UNIVERSITÀ DEGLI STUDI DI TRIESTE

UNIVERSITÀ DEGLI STUDI DI UDINE

Dottorato di Ricerca Interateneo in
Ingegneria Civile–Ambientale e Architettura

Curriculum: Ingegneria Civile

Settore Scientifico Disciplinare: ICAR/09 Tecnica delle costruzioni

XXXVIII Ciclo

SEISMIC STRENGTHENING OF EXISTING MASONRY BUILDINGS WITH LOW-INVASIVE TECHNIQUES

Dottorando
Emanuele Rizzi

Coordinatore
Prof. Alberto Sdegno

Supervisore di Tesi
Prof. Ing. Natalino Gattesco

Co-Supervisore di Tesi
Dr. Ing. Ingrid Boem

Anno Accademico 2024/2025



UNIVERSITÀ DEGLI STUDI DI TRIESTE



UNIVERSITÀ DEGLI STUDI DI UDINE

hic sunt futura

XXXVIII INTER-UNIVERSITY RESEARCH DOCTORATE PROGRAMME IN CIVIL-ENVIRONMENTAL ENGINEERING AND ARCHITECTURE

SEISMIC STRENGTHENING OF EXISTING MASONRY BUILDINGS WITH LOW-INVASIVE TECHNIQUES

Scientific-disciplinary sector: ICAR/09 CONSTRUCTION ENGINEERING

CANDIDATE **Emanuele Rizzi**

COORDINATOR **Prof. Arch. Alberto Sdegno**

SUPERVISOR **Prof. Ing. Natalino Gattesco**

CO-SUPERVISOR **Dr. Ing. Ingrid Boem**

ACADEMIC YEAR 2024/2025

Abstract

This PhD thesis investigates the seismic performance of historic masonry structures strengthened with Composite Reinforced Mortar (CRM) systems. Despite their growing use in heritage rehabilitation, CRM systems still lack dedicated design provisions, and only limited experimental data are available, particularly for single-sided applications. This research addresses these gaps by combining experimental testing, analytical modelling, and numerical simulations to evaluate the effectiveness, durability, and predictive modelling of CRM-strengthened masonry.

An extensive experimental campaign was carried out on material samples, masonry elements (piers, spandrels, and ring beams), and a two-story pilot building, under both in-plane (IP) and out-of-plane (OOP) loading. Tests were performed on unreinforced (URM), single-sided (R1), and double-sided (R2) strengthened specimens. The results confirmed that CRM systems substantially enhance strength, ductility, and energy dissipation capacity, while promoting more distributed cracking and stable post-peak behavior. Two-sided applications provided further improvements in both strength and deformation capacity. The use of transversal connectors effectively prevented wythe separation in two-leaf walls, ensuring composite action between the coating and the substrate.

Durability tests on glass-fibre meshes and textile-reinforced mortars highlighted a significant degradation of tensile properties under alkaline exposure and elevated temperature, confirming the importance of environmental effects on long-term performance. However, accelerated ageing protocols still require correlation with real-time exposure to reliably estimate service life.

Analytical correlations were developed and calibrated to predict the strength and deformation capacity of CRM-reinforced elements, showing good agreement with the experimental data for both in-plane and out-of-plane behavior. At the structural scale, detailed nonlinear numerical models in Abaqus captured the observed damage mechanisms with high accuracy. Simplified equivalent frame models implemented in Midas Gen provided a computationally efficient tool for evaluating the global seismic performance of CRM-strengthened buildings. The application of this method to benchmark configurations and to the pilot building demonstrated its reliability for practical design purposes.

Overall, this research contributes to the understanding and design of CRM interventions for the seismic strengthening of historic masonry. It provides validated experimental evidence, practical analytical correlations, and calibrated numerical approaches that together form a robust basis for future code development and engineering practice. The outcomes also highlight the need for further long-term durability studies and large-scale experimental validation to fully establish CRM systems as a reliable, low-invasive strengthening solution for heritage preservation.

Keywords: Masonry structures – Seismic engineering – Experimental testing - Composite Reinforced Mortar - Composites

Acknowledgements

I would like to express my sincere gratitude to the Interreg Italy-Slovenia Cooperation Program 2014–2020, which primarily funded the CONSTRAIN project. I also gratefully acknowledge the financial support of the Department of Civil Protection (ReLUIS 2019–2021 and 2022–2024).

The Abaqus software license was kindly granted by Prof. Chiara Bedon, and the software Midas GEN was provided by CSP Fea s.c.

I am deeply grateful to my supervisor, Prof. Eng. Natalino Gattesco, for his guidance, demanding standards, and for teaching me the importance of curiosity in research.

My sincere thanks go to Eng. Franco Trevisan, technician of the Laboratory for Testing Materials at the University of Trieste, for his valuable assistance during the execution of the experimental tests.

I also wish to thank Andrea and Cecilia Zampa, and the staff of Fibre Net S.r.l. (Pavia di Udine, Italy). I am particularly grateful to Allen Dudine, Carlos Passerino, and Salvatore Grassia for their time, help, and trust during my activities in the company's laboratories. The financial contribution of Fibre Net S.r.l. to the development and execution of the tests is gratefully acknowledged.

I am thankful to the staff of the Laboratory of Civil Engineering at the University of Brescia, in particular Prof. Fausto Minelli, Dr. Luca Facconi, and Dr. Sara Lucchini, for their support in organizing and conducting the pilot building tests and for drafting the article on the results.

My gratitude extends to my colleagues at the Department of Engineering and Architecture of the University of Trieste: Eng. Sara Verza, Dr. Matteo Barnaba, and Eng. Alessia Bez, for their help during the experimental and numerical activities of the CONSTRAIN project. I am especially thankful to Dr. Eng. Ingrid Boem, whose suggestions, data analyses, and analytical correlations greatly contributed to this research.

I am also grateful to Prof. Matija Gams and Eng. Veronika Pučnik from the Faculty of Civil Engineering and Geodesy for their collaboration on the experimental tests on spandrels, and in particular to Prof. Gams for his assistance in drafting the first articles derived from these results.

Finally, my heartfelt thanks go to Monika, for her patience and love during the final stages of this research; to my parents, relatives, and all my friends, for their constant encouragement and support.

Emanuele

Trieste, December 16, 2025

Table of contents

Abstract i

Acknowledgements iii

1 Introduction 1

1.1 Aims and scope 2

1.2 Seismic performances of unreinforced masonry 4

1.2.1 Inadequate structural integrity 4

1.2.2 Inadequate structural layout 6

1.2.3 Inadequate integrity and strength of masonry 6

1.3 Experimental testing of unreinforced masonry 10

1.3.1 Material tests 10

1.3.2 Laboratory tests on structural elements and buildings 11

1.3.3 In-situ tests 16

1.4 Modelling of unreinforced masonry 18

1.4.1 Overview of numerical modelling strategies 20

1.5 Strengthening techniques for masonry buildings 24

1.6 TRM technique and characterisation 29

1.6.1 Testing TRM 32

1.6.2 Durability of FRP materials 34

2 Experimental testing for durability 37

2.1 Project coordination and communication structure 38

2.2 Testing methodologies and groups 40

2.2.1 Materials 42

2.3 Conditioning of yarn and GFRP grid specimens 49

2.4 Conditioning of FRCM coupons 51

2.5 Tests on yarns 53

2.5.1 Labelling 53

2.5.2 Tensile testing 53

2.5.3 Results 57
2.6 Tests on GFRP grids 59
2.6.1 Labelling 59
2.6.2 Cross section determination on FRP bars 59
2.6.3 Tensile testing 60
2.6.4 Results 62
2.7 Tests on mortar prisms 67
2.7.1 Labelling 67
2.7.2 Preparation and curing 67
2.7.3 Bending and compression tests 67
2.7.4 Results 68
2.8 Tests on FRCM coupons 69
2.8.1 Labelling 69
2.8.2 Tensile testing 69
2.8.3 Results 70
2.9 Conclusions 73
3 Experimental campaign on CRM strengthened masonry structural elements 75
3.1 Masonry characteristics 77
3.2 Strengthening techniques characteristics 81
3.2.1 Description of the CRM strengthening intervention 81
3.2.2 Description of the strengthening intervention of masonry ring beams with FRP meshes embedded in bed joints 84
3.2.3 Description of the strengthening intervention of masonry ring beams with externally bonded FRP strips 85
3.3 Strengthening materials characterization 86
3.4 In-plane behaviour of piers 90
3.4.1 Literature review 90
3.4.2 Description of the samples 92

3.4.3 Test setup 95
3.4.4 Results 100
3.4.5 Analysis of results and comparison 126
3.5 In-plane behaviour of spandrels 135
3.5.1 Literature review 135
3.5.2 Description of the samples 136
3.5.3 Test setup 138
3.5.4 Results 143
3.5.5 Analysis of results and comparison 162
3.6 Out-of-plane behaviour of masonry piers 169
3.6.1 Literature review 169
3.6.2 Description of the samples 171
3.6.3 Test setup 173
3.6.4 Results 176
3.6.5 Analysis of results and comparison 182
3.7 Roof ring beams with FRP meshes embedded in bed joints 184
3.7.1 Literature review 184
3.7.2 Scope and methods 185
3.7.3 Results 190
3.7.4 Analysis of results and comparison 191
3.8 Ring beams with externally-bonded FRP strips 195
3.8.1 Description of the samples 195
3.8.2 Test setup 196
3.8.3 Results 200
3.8.4 Analysis of results and comparison 205
3.9 Pushover test on a full-scale masonry building 207
3.9.1 Literature review 207

3.9.2 Scope and methods 210
3.9.3 Retrofitting technique 214
3.9.4 Test setup 217
3.9.5 Results of the pushover tests 221
3.9.6 Analysis of results and comparison 229
3.9.7 Vibration analysis 233
4 Analytical estimation of the seismic behaviour of CRM strengthened structural elements 237
4.1 Analytic estimation of the in-plane resistance of piers 240
4.1.1 Application and validation 245
4.2 Analytic estimation of the in-plane resistance of spandrels 250
4.2.1 Application and validation 256
4.3 Analytic estimation of the out-of-plane resistance of piers 260
4.3.1 Application and validation 263
4.4 Analytic estimation of resistance of roof ring beams with FRP meshes embedded in mortar joints 266
4.4.1 Application and validation 269
4.5 Analytic estimation of resistance of ring beams with externally-bonded FRP strips 272
4.5.1 Application and validation 273
5 Numerical modelling 275
5.1 Detail finite element analysis modelling 277
5.1.1 Material properties 277
5.1.2 Post-failure behaviour 277
5.1.3 Modelling of the reinforcement coating 279
5.2 Shear-compression numerical models 282
5.2.1 Stone masonry piers 283
5.2.2 Single leaf brick masonry specimens 288

5.2.3 Two leaf brick masonry specimens 292
5.3 Shear-bending numerical models 297
5.3.1 Stone masonry specimens 298
5.3.2 Single leaf brick masonry specimens 303
5.3.3 Two leaf brick masonry specimens 306
5.4 Equivalent frame modelling 311
5.4.1 Equivalent frame method 311
5.4.2 The software Midas Gen 312
5.4.3 Benchmark examples 322
5.5 Pilot building simulation using the Equivalent frame model 341
5.5.1 Material properties 341
5.5.2 Plastic hinges properties 343
5.5.3 Numerical analysis of the unreinforced pilot building 344
5.5.4 Numerical analysis of the strengthened pilot building 348
6 Conclusions and future work 353
6.1 Summary 353
6.2 Conclusions 354
6.2.1 Effectiveness of CRM reinforcement 354
6.2.2 Durability of CRM composites 357
6.2.3 Analytical estimation of the seismic behaviour of CRM-strengthened masonry 358
6.2.4 Numerical modelling insights 359
6.3 Future Work 360
References 361
Appendix A 381
Appendix B 391
Simplified numerical analyses on pier elements 392

Simplified numerical analyses on spandrel elements.....416
Simplified numerical analyses on portal frames 425
Simplified numerical analyses on single story walls 452
Simplified numerical analyses on two-story walls.....476

1 Introduction

Nowadays, most of the Italian and European building heritage in historic centres is made of unreinforced masonry. Many of these buildings were constructed before seismic actions were fully understood by builders and engineers, and before modern seismic regulations were applied. As a result, existing masonry buildings are frequently susceptible to severe damage or even total collapse when subjected to strong earthquakes. This susceptibility has been documented in several recent seismic events, including the 2009 L'Aquila earthquake in Central Italy, the 2012 Emilia earthquakes in Northern Italy, the 2016–2017 Central Italy seismic sequence, as well as European events such as the 2019 North-West Albania earthquake and the 2020 Zagreb earthquake in Croatia [1–6,6,7]. These events have evidenced the importance of studying and preserving these structures, to prevent loss of human life, reduce economic damage, and preserve social, cultural, and architectural heritage.

From a sustainability perspective, conserving existing masonry structures reduces the demand for new construction materials and minimizes construction waste, but their conservations present unique challenges. Over time, materials can degrade due to environmental factors, such as urban pollution, moisture (rising damp, water infiltration, condensation), freeze-thaw cycles, and biological growth [8]. Additionally, previous restoration efforts may have employed incompatible materials, worsening deterioration [9]. Planning conservation strategies requires a thorough understanding of the materials and construction techniques used in the original masonry. This includes detailed analysis of mortar composition, stone or brick types, and construction methods. Modern conservation practices emphasize the use of compatible materials and reversible techniques to ensure that interventions do not alter the original fabric of the structure.

In the Italian context, the costs of strengthening interventions complicate preservation efforts. Limited public and private funding mean that costly interventions must be carefully planned to maximize their impact. To this end, the development of cost-effective and technically efficient structural reinforcement strategies is a major concern for both practitioners and researchers, to ensure structural safety and preserve existing masonry buildings.

1.1 Aims and scope

This PhD thesis addresses the challenging topic of assessing the seismic performance of historic masonry structures strengthened with Composite Reinforced Mortar (CRM) systems. The study is motivated by the limited experimental data currently available for masonry walls strengthened on one side and the lack of systematic comparisons with two-sided reinforcement. The dual aim of this research is, first, to investigate the mechanical behavior and durability of CRM-strengthened masonry, focusing on both single-sided and double-sided applications, and second, to evaluate numerical modelling strategies capable of predicting the structural response of such interventions, from detailed element-level simulations to simplified approaches suitable for the analysis of real-scale structures.

The initial phase of the research focuses on experimental investigations, which are crucial due to the lack of available data on single-sided CRM applications. Laboratory tests were conducted on materials, masonry piers, spandrels, roof ring beams and a two-story pilot building under in-plane and out-of-plane loading, both unstrengthened (URM) and strengthened on one or both sides (R1 and R2 configurations). Particular attention was given to two-leaf walls, which are prone to separation of the wythes; this issue was addressed experimentally using transversal connectors. In addition, accelerated ageing tests were also performed to evaluate the durability of the composite materials, a topic that remains an open research topic. The experimental campaign enabled a detailed characterization of the stiffness evolution, failure mechanisms, and energy dissipation of CRM-reinforced masonry, providing the basis for defining reliable analytical correlations for estimating strength and deformation capacities of reinforced elements.

Complementary to the experimental program, detailed numerical models were developed and validated in the Abaqus software to account for nonlinearities at the material level (masonry and strengthened mortar matrix) using a continuum finite element modelling approach. This allows to investigate on the complex failure mechanisms, providing an objective basis for validating analytical correlations. To extend the investigation to the building scale, simplified models based on the equivalent frame method were employed in the Midas Gen software. The application of this method was used for simulating benchmark examples of wall configurations of increasing complexity, and the pilot building tests, and it allowed for a preliminary assessment of CRM behavior in entire structures, demonstrating the potential of efficient, yet reliable, modelling strategies for

practical engineering applications. The developed method was applied to benchmark examples of wall configurations of increasing complexity.

The main contribution of this work lies in improving the understanding and guidance for CRM interventions, since, to date, there are no specific design provisions for CRM systems, despite their widespread use. In professional practice, engineers often rely on the correlations and design approaches originally developed for FRCM systems (ACI 549.6R-20 [10], CNR DT 215/2018 [11]),adapting them to CRM applications. In this study, analytical correlations are proposed for estimating the strength of CRM-reinforced elements, and a common deformation capacity is evaluated for elements strengthened on either one or both sides. Practical recommendations are provided for addressing construction issues, such as leaf separation and material interface behavior. The results serve as a solid basis for future research and practical applications, including durability considerations.

This thesis combines laboratory testing, analytical correlations and numerical simulations, to better understand how CRM strengthening works in historic masonry. The goal is to provide practical guidance for designing effective interventions, improving both the performance and durability of these structures under seismic loads.

1.2 Seismic performances of unreinforced masonry

For any structure, seismic acceleration generates forces whose amplitude depends on the building's natural periods of vibration. These periods are influenced by the structural configuration and geometry, mass distribution, stiffness of elements, continuity and connection between structural components, boundary conditions, and soil-structure interaction [12,13]. Irregular layouts, openings, or discontinuities can introduce local modes and torsional effects, affecting how seismic forces are distributed and resisted [14].

The seismic performance of unreinforced masonry (URM) structures has been extensively studied over the past century. While the primary failure mechanisms are well-documented, accurately assessing the behavior of masonry remains challenging due to inherent uncertainties in material properties and the complex, anisotropic nature of the material. Ensuring the seismic safety of existing masonry buildings requires a thorough assessment of their structural performance [15]. When such assessments indicate insufficient capacity, it becomes essential to define and implement appropriate strengthening strategies aimed at improving their overall seismic behavior. Post-earthquake surveys have identified several recurring weaknesses that typically lead to structural failure, including:

- Inadequate connection between structural elements and lack of box-like structural behaviour,
- Inadequate structural layout of walls (in floor plan and in elevation),
- Inadequate integrity and strength of masonry.

1.2.1 Inadequate structural integrity

A recurrent structural vulnerability in existing masonry constructions is the insufficient connection between orthogonal walls, between walls and floors and a lack of stiffness of the latter. As extensively documented in the literature [16–18], inadequate connections hinder the capacity of the building to behave as an integrated structural system. Under seismic excitation, this vulnerability promotes the development of cracks at wall intersections, causing the structure to separate into independent macroelements, each resisting seismic loads autonomously. In such cases, the global seismic capacity is governed by the weakest element, which can fail at relatively low earthquake intensities. By contrast, when wall-to-wall and wall-to-floor connections are efficient and the floors are stiff enough in their plane, all elements work together in resisting earthquake loads,

enhancing resistance and ductility to earthquake induced forces. The behaviour of the structure in the latter case is sometimes called box-like behaviour [19]. Figure 1.1 illustrates this concept.

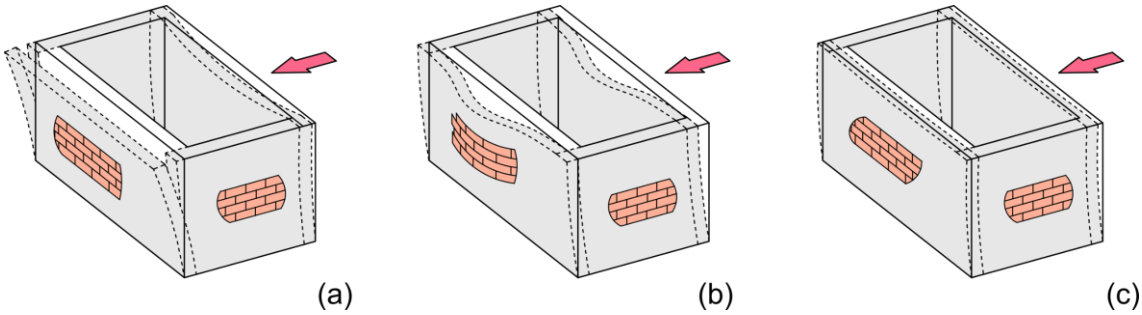


Figure 1.1. Response of structures with different strength of connections: a) poor connection between walls and weak floor structure; b) proper connection between walls but weak in-plane floor structure and c) proper connection between walls and strong in-plane floor structure

Further potential threats may also be related to the building configuration, like the presence of extended gable walls, arches, vaults, and untied inclined roofs, which increase the horizontal loads supported by the bearing walls. Strengthening interventions for existing masonry should therefore prioritize the improvement of wall-to-wall and wall-to-floor connections, through the installation or reinforcements like ties and chains, in order to prevent loss of structural integrity. Failures due to loss of box action are often catastrophic, as shown in Figure 1.2, where perimeter walls and floor connections failed, leading to collapse.

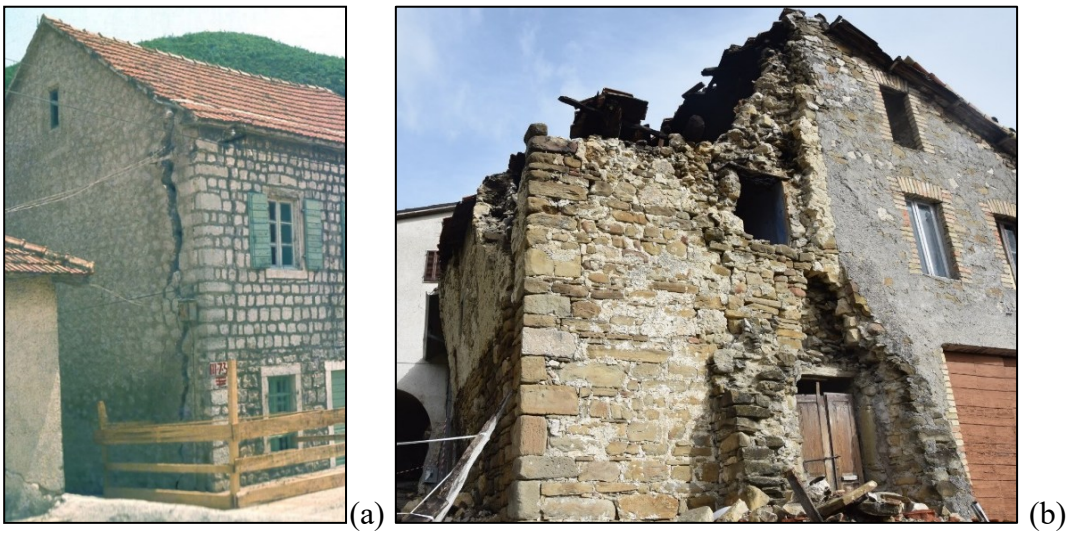


Figure 1.2. Loss of structural integrity: a) separation of perimeter walls (Montenegro, 1979), b) insufficient connection to floor structures (Borgo, 2016)

1.2.2 Inadequate structural layout

Buildings with irregular wall distribution in plan or elevation are also prone to earthquake damage. Uneven arrangements of load-bearing walls often produce a structure that is strong in one direction but weak in another (Figure 1.3). Similarly, irregularities in elevation, such as large openings at the ground floor, often create soft storeys, which are highly vulnerable during seismic events (Figure 1.4). Torsional effects can also become critical when the distribution of masonry load-resisting elements is irregular, either in plan or along the height of the structure. Such deficiencies severely reduce the building's ability to dissipate seismic energy, frequently resulting in collapse.

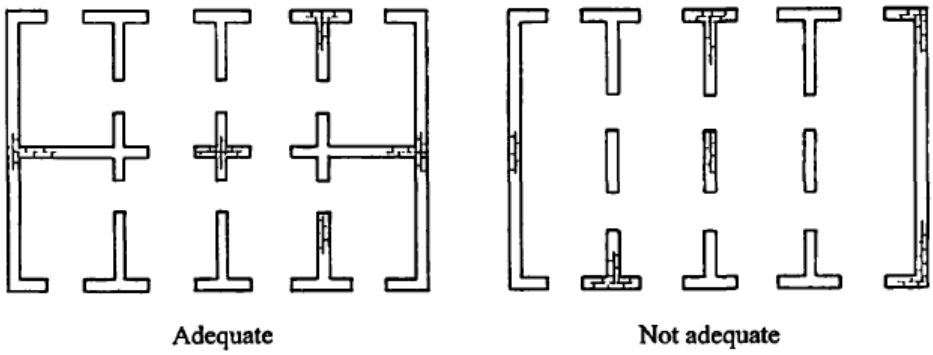


Figure 1.3. Distribution of structural walls in plan [18]



(a) (b)

Figure 1.4. Failure of soft storey: a) (Skopje,1963), b) (Neftgork, 1995)

1.2.3 Inadequate integrity and strength of masonry

Even when masonry structures present proper layout and effective connections, their seismic performance is highly dependent on the masonry mechanical properties. Unreinforced stone or brick masonry is generally characterized by high compressive strength but very limited shear resistance and negligible tensile capacity [20,21]. While

these properties render masonry suitable for supporting vertical loads, they also make it particularly vulnerable to horizontal seismic actions, both in-plane and out-of-plane.

In existing masonry buildings, both local and global failure mechanisms may occur under horizontal loads. Local mechanisms typically involve individual wall panels or larger portions of the structure and often result from out-of-plane actions. Their development is generally favoured by inadequate connections, either between walls and floors or at wall-to-wall intersections. Global mechanisms, conversely, affect the structure as a whole, mainly mobilizing the masonry walls in their own plane. Structural safety must be evaluated with respect to both types of mechanisms.

In masonry structures, perforated walls consist of two primary macro-elements: piers and spandrels. Piers are the vertical wall segments located between openings (such as windows and doors), while spandrels are the horizontal wall strips situated above or below adjacent openings or between an opening and the roof. Piers primarily resist vertical loads and in-plane shear, while spandrels provide horizontal connectivity, redistributing forces between adjacent piers [18].

The study of post-earthquake damage evidenced that pier elements can undergo different failure mechanisms under the combined action of vertical and horizontal loads. The principal in-plane failure mechanisms (Figure 1.5) observed include:

- **Diagonal shear cracking**
  linear or stair-step cracks developing along the compressed diagonal.
- **Sliding shear failure**
  horizontal cracks along mortar bed joints, driven by interface friction, typically occurring under low vertical stress levels.
- **Compression-bending failure or rocking**
  localized damage at the base and top cross-sections, characterized by horizontal cracks in tension zones and possible crushing of masonry at the compressed toe regions.

The failure mechanisms depend on geometry, boundary conditions, vertical stress, type of masonry, bonding and coursing of units and quality of the materials. However, diagonal shear cracking is the most commonly encountered failure mode in piers of traditional masonry [17], which is characterized by X shaped cracks due to cyclic actions (Figure 1.6). To address these vulnerabilities, various reinforcement strategies are employed,

including the application of strengthening coatings that provide higher tensile resistance to the masonry elements, grout injections, and the installation of connecting ties to improve structural integrity.

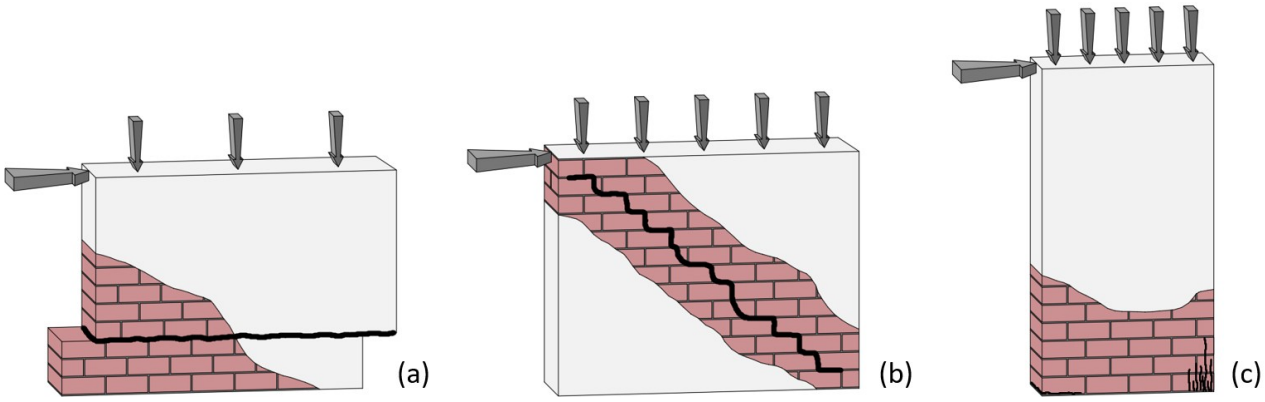


Figure 1.5. Failure mechanism of masonry: a) sliding shear failure; b) diagonal shear cracking; c) compression-bending failure

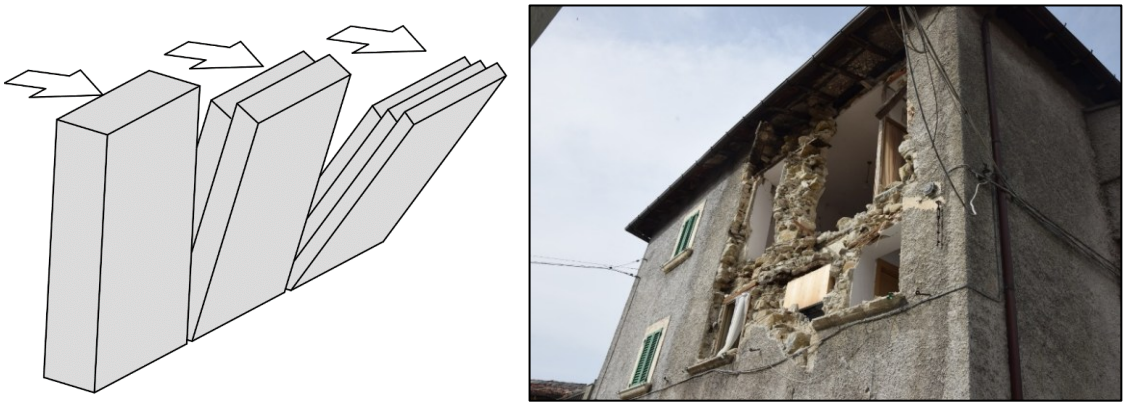
Masonry spandrels, on the other hand, are subject only to shear forces and bending moments and very low compressive stresses. For this reason, in absence of a horizontal element capable of resisting tensile forces (e.g. steel ties or floor curbs) their resistance against the rocking mechanism is very limited. The presence of effectively connected tie rods at floor level capable of resisting tensile forces counteract the rocking of piers. By restraining this separation, tie rods increase the compression within the spandrel elements, which in turn enhances their shear-flexural resistance. As a result, an inclined strut mechanism is activated, similar to that observed in vertical piers subjected to combined axial load and bending, causing typically diagonal cracks (Figure 1.6).



(a) (b)

Figure 1.6. Typical diagonal shear damage in piers of ground storey: a) Budva, 1997 and b) Umbria, 1997

A further weakness in existing construction is the presence of multi-wythe load-bearing walls, with an inner cavity filled with scrap material and low-strength mortar. These walls do not present adequate transverse connections and are prone to delamination or wythe separation under both in-plane and out-of-plane loads (Figure 1.7). To achieve monolithic behavior, interventions such as elements connecting wythes through the thickness or grout injection into cavities are required.



(a) (b)

Figure 1.7. a) out-of-plane behaviour of a single-leaf wall and a multi-wythe wall: b) out-of-plane failure of a two-wythe wall (Borgo, 2016)

Due to the inherent uncertainty in the mechanical properties of existing masonry structures, a large number of in-situ and laboratory experimental tests have been developed to assess their behaviour when subjected to seismic loads.

1.3 Experimental testing of unreinforced masonry

The experimental characterization of unreinforced masonry is fundamental for understanding its mechanical behavior and for calibrating both analytical and numerical models. Unlike homogeneous materials such as steel or concrete, masonry is a composite and anisotropic material, composed of units (bricks, stones, or blocks) and mortar joints. The mechanical properties of the masonry strongly depend on the geometry, texture, quality of workmanship and materials, and the unit-mortar interaction.

Since the 1970s, a wide range of experimental campaigns have been carried out, both in laboratories and directly on site, with the aim of investigating the seismic response of unreinforced masonry structures. Since then, the testing approaches have been refined to better reproduce the actual conditions experienced by masonry under earthquake loading. Different experimental strategies have been adopted, varying from small-scale models to full-scale specimens to fulfil structural representativeness requirements. The loading conditions have also been explored through different protocols, including static and dynamic tests, monotonic and cyclic loading, as well as in-plane and out-of-plane actions [18,22–32].

Experimental tests on masonry can be divided into:

- Material tests, performed on masonry components (units and mortar) or small assemblies;
- Structural element tests, performed on walls, panels, or large-scale specimens;
- In-situ tests, applied directly on existing structures for mechanical characterization, which can generally be classified into destructive and non- or semi-destructive.

1.3.1 Material tests

The mechanical characterization of masonry materials represents the initial step in defining the mechanical behavior of masonry assemblages. Masonry units (bricks, stones and blocks) are tested according to European harmonized standard procedures EN 772. This series of standards defines the procedures for determining the physical and mechanical properties of individual units. The most relevant test concerns the determination of the compressive strength (EN 772-1 [33]), obtained by loading individual units between two steel plates at a constant rate until failure. The compressive strength is the basis for the classification of the units and for the estimation of the masonry

compressive strength according to design standards, such as EN 1996-1-1 [34]. Additionally, the EN 772 includes procedures for determining bulk density, water absorption, initial rate of suction, and dimensional tolerances.

Mortar specimens are tested according to EN 1015-11 [35]. This standard specifies the determination of compressive and flexural strength on prismatic samples, typically of dimensions 40×40×160 mm (Figure 1.8a). The specimens are cured under controlled temperature and humidity conditions before testing. The flexural test is carried out first using a three-point bending setup, after which the two resulting halves are used to determine the compressive strength.

The shear behavior of mortar joints is characterized by testing small masonry assemblages composed of two or three units bonded with mortar (Figure 1.8b,c), to determine the initial shear strength and friction coefficient of mortar joints, according to EN 1052-3 [36].

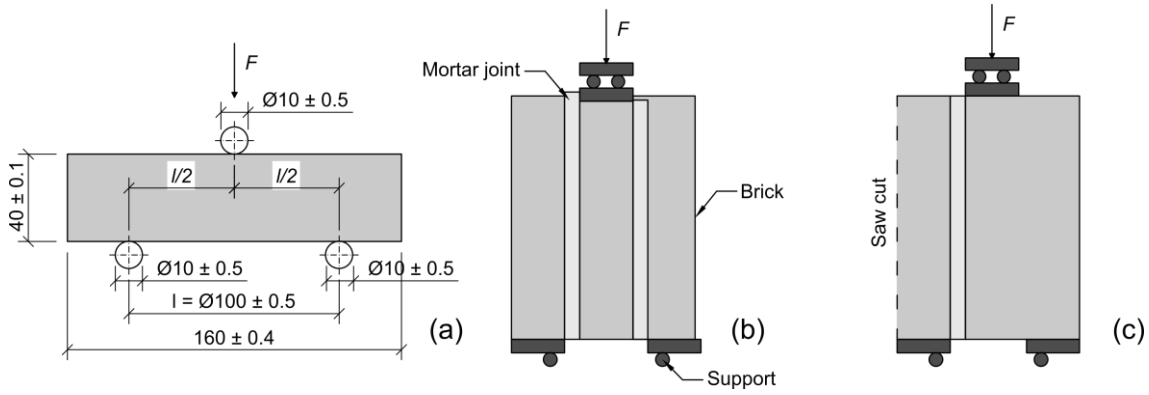
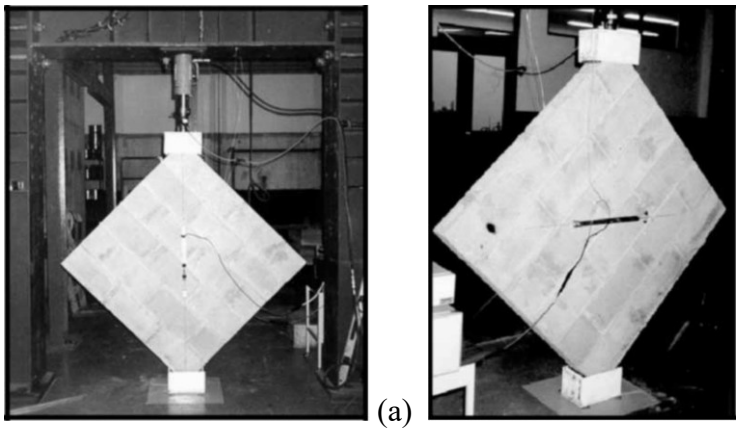


Figure 1.8. a) flexural test on masonry samples; b) and c) shear tests on masonry assemblages

1.3.2 Laboratory tests on structural elements and buildings

Tests on small-scale wallettes are commonly used to capture the combined effect of units and mortar. Wallets can be tested in uniaxial compression, to derive vertical compressive strength and elastic modulus of masonry, according to EN 1052-1 [37] or ASTM C1314 [38] and in diagonal compression to estimate shear strength and shear modulus, according to ASTM E519 [39] (Figure 1.9).



(a) (b)

Figure 1.9. ASTM E 519 test setup (a) with reaction frame (b) with instrumentation and loading shoes [29]

The diagonal compression test, although still widely used and referenced in design codes, is gradually being replaced by combined compression-bending and shear tests on piers, commonly referred to as shear-compression tests, which are considered more representative of the actual boundary conditions experienced by walls in real structures. Several authors have carried out experimental compression-bending and shear tests to investigate the structural response of historical masonry under combined vertical and lateral loading [23,27,30,32]. These tests provide direct information on the shear response of the material under conditions that resemble in-plane seismic actions. In these tests, wall specimens are subjected to a combination of constant vertical precompression and increasing or cyclic horizontal loads imposed at the top of the wall. The vertical load simulates the effect of gravity loads acting on the wall in its actual configuration, while the horizontal load reproduces the in-plane seismic action. The interaction between vertical stress and shear strength is one of the key aspects of masonry behavior. Under service conditions, increasing levels of compression generally enhance the shear resistance of the wall by increasing the friction between the masonry and the mortar.

The outcome of shear-compression tests provides a load-displacement curve (Figure 1.10) from which the following parameters for seismic assessment are derived:

- Shear strength and drift capacity;
- Failure mechanisms (sliding shear, diagonal shear cracking or compression-bending failure);
- Hysteretic behavior and energy dissipation.

These parameters are widely adopted in analytical and numerical models for the seismic analysis of masonry buildings. The crack patterns observed during the tests also offer valuable insight into the governing failure mechanisms.

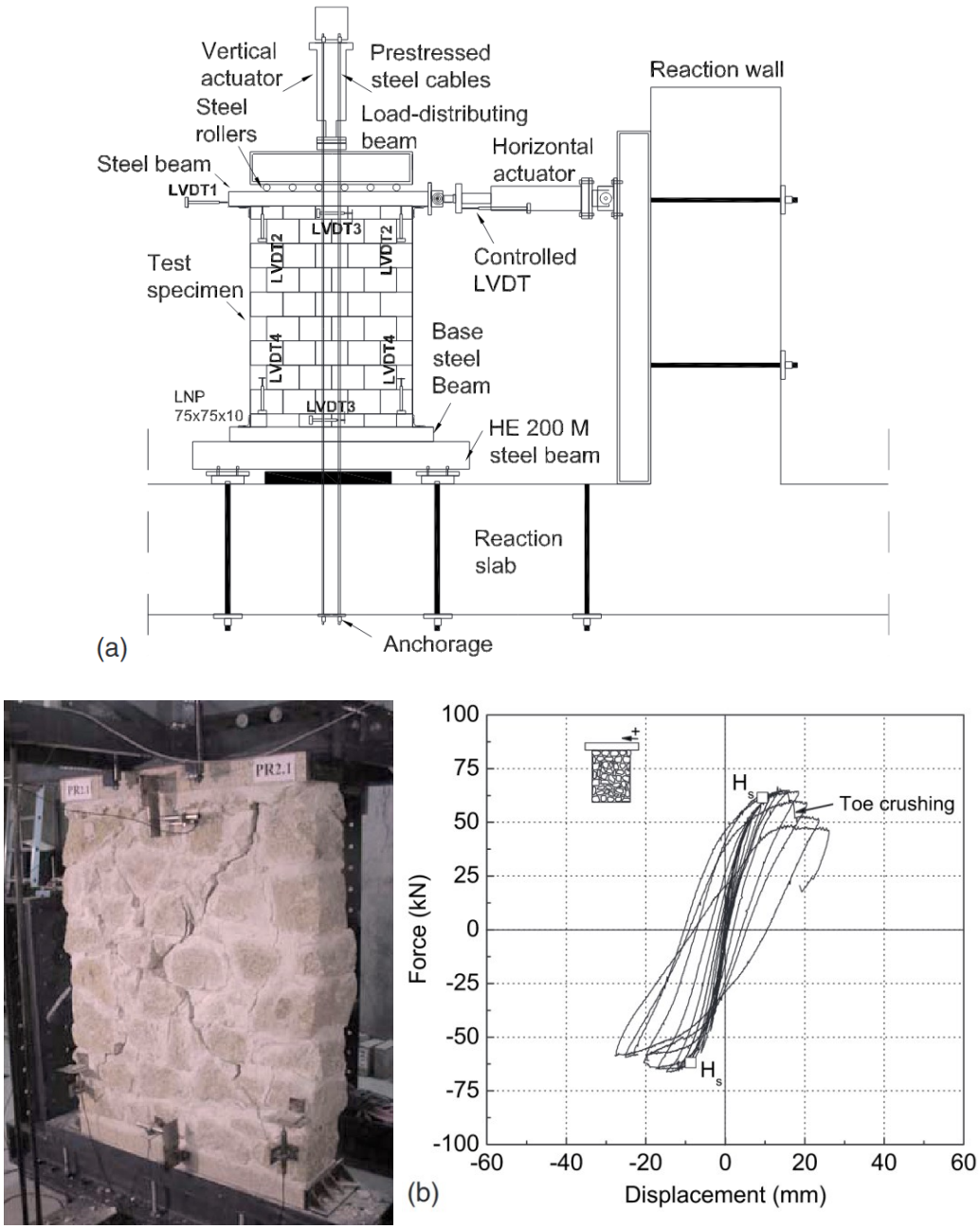


Figure 1.10. a) typical compression-bending and shear test setup and b) lateral displacements-lateral resistance hysteresis loops, obtained during seismic resistance test of a masonry wall (H_S is the cracking load) [32]

Compared to piers, spandrels have historically received less attention in experimental research mainly due to the complexity of their behavior under combined loading conditions. In recent decades, however, several experimental studies have been conducted

to better understand their structural role and failure modes [22,24,25,40]. These tests are typically performed on full-scale H shaped specimens representing a spandrel and two adjacent piers subjected to compressive stresses. Experimental campaigns have considered both configurations with steel/composite ties at the floor level, which counteract the rocking of piers, and configurations without ties, to reproduce more vulnerable historical conditions.

Three main testing setups were designed in the literature for testing masonry spandrels. The first setup (Figure 1.11a) was adopted by both Augenti et al. [41] and Ismail and Ingham [42] and consisted of "TT-shaped" sample panels composed of two piers fixed at the base and loaded with a constant vertical load at the top, coupled with a spandrel. Additionally, a reversed cyclic loading was applied at the top of the samples. The second setup (Figure 1.11b), adopted by Gattesco et al. [24], consisted of an "H-shaped" masonry panel (two lateral pier portions joined by a central spandrel), with piers clamped under a constant axial stress; one pier was fixed at the base while the other was subjected to cyclic up–down lifts. While these boundary conditions do not enable an accurate representation of the pier response, since in realistic perforated walls the pier cross sections at midstory height generally rotate, they do not significantly affect the spandrel behavior and allowing to measure the forces generated in the spandrel. The third setup (Figure 1.11c), proposed by Beyer et al. [22], also concerned "H-shaped" masonry panels with pre-compressed piers. The sample stands on two stiff steel beams that are supported on hinges at the centre line of the piers and connected to actuators at their ends that were moved with the same velocity in opposite directions. Additionally, one of the two supports of the beams allow also a sliding movement along the longitudinal axis of the beam. As a result, the two horizontal lever beams rotate the two piers with the same drifts, causing the shear and bending to the spandrel and the horizontal sliding does not restrain the axial elongation of the spandrel.

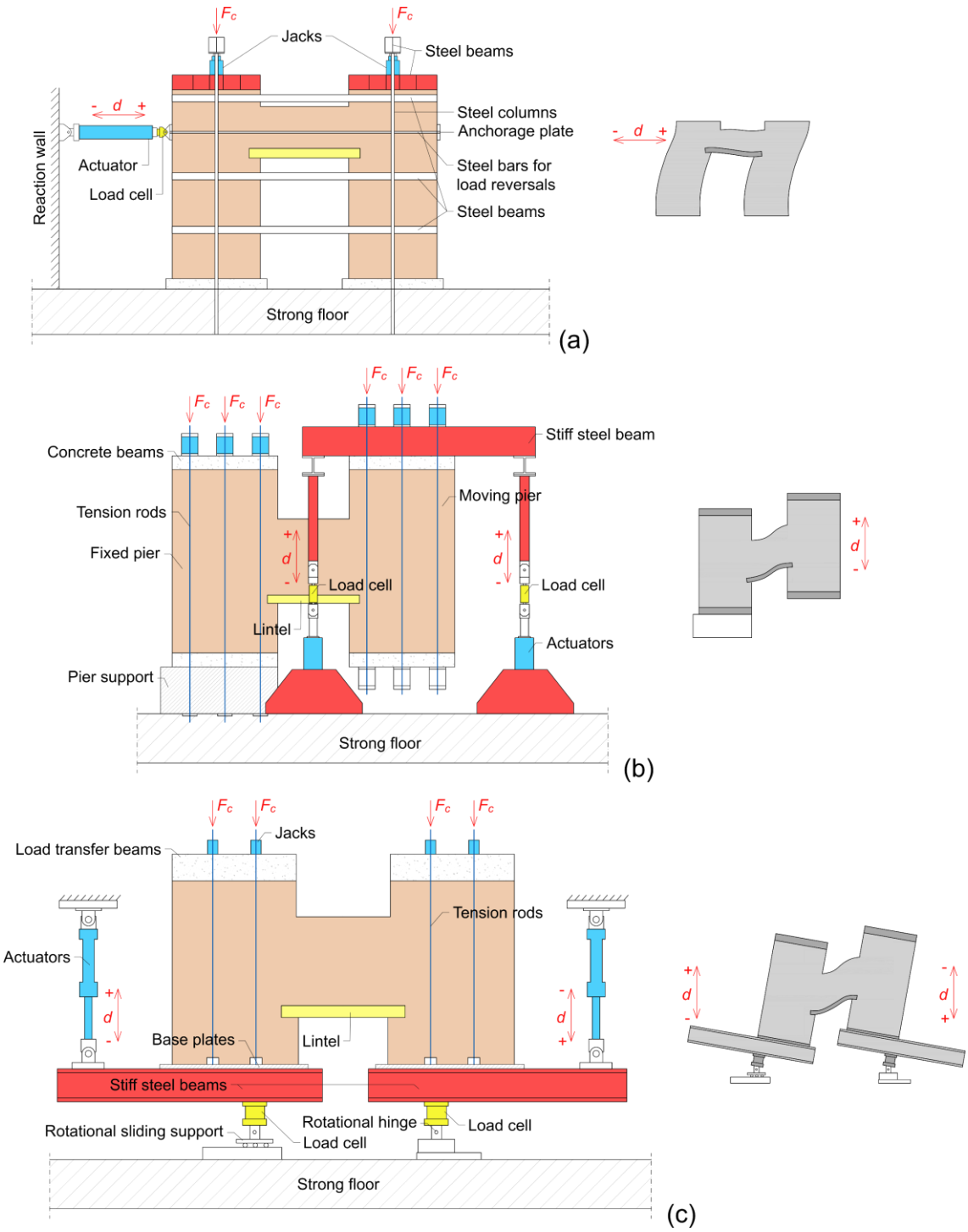


Figure 1.11. Drawings of the test setups adopted in the literature for masonry spandrel testing: a) Augenti et al. [41] and Ismail and Ingham [42]; b) Gattesco et al. [24]; c) Beyer et al. [22]

Static and dynamic laboratory tests on full-scale or scaled masonry buildings were also performed in the literature [28,31]. Dynamic testing, in particular, offers valuable insights into the seismic performance of masonry structures. These tests are conducted using large-scale shaking tables, which simulate earthquake ground motions. Many of these experimental campaigns have focused on assessing the effectiveness of traditional

seismic retrofitting techniques designed to promote a “box-type” global structural behavior [28,43–45]. Although large-scale tests are limited in number due to the complexity of experimental setups and the high costs involved, these investigations provide critical data for validating simplified predictive models from testing single masonry panels [46,47].

1.3.3 In-situ tests

For existing masonry, in-situ tests are fundamental for assessing the mechanical properties of materials and structural elements. Unlike laboratory tests, which are typically conducted on newly built specimens under controlled conditions, in-situ investigations capture the variability, heterogeneity, and degradation phenomena that characterize historical masonry. Over the past decades, several testing procedures have been developed and standardized, which can generally be classified into destructive and non- or semi-destructive. These approaches provide complementary information and, when combined, allow for a more reliable mechanical characterization of existing masonry. At present, most of the non-destructive procedures can give only qualitative results

Among the most common semi-destructive techniques used are flat-jack tests [48–51]. The single flat-jack test measures the state of stress in the wall, while the double flat-jack test provides estimates of the elastic modulus and the strength.

Another semi-destructive in-situ technique is the shove test [52,53]. This test provides an estimation of the shear strength and friction coefficient of the mortar joints under the existing vertical stress state in periodic masonry. Although the results are affected by the local conditions of the tested area, it is recommended to perform a significant number of repetitions to obtain statistically reliable values.

Non-destructive in-situ techniques frequently discussed in the literature include infrared thermography, sonic tests, ground-penetrating radar (GPR), and vibration-based monitoring [48]. The accelerometers are also used to identify the global dynamic properties of a building, such as natural frequencies and mode shapes, which are fundamental for seismic vulnerability assessment. Each of these methods can provide complementary insights into the structural consistency of masonry:

- thermography can highlight discontinuities (inclusions of different materials, water and heating systems), hidden voids and moisture;

- sonic and ultrasonic tests can detect voids, flaws and crack or damage patterns,
- ground-penetrating radar (GPR) allows for the detection of possible damage within the walls, to detect and quantify the presence of moisture, to reconstruct the morphology of wall sections, particularly in multi-leaf stone and brick masonry and to locate inclusions of different materials, such as steel or wood, and to identify large voids that could compromise structural integrity;
- vibration monitoring makes it possible to detect eventual anomalies in the diagnosis phase.

In-situ destructive testing of masonry elements to determine the shear strength is actually performed through two main procedures: diagonal compression tests and shear-compression tests (Figure 1.12b) [54–56]. In both tests, the panels are mechanically isolated by cutting their perimeter edges. The shear strength resulting from the two tests typically differs, highlighting the problem of choosing the method that best simulates the real behavior of the masonry when stressed by lateral loads.

In diagonal compression tests (Figure 1.12a), the isolated masonry panel is square (typical dimensions of approximately 120×120 cm). A set of metallic elements is then fixed at two opposing corners of the wall panel, and a hydraulic jack is interposed at one corner to apply the load. Usually, the panel remains partially anchored to the rest of the wall through the lower horizontal edge. This test simulates a pure shear stress state from which the shear strength is evaluated.

In the shear-compression test (Figure 1.12b), the isolated masonry panel is higher than it is wide. A test apparatus is used to induce a constant vertical stress in the panel, while a horizontal load is introduced at mid-height by means of hydraulic jacks anchored to a nearby opening. Typically, the test apparatus overhanging the panel is not sufficient to provide a perfect constraint; thus, the upper half of the panel can translate and rotate, while the lower half, connected to the rest of the masonry, can be considered as perfectly fixed. This results in a lack of symmetry in the shear distribution between the upper and lower halves of the panel, which must be considered when analysing the data. Consequently, the lower half of the panel is always more stressed and the failure always localizes here. This test reproduces more realistically the stress state that piers undergo under seismic actions.

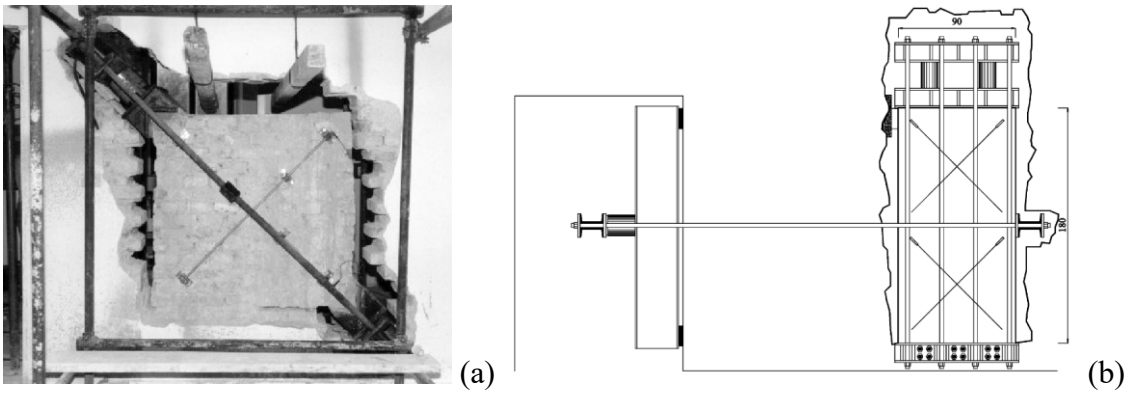


Figure 1.12. In situ layout of a a) diagonal compression test and b) shear-compression test [56]

1.4 Modelling of unreinforced masonry

The structural modelling of unreinforced masonry (URM) presents significant challenges due to the material's heterogeneity, anisotropy, and nonlinearity. The extensive testing performed on masonry elements, allowed to define and validate accurate analytical models to determine the maximum shear force that a masonry panel can resist. The interpretation of failure modes discussed in §1.2.3, are typically addressed in the literature through simplified strength criteria, which allow accounting for the dependence on multiple factors, such as: the resistance characteristics of the individual masonry components (mortar, blocks), the geometry of the panel (in particular its slenderness), the normal stress acting on the panel and the static scheme (e.g. Italian Building Code [15], EN 1996-1[34], FEMA 306 [57], ACI 530-05 [58], DIN 1053-100 [59]). The resistance criteria adopted in national and international design codes are generally consistent with the assumption that the maximum shear capacity of the panel is reached when the stress state reaches the ultimate strength of the material in a specific point or section of the panel [60]. Comprehensive reviews of the theoretical background of the analytical methods have been provided by Magenes and Calvi [61] and Calderini et al.[62].

For the in-plane bending behaviour of masonry panels, leading to a rocking failure in compression, the typically used analytical models consider the base section of the panel to assess the stress state. They evaluate the maximum normal stress acting on the bed joints plane, which is calculated on the basis of the beam theory, neglecting the tensile strength of the material and assuming an appropriate normal stress distribution at the compressed toe.

For the shear behaviour, two different models have been developed to represent failure mechanisms: models that describe masonry as a composite, considering its constituting components (joints and blocks) separately, and models that assume masonry as an equivalent isotropic material, considering the development of a crack along a principal stress direction. The first models developed in the literature and adopted in codes to describe the sliding shear failure of masonry along joints are based on a Mohr-Coulomb-type criterion. These models consider cohesion and friction parameters, considering the actual compressed part of the reference section. The second model, describing diagonal cracking through joints, was originated from tests performed in Ljubljana (Slovenia) [63,64] on URM piers with fixed boundary conditions. This model is based on the assumption that diagonal shear failure is reached when the principal stress at the centre of the pier attains a critical value, which is defined as a reference tensile strength of masonry.

By comparing these three mechanisms, the failure criterion of the panel under varying axial loads can be determined as the minimum envelope of the limit strength domains associated with the different failure modes (Figure 1.13).

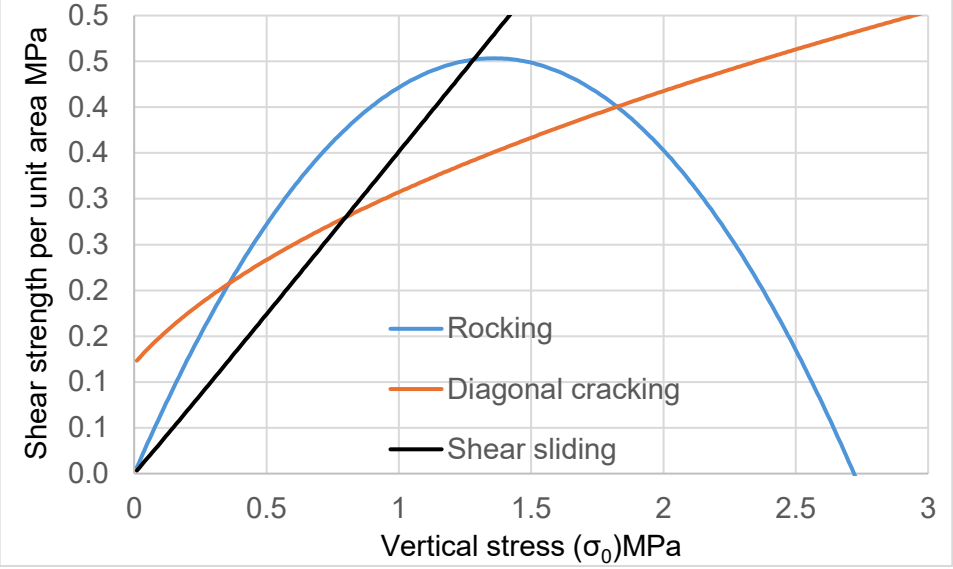


Figure 1.13. Strength domain of the shear resistance of a compressed masonry panel (length = 2250 mm, thickness = 250 mm, height = 3375 mm, compressive resistance = 3.2 MPa, equivalent masonry shear strength for $\sigma_0 = 0$ for the "Turnšek and Čačovič" formula = 0.12 MPa, equivalent masonry shear strength for $\sigma_0 = 0$ for the shear sliding formula = 0.20 MPa)

For spandrels, in the absence of elements capable of resisting tensile forces (e.g., steel ties or floor curbs), their capacity to resist the rocking mechanism is generally neglected in European design codes [34]. However, experimental evidence shows that a limited

resistance is provided by the compressive axial force on adjacent piers, granting an interlocking effect of masonry units at both ends of the element. This effect is considered by the Italian Building Code [65] and by the technical guideline FEMA 306 [57]. An analytical validation of the latter formulation for unreinforced masonry spandrels was carried out by Rinaldin et al. [46], who compared it with experimental tests results.

1.4.1 Overview of numerical modelling strategies

In the field of Finite Element Analysis (FEA), various modelling strategies have been proposed in the literature to simulate the behaviour of masonry structures under static and dynamic loads. These can be broadly classified into three main approaches [66–69]:

- **micro-modelling**, in which units and mortar in the joints are represented by continuum elements, whereas the unit-mortar interface is represented by interface elements (Figure 1.14a,b);
- **macro-modelling**, in which units, mortar and unit-mortar interface are smeared out in a homogeneous continuum (Figure 1.14c);
- **structural component models**, where elements are represented with beam elements or macro-elements and their constitutive laws are directly provided in terms of internal forces such as shear force or bending moment.

Micro-modelling represents each unit and the mortar joints as distinct elements, allowing for detailed simulation of local failure mechanisms, such as cracking and crushing at the unit-mortar interface. A simplified approach to micro modelling proposes to combine the mortar thickness into interface elements with assigned nonlinear behaviour between rigid or elastic blocks [70]. This detail level provides higher accuracy than macro-models but at a high computational cost, making this type of modelling suitable primarily for small-scale components or local analyses.

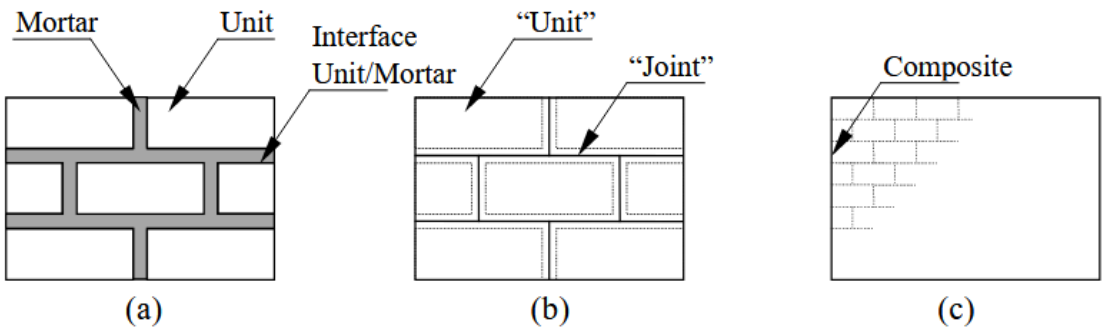


Figure 1.14. Modelling strategies for masonry structures: (a) detailed macro-modelling; (b) simplified micro-modelling; (c) macro-modelling [67]

As an alternative to FEA, the Discrete Element Methods (DEM) has been investigated in the recent years [71–73]. This method belongs to the simplified micro-modelling approach and involves modelling the units as particle entities interacting along their boundaries through contact models. DEM are used in explicit dynamic analyses for simulating the masonry behaviour under dynamic actions. Additionally, the combined Finite-Discrete Element Method (FDEM) implements a finite element mesh discretization of the particle [74,75].

Macro-modelling idealizes masonry as a homogeneous material with equivalent mechanical properties [70,76,77]. Its nonlinear behaviour is modelled through continuum damage mechanics constitutive laws (e.g. concrete damage plasticity, total strain crack, Drucker-Prager). A comparative study of three different macroscale material models for predicting the in-plane behavior of masonry was conducted by Zizi et al. [69], highlighting the importance of carefully calibrating the damage model parameters. These parameters should be derived from experimental tests on large-scale masonry specimens, such as piers and spandrels, or from the results of micro-element discrete numerical analyses, which can provide the calibration data. The reduced computational cost due to the lower degrees of freedom of the models, makes this approach suitable for simulating the global response of structural elements and small buildings under static or dynamic loads. Furthermore, macro-modelling is used to represent the behaviour of non-periodic masonry, such as irregular stone.

For practical engineering applications, structural component models based on beam or macro-elements are generally adopted for the seismic assessment of whole masonry buildings. The macro-element method was inspired by the POR method [78], developed

with the experience obtained with the Skopje (Slovenia) earthquake in 1963, and, was historically the first seismic assessment method for masonry structures in Italy [68].

The progress in the analytical methods in the following years led to the development of the so called Equivalent Frame Method (EFM), implemented in various forms by different authors [79–83]. This method consists in schematizing the structure into an equivalent frame system composed of vertical and horizontal resisting structural macro-elements (i.e. the piers and the spandrels) connected by means of rigid nodes (Figure 1.15). Each macro-element is represented as a beam element along its principal centroid axis, with nodes positioned at the intersections with the centroid axes of the orthogonal connected elements. Alternative macro-element formulations have also been proposed, like those based on two-dimensional elements [84]. Infinitely rigid segments at the ends of the masonry macro-elements allow to model the reduced deformability of the structural nodes. The elastic deformation of the structural elements depends on the elasticity of the macro-elements, while the inelastic response is lumped in rotational and shear plastic hinges. The rotational plastic hinges at the ends of the macro-elements simulate the inelastic in-plane bending response, while the shear plastic hinge at mid-length represents the inelastic in-plane shear response.

The equivalent frame idealization presents limitations in presence of irregular layouts of openings in perforated wall panels. In these cases, the application a priori of the modelling rules proposed in the literature [79,85,86], may lead to epistemic modelling errors. Different studies have investigated on the reliability of these rules in equivalent frame modelling of some case study walls with irregular openings layout [87,88], highlighting some inaccuracies in the stiffness, shear force and drift values.

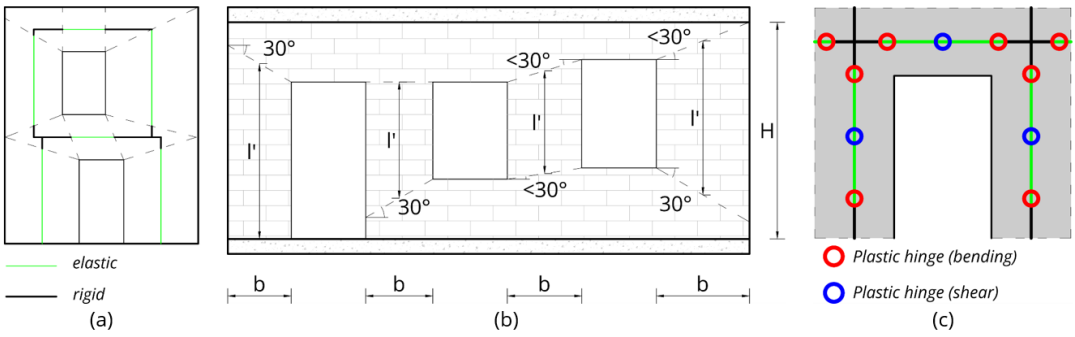


Figure 1.15. Modelling of a masonry wall accordingly to the Equivalent frame method (a), definition of the effective pier length (b), and location of the lumped plasticity hinges (c)

The EFM method is mainly used to perform nonlinear static (pushover) or dynamic analyses. The nonlinear static (pushover) analyses proved to be a reliable tool for obtaining a realistic prediction of the resistance and displacement capacities with relatively low computational effort, provided that there is proper calibration of the mechanical parameters and a thoughtful schematization of the resisting elements. The resisting elements (i.e. the piers and the spandrels), are usually schematised by means of mono-dimensional, elastic beam elements, with rigid parts at both ends, defining the "Equivalent Frame" model of the structure. Recent studies have has extended the application of this methodology also for the simulation of shaking table tests on full-scale buildings [89–91].

Out-of-plane mechanisms are usually assessed through limit analysis methods, in terms of both strength and displacement capacity [92,93]. The analyses consider: the compressive strength of masonry, wall texture, quality of connections, and the presence of tie rods or chains. Limit analysis play a fundamental role in analysing the seismic performance of structural elements in monumental buildings, as highlighted by the Italian Ministry of Cultural Heritage [94]. These structures are often characterized by large spans and heights, weak connections between walls, arches, vaults, and roofs. As a result, they do not behave as a single unit under seismic action, but rather tend to separate into distinct macro-elements. For ordinary masonry buildings, a list of the most recurrent out-of-plane failure mechanisms is provided by Milano et al. [95]. To analyse out-of-plane mechanisms, in recent years, numerical approaches based on the DEM and FDEM approaches have been reported in the literature [75,96–98]. Early applications of DEM mainly focused on historical constructions, typically involving relatively simple systems composed of a limited number of blocks [99]. Advances in computational power have since enabled the modelling of more complex masonry assemblages with thousands of discrete elements, allowing for a realistic assessment of their seismic performance through both pushover methods [98] and dynamic analyses [100]. These models have been successfully used to reproduce experimental tests on masonry walls subjected to out-of-plane loading [101,102].

1.5 Strengthening techniques for masonry buildings

Designers need to consider many criteria when deciding upon structural strengthening interventions. The structural resistance of the building must be first assessed to define efficient technical measures needed to improve structural deficiencies. Before deciding on the intervention, general criteria need to be considered (e.g. costs of intervention and the importance of the building, availability of adequate technology and skilled workmanship to implement the proposed measures, duration of the works and problems of occupancy, etc.). Moreover, in the case of heritage buildings or buildings protected by superintendencies, the principles of preservation of the historical value of architectural heritage should also be taken into account [18]. In this case, it is preferred that the adopted techniques are reversible, allowing future removal or replacement should more effective solutions become available. Moreover, the interventions must guarantee a durability comparable to that of the existing structure, as required by the guidelines of the Ministry of Cultural Heritage [94].

Strengthening interventions can be classified into:

1. Interventions aimed at improving structural integrity (e.g. by improving the connections between structural elements, stiffening floors, retrofitting roofs, and reducing the thrust of arches and vaults);
2. Interventions aimed at improving structural layout by improving the regularity of the structure;
3. Interventions aimed at increasing the integrity and strength of masonry elements;
4. Foundation interventions.

Improving structural integrity should be prioritized in every strengthening intervention by improving wall-to-wall and wall-to-floor connections, as well as stiffening of timber floors. Traditionally, ties with anchors were used to strengthen the connections between structural elements. The anchors prevent the slippage of a tie rod from the masonry or timber elements. They also contain the horizontal thrusts of arches, vaults, and wooden trusses in roofs, and prevent the overturning of the walls by connecting them to the floor diaphragm [103,104]. Anchors can be with a distribution plate or an injected expansion bulb, or grouted. In the past, reinforced concrete anchors using the so-called "dovetail" devices had been proposed for seismic applications. The latter solution should be

completely abandoned, as it is very invasive, ineffective statically as the connections are very limited in number, and harmful due to the damage to the surrounding masonry [105].

Ancient timber floors are characterized by low in- and out-of-plane stiffness and weak connections with the surrounding walls. A simple technology employed to provide a resisting floor diaphragm involves adding a thin collaborating reinforced concrete slab (50mm), properly connected to the walls through injected steel bars, embedded within the slab. This intervention might be unsuitable for the floor and roof strengthening due to the significant weight increase [104]. Furthermore, this technique might not meet the reversibility and material compatibility criteria for protected cultural heritage buildings. The effectiveness of the stiffening system depends entirely on the collaboration between the concrete slab and the wooden beams, which is obtained through the use of different connectors [106].

More recently, dry solutions have been preferred for strengthening wooden floor structures. Typically, the solution of the timber diaphragm, which consists in nailing overlaying wooden panels to the existing wooden planks, is preferred. This approach is highly reversible and minimally invasive, while effectively improving the in- and out-of-plane stiffness of the floor and avoiding significant increases in seismic mass, and thus in seismic action [105]. In addition to or as an alternative to this system, other reinforcement strategies can be employed, such as diagonally placed steel strips, gang nails, or carbon fibre reinforced polymer (CFRP) strips.

The use of steel strips involves placing thin steel plates at each wooden joist, above the existing boarding, and fastening them to the beams with steel dowels. The system is completed by a set of diagonal steel strips, welded to a perimetric steel profile to create a lattice truss [107]. The gang nail system, on the other hand, consists of using steel nail plates at the joints between adjacent boards to prevent slip and increase the in-plane shear resistance of the floor [108,109]. Finally, CFRP strips can be bonded to the wooden surface using two-component epoxy resin, typically arranged diagonally to counteract shear deformation within the floor plane. Although this technique offers significant stiffness and tensile strength improvements, its reversibility is limited due to the partial penetration of the resin into the wood fibres [108].

For all these strengthening strategies, the effectiveness of the intervention relies on the realization of a horizontal lattice truss, to give the floor good in-plane stiffness so as to be

able to transfer horizontal seismic action to the shear walls and to prevent out-of-plane displacements of the walls perpendicular to the seismic direction. Steel L-profiles are usually installed along the edges of the floor, fixed to the joists and boards through dowels, to the reinforcing system, and to the masonry walls, through injected dowels.

Moreover, in wooden floors suffering from excessive out-of-plane deformability, wooden beams can be strengthened by using FRP or steel strips on the lower surface of the beams. Many layouts of the strips can be used. FRP strips can be glued to the beam with epoxy resin, and steel strips can be glued or nailed to the beam [110].

The structural layout is typically improved by adding new masonry walls or closing some openings in existing walls. These interventions aim to achieve a similar number of resisting elements in both perpendicular directions, and to have a layout of walls in which the centre of mass and centre of rigidity in a floor are as close as possible and aligned in all floors of the structure.

After improving the structural integrity, masonry walls will typically exhibit in-plane failure mechanisms. The most diffuse traditional strengthening systems for masonry structural elements consisted in wall jacketing with steel-reinforced concrete coatings, grout injections and unreinforced or steel-reinforced repointing of mortar joints [111–115].

Wall jacketing with steel reinforced concrete coatings consists in the of a welded steel mesh (diameter 4 to 8 mm) on both faces of a wall, connecting the two meshes with steel connectors passing through the wall thickness (4-6/m^2) and applying on the two faces a cement mortar based coating (thickness 50-100 mm) [18,114]. The two concrete slabs should work together with the masonry, improving the tensile and shear strengths of the wall, but also enhancing its stiffness. However, the increased stiffness may have negative effects on the overall seismic behaviour [116]. This technique was extensively applied particularly to irregular multiple leaf stone-walls in Italy and it is recommended by the Italian Code [65], but it was not always applied correctly (discontinuities between the walls, lack of overlapping between two different sheets of the mesh, absence of steel transversal connectors and use of too short connectors, and lack of intervention uniformity), frequently leading to local failures of jacketed walls and uneven distribution of stiffnesses in the structure.



(a) (b) (c) (d)

Figure 1.16. (a) Failure due to insufficient steel mesh overlapping and (b) insufficient transversal ties confining action; (c) lack of connection between nets; (d) absence of connectors [116]

Grout injections are used to fill the voids, cracks and gaps between two or more leaves, thus increasing the continuity of the masonry and hence its strength. The intervention consists of the injection of a highly fluid binder mixture, typically based on resins, cementitious, or lime-based materials [117]. To avoid leakage, the joints among the elements, cracks and discontinuities are sealed. The injection is performed at low pressure (typically by gravity) to avoid either air being trapped within the cracks and fine voids or even wall disruption. The injections are performed from the bottom up in several lifts. The quantity of injected material varies greatly with the type of masonry. Extensive research has been conducted to assess the effectiveness of this technique [118,119]. The effectiveness of the injections depends on the compatibility of physical, chemical and mechanical properties of the original masonry and the injected material [116]. This technique is not suitable for certain wall types, such as single-leaf masonry or walls with a low percentage of internal voids. Non-destructive tests as sonic or thermography tests can also be carried out on site, before and after injection to detect the penetration and diffusion of the grout [120].

Repointing of mortar joints was investigated for its use in masonry with low quality mortar and strong units [18]. The technique consists in removing part of the existing mortar, up to 1/3 of the wall's thickness, and replacing it with a higher quality mortar. To prevent vertical instability, the wall is first repointed on one side and, after sufficient strength of the mortar is attained, the procedure is repeated on the opposite side. The

addition of steel reinforcement bars in the bed joints was also investigated, although the studies did not observe any significant shear strength increase [111,115].

Although the techniques involving the use of cement-based mortars, concrete and steel elements were widely used in the past, with time they evidenced critical aspects concerning deterioration and incompatibility with the historic materials. As a result, in recent years the use of lime-based mortars for the restoration of historic buildings has seen a great upsurge, due to their chemical and mechanical compatibility with original materials and their higher deformability, which allows them to better accommodate structural movements [121]. Moreover, cement-based mortars and concrete reduce the vapor permeability of the masonry, resulting sometimes in a damage of the surface finishes. In steel reinforced concrete jacketing, a low durability of the technique was often observed, due to insufficient thickness of the steel cover with consequent steel corrosion [116].

For these reasons, innovative strengthening techniques were proposed, based on Fibre-Reinforced Polymers (FRPs). These are used as noncorrosive reinforcements for plasters, which are applied on the surface of the walls [122,123]. In addition, replacing traditional cement-based or resinous matrices with natural binders has improved the mechanical and chemical compatibility between the reinforcement system and the masonry substrate, complying structural and conservation needs.

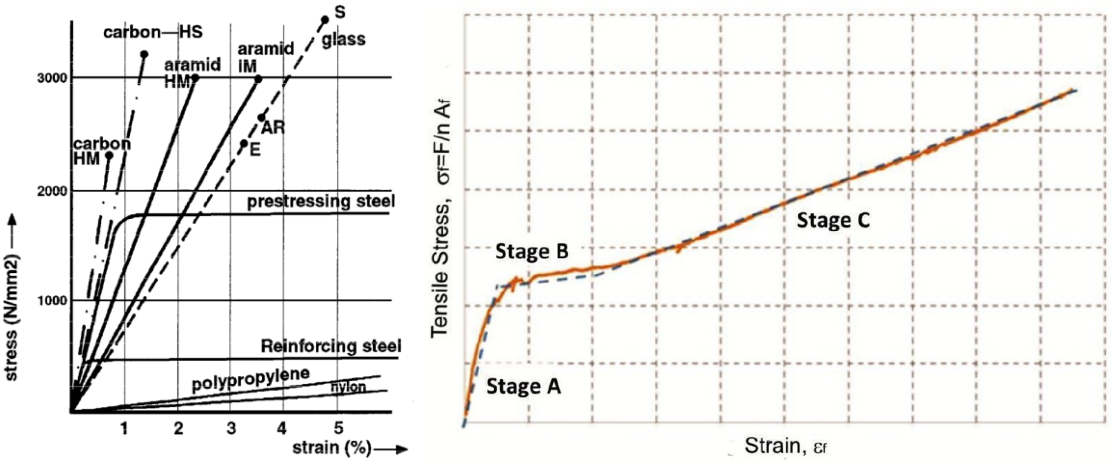
1.6 TRM technique and characterisation

Textile Reinforced Mortars (TRM) strengthening techniques consist of plastering the walls by means of mortar layers with embedded grids of textiles made of long fibres (e.g., glass, carbon, basalt, aramid, steel and polyparaphenylene benzobisoxazole). Fibres may be coated in a polymeric matrix (usually epoxy, vinylester or polyester thermosetting resin). In recent years, due to a growing environmental awareness, also natural fibres (such as jute, flax, hemp, etc.) have been investigated by many researchers [124,125], although their mechanical properties are significantly lower than those of other fibres. The advantages of the system concern the coupling of a non-corrosive reinforcement with an inorganic matrix, which is mechanically and chemically compatible with historical masonry, in terms of bond to the rough surface and breathability, resulting in a composite layer capable of increasing the stiffness, tensile strength and displacement capacity of the masonry. Furthermore, the inorganic matrix allows a higher vapor permeability of the masonry surface. A permeable coating allows moisture trapped in the material to exit, preventing issues like freeze-thaw cycle damage and efflorescence. TRM systems can also sometimes be applied with minimal impact on the aesthetics of the original surface. Various combinations of mortar matrices and textile reinforcements result in different types of TRM composites, commonly referred to as: FRM (fabric reinforced mortar), FRCM (fibre-reinforced cementitious matrix/mortar), TRC (textile reinforced concrete), IMG (inorganic matrix-grid composites) and CRM (composite reinforced mortar) [126].

These materials were introduced as an alternative to Fibre Reinforced Polymers (FRP), first introduced in the 1980s and extensively applied to both masonry and reinforced concrete structures, overcoming several limitations associated with polymeric matrices. Such limitations concern the mechanical properties and bonding degradation due to moisture, temperature and UV radiation [127–130]. Other complications concern the low fire resistance, difficulty of applying FRP on humid surfaces, high possibility of harming the workers during application of epoxies, high cost of resin, strength incompatibility between masonry and fibres and poor bond on rough surfaces [131].

From a constitutive standpoint, TRMs are heterogeneous and anisotropic materials. Their mechanical behavior is governed by the properties of both the fibres and the mortar matrix, as well as by the bond mechanisms at the textile-mortar and mortar-masonry interface. In

polymer coated fibres, the polymer matrix protects the fibres and transfers stresses between the fibres and the matrix. The fibres in tension, generally exhibit a linear elastic behaviour until failure (Figure 1.17a), while the composite is characterized by a tri-linear stress-strain behaviour: an initial uncracked elastic phase dominated by the mortar, a crack development phase in which the load is progressively transferred to the fibres, and a final hardening phase governed by the textile until failure (Figure 1.17b).



(a) (b)

Figure 1.17. Tensile stress-strain behavior of various reinforcing fibres [132]; b) example of tensile stress-strain curve [133]

The fibres commercially used in TRMs consist of continuous thin filaments (about 10 μm in diameter), arranged in various configurations (tow, spun yarn, roving). The tapes are produced by combining several hundred tows or yarns, by aligning, stitching together, or fixing them onto a support. The classification of fibres is based on their chemical composition and linear mass, which is expressed in Tex, equivalent to 1 g per kilometre of fibre, according to ISO 1144:1973(E) [134].

The most widely used fibres are glass fibres, due to their availability and low cost. However, it is essential to note that glass fibres are susceptible to alkali attack when embedded in a mortar with an alkaline environment. Therefore, alkali-resistant (AR) glass fibres must be used.

There are two main types of systems proposed in the literature, mainly differing in the type and thickness of the matrix (cement- or natural hydraulic lime-based), ranging from 10-15 mm thin coatings to about 30-40 mm thick layers, and in the type of reinforcements: fibre meshes (from 10×10 mm up to 30×30 mm grid dimension) in thin coatings and

preformed composite meshes (from 33×33 mm up to 99×99 mm grid dimension) in thick layers. The former is typically referred to as Fabric-Reinforced Cementitious Matrix (FRCM) systems (Figure 1.18a), while the latter is known as Composite Reinforced Mortar (CRM) systems (Figure 1.18b). Recently, the Italian Superior Council for Public Works published two technical guidelines that formally define and regulate the use of composite strengthening systems for existing masonry structures [135,136]. The first document, issued in 2019, standardizes the CRM technique for structural retrofitting. The second guideline, published in 2022, concerns the use FRCM systems for the strengthening of existing constructions. These two documents represent an important step toward the harmonization and qualification of composite materials employed in structural rehabilitation in Italy.

These techniques (Figure 1.18) can be adopted to improve the resistance, displacement and dissipative capacities of existing masonry elements in both in-plane and out-of-plane directions. The effectiveness of these approaches has been widely demonstrated through numerous experimental investigations reported in the literature [126].

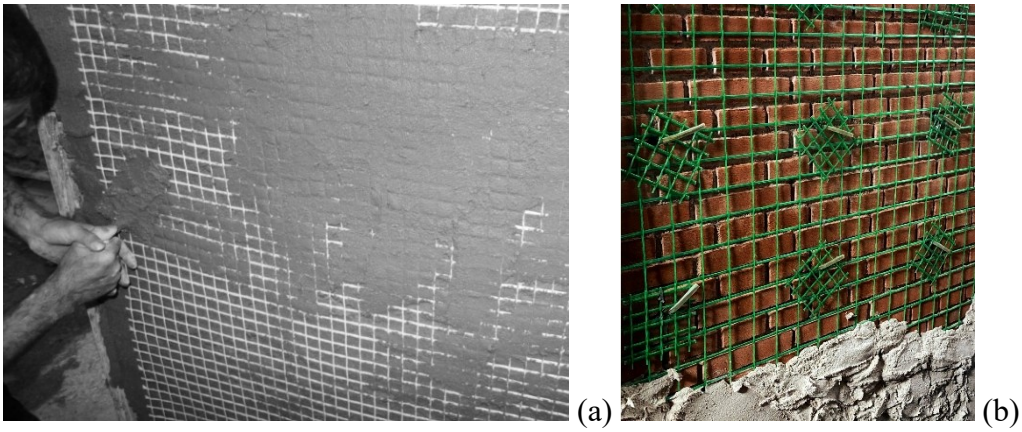

(a) (b)

Figure 1.18. Application of the (a) FRCM [137] and (B) CRM strengthening technique on a masonry wall

The different in-plane deformability of the reinforced coating and the masonry panel, determine a significant demand on the coating-to-masonry bond. The stress is increased further by lateral load reversals that occur during earthquakes, in addition to the compressive load. These two effects usually cause the wall to shrink slightly during an earthquake, while the coating cannot easily deform in the same way [138], potentially causing catastrophic failure. Thus, in both systems, specifically designed mechanical connectors are needed to ensure the composite action between the masonry and the strengthening layer, especially after the original bond is lost [139]. Nowadays, FRCM

systems involve the installation of composite fibre-resin rods which are injected into the masonry, while the opposite end features a staple that is impregnated in situ, above the reinforcement mesh. Differently, CRM systems typically adopt L-shaped connectors that are injected into the wall. The requirement of anchors is extensively observed in research based on cyclic shear compression tests [140–145].

Normally, the coatings are applied on both sides of the wall and anchored with connectors that pass through the entire wall thickness. Such a sandwich application displays obvious mechanical benefits and reduces the demand on the bond. However, to reduce the cost of intervention in moderate seismicity regions, several studies have explored single-sided applications, which have shown promising results [41,141–143,146–149]. In some applications, during in-plane tests, parasitic out-of-plane bending emerged due to the stiffness un-symmetry. In multi-leaf walls, single-sided applications require particular attention to detailing, with the prior installation of transverse connectors to ensure composite action across the entire wall thickness.

All the intervention details require study to validate the strengthening system, which can only be accomplished through experimental testing under simulated seismic loads.

1.6.1 Testing TRM

The performance of TRM coatings on masonry walls has been extensively studied in the literature. Typically, experimental tests on full-scale masonry elements are cyclic quasi-static and include: in-plane compression-bending and shear tests [138,150–160] and diagonal compression tests [124,125,146,150,161–180]; out-of-plane three- and four-point bending or airbag tests [26,42,42,150,157,171,181–189]; and tests on whole buildings [190–194].

These tests are conducted on both unstrengthened and retrofitted samples, tested under the same boundary and loading conditions, to evaluate the improvements in strength, deformation capacity, and energy dissipation provided by the TRM intervention. Additionally, dynamic laboratory tests (shaking table tests) on individual elements or scaled buildings have been carried out to reproduce the seismic response of strengthened masonry and to validate the reliability of simplified experimental and numerical models [44,45,192,195–199]. Papanicolaou et al. performed a large-scale test campaign on TRM [130,187], focusing on hollow clay masonry. Research into TRM has accelerated since, as summarised in recent papers by De Santis et al. [200] and Kouris and Triantafillou

[201]. Additionally, TRM research examined different scale levels, ranging from single material components [202] to masonry walls and structures [126]. The tests on full-scale TRM-strengthened masonry elements are particularly significant, as they explain the resisting mechanisms in structures under realistic boundary and loading conditions and the actual interaction among layers. Cyclic in-plane compression-bending and shear tests [150,151] and out-of-plane (OOP) bending tests [26,42,203] evidenced the capability of these reinforcement systems to increase the in- and out-of-plane strength of masonry elements and increasing significantly the plastic deformation. Additionally, experimental investigations on masonry vaults [204,205], have shown improved seismic behaviour, evidencing also the importance of the connections between the vault and the abutments [206,207].

Material level characterization tests on TRM generally includes tensile tests on individual materials (yarns, textiles, mortar) tensile tests on TRM coupons (Figure 1.19a), shear–bond tests on TRM layers applied to masonry substrates (Figure 1.19b) and pull-out tests (Figure 1.19b). The compressive behaviour is mainly due to the mortar in compression; thus, compression tests are performed only on mortar prisms, according to EN 1015-11 [35]. The global equivalent cross section of the wires is measured according to the procedure presented in CNR DT 203/2006, Appendix B [208] using a graduated cylinder.

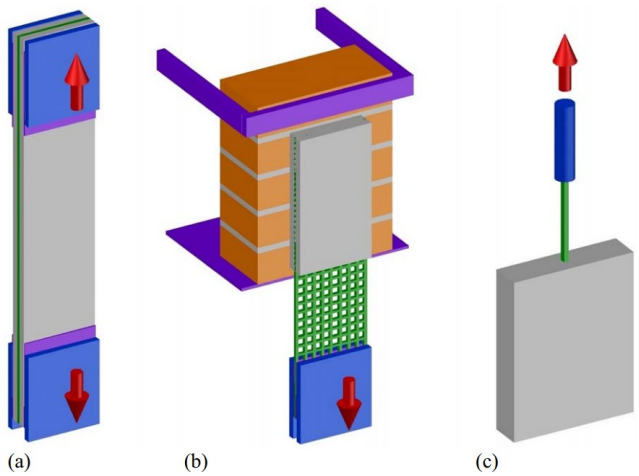


Figure 1.19. Characterization tests for TRM: (a) direct tensile tests; (b) shear bond tests; and (c) pull-out tests [209]

Significant contributions in this field have been made by the RILEM Technical Committee 250-CSM (2012–2019), which coordinated different European research institutions on the study of TRMs reinforced with synthetic and inorganic fibres [210–214]. More recently, research has also focused on the potential of natural fibres as a

sustainable alternative for TRM reinforcement [215–217]. Current research efforts are focused on defining qualification procedures, testing methods, and design criteria for TRM systems, analogous to those already established for FRP composites.

1.6.2 Durability of FRP materials

Durability still represents one of the main concerns for FRP composites in civil engineering and continues to limit their widespread adoption by structural designers. [218]. In Italy, ordinary civil structures are designed to remain in service for up to 50 years; therefore, the development and validation of comprehensive inspection and maintenance plans are essential, based on experimental assessments of long-term durability. The primary environmental factors influencing degradation include moisture, alkaline exposure, creep and relaxation, fatigue, fire, thermal effects (such as freeze-thaw cycles), and ultraviolet radiation.

In the framework of TRM strengthening interventions, the deterioration of matrices (hydrolysis, swelling and plasticisation) in water environments may reduce the coupling effect at the interface between the fibres and the matrix, consequentially decreasing the mechanical properties of the strengthening intervention [219]. Several studies are focusing on assessing the long-term performances on the use of FRP materials embedded into organic matrixes (e.g. activities of the RILEM Technical Committee 290-IMC, started in 2019), which can achieve high pH values in lime- or cement-based mortars, and may induce degradation of the glass fibres [220].

The extent of degradation (physical, chemical, mechanical) depends on the type of fibres and matrix, the manufacturing process, and the severity of environmental exposure. The resin in FRP materials act as a barrier preventing the degradation of the glass fibres from the corroding agents. However, water can possibly transport alkalis through micro-cracks, allowing for degradation of the fibres. The water can also damage the fibre/resin interface or the resin itself through plasticisation and hydrolysis, which leads to permanent changes in the resin structure [219]. Moreover, the temperature can alter the structure of organic resins, facilitating water/alkali penetration and accelerating degradation.

Current knowledge about durability is primarily derived from accelerated ageing tests; however, the correlation between these results and those obtained from real-time exposure remains an open issue [209]. Different accelerating aging protocols are used to investigate on the TRM durability, but generally these involve immersion of the samples in alkaline

solutions maintained at controlled temperature for extended periods (up to 9000 hours), to simulate long-term degradation.

Previous research on bare fibre-based textiles evidenced a higher degradation from alkali baths on the tensile strength of E-glass and basalt dry fibres, in respect to alkali resistant (AR) glass and PBO, while carbon fibres were very limitedly influenced [221]. The enhanced durability of AR glass fibres is due to their zirconium dioxide content (≥ 16% content in mass) which provides high alkali resistance. They were originally developed for glass fibre-reinforced concrete (GFRC) applications, glass fibre-reinforced concrete premix, fibre-reinforced concrete, and other cementitious based products [222–224], although the standards are now also applied for use in TRM systems.

Much of the information available at the moment on these materials and strengthening systems are related to their short-term behaviour; thus, the experimental evaluation of the long-term structural properties of TRM strengthened masonry structures under various environmental exposure conditions and combinations is therefore essential. According to this scientific target, research groups all over the world, involved in this research field, aim at focusing their efforts studying the state-of-the-art regarding the durability of individual FRCM/TRM and CRM materials, and the durability of masonry assemblages strengthened with such materials. Furthermore, experimental studies aimed at determining a set of standardized tests, to be used for the mechanical characterization of FRCM/CRM, subjected to environmental actions are undergoing. The tests are conducted on individual materials (matrices and textiles), composites (FRCM/CRM), substrates (masonry of selected configurations) and on the combined system (masonry and FRCM/CRM layers). The main degradation agents investigated in terms of exposure conditions are: the presence of alkaline ions in the matrix (for glass and basalt fibres due to their known vulnerability to alkali) and the effect of extreme moisture/temperature scenarios.

In the RILEM 290-IMC project[1], titled “Durability of Inorganic Matrix Composites used for Strengthening of Masonry Constructions”, different textiles and mortars, according to the availability of manufacturing companies, were tested. The results will be used for formulating preliminary degradation laws expressed as a function of the investigated

[1] https://www.rilem.net/groupe/290-imc-durability-of-inorganic-matrix-composites-used-for-strengthening-of-masonry-constructions-384

variables. A further goal is to correlate the effect of accelerated tests with natural time conditions.

Furthermore, the ongoing research aims at proposing guidelines for testing and simulation of environmental factors, which may serve as a basis for the development or refinement of future design recommendations for inorganic mortar-based strengthening systems for existing masonry structures.

2 Experimental testing for durability

This study presents a set of experimental tests carried out within the framework of the RILEM Technical Committee 290-IMC (Inorganic Matrix Composites for the strengthening of masonry), established in 2019 within Cluster E. The Committee is chaired by Prof. Maria Antonietta Aiello, with Dr. Catherine Papanicolaou as Deputy Chair.

The main objective of this project is to improve the understanding of the long-term durability and structural reliability of masonry elements strengthened with inorganic matrix composite systems, namely FRCM/TRM and CRM, when exposed to aggressive environmental conditions.

The main objective of the project is to investigate the long-term durability and structural reliability of masonry elements strengthened with inorganic matrix composite systems, including FRCM/TRM and CRM, under various environmental conditions. The relevance of the project derives from the growing use of these materials in the strengthening of existing and historical masonry structures, for which reliable information on long-term performance is still limited.

To achieve these goals, the project is organized into four Working Packages (WP), which focus on the following specific tasks:

WP1. *State-of-the-Art* – A detailed assessment of the durability of individual FRCM/TRM and CRM materials, as well as masonry assemblies strengthened with such systems, is performed. This study highlights current knowledge gaps and defines the basis for subsequent experimental programs.

WP2. *Experimental and analytical research* – Experimental campaigns standardize testing procedures for the mechanical characterization of FRCM/TRM/CRM systems subjected to detrimental environmental actions. Tests are conducted at multiple scales, including individual materials (fibres, mortars, resins), composite systems (FRCM/TRM/CRM), masonry substrates, and the combined system (masonry and composite overlay). Two critical exposure aspects are studied: (i) the effect of alkaline ions on fibre durability (notably glass and basalt), and (ii) the impact of extreme moisture and temperature conditions. Different types of fabrics, mortars, and masonry substrates are investigated to account for variations in

currently available systems. The analytical study is aimed to formulate preliminary degradation laws expressed as a function of the investigated variables and correlate accelerated testing results with natural conditions, to predict long-term structural efficiency.

WP3. *Proposal of recommendations* – Based on experimental and analytical outcomes, recommendations are developed for testing protocols, environmental simulations, and the implementation of future design guidelines for inorganic mortar-based strengthening systems.

WP4. *Dissemination of knowledge* – The project emphasizes the exchange of knowledge among multidisciplinary stakeholders, including academia, research institutions, manufacturing companies, contractors, and practitioners, through seminars, workshops, and training courses.

Within this framework, the experimental campaign presented in this chapter focuses on the assessment of the durability of inorganic matrix composite systems, contributing to the broader objectives of the RILEM 290-IMC project by providing data on the evolution of mechanical properties and bond behaviour after environmental exposure.

2.1 Project coordination and communication structure

The study comprises 20 systems, provided by 8 distinct companies, and subjected to experimental testing by 3 different laboratories (round robin testing system). Most of these laboratories have undertaken the assessment of 2 systems, while 6 laboratories have conducted tests on 3 systems each, and 1 laboratory is responsible for evaluating a single system. The list of the systems tested by the laboratories is presented in Table 2.1.

To enhance the efficiency of testing coordination for each individual system or groups of systems and to facilitate effective communication with the respective companies, a Reference Lab has been designated for each system or group of systems. The Reference Labs are tasked with:

- Collection of all necessary information required for the delivery of materials to the collaborating labs in the group and forward them to the company.
- Coordination of the initiation of tensile coupon testing for untreated specimens to minimize discrepancies between different labs testing the same system.

- Collection of test data from all collaborating labs in the group and communicate with the TC Chair for troubleshooting matters or other concerns.

The companies have been tasked to dispatch their product(s) to each laboratory within the testing group upon receiving the relevant information, along with providing explicit instructions to the laboratories regarding the handling of materials. Furthermore, it was advised for each test group to adopt a common starting point for the testing campaign.

Table 2.1. Systems tested within the RILEM 290-IMC project

BASF Glass1 (lime mortar)	BASF Glass2 (fibre-reinforced lime mortar)	Biemme Glass (lime mortar)	MAPEI CRM (AR glass and lime mortar)
TICM (Carbon and lime mortar)	GP&Intech Glass (lime mortar)	GP&Intech Basalt (lime mortar)	GP&Intech Glass CRM (lime mortar)
KIMIA Basalt (lime mortar)	KIMIA Juta (lime mortar)	KIMIA Flax (lime mortar)	SIKA Glass (cement mortar)
FIBRENET FRCM GLASS1 (lime mortar)	FIBRENET FRCM GLASS2 (cement mortar)	FIBRENET CRM-GLASS1 (lime mortar)	FIBRENET CRM - GLASS2 (cement mortar)
FIBRENET FRCM -JUTA1 (lime mortar)	FIBRENET FRCM -JUTA2 (cement mortar)	FIBRENET FRCM - JUTA3 impregnated (lime mortar)	FIBRENET FRCM - JUTA4 impregnated (cement mortar)

2.2 Testing methodologies and groups

The University of Trieste's Laboratory for Testing Materials and Structures has been assigned the assessment of the following systems provided by the Fibre Net company:

- CRM-GLASS1 (lime mortar)
- FRCM-GLASS1 (lime mortar)

Additionally, it served as the reference laboratory for Fibre Net CRM-GLASS-1 (lime mortar) and Fibre Net CRM-GLASS-2 (cement mortar). In the tables below, the work groups for the three systems are presented.

Table 2.2. Work groups for the strengthening systems investigated

Fibre NET CRM-GLASS1 (lime mortar)	**Fibre NET FRCM-GLASS2 (cement mortar)**	**Fibre Net FRCM-GLASS1 (lime mortar)**
University of Trieste (Reference Lab)	CUT_Cracow University	University of Trieste (Reference Lab)
Politecnico di Milano	Politecnico Milano	University of Xi'an Jiatong - Liverpool
ITC - CNR - Antonio Occhiuzzi	ITC - CNR - Antonio Occhiuzzi	University of Calabria

The tests were conducted on specimens in their unconditioned state for reference and on specimens subjected to alkaline environments pertinent to the specific system. The experimental campaign adopted the following environmental exposures:

- **Environment A** (lime mortar)
  Temperatures: T1 = 23°C; T2 = 40°C
  Chemical composition: 0.16% Ca(OH)2
- **Environment B** – Portland cement mortar
  Temperatures: T1 = 23°C; T2 = 40°C
  Chemical composition: 0.16% $Ca(OH)_2$; 1% NaOH ; 1,4% KOH
- **Environment C**
  Temperatures: T1 = 23°C, T2=40°C, T3 = 60°C
  Chemical composition: as per ASTM D7705/D7705 M [225]

Depending on the type of mortar employed in the FRCM/CRM system, either environments A or B were adopted. Environment C, on the other hand, was exclusively utilized for the FRP mesh in CRM Systems.

For CRM systems, the experimental campaign was focused only on the FRP grid used as reinforcement within the mortar, coherently with the available European Assessment Documents (EAD) [226]. Conversely, in FRCM systems, the tests are conducted on fibre-reinforced mortar coupons, following the instructions outlined in the available EAD [133]. Additionally, the test campaign comprehends tests on dry fibre yarns and the mortar used in the system, according to ISO 3341 [227] and EN 1015-11 [35], respectively. The quantity of tests conducted during the campaign is detailed in Table 2.3 and Table 2.4. A few additional specimens were produced to account for unforeseen losses.

Table 2.3. Number of minimum tests for the CRM systems

CRM					
Environment (temperature)	Conditioning time (hours)	Dry fibre yarns	WARP FRP grid	WEFT FRP grid	Mortar triplets
Unconditioned	-	5	5	5	1
A or B (23°C)	1000	5	5	5	-
	2000	5	5	5	-
	3000	5	5	5	-
A or B (40°C)	1000	5	5	5	-
	2000	5	5	5	-
	3000	5	5	5	-
C (23°C)	1000	-	5	5	-
	3000	-	5	5	-
	6000	-	5	5	-
C (40°C)	1000	-	5	5	-
	3000	-	5	5	-
	6000	-	5	5	-
C (60°C)	1000	-	5	5	-
	3000	-	5	5	-
	6000	-	5	5	-

Table 2.4. Number of minimum tests for the FRCM system (lime mortar).

FRCM					
Environment (temperature)	Conditioning time (hours)	Yarns	FRCM	FRCM with aged textiles	Mortar triplets
Unconditioned	-	5	5	-	1
A (23°C)	1000	5	-	5	-
	2000	5	-	5	-
	3000	5	-	5	-
A (40°C)	1000	5	-	5	-
	2000	5	-	5	-
	3000	5	-	5	-
Water (23°C)	1000	-	5	-	1
	2000	-	5	-	1
	3000	-	5	-	1
Water (40°C)	1000	-	5	-	-
	2000	-	5	-	-
	3000	-	5	-	-

2.2.1 Materials

Each laboratory received the materials listed in Table 2.5 and Table 2.6 for their respective systems. Using their equipment, each laboratory has prepared specimens with the provided materials and conducted tests on them.

Table 2.5. List of materials sent to the laboratories for the Fibre Net CRM-GLASS1 and GLASS2 systems (measures in mm)

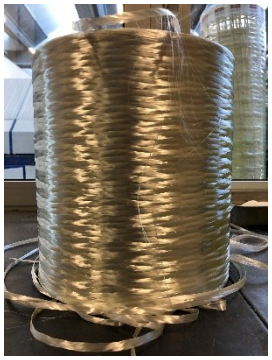
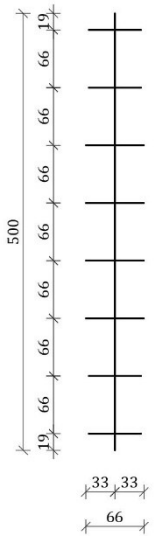
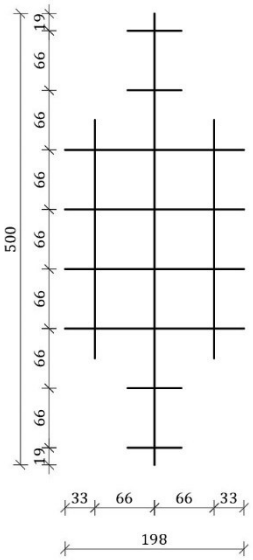
50 meters of dry bundle taken from the production reel of reinforcing nets.	FRP grid specimens Flat reinforcement (WEFT)	FRP grid specimens Twisted reinforcement (WARP)	1 bag of lime/cement mortar 25 kg (System CRM matrix)
			

Table 2.6. List of materials sent to the laboratories for the Fibre NET FRCM-GLASS1 system

50 meters of dry bundle taken from the production reel of reinforcing nets.	15 running meters of mesh having a width of 1 m for tests on dry mesh and FRCM	1 bag of lime mortar 25 kg (System CRM matrix)
		

The specific products subjected to testing are provided by the composite factory Fibre Net, located in Pavia di Udine, Italy. The GFRP mesh is commercially known as FBMESH66X66T96AR, while the thermo-welded fibreglass mesh for the FRCM system is named FB-VAR220R12.

The dry fibreglass yarn coils provided by the manufacturer have a linear density of 2400 Tex, a filament diameter of 17 μm and 24 μm, and are certified to lose less than 10% of their strength after being immersed in a solution of 20% NaOH at 50°C for 24 hours.

The thermosetting resin used to produce the GFRP mesh is a mixture consisting of 75% vinyl ester resin (vinyl ester epoxy; the catalyst is benzoyl peroxide, while the thixotropic agent is pyrogenic silica, with the addition of a green pigment) and 25% orthophthalic polyester resin (epoxy-bisphenol A-based vinyl ester resin, diluted in styrene).

The production of the GFRP meshes involves the weaving of dry Alkali-Resistant glass fibres (Figure 2.1a) after soaking them in the thermosetting resin (epoxy vinyl ester, Figure 2.1b). Before the resin sets, the mesh is formed by twisting the wires in one direction (warp) across the wires in the perpendicular direction (weft); thus, the fibres in the weft direction remain parallel. After the resin has set, the GFRP meshes are produced in rolls (Figure 2.1c) with twisted fibre wires in the warp direction and parallel fibre wires in the weft direction; thus, for ease of installation, the warped fibre wires are commonly oriented in the vertical direction of a masonry wall. Additionally, preformed GFRP angle brackets (Figure 2.1d), generally counting six vertical wires on each side, are also produced to be employed to ensure the continuity of the reinforcement at wall corners.

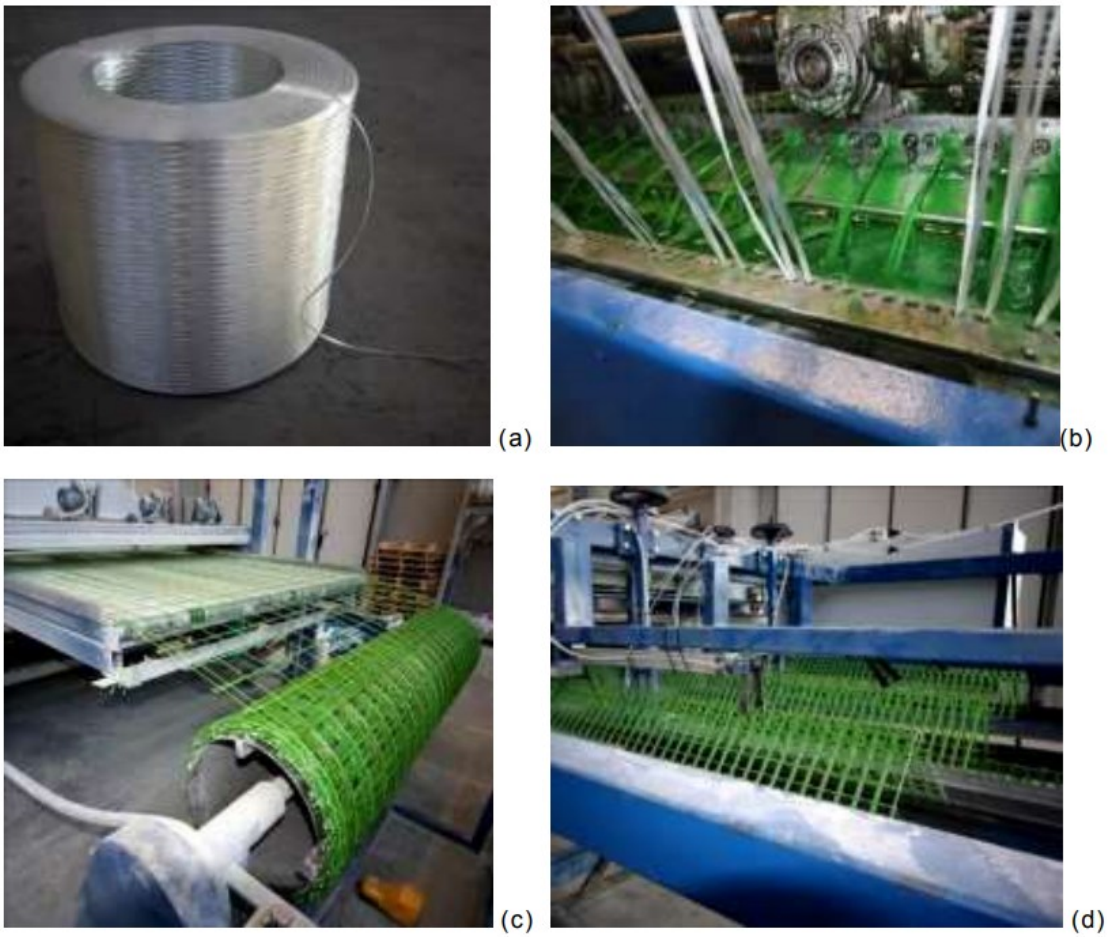


Figure 2.1. Production of the GFRP meshes: (a) spools of dry Alkali-Resistant glass fibres wires, (b) soaking of dry fibres wires in the thermosetting resin, (c) storage of the GFRP mesh in rolls and (d) production of the angle brackets for corner devices [228]

Among the preformed GFRP meshes formats, the 66x×66 mm^2 grid with a single fibre cross section is the most widely used configuration for the strengthening of existing masonry structures (Figure 2.2).

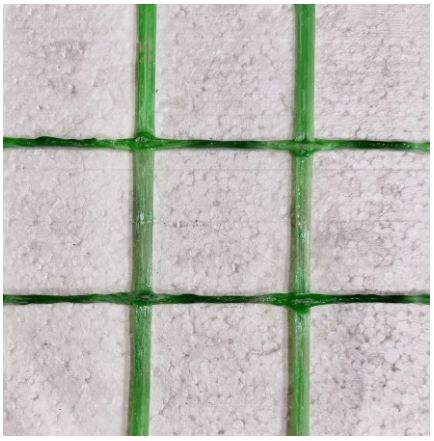


Figure 2.2. Details of 66×66 mm^2 GFRP mesh tested: the weft (parallel fibre wires) is vertical and the warp (twisted fibre wires) is horizontal

The mortars utilized in the systems are commercially available under the names Epoca calce NHL 115 (lime mortar) and Materia rinforza RZ 215 (cement mortar). The key material properties are detailed in the following tables.

Table 2.7. Technical sheet of the GFRP mesh used in the CRM system

Commercial name	FBMESH66X66T96AR
Type of fibres	Alkali resistant glass type EC-R
Type of resin	Thermosetting epoxy vinyl ester
Weight	420 g/m2
Mesh size - CNR-DT 203/2006 [208]	66×66 mm
Weft linear mass	9600 Tex
Warp linear mass	9600 Tex
Nominal Fibre Area - CNR-DT 203/2006 [208]	3.6 mm2
Bars/meter/side - CNR-DT 203/2006 [208]	15
Fibre content by weight (average weft - warp)	70%
Nominal Section of a Single Bar - ISO 10406-1 [229]	11.6 mm2 (WEFT)
	8.9 mm2 (WARP)
Tensile strength of the mesh - ISO 10406-1 [229]	Average: 79.5 kN/m
	Characteristic: 67.5 kN/m
Tensile strength of the bar - ISO 10406-1 [229]	Average: 5.3 kN
	Characteristic: 4.5 kN
Tensile stress of the composite - ISO 10406-1 [229]	Average: 490 MPa
	Characteristic: 385 MPa
Average axial stiffness at tensile strength of the bar - ISO 10406-1 [229]	275 kN
Average elongation at break of the bar - ISO 10406-1 [229]	1.90%
Average knot tear strength	0.28 kN

Table 2.8. Technical sheet of the dry fibreglass mesh for the FRCM system

Commercial name	FB-VAR220R12
Type of fibres	Alkali resistant glass type EC-R
Fibre density	2.65 g/cm^3
Total weight of fibreglass - ISO 3374 [230]	200 g/m2
Weight of fibreglass for each main direction - ISO 3374 [230]	100 g/m2
Mesh size - CNR-DT 203/2006 [208]	12 mm
Mesh section - CNR-DT 203/2006 [208]	40 mm2/m
Tensile breaking load 0°	≥ 56 kN/m
Tensile breaking load 90°	≥ 56 kN/m
Tensile breaking stress of the fibre	1400 MPa
Elastic modulus of the fibre	≥ 74 GPa
Elongation at break of the fibre	2%

Table 2.9. Technical sheet of the lime mortar used in both CRM and FRCM systems.

Commercial name	EPOCA CALCE - NHL 115
Mortar class - EN 998-2 [231]	M15
Bulk density	1.40 ± 0.1 kg/L
Bulk Density of the mix - EN 1015-6 [232]	1.80 ± 0.1 kg/L
Compression strength (28 days) EN 1015-11 [35]	≥ 15 MPa
Flexural strength (28 days) EN 1015-11 [35]	≥ 2.0 MPa
Elastic modulus in compression - EN 13412 [233]	≤ 10 GPa
Mix design water percentage	18%

Table 2.10. Technical sheet of the cement mortar used in the CRM system.

Commercial name	MATERIA RINFORZA RZ 215
Mortar class - EN 998-2 [231]	M15
Bulk density	1.40 / 1.70 kg/L
Compression strength (28 days) EN 1015-11 [35]	≥ 15 MPa
Flexural strength (28 days) EN 1015-11 [35]	≥ 4.0 MPa
Elastic modulus in compression - EN 13412 [233]	≥ 10 GPa
Mix design water percentage	17 / 19 %

The test methodologies adopted at the laboratories, and the results for each test are reported in the following chapters. The tests on yarns were carried out at the laboratory of the company Fibre Net, while the tests on GFRP grids were performed at the laboratory of the University of Trieste.

The tests for the FRCM system were abandoned after initial testing due to low adherence of the dry fibreglass mesh to the mortar provided by the company. The mesh slipped within the sample after the formation of the first crack in the mortar, and the stage B and C behaviours outlined in Figure 1.17 could not be observed. The test results and their discussion are reported in §2.8.

2.3 Conditioning of yarn and GFRP grid specimens

Two plastic tanks containing the conditioning solutions were prepared for the 23°C exposure:

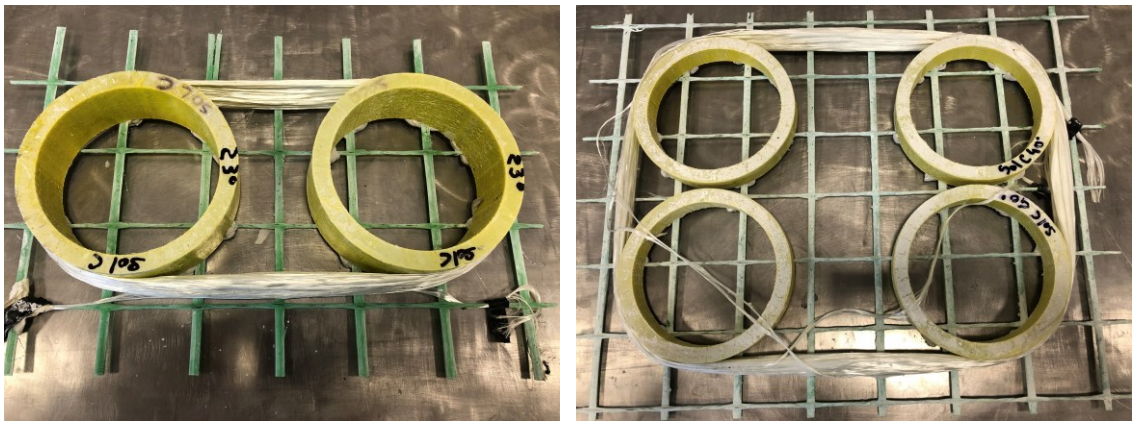
- Tank 1 (Solution A): 66 litres with 0.32% $Ca(OH)_2$
- Tank 2 (Solution C): 63 litres with 1.185% $Ca(OH)_2$, 0.09% NaOH, and 0.42% KOH

The tanks were left in the laboratory to allow the solutions to reach thermal equilibrium before immersing the specimens. For solution C tanks, a small circulation pump (less than 1% of the solution volume in 1 minute) was installed to prevent excessive solid deposit of $Ca(OH)_2$ over the samples.

Additionally, stainless steel tanks (550×450×130 mm) were filled with the two solutions and placed inside climate chambers at 40°C and 60°C. Before inserting the specimens, the temperature was monitored to ensure stability and minimize temperature fluctuations. Continuous temperature control was performed using thermocouples connected to a central monitoring unit. Both yarn and GFRP mesh samples were conditioned in the same tanks.

Yarns were wound around composite pultruded circular profiles (diameter of 160 mm, height 50 mm) fixed on composite grids measuring:

- 470 x 300 mm for conditioning at 23°C in PVC tanks (Figure 2.3a);
- 470 x 530 mm for conditioning at 40°C in stainless steel tanks (Figure 2.3b).



(a) (b)

Figure 2.3. Winding system for conditioning dry fibreglass yarns in tanks: a) double-tube winding system; b) quadruple-tube winding system

Aged yarn specimens have been tested in a dry condition, after accurately washing the yarns with sprinkle water, to avoid damaging the delicate fibres. Then the yarns were left to dry in laboratory conditions for at least 3 days before testing. The specimens were unwound in a manner that prevented damage to the yarns and avoided significant changes in twist.

The FRP grids were cut into panels directly after production, without being rolled for storage, and then conditioned in 5 stainless steel tanks. Between the samples, composite bars with a circular cross section (8 mm diameter) were used as spacers, to allow for a better interaction between the specimen and the solution (Figure 2.4a). Specimens were cut after the conditioning process using an angle grinder equipped with a disk for cutting steel. Due to limitation sizes of the available steel tanks, some panels had a minimum length of 490 mm instead of 500 mm.

Aged specimens have been tested in a dry condition, after accurately washing the yarns with water and removing the excess solid deposit of $Ca(OH)_2$ on the surfaces (Figure 2.4b). Then the panels were left to dry in laboratory conditions for at least 7 days before cutting and testing.



(a) (b)

Figure 2.4. a) conditioning of FRP grids in tanks; b) washing of FRP grids after conditioning

2.4 Conditioning of FRCM coupons

The dimensions of the FRCM coupons were 500x60x10 mm, comprising 5 longitudinal yarns. FRCM coupons were fabricated using dry fibreglass mesh cut to the dimensions of 500x60 mm, utilizing steel moulds lubricated with mineral oil to facilitate demoulding (24-48h after production casting). A 5 mm layer of mortar was prepared in the mould and levelled before inserting the mesh (Figure 2.5). The coupon was then completed with the remaining 5 mm of mortar.

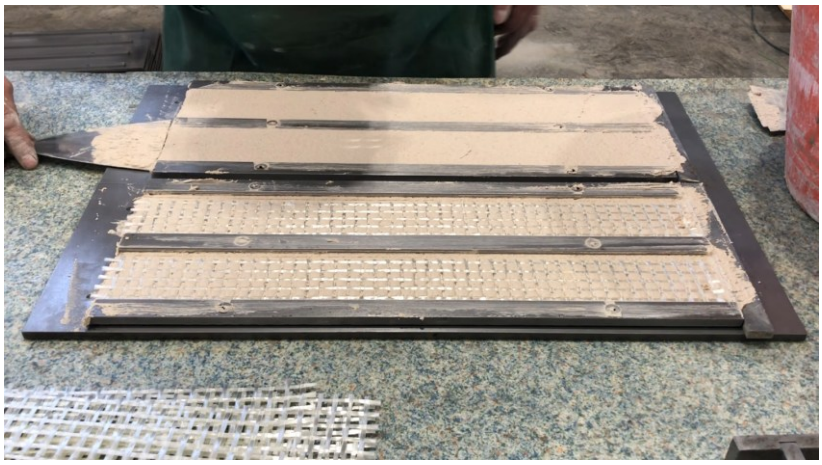


Figure 2.5. Preparation of FRCM coupons

After demoulding (24–48 hours post-production), the specimens were left in plain water at the specified temperatures (23 °C or 40 °C) for 1000 h, 2000 h, and 3000 h. They were then left to dry under laboratory conditions for 168 h (7 days) and subsequently tested at ages of 1168 h, 2168 h, and 3168 h (five specimens for each duration).

For unconditioned FRCM, the tensile coupons were immersed in plain water at normal temperature (23 °C) for 21 days. They were then left to dry under laboratory conditions for 7 days and subsequently tested at an age of 28 days.

For FRCM aged textile samples, the dry fibreglass mesh was pre-cut to size and conditioned in two stainless steel tanks, with FRP grid elements used as spacers in between (Figure 2.6a). Each group of textiles was exposed to a different exposure scenario (six scenarios: 1000 h, 2000 h, and 3000 h for T1 and T2). The textiles were then left to dry for at least 7 days before preparing the FRCM coupons. After demoulding, the coupons were cured in the same environments as the textiles and for the same conditioning durations (Figure 2.6b).

All specimens were left to dry in laboratory conditions for 7 days before testing.



(a) (b)

Figure 2.6. a) preparation of dry fibreglass meshes for immersion; b) conditioning of FRCM coupons

2.5 Tests on yarns

2.5.1 Labelling

The specimens were labelled with an alphanumeric string segmented into four components: specimen type (Y = yarn), environmental conditions and temperature (U = unconditioned; A23/40 = environment A at 23/40°C), conditioning duration in hours, and sample identification number (e.g., Y-A23-2000-2).

2.5.2 Tensile testing

Tests were carried out according to ISO 3341:2000 [227], using an electromechanical universal testing machine Galdabini Sun 2500, which features a constant rate of elongation (CRE). A control unit was used to record the load applied to the specimen and the displacement between the clamps, since installing a displacement transducer directly on the specimen was not advisable due to the deformability of the fibre yarns. The maximum error in the indicated force, at any point in the range in which the machine is used, did not exceed 1% of the true force and the error in the indicated clamp separation did not exceed 0.01 mm. The tests were stopped upon reaching a 50% decrease in resistance. The load and the displacement were recorded at a frequency of 10 Hz.

According to the standard, the design of the clamps is critical to obtaining correct breaks and consistent results. The clamps shall be capable of holding the specimens without slippage and without visible damage and shall be designed so that breaks do not occur within 10mm of the jaws. During testing, locating failure on the specimen proved challenging due to the high thread count. Consequently, various types of clamping systems were evaluated in our tests to assess their impact on the results. The gripping methods tested are presented in Figure 2.7.

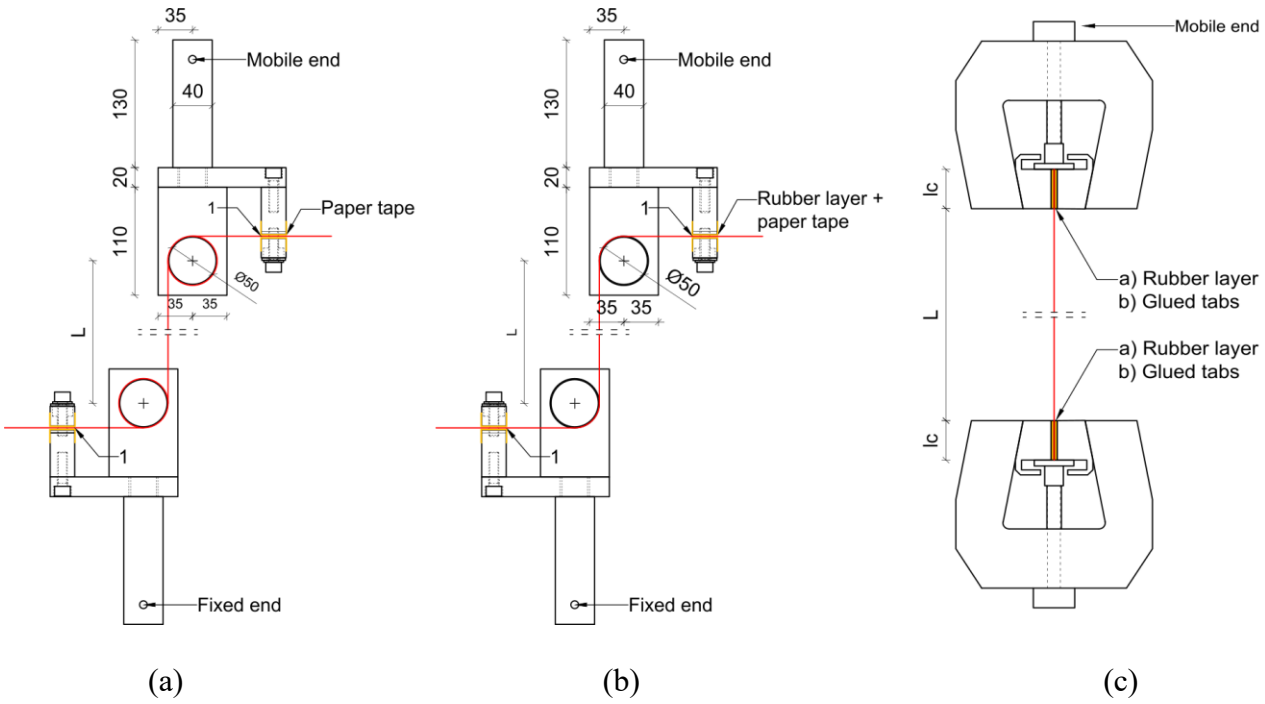


Figure 2.7. Clamp configurations for dry fibre yarns used at UniTS: (a) radiused clamps; (b) radiused clamps with full yarn wrap; (c) wedge jaws with different interposed layers (dimensions in mm)

The radiused clamps have a diameter of 50 mm, and the two faces of the grips, which hold the specimen, were covered with paper adhesive tape to facilitate gripping of the yarn without causing damage. The gauge length (L) for specimens was 500mm. A pretension f 9 N (3.75 mN/Tex) was applied before staring the tests.

In the first gripping method that was tested (Figure 2.7a), the yarn was wrapped around the radiused clamps once, before being secured in the fixation system (labelled as number 1 in the figure). This system was tested because, as the tension in the yarn increased, the force of wrapping also increased, reducing potential slippage.

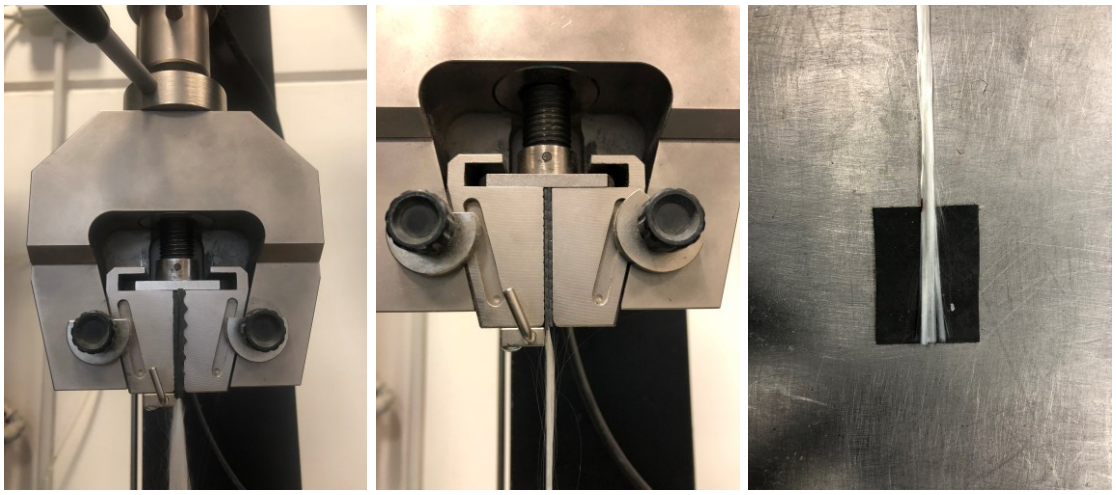
However, during the testing of aged specimens, localized fibre failures were observed in the wrapping region already at the specimen installation stage. These premature failures are attributed to the increased fragility of the fibres after ageing, which resulted in a reduced tensile capacity of the corroded fibre sections. In this condition, the additional stresses induced by yarn wrapping around the clamp were sufficient to trigger fibre rupture, even before the application of the pretension load.

Therefore, the observed failures cannot be attributed solely to the gripping system itself, but rather to the combined effect of the test set-up and the degradation of the fibres due to ageing. To mitigate this issue and reduce stress concentrations at the clamp, a second

gripping method without yarn wrapping around the radiused clamps was adopted (Figure 2.7b), with the aim of limiting premature fibre breakage during specimen installation. This method also involved the addition of a white rubber layer to the fixation system, placed under the paper tape. Despite this modification, some fibre ruptures were still observed prior to testing. Therefore, to further address this issue, a third gripping method was adopted, consisting of a gripping system with steel wedge jaws (Figure 2.7c), in which different materials were tested in the gripping area:

- Rugged rubber with a thickness of 3 mm (Figure 2.8a);
- Smooth rubber with a thickness of 1 mm (Figure 2.8b, c);
- Glued tabs (Figure 2.9).

The systems tested are presented in Figure 2.8.



(a) (b) (c)

Figure 2.8. Clamping jaws with interposed rubber layers: (a) 3 mm thickness; (b) 1 mm thickness and c) positioning of the yarn on the rubber layer

For glued tabs, they were made of pultruded plates (35x40 mm) with a thickness of 5 mm, glued with epoxy resin with the material properties reported in Table 2.11. Prior to gluing, the specimens were kept straight by using steel weights on both sides (Figure 2.9).

An overview of the different tested gripping methods is presented in Table 2.12.

.

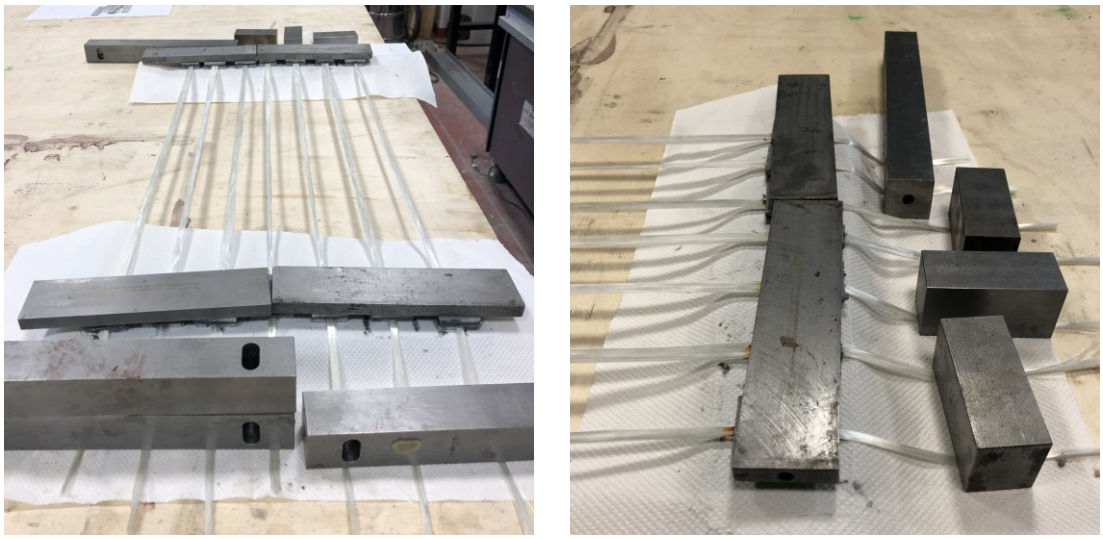


Figure 2.9. Preparation of glued tabs in dry fibreglass yarn tests

Table 2.11. Technical sheet of the epoxy resin used for gluing tabs in yarn tests

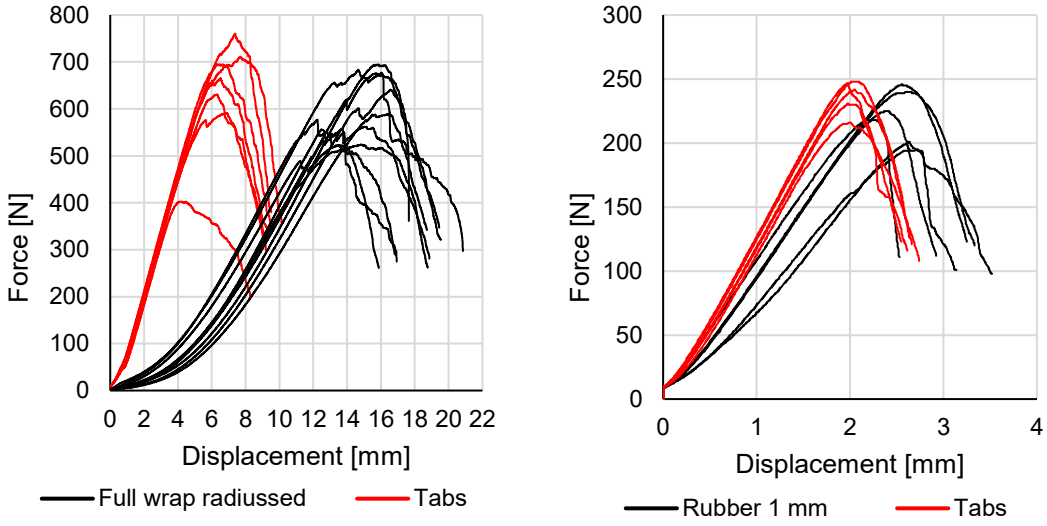
Commercial name	FB-RC30/3
Type of resin	Two-component thixotropic epoxy
Full curing time at 20 °C	7 dd
Tensile strength [234]	60 MPa
Tensile elastic modulus [234]	3000 MPa
Elongation at break [234]	2.9 &
Compressive strength [235]	60 MPa

Table 2.12. List of clamping systems tested for different clamping systems

Environment (temperature)	**Conditioning time** (hours)	**Radiused wrapped**	**Radiused**	**Jaws rubber 3 mm**	**Jaws rubber 1 mm**	**Jaws with glued tabs**
Unconditioned	-	X	-	-	-	X
A (23°C)	1000	X	-	-	-	X
	2000	-	-	-	-	X
	3000	-	-	X	X	X
A (40°C)	1000	X	-	-	-	X
	2000	X	X	-	-	X
	3000	-	-	X	-	X

All the clamping systems tested exhibited higher displacements between the clamps compared to the glued tabs. For this reason, the latter was considered more accurate in

determining the elongation at break (see comparison in *Figure 2.10*) and was adopted for all the tests.



(a) (b)

Figure 2.10. Comparison between clamping systems: (a) unconditioned yarn tests; (b) A23-3000 tests.

2.5.3 Results

For each set of specimens, the arithmetic means of the following properties were determined:

- breaking force (in Newtons);
- elongation at break, expressed as a percentage of the gauge length;
- breaking strength, calculated in Newtons per Tex from the mean breaking load.

The results of the tensile tests are reported in Table 2.13 and Figure 2.11. The plots of the force-displacement curves are reported in Appendix A.

Table 2.13. Results of the tensile tests on dry fibreglass yarns

Temperature	**Ambient**	**23°C**			**40°C**		
Conditioning time (h)	Unconditioned	1000	2000	3000	1000	2000	3000
Average Breaking Force (N)	675.7	428.3	301.6	236.4	178.8	165.0	109.3
Standard deviation (N)	54.8	32.4	12.5	12.0	22.1	33.0	5.9
Average elongation at break (%)	1.39%	0.72%	0.55%	0.41%	0.32%	0.37%	0.21%
Standard deviation (%)	0.10%	0.06%	0.02%	0.01%	0.05%	0.08%	0.02%
Average Breaking Strength (N/Tex)	0.282	0.178	0.126	0.099	0.075	0.069	0.046

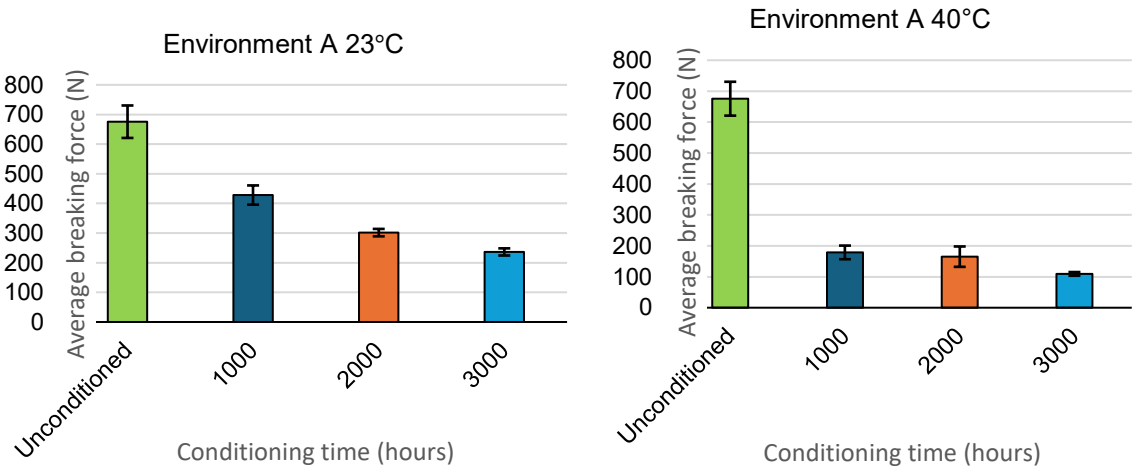


Figure 2.11. Results of the tensile tests on dry fibreglass yarns

The conditioning significantly reduced the strength of the dry fibreglass yarns in respect to the unconditioned specimens by the following quantities:

Environment A 23°C:

- -36.6 % at 1000 h;
- -55.4 % at 2000 h;
- -65.0 % at 3000 h.

Environment A 40°C:

- -73.5 % at 1000 h;
- -75.6 % at 2000 h;
- -83.8 % at 3000 h.

The elongation at rupture decreased proportionally with specimen strength as a result of progressive corrosion-induced damage.

2.6 Tests on GFRP grids

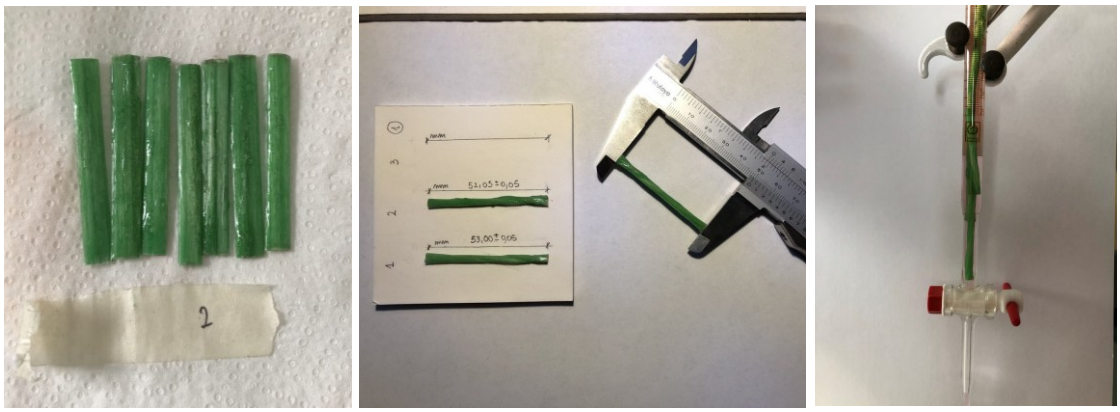
2.6.1 Labelling

Specimens are labelled with an alphanumeric string segmented into four components: specimen type (WA=warp direction, WE=weft direction), environmental conditions and temperature (U=unconditioned; A/C 23/40/60=environment A/C at 23/40/60°C), conditioning duration in hours, and sample identification number (e.g., WA-C60-6000-3).

2.6.2 Cross section determination on FRP bars

To evaluate the cross section, the CNR-DT 203/2006 [208] proposes the method of ACI 440.3R-04 [236], initially applied to FRP bars and adapted to GFRP meshes. The principle of the method is to determine the cross section from the length of the specimen and its volume, measured by the displacement of the liquid inside a graduated cylinder or burette, as also proposed by EAD 340392-00-0104 [226]. Additionally, according to ISO 10406-1 [229] (section 5), the minimum length of samples should be at least 100 mm. The volume measurement was conducted with a class A graduated burette with a capacity of 25 ml and a sensitivity of 0.025 ml. To fill the burette, 70.5° ethanol alcohol was used to reduce the amount of air bubbles trapped inside the liquid. The measurement was conducted at least one minute after the immersion of the specimens.

For all tensile tests, the cross-section considered was that of the unconditioned FRP grids. A minimum of 5 specimens were tested for each winding direction (WARP and WEFT). Each specimen comprised 7 segments, each approximately 50 mm in length, ensuring they were cut orthogonally to their longitudinal direction (Figure 2.12).



(a) (b) (c)

Figure 2.12. Cross section determination on FRP bars: a) specimens; b) length measurements with a calliper; c) volume measurement with a graduated burette.

Table 2.14. Results of the cross-section determination on FRP bars

WARP sample	**A_{mean}** (mm^2)
1	10.7 ± 0.2
2	7.3 ± 0.2
3	7.2 ± 0.2
4	8.7 ± 0.2
5	8.1 ± 0.2

WEFT sample	**A_{mean}** (mm^2)
1	13.2 ± 0.2
2	10.8 ± 0.1
3	11.5 ± 0.2
4	12.6 ± 0.2
5	10.8 ± 0.1

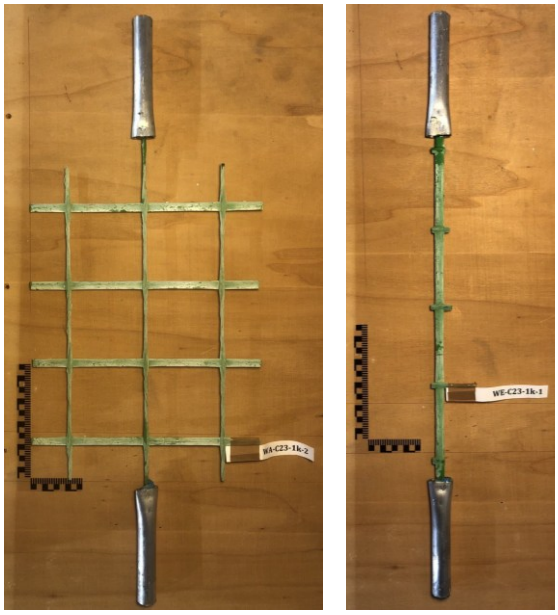
The mean cross-sectional areas for WARP and WEFT samples are 8.4±0.2 mm^2 and 11.6±0.2 mm^2, respectively.

2.6.3 Tensile testing

Tests were carried out according to EAD 340392-00-0104 ANNEX B [226]. To prevent the rupture of the specimen in the grip zone, a pair of tabs was installed to the ends of the specimens. The tabs were made using aluminium tubular profiles (16 mm diameter, 1.5 mm thickness, 100 mm length), filled with low viscosity epoxy resin with the mechanical properties reported in Table 2.15. The sample was kept centred in the tab by utilizing a cap made of ethylene-vinyl acetate at both ends, with a centred hole. The end of the tube pointing towards the specimen was closed by deforming it with a bench vise when the resin was still liquid, by taking care to not damaging the specimen. This measure was introduced to prevent slippage of the whole resin block from the aluminium cylinder.

Table 2.15. Technical sheet of the epoxy resin used for gluing tabs in FRP grid tests

Commercial name	Kerabuild Epofill
Type of resin	Two-component epoxy
Density of the mixture	1100 kg/m^3
Viscosity of the mixture	380 mPa×s



(a) (b)

Figure 2.13. WARP (a) and WEFT (b) samples before testing

The tensile testing machine adopted is equipped with a calibrated load cell (20 kN capacity) classified in class 1 with reference to EN ISO 6892-1 [237]. The clamping heads are made with wedge tensile grips. The load cell was zeroed before installing the samples, and the initial conditions were restored with the sample installed before starting the recording, considering the axial rigidity of the sample. One displacement transducer with a measurement length of 100 mm with a sensitivity of 1/1000 mm was installed at the centre of the sample on a gauge length of 70 mm to calculate the strain until failure (Figure 2.14a, b). The load and the displacement were recorded at a frequency of 10 Hz.



(a) (b)

Figure 2.14. Installation of WARP (a) and WEFT (b) samples in the testing machine.

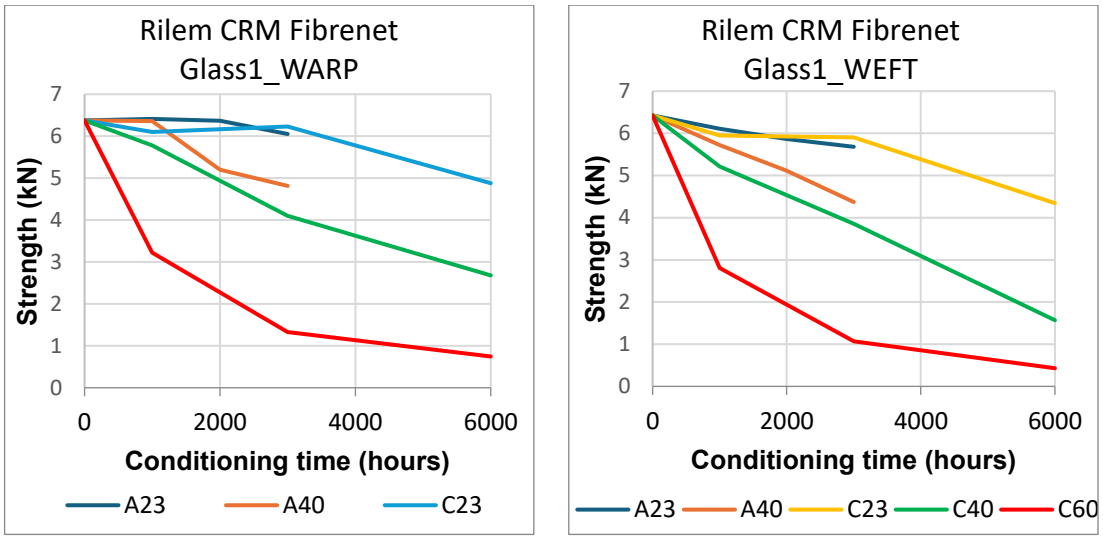
The tests were conducted manually, trying to maintain a constant rate of loading between 0.5% and 1.5% strain per minute, as specified in ISO 10406-1 (Section 6).

2.6.4 Results

For each set of specimens, the tensile load, tensile strength, Young's modulus, and ultimate strain were calculated as described in ISO 10406-1. The Young's modulus was calculated based on the stress-strain curve obtained from the load levels at 20% and 50% of the tensile capacity. The ultimate strain was defined as the strain corresponding to the ultimate tensile capacity, given that displacement measurements were available up to failure. In cases where the displacement measurements were not available up to failure, the ultimate strain was computed by dividing the ultimate stress by the elastic modulus.

The results of the tensile tests are reported in and in Figure 2.16, Figure 2.17 and Figure 2.18. The plots of the force-displacement curves are reported in Appendix A.

The conditioning process resulted in a reduction in the strength of the FRP grid bars compared to the unconditioned specimens, with more significant reductions observed in hotter conditioning environments, as indicated in Table 2.16 and Figure 2.15.



(a) (b)

Figure 2.15 Strength vs conditioning time results of tensile tests on GFRP mesh wires: (a) WARP and (b) WEFT

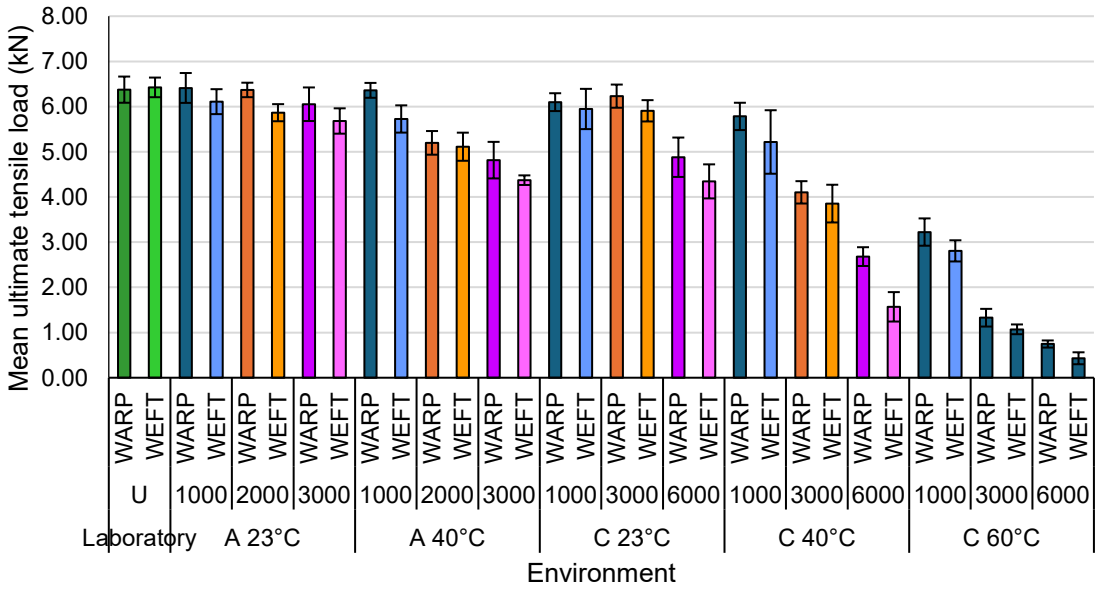


Figure 2.16. Mean ultimate tensile load (kN)

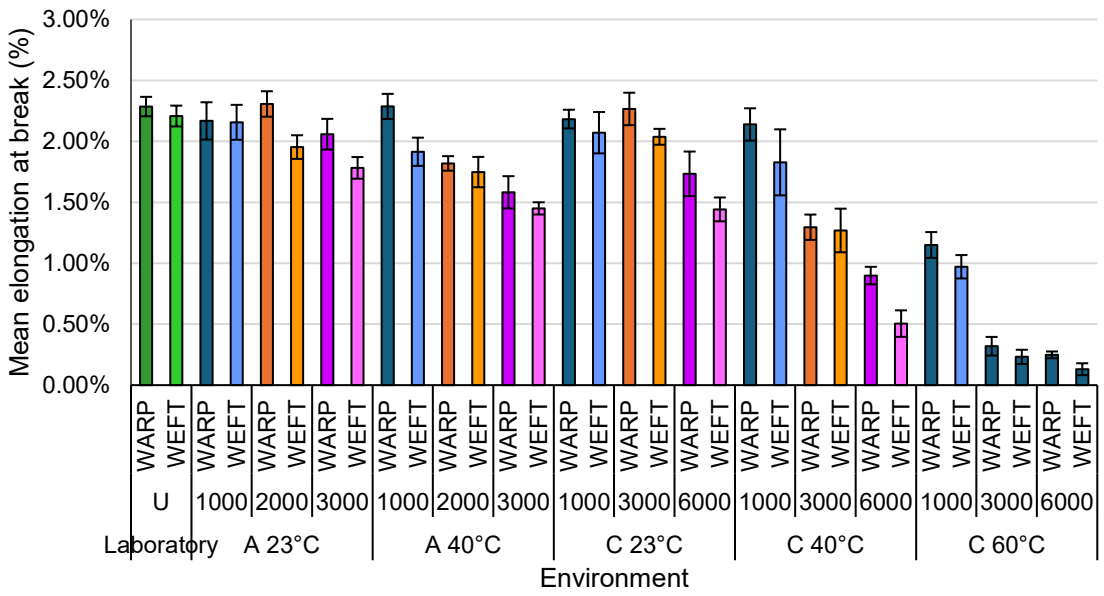


Figure 2.17. Mean elongation at break (%)

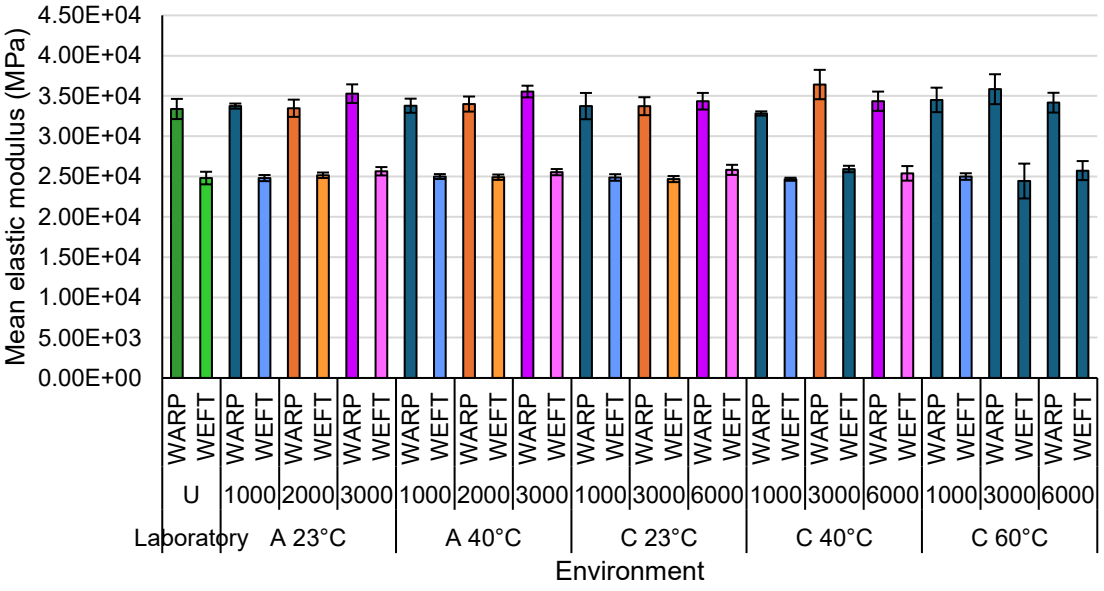


Figure 2.18 Mean elastic modulus (MPa)

Table 2.16. Ratios between the strength of conditioned and unconditioned specimens

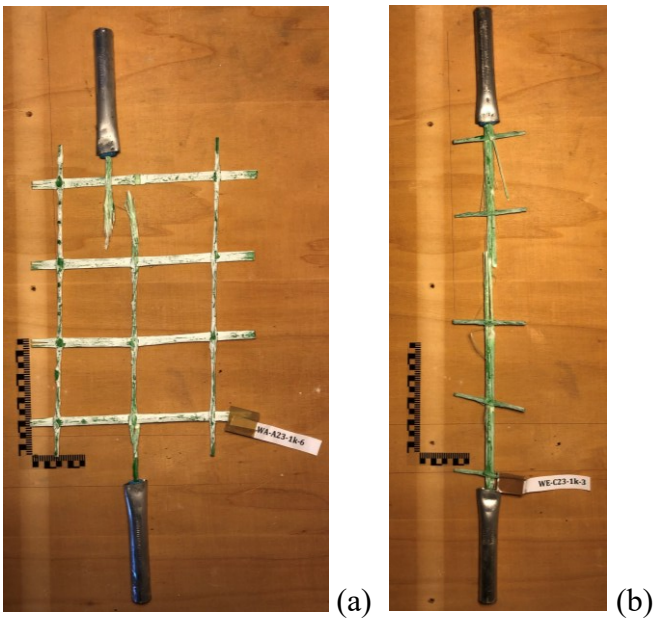
Environment (temperature)	**Conditioning time** (hours)	**WARP FRP grid**	**WEFT FRP grid**
A (23°C)	1000	100%	95.8%
	2000	99.9%	92.0%
	3000	94.9%	89.1%
A (40°C)	1000	99.8%	89.8%
	2000	81.5%	80.2%
	3000	75.5%	68.6%
C (23°C)	1000	95.7%	93.3%
	3000	97.7%	92.7%
	6000	76.5%	68.2%
C (40°C)	1000	90.7%	81.8%
	3000	64.4%	60.4%
	6000	42.0%	24.6%
C (60°C)	1000	50.6%	44.0%
	3000	20.8%	16.8%
	6000	11.7%	6.8%

The elastic modulus remained unaffected by the conditioning, in agreement with the results from the yarn tests (

Appendix A), tensile fatigue testing reported in the literature [238], and tensile tests on FRP bars documented in another study [239].

In general, the WEFT samples exhibited lower resistance compared to the WARP samples, with a difference of approximately 5-10% in resistance for conditioning environments at 23°C and 40°C, except for the C40 environment at 6000h which showed a resistance ratio of 58%. For the C60 environment, the resistance ratios were 87.1%, 80.6%, and 57.7% for conditioning times of 1000 hours, 3000 hours, and 6000 hours, respectively.

In WARP samples, failures predominantly occurred near the first node, adjacent to the tab (Figure 2.19a). In WEFT samples, failure was more widespread, characterized by longitudinal fracturing of the external fibres across the sample (Figure 2.19b).



(a) (b)

Figure 2.19. Typical failure modes of WARP (a) and WEFT (b) samples during tensile testing

2.7 Tests on mortar prisms

2.7.1 Labelling

Specimens are labelled with an alphanumeric string segmented into three components: system type (CRM), environmental conditions and temperature (U = unconditioned) and sample identification number (e.g., CRM-U-1).

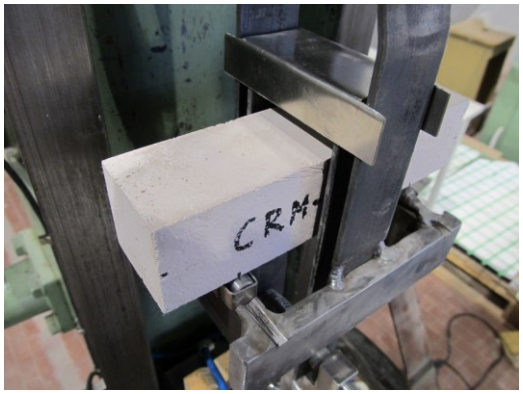
2.7.2 Preparation and curing

The mortar used in each system was utilized for sampling one set of three mortar prisms (160x40x40 mm), which underwent curing and testing under laboratory conditions, following the specifications outlined in UNI EN 1015-11 [35]. The mortar prisms were cured at 20°C in a polyethylene bag for the first 7 days, after which they were transferred to a metallic grid in an environment with a relative humidity of 65% ± 5% until the day of testing, which occurred at 28 days of curing.

2.7.3 Bending and compression tests

The three-point bending tests (Figure 2.20a) to assess the flexural tensile strength of mortar was carried out using a tensile testing machine equipped with a calibrated load cell (20 kN capacity) classified in class 1 with reference to EN ISO 6892-1. The load cell was zeroed after installing the sample. The distance between supports was 100 mm.

The compression tests (Figure 2.20b) were conducted following the flexural tests on prism halves, using rectified steel plates with a Vickers hardness of at least 600 HV, measuring 40x40 mm.


(a)

(b)

Figure 2.20. Test setups for flexural tests on mortar prisms (a) and compression tests on prism halves (b)

The tests were conducted manually, trying to maintain a constant rate of loading between 10 N/s and 50 N/s for flexural tests and approximately 400 N/s for compression tests. The load and the displacement were recorded at a frequency of 10Hz.

2.7.4 Results

To determine the mass weight of the mortar, the dimensions and weights of the prisms were measured with a calibrated calliper and a scale with a sensitivity of 1 g, respectively. The flexural and compressive resistance of the specimens was determined by calculation according to UNI EN 1015-11. The results are summarized in Table 2.17.

Table 2.17. Results of the flexural and compression tests on mortar prisms

FLEXURAL TEST #	1	2	3	4	5	6
Label	CRM-U-1	CRM-U-2	CRM-U-3	CRM-U-4	CRM-U-5	CRM-U-6
Age of the specimen (h)	667	667	667	660	660	660
Specific weight (kg/m^3)	2026	2032	2032	2003	2009	2001
Flexural Strength (MPa)	3.84	5.21	4.41	4.14	3.64	3.59
COMPRESSION TEST #	1	2	3	4	5	6
Compressive Strength (MPa)	24.16	23.35	23.03	22.95	23.22	23.32

The average compressive strength is 23.34 MPa (CoV=1.9%), while the average flexural tensile strength is 4.14 MPa (CoV=14.7%). According to the technical sheet, the flexural tensile strength at 28 days of curing should be ≥ 2 MPa, while the compressive strength at the same curing time should be ≥ 15 MPa.

The tests on mortar conditioned in water for up to 3000h were not performed as these tests were part of the FRCM testing which was discontinued due to the inefficiency of the system, as reported in the following section.

2.8 Tests on FRCM coupons

As mentioned previously, the tests were discontinued due to the slippage of the mesh within the mortar during tensile testing.

2.8.1 Labelling

Specimens are labelled with an alphanumeric string segmented into four components: specimen type (FRCM), environmental conditions and temperature (U=unconditioned; A/W 23/40=environment water/A at 23/40°C), conditioning duration in hours, and sample identification number (e.g., FRCM-W40-1000-4).

2.8.2 Tensile testing

The tensile testing machine that was designed (Figure 2.21) is equipped with a calibrated load cell (50 kN capacity) classified in class 1 with reference to EN ISO 6892-1. The clamping heads are made with bolted steel plates with added steel spacers (8 mm in thickness) to provide sufficient clearance for attachment to the ball joints. The grips are rotationally self-aligning to minimize bending stresses in the coupon. The specimens were equipped with a set of glued tabs in the gripping area to ensure homogenous distribution of stresses. The tabs were made of pultruded plates (60x100 mm) with a thickness of 5 mm, glued with epoxy resin with the material properties reported in Table 2.10. A pretension of 5% of the foreseen failure load is applied to the specimen. Previous studies [213] on the same system suggest an anticipated ultimate load of 2.9 kN, resulting in a pretension of 0.15 kN. The four bolts on each plate were tightened with a torque of 50 Nm each to ensure sufficient static friction force on the sample for the anticipated ultimate load.

The load cell was zeroed after installing the sample. Two displacement transducers, with measurement lengths of 25 mm and a sensitivity of 1/100 mm were installed on each side of the specimen with steel brackets, with a gauge length of 265 mm to calculate the strain until failure. The load was applied under displacement control, with a constant rate of 0.2 mm/min in the non-cracked phase and crack formation phase and it was increased manually at 0.5 mm/s after the first crack formed. Due to the control unit limitations, the load and the displacement were recorded at a frequency of 1 Hz.

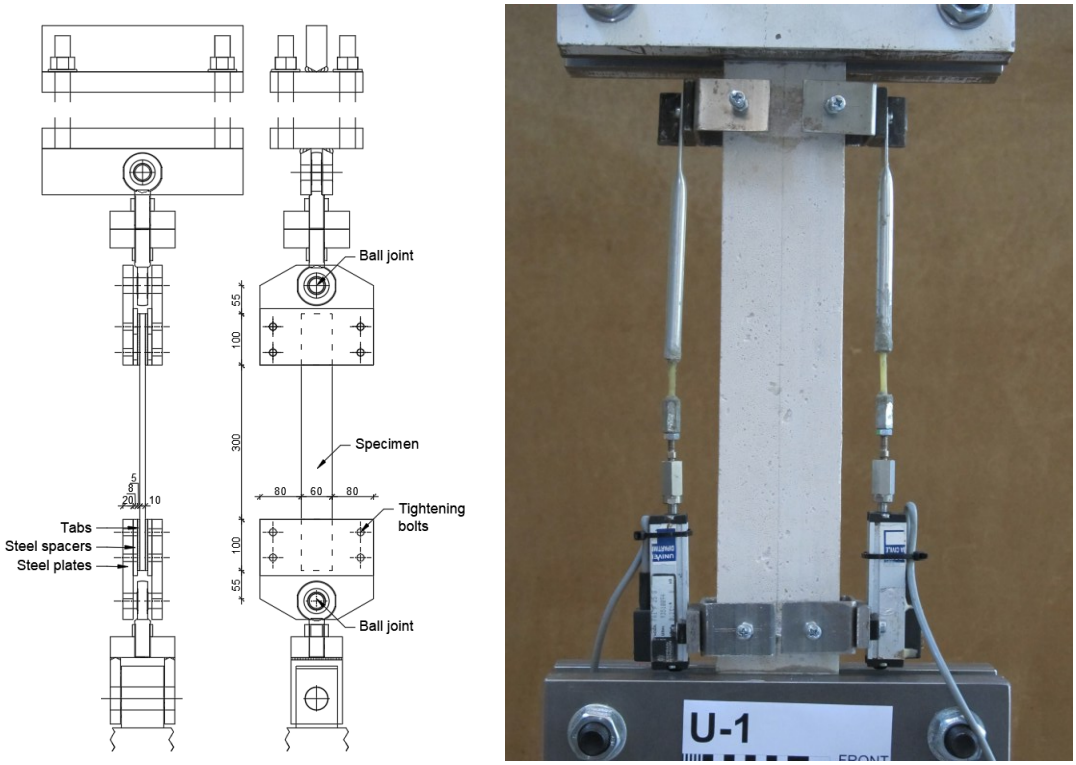


Figure 2.21. Test setup for FRCM tensile tests

The low bending resistance of the samples made their installation in the machine complicated, due to the presence of the ball joint hinge at the base and the tightening mechanism with bolts, resulting in their cracking before starting the test.

2.8.3 Results

Three tests were conducted on samples FRCM-U-2, 6, and 7. During the tests on samples 2 and 7, a crack developed outside the gauge length (Figure 2.23a), resulting in the inability to maintain a constant rate of loading. In sample 6, two cracks were deliberately induced at approximately one-third of the gauge length prior to testing to assess the system's ability to distribute stresses between the mesh and the mortar. In the latter case (Figure 2.23b), only one of the cracks propagated, indicating slippage of the mesh within the sample. The test results are presented in Figure 2.22.

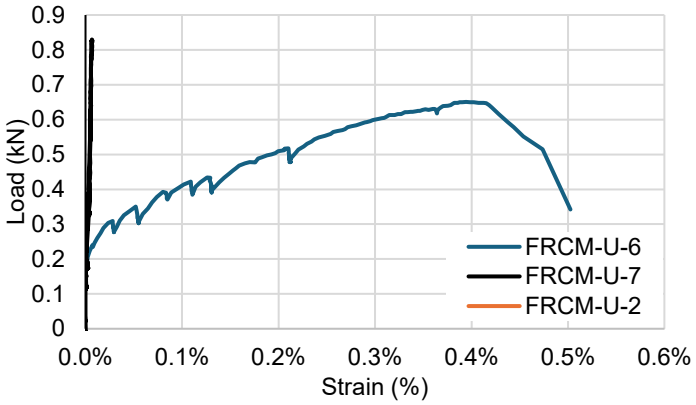


Figure 2.22. Results of the FRCM tensile tests

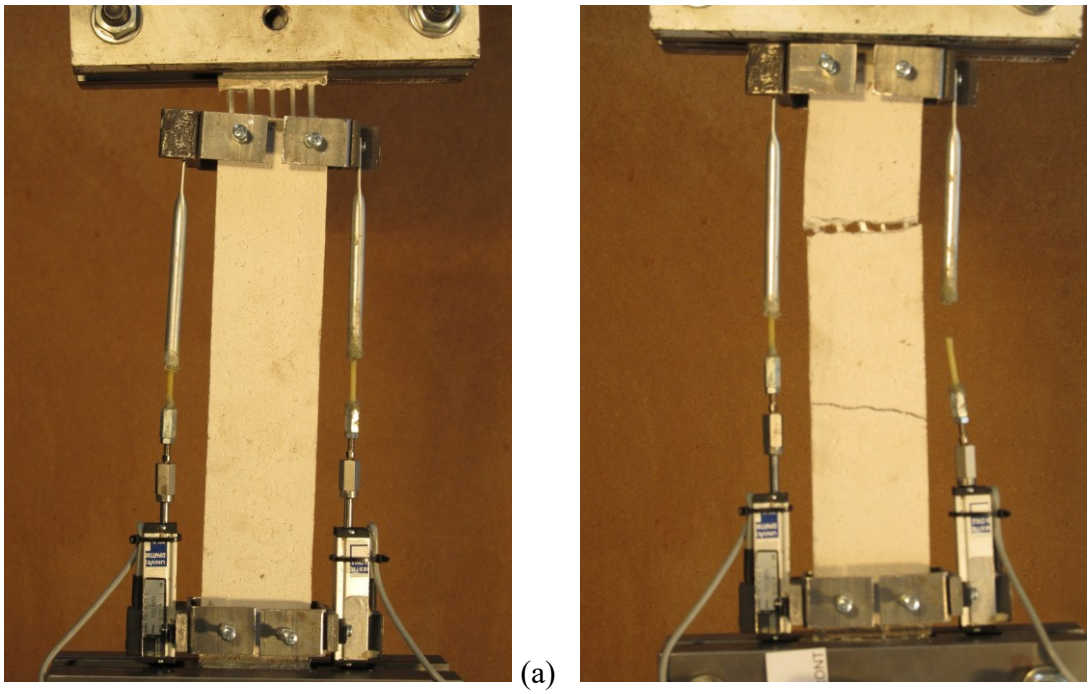


Figure 2.23. Crack pattern of the tensile tests on FRCM coupons: a) FRCM-U-2; b) FRCM-U-6

The resistances recorded by the system indicate that slippage began at an average value of 0.70 kN, which is approximately 24% of the anticipated failure load. Further investigation led to the conclusion that the system should have included an adhesion-promoting component applied at the mesh-mortar interface. As this component was not supplied by the manufacturer, the testing campaign on this system was discontinued. Future investigations should therefore assess the performance of the system including the adhesion promoter.

Similar issues were reported by the laboratory of Xi'an Jiaotong–Liverpool University, which employed a comparable test setup. Conversely, the laboratory of the University of Calabria, using a universal testing machine equipped with properly aligned grips, obtained improved results and was able to observe multiple cracking, although this behavior was limited to unconditioned specimens.

2.9 Conclusions

Durability and long-term performance of composite strengthening systems remain a critical concern for the rehabilitation of masonry structures. The results of the present study demonstrate that environmental exposure at elevated temperature in alkaline conditions, significantly affects the mechanical behavior of TRM and FRP materials, with notable reductions in tensile strength and elongation at break, observed in both dry fibreglass yarns and GFRP grids. Moreover, the tests highlighted practical issues in current testing regulations, such as slippage and difficulties in clamping dry fibre yarns, which can influence the reliability and reproducibility of experimental measurements. Bonding the yarns with epoxy on pultruded sheets and maintaining them under slight tension during curing allowed the tests to exploit the tensile capacity of the yarns, using wedge jaws to fix the specimens in the testing machine.

After 3000 hours of conditioning, tensile tests revealed that the strength of dry fibreglass yarns decreased by 65% and 84% at 23°C and 40°C, respectively. The current observations can be the criticalities of the clamping system proposed in the guidelines for testing: the radiused clamps caused partial premature fibre breaks. Additionally, wrapping the yarn on the steel cylinder increased slippage. Using wedge jaws with glued tabs provided the most reliable measurements.

For the FRP grids, strength reductions depended on both the exposure conditions and the fibre orientation. WARP fibres consistently retained higher strength than WEFT fibres, with differences of 5-10% in most cases. After 3000 h at 40 °C, the strength of WARP fibres decreased to 76% under Environment A and 64% under Environment C, while WEFT fibres dropped to 69% and 60%, respectively. On average, Environment C was more aggressive than Environment A. Failure modes also varied with orientation: WARP samples fractured mainly near the first node, whereas WEFT samples showed longitudinal fibre breaks along the sample. The adopted test setup allowed to fully exploit the tensile capacity of the bars, with all failures occurring outside the gripping area.

Although the mortar was classified as M15, it exhibited significantly higher strengths after 28 days, showing a compressive strength of approximately 23 MPa in compression and 4 MPa in flexural tension.

The FRCM system did not achieve the anticipated tensile performance because the dry fibreglass mesh slipped within the mortar, emphasizing the necessity of including

adhesion-promoting components in the design of composite systems. In some tests, cracks appeared outside the gauge length, highlighting the challenge of accurately monitoring displacements during tensile testing. Due to the low flexural resistance of the coupons, a test setup with properly aligned tensile grips is preferable to minimize accidental failures during the installation of the samples.

Although accelerated ageing tests are effective for identifying degradation trends but still require correlation with real-time exposure to predict service life. Future research should aim to establish these correlations.

3 Experimental campaign on CRM strengthened masonry structural elements

The tests performed in this study are part of the test campaign carried out within the Interreg CONSTRAIN Project[2]. To investigate the effectiveness of the CRM coating system under seismic conditions, the experimental campaign included: tests on materials, compression-bending and shear tests on piers, shear-bending tests on spandrels, OOP tests of top bond beams and full-scale cyclic tests on a two-storey rubblestone masonry building, as presented in Table 3.1. The objective of these tests is not only to assess the improvement in seismic performance but also to determine whether the coating and the existing brick masonry can work together as a composite load-bearing structural element under demanding earthquake loading conditions.

The results of the tests presented in this study have been published in six papers [142], [147], [141], [144], [240], [148].

[2] https://2014-2020.ita-slo.eu/en/constrain

Table 3.1: Summary of the experimental program carried out within the CONSTRAIN project

Type of test	Masonry type	Sample ID	Strengthening
In-plane tests on masonry piers	Stone R2	P-R2U	/
	Stone R2	P-R2R-1	CRM on one-side
	Stone R2	P-R2R-2	CRM on two-sides
	Solid brick B2	P-B2U	/
	Solid brick B2	P-B2R-1	CRM on one-side
	Solid brick B2	P-B2R-2	CRM on two-sides
	Solid brick B1	P-B1U	/
	Solid brick B1	P-B1R	CRM on one-side
In-plane tests on masonry spandrels	Stone R2	S-R2U-1	/
	Stone R2	S-R2R-1	CRM on one-side
	Stone R2	S-R2U-2	/
	Stone R2	S-R2R -2	CRM on two-sides
	Solid brick B2	S-B2U-1	/
	Solid brick B2	S-B2R-1	CRM on one-side
	Solid brick B1	S-B1U-1	/
	Solid brick B1	S-B1R-1	CRM on one-side
Out-of-plane tests on piers	Stone R2	B-R2	CRM on one-side
	Solid brick B2	B-B2	CRM on one-side
	Solid brick B1	B-B1	CRM on one-side
Out-of-plane tests on roof ring beams	Stone R2	T-R2	GFRP mesh in bed joints
	Solid brick B1	T-B1	GFRP mesh in bed joints
Out-of-plane tests on floor ring beams	Stone R2	C-R2	CFRP eccentric strips
	Solid brick B1	C-B1	CFRP eccentric strips
Pushover tests on a pilot building	Stone R2	PB-U	/
	Stone R2	PB-R	CRM on one-side

The main characteristics for the materials adopted in the tests that were performed in this study are reported in the following.

3.1 Masonry characteristics

Three different masonry types were considered in the experimental campaign (Figure 3.1): double leaf rubble stone masonry, 350 mm thick (**R2**), double leaf solid clay brick masonry, 250 mm thick (**B2**) and single leaf solid clay brick masonry, 250 mm thick (**B1**).


(a)

(b)

Figure 3.1. Masonry types (a) R2, (b) B1 and B2

The stone units were a mix of two Credaro[3] stones: Berrettino (sandstone) and Medolo (limestone), with approximate compressive and flexural strengths of 160 MPa and 20 MPa, respectively. The units had approximate dimensions of 150×100×210 mm (width x height x length), laid in a two-leaves masonry configuration, although there was substantial size variability between the elements. These stones are sandstone type with a calcareous composition. Berrettino is a mainly carbonate (calcarenite) rock made of minute detrital grains with evident stratification and a yellow-brown or pink colour. In contrast, Medolo comprises almost entirely microcrystalline calcium carbonate (crystalline limestone) with a very fine grain size and a hazelnut-grey colour. The thickness of the joints was about 10 mm but varied significantly due to the irregular shape of the stones.

The solid clay bricks (120×55×250 mm, width x height x length) had a surface roughness replicating the typical appearance of old masonry structures and had a nominal compressive strength of 18 MPa. The bricks in the samples were arranged in two different bond patterns with mortar joints about 10 mm thick. The first (for masonry B2) replicated a double-leaf masonry wall composed of two adjacent, independent wythes made up

[3] http://www.naturalstoneinfo.com/download/bgcamcom.pietra_credaro.pdf

following the “stretcher bond”; headers were provided at the ends of alternating rows. The second (for masonry B1) followed the “English bond”, alternating courses of headers and stretchers, with headers laid centred over the stretchers in the course below.

The concrete foundation blocks used as a base to construct the samples were wetted before the first layer of mortar was spread, and the stones/bricks were soaked in water before construction. The stones were shaped by a hammer before laying.

All the masonry types were assembled with a natural lime mortar simulating the weak mortar typically found in historical buildings [241]. It was a mixture of natural hydraulic lime and sand, in a lime-to-sand ratio of 1:7 by mass (i.e., 200 kg hydraulic lime and 1400 kg of sand per m^3 of mortar). The aggregate’s grain size distribution ranged from 0.05 to 3 mm, with approximately 45% of the sand particles being smaller than 0.5 mm (Figure 3.2). To determine the bending and compressive strengths, standard prisms (160×40×40 mm) were sampled during construction for different samples. The prisms were later tested in accordance with EN 1015-11 (Figure 3.3) [35]. The mean values of flexural ($f_{b,f}$) and compressive strength ($f_{b,c}$) are reported in Table 3.2.

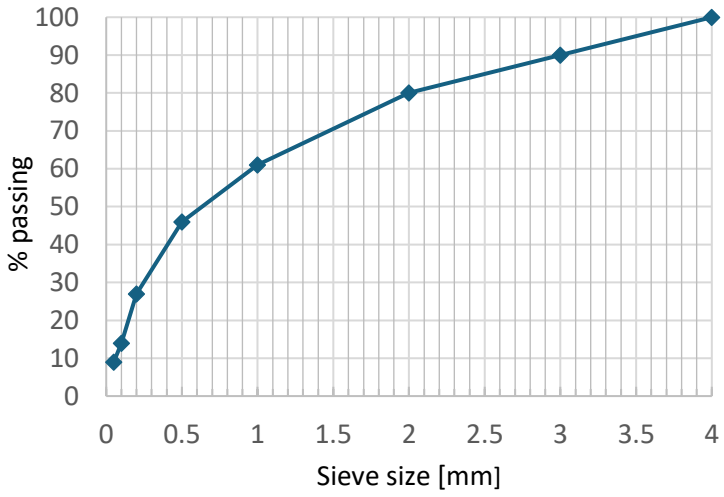


Figure 3.2. Sieve mortar curve

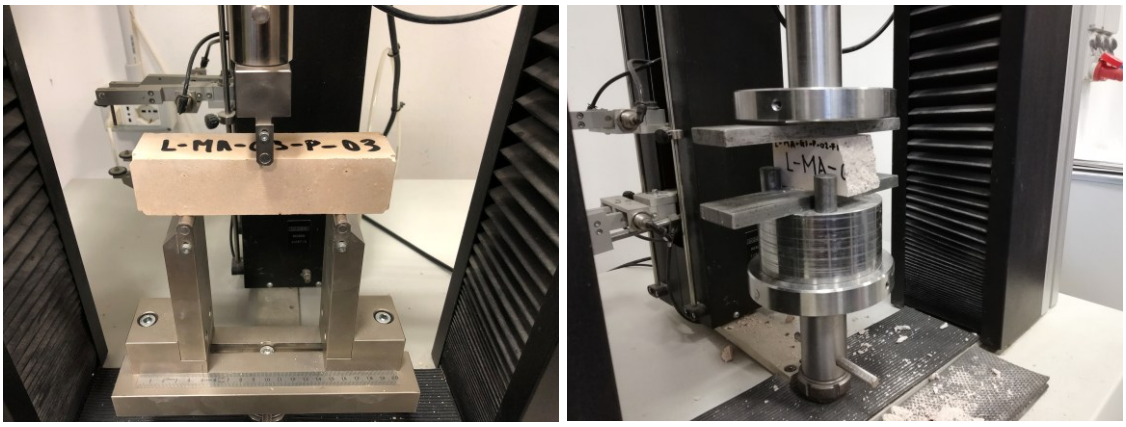


Figure 3.3. Testing flexural (left) and compressive strength (right)

Table 3.2 Mechanical properties from tests on masonry prisms

Ref. sample name	n° samples	Age [days]	Mechanical properties	
			$f_{b,f}$ [MPa] (CoV %)	$f_{b,c}$ [MPa] (CoV %)
S-R2-1, A3_1, A3_1	-	-	0,23 (18 %)	1,11 (17 %)
S-R2-2	21	36	0,36 (23%)	1,95 (12 %)
S-B1	/	/	/	/
S-B2	21	38	0,30 (15 %)	1,86 (6 %)
A2_1, A2_2	6	34	0,30(10 %)	1,50 (9 %)
A1_1, A1_1	6	97	0,29 (12 %)	1,63 (7 %)
T1	12	43	0,76 (10 %)	1,99 (11 %)
T2	6	43	0,59 (5 %)	1,62 (7 %)
P-R2U, P-R2R-1, P-R2R-2, B-R2	12	66	0.17 (16%)	0,93 (5 %)

For each of the three masonry types, monotonic compressive tests were carried out on two masonry wallets (500 mm width, 1000 mm height) according to EN 1052-1 [37]; the main test results are summarized in Table 3.3 - Table 3.5.

Table 3.3 Mechanical properties of stone masonry (R2)

Sample ID	Peak force [kN]	Compressive strength [MPa]	Young modulus [MPa]	Ultimate strain [%]
A3_1	451.64	2.58	1162.0	1.2 %
A3_2	416.96	2.38	986.4	2.8 %
Average	434.30	2.48	1074.2	2 %

Table 3.4 Mechanical properties of double-leaf brick masonry (B2)

Sample ID	Peak force [kN]	Compressive strength [MPa]	Young modulus [MPa]	Ultimate strain [%]
A2_1	875.60	6.86	2073.5	1.1
A2_2	750.68	6.00	2293.1	*
Average	813.14	6.43	2183.3	1.1

* Instruments were damaged after reaching a strain of 0.37%

Table 3.5 Mechanical properties of single-leaf brick masonry (B1)

Sample ID	Peak force [kN]	Compressive strength [MPa]	Young modulus [MPa]	Ultimate strain [%]
A1_1*	490.3	3.8	1589.1	0.35
A1_2	852.4	6.7	2341.1	**
Average	852.4	6.7	2341.1	-

* Failure of the sample was eccentric. Values are not considered.
** Instruments were damaged after reaching a strain of 0.3%

3.2 Strengthening techniques characteristics

3.2.1 Description of the CRM strengthening intervention

The technique consisted in the application, on the masonry surface of a mortar coating with preformed Glass Fibre-Reinforced Polymer (GFRP) composite meshes embedded, in combination with the introduction of transversal connectors. The minimum coating thickness (due to surface roughness) was 30 mm. In addition, FRP "L"-shaped connectors are inserted into holes drilled in the masonry and injected with vinyl ester epoxy resin. Additionally, in front of each connector, a FRP mesh sheet is positioned to distribute stresses within the coating.

In case of application of CRM at both sides of the masonry (Figure 3.4a), the holes and the connectors pass through the thickness of the masonry, granting a minimum overlapping within the masonry thickness of 150 mm. In case of application of CRM only on one side of the masonry (Figure 3.4b), a single connector is inserted with a bonding length of 200 mm. However, in case of double or multiple leaves masonry, additional transversal connectors (called "artificial diaton") are also introduced, involving almost the whole masonry thickness, to create the connection between leaves and prevent leaves separation and delamination phenomena (Figure 3.4c). The artificial diaton is composed of a threaded M16 steel bar centred in a cement-based mortar core, which was injected in a transversal hole drilled in the masonry by using a water-cooled core drilling machine, and with a perforated steel washer (150 mm diameter, 4 mm thick) screwed at the head. The term "artificial diaton" recognises a transversal tying element not originally present in the masonry and introduced during the strengthening intervention. In contrast, "non-artificial diaton" or, simply, "diaton", commonly refers as a large stone element arranged as header during the wall construction, connecting the leaves. A perforated thick stainless-steel washer is then installed on the threaded bar to connect the diaton to the reinforcing mesh and interlock with the surrounding mortar.

The strengthening procedure on two sides of the masonry (similar to one-sided application) involved several sequential operations. First, the existing plaster was removed and the mortar joints were scarified by approximately 10 mm. Passing through holes (24 mm diameter) for L-shaped connectors were drilled near mortar joints and cleaned with compressed air. The reinforcing mesh was applied on the wall sides and spacers were installed to position the mesh at the middle of the coating thickness. An

overlap of at least 150 mm was ensured between adjacent mesh sheets. Then, GFRP mesh devices (33 mm grid dimension, 150×150 mm dimension) were positioned cantered at each hole, and the L-shaped connectors were injected into the wall with epoxy resin, providing an overlap of at least 200 mm within the masonry. Finally, the wall surface is moistened before applying the new mortar coating on both sides of the wall.

In case of walls with multiple leaves, for the installation of artificial diatons, the steps were as follows: drilling the masonry with a water-cooled coring machine (50 mm diameter) near the mortar joints, inserting an M16 stainless steel threaded bar in the centre of each hole, moistening the surface, and injecting high strength mortar until the hole is completely filled.

For the test on the building, stainless steel threaded bars acting as dowels were also installed at the base of the wall, anchored in the foundation with epoxy resin and positioned at mid-thickness of the plaster layer to ensure the connection of the strengthening system with the foundation and avoiding the overturn of the building. While in the tests on single structural elements, the connection of the coating at the edges of the element, to simulate the reinforced plaster continuity, was guaranteed through special devices.

A summary of the applied technique to different masonry types is represented in Figure 3.5 and Figure 3.6.

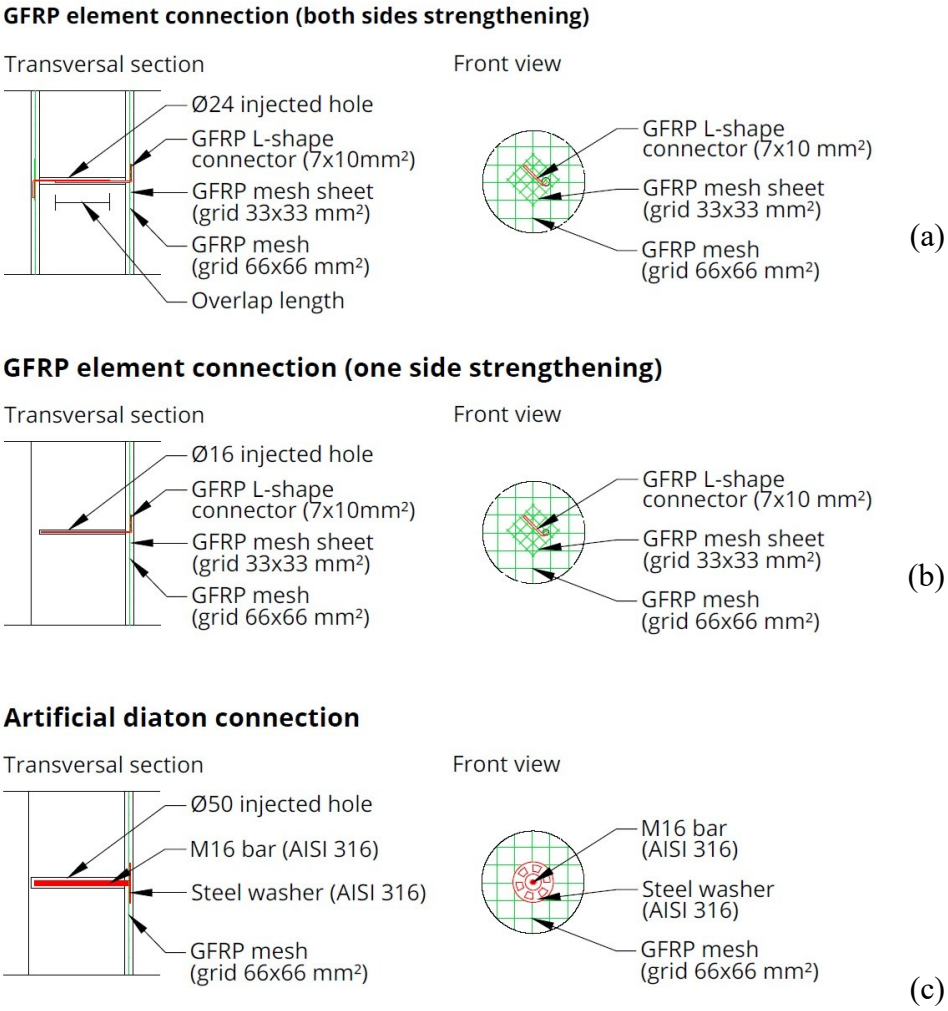


Figure 3.4. Main features of the transversal connectors for the CRM strengthening technique: FRP connection for double-sides (a) and single-side (b) application, and additional "artificial diaton" connection for multiple leaves masonry (c)

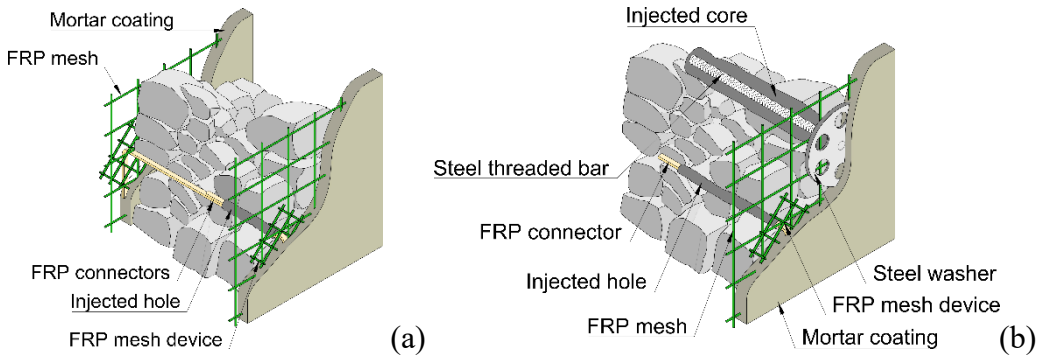
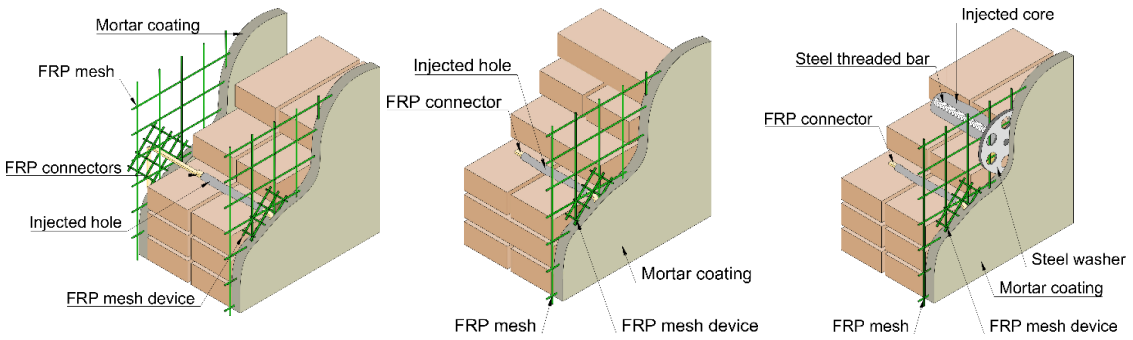
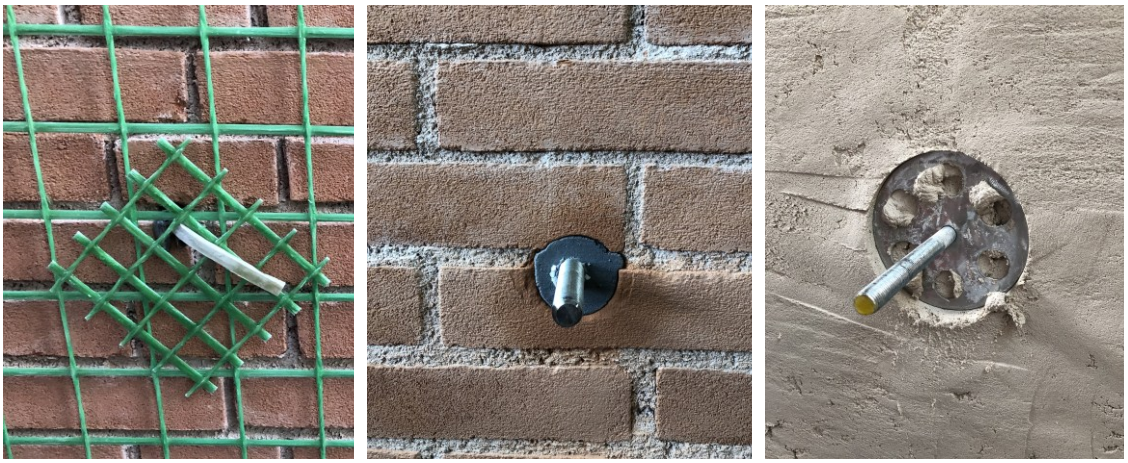


Figure 3.5. CONSTRAIN strengthening of stone masonry walls: strengthening on both sides (a), and on only one side (b)



(a) (b) (c)

Figure 3.6. CONSTRAIN strengthening of brick masonry walls: strengthening on both sides (a), and on only one side, in the case of single (b) or multiple (c) leaf wall



(a) (b) (c)

Figure 3.7. Application of coating: a) L connector after installation of the GFRP mesh; b) protruding threaded steel bar of the embedded steel connector after mortar application, c) injected steel connector bar and washer during manual application of the coating

3.2.2 Description of the strengthening intervention of masonry ring beams with FRP meshes embedded in bed joints

The technique can be generally adopted for the reconstruction of the roof masonry ring beams by embedding FRP pre-formed meshes in the bed joints (Figure 3.8), so to improve the out-of-plane response of the walls and foster the global, box-like behaviour of the masonry structure, contrasting overturning phenomena. It is observed that the intervention is also capable of improving the in-plane performances of the upper masonry spandrels.

In particular, Glass fibres meshes are herein considered (GFRP).



Figure 3.8. Reconstruction of the roof masonry ring beams FRP meshes embedded in bed joints

3.2.3 Description of the strengthening intervention of masonry ring beams with externally bonded FRP strips

The technique can be generally adopted to improve the out-of-plane response of masonry walls and foster the global, box-like behaviour of the masonry structure. It consists of bonding Fibre-Reinforced Polymer (FRP) strips onto the outer surface of the masonry ring beams in a building (Figure 3.9). Being the reinforcement eccentric (since FRP is applied on only one side), the continuity of the strip around the corner is crucial.

It is observed that the intervention is also capable of improving the in-plane performances of the masonry spandrels, since a horizontal tensile-resistant element is introduced.

In particular, unidirectional Carbon fibre strips are considered (CFRP). To apply the strips, the masonry surface was first levelled by applying a flat and smooth layer of a rapid-setting, thixotropic cementitious grout. Then, a first layer of epoxy resin was spread and the strip was applied; on top of the strip, a new layer of epoxy resin was spread.

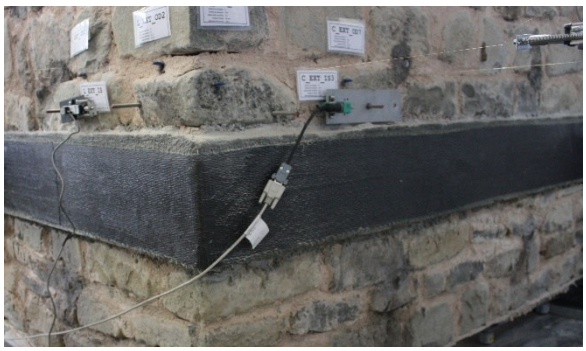


Figure 3.9. CFRP strip externally bonded on a masonry ring beam

3.3 Strengthening materials characterization

For the CRM, a pre-mixed commercial natural hydraulic lime mortar was used for the coating. To determine the bending and compressive strengths, standard prisms (160×40×40 mm) were sampled during construction for different samples. The prisms were later tested in accordance with EN 1015-11 [35]. Additionally, the Young's modulus at one third of the rupture load was measured on at an age on 76 days on four cylindrical samples, with dimensions diameter/length = 100/200 mm, which were sampled during the construction of the pilot building and tested in accordance with EN 12390-13 (Figure 3.4) [242]. The measured Young's modulus was equal to 10091 MPa (CoV 2.66%).

The mean values of flexural ($f_{c,f}$) and compressive strengths ($f_{c,c}$) are reported in Table 3.6. The mortar strength varied significantly among different samples, likely due to its high viscosity, which made it difficult to remove air bubbles during sampling, even though the sampling procedure prescribed by the technical standards was followed.

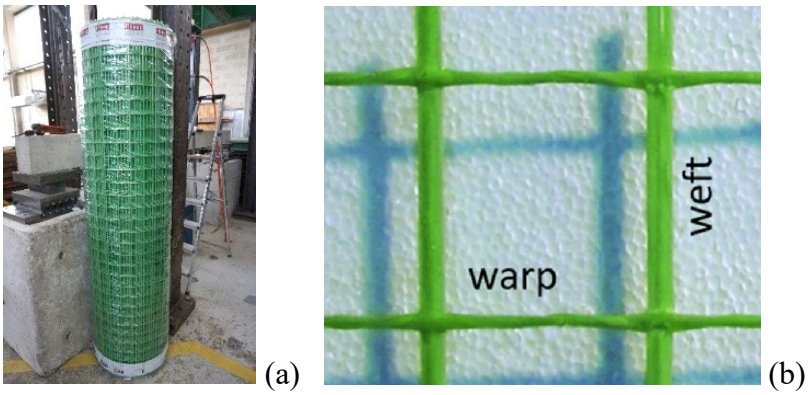
Table 3.6 Mechanical properties of mortar for strengthening

Ref. sample name	n° samples	Age [days]	Mechanical properties	
			$f_{c,f}$ [MPa] (CoV %)	$f_{c,c}$ [MPa] (CoV %)
S-R2-1	3	40	4,2 (5 %)	22,9 (10 %)
S-R2-2	12	38	5,6 (4%)	24,6 (5 %)
S-B1	12	84	4,4 (7 %)	20,1 (8 %)
S-B2	15	39	3,9 (15 %)	15,0 (20 %)
P-R2R-1, P-R2R-2, B-R2	6	35	3,0 (10 %)	30,1 (4%)



Figure 3.10. Testing elastic modulus

The preformed FRP meshes (Figure 3.11) embedded within the coating were composed of long Alkali-Resistant glass fibres embedded in a thermosetting resin made of epoxy vinyl ester with benzoyl peroxide as catalyst (Glass FRP - GFRP). They had a 66×66 mm grid dimension and were composed of twisted-fibre wires in the warp direction, weaved on parallel-fibre wires in the weft direction (dry fibre cross-sectional area in the wire of 3.8 mm^2). The tensile strengths and axial stiffness of GFRP wires were determined through tensile tests, according to ISO 10406 [243], as summarized in Table 3.7. The same type of meshes were used also for the masonry ring beams samples with meshes embedded in bed joints.



(a) (b)

Figure 3.11. GFRP mesh for the CRM system: (a) general view of the mesh rolls and (b) detail

Table 3.7 Mechanical properties of the GFRP mesh: tensile resistance T_G, ultimate strain $\varepsilon_{u,G}$ and axial stiffness EA_G

Property	Twisted fibres wires		Parallel fibres wires	
	Mean	**COV (%)**	**Mean**	**COV (%)**
T_G (kN)	5.11	2.4	5.93	3.9
$\varepsilon_{u,G}$ (%)	1.85	1.9	2.03	4.2
EA_G (kN)	276.7	2.6	291.2	1.6

The GFRP L-shaped connectors are composed of AR glass fibres oriented in parallel across the longitudinal direction. The fibres are embedded in a thermosetting resin made of epoxy vinylester with benzoyl peroxide as catalyst. They had a cross-section of 7×10 mm, with a dry fibre cross section of 32.4 mm^2 (nominal characteristic tensile strength of 17 kN and ultimate strain of 1.9 %.) - Figure 3.12a. The holes drilled in the masonry had a diameter of 24 mm for double-side application (with connectors overlapping length of

at least 200 mm), and of 16 mm for single-sided. The holes were injected with bi-component vinyl ester chemical anchor. The GFRP mesh sheets were 165×165 mm, with a 33x33 mm mesh grid dimension (Figure 3.12b).


(a)

(b)

Figure 3.12. GFRP transversal connections: (a) the "L"-shape connector and (b) the mesh sheets

The artificial diatons (Figure 3.13) were made with a 16 mm diameter threaded stainless steel bar (AISI 316) embedded in a 50 mm diameter core of high resistance thixotropic cement-based mortar and were provided at the head with a perforated stainless-steel washer (4 mm thick, 150 mm diameter), with a nut welded at the centre, screwed on the head of the threaded bar. The technical sheet of the mortar for the injection is reported in Table 3.8. The mixing water adopted for the mortar was 15% in mass and the mixture had a pot life of 60 minutes.


(a)

(b)

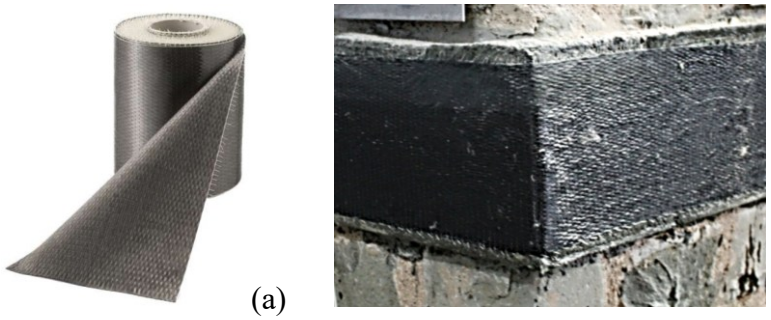
Figure 3.13. Artificial diaton: (a) assembling of the steel connector and (b) detail of the perforated head washer

Table 3.8 Characteristics of the mortar used to inject the diatons.

Property	Value	Test Method
Density of hardened product	2.2 kg/L	EN 12190
Elastic modulus	≥ 27.2 GPa	EN 13412
Adhesion to concrete at 28 days	≥ 2.0 MPa	EN 1542
Compressive strength (1, 7, 28 days)	≥ 20 / 50 / 60 MPa	EN 12190
Flexural strength (1, 7, 28 days)	≥ 5.0 / 8.5 / 9.5 MPa	EN 196-1

Generally, the number, position and diameter of connectors are crucial for the transversal tying and depend on the masonry texture, thickness and mechanical characteristic. In lack of a specific design procedure, reference was made to the literature. In particular, the GFRP injected connectors were distributed by considering the range 4–6/m^2 suggested by Tomaževič [18] for traditional reinforced-cement coating. For dimensioning the artificial diatons, reference was made to the ranges suggested by Castori et al. [244] for historic hard-stone masonry (barely cut stones and pebbles assembled with lime-based mortars): connector diameter: 16-20 mm; hole diameter to connector diameter ratio: 3-4; connectors distance to hole diameter ratio: 9-11.

The unidirectional CFRP strips for reinforcing the masonry ring beams with the externally bonded strengthening system (Figure 3.14) had a width of 200 mm and a dry fibre cross-section of 66.6 mm^2 (fibre mass per unit area 600 g/m^2). Epoxy-impregnated CFRP coupons provided mean values of tensile strength and Young modulus of 1314.3 MPa (CoV = 8.7%) and 353 GPa (CoV = 13.6%), respectively.



(a) (b)

Figure 3.14. CFRP strips: (a) dry fibres roll and (b) detail of application

3.4 In-plane behaviour of piers

The tests performed in this study were carried out according to the test setup proposed by Gattesco et al. [152], and were performed at the University of Trieste (Italy). The tests aimed to evaluate and compare the in-plane performances of the piers before and after applying CRM coatings. The slender ratio of piers was approximately 1.31. Two CRM coating configurations were considered: both wall sides or only one side. For specimens made of single-leaf brick masonry, only the one-sided application was investigated, as the two-sided configuration was expected to show a similar behavior to that of double-leaf brick walls strengthened on both sides, due to the confinement effect provided by the strengthening system.

3.4.1 Literature review

Three main testing setups were designed in the literature for shear-compression testing masonry piers. The first reproduced a shear-type scheme (Figure 3.15a), avoiding rotations at the panel top [150–153,155]. This setup recreates the typical boundary condition of piers in a building with strong spandrels. The second setup reproduced a cantilever scheme (Figure 3.15b), which allows free rotation at the top [138,154,156–160], being representative of buildings with weak spandrels. The third setup (Figure 3.15a), adopted by Messali et al. [156] used a “reversed-T” testing procedure, in which the free rotation at the top was permitted, according to the zero-moment condition which occurs approximately at the half-height of piers under the shear-type scheme. This type of test allowed to investigate more realistically the diffusive flexural damage at the edge of the pier and clearly evidenced the role of the embedded reinforcement in contrast to rocking, carrying tensile strength. To counteract the bending effect due to the free rotation at the top, Guerreiro et al. [153] reduced the height of the horizontal load, so to investigate the behavior of piers dominated by the shear contribution.

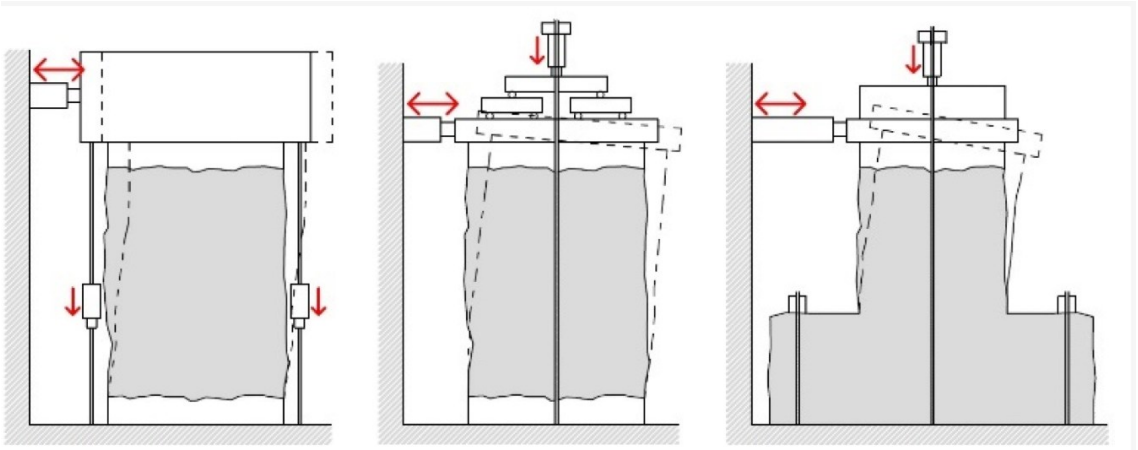
As reported by Boem [126] in its state of the art review, the shear-compression tests available in the literature on TRM-strengthened panels typical concern samples having widths generally ranging from 800 to 3000 mm, with slender ratios from 0.68 to 1.6; axial stress level ranges from 2.5% to 10% of the masonry compressive stress, and up to 30% in some cases. The tests also evidenced the following points:

In the tests with a shear-type loading scheme:

- The typical failure mode was diagonal cracking;
- Comparisons between specimens strengthened with plain plaster and those with plaster embedding the reinforcement clearly demonstrated the latter's effectiveness in promoting distributed cracking and enhancing energy dissipation.
- Compressive stress concentration at the corner sometimes showed local debonding phenomena at the mortar-masonry interface.
- In the samples with high axial stress levels, debonding became more diffuse across the wall, compromising the collaboration between the TRM and the masonry, and evidencing the need of stronger anchors to contrast this effect.

In the tests with a cantilever-type loading scheme:

- The typical failure mode was flexural, characterized by toe crushing without relevant diagonal cracks;
- these tests also evidenced the importance of proper anchoring of the TRM layers at the wall extremities to improve performance against the rocking-induced bending mechanism.



(a) (b) (c)

Figure 3.15. Schematization of different setups for tests on masonry piers under in-plane loading: (a) shear type, (b) cantilever and (c) reversed-T shape [126]

The tests reported and analysed in the following aim at providing original results on piers tested under representative loads and boundary conditions in the laboratory. The main features of the samples and the testing apparatus are reported in the following sections; then, the test results are described in terms of capacity curves and damage pattern evolution. Finally, the results are analysed and compared, providing useful information

on the effectiveness of the CRM coating in terms of resistance, displacement, stiffness and dissipative capacities.

3.4.2 Description of the samples

The research considers rectangular pier samples (masonry panels having a width of 1500 mm and a height of 1960 mm). Each specimen was built between a bottom and a top reinforced concrete (RC) beam 300 mm height, 1500 mm long and with a thickness equal to that of the plain masonry. Three different masonry types were considered: R2, B2 and B1.

A total of eight panels were built and tested (Table 3.9): three in rubble stone masonry (R2), three in double leaf solid brick masonry (B2), and two in single leaf solid brick (B1) masonry. Both a reference wall and a wall strengthened by coating one or two sides were tested to observe the effects of strengthening. For the two-leaf masonry, which is susceptible to separation of the leaves, an additional sample with coating applied to both sides was added for comparison. In the strengthened samples, to reproduce the continuity of the strengthening system at the piers' extremities, as in actual structures, the CRM layer was extended over the upper and lower RC beams and fixed with a steel plate, which was bolted to the RC beams. The sample construction (Figure 3.16) and the positioning of the GFRP connectors and of GFRP connectors combined with artificial diatons is schematized in Figure 3.17, Figure 3.18 and Figure 3.19.

In all of the samples, to avoid the sliding of the wall at the masonry – concrete interface, in the first and last mortar bed joints, a mass of 2.5 kg of R 32.5 pozzolanic cement was added to the mix for every 25 kg of dry mortar. The thickness of the joints was about 1 cm but varied significantly due to the irregular shape of the stones.



(a) (b)

Figure 3.16. Construction of (a) brick and (b) stone masonry walls

Table 3.9: Summary of the experimental tests on piers

Sample ID	Masonry type	Strengthening system	Connectors
P-R2U	R2	/	/
P-R2R-1	R2	CRM on one-side	GFRP + diatons, 1 side
P-R2R-2	R2	CRM on two-sides	GFRP, passing-through
P-B2U	B2	/	/
P-B2R-1	B2	CRM on one-side	GFRP + diatons, 1 side
P-B2R-2	B2	CRM on two-sides	GFRP, passing-through
P-B1U	B1	/	/
P-B1R-1	B1	CRM on one-side	GFRP, 1 side

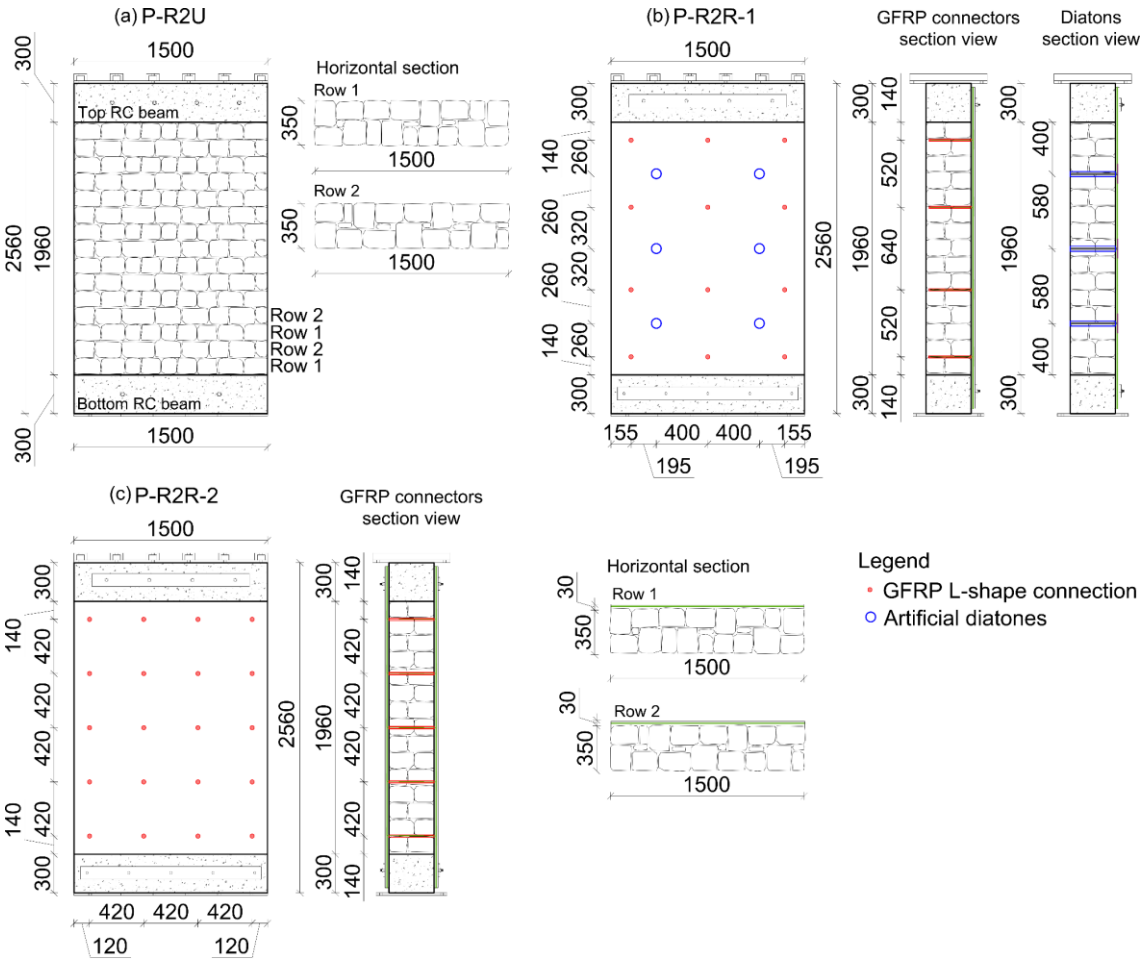


Figure 3.17. Lateral and cross-sectional views of sample (a) P-R2U and (b) P-R2R-1 and (c) P-R2R-2 (dimensions in mm)

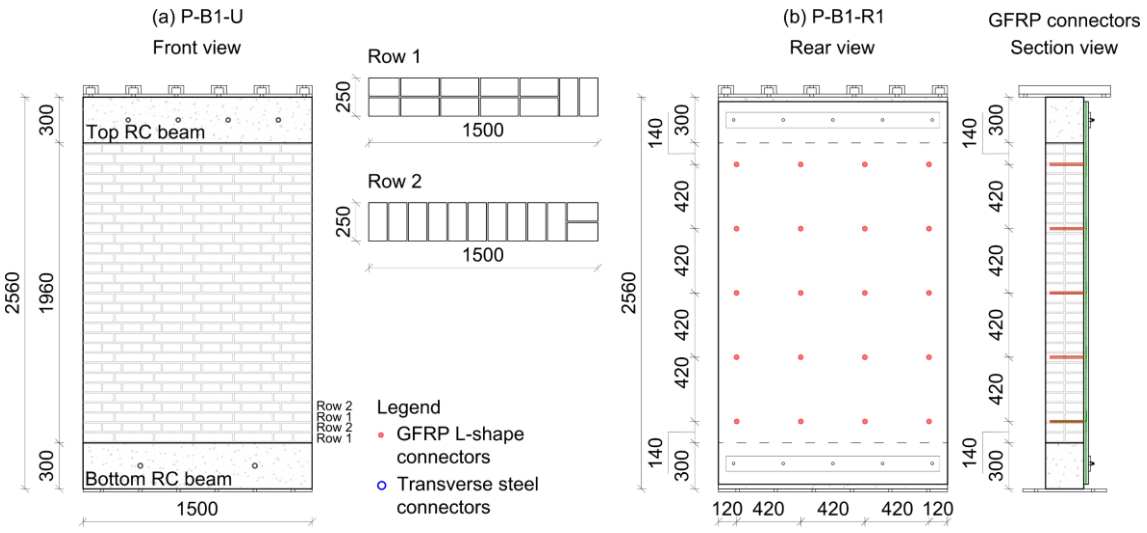


Figure 3.18. Lateral and cross-sectional views of samples (a) P-B1-U and (b) P-B1-R1 (measures in mm)

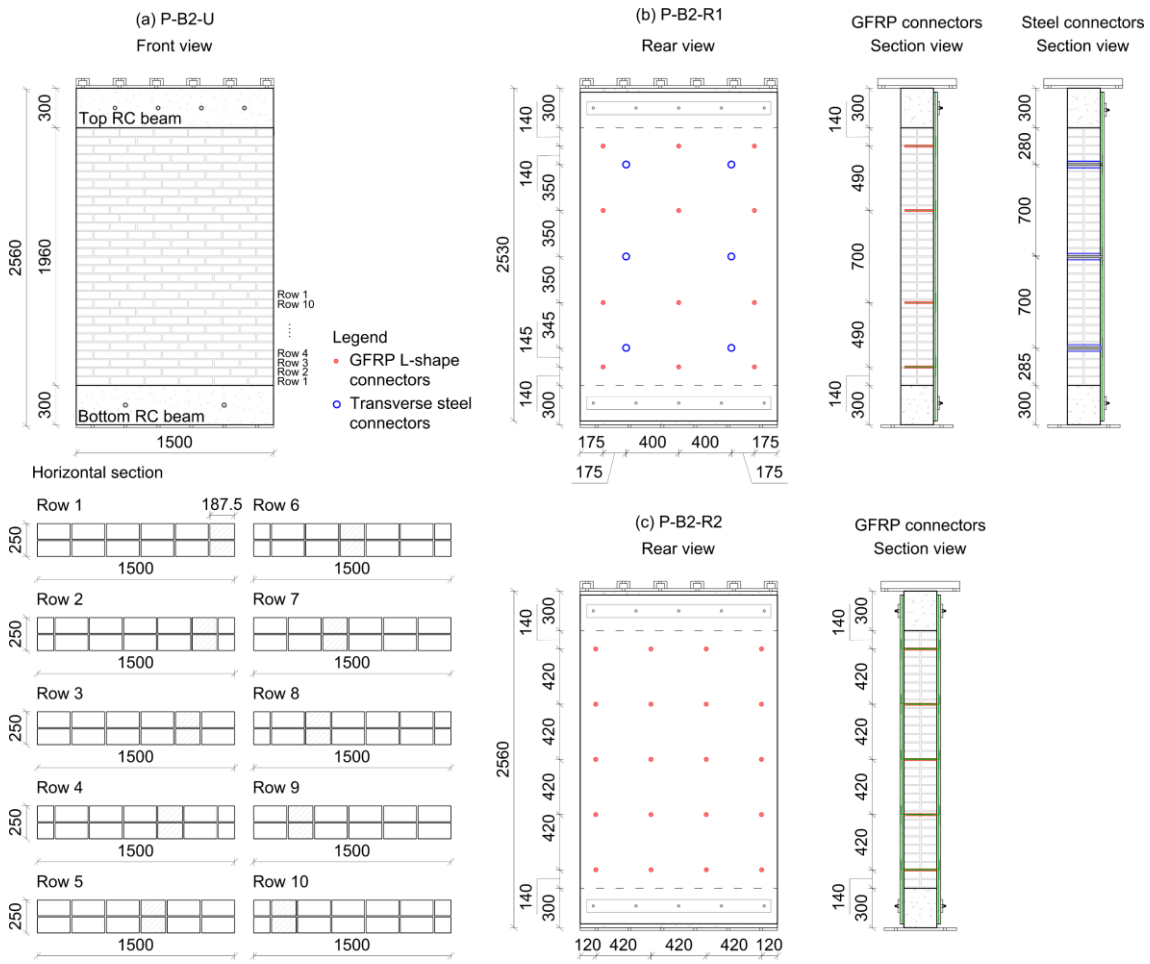


Figure 3.19. Lateral and cross-sectional views of samples (a) P-B2-U, (b) P-B2-R1 and (c) P-B2-R2 (measures in mm)

3.4.3 Test setup

The test setup is schematized in Figure 3.20: the lower RC beam was bolted to a stiff steel beam fixed to the laboratory floor. The RC beam at the top of the sample was bolted to the upper stiff steel beam of the testing apparatus. At the lateral extremities of the upper steel beam, two electro-mechanical actuators, connected to the floor, were installed to control the amount of vertical axial load and the rotation at the top. During testing, they were governed so as the applied axial load was maintained constant during the tests (axial stress level was 0.5 MPa) and the rotations of the upper steel beam were constrained. A third actuator, positioned at the side of the upper steel beam (left side), at its mid-height, applied the lateral loading, which was applied by cycles with increasing displacement amplitude in negative and positive directions. Because of the slow speed of the electro-mechanical actuators, each load amplitude was only repeated once (instead of the usual three times). The load protocol was based on protocols usually used to assess seismic resistance and experience [18,47].

During the tests, the two steel rods prevented OOP displacements at the upper RC element level. The rods were connected to an external fixed support.

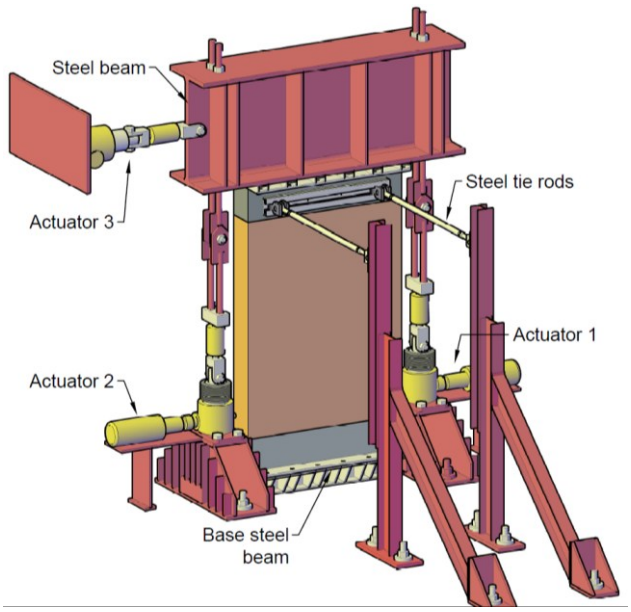


Figure 3.20. Front view of the test setup for in-plane shear-compression tests

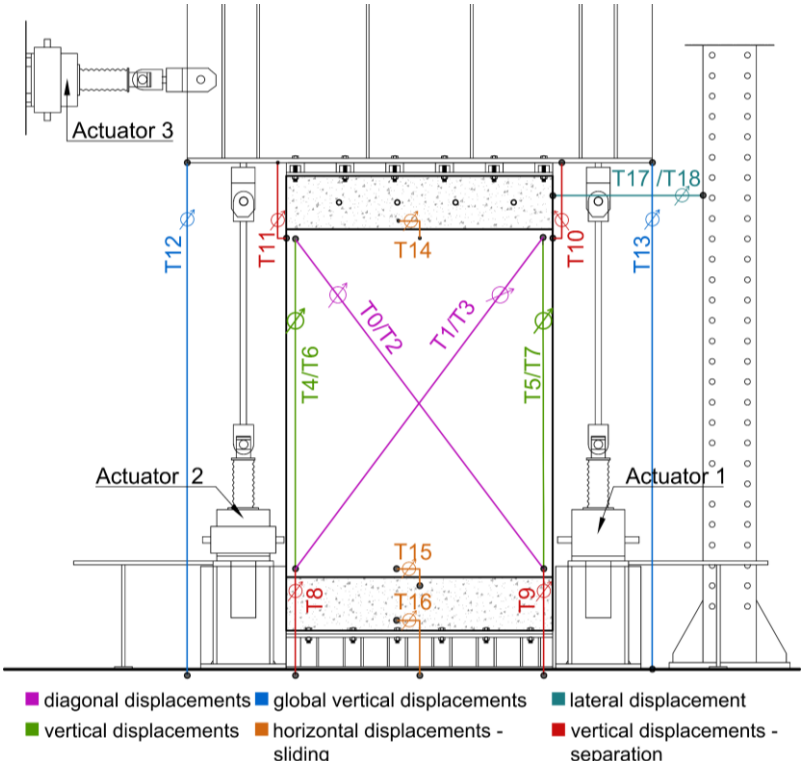
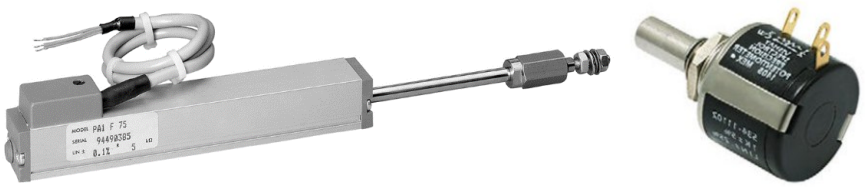


Figure 3.21. Instrumentation for in-plane shear-compression tests

The displacements were measured through linear potentiometric transducers with a stroke of 25 mm and 50 mm (Figure 3.20) and multi turn wire wound potentiometric transducers

(Figure 3.22). These work by transforming the relative displacement of the shaft (linear) or its winding (wire wound) in an electric resistance that is read by the control unit, that converts it in an equivalent displacement, based on the instrument calibration constant. The installation of instruments was performed through the use of metal brackets fixed to the wall and an inextensible metal wire connected through lead masses that allowed to extend the measurement base length.



(a) (b)

Figure 3.22 (a) linear potentiometer transducer; (b) multi-turn wire wound potentiometer transducer

Each specimen was equipped with 19 displacement transducers, as shown in Figure 3.21. The transducers measured lateral displacements, axial and shear deformations, uplift and slip relative to the foundation. In particular, transducers T0/T2 and T1/T3 measured the diagonal variation on both faces of the specimen. Transducers T4/T6 and T5/T7 surveyed the vertical deformation of the specimen at the left and right vertical edges, respectively. The vertical displacement between the specimen's first masonry row and the floor was measured using transducers T8 and T9, while the uplift of the stiff steel beam at the top of the specimen was monitored with transducers T10 and T11. In addition, transducers T12 and T13 monitored the distance between the top steel beam and the floor. Simultaneously, the masonry-concrete slip at the top and bottom edges of the specimen was surveyed via transducers T14 and T15. Transducer T16 was designated for measuring the slip of the bottom concrete element relative to the floor base steel beam. Transducers T17 and T18 measured the horizontal displacement at the top of the specimen. Finally, vertical and lateral forces were measured by three load cells.

A digital image correlation (DIC) system measured the displacement and strain fields on one wall surface. The cameras had a resolution of 45.7 Megapixels. The DIC system works by comparing photographs taken at different times. A pair of cameras are used to obtain a 3D position using the stereo vision principle. The system is calibrated before the test to give accurate measurements, although it works better on flat surfaces. The main

computational challenge lies in identifying the same points in images acquired by both cameras at different times. For this process to be effective, adequate illumination, preferably uniform and constant throughout the test, and a random speckle pattern (Figure 3.24) on the measured surface are required. This type of measuring system can be used for several purposes, as reported in Oats et al. [245], but it is particularly useful for masonry elements because it allows the detection of cracks in the early stages when the damage cannot be seen by the naked eye. In Howlader et al. [246], the same methodology has been adopted for in-plane tests on masonry walls. The study also discusses on the high accuracy that can be reached, analysing the ideal step size to guarantee an accurate data extraction.

The side of the wall facing the cameras was painted with a contrasting random speckle pattern, painted manually using white paint as background and black dots, while the other side was painted white to facilitate the visual examination of cracks. The advantage of the system is that it gives the displacement field over the entire visible surface. Strains and other quantities can be calculated based on measured displacement fields.

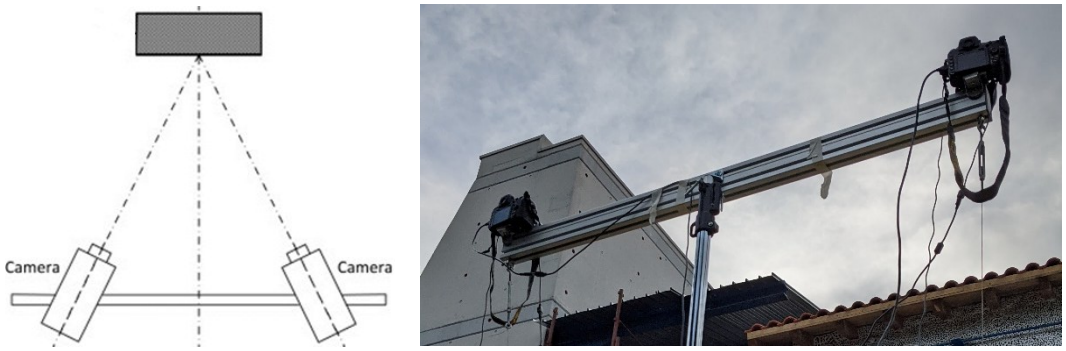


Figure 3.23. The concept of locating a point in 3D using two cameras, left. The cameras used during the tests, right

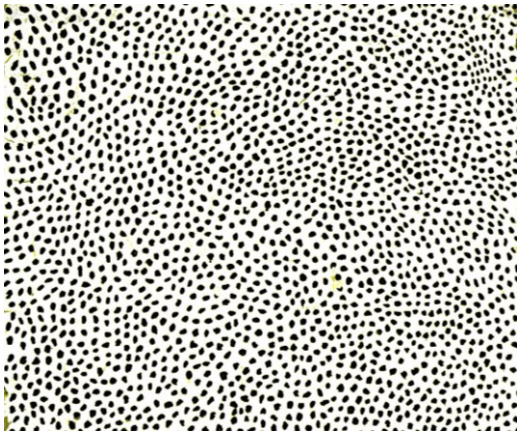


Figure 3.24. Random speckle pattern painted on the surface of the pier P-R2U

The loading protocols are shown in Figure 3.25 and Figure 3.26. The tests were terminated when collapse was imminent, after a reduction in peak force of at least 20% was attained. The loading cycles at each drift level were not repeated due to the limited actuator speed (maximum 10 mm/min).

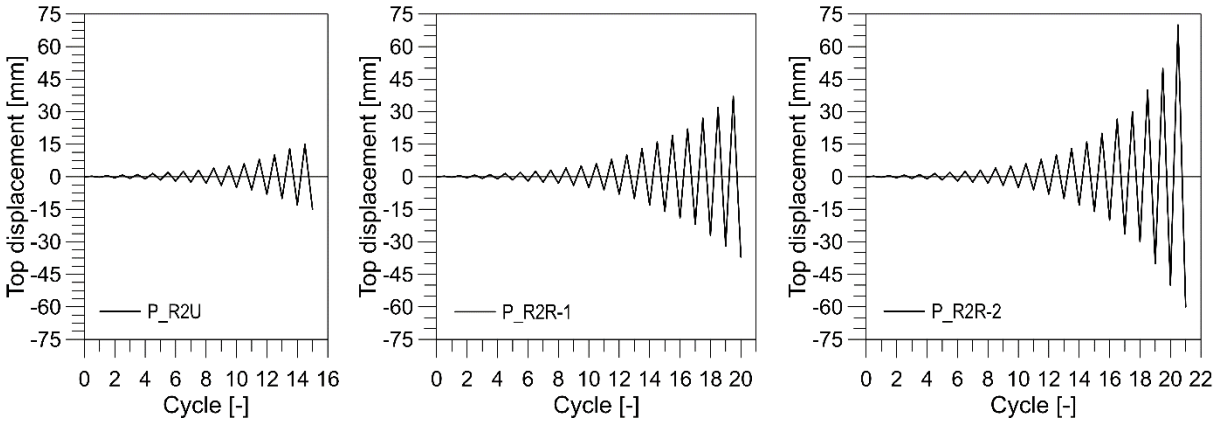


Figure 3.25. Loading cycles for the stone piers

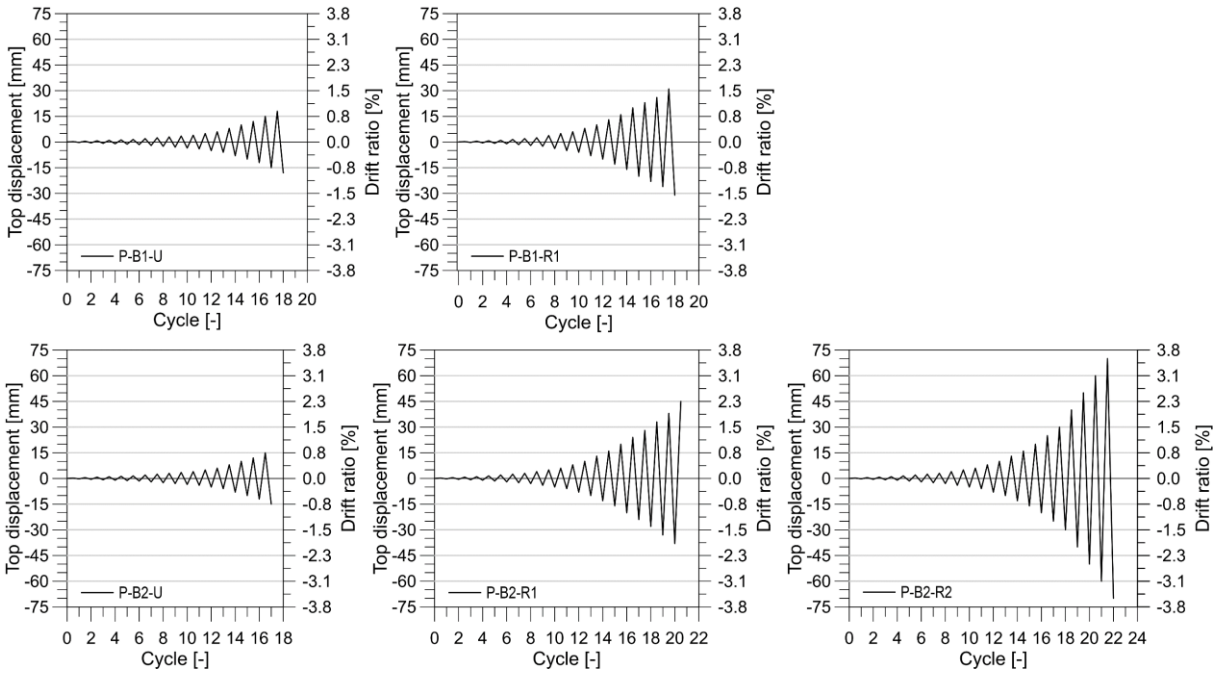


Figure 3.26. Loading cycles for the brick piers

The behaviour of each sample is described in the following, reporting also monitored loads and displacements and evolution of the crack pattern, which was surveyed with the DIC system on one side and by means of manually drawing above newly formed cracks with a black marker on the other. The main results are then summarized and compared.

The global behaviour of each pier is described in terms of capacity curves, which show the applied horizontal load V_P (shear force) as a function of the horizontal displacement of the top RC beam d_P. The pier drift γ_P was determined by dividing d_P by the pier's height (1960 mm).

According to the typical in-plane failure mechanisms of historic masonry elements, two groups of cracks were generally expected: mainly hotiontal cracks at the corners of the pier, related to in-plane bending failure, and diagonal cracks in the center of the pier, indicative of an in-plane shear mechanism. For monitoring such occurrances, the relative displacements along the diagonals (d_1 and d_2) and throughout the piers height (d_{vL} and d_{vR}, at left and right side) were monitored at both sides of the pier samples. The diagonal displacements were measured on a base length of about 2365 mm centred in the pier area; the vertical on a base length of about 1960 mm.

In addition, the global vertical displacements between the upper steel beam and the laboratory floor were also measeured (d_{Vtot}) to monitor possible additional movements external to the deformations of the masonry sample. Positive displacements conventionally refer to elongations.

3.4.4 Results

3.4.4.1 Test P-R2U

The first damage was observed almost in the middle of the wall, where a sub-vertical crack formed. Then, the crack grew in length with increasing load and other cracks formed from the centre of the panel, with an inclined trend. The diagonal cracks grew and eventually connected the corners of the wall. At the end, the unreinforced stone masonry pier responded in shear, characterised by diagonal cracks: the cracks ran almost exclusively through joints and involved the whole masonry thickness. The progressive opening of diagonal cracks was detected by the diagonal transducers (positive values that alternatively occurred at the opposite diagonals); the vertical transducers evidenced a gradual shortening of the sample during the test.

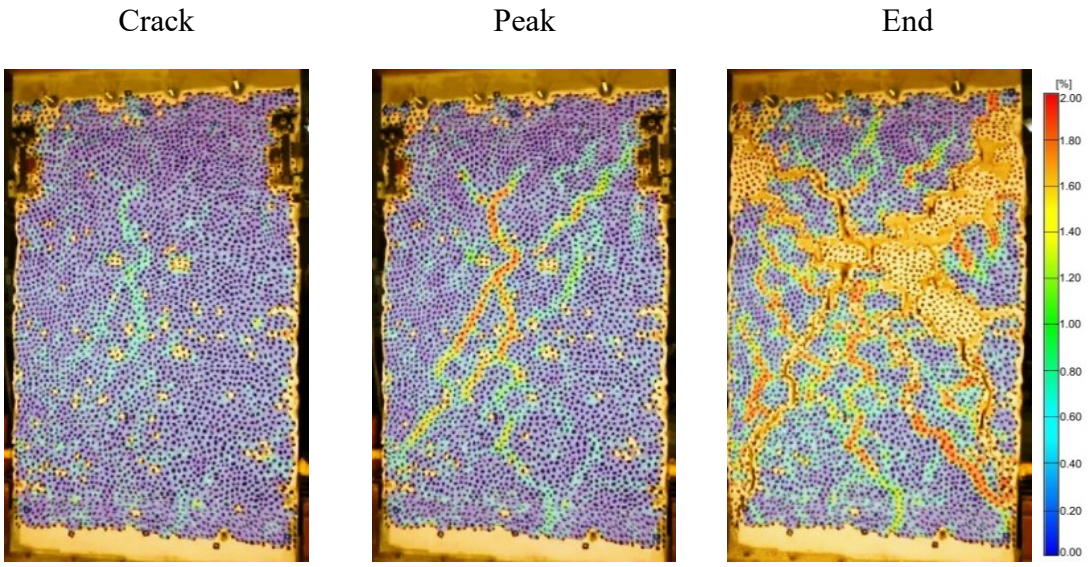


Figure 3.27 Crack pattern on the back side of wall P-R2U, with the positive loading direction toward the left side of the images

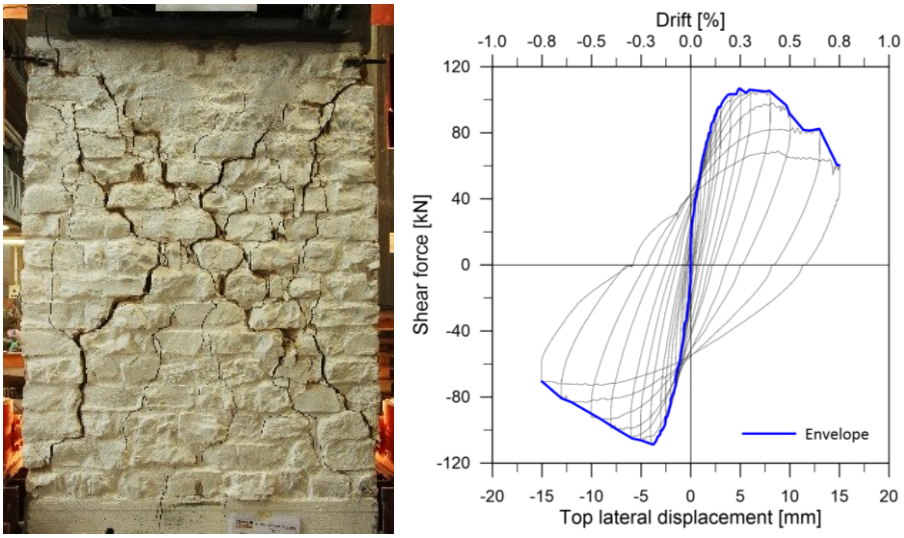


Figure 3.28 P-R2U: a) crack pattern on the front side of the wall and b) force-displacement curve

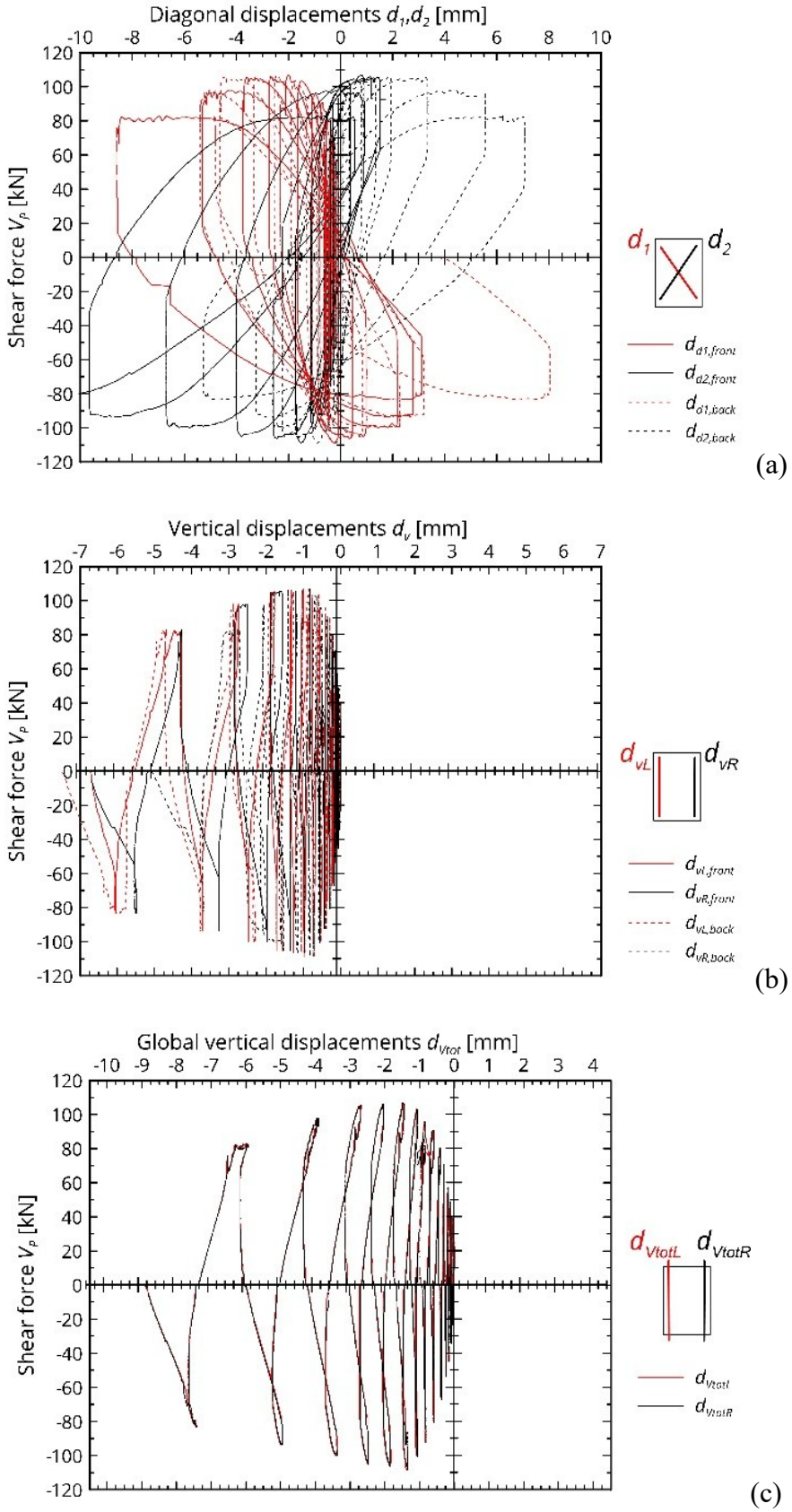


Figure 3.29 Main results of test P-R2U a) displacements along the diagonals; b) vertical displacements along the side of the wall; c) total vertical displacements between the base and the top stiff beams

3.4.4.2 Test P-R2R-1

It is observed that, before the beginning of the test, the sample had minor cracks in the first mortar bedding and at the base of the coating. This may have likely led to a lower-than-expected initial stiffness, which resulted quite similar to that of the unstrengthened sample.

During the test, damage developed differently on the strengthened and unstrengthened sides: the response and damage on the unstrengthened (front) side were again in shear, which was clear from the diagonal cracks. On the strengthened (back) side, the cracks in the coating were almost vertical initially, at the centre of the sample, only starting to incline when approaching to the maximum resistance; horizontal cracks in the coating also appeared near the corners, indicating the activation of bending. Despite these horizontal cracks, the governing mechanism was shear, as evidently from the alternating elongations detected by the diagonal transducers, whereas the global vertical displacements almost remained negative. (d_{Vtot}) The vertical transducers applied at the two sides of the sample (d_V) behaved differently: those on the unstrengthened side mainly measured a gradual compression, while those applied on the mortar coating detected elongations, likely related to the activation of the bending mechanism.

The cracking in the unstrengthened side was concentrated in a few large cracks, whereas the cracking in the coating was widely spread out in much more cracks. Finally, almost at the end of the test, a vertical crack was observed at the sides of the sample and the coating diffusely lost bond with the masonry, except where transversal connectors were present, and the also the coating near some of the steel connectors crumbled and the GFRP mesh fractured.

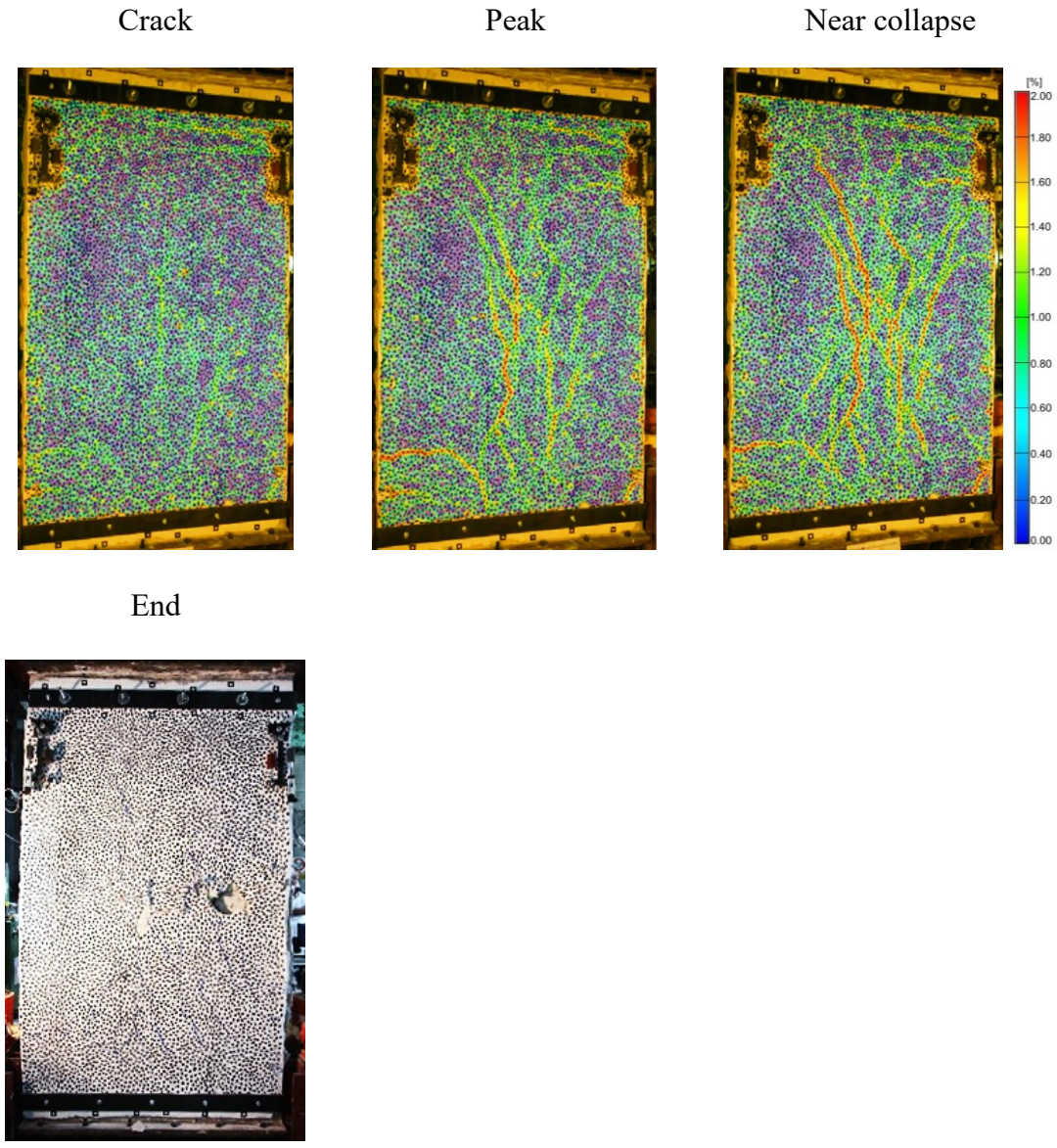


Figure 3.30 Crack pattern on the back side of wall P-R2R-1, with the positive loading direction toward the left side of the images

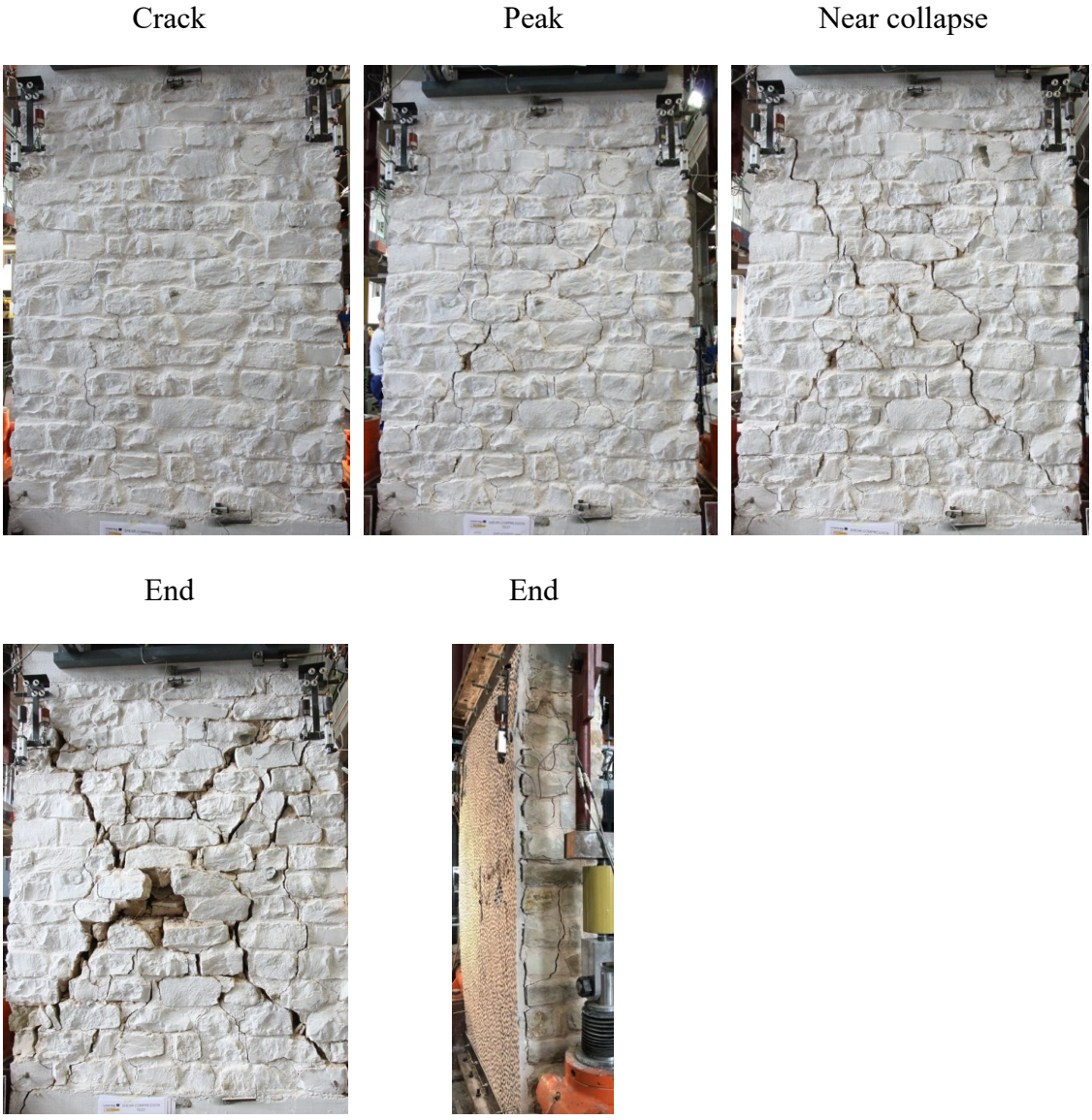


Figure 3.31 Crack pattern on the front side of wall P-R2R-1

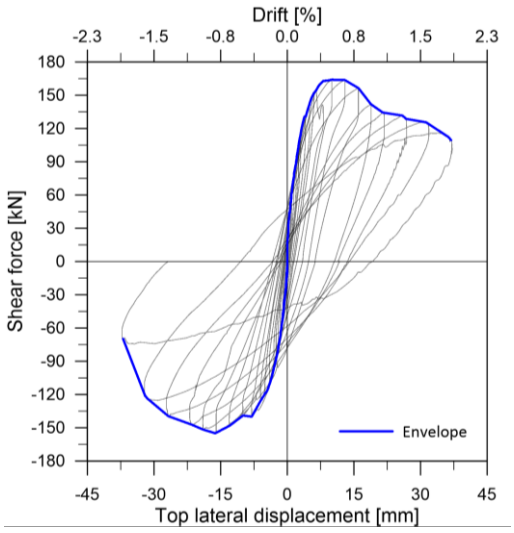


Figure 3.32 Force-displacement curve of test P-R2R-1

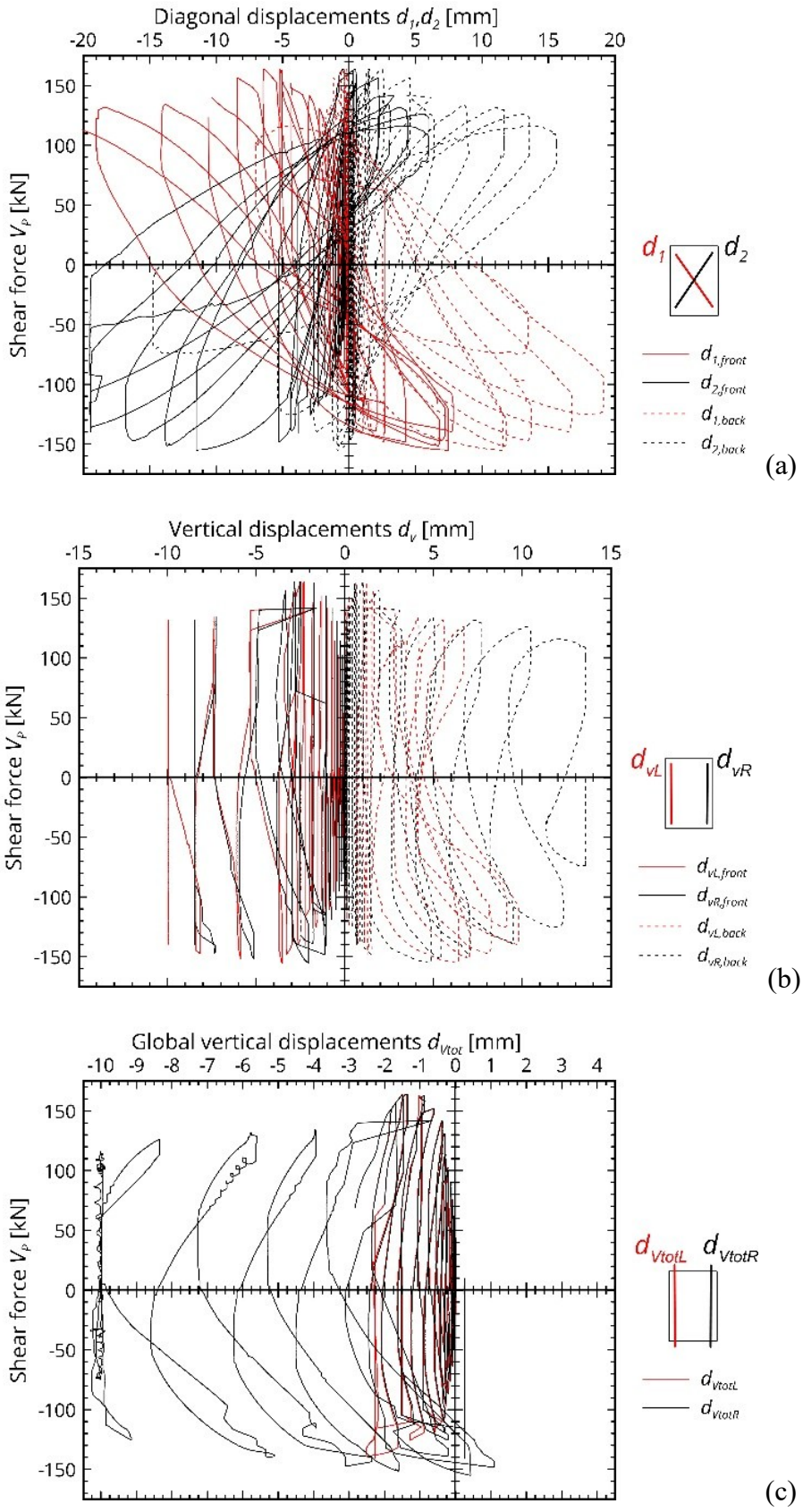


Figure 3.33 Main results of test P-R2R-1 a) displacements along the diagonals; b) vertical displacements along the side of the wall; c) total vertical displacements between the base and the top stiff beams

3.4.4.3 Test P-R2R-2

The first cracks were horizontal at the bottom and top corners, indicating the activation of bending damage; however, also some sub-vertical cracks formed at the centre of the sample.

When approaching to the maximum resistance, other horizontal, parallel cracks occurred at the corners and several inclined cracks propagated diagonally from the centre of the panel, Horizontal and inclined cracks, widely spread over a large area, indicated the combined activation of bending and shear mechanisms. This was evident also from the consistent elongations monitored by both diagonal and vertical transducers installed on the sample.

Close to the end of the test, the coating diffusely lost the bond with masonry, by connectors. Also, a vertical crack between the wythes developed and gradually widened until the end of the test.

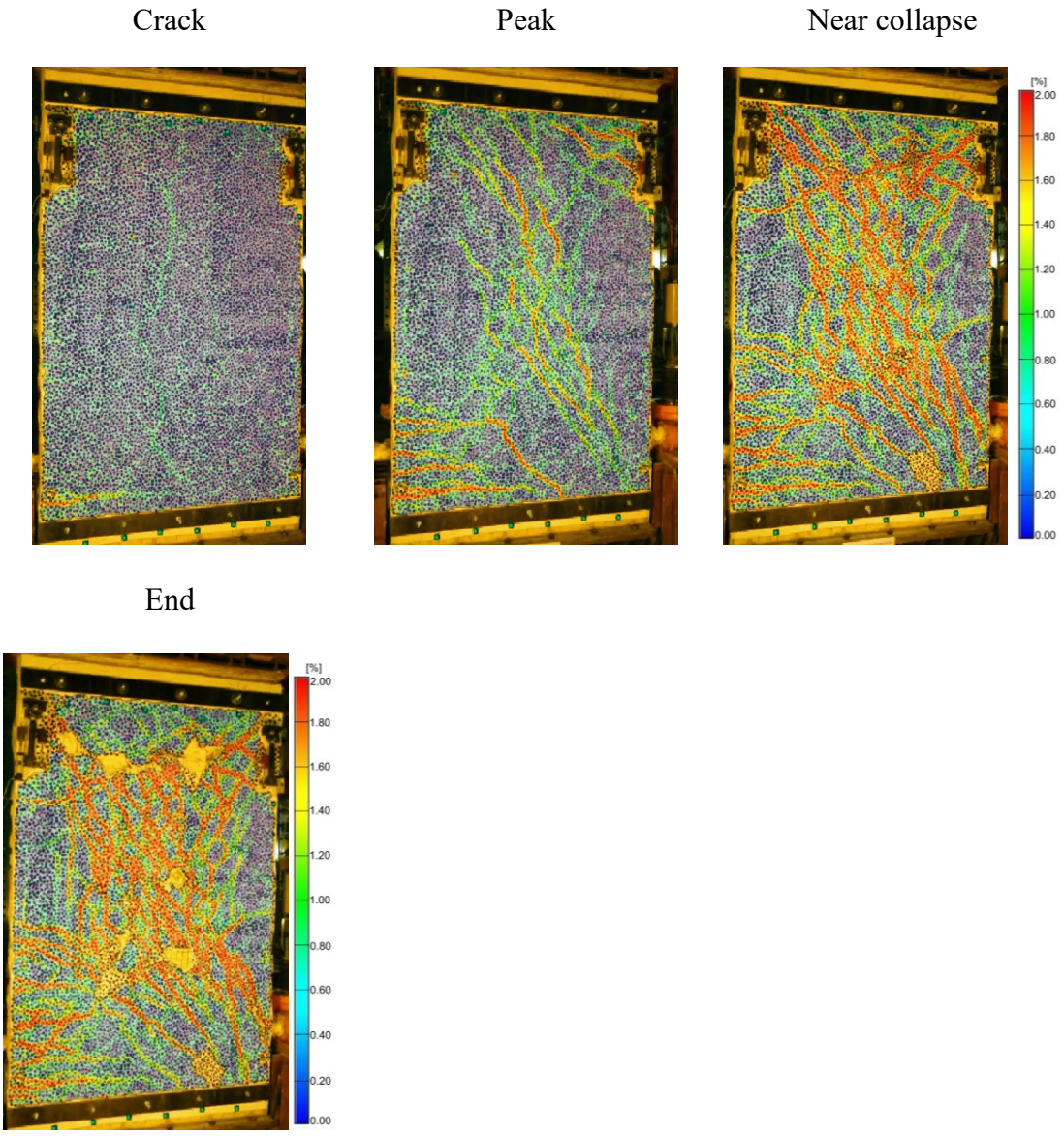


Figure 3.34 Crack pattern on the back side of wall P-R2R-2, with the positive loading direction toward the left side of the images

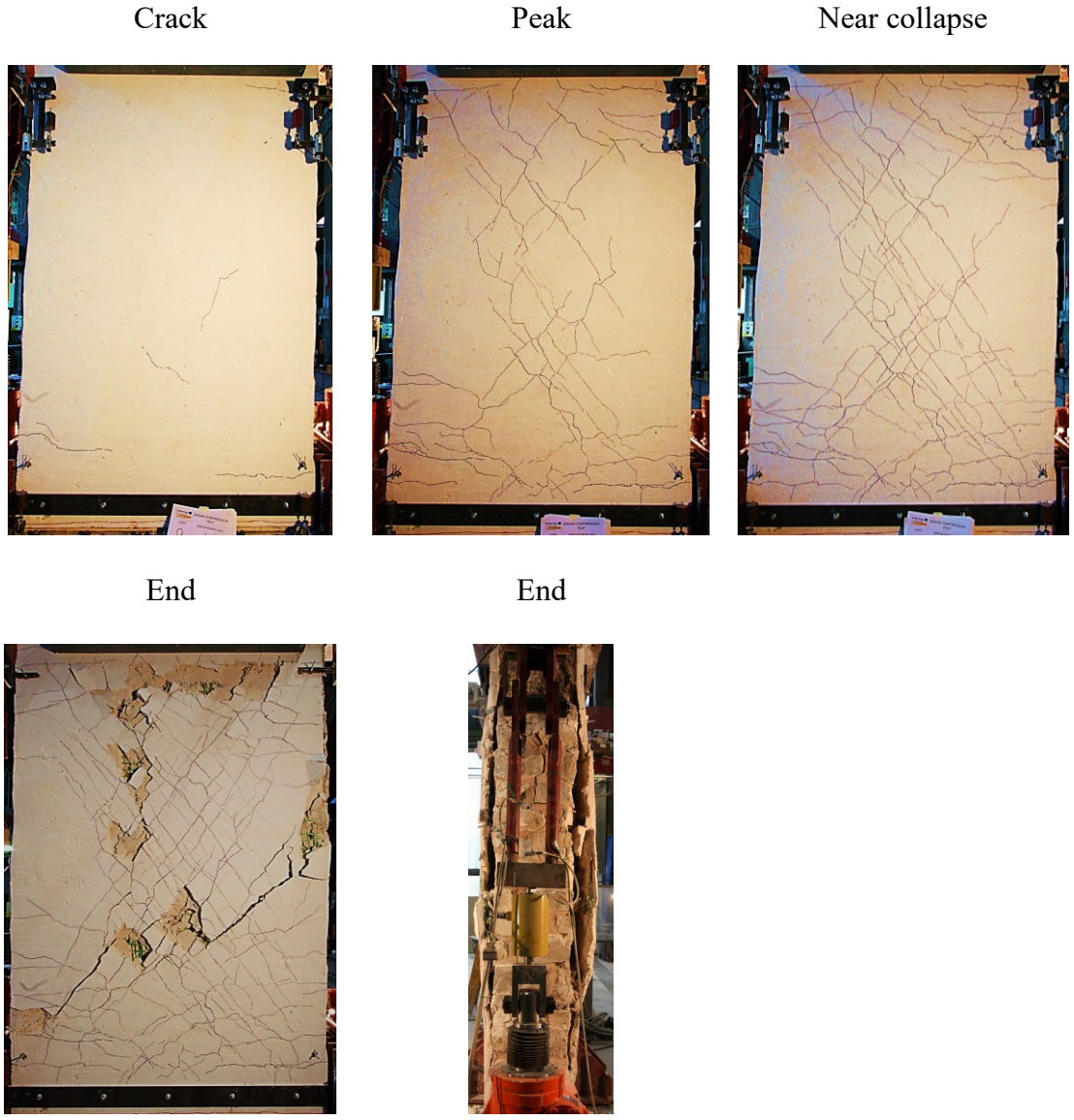


Figure 3.35 Crack pattern on the front side of wall P-R2R-2

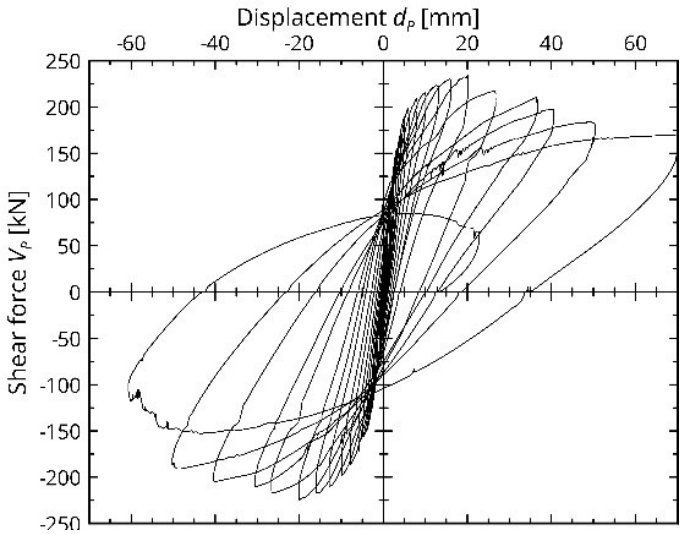


Figure 3.36 Force-displacement curve of test P-R2R-2

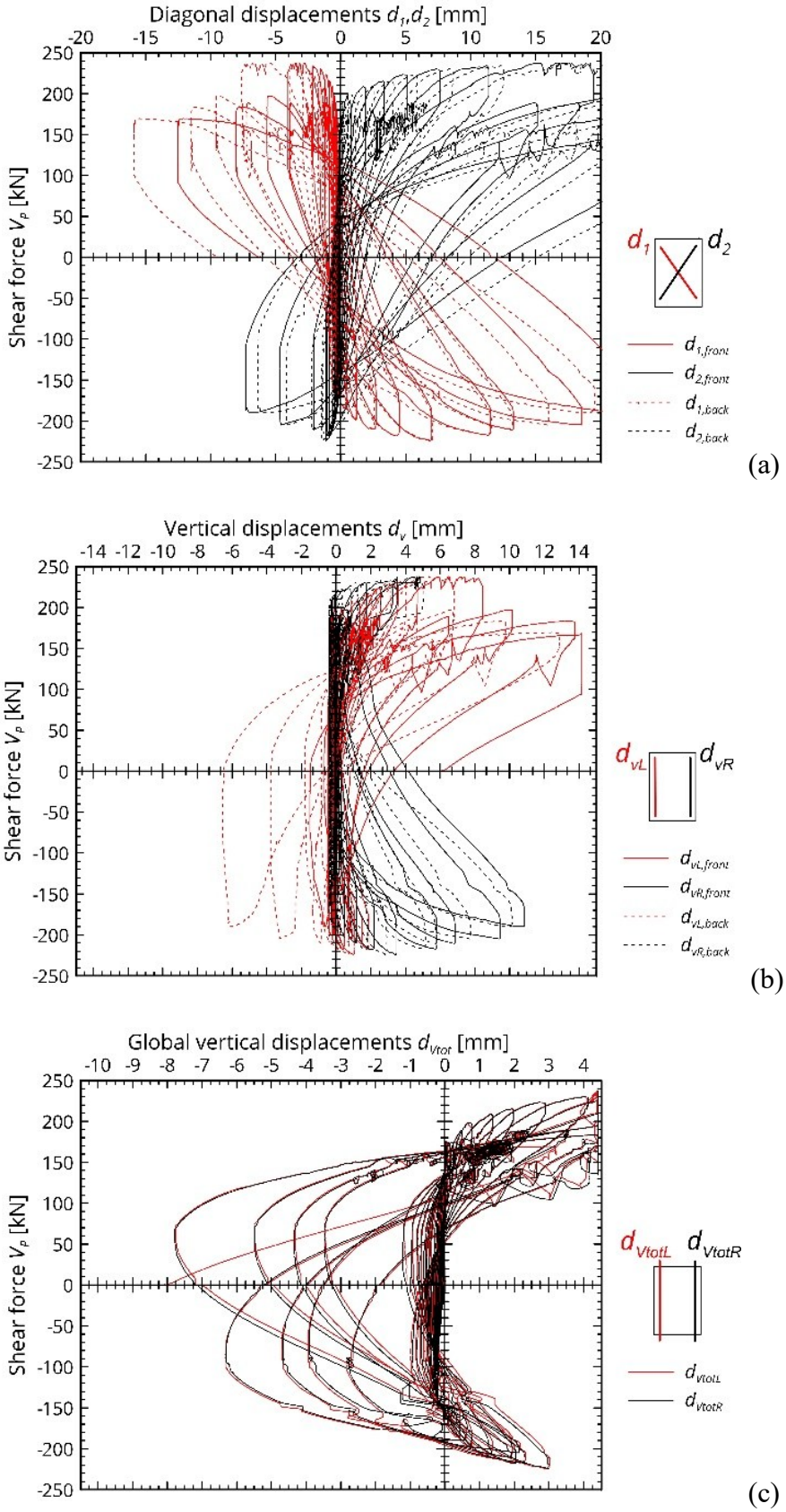


Figure 3.37 Main results of test P-R2R-2: a) displacements along the diagonals; b) vertical displacements along the side of the wall; c) total vertical displacements between the base and the top stiff beams

3.4.4.4 Test P-B2U

The pier responded in shear, characterised by diagonal cracks: the first cracks were scattered in bricks and head joints, starting from the centre of the panel and then developing along the diagonal trajectories throughout the whole thickness. The diagonal cracks were monitored by the diagonal transducers (positive values occurring alternatively at the opposite diagonals). The progressive shortening of the sample was surveyed by the vertical transducers (negative values). During the test, also significant cracking at the sides of the sample, due to separation of the leaves, was observed.

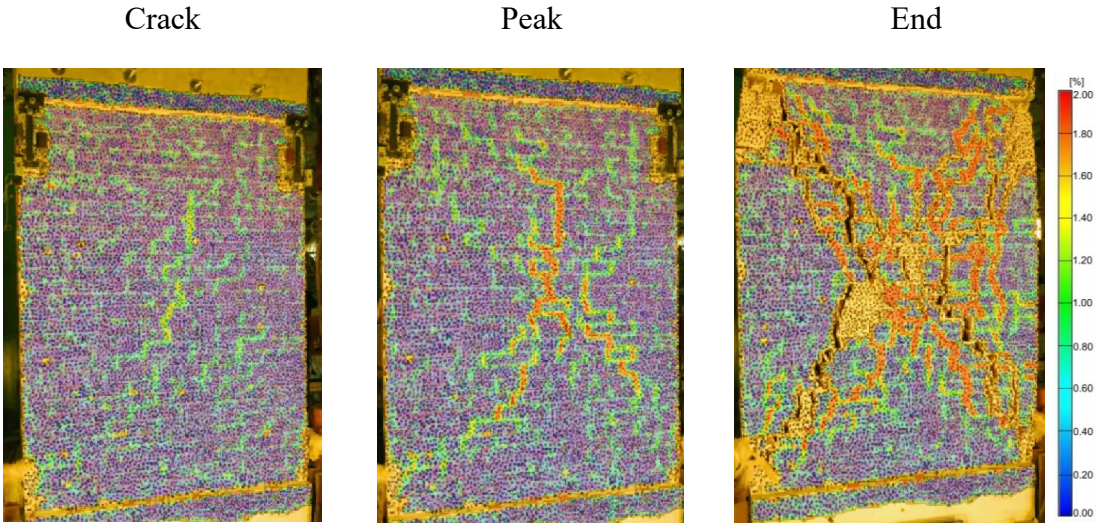


Figure 3.38 Crack pattern on the back side of wall P-B2U, with the positive loading direction toward the left side of the images

End End



Figure 3.39 Crack pattern on the front side of wall P- B2U

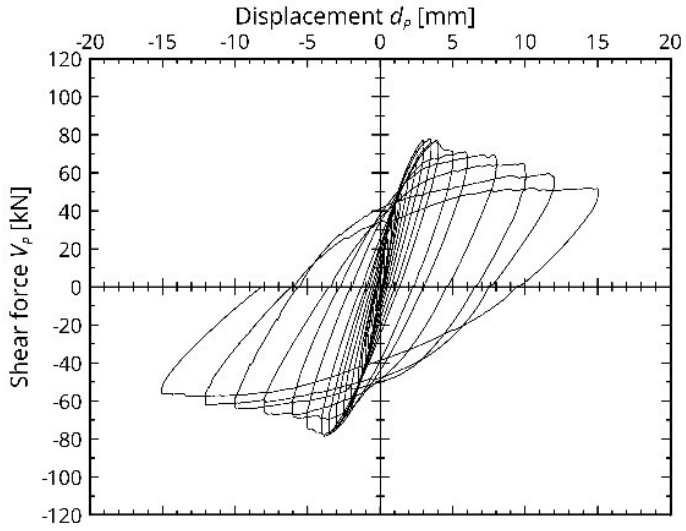


Figure 3.40 Force-displacement curve of test P- B2U

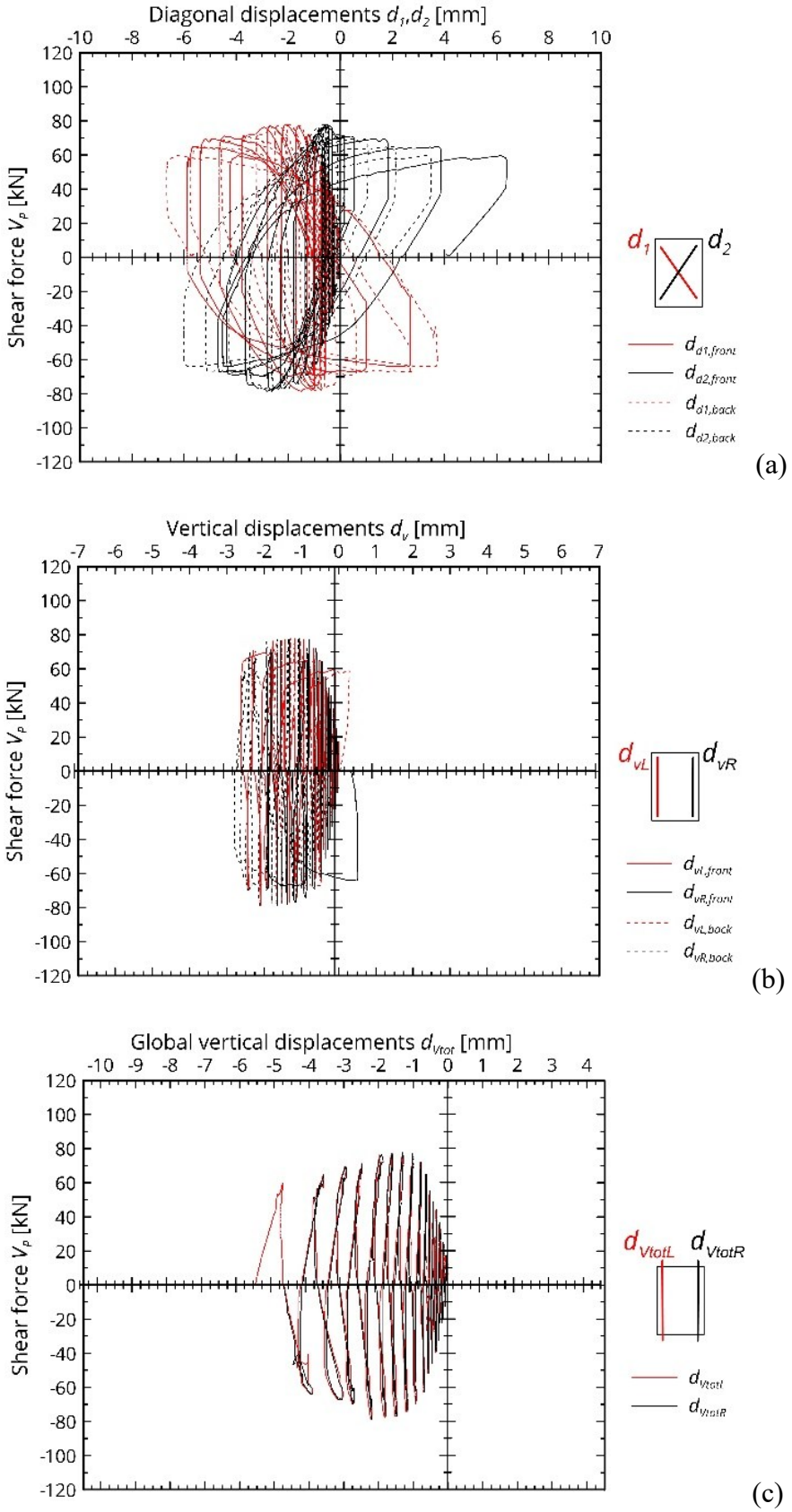


Figure 3.41 Main results of test P- B2U: a) displacements along the diagonals; b) vertical displacements along the side of the wall; c) total vertical displacements between the base and the top stiff beams

3.4.4.5 Test P-B2R-1

The initial damage in the wall manifested as horizontal cracks at the top and bottom corners. With increasing load, the horizontal cracks propagated until peak resistance, when suddenly an inclined crack formed in the coating and also on the unstrengthened side. In the post-peak response, diagonal cracks in both the coating and the masonry were active and gradually propagated and the separation of the leaves was also observed. At the end of the test, the leaf with the coating diffusely separated and heavily leaned out. However, the transversal connectors prevented the overturning. The combination of several horizontal and inclined cracks in the coating reflected the combined activation of bending and shear mechanisms, as detected also by positive values achieved by both diagonal and vertical transducers.

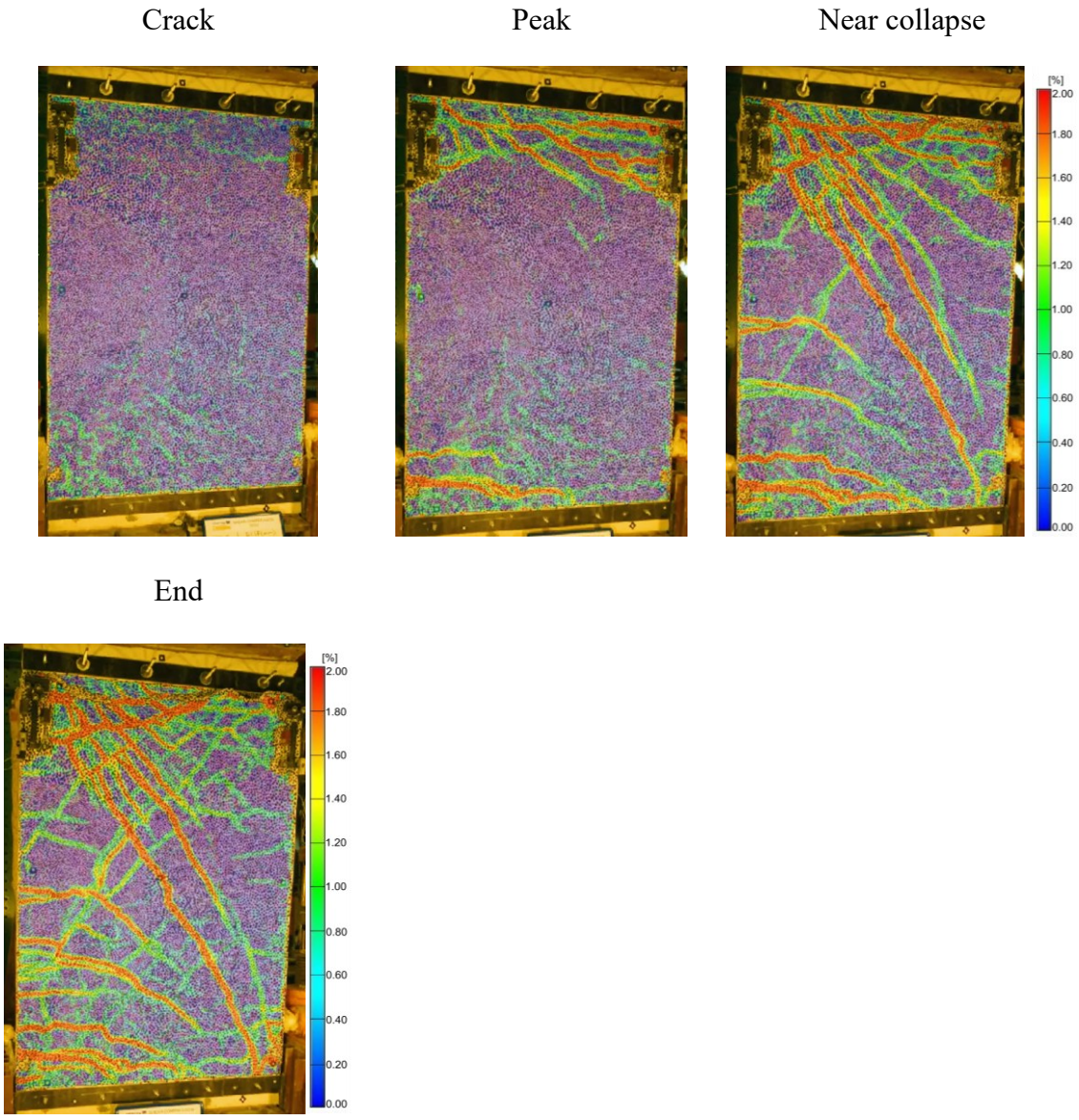


Figure 3.42 Crack pattern on the back side of wall P-B2R-1, with the positive loading direction toward the left side of the images



Figure 3.43 Crack pattern on the front side of wall P-B2R-1

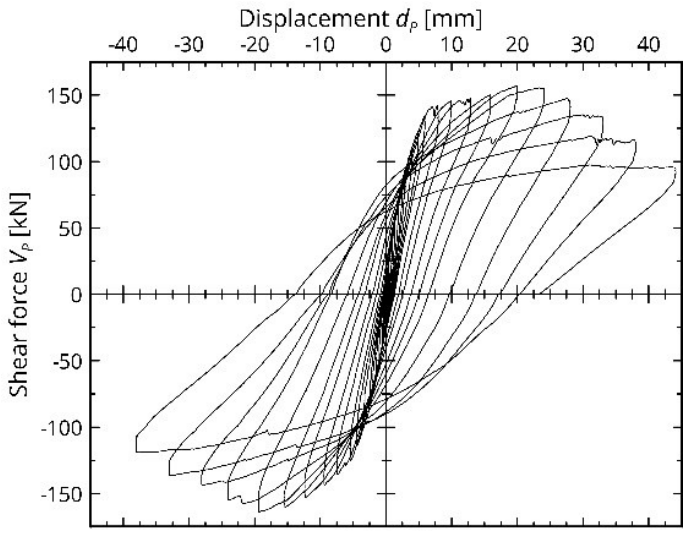


Figure 3.44 Force-displacement curve of test P-B2R-1

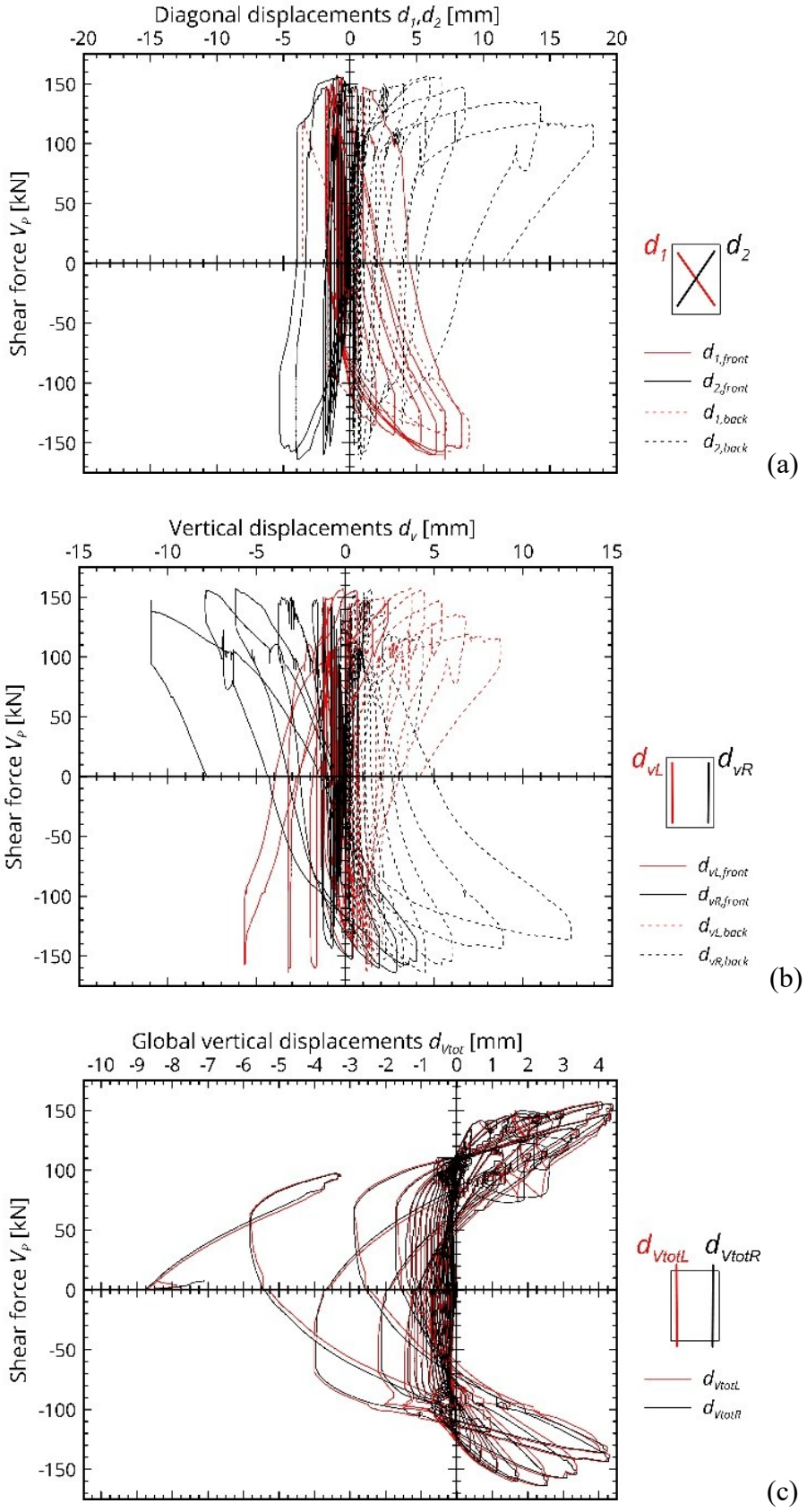


Figure 3.45 Main results of test P-B2R-1: a) displacements along the diagonals; b) vertical displacements along the side of the wall; c) total vertical displacements between the base and the top stiff beams

3.4.4.6 Test P-B2R-2

The first damage was horizontal cracking at the base and top corners of the wall. This type of damage gradually propagated until peak resistance was reached. In post peak stage, the bending response remained dominant, but inclined cracks also appeared. The GFRP mesh fracture at the top of the wall was observed at collapse. Nor evident leaves separation of coating debonding were observed.

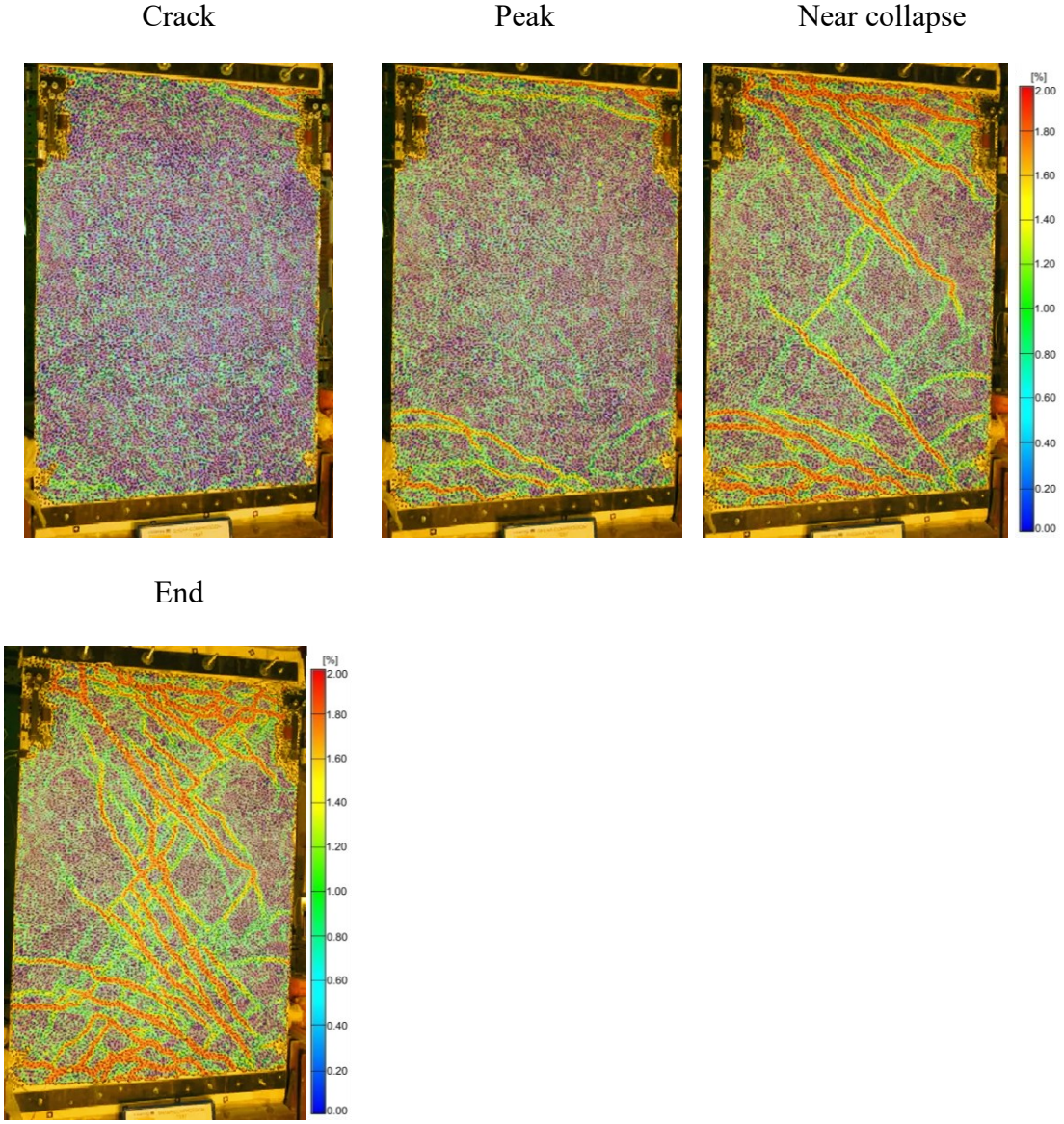
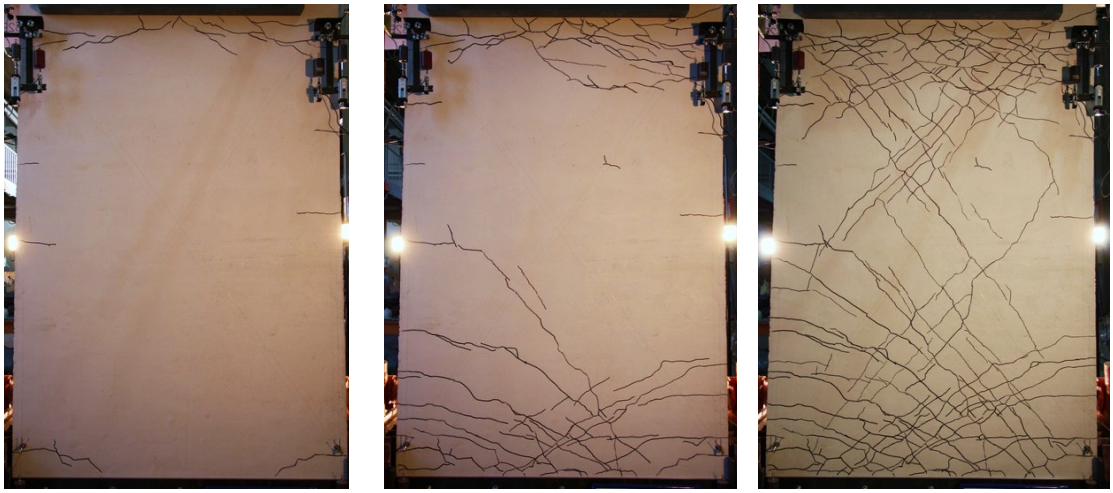


Figure 3.46 Crack pattern on the back side of wall P-B2R-2, with the positive loading direction toward the left side of the images

Crack Peak Near collapse



End

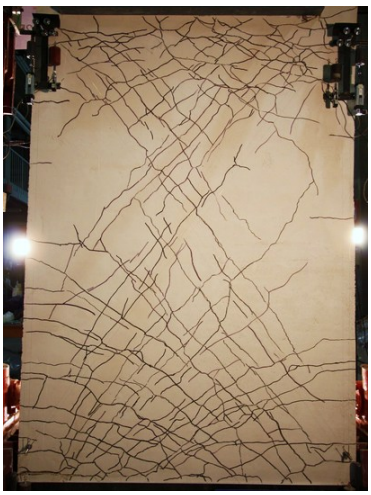


Figure 3.47 Crack pattern on the front side of wall P-B2R-2

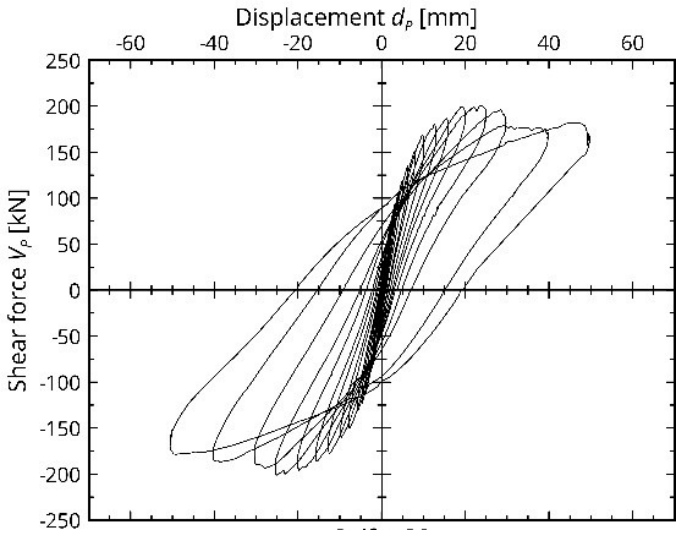


Figure 3.48 Force-displacement curve of test P-B2R-2

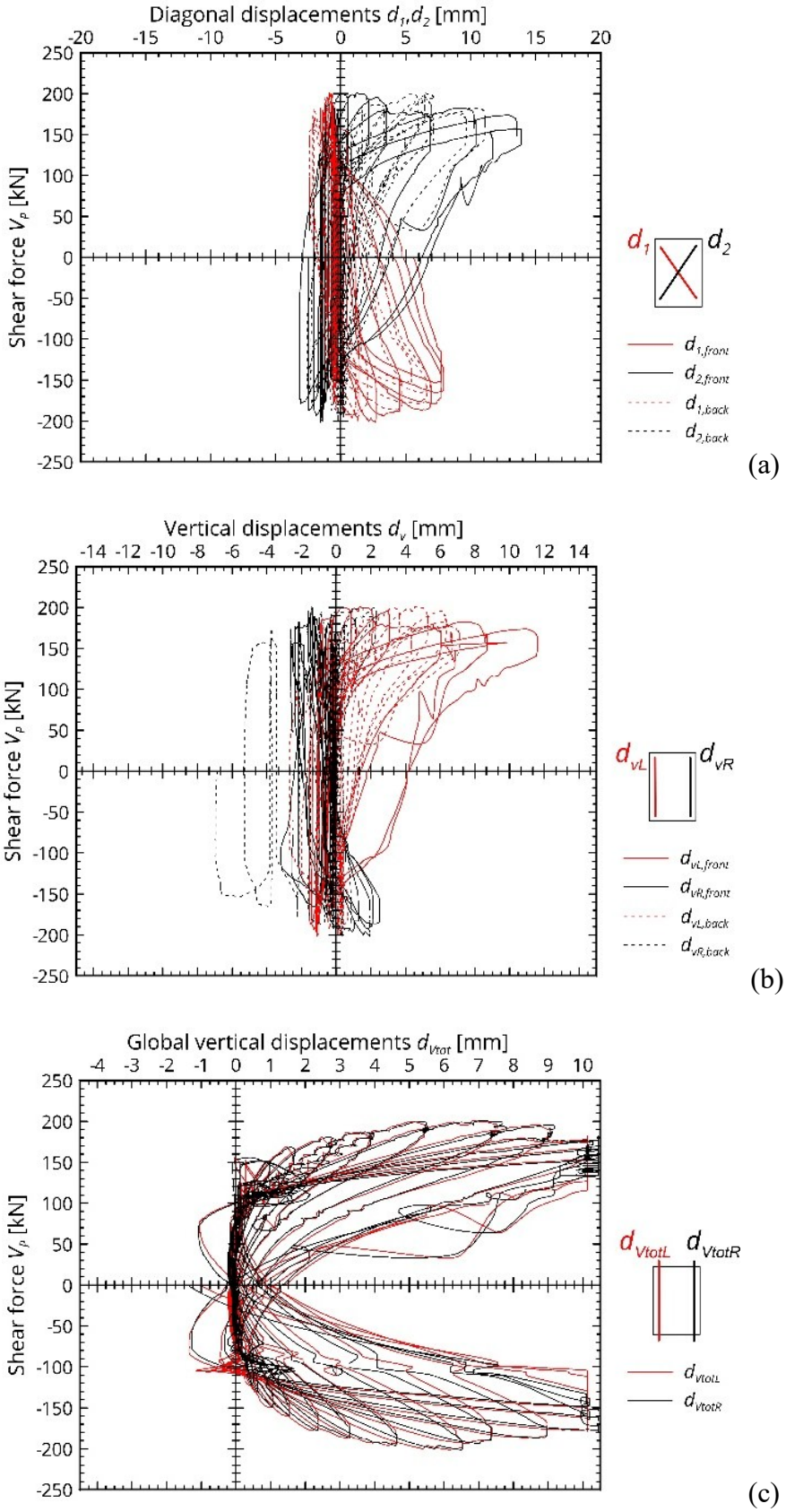


Figure 3.49 Main results of test P-B2R-2: a) displacements along the diagonals; b) vertical displacements along the side of the wall; c) total vertical displacements between the base and the top stiff beams

3.4.4.7 Test P-B1U

The first damage was horizontal cracks at the opposite corners, due to bending mechanism. Shortly after, a vertical crack at the centre of the wall opened. Approaching to the peak resistance, the vertical crack elongated at an angle towards the corners of the wall. Inclined cracking indicates shear response took over (as also detected by diagonal transducers) and continued until collapse was achieved.

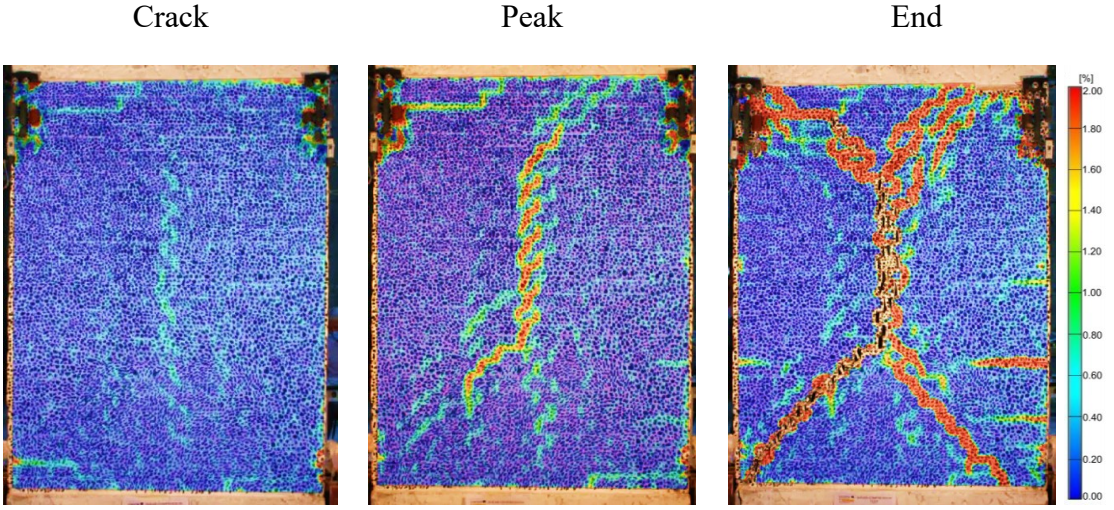


Figure 3.50 Crack pattern on the back side of wall P-B1U, with the positive loading direction toward the left side of the images

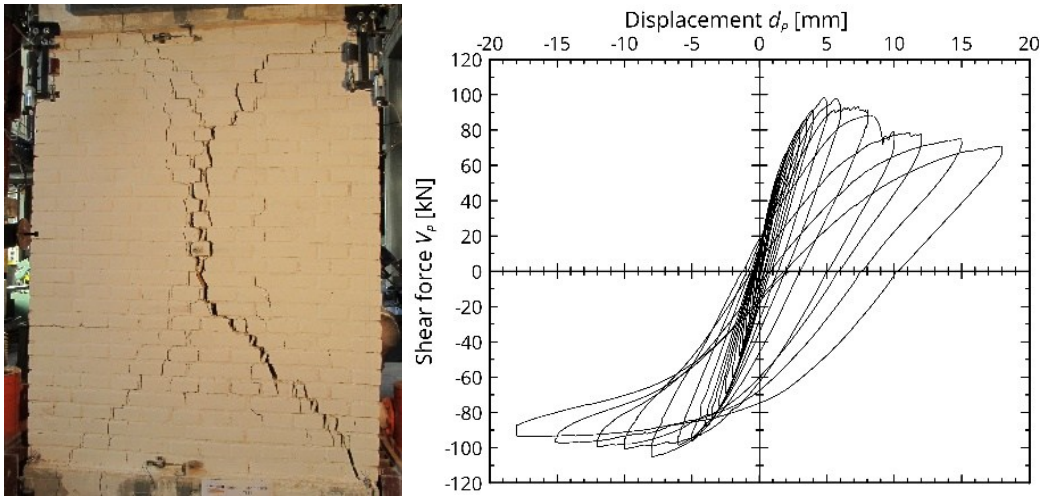


Figure 3.51 Test P-B1U: a) crack pattern on the front side of the wall and b) force-displacement curve

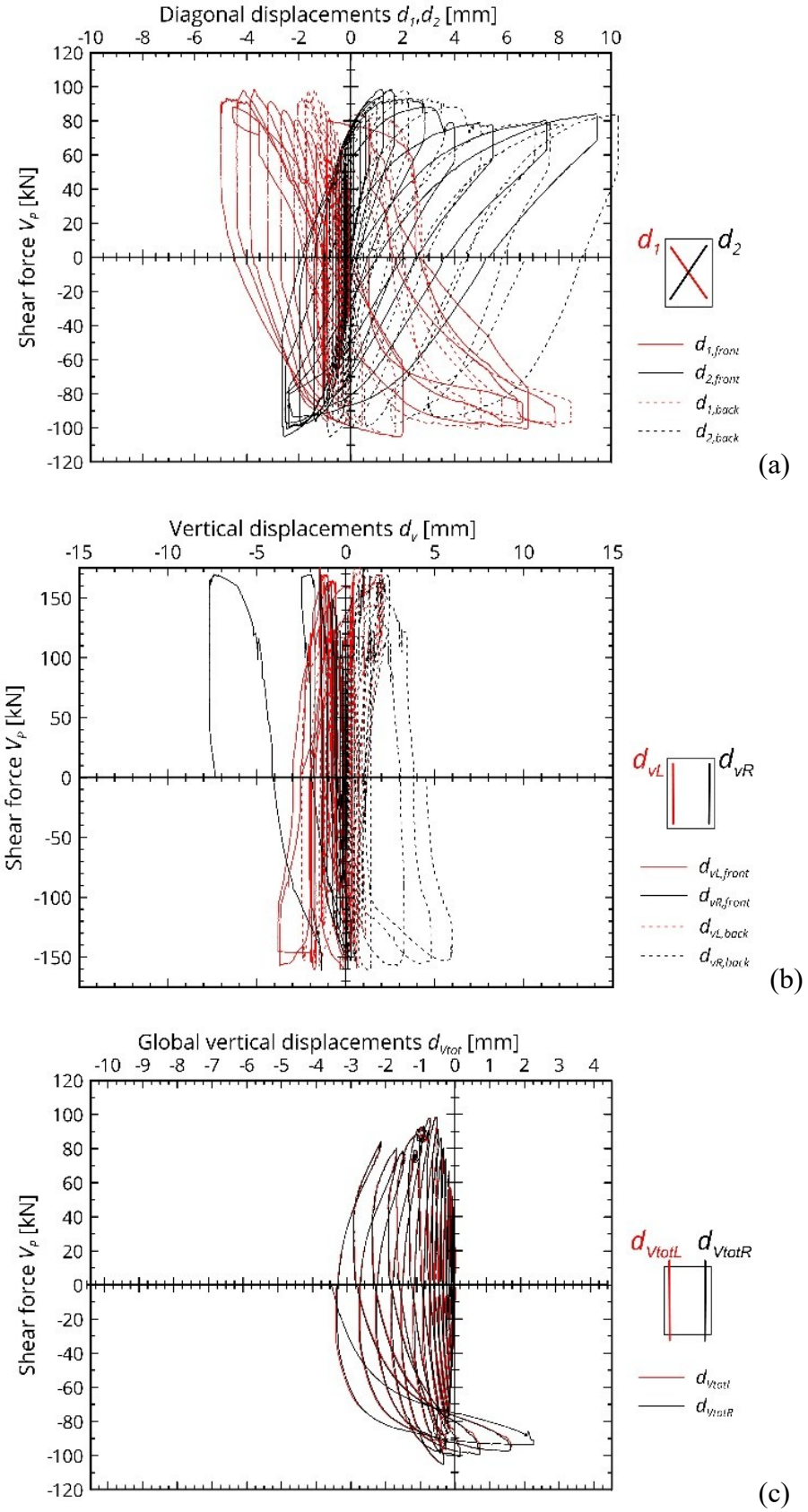


Figure 3.52 Main results of test P-B1U a) displacements along the diagonals; b) vertical displacements along the side of the wall; c) total vertical displacements between the base and the top stiff beams

3.4.4.8 Test P-B1R-1

The sample initially developed horizontal cracks on both the coating and the unstrengthened side. With increasing load, the horizontal cracks in the coating extended and propagated, but on the unstrengthened side some inclined cracks appeared in addition to the horizontal cracks, intersecting in the upper half of the wall. Shortly before peak resistance was reached, inclined cracks appeared also in the coating. After peak resistance, the inclined cracks were active and horizontal cracks barely activated. This continued until the end of the test. Although the inclined cracks were not exactly diagonal (from corner to corner), response was predominantly in shear.

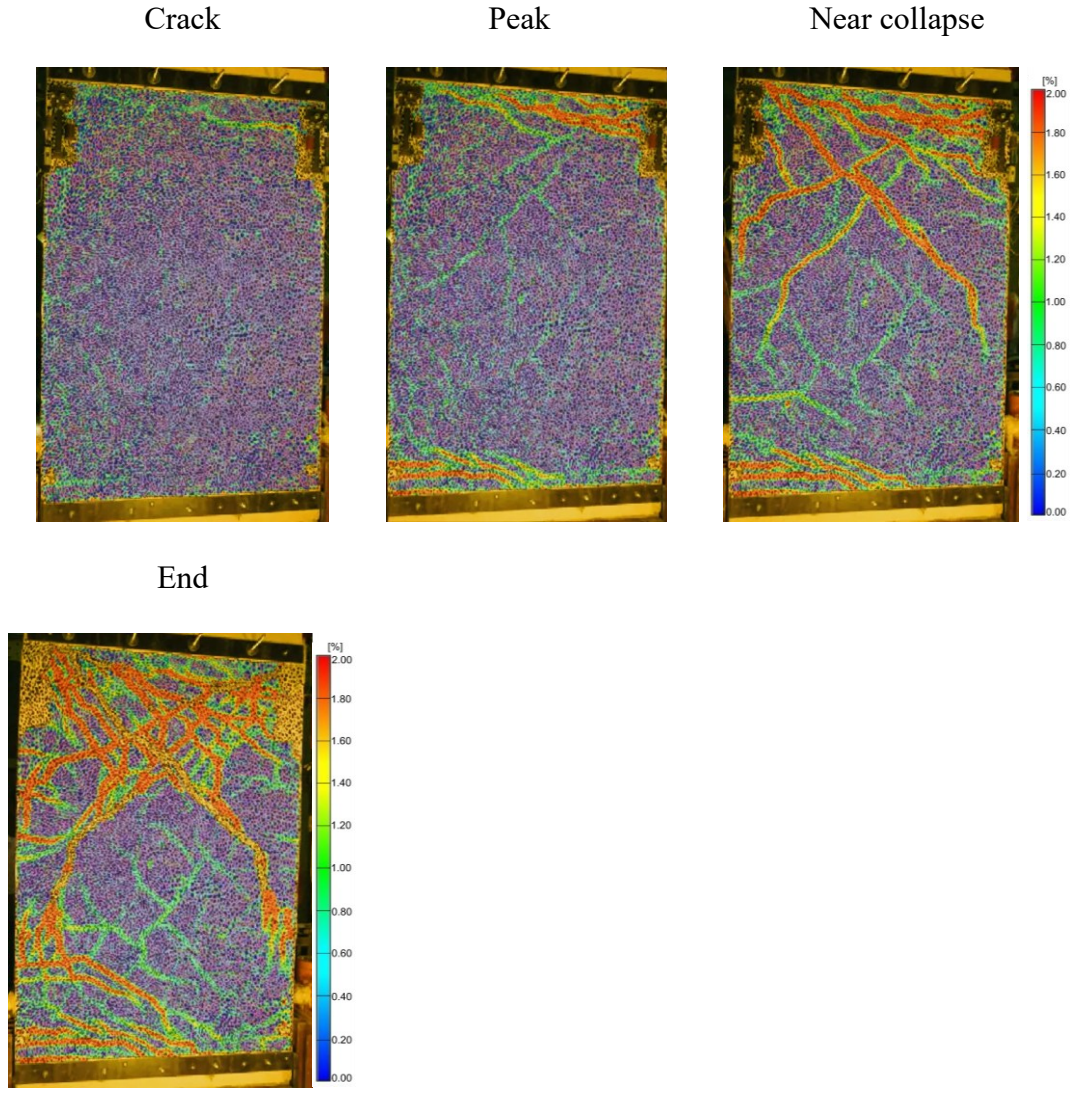


Figure 3.53 Crack pattern on the back side of wall P-B1R-1, with the positive loading direction toward the left side of the images

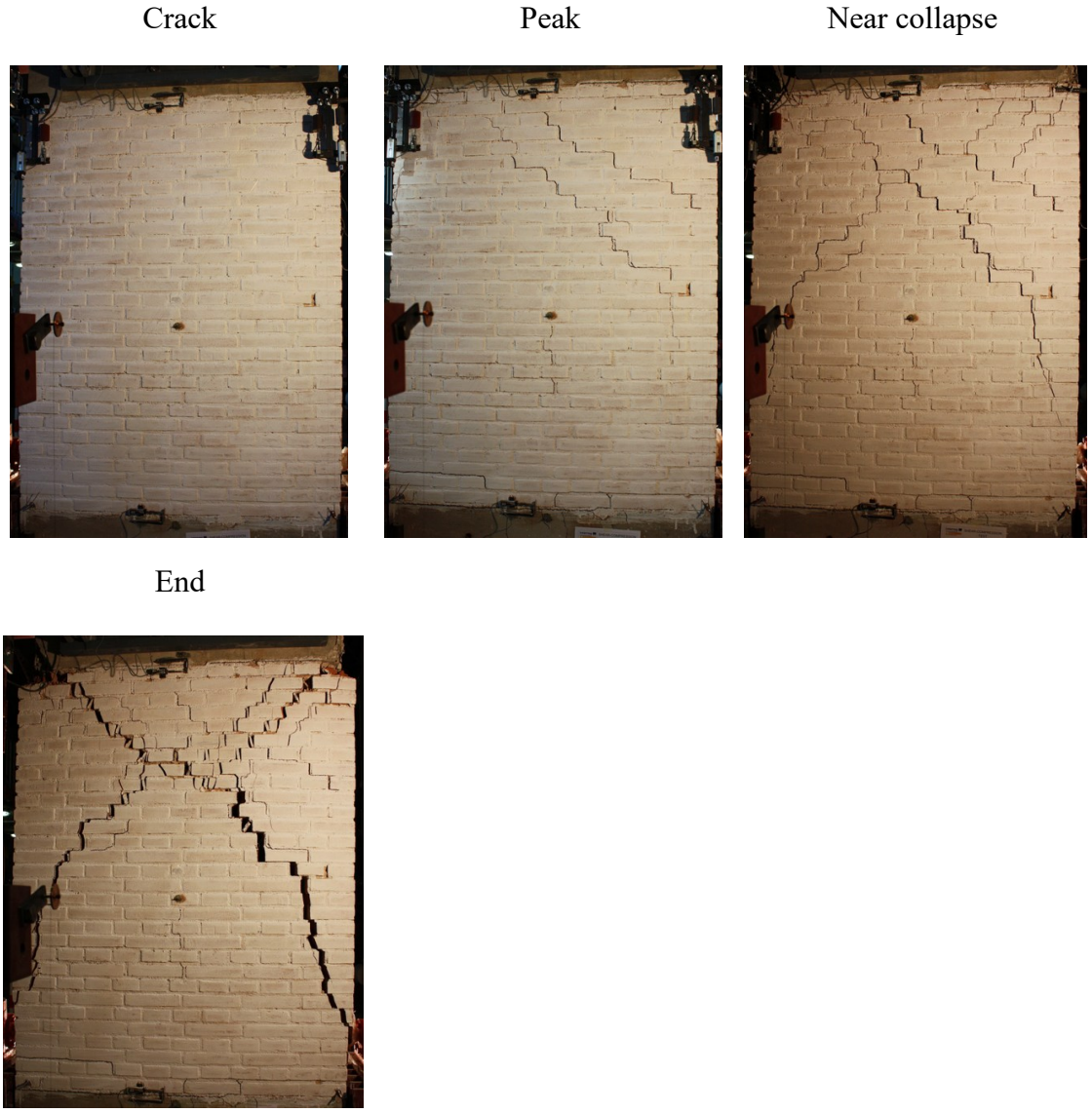


Figure 3.54 Crack pattern on the front side of the wall P-B1R-1

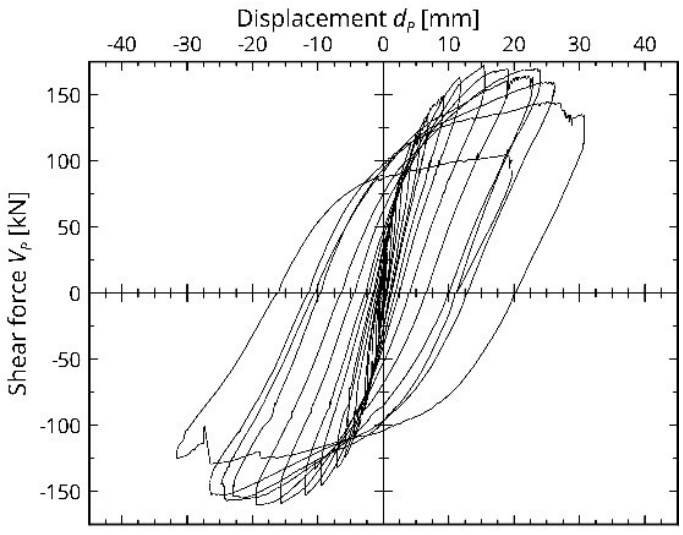


Figure 3.55 Force-displacement curve of test P-B1R-1

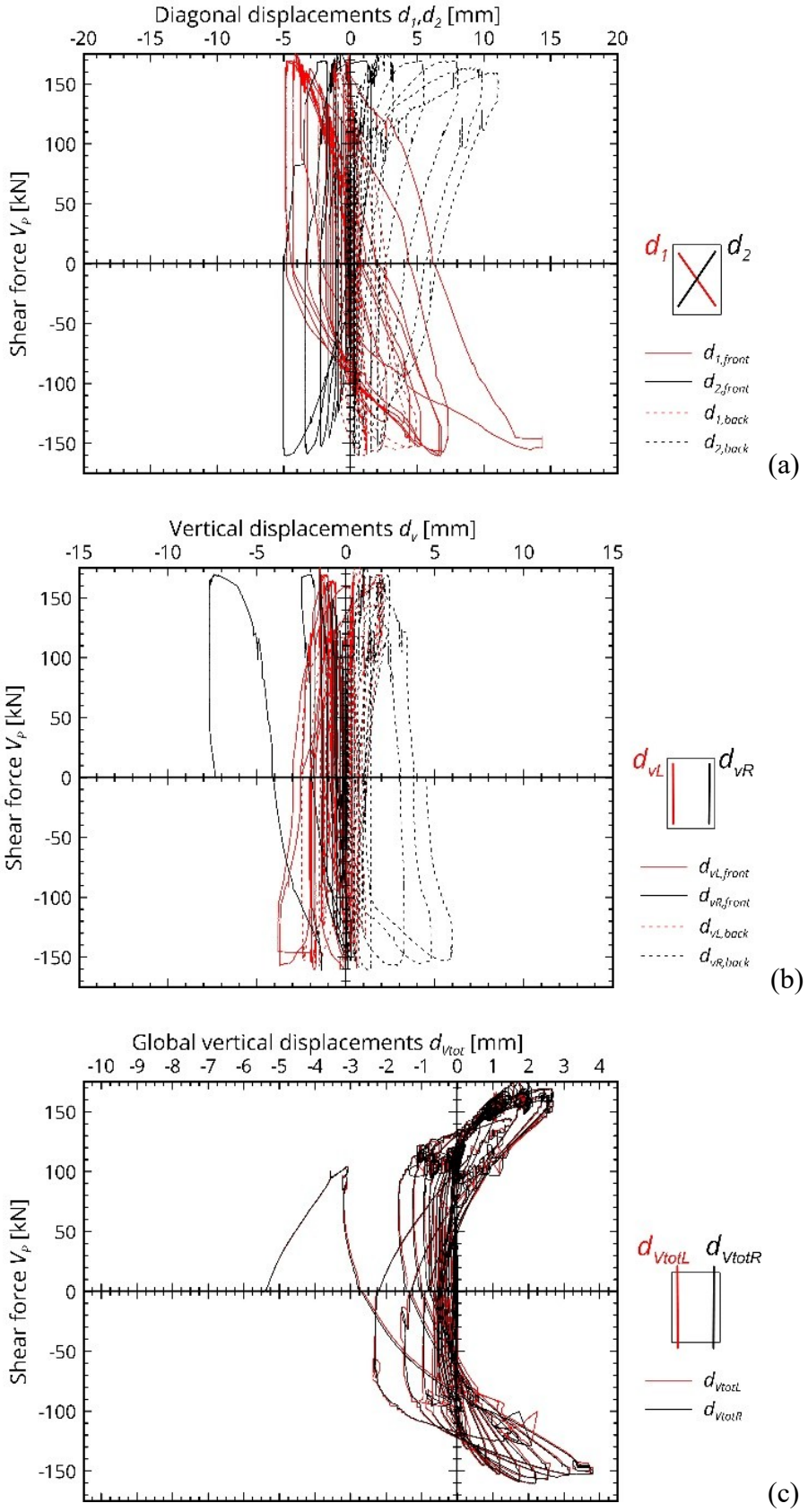


Figure 3.56 Main results of test P-B1R-1 a) displacements along the diagonals; b) vertical displacements along the side of the wall; c) total vertical displacements between the base and the top stiff beams

3.4.5 Analysis of results and comparison

The capacity curves comparison of unstrengthened and CRM strengthened pier samples is reported in Figure 3.57. The values of V_P and d_P obtained from the eight experimental tests are summarized in Table 3.10 and in Figure 3.58 for first cracking, peak load and end of the test (*Cr, Pk, End*).

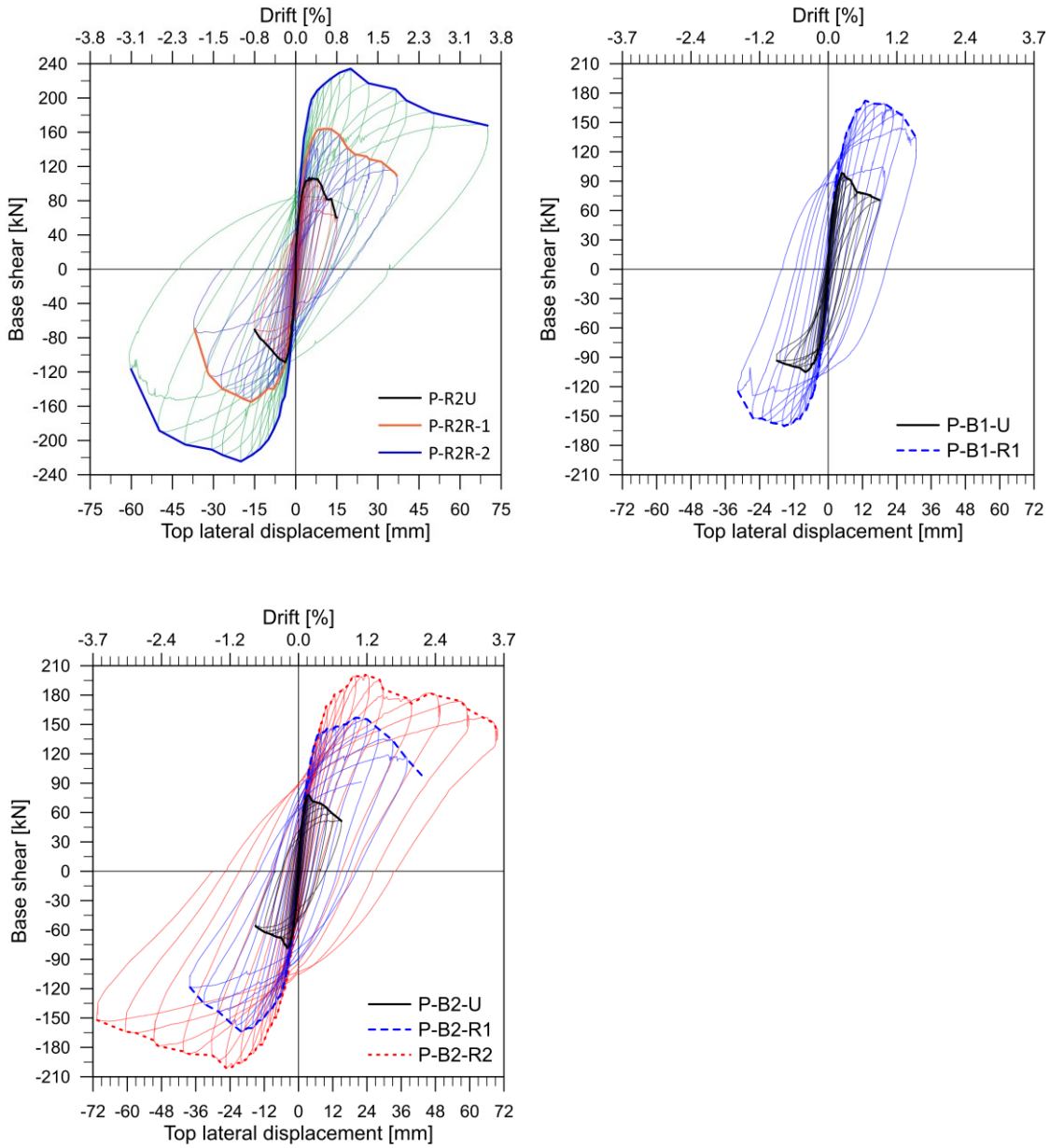


Figure 3.57 Comparison of capacity curves of unstrengthened and CRM strengthened pier samples

Table 3.10 Values of the lateral load (V_P) and horizontal displacement (d_P) measured in positive and negative loading directions, for the first cracking, peak load and end of the test.

	First cracking (*Cr*)		**Peak load (*Pk*)**		**End of test (*End*)**	
ID	V_P **[kN]**	d_P **[mm]**	V_P **[kN]**	d_P **[mm]**	V_P **[kN]**	d_P **[mm]**
P-R2U	83.2	2.0	106.8	4.9	74.7	13.0
	-84.8	-2.0	-108.8	-3.9	-76.2	-13.1
P-R2R-1	91.7	2.3	164.0	12.9	114.8	35.1
	-97.6	-2.5	-155.0	-16.2	-108.5	-32.2
P-R2R-2	157.2	3.7	234.3	19.8	164.0	68.0
	-157.6	-4.7	-224.5	-19.9	-157.1	-50.7
P-B2U	64.2	2.0	78.0	3.1	54.6	12.1
	-62.1	-2.0	-78.6	-4.0	-55.0	-15.0
P-B2R-1	98.0	3.2	157.0	20.1	109.9	38.1
	-95.0	-3.3	-164.0	-20.0	-114.8	-38.0
P-B2R-2	88.2	2.8	200.7	24.1	140.5	69.7
	-84.5	-2.6	-201.4	-25.1	-141.0	-70.4
P-B1U	55.7	1.3	98.5	4.8	68.9	18.1
	-63.4	-1.8	-105.3	-7.9	-73.7	-18.0
P-B1R-1	109.5	3.6	172.2	13.0	120.6	30.8
	-98.4	-3.0	-160.5	-16.1	-112.4	-31.6

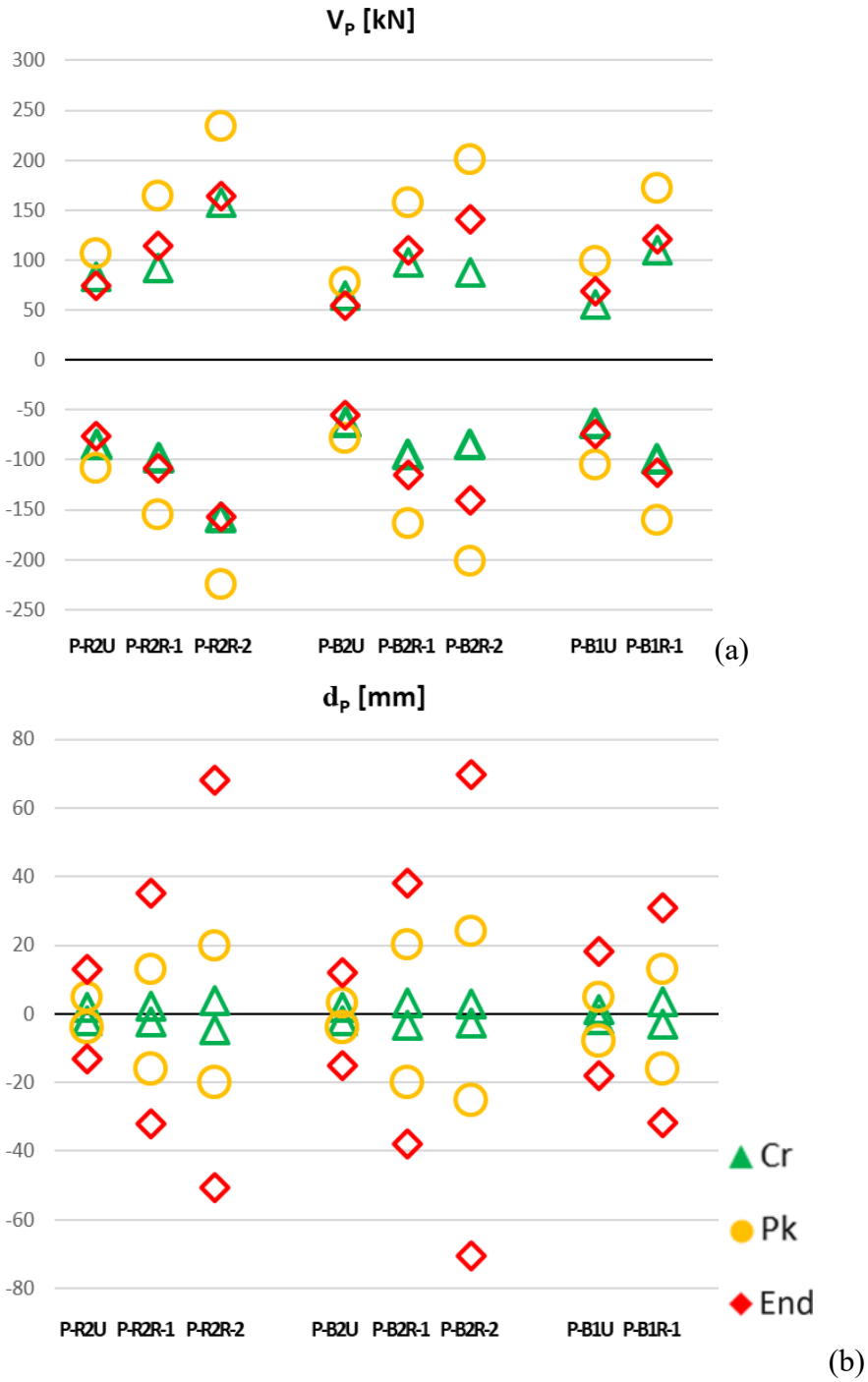


Figure 3.58 Main test results of "P" samples: first cracking, peak and near collapse forces (a) and top horizontal displacements (b).

In all the unstrengthened masonry piers, the failure was governed by a pure diagonal cracking mechanism; the cracks had a stair-stepped trend and involved mainly the mortar joints (both head and bed joints). The stone masonry P-R2U attained to a mean peak load of 107.8 kN, quite similar to that of the single leaf brick masonry P-B1U (101.9 kN); a lower resistance was attained by the double leaf brick masonry P-B2U (78.3 kN). The displacement at the end of the test was quite high for P-B1U (18.1 mm), compared with

the ultimate limit drift of 0.005 for shear failure specified by the Italian code. The displacements at the end of the tests were lower for P-R2U and P-B2U (about 13.1-13.6 mm), due to the weak wythes connection. An evident leaf separation actually occurred in P-B2U, just after the peak load.

In the samples strengthened at one side only, the diagonal cracking mechanism was evidently detectable on the plain masonry side; diagonal cracks also occurred in the coating on the strengthened side, but in combination with horizontal and inclined cracks originating from the corners at the bottom and top of the pier, indicating also the activation of the in-plane bending mechanism. After reaching the peak load and approaching to collapse, leaf separation and coating debonding started to occur in P-R2R-1 and P-B2R-1 masonry and the coating debonding also activated in P-R2R-1. However, the presence of the transversal anchors contrasted the layer separation and overturning.

A very largely diffused crack pattern occurred in the two-sides strengthened samples, for the combined activation of diagonal cracking and bending mechanisms. The coating debonding (and the leaf separation in P-R2R-2) also activated when the collapse was incipient.

In the stone rubble masonry, the one-side CRM strengthening intervention led to an increase of the pier resistance of 1.48 times and determined an ultimate displacement 2.58 times higher in respect to the plain masonry. In case of strengthening at both sides, such increments resulted, respectively, 2.13 and 4.55 times. Actually, the one-side application provided values of strength and ultimate displacement almost in-between the plain and the two-sides strengthened configurations.

In the double leaf brick masonry, the peak resistance and the ultimate displacement of the one-side reinforced configuration were, respectively, 2.05 and 2.81 times those of the plain masonry. In case of strengthening at both sides, the increments were of 2.57 and 5.17 times.
The one-side reinforcement applied on the single leaf brick masonry determined a pier resistance and ultimate displacement of 1.63 and 1.73 times those of the plain masonry.

The cyclic tests allow also to draw the trends of the piers cycle stiffness, K_P (evaluated as the slope of the peak-to-peak line within each loop of the V_P–d_P curve) by varying d_P (Figure 3.60). An elastic deformability of the apparatus was estimated from the displacements of instruments T8-T11, which resulted on average in 56 kN/mm, showing

a reduced stiffness of the sample. The stiffness degradation with increasing distortion shows an approximately power-law trend, with a softer degradation in the strengthened samples, in respect to the unstrengthened ones. At the end of the tests, the cycle stiffness degraded by about 90–95% of the initial value.

The cumulative input energy (E_{in}) and the dissipated hysteretic energy (E_{hys}) were quantified (Figure 3.61), as well as the Ehys/Ein ratios (Figure 3.62). Ein is the cumulative work to deform the sample from the beginning of the test to a specific target value of displacement d_P. For each loading cycle, it corresponds to the area under the positive and negative branches of the hysteretic loop of the F_P-d_P graph. Similarly, the cumulative dissipated hysteretic energy E_{hys} is the sum of all the areas included in the hysteretic loops.

Finally, an estimation of the equivalent hysteretic damping with varying target displacement was performed (Figure 3.63), accordingly to the procedure The hysteretic response yields an approximate value of the equivalent hysteretic damping of the structure, which can be determined using the equation proposed by Chopra [12] and ATC FEMA 440 [247]:

$$\xi_{hys,i} = \frac{E_{hys,i}}{4\pi\, E_{s0,i}} \tag{3.1}$$

where $E_{hys,i}$ is the hysteresis energy dissipated within each cycle and $E_{s0,\mathrm{i}}$ is the strain energy associated with the secant stiffness of the structure in the ith cycle, as illustrated in Figure 3.59 and calculated using Eq. (3.2).

$$E_{s0,i} = \frac{1}{2} \cdot k_{s,i} \cdot \delta_{avg,i}^2 \tag{3.2}$$

where $k_{s,i}$ is the secant stiffness of the i-th cycle and $\delta_{\mathrm{avg,i}}$ is the average of the positive and the absolute value of the negative maximum displacements reached in the cycle. The $k_{s,i}$ was calculated according to Eq.(3.3).

$$k_{s,i} = \frac{V_{max,i} + |V_{min,i}|}{\delta_{max,i} + |\delta_{min,i}|} \tag{3.3}$$

where $\delta_{max,i}$ and $\delta_{max,i}$ are the maximum and minimum displacements, and $V_{max,i}$ and $V_{min,i}$ are the corresponding shear strengths, respectively, recorded in the in the i-th cycle.

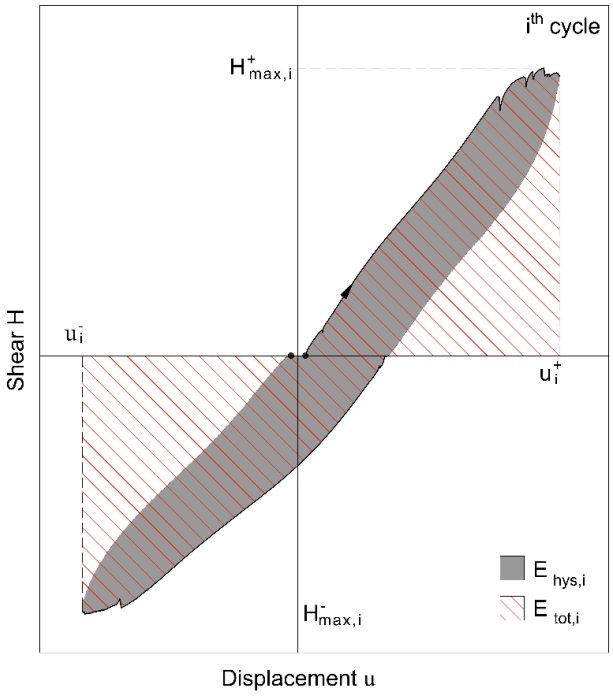


Figure 3.59 Total and hysteretic energy

The value of the equivalent hysteretic damping is used in many building codes ([247], [15]) to evaluate the resisting ground acceleration of a building with the use of the Capacity spectrum method.

In general, significantly higher input and dissipated cumulative energies resulted from the strengthened samples, in respect to the plain masonry (Table 3.11). The cumulative dissipated hysteretic energy for rubble stone, at the end of the tests, increased by 3.39 and 7.18 times compared to unstrengthened state, for piers P-R2R-1 and P-R2R-2, respectively. In case of two leaf brick masonry, the cumulative dissipated hysteretic energy was increased 5.46 and 8.73 times for piers P-B2R-1 and P-B2R-2, respectively. In case of single leaf brick masonry, the single sided application of coating increased the amount of hysteretic cumulative dissipated hysteretic energy by a factor of 4.45.

Initially, the equivalent hysteretic damping, ξ_{hys}, ranged within 0.1-0.2, then experienced a rapid drop (more substantial in the strengthened samples) before increase again and reaching higher values (generally, up to 0.25-0.30).

Table 3.11 Cumulative input energy E_{in} and dissipated hysteresis E_{hys} at peak load (Pk) and at the end of the test (End), mean dissipated energy ratio in the cycles (E_{hys}/E_{in}). The ratios between strengthened and unstrengthened samples, for both E_{in} and E_{hys} are also calculated.

Sample	Peak load (Pk)					End of the test (End)				
	E_{in} [J]	$E_{in,R}/E_{in,U}$ [-]	E_{hys} [J]	$E_{hys,R}/E_{hys,U}$ [-]	E_{hys}/E_{in} [-]	E_{in} [J]	$E_{in,R}/E_{in,U}$ [-]	E_{hys} [J]	$E_{hys,R}/E_{hys,U}$ [-]	E_{hys}/E_{in} [-]
P-R2U	2.84	1.00	2.02	1.00	0.71	11.95	1.00	9.62	1.00	0.81
P-R2R-1	16.33	5.74	12.21	6.06	0.75	44.65	3.74	32.59	3.39	0.73
P-R2R-2	27.06	9.52	14.44	7.16	0.53	101.13	8.46	69.10	7.18	0.68
P-B2U-1	2.02	1.00	1.14	1.00	0.56	8.04	1.00	6.11	1.00	0.76
P-B2R-1	18.92	9.39	9.51	8.31	0.50	52.41	6.52	33.36	5.46	0.64
P-B2R-2	27.01	13.40	11.42	9.98	0.42	87.72	10.91	53.32	8.73	0.61
P-B1U-1	4.85	1.00	2.43	1.00	0.50	13.59	1.00	7.04	1.00	0.52
P-B1R-1	14.79	3.05	7.05	2.91	0.48	47.58	3.50	31.33	4.45	0.66

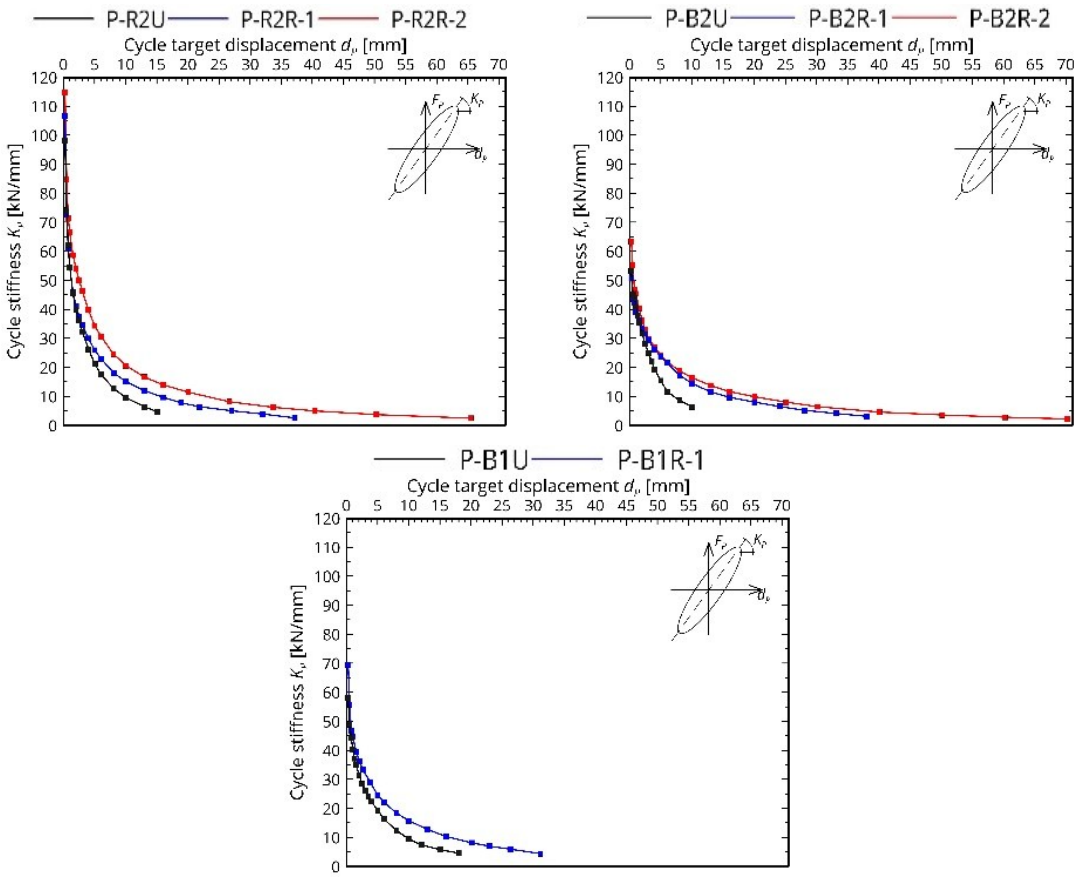


Figure 3.60 Piers' evolution of cycle lateral stiffness

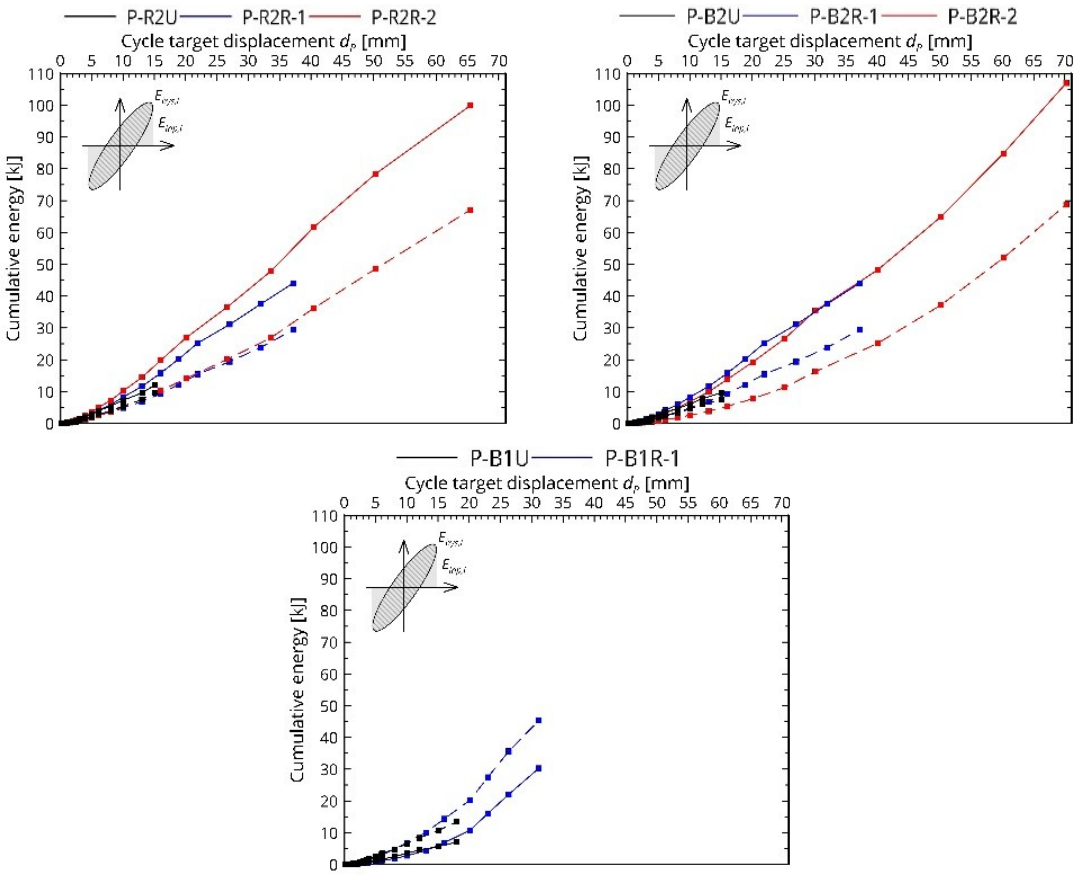


Figure 3.61 Piers' energy dissipation

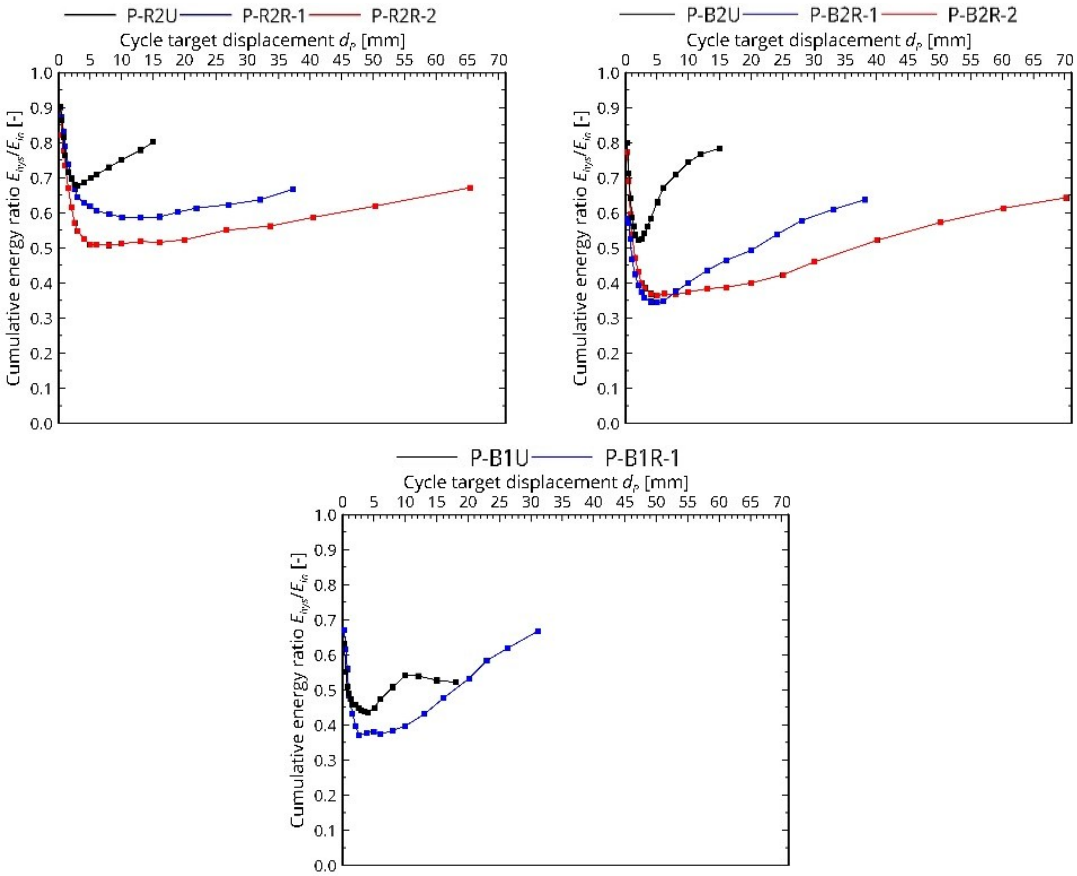


Figure 3.62 Piers' evolution of the cumulative energy ratio E_{hys}/E_{in}

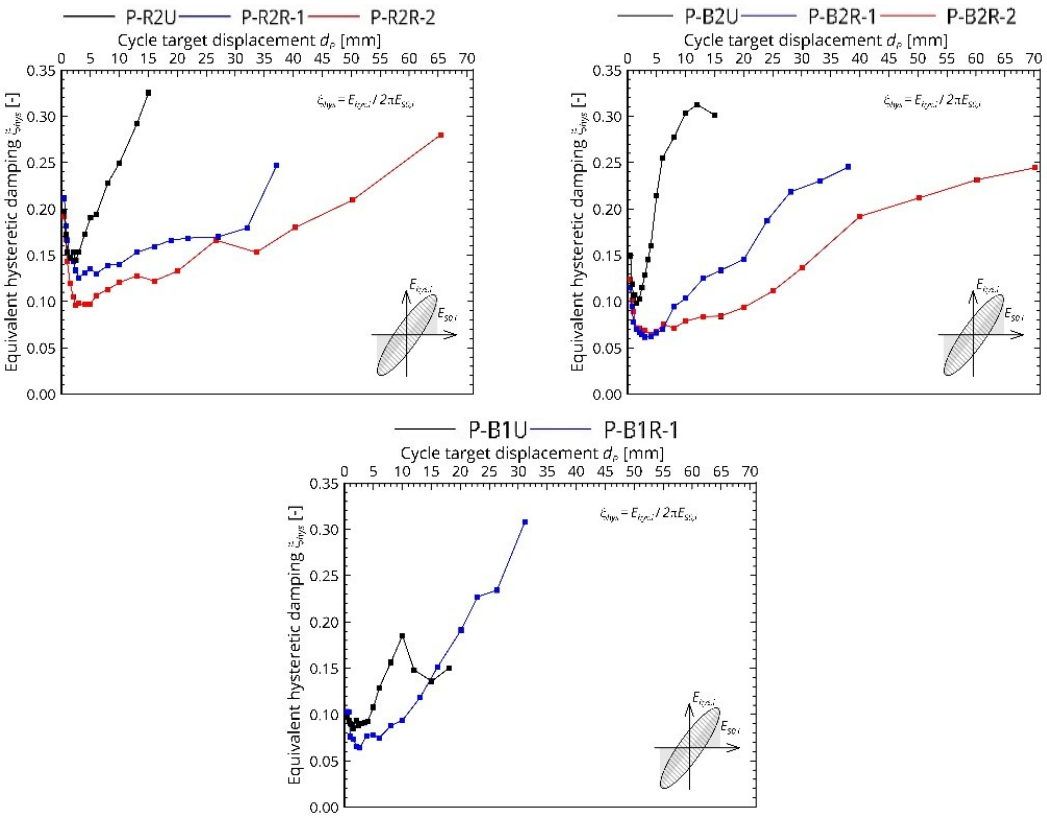


Figure 3.63 Piers' evolution of the equivalent hysteretic damping ratio ξ_{hys}

3.5 In-plane behaviour of spandrels

The tests performed in this study were carried out according to the test setup proposed by Beyer et al. [22], and were performed at the University of Ljubljana (Slovenia). The tests aimed to evaluate and compare the in-plane performances of the spandrels before and after applying CRM coatings. Two CRM coating configurations were considered: both wall sides or only one side. The two-sided coating was expected to perform better, having twice the reinforcement, symmetry and, to some extent, masonry confinement provided by the passing-trough transverse connectors.

3.5.1 Literature review

The application of one-sided, composite fibre-reinforced mortar coatings on spandrels has not yet been addressed in the literature. Few studies are available on TRM strengthened spandrels [41,42]. Both studies investigated on the seismic behaviour of spandrels strengthened with the FRCM system applied on both sides. From studies conducted on TRM strengthened walls it's difficult to draw general conclusions about the effect of single-sided applications compared with double-sided one, since the observations are based on simplified tests in terms of load pattern and boundary conditions, which do not represent the actual conditions. Moreover, multiple-leaf or irregular masonry is not typically considered, although they are more likely to present criticalities due to single-side strengthening. For example, in [152] and [158], debonding of the CRM coating and masonry leaf separation occurred in rubble stone masonry piers subjected to shear-compression tests because the transversal anchors were too weak.

The tests reported and analysed in the following aim at providing original results on spandrels tested under representative loads and boundary conditions in the laboratory. Furthermore, the highly vulnerable double-leaf rubble stone masonry typology is considered. The main features of the samples and the testing apparatus are reported in the following sections; then, the test results are described in terms of capacity curves and damage pattern evolution. Finally, the results are analysed and compared, providing useful information on the effectiveness of the CRM coating in terms of resistance, displacement, stiffness and dissipative capacities.

3.5.2 Description of the samples

The research considered of "H"-shape masonry panels aimed at recreating the spandrel area and two adjacent piers. To facilitate a uniform load distribution in testing, reinforced concrete beams were created at the base and at the top of each masonry column.

All three masonry types were considered (R2, B2 and B1). In the rubble stone samples, a timber lintel (2 beams, cross section 170×170 mm), indenting in each lateral column for 150 mm, was introduced under the spandrel, to reproduce the typical arrangements in historical stone buildings. Differently, in the solid brick samples, a masonry jack arch was created at the spandrel intrados, with couples of bricks arranged alternatively as headers or stretchers (height 250 mm).

A total of four "H"-shape panels were built and tested (Table 3.12): two in rubble stone masonry (R2), one in double leaf solid brick masonry (B2), and one in single leaf solid brick (B1) masonry. Initially, the panels were tested in their unstrengthened state, up to a damage level close to the ultimate to serve as a reference. Then they were repaired, retrofitted and tested again, up to a near-collapse condition. The repair involved sealing of cracks and later injection with *Kemagrout CI50*[4], a low viscosity mixture of cement and plasticizing additives with shrinkage compensation and high initial and final strength. For the two-leaf stone masonry, two samples were tested: one with the coating on one side with artificial diatons and a sample with the coating applied to both sides.

The sample dimensions and the positioning of the GFRP connectors and of GFRP connectors combined with artificial diatons is schematized in Figure 3.64.

[4] https://formatiq.pl/produkt/kemagrout-ci-50-mieszanka-cementow-i-dodatkow-uplastyczniajacych/

Table 3.12: Summary of the experimental tests on spandrels.

Sample ID	Masonry type	Strengthening system	Connectors
S-R2U-1	R2	/	/
S-R2R-1	R2	CRM on one-side	GFRP + diatons, 1 side
S-R2U2	R2	/	/
S-R2R-2	R2	CRM on two-sides	GFRP, passing-through
S-B2U	B2	/	/
S-B2R	B2	CRM on one-side	GFRP + diatons, 1 side
S-B1U	B1	/	/
S-B1R	B1	CRM on one-side	GFRP, 1 side

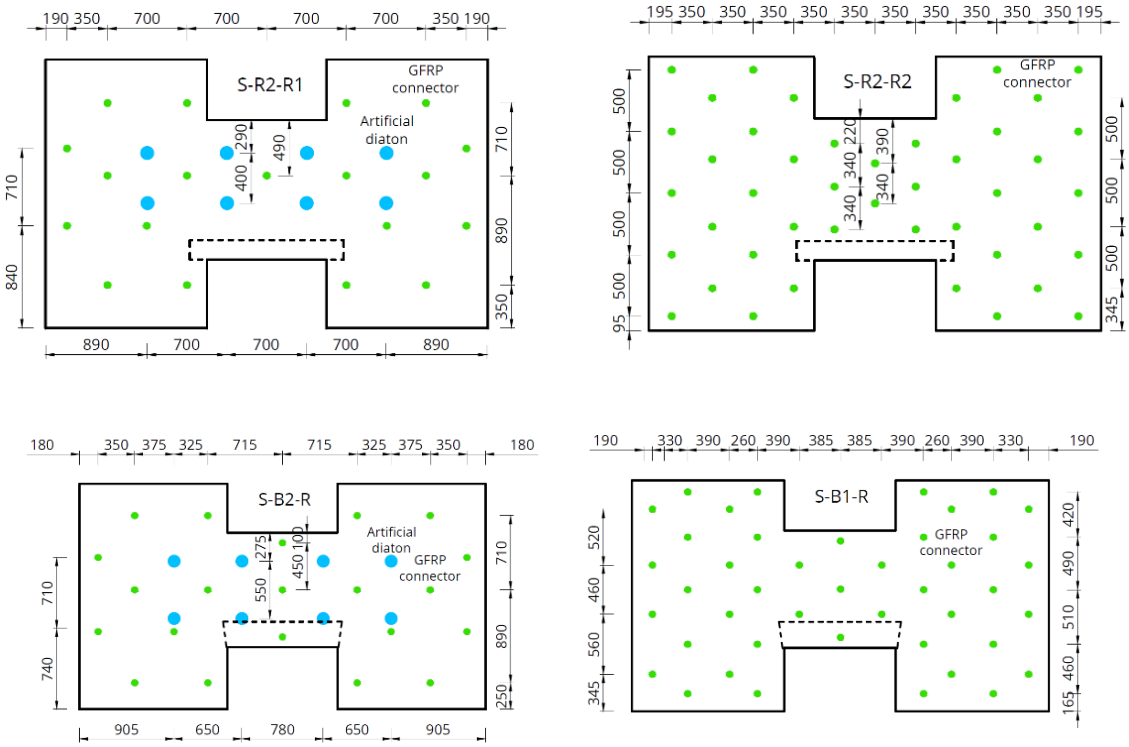


Figure 3.64 Positioning of the connectors in CRM strengthened spandrel samples (measures in millimetres)


(a)

(b)

Figure 3.65 Construction of samples a) S-R2-1 and b) S-B2-1

3.5.3 Test setup

The test apparatus (Figure 3.66 Schematization of the test setup for spandrels.) consisted of two independent horizontal steel beams (HEB 400), placed on support knuckle joints (equipped with load cells). The joints allowed the possibility of carrying loads in both compression and tension. Both joints were rotational; in addition, the right joint, allowed horizontal translations. Each external wall column of the H-shape masonry sample was positioned on one of the steel beams, vertically centered with the knuckle joint. Two servo-hydraulic actuators (250 kN load capacity and 200 mm stroke cpacity each) ortiented vertically were attached to the free, external ends of the steel beams and locked on independent steel frames. Four hydraulic actuators (500 kN capacity) were installed on the columns to apply an axial compressive load. Each piston was contrasted at the top by steel elements connected to the steel beams at the base by means of threaded rods. The four pistons were connected in parallel and introduced a constant force (correspondent to an axial stress level of about 0.33 MPa on the masonry columns). During the tests, the two external actuators moved at the same speed in opposite directions. The sepped was maintained The rotation θ, evaluated in accordance with Eq. (3.4):

$$\theta = \frac{(w_{Lm} + w_{Li})}{b_p} = \frac{(w_{Rm} + w_{Ri})}{b_p} \qquad (3.4)$$

where w_i and w_m are the vertical displacements at the inner and outer corners of the piers, measured at the intrados of the left (L) and right (R) lever beams, respectively, and b_p is the pier width. The vertical distortion δ_{sp} applied to the spandrel was estimated using Eq. (3.5).

$$\delta_{sp} = \theta \cdot (b_p + b_{sp}) \tag{3.5}$$

where b_{sp} is the spandrel width.

This caused shear and bending in the spandrel. The load was applied cyclically in the positive (clockwise rotation of the beams) and negative directions (anti-clockwise rotation), gradually increasing the target amplitude and performing three repetitions for each.

Considering the balance of vertical forces, the shear force acting on the spandrel was given by the sum of the load transmitted by the outer actuator and the vertical reaction at the support on the left (or right) lever beam. The mean value between both sides was considered, according to Eq. (3.6):

$$V_{sp} = \frac{V_{Lsp} + V_{Rsp}}{2} = \frac{\left(C_{Lp} + C_{Ls}\right) + \left(C_{Rp} + C_{Rs}\right)}{2} \tag{3.6}$$

The testing apparatus and load pattern basically reproduced those designed by Beyer and Dazio [22]. The main difference stood in the absence of the horizontal rods introducing an axial force into the spandrel. In fact, the tests were specifically carried out to detect the coupling effect of the spandrel due to the CRM application, not influenced by any other horizontal constrain; any tying effect would have reasonably increased the sample performances. In addition to the reference approach, RC elements (cross-section of 250×250 mm^2) were positioned at the base and top of each masonry pier of the sample, to facilitate a uniform load distribution and transfer during testing.

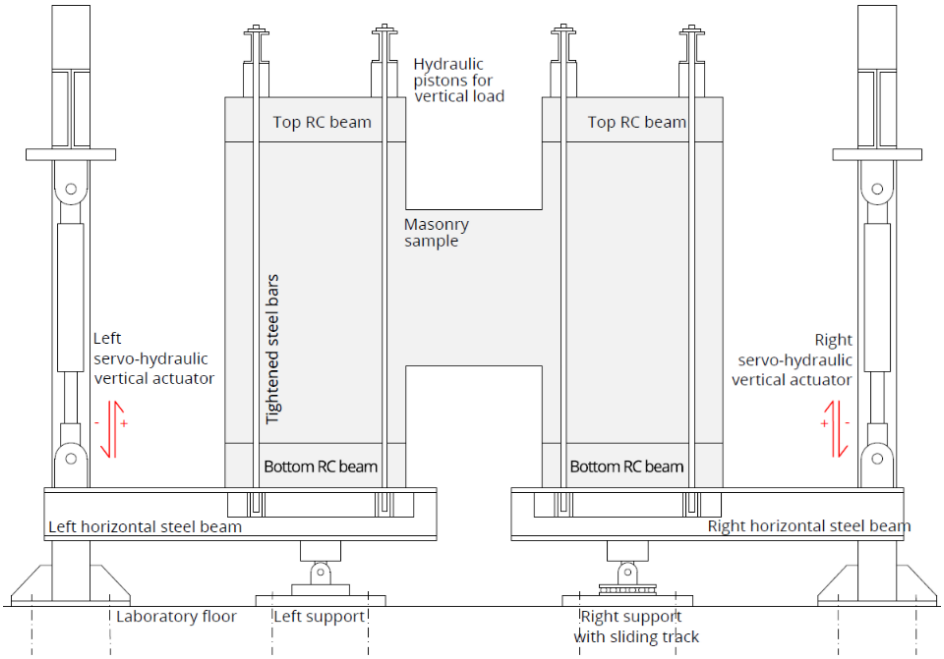


Figure 3.66 Schematization of the test setup for spandrels.

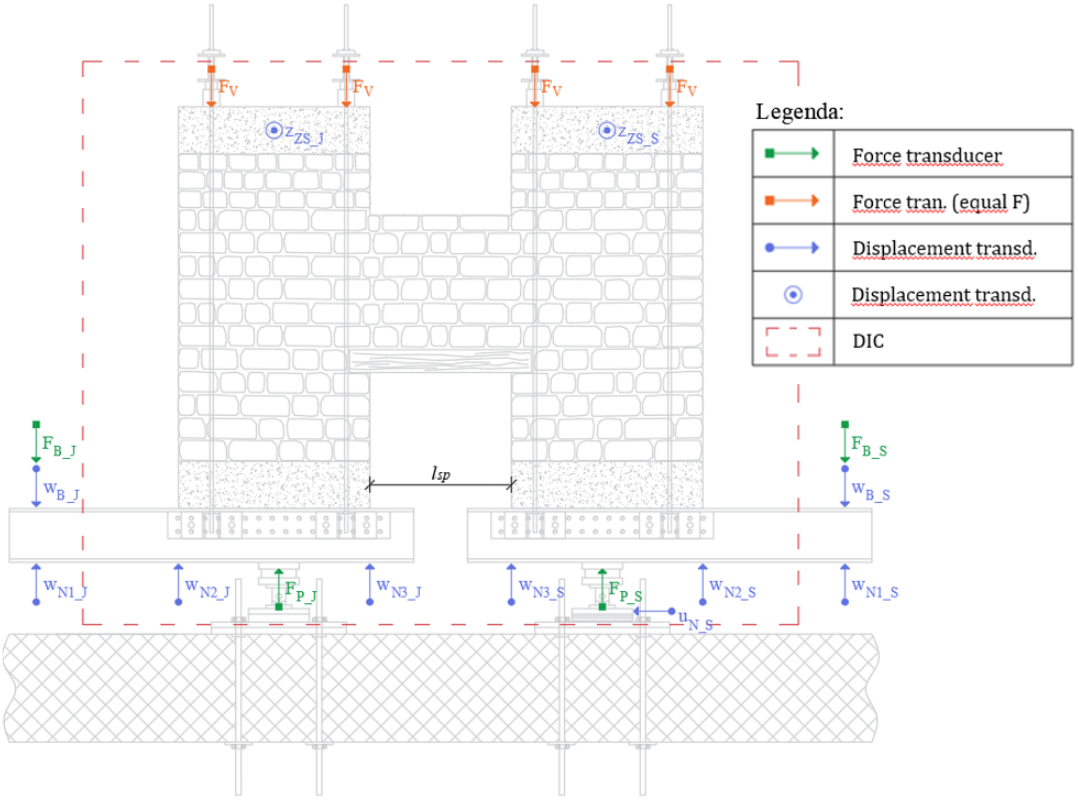


Figure 3.67 Instrumentation for in-plane tests on spandrels

The displacements were measured through Linear Variable Differential Transformers (LVDTs) with a stroke from 50 mm and 500 mm. Contrary to potentiometer transducers, LVDTs do not rely on mechanical contact for signal transmission, which makes them less

sensitive to wear, friction, and electrical noise. They function based on electromagnetic principles, based on a movable ferromagnetic core that shifts within a set of coils. As the core moves, it alters the magnetic field and induces a change in voltage proportional to the displacement.



Figure 3.68 Linear variable differential transformer

Each specimen was equipped with 11 LVDTs, as shown in Figure 3.67. A series of six potentiometer transducers (labelled "w" in Figure 3.67) were fixed to the laboratory floor in order to measure the vertical displacements at the intrados of the two beams at different positions, which corresponded to the external actuators and the outer and inner corners of the masonry columns. Two instruments (labelled "z" in Figure 3.67) measured the out of plane displacement at the centre of the top RC beam of the piers. The instrument $u_{N,s}$ measured the sliding of the right support, while two instruments measured the vertical displacement of the steel beams in correspondence of the servo-hydraulic actuators.

A digital image correlation (DIC) system measured the displacement and strain fields on one wall surface. A random speckled pattern was painted on the front wall surface to facilitate identification of the same measurement points in pictures taken from both cameras, while the spandrel area on the back of the wall was painted white to facilitate the visual examination of cracks. The principal tensile strain field monitored through the DIC system was particularly useful for observing crack development in the spandrels. It was particularly interesting to compare the crack patterns with the attainment of first cracking (Cr), peak load (Pk) and near collapse (Nc). This latter was assumed to have been attained for a 30% shear load decrease from the peak load.

The loading protocol is shown in and Figure 3.26. The tests were terminated when collapse was imminent, after a reduction in peak force of at least 20% was attained.

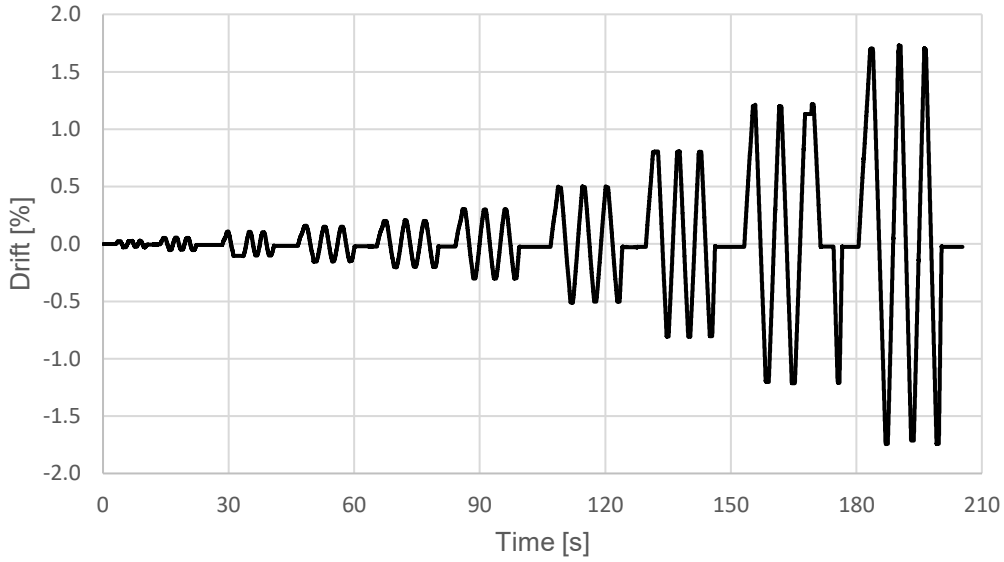


Figure 3.69 Loading program for the spandrel S-B2-R

The behaviour of each sample is described in the following, reporting also monitored loads and displacements and evolution of the crack pattern (surveyed at the front side by means of a Digital Image Correlation system). The main results are then summarized and compared.

The global behaviour of the spandrels is described in terms of capacity curves, representing the shear load, V_S, varying the vertical distortion d_S. The shear load V_S was obtained from the vertical translation equilibrium of the external vertical forces acting on the left half (as well as right half) of the sample, i.e. load applied by the outer actuator and the reaction at the support. The distortion d_S was calculated by using the following equation:

$$d_S = \left(\delta_{V,r} - \delta_{V,l}\right) \cdot \left(\frac{b_{sp}}{2} + \frac{b_P}{2}\right) \Big/ \left(\frac{b_P}{2}\right) \qquad (3.7)$$

where δ_V is the vertical displacement in correspondance on the inner corners of the two masonry columns (right – r, and left – l). The spandrel drift γ_S was determined by dividing d_S by the spandrel's length.

In addition to the distortion, the horizontal sliding of the right support (d_H) was monitored during the tests.

According to the typical in-plane failure mechanisms of historic masonry elements, two groups of cracks were generally expected: mainly vertical cracks at the spandrels ends,

related to in-plane bending failure, and diagonal cracks within the spandrels, indicative of an in-plane diagonal shear mechanism. For monitoring such occurrances, the DIC system was employed to evaluate the trends of the equivalent horizontal strains at the top and the bottom of the spandrels (ε_{top} and ε_{bot}, respectively) and of the equivalent strains across the spandrels diagonals (ε_{d1} and ε_{d2}, respectively). Strains ε_{top} and ε_{bot} were calculated on a base length of about 1780 mm; ε_{d1} and ε_{d2} were calculated on a base length of about 700 mm centred in the spandrel area. In general, the monitored strains were positive (tensile strains), regardless of the loading direction, consistently with the formation of the cracks. Not-negligible residual strains were expected, as long as damage progressed.

3.5.4 Results

3.5.4.1 Test S-R2U-1

The first cracking appeared at the spandrels opposite corners. The cracks gradually expanded, following the mortar joints in an almost vertical pattern until they spanned the entire height. Similar cracks emerged on both sides of the sample, spanning the full thickness of the wall. A significant drop in stiffness then occurred, and the cracking evolved asymmetrically. When loaded in the positive direction, damage was concentrated in the two vertical cracks at the spandrel ends. In contrast, a diagonal crack appeared when loaded in the negative direction, originating from the top-right corner, where the damage was primarily focused. Despite these differences, the load decrease was gradual in both cases. A mixed failure mode, involving both bending and shear, was observed. The horizontal displacements at the right support noticed the right pier pulled away from the left one; residual slip significantly increased with the number of load cycles. The horizontal strains at top and bottom resulted almost comparable, while diagonal strains were not, due to the activation of the inclined crack along one diagonal only.

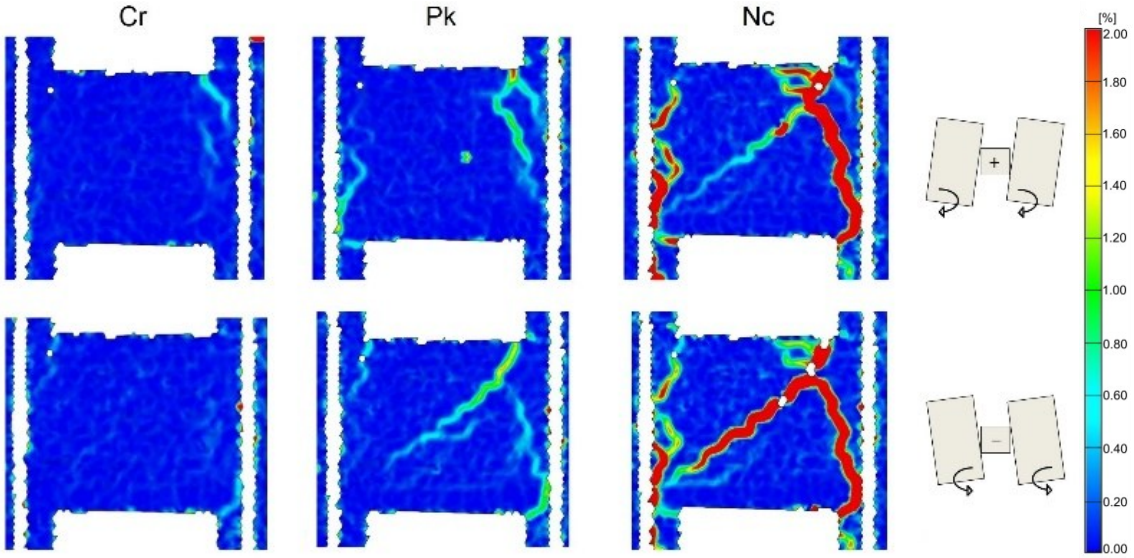


Figure 3.70 Crack pattern on the front side of spandrel S-R2U-1

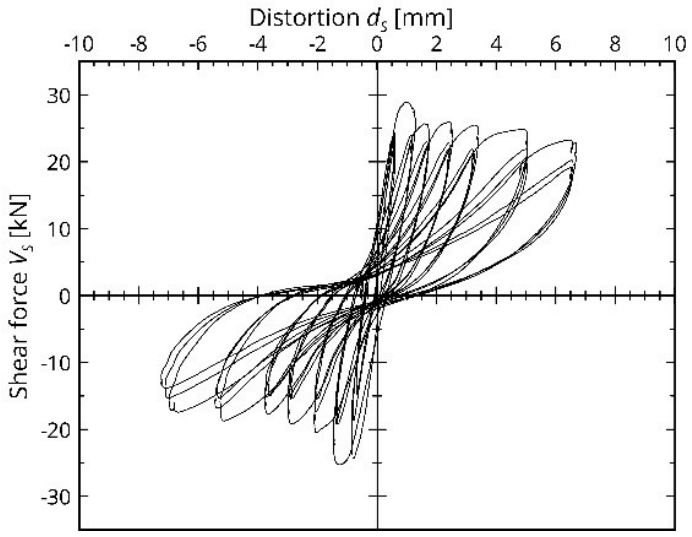


Figure 3.71 Force-displacement curve of test S-R2U-1

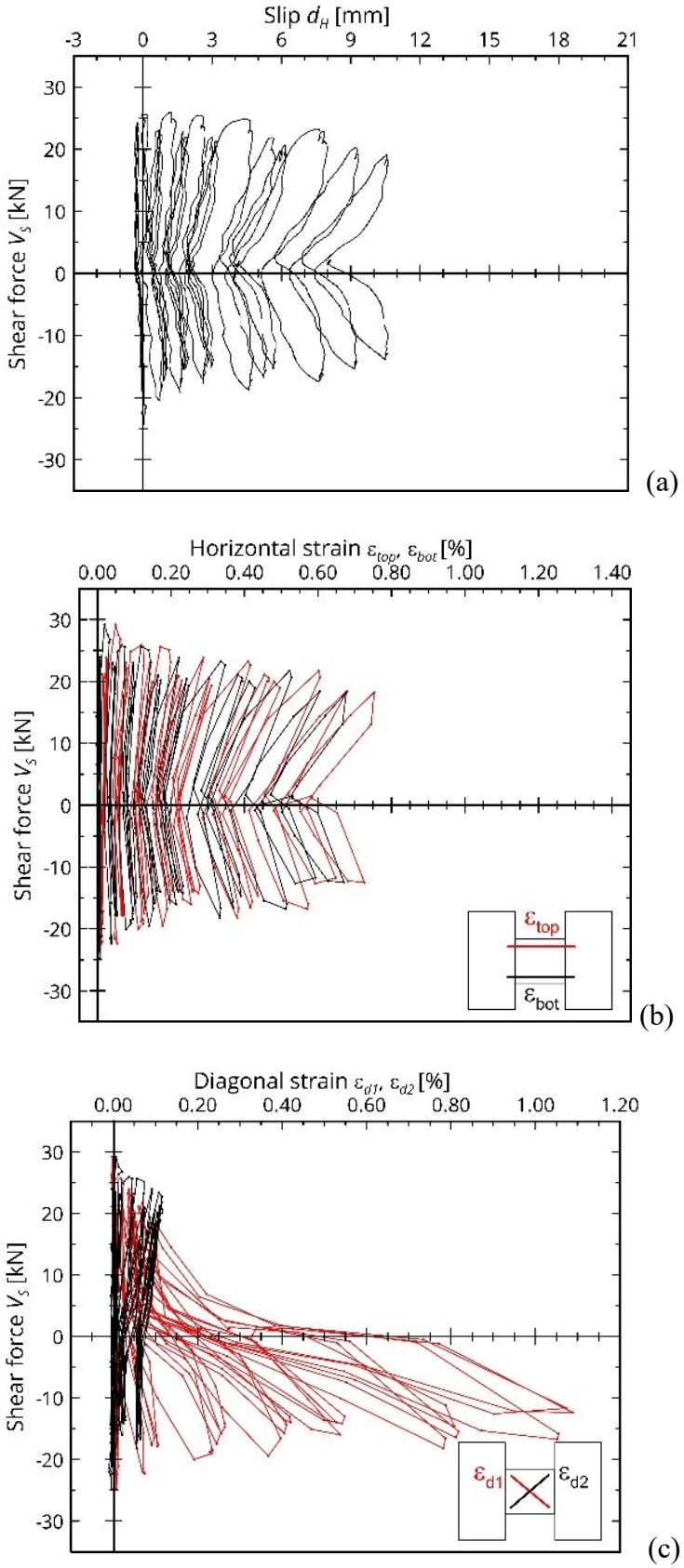


Figure 3.72 Main results of test S-R2U-1 a) separation between the piers; b) horizontal strain of the spandrel; c) diagonal strain of the spandrel

3.5.4.2 Test S-R2R-1

The first cracks occurred at the opposite corners of the spandrel and initially involved only the mortar of the coating; then the cracks extended almost vertically, also new parallel cracks formed nearby. Inclined and diagonal cracks developed, spreading over the entire coating surface till the progressive failure of the GFRP wires, leading to a rapid load decrease. Mainly the horizontal wires at the spandrel corners fractured, indicating that final failure was due to bending, despite numerous diagonal cracks. During the test, the bond of the coating with the masonry was gradually lost over a large area of the cracked spandrel; no separation between the wall leaves was observed. On the unstrengthened back side, the masonry cracks were fewer than on the strengthened front side and reproduced the crack pattern of a plain wall, S-R2U-1. The right support began sliding quite early, as the first cracks occurred; the residual sliding progressed with the cycles. The horizontal strains progressed almost symmetrically, and so did the diagonal strains.

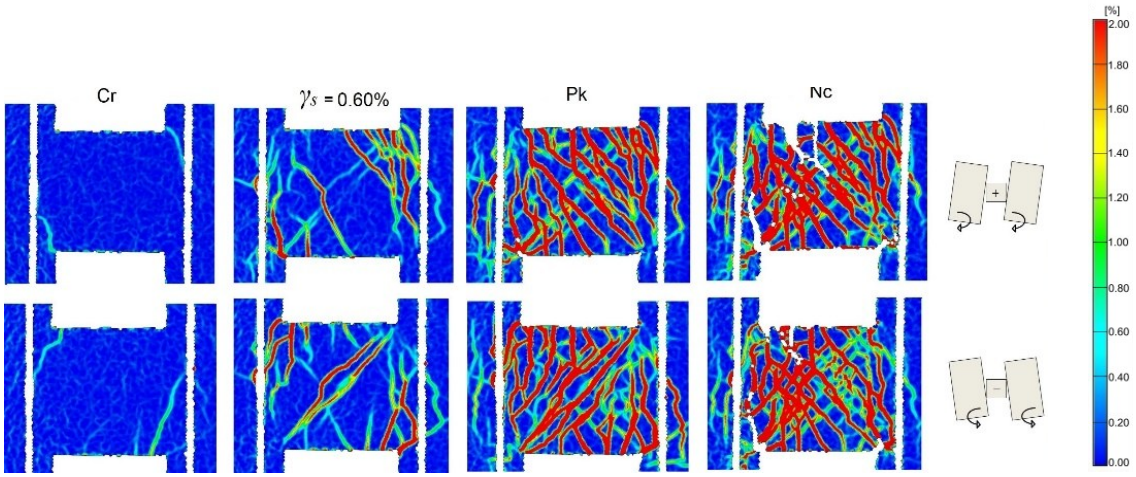


Figure 3.73 Crack pattern on the front side of spandrel S-R2R-1



Figure 3.74 Crack pattern on the back side of the spandrel S-R2R-1


(a)

(b)

Figure 3.75 Details of the failure of some GFRP wires at the (a) left and (b) right lower corner of the spandrel (the coating was manually removed at the end of the test)

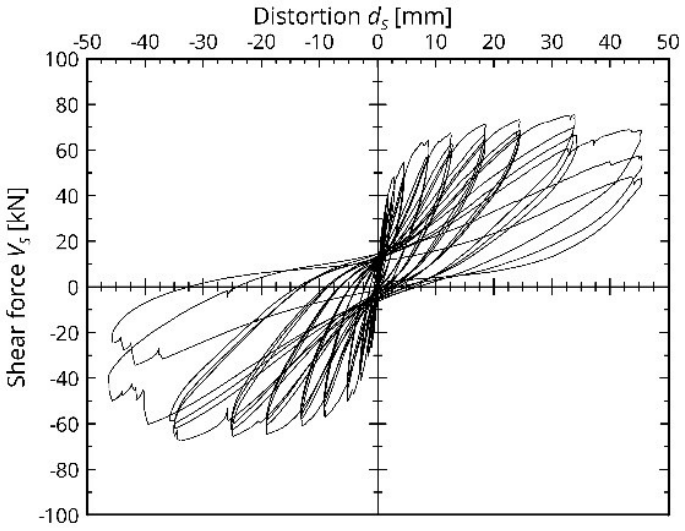


Figure 3.76 Force-displacement curve of test S-R2R-1

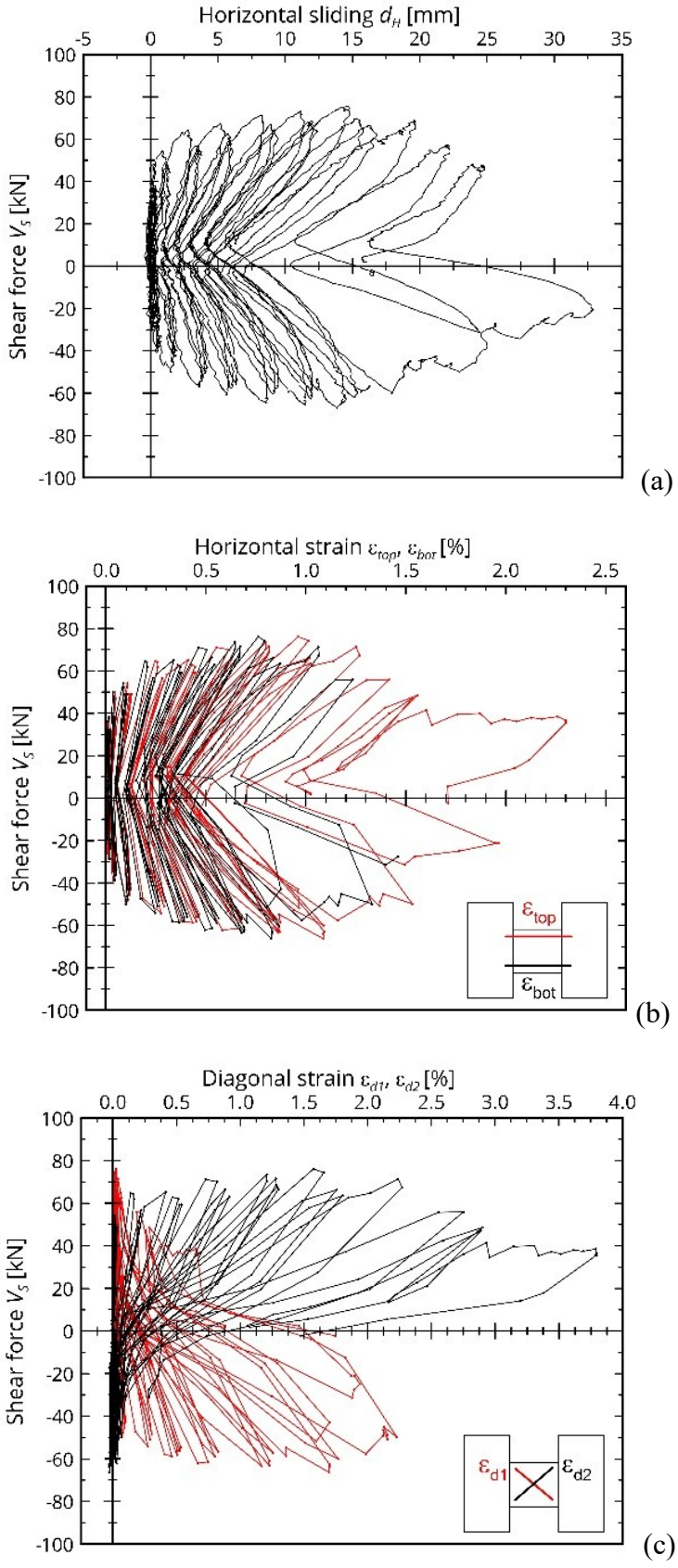


Figure 3.77 Main results of test S-R2R-1 a) separation between the piers; b) horizontal strain of the spandrel; c) diagonal strain of the spandrel

3.5.4.3 Test S-R2U-2

The first cracks appeared at the opposite corners and the damage concentrated in two main, almost vertical cracks at the spandrel extremities, indicating failure governed by the bending mechanism (diagonal strains were quite negligible). Similar cracks emerged on both sides of the sample, spanning the full thickness of the wall. After the peak load, a gradual drop or resistance was surveyed, also with the progressive gradual residual slip between the piers. The horizontal strains at top and bottom were almost comparable.

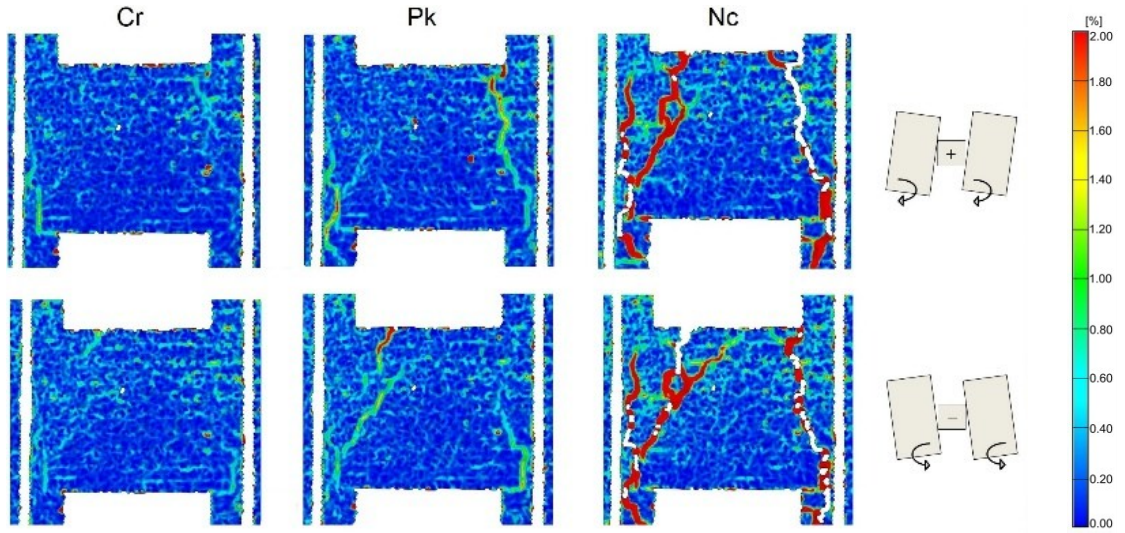


Figure 3.78 Crack pattern on the front side of spandrel S-R2U-2

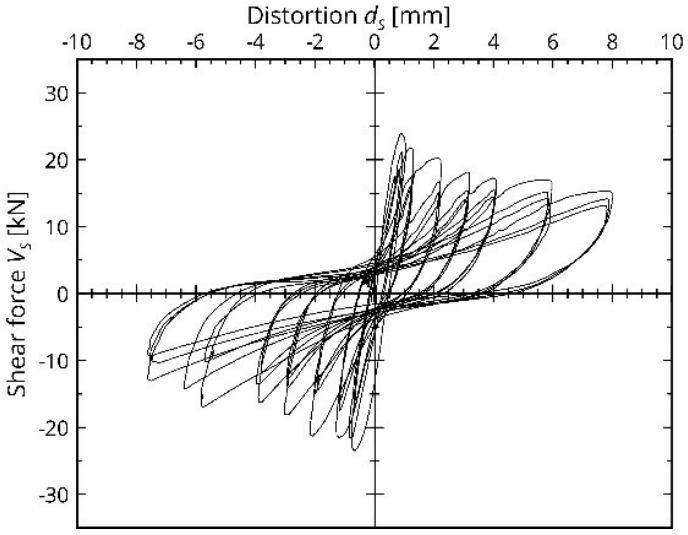


Figure 3.79 Force-displacement curve of test S-R2U-2

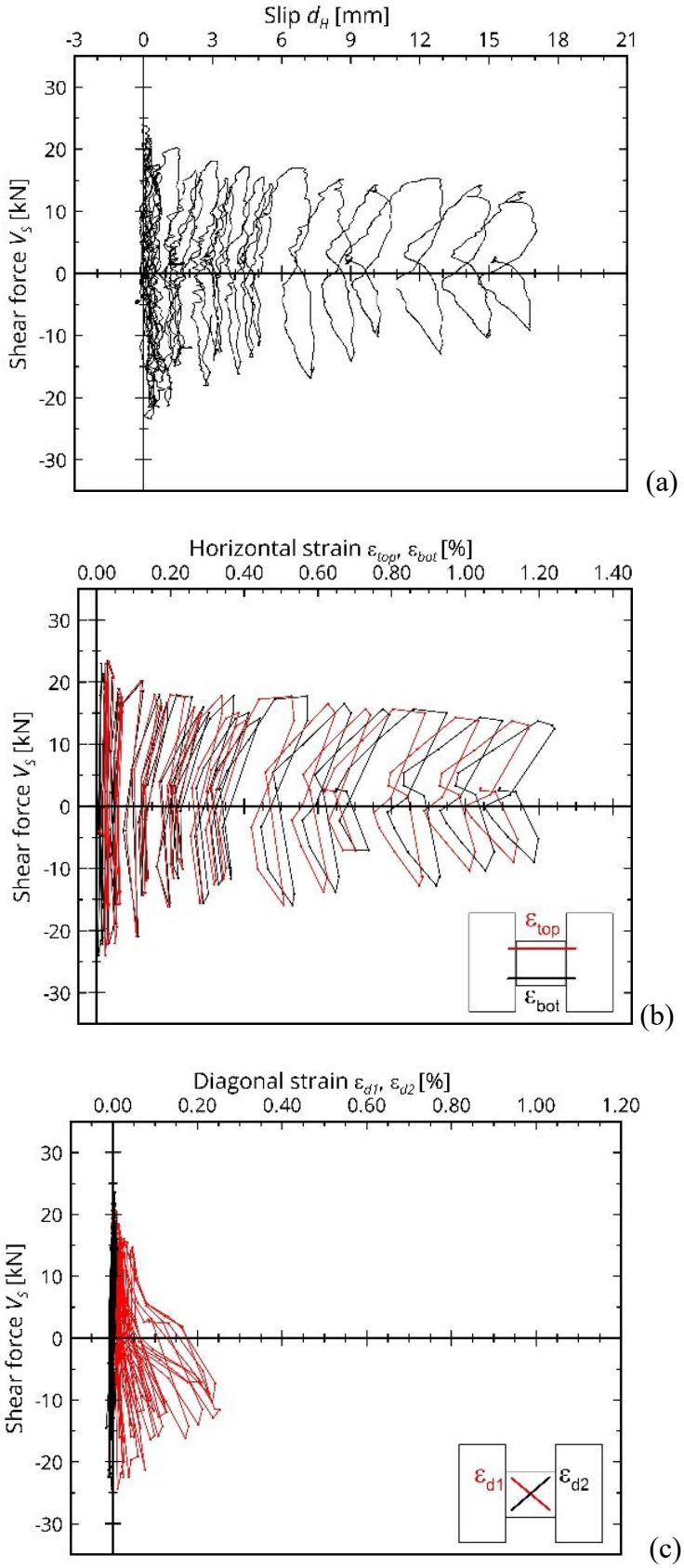


Figure 3.80 Main results of test S-R2U-2 a) separation between the piers; b) horizontal strain of the spandrel; c) diagonal strain of the spandrel

3.5.4.4 Test S-R2R-2

The first cracks formed in the coating, at opposite corners of the spandrel, displaying a vertical pattern. These cracks progressively extended and, due to load reversal, spanned the entire height of the spandrel. Additional vertical cracks appeared near the previous ones, followed also by inclined cracks in the coating within the spandrel area, so that the entire coating surface was covered by cracks once the peak resistance was reached. The collapse mode was flexural: the vertical crack at the right end of the spandrel widened, leading to the failure of the GFRP wires crossing the crack, on both the front and back sides. At the end of the test, some debonding of the coating from the masonry was observed around the wider cracks. Additionally, initial separation of the wall leaves was detected in the pier portions below the lintel. The horizontal sliding at the right support was quite limited until peak load; after that, increasing values were recorded, along with significant residual slip.

Actually, during the data post-processing, it emerged that a malfunction determined an unexpected, progressive reduction of the axial pre-stress level after the first cracking. With the reduced vertical load, N_S, horizontal cracks formed at the base of both piers, at the interface between the masonry and the RC beams: a crack opened from the inner corner of the left pier when loading in the positive direction, and from the inner corner of the right one for the opposite loading. The alternated opening of these cracks limited the actual rotation of the cracked pier in respect to that imposed by the apparatus, affecting the net spandrel distortion. The bottom horizontal strains resulted significantly higher that the top ones; diagonal strains were comparable.

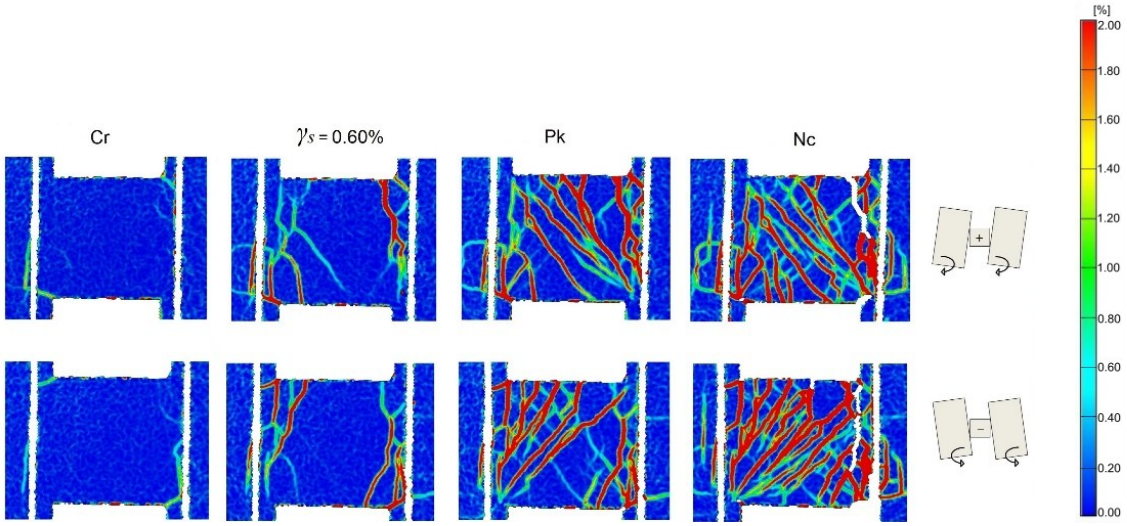


Figure 3.81 Crack pattern on the front side of spandrel S-R2R-2

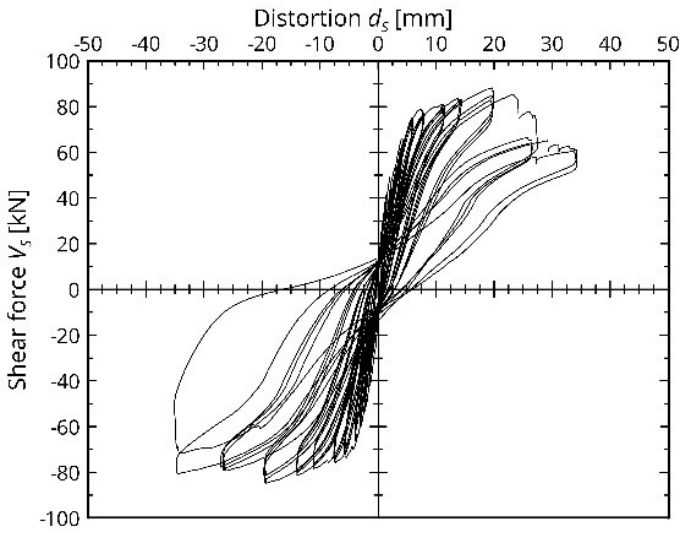


Figure 3.82 Force-displacement curve of test S-R2R-2



Figure 3.83 Crack pattern on the back side of the spandrel S-R2R-2

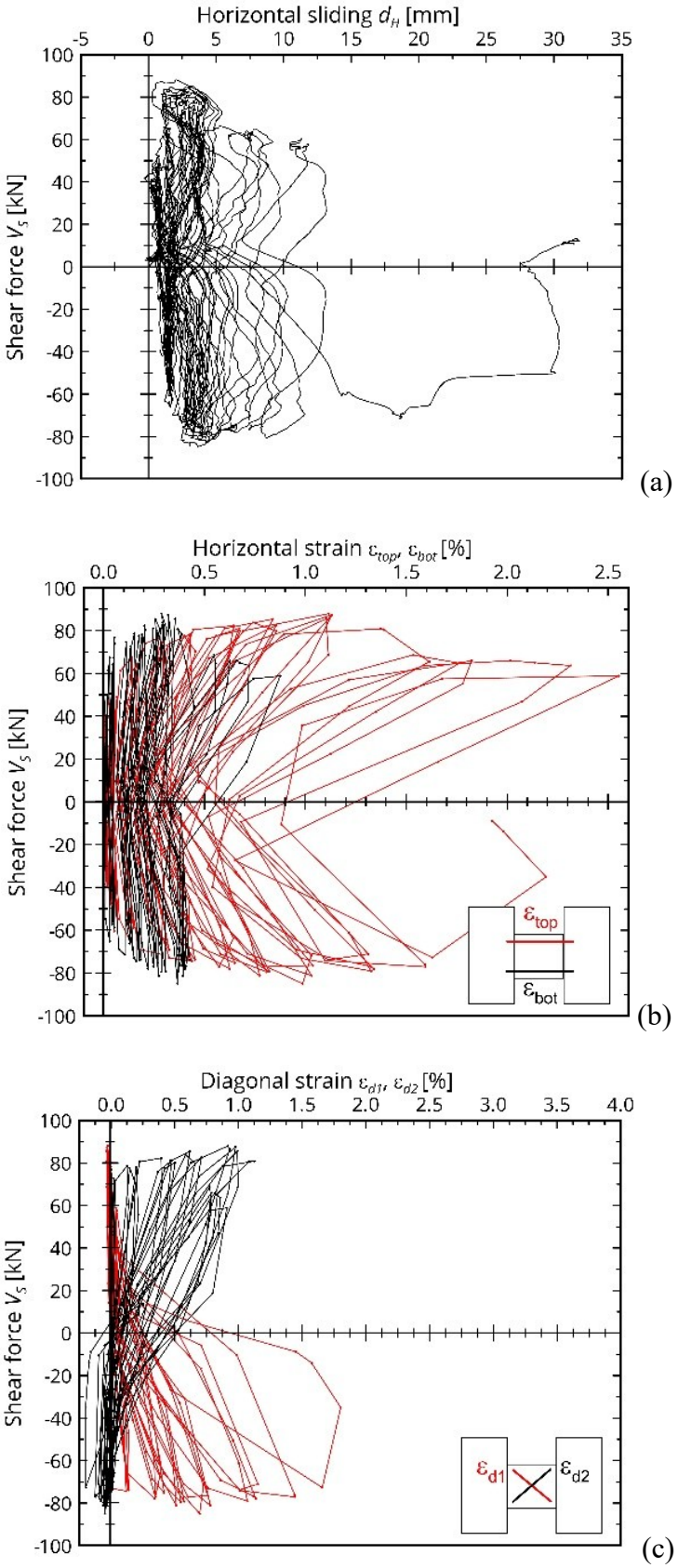


Figure 3.84 Main results of test S-R2R-2 a) separation between the piers; b) horizontal strain of the spandrel; c) diagonal strain of the spandrel

3.5.4.5 Test S-B2U

The first significant cracking occurred almost at the attainment of the peak load: the cracks were inclined, running mostly through the mortar joints (diagonal shear failure mechanism) and determined an abrupt resistance decay and a large horizontal sliding at the base right support. This triggered the lower portion of the masonry spandrel (mainly, the jack arch), fully surrounded by cracks, to detach from the upper portion at the end of the test. The crack pattern was identical on both sides of the sample, spanning the full thickness of the wall. The horizontal strains at top and bottom resulted almost comparable, as well as the diagonal strains (which clearly detected the occurrence of symmetric diagonal cracking).

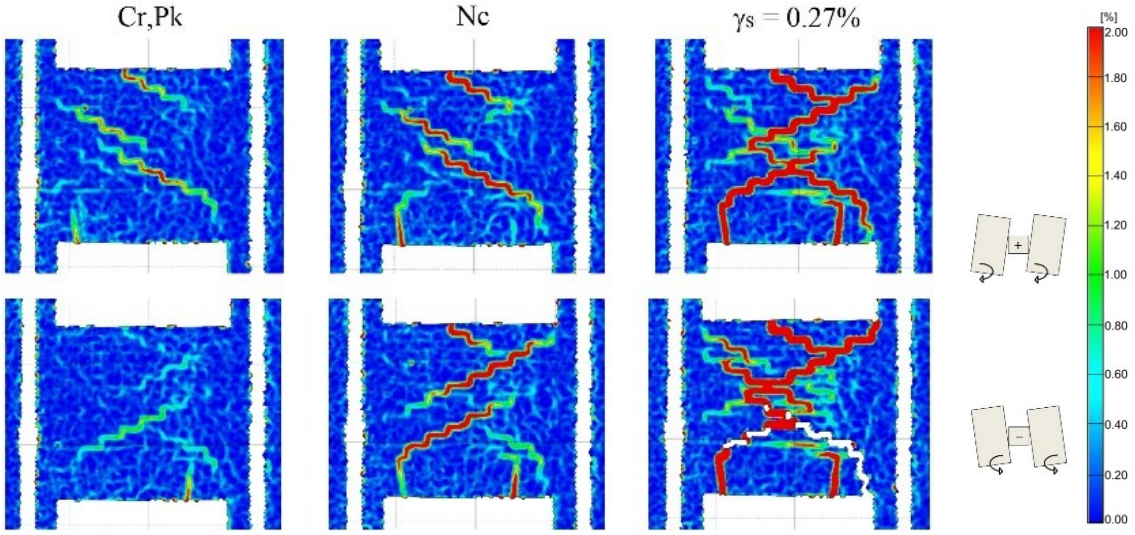


Figure 3.85 Crack pattern on the front side of spandrel S-B2U

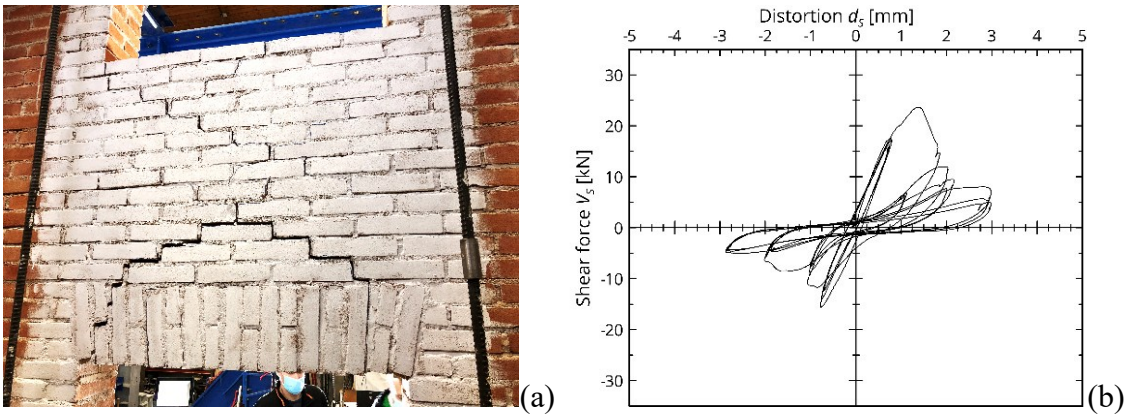


Figure 3.86 Test S-B2U: a) crack pattern on the back side of the spandrel, b) force-displacement curve

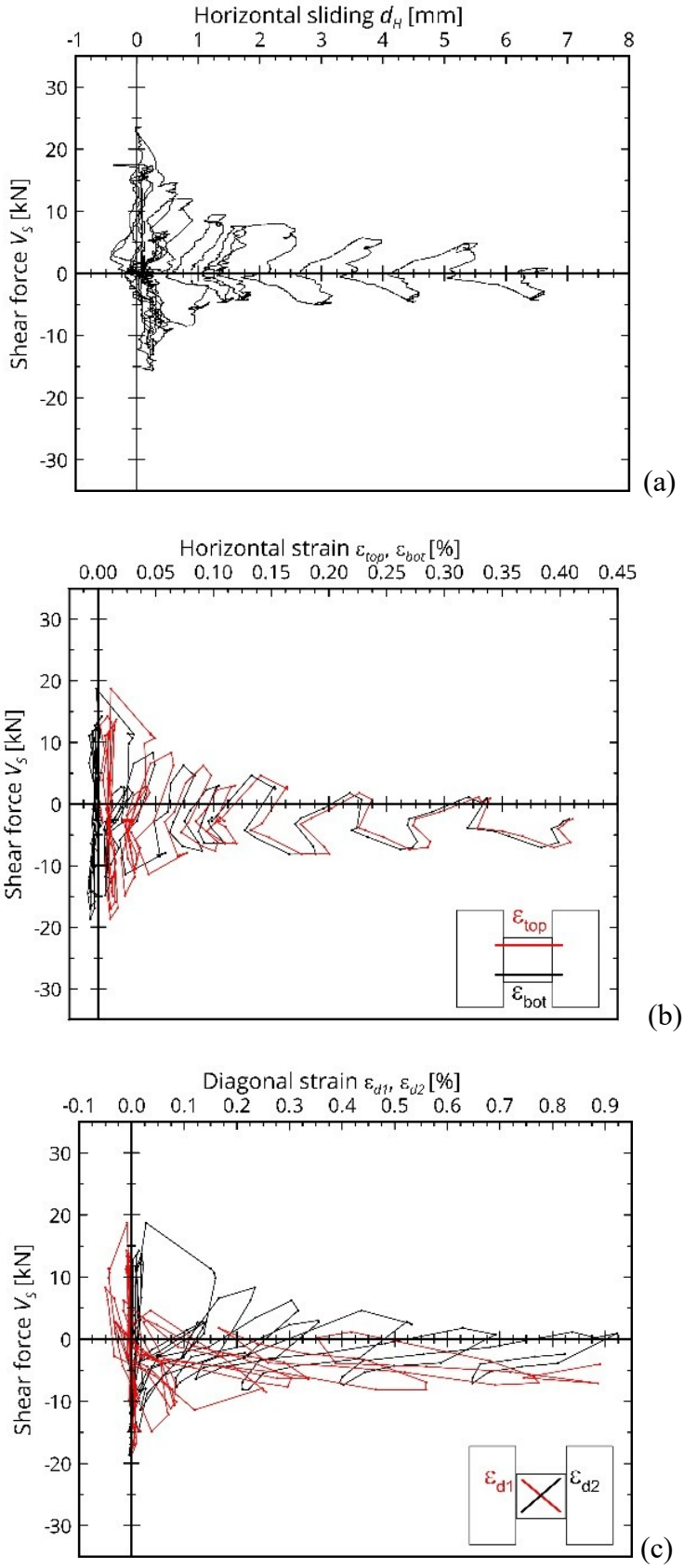


Figure 3.87 Main results of test S- B2U: a) separation between the piers; b) horizontal strain of the spandrel; c) diagonal strain of the spandrel

3.5.4.6 Test S-B2R

The first cracks formed in the coating, at diagonally opposite corners of the spandrel, then the cracks progressively spread: they were initially almost vertical, but then also diagonal cracks appeared in the centre. When peak load was reached, the cracks covered the entire spandrel surface. On the reverse side (unstrengthened masonry), the cracks also gradually diffused, but the trend was that of stepped cracking that mainly followed previously repaired cracks. The lower masonry portion of the spandrel (the jack arch) tended to detatch (similar to what occurred in the unstrengthened configuration). The final collapse was due to failure of some vertical GFRP wires around the left end of the spandrel, reminiscent of vertical shear sliding. No layer separation emerged between the wall leaves but some debonding of the coating around the cracked areas; however the composite action was maintained until the end. The horizontal strains progressed almost symmetrically, and so did the diagonal strains.

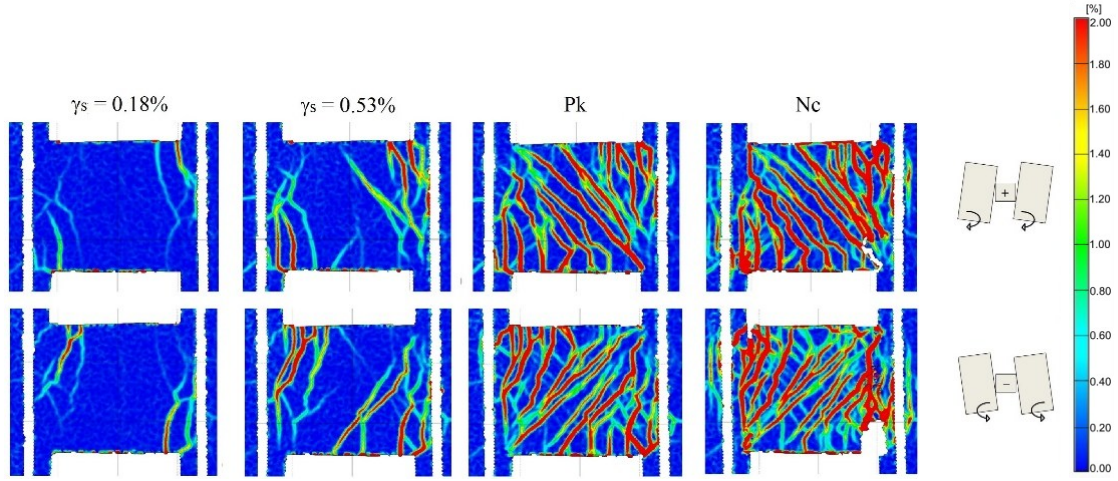


Figure 3.88 Crack pattern on the front side of spandrel S-B2R

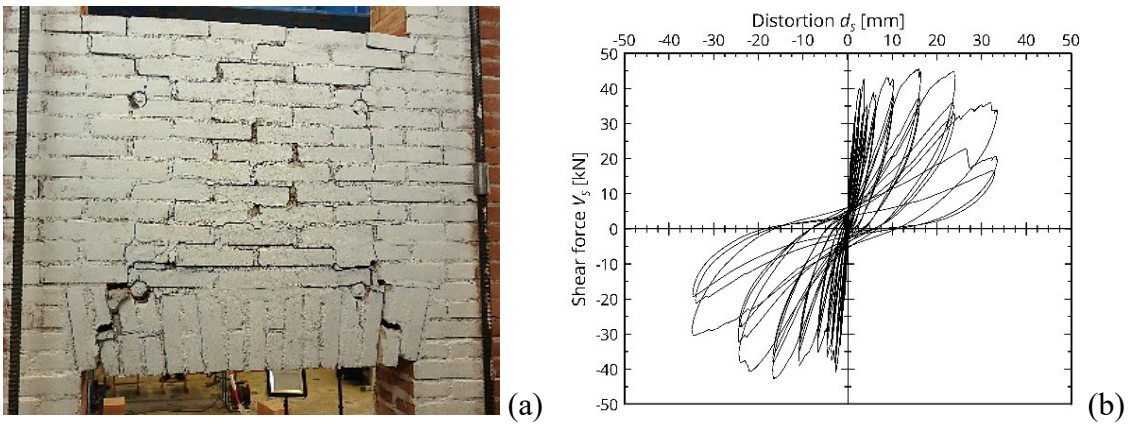


Figure 3.89 Test S-B2R: a) crack pattern on the back side of the spandrel, b) force-displacement curve

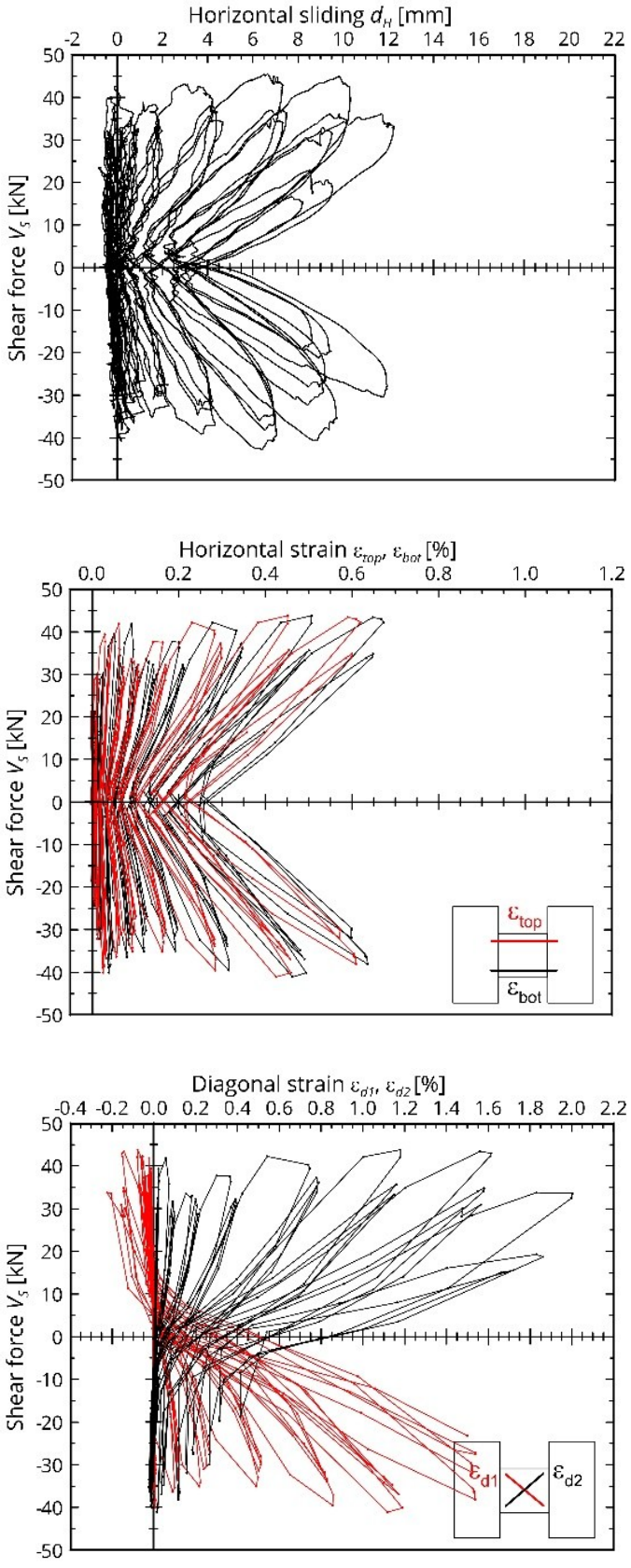


Figure 3.90 Main results of test S- B2R: a) separation between the piers; b) horizontal strain of the spandrel; c) diagonal strain of the spandrel

3.5.4.7 Test S-B1U

The first cracks occurred at the ends of the jack arch, first at the left corner of the spandrel (when loading in the positive direction) and then suddenly also in the right corner (when loading in the negative one). When reaching peak load, cracks also formed around the top corners of the spandrel, leading to activation of the bending failure mechanism. The upper cracks then opened with an inclined pattern, while the lower cracks opened almost vertically, causing a rapid load drop. A horizontal crack also appeared at the top of the jack arch. After the peak load, the right pier moved horizontally, regardless of the loading direction. By the end, the arch was completely surrounded by cracks and on the verge of collapse. The damage pattern on the back of the wall mirrored that on the front, with cracks running almost exclusively through the mortar joints. The horizontal strains at top and bottom were almost comparable; the diagonal strains resulted almost negligible.

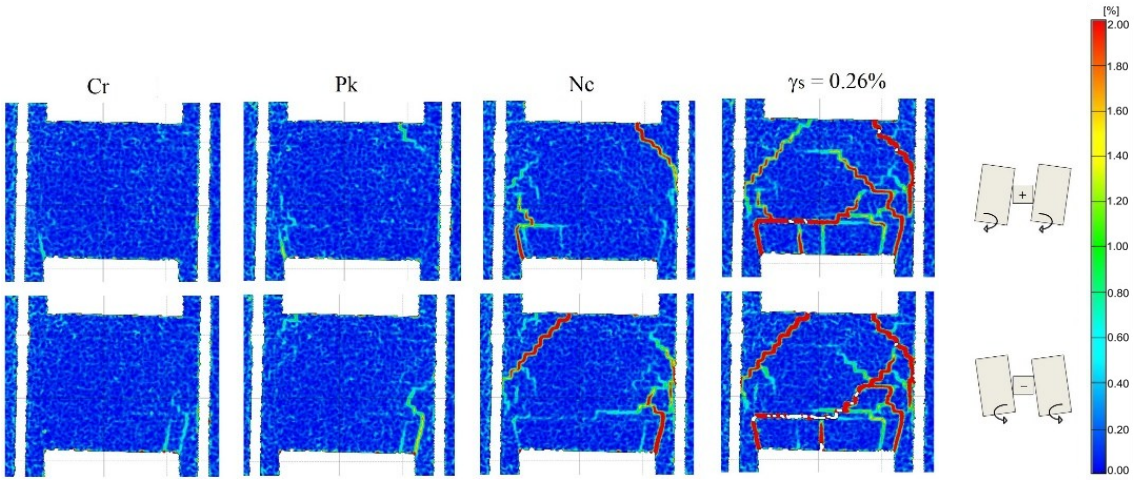


Figure 3.91 Crack pattern on the front side of spandrel S-B1U

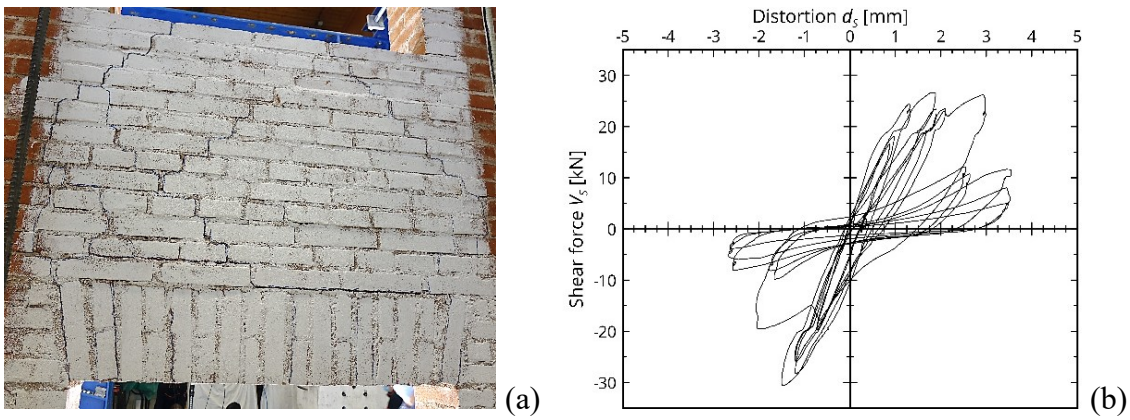


Figure 3.92 Test S-B1U: a) crack pattern on the back side of the spandrel, b) force-displacement curve

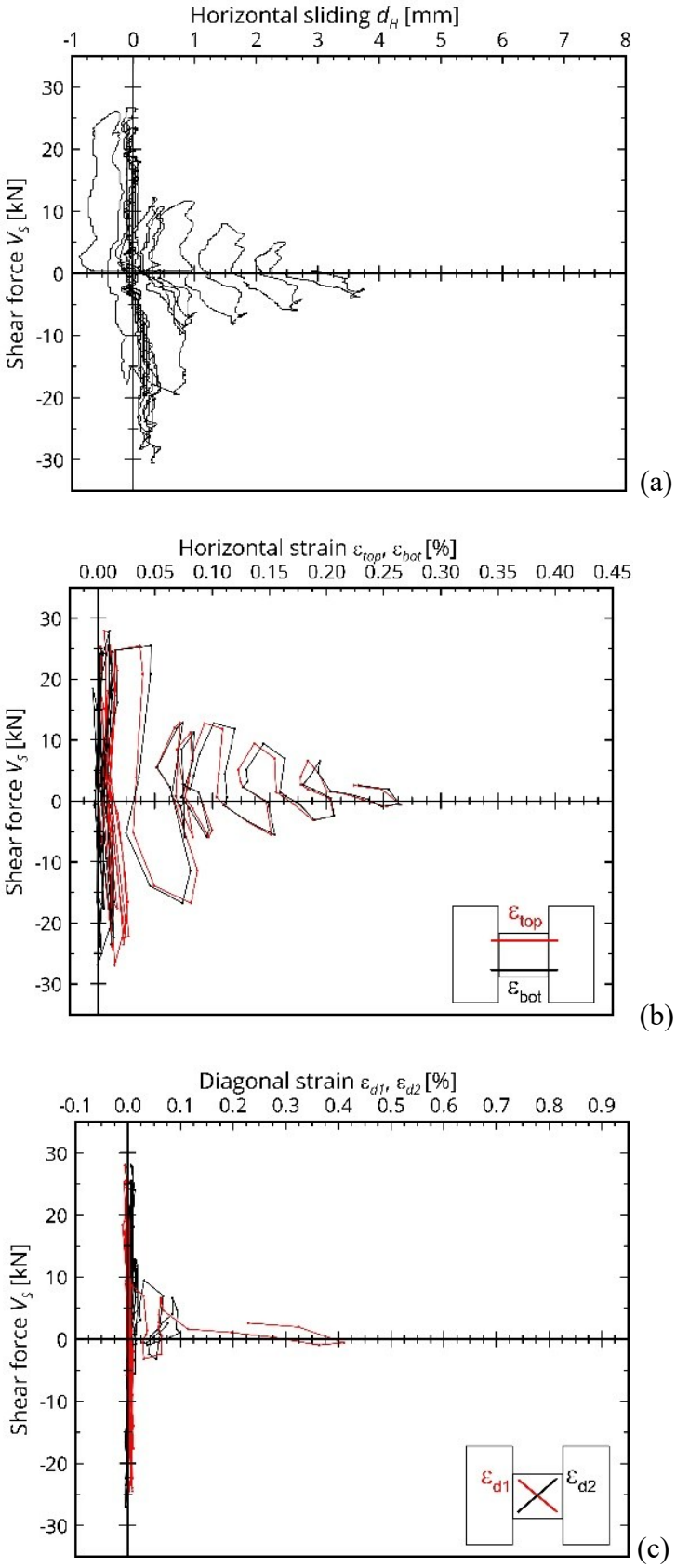


Figure 3.93 Main results of test S- B1U: a) separation between the piers; b) horizontal strain of the spandrel; c) diagonal strain of the spandrel

3.5.4.8 Test S-B1R

Cracks in the coating firstly activated in the spandrel's lower corners and then, at the top corners. Such cracks progressed almost vertically, meanwhile other incluned cracks gradually occurred in the vicinity. At the reaching of the peak load, the entire coating was diffusely covered by cracks, and the cracks at the centre of the spandrel were diagonal. Then, the horizontal GFRP wires at the right end of the spandrel progressively failed in tension, starting from the bottom corner. The coating debonded in the cracked areas, but the anchors and the diatones maintained composite action. The unstrengthened side experienced inclined cracks very similar to those observed in the test of the unstrengthened wall, S-B1-U. The crack above the jack arch opened again, but the arch fallin was prevented. The sliding of the right support was significant and also in the residual sliding. Both the horizontal strains and the diagonal ones progressed almost symmetrically.

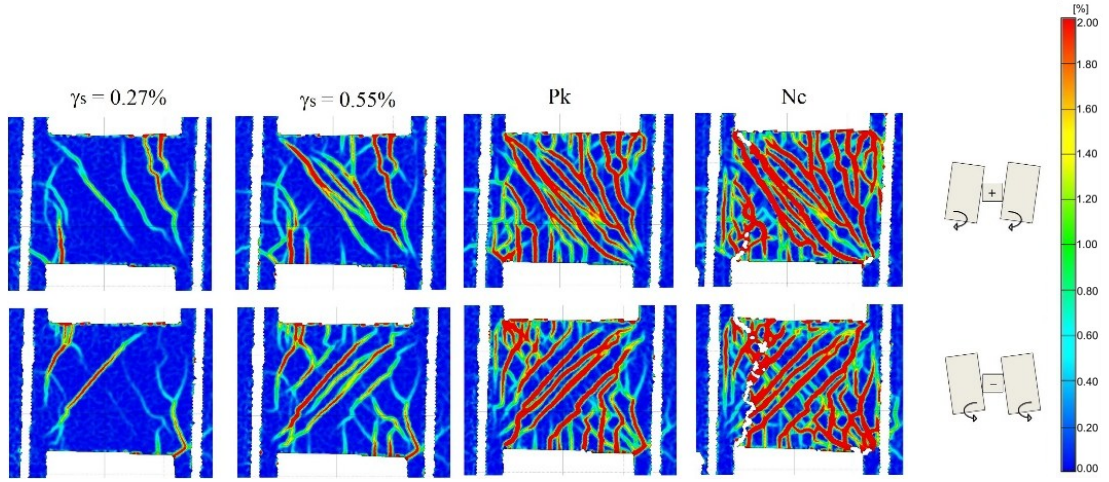


Figure 3.94 Crack pattern on the front side of spandrel S-B1R

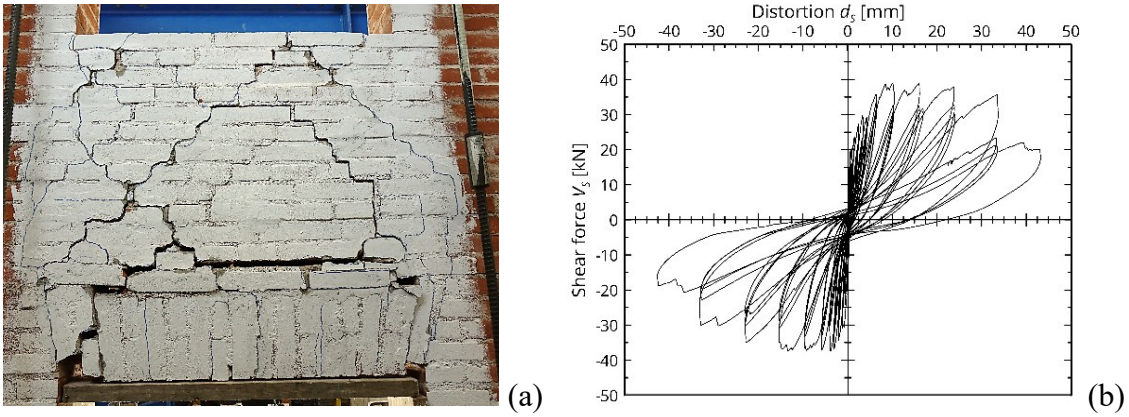


Figure 3.95 Test S-B1R: a) crack pattern on the back side of the spandrel, b) force-displacement curve

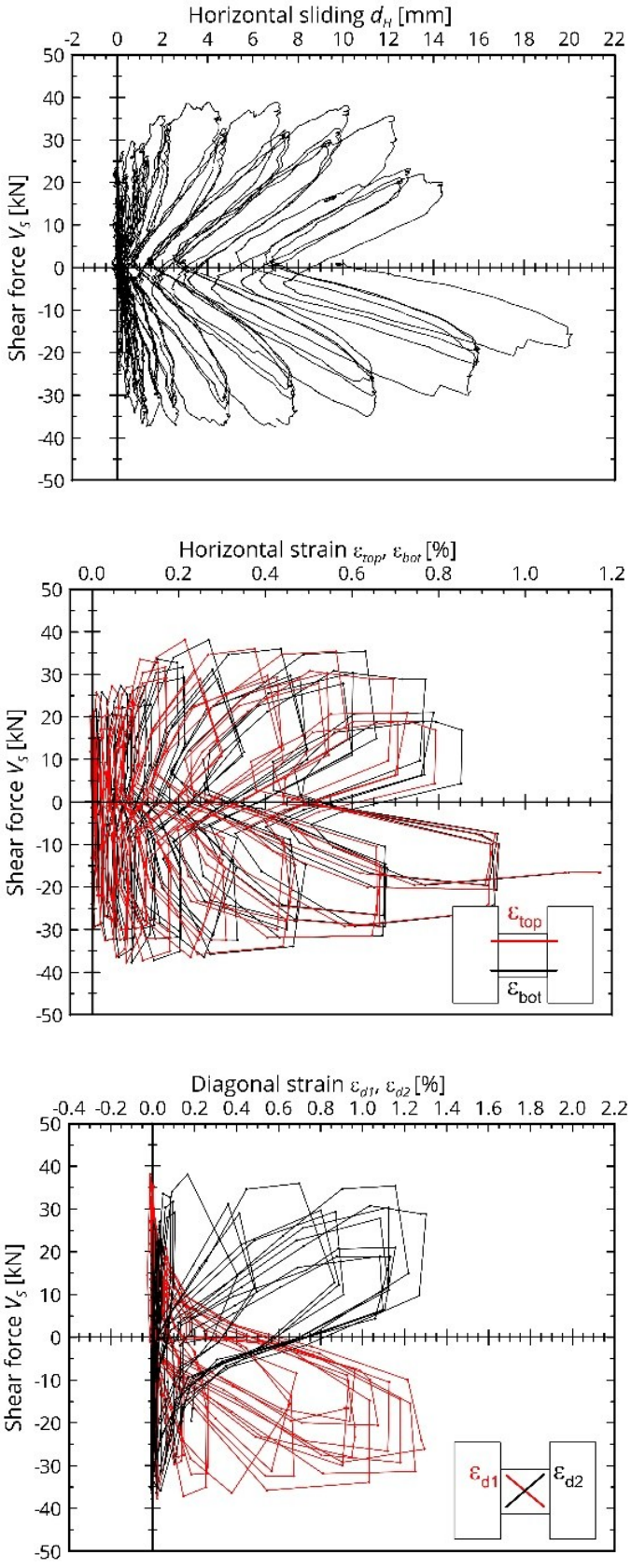


Figure 3.96 Main results of test S- B1R: a) separation between the piers; b) horizontal strain of the spandrel; c) diagonal strain of the spandrel

3.5.5 Analysis of results and comparison

The capacity curves of unstrengthened and CRM strengthened spandrel samples are compared in Figure 3.97. The values of shear force V_S and distortion d_S obtained from the eight experimental tests are summarized in Table 3.12 and in Figure 3.98 for the three limit state, namely, first cracking, peak load and near collapse (*Cr*, *Pk*, *Nc*). The latter was identified at the occurrence of a 30% load decrease after the peak load.

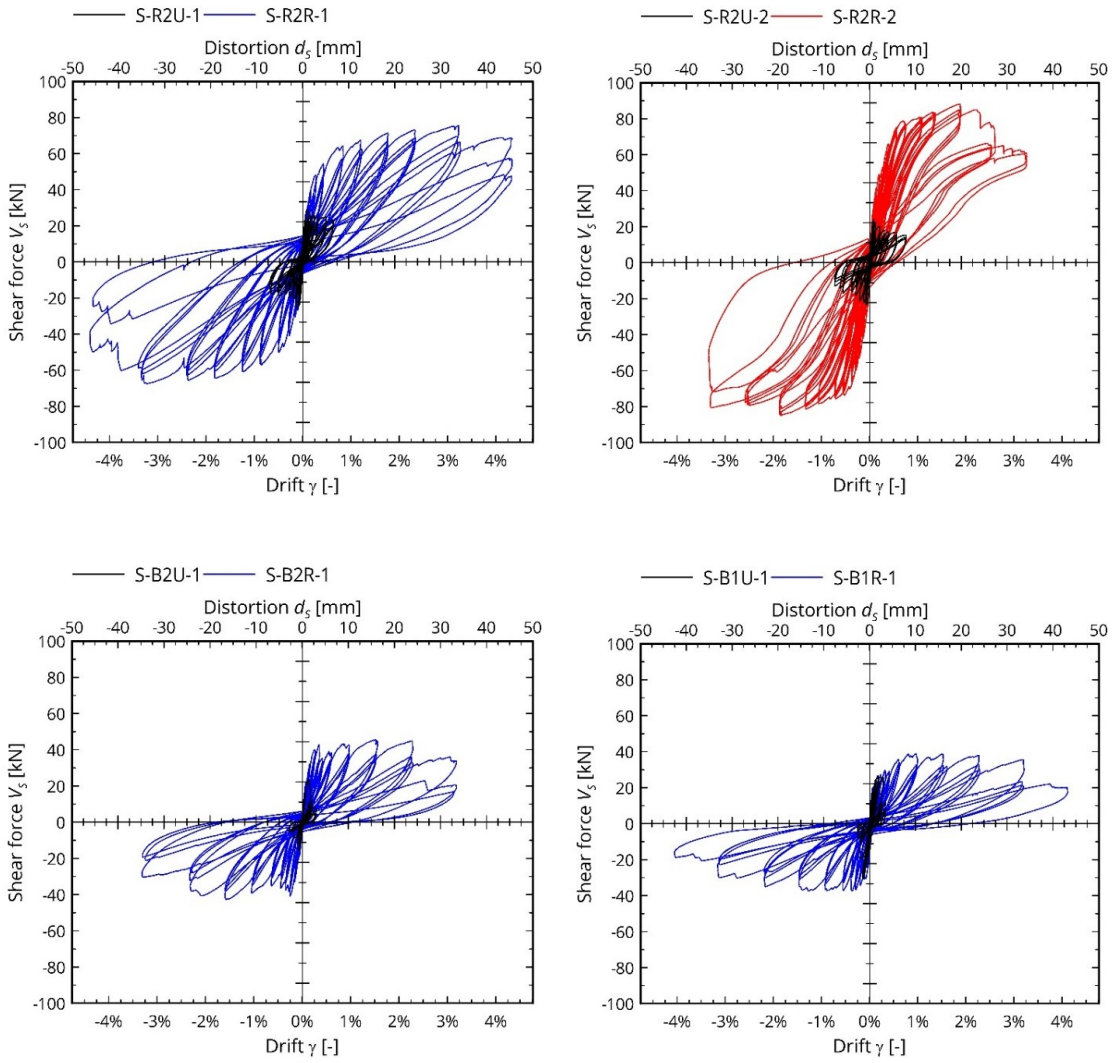


Figure 3.97 Comparison of capacity curves of unstrengthened and CRM strengthened spandrel samples

Table 3.13 Values of the shear force (V_S) and distortion (d_S) measured in positive and negative loading directions, for the first cracking, peak load and near collapse limit states

ID	**First cracking (*Cr*)**		**Peak load (*Pk*)**		**Near collapse (*Nc*)**	
	***V*$_S$ [kN]**	***d*$_S$ [mm]**	***V*$_S$ [kN]**	***d*$_S$ [mm]**	***V*$_S$ [kN]**	***d*$_S$ [mm]**
S-R2U-1	23.3	0.28	28.9	0.49	20.2	4.27
	-24.0	-0.33	-25.3	-0.55	-17.7	-4.23
S-R2R-1	29.7	0.26	75.5	18	52.8	24.7
	-26.7	-0.29	-67.5	-17.6	-47.2	-24.6
S-R2U-2	22.1	0.19	23.9	0.26	16.7	3.22
	-22.4	-0.12	-23.5	-0.19	-16.4	-3.15
S-R2R-2	48.6	0.63	88.1	17.8	61.7	31.69
	-53.0	-0.71	-84.8	-17.6	-59.4	-32.15
S-B2U-1	+23.6	+0.44	+23.6	+0.44	+16.5	+0.85
	-15.7	-0.30	-15.7	-0.30	-11.0	-0.55
S-B2R-1	+21.6	+0.26	+45.5	+8.4	+31.9	+18.05
	-23.8	-0.29	-42.7	-8.4	-29.9	-18.50
S-B1U-1	+22.9	+0.29	+26.6	+0.59	+18.6	+1.09
	-26.8	-0.26	-30.6	-0.54	-20.1	-1.17
S-B1R-1	+19.6	+0.33	+38.9	+8.7	+27.2	+18.4
	-23.2	-0.14	-37.4	-7.5	-26.2	-18.4

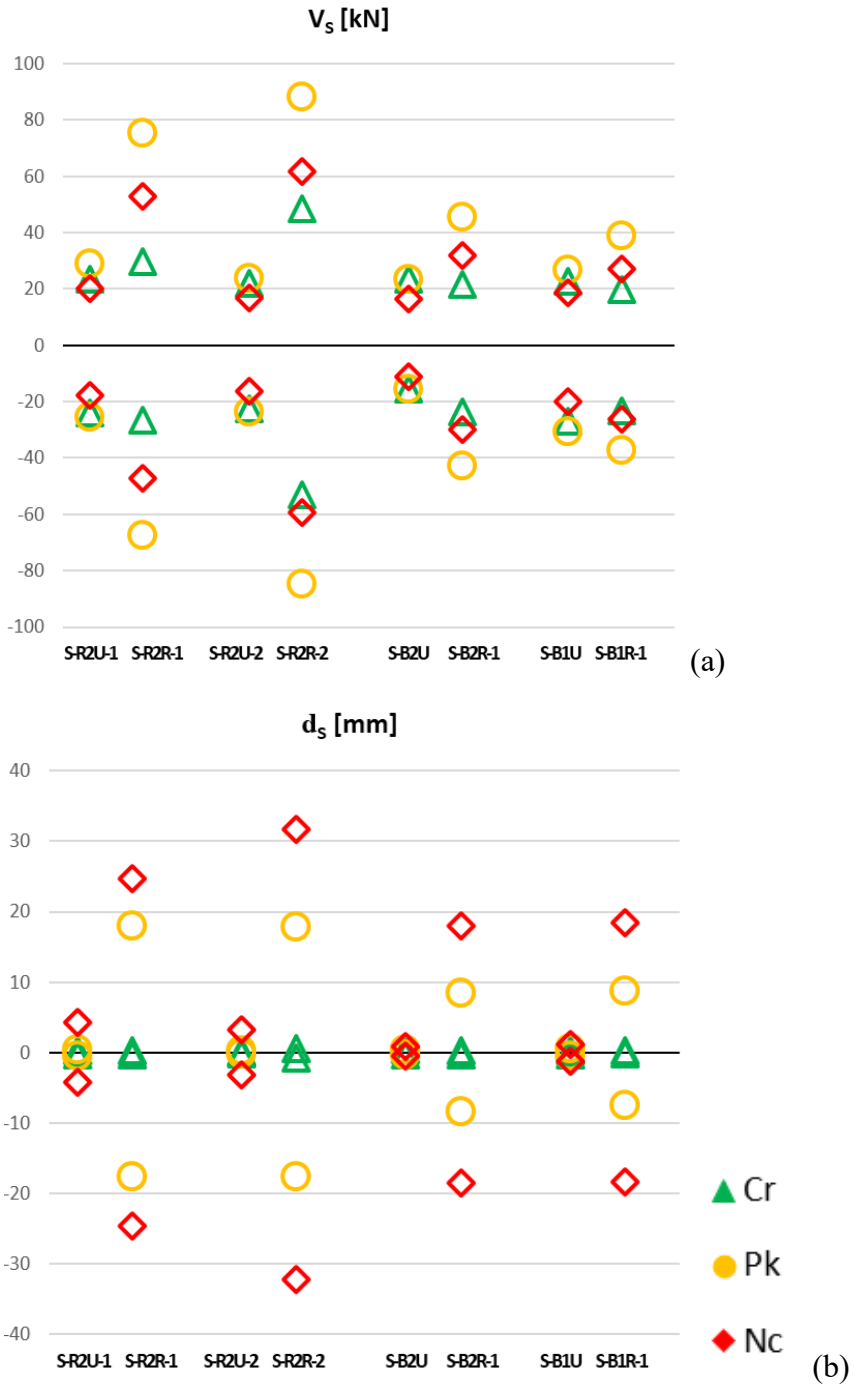


Figure 3.98 Main test results of "S" samples: first cracking, peak and near collapse forces (a) and distortion (b)

The failure of the two unstrengthened rubble stone spandrels and of the single-leaf solid brick masonry was dominated by the bending mechanism, as evidenced from the typical crack pattern with sub-vertical cracks at the spandrel ends (with cracks running mostly through the mortar joints). Very similar peak resistance values were attained: 27.1 kN for S-R2U-1, 23.7 kN for S-R2U-2 and 28.6 kN for S-B1U. In contrast, the unreinforced masonry spandrel made of double-leaves solid brick failed by shear (diagonal cracks,

mean peak load 19.7 kN). The capacity curves showed a quite ductile response for the stone samples with the timber lintel (ultimate displacements 4.25 mm and 3.19 mm, for S-R2U-1 and -2), while the response was brittle in case of masonry arch (0.7 mm for S-B2U and 0.3 mm for S-B1): at the end of the tests, the arch was completely surrounded by cracks and was about to fall.

In the strengthened spandrels, the first nearly vertical cracks formed in the coating, at the extremities of the spandrel (activation of bending mechanism), but then progressively spread, and diagonal cracks also appeared (activation of diagonal cracking mechanism), covering the entire spandrel. At the end of the tests, the bond between the coating and the spandrel was lost in the cracked areas, but the anchors assured the composite action until the end, when the GFRP wires progressively failed in tension at the extremities. It resulted mean peak loads of 71.5 kN for S-R2R-1, 44.1 kN for S-B2R-1 and S-B1R-1; the mean ultimate displacements were 24.7 mm, 18.3 mm and 18.4 mm, respectively. For the sample S-R2R-2, the mean peak resistance and ultimate displacement values were 86.5 kN and 31.9 mm. However, as already noted, the accidental malfunction of the vertical pressure control system limited the pier rotation, affecting the net spandrel distortion.

In the rubble stone masonry, the one-side retrofitting intervention increased the spandrel resistance to 2.8 times of original and the ultimate distortion by 6.6 times with respect to the plain masonry. In case of retrofitting at both sides, the improvement was 3.4 and 8.6 times for the same quantities (lower than expected due to the anomaly in the vertical loading system). In the sigle-leaf solid brick masonry, the peak force of the one-side retrofitted configuration was 2.24 times that of of the unstrengthened one and the distortion more than 26.1 times higher. In the double-leaves solid brick masonry, increment ratios were, respectively, 1.33 and 16.3 times.

The cyclic tests allow also to draw the trends of the spandrels cycle stiffness, K_S (evaluated as the slope of the peak-to-peak line within each loop of the V_S - d_S curve) by varying the distortion d_S (Figure 3.99a). The stiffness degradation with increasing distortion shows an approximately power-law trend, with a softer degradation in the strengthened samples, in respect to the unstrengthened ones. The stiffness gap within the three loops of a single target displacement was quite low. At the end of the tests, the cycle stiffness degraded by about 90–95% of the initial value.

The cumulative input energy (E_{in}) and the dissipated hysteretic energy (E_{hys}) were quantified (Figure 3.100), as well as the E_{hys}/E_{in} ratios (Figure 3.101). E_{in} is the cumulative work to deform the sample from the beginning of the test to a specific target value of distortion. For each loading cycle, it corresponds to the area under the positive and negative branches of the hysteretic loop of the F_S-d_S graph. Similarly, the cumulative dissipated hysteretic energy E_{hys} is the sum of all the areas included in the hysteretic loops. Three points for each target displacement are reported because of the three iterations cyclic.

For the strengthened samples, an approximate estimation of the equivalent hysteretic damping with varying target displacement was performed (accordingly to the procedure reported in FEMA 440 [247]) (Figure 3.102).

In general, significantly higher input and dissipated cumulative energies resulted from the strengthened samples, in respect to the plain masonry (Table 3.14). The cumulative dissipated energy at near collapse increased by 21-22 times for R2, by 66 times for B2 and by 26 times for B1. At a given target drift, the reduction in ξ_{hys} result greater between the second and third cycles than between the first and second. Approaching the peak load ξ_{hys} was about 0.11 in S-R2R-1 and 0.08 in S-R2R-2; at the near-collapse limit, ξ_{hys} 0.14 and 0.09, respectively. The values of ξ_{hys} at peak load (0.10–0.11) and near collapse (0.13) almost coincided in S-B1R-1 and S-B2R-1.

Table 3.14 Cumulative input energy E_{in} and dissipated hysteresis E_{hys} at peak load (Pk) and at near collapse (Nc), and mean energy ratio in the cycles (E_{hys}/E_{in})

ID	Peak load (*Pk*)			Near collapse (*Nc*)		
	E_{in} [J]	E_{hys} [J]	E_{in}/E_{hys} [-]	E_{in} [J]	E_{hys} [J]	E_{in}/E_{hys} [-]
S-R2U-1	119.8	78.6	0.66	1233.0	807.8	0.66
S-R2R-1	18496.4	9462.8	0.51	30045.2	16591.2	0.55
S-R2U-2	34.9	23.5	0.67	831.1	641.1	0.77
S-R2R-2	16100.1	5941.8	0.35	35706.6	14362.3	0.40
S-B2U-1	83.8	48.2	0.58	125.2	77.9	0.62
S-B2R-1	4069.1	1883.4	0.46	9560.2	5109.7	0.53
S-B1U-1	152.3	66.8	0.44	334.6	174.0	0.52
S-B1R-1	3333.4	1757.2	0.53	8006.4	4463.2	0.56

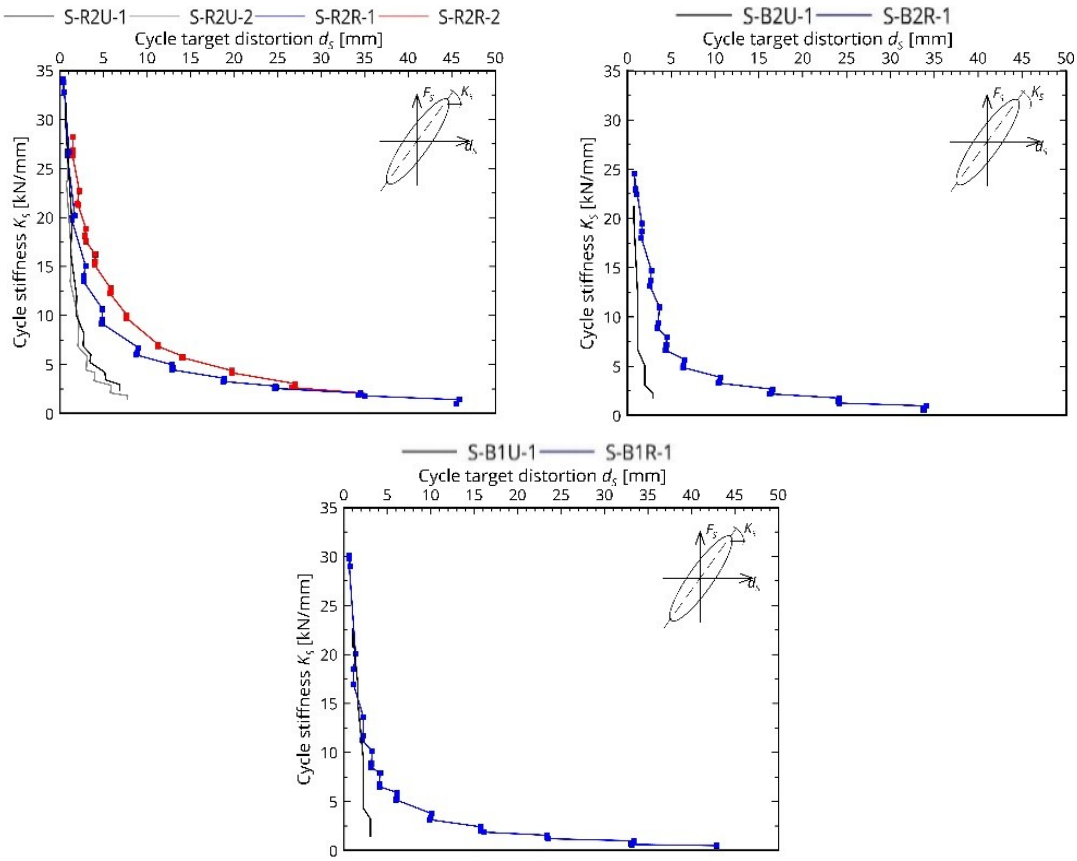


Figure 3.99 Spandrels' evolution of cycle lateral stiffness

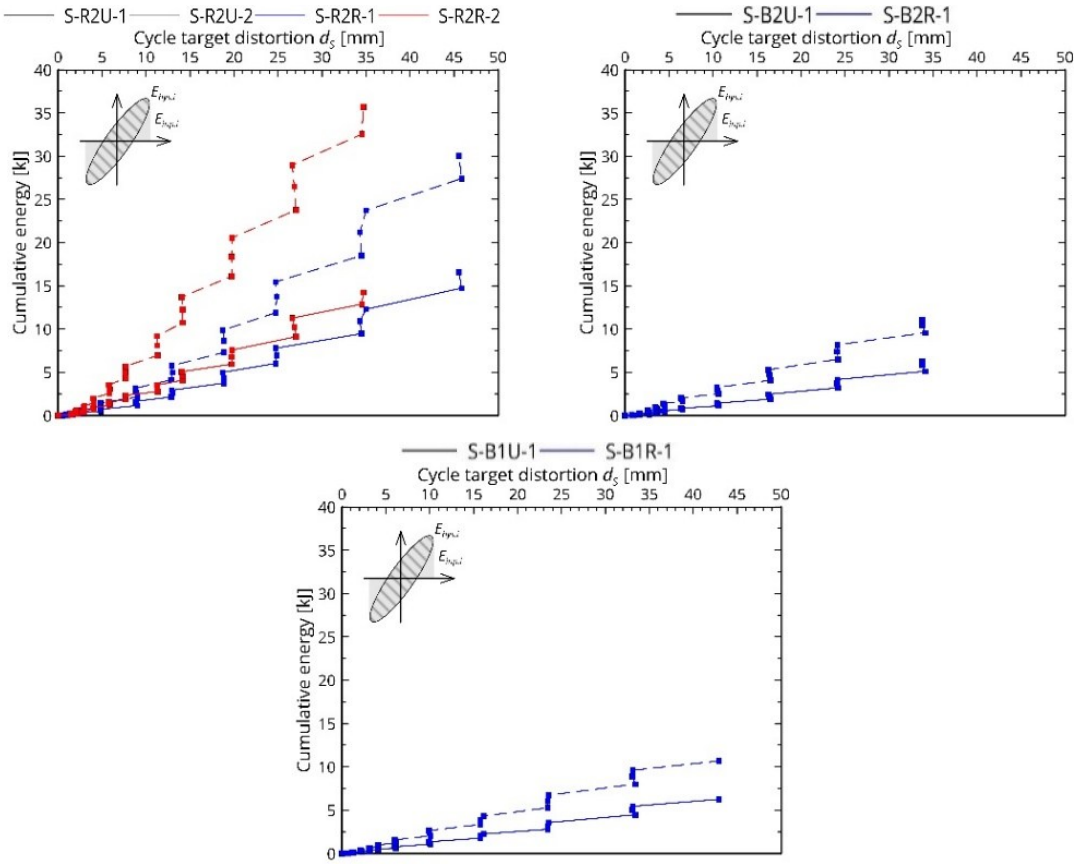


Figure 3.100 Spandrels' energy dissipation

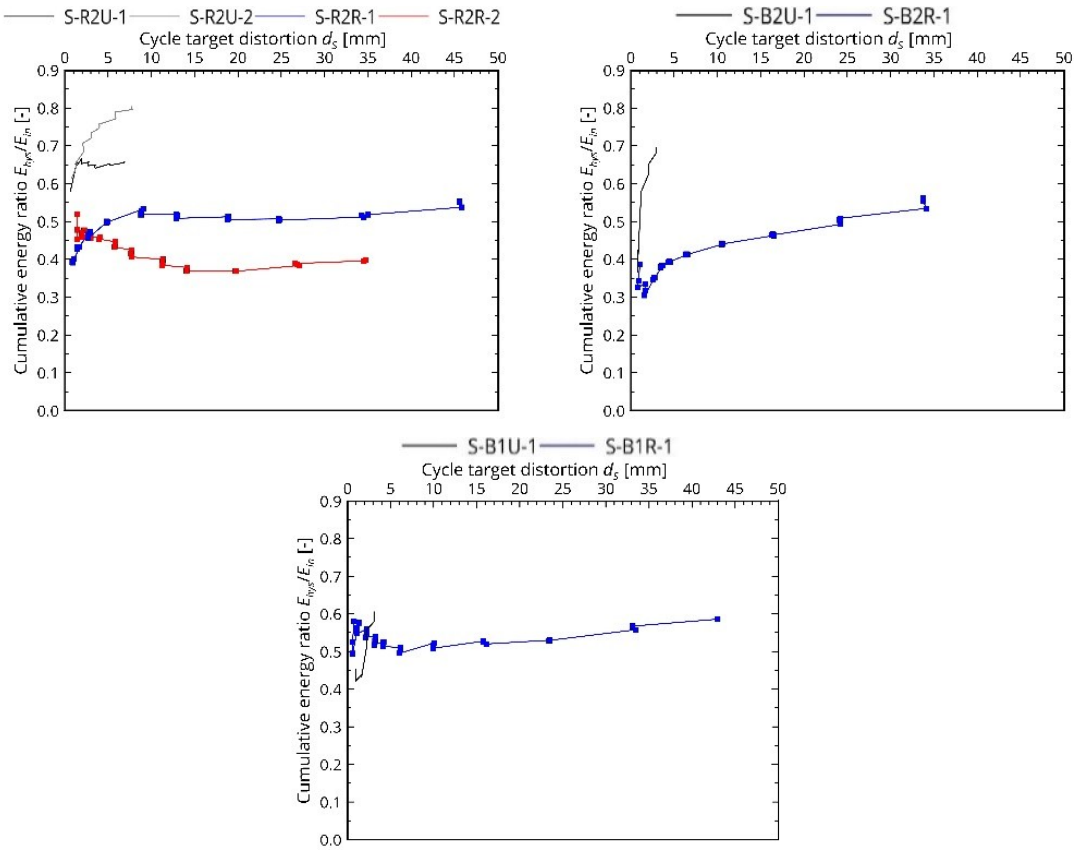


Figure 3.101 Spandrels' evolution of the cumulative energy ratio E_{hys}/E_{in}

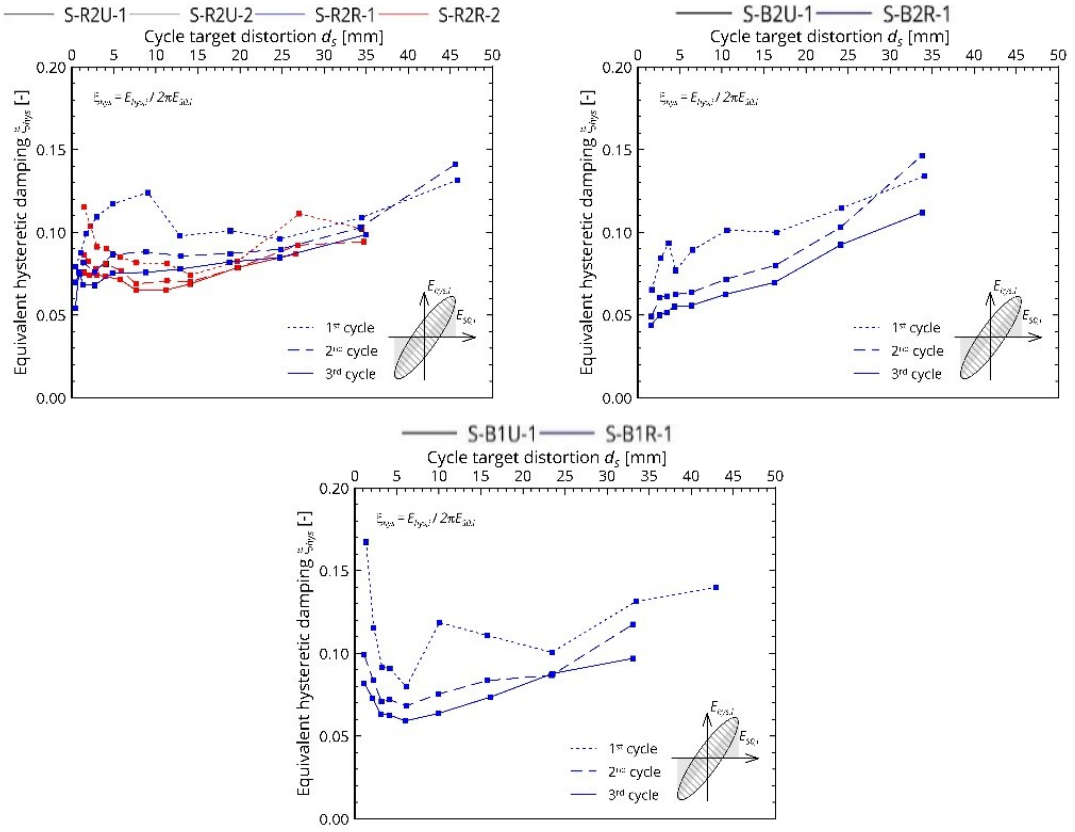


Figure 3.102 Spandrels' evolution of the equivalent hysteretic damping ratio ξ_{hys}

3.6 Out-of-plane behaviour of masonry piers

In this section, the out-of-plane (OOP) performance of masonry walls strengthened with a CRM coating is investigated. The tests were performed at the University of Trieste (Italy). Each sample represented the behavior of both the strengthened and unstrengthened wall panels. The CRM coating was applied on one side only, and its continuity between floors was not simulated. Thus, when the load was applied toward the unreinforced side, the wall behaved as an unreinforced specimen, allowing the comparison between the two configurations.

3.6.1 Literature review

Two main testing setups are adopted in the literature for testing the TRM effectiveness against out-of-plane failure, concerning three-point [150,157,171,185,187] and a four-point bending flexural scheme [26,184,186,188,189]. Some alternative setups considered air-bag tests [42,181], uniform loading [203], eccentric compression [182] and bi-dimensional bending with un-symmetric boundary conditions [183].

Depending on the geometry, material properties, loading type, and boundary conditions, the out-of-plane (OOP) failure of TRM-strengthened masonry typically occurs through the rupture or the debonding of the TRM on the tensed side, for crushing on the compressed side, for shear failure or, in very weak masonry, for leaf separation or disaggregation (Figure 3.103).

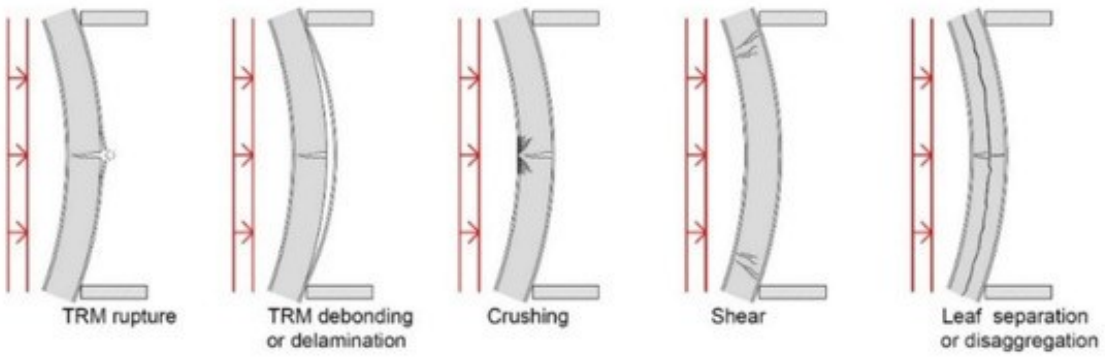


Figure 3.103 Out-of-plane loading: typical failure mode of TRM-strengthened masonry elements [126]

As reported by Boem [126] in its state of the art review, the out-of-plane tests available in the literature on TRM-strengthened panels typical concern samples arranged

horizontally, having widths generally ranging from 100 to 440 mm and lengths until 1500 mm. The bending is generally perpendicular to the bed joints, although also bending parallel to joints was tested [187,188,248]. The vertical arrangement was adopted for masonry walls up to 3670 mm tall and, in some cases, pre-loaded with an additional axial compression [42,203]. Typically, the load was applied monotonically up to failure, or following loading-unloading procedures. Typical results show the load at varying of the mid-span deflection. The tests also evidenced the following points:

- The application of TRM generally improved both the strength and displacement capacities of the masonry.
- Strengthened specimens typically exhibited multiple parallel cracks in the mortar matrix, demonstrating the ability of the embedded reinforcement to redistribute flexural stresses, as confirmed by comparison with samples coated only with bare plaster.
- The load-displacement curves usually displayed a bilinear trend, corresponding to uncracked and cracked stages.
- Negligible benefits were observed in specimens with TRM applied solely on the compressed side. In this regard, D'Ambrisi et al. [150] performed a study on the out-of-plane behavior of full-scale fired clay brick masonry piers (800 × 1600 × 220 mm) strengthened with a CRM system with a polymeric mesh with triangular grids embedded. The experimental setup consisted of two reinforced concrete curbs placed at the top and bottom of each specimen, with blocked rotations at the wall's extremities, and a constant vertical compression of 0.5 MPa was first applied, followed by a horizontal load. In the experimental campaign, a sample with the CRM coating applied on the compressed side was tested, showing a strength increase of about 40% and a fourfold improvement in ductility. Although, from the paper it's not clear whether the continuity of the reinforcement between floors was simulated.
- The orientation of the masonry bed joints had limited influence on the response of strengthened samples, as the masonry tensile contribution was minor.
- In systems combining high-performance reinforcements with weak bonding at the coating-masonry interface, the failure mode often shifted from TRM tensile rupture to delamination, debonding, or shear collapse.

Shaking table tests were also performed on unreinforced and repaired masonry samples using shaking table tests [249], showing that pseudo-static loading procedures are

generally more severe than actual seismic actions. These dynamic tests confirmed the effectiveness of the embedded reinforcement, although some local debonding was observed. Moreover, the presence of transversal ties effectively prevented leaf separation or disaggregation and in ensured stress transfer between the masonry and the reinforcing fabric at advanced damage levels.

The tests reported and analysed in the following aim at providing original results on piers tested in a three-point bending boundary condition in the laboratory. The main features of the samples and the testing apparatus are reported in the following sections; then, the test results are described in terms of capacity curves and damage pattern evolution. Finally, the results are analysed and compared, providing useful information on the effectiveness of the CRM coating in terms of resistance, displacement, stiffness and dissipative capacities.

3.6.2 Description of the samples

The research considered rectangular masonry panels having a width of 1030 mm and a height of 2480 mm. Each specimen was built between a bottom and a top reinforced concrete (RC) beam 250 mm height, 1030 mm long and with a thickness equal to that of the plain masonry. A total of three panels were built and tested (Table 3.15), one for each masonry type: R2, B2 and B1. The samples were strengthened with the CRM system applied at one side only. The positioning of the GFRP connectors and of GFRP connectors combined with artificial diatons is schematized in Figure 3.104 and Figure 3.105.

The boundary conditions analysed represent an extreme and simplified case for the pier subjected to out-of-plane forces, aimed at studying the behavior of the section with and without the contribution of the reinforcement. In actual applications, the reinforcement can improve response in both loading directions, provided the continuity of the reinforcement between stories and its connection to the foundation are ensured. Under reverse cyclic loading, this contribution is particularly beneficial, as it enables the tensile capacity of the coating to be mobilized regardless of the direction of the seismic action.

Table 3.15: Summary of the experimental out-of-plane tests

Sample ID	Masonry type	Strengthening system	Connectors
B-R2	R2	CRM on one-side	GFRP + diatons, 1 side
B-B2	B2	CRM on one-side	GFRP + diatons, 1 side
B-B1	B2	CRM on one-side	GFRP, 1 side

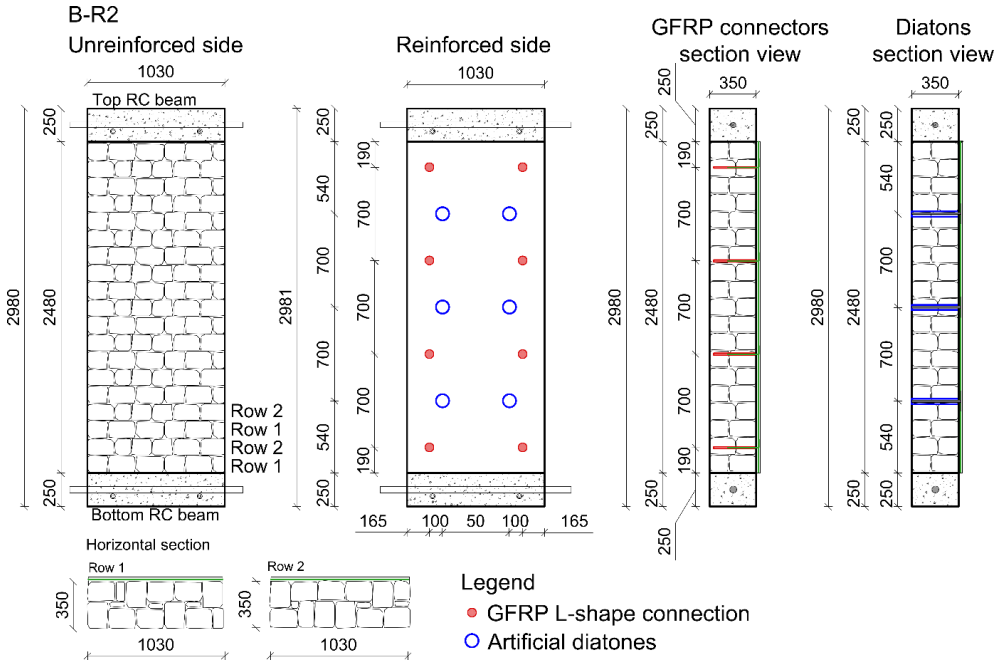


Figure 3.104 Lateral and cross-sectional views of sample B-R2 (measures in mm)

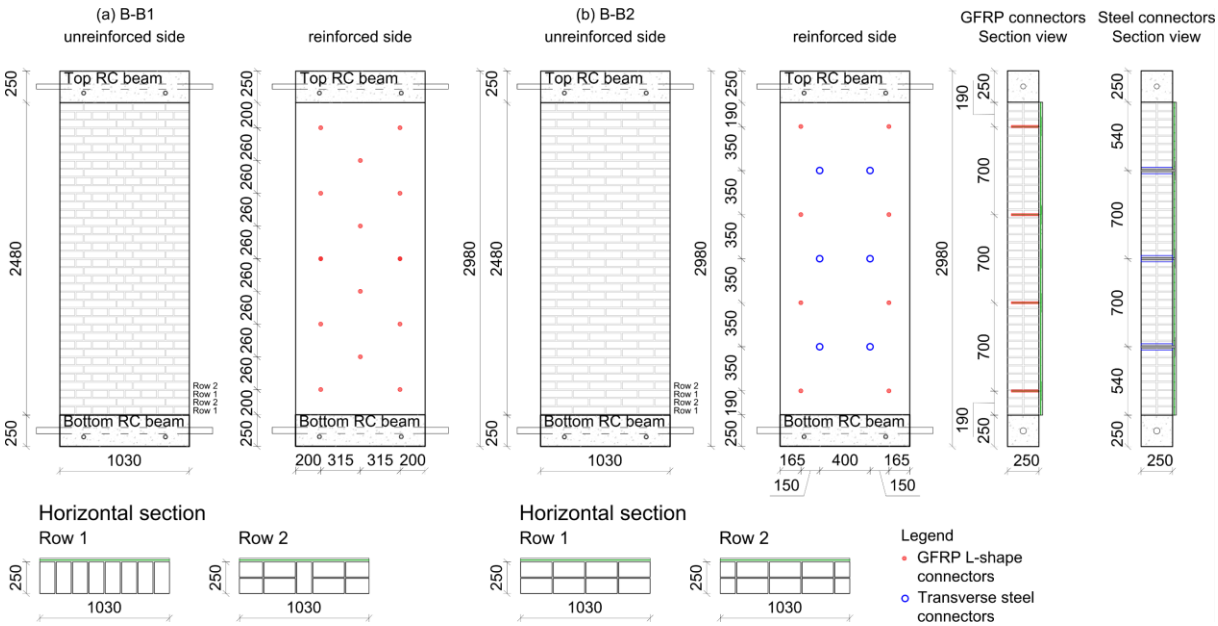


Figure 3.105 Lateral and cross-sectional views of samples (a) B-B1 and (b) B-B2 (measures in mm)

3.6.3 Test setup

The test setup, schematized in Figure 3.106, was a vertical three-point bending test with the samples hinged at the top and bottom. Similarly as in other research of OOP response (e.g. Ismail and Ingham 2016), compressive axial load was not simulated. The apparatus was composed of a steel truss reaction frame, four restraining bars, a trolley for the load distribution system and a hydraulic actuator. A smooth horizontal steel bar (40 mm diameter) running through each RC beam allowed to connect the wall to the reaction frame, by means of four restraining bars provided with knuckle joints. Additionally, the restraining bars were maintained in parallel alignment by two 48.3 mm diameter steel tubular profiles, connected with swivel clamps between each pair. All the samples were arranged so that the CRM-strengthened side was that on the front side. Each end of the lower smooth bar was placed on a steel spacer, so that the sample was suspended at the base, allowing free rotation.

During testing, the actuator, positioned horizontally at the mid-height of the samples, at the rear side, moved a loading trolley to apply the out-of-plane loading cycles. Additionally, to ensure a uniform loading surface, a 10 mm thick chalk and lime mortar layer was applied to the unstrengthened wall surface in correspondence of the loading beam

Since no compression was acting in the walls except for self-weight, and the friction between the RC blocks and the wall was relatively low, steel tubular tensioners were installed to increase the friction and prevent shear slip at the RC block-masonry interface (top and bottom). These devices (Figure 3.107), increased friction via compression between the blocks and the wall by manually tightening the nuts. The tensioners were installed between the RC blocks and class 8.8 M22 threaded steel bars, which passed through the third bed joint and were manually tightened.

Each specimen was equipped with nine displacement transducers, as shown in Figure 3.106b, and two load cells. The displacement transucers were used to measure out-of-plane displacements at the top, middle and bottom of the sample, and rotations of the top and bottom RC elements. Two transducers were placed at the sides of the walls to measure vertical deformations at the mid-height of the pier. The load cells measured the force acting on the wall. Instruments T1 to T4 were averaged to measure the OOP displacement of the middle section, while instrument T5 was used to detect leaf separation in the

double-leaf sample. The strengthened surface of the wall was painted with a contrasting random speckle pattern to measure the displacement and strain fields using the DIC system. A coat of white paint was applied to the unstrengthened side to facilitate crack identification.

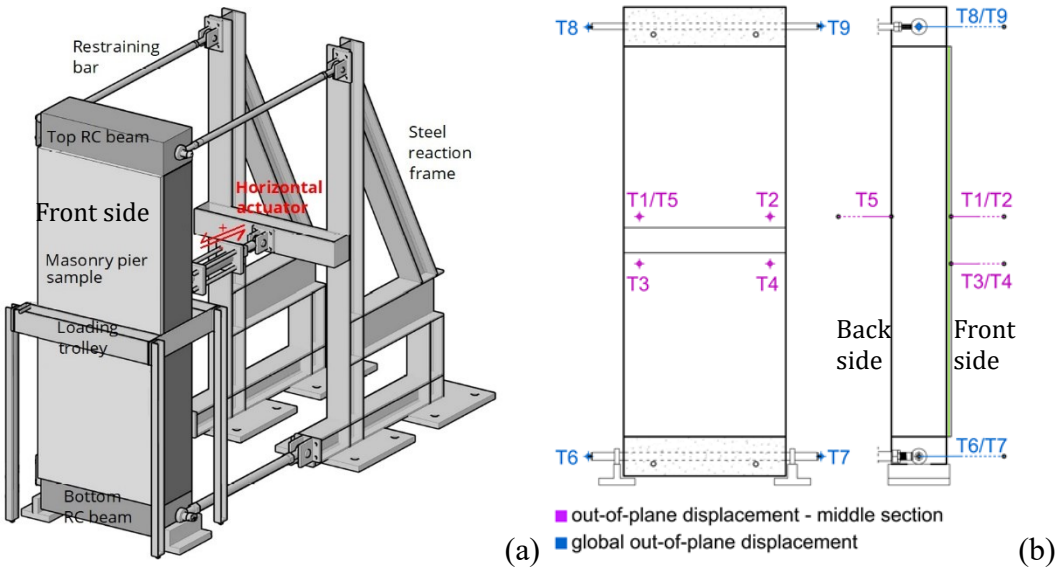


Figure 3.106 Test setup for out-of-plane tests: (a) front view; (b) instrumentation.

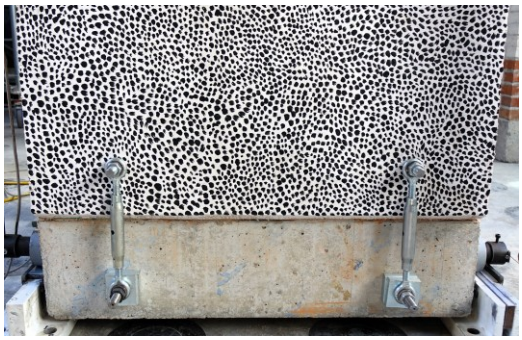


Figure 3.107 Steel tensioners at the bottom of the pier B-2

The loading cycles were performed at increasing displacements, acting in the positive (pushing from the rear to the front side) and negative (pulling from the front to the rear side) directions and gradually increasing the target amplitude. Each load amplitude was repeated only once before it was increased. When a net deflection equal to 1/100 of the sample height was reached, the test was prosecuted by pushing monotonically.

When pushed, the coating was in tension, simulating the strengthened wall response; when pulled, the coating was in compression, which simulated the unreinforced wall response.

The loading programs are shown in Figure 3.108. The tests were concluded when collapse was imminent.

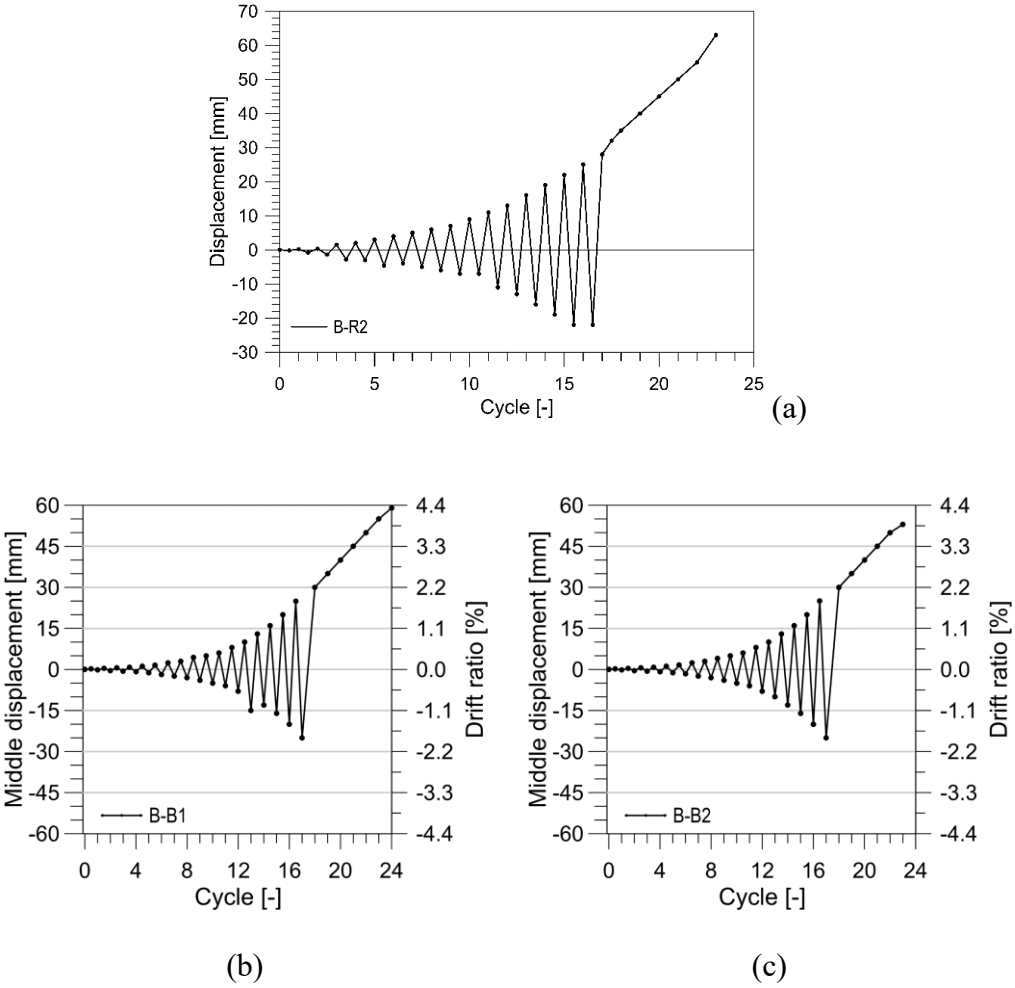


Figure 3.108 Loading cycles for the piers a) B-R2, b) B-B1 and c) B-B2

The behaviour of each sample is described in the following, reporting also monitored loads and displacements and evolution of the crack pattern (surveyed at the front side by means of a Digital Image Correlation system). The main results are then summarized and compared.

The global behaviour of the samples is described in terms of capacity curves, representing the applied horizontal load F_B varying the net horizontal deflection d_B, at the mid-height of the sample.

3.6.4 Results

3.6.4.1 Test B-R2

The first crack occurred at first on the unreinforced side, when pulling, near the mid-height; then also on the strengthened side, when pushing. As the displacement amplitudes increased, the crack pattern on the unstrengthened side remained the same as the single crack opened increasingly more. On the other side, several new horizontal cracks opened on the strengthened side, involving an increasingly wider sample portion. The cracks in the coating multiplied and spread over almost 2/3 of the pier height. The final collapse was due to the tensile failure of the GFRP vertical wires crossing a crack around the mid-span.

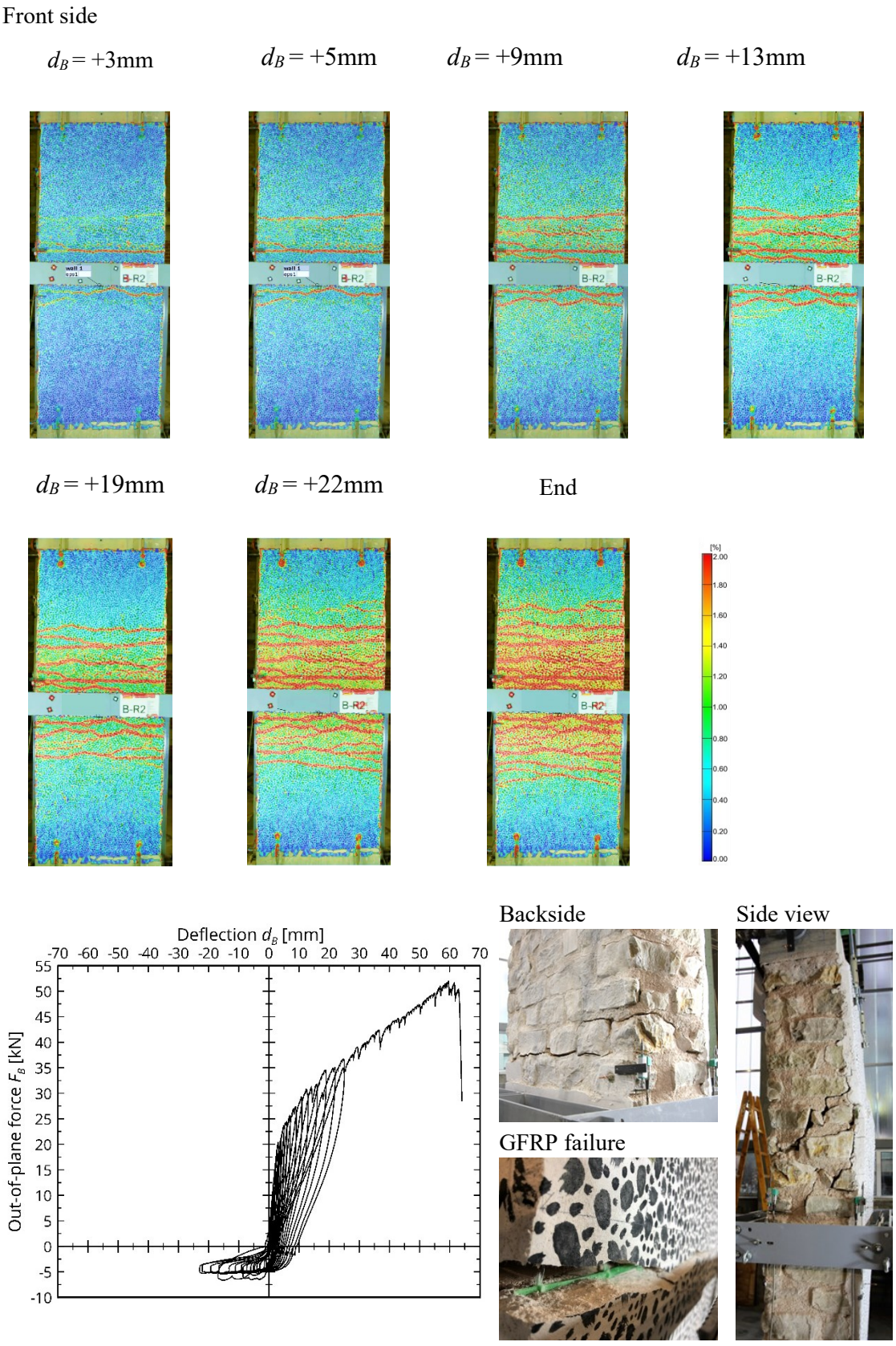


Figure 3.109 Main results of test B-R2

3.6.4.2 Test B-B2

A single horizontal crack occurred on the unreinforced side, in the middle section, which then gradually opened during the pulling stages. On the coated side, the first crack appeared next to the mid-height and had a sub-vertical trend. As the pushing load increased, new cracks appeared in the coating. All cracks in the coating were primarily horizontal. The cracks originated from the midsection and gradually spread toward the top and bottom of the pier, involving more than 2/3 of the height. At collapse, the GFRP vertical wires in the coating fractured around the mid-span.

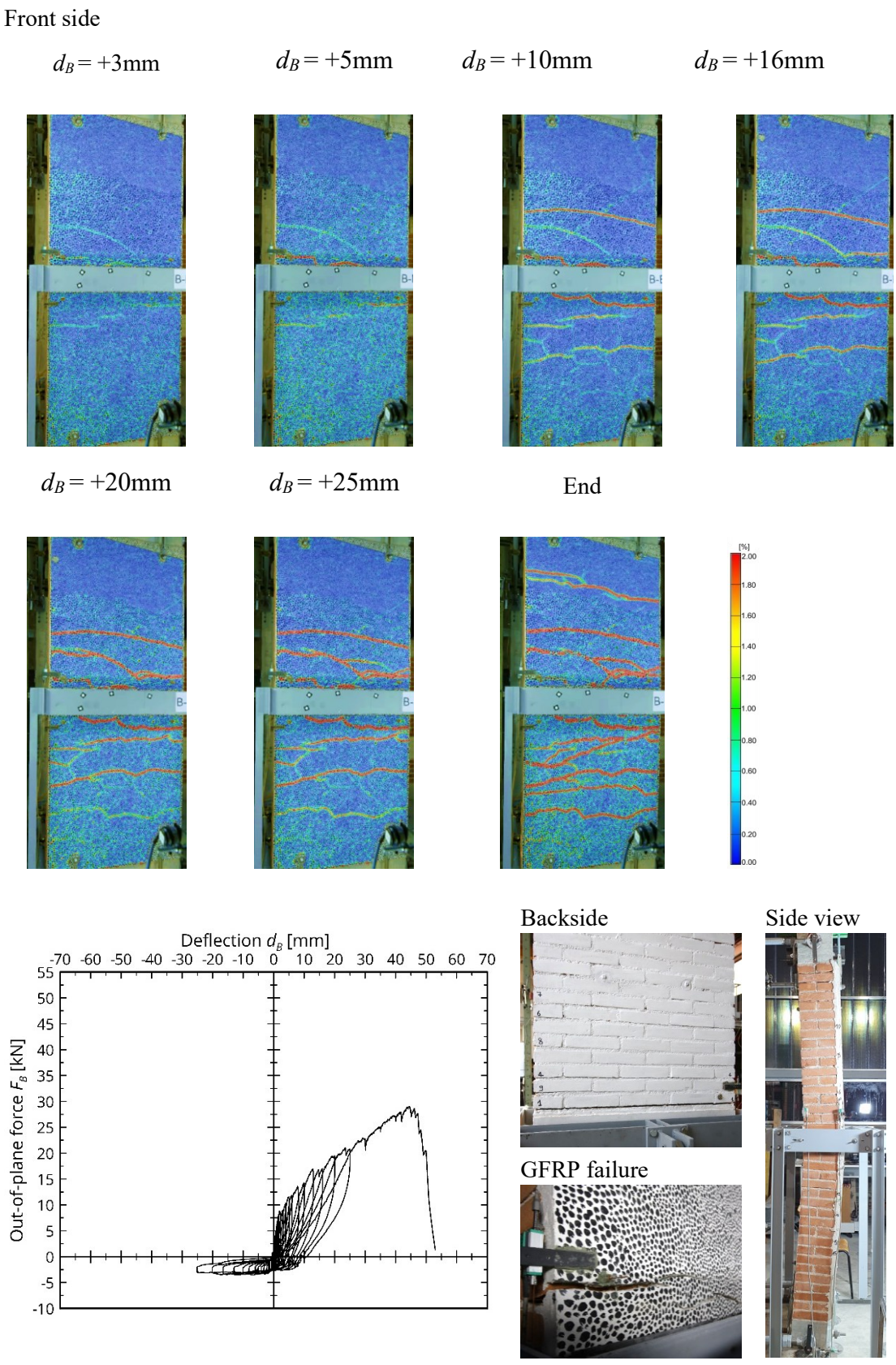


Figure 3.110 Main results of test B-B2

3.6.4.3 Test B-B1

The first crack appeared when pulling and was horizontal in the mid-height bed joint of the unreinforced side; a second horizontal crack formed slightly upper when the deflection was increased. On the coated side, the first horizontal crack appeared at mid-height. As the pushing load increased, new cracks appeared in the coating. All cracks in the coating were primarily horizontal**.** The cracks originated from the midsection and gradually spread toward the top and bottom of the pier, involving almost 2/3 of the height. At collapse, the GFRP vertical wires in the coating fractured at the mid-span.

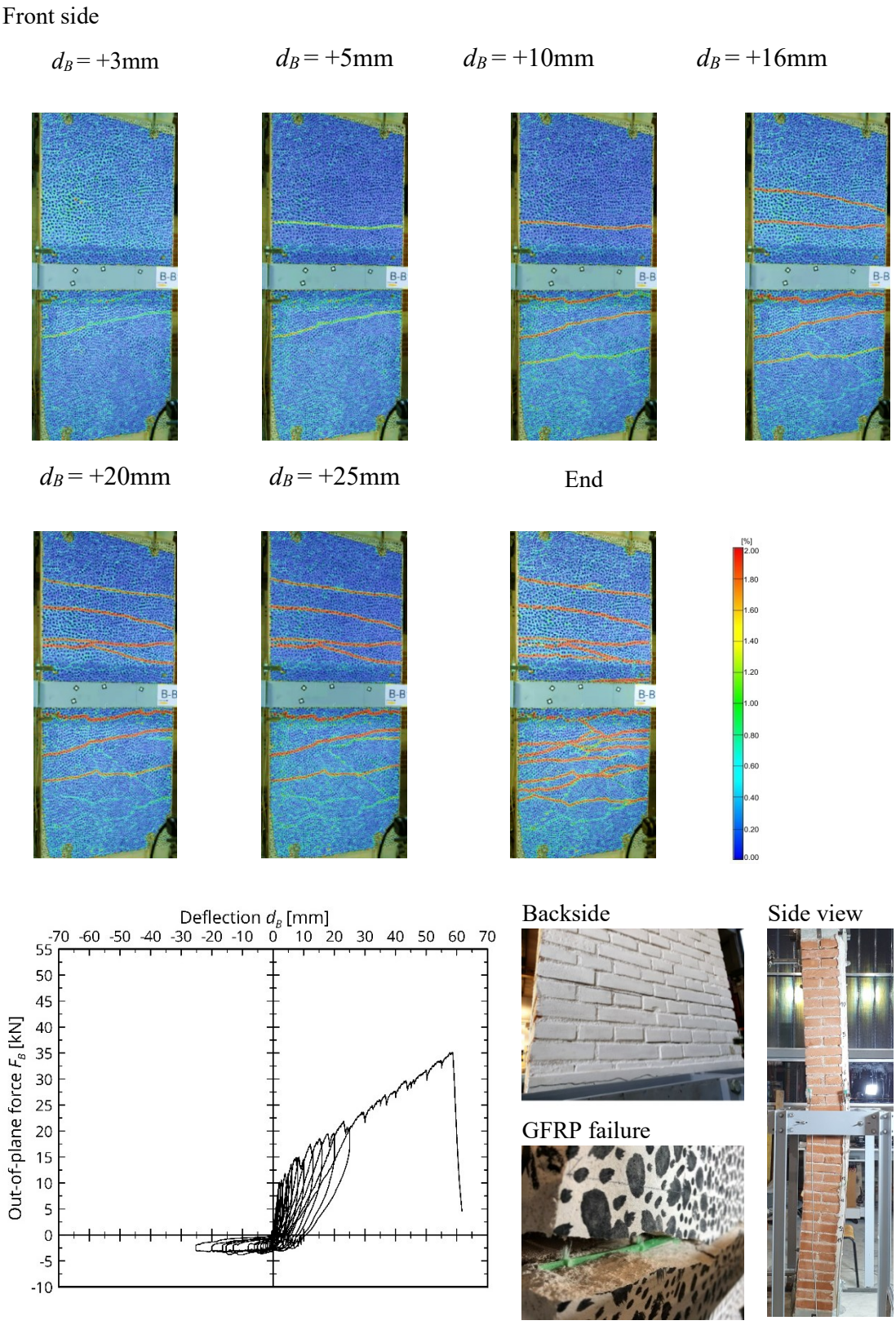


Figure 3.111 Main results of test B-B1

3.6.5 Analysis of results and comparison

The values of F_B and d_B obtained from the three experimental tests are summarized in Figure 3.112 and Table 3.16, for first cracking ald ultimate load (*Cr*, *Ul*). When pushing, the ultimate load is taken in correspondance of the peak load; when pulling, the value correspondant to a net deflection equal to 1/150 the height is assumed.

It is observed that the comparison between the sample performances in pushing and pulling directions almost provided a comparison between CRM-strengthened and unstrengthned masonry. In fact, the contribution of CRM in compression is almost negligible (except for the small additional thickness, due to the mortar).

Table 3.16 Values of the out-of-plane horizontal load (F_B) and net deflection (d_B) measured in positive and negative loading directions, for the first cracking and ultimate load

ID	**Side in tension**	**First cracking (*Cr*)**		**Ultimate load (*Ul*)**	
		F_B [kN]	**d_B [mm]**	**F_B [kN]**	**d_B [mm]**
B-R2	URM	-6.49	-2.81	-5.15	-16.7
	CRM	20.4	3.28	52.0	59.6
B-B2	URM	-3.42	-3.15	-3.43	-16.7
	CRM	8.83	2.25	29.0	44.5
B-B1	URM	-3.37	-3.1	-3.32	-16.7
	CRM	9.80	1.90	35.1	58.6

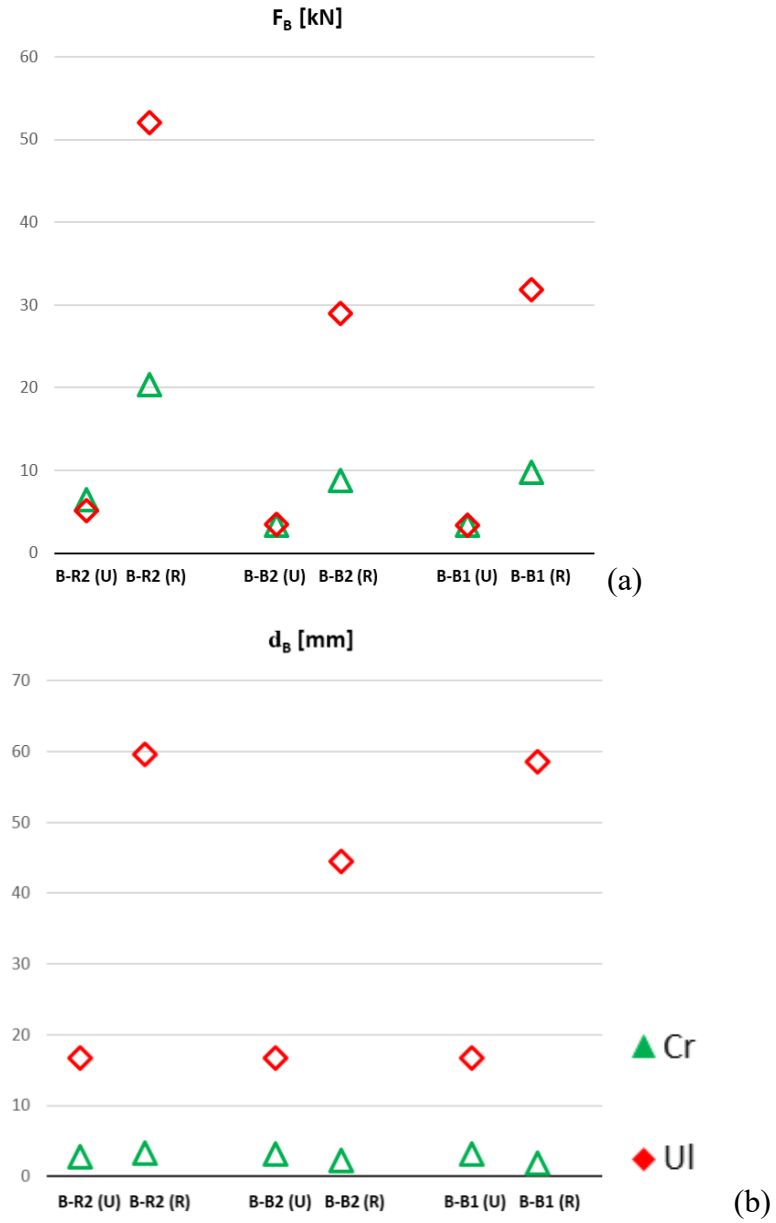


Figure 3.112 Main results of out-of-plane tests: first cracking, peak and near collapse forces (a) and net deflections (b)

In general, on the unstrengthened side, the failure mechanism was characterized by the opening of one or two nearly horizontal cracks in masonry bed joints. Differently, on the strengthened side, many cracks in the coating widely spread from the central section: the CRM and the masonry performed as a composite element; when the collapse occurred, the vertical GFRP wires fractured due to tension, indicating it was exploited at its maximum.

Significant improvements were attained in terms of resistance (ratio between ultimate forces): 10.1 in B-R2, 8.5 in B-B2 and 10.6 in B-B1. The failure on the fibres occurred at 45.8 times the span in B-R2, 61.4 in B-B2 and 46.6 in B-B1.

3.7 Roof ring beams with FRP meshes embedded in bed joints

The tests performed in this study were performed at the University of Ljubljana (Slovenia). The tests aimed to evaluate and compare the out-of-plane performances of the ring beams strengthened with GFRP meshes embedded in mortar joints.

3.7.1 Literature review

The vulnerability of existing buildings characterized by unidirectional timber floors and roofs without ties was clearly evidenced by the post-earthquake studies and surveys [251–253], evidencing the dangers and potential damage of out-of-plane (OOP) failure of masonry walls [254]. Past research has demonstrated how properly designed floor tie rods or RC ring beams at roof and floor levels can mitigate local OOP response in favour of global, box-like behaviour of the structure [18,255,256].

As shown by Guadagnuolo and Faella [257], solutions for ring beams that are more compatible with the low mechanical characteristics of historic masonry through the use of fibre-based composites are emerging as promising alternative. The potential of this type of solutions for the reinforcement of masonry buildings is significant in enhancing both the in-plane and out-of-plane behaviour of masonry walls and vaults, as beneficial in cracking control, ductility improvement and energy dissipation increase. However, focusing on the applications of fibre-based composites to achieve the tying (ring) effect in masonry beams, just a few references are there in the literature. For example, Borri et al. [258] and Sisti et al. [259] tested masonry ring beam samples with Glass Fibre Reinforced Polymer (GFRP) pre-formed meshes embedded in the mortar joints in monotonic bending. The compatibility of the two materials led to composite action and enhanced load-bearing capacities for loads orthogonal and parallel to the bed joints. Additionally, De Santis and de Felice [195] performed shaking table tests on a small rubble stone masonry structure strengthened with GFRP meshes embedded in the plaster of the outer façade, combined with transversal GFRP connectors (Composite-Reinforced Mortar technique, CRM); the externally bonded coating opposed the separation of orthogonal walls and roof thrusts. Jasieńko et al. [260] experimentally analysed wrapping of masonry domes with organic and inorganic matrices. In summary, fibre-based composite materials were used in some successful experimental applications to provide a tying effect, but anchoring or wrapping emerged as crucial for achieving optimal performance.

The embedment of FRP meshes in the horizontal joints of mortar in masonry crowning beams is suggested by the Italian CNR guidelines CNR-DT 215/2018 [11] as a technique to foster the box-type behaviour of the masonry structure and prevent the OOP overturning collapse mechanisms. Similarly, the use of FRP horizontal strips glued with organic resins, properly anchored to the orthogonal walls and optimally embracing the whole structure's perimeter, is recognised as an effective strengthening solution against OOP loads by the Italian CNR guidelines CNR-DT 200 R1/2013 [261]. The analytical methods for the strength of fibre reinforced ring beams are typically based on the composite beam theory, which appears to be valid [126,257–259,262–268], although few experimental studies have confirmed this. Of note, externally bonded reinforcements are eccentric systems, and their behaviour under load reversals still needs to be adequately addressed. Moreover, monotonic OOP tests, as presented in [269] and [270] are not sufficiently representative, and even in the case of fibre-reinforced bed joints, which are symmetric, load reversal may lead to premature debonding.

The tests reported and analysed in the following focus on these issues, providing original new results. The campaign investigates on the seismic behaviour of full-scale masonry crowning beams with GFRP-strengthened bed joints.

3.7.2 Scope and methods

The experiment was designed to schematically reproduce the typical loading condition in masonry walls at the floor/roof level induced by the seismic action in structures without horizontal diaphragm loading, as schematically shown in Figure 3.113a. The strengthening technique for OOP loads, based on fibre-based composite materials consists of embedding GFRP meshes in the bed joints. The system is symmetric and simple straight beam samples are considered, as shown in Figure 3.113b. The effect of GFRP anchorage at corners may improve the global behaviour, but is ignored in these tests and will be investigated in the tests on ring beams with externally bonded FRP strips. Figure 3.114 shows the GFRP mesh in rubble stone masonry during construction. The seismic action was simulated, in a simplified way, by applying a concentrated OOP load in a quasi-static cyclic manner in the middle of the samples, as shown by blue and red arrows in Figure 3.113b.

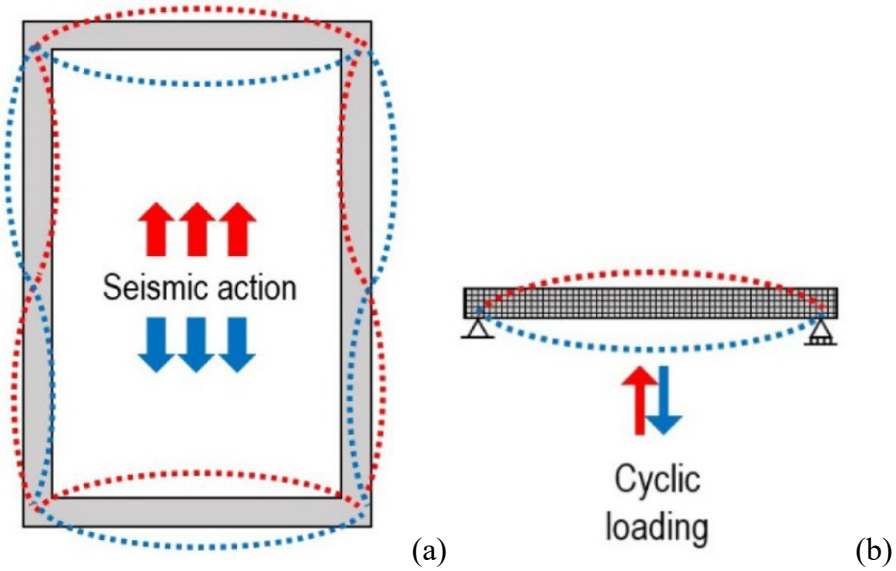


Figure 3.113 Schematization of general issue (a) and in a plan view and of the experimental patterns for testing GFRP meshes embedded in bed joints

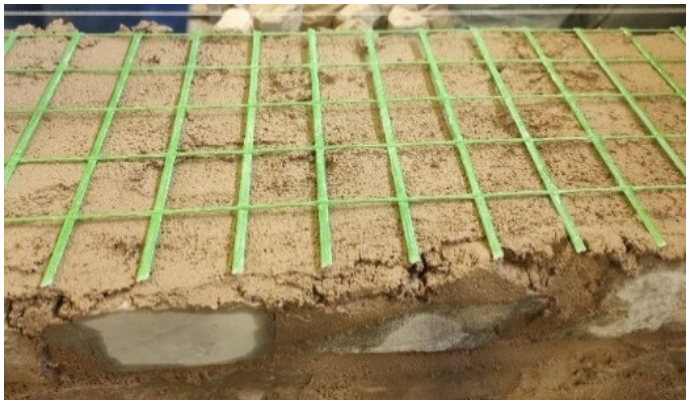
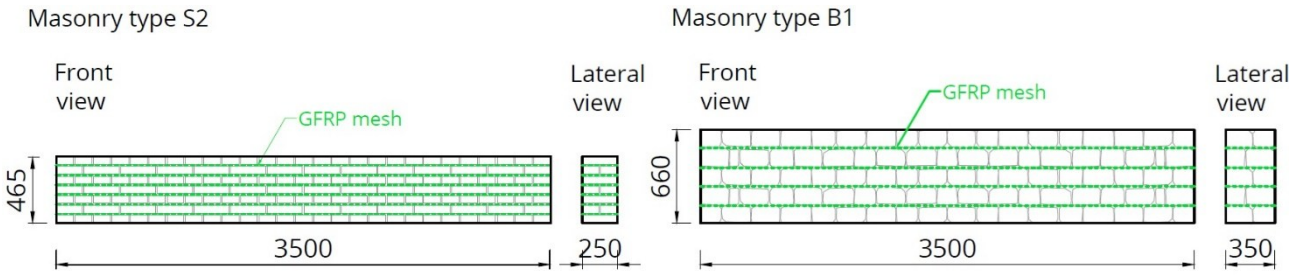


Figure 3.114 Mesh embedded in the bed joint

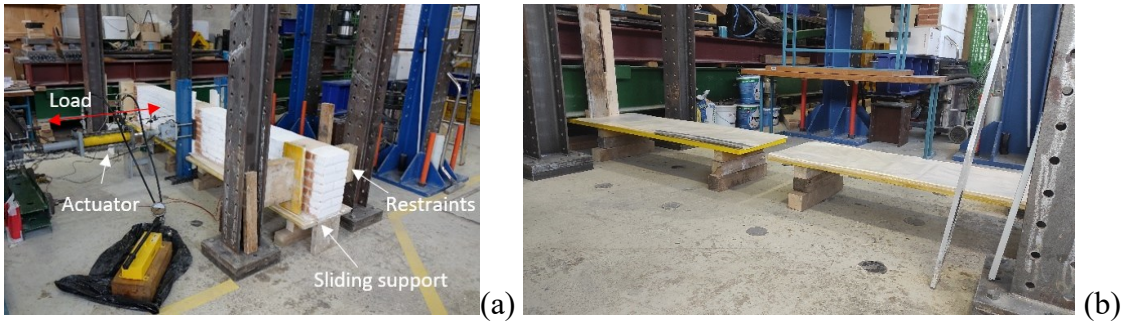
The masonry ring beam samples with GFRP meshes embedded in the bed joints (“T”) were 3500 mm long. The first sample was made of 350 mm thick double-leaf rubble stone masonry (“T-R2”), which was 660 mm tall and had four reinforced bed joints (Figure 3.115a). The other sample was made of 250 mm-thick single-leaf solid clay brick masonry (“T-B1”) that was 465 mm tall, with six reinforced bed joints (Figure 3.115b).



(a) (b)

Figure 3.115 Main geometric characteristics of the roof ring beam masonry samples: (a) T-R2 and (b) T-B1

The experimental setup consisted of the horizontal sliding system (supporting the sample vertically), horizontal restraining system, and loading system (Figure 3.116a). The sliding system consisted of a smooth, flat surface covered with two plastic sheets with grease in between (Figure 3.116b). The restraining system comprised four stiff steel columns connected to the laboratory basement (two at each side), which was connected to the sample with hinged rods that provided support against out-of-plane horizontal sliding, but allowed rotations. The net span between the supports was 3000 mm. The loading system was a horizontal actuator located at the midspan of the sample and connected on one side to a concrete ballast and on the other to a steel frame on a trolley. Thin elastic rubber strips at the contact between the wall and the load beam were used to reduce load concentrations at transfer points. The load was applied cyclically, alternatively pulling (negative loading) and pushing (positive loading), gradually increasing the amplitude of the deflection.



(a) (b)

Figure 3.116 (a) Wooden support for the samples with sliding surface; (b) Sample, restraining frame and the actuator

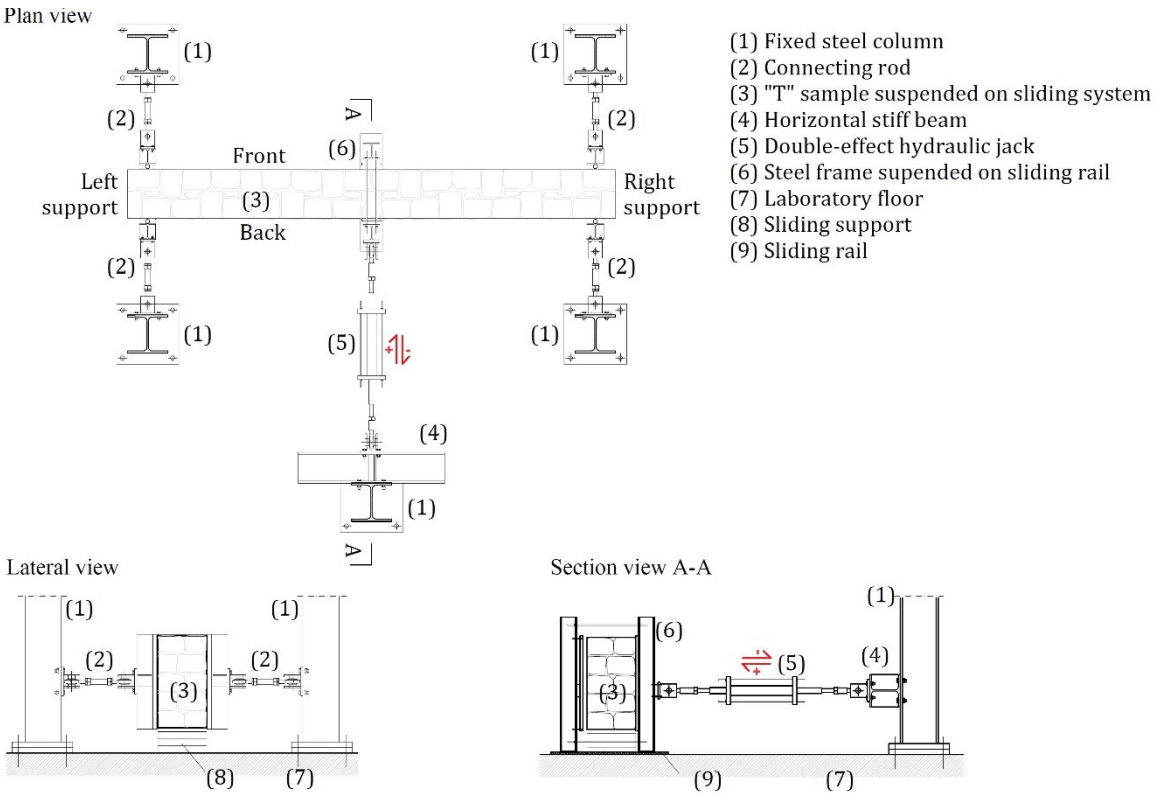


Figure 3.117 Experimental setup for "T" samples

The instrumentation consists of two load cells on the actuator (one for pushing and one for pulling) and six displacement transducers. A pair of transducers were mounted on the left side (near support), at the centre (next to the actuator) and on the right side (near support), as shown in Figure 3.118. The recordings of paired displacement instruments were averaged.

The instrumentation consisted of two load cells for measuring the force in the actuator ($P-$, $P+$) and six displacement transducers monitoring the absolute horizontal OOP displacements. A pair of transducers was installed in the vicinity (~ 150 mm) of the midspan (δ_{M1}, δ_{M2}) and at the left (δ_{L1}, δ_{L2}) and right (δ_{R1}, δ_{R2}) supports. For each pair, one transducer was installed near the top and one near the bottom of the wall (Figure 3.118). The sample net deflection δ_m was evaluated as:

$$\delta_m = \frac{(h_{M1} + h_{M2})}{2} - \frac{(h_{L1} + h_{L2}) + (h_{R1} + h_{R2})}{4} \qquad (3.8)$$

The amplitude of the net deflection was cyclically increased during the tests, according to the protocols illustrated in Figure 3.119; at the first failure of the GFRP mesh in one loading direction, the test was continued by monotonically loading in the opposite direction until failure.



Figure 3.118 Locations of displacement transducers

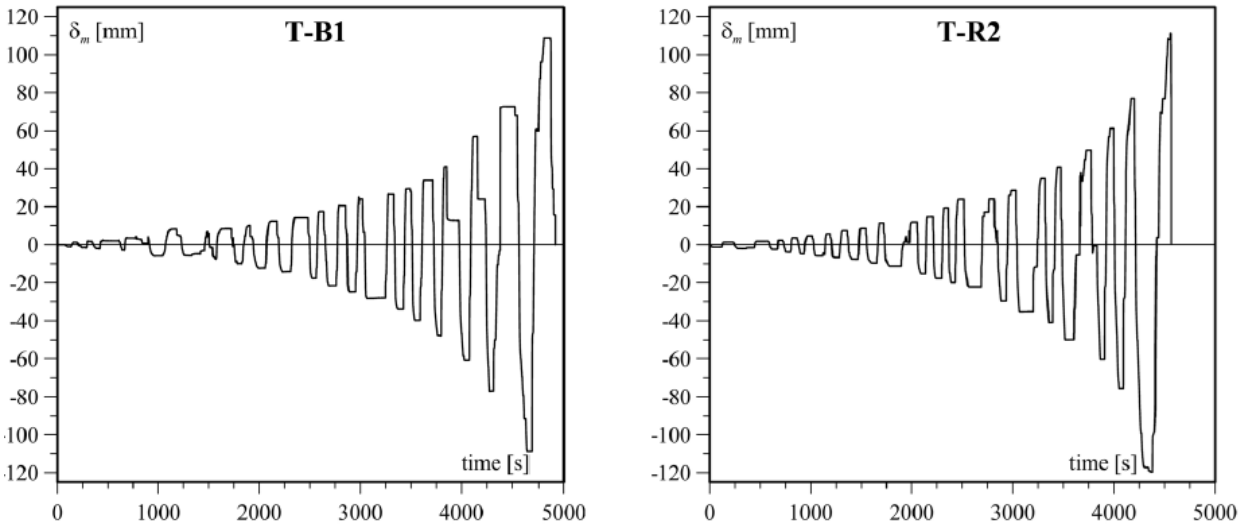


Figure 3.119 Loading protocols followed during the tests (evolution of the net deflection in time)

The main results are summarized in the following, reporting also monitored loads and displacements and evolution of the crack pattern (visual surveyed during the test).

The global behaviour of the samples is described in terms of capacity curves, representing the out-of-plane horizontal load, F_T, varying the net horizontal deflection at the midspan, d_m.

3.7.3 Results

3.7.3.1 Test T-R2

A first pair of central cracks opened on the rear face, when pulling, and just after of the front face, inversing the load direction. The cracks followed an almost vertical trend along the mortar joints. With increasing load, the deflection increased, and new sub-vertical cracks formed. The cracks progressively formed alternately at front and back, according to the loading direction. When the number of cracks stabilized, a gradual and significant widening of the central cracks emerged at increasing deflection. The collapse was due to the fracture of the GFRP longitudinal wires near the back side, when pulling, and then near the front side, when pushing. The behaviour was almost symmetric in the two directions.

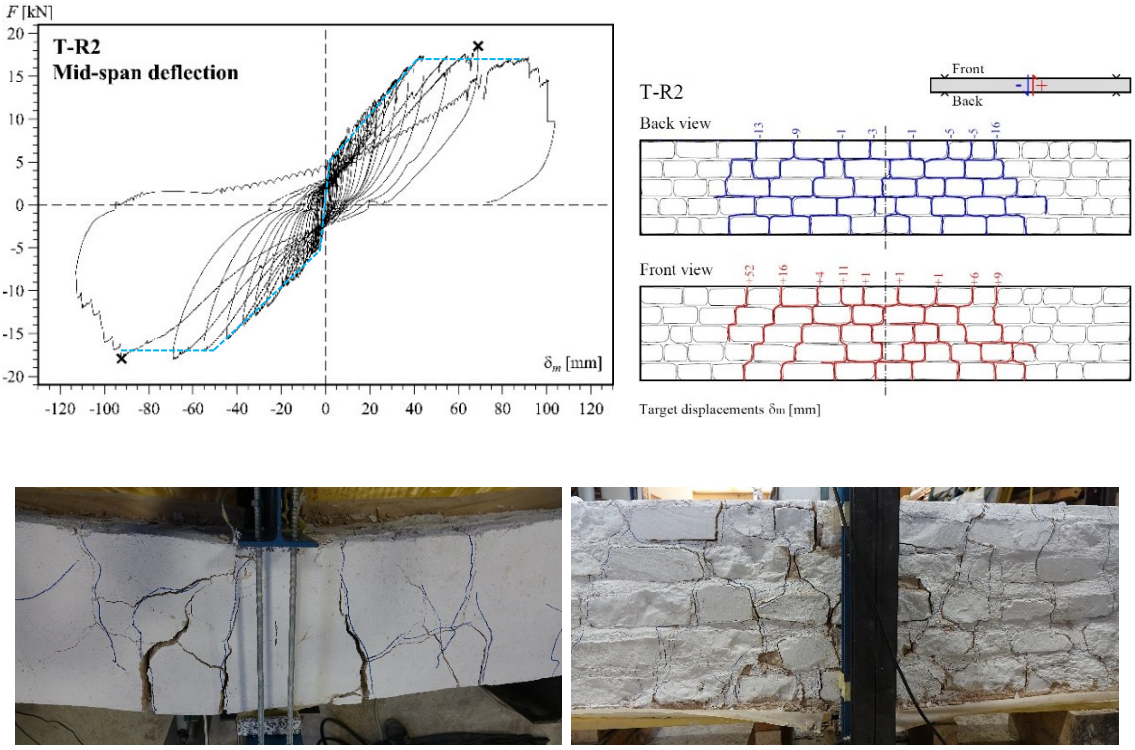


Figure 3.120 Main results of test T-R2

3.7.3.2 Test T-B1

A first pair of cracks formed in the vicinity of the midspan, when pushing. The cracks were vertical but followed the joints at the front side. As the load direction was inversed, the cracks on the front side closed, and the cracks on the back side opened. With increasing load, the new sub-vertical cracks (following the joints) developed almost throughout the whole sample height, gradually covering an increasingly wider portion of the sample. Once the formation of most of the cracks was completed, the existing cracks widened with the deflection increase. Near the ultimate state, a continuous horizontal discontinuity at the upper bed joint caused a gradual separation of the last brick row from the lower part of the sample on the left side; thus, the last layer of reinforcement mesh lost part of its effectiveness. At the test prosecuted, some longitudinal GFRP wires on the rear face fractured at the mid-span; similarly, at the opposite loading direction, the GFRP wires on the front face fractured at the mid-span. The behaviour was quite asymmetric in the two loading directions (the hardening was stiffer in pulling).

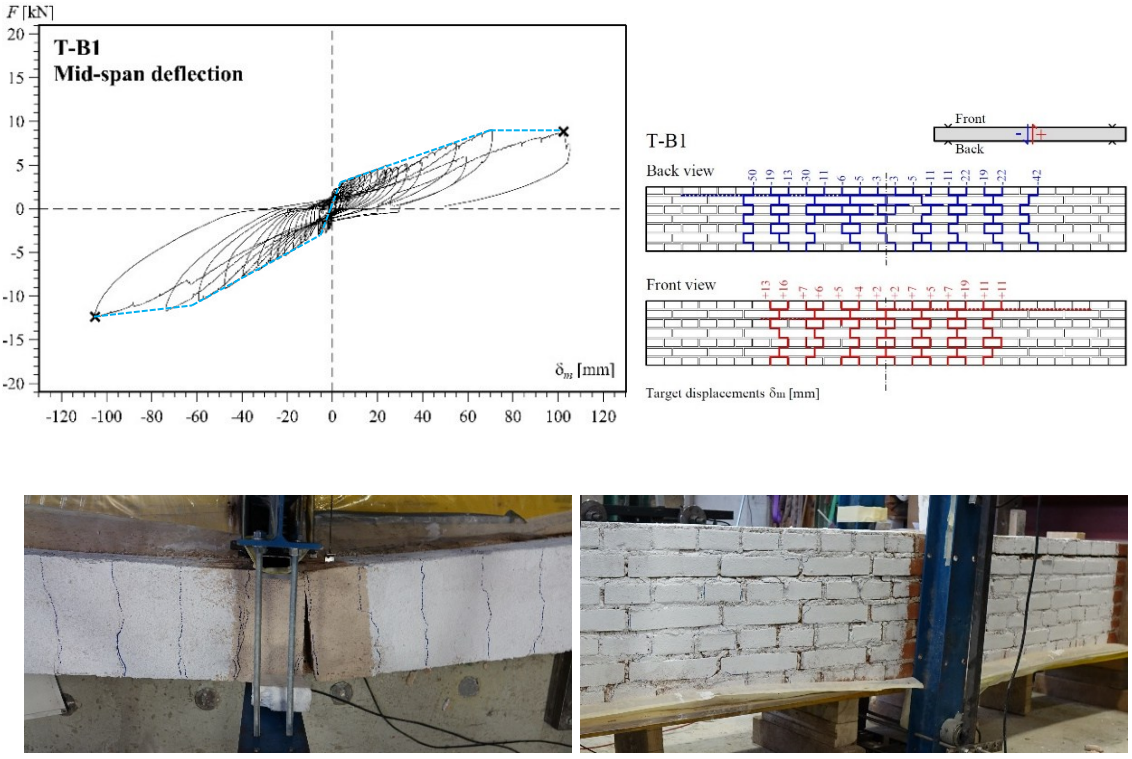


Figure 3.121 Main results of test T-B1

3.7.4 Analysis of results and comparison

Generally, the first cracks in the masonry formed on the tensed side, in the vicinity of the midspan. As the load direction was inversed, the cracks on one side closed, and the cracks

on the other side opened. With increasing load, new sub-vertical cracks developed on the tension side, almost throughout the whole sample height, gradually covering an increasingly wider portion of the sample (of a width of about 1800 mm). Moreover, as the deflection increased, the existing cracks widened. Both samples attained to peak load just before some longitudinal GFRP wires fractured on the tensed side, at the mid-span; then the load rapidly dropped down.

The backbone of the load-deflection F_T-d_m curves assumed a roughly tri-linear trend: the first elastic part with an initial stiffness, a second plastic part with hardening, and a third part with near-zero stiffness.

The main results of the two tests in terms of load and deflection at first cracking (*Cr*) and at collapse (*Ul*) are summarized in Table 3.17 and Figure 3.122. For sample T-R2, the resistance of almost 18.3 kN at about 1/44 of the net span for both directions. Sample T-B1 reached 12.4 kN and 9.0 kN in pulling and pushing, respectively; the difference was likely influenced by the detachment of the upper rows mentioned before. However, the ultimate deflections were similar (about 1/29 the net span).

Table 3.17. Main results of tests on masonry ring beams with FRP meshes embedded in bed joints, in terms of load and deflection at first cracking (Cr) and at collapse (Ul)

Sample	**Load direction**	**First cracking (*Cr*)**		**Ultimate load (*Ul*)**	
		F_T [kN]	**d_m [mm]**	**F_T [kN]**	**d_m [mm]**
T-R2	Pull (−)	−2.3	−1.0	−18.0	−68.8
	Push (+)	+5.2	+0.8	+18.6	+69.0
T-B1	Pull (−)	−3.1	−2.7	−12.4	−105.1
	Push (+)	+2.6	+2.3	+9.0	+101.9

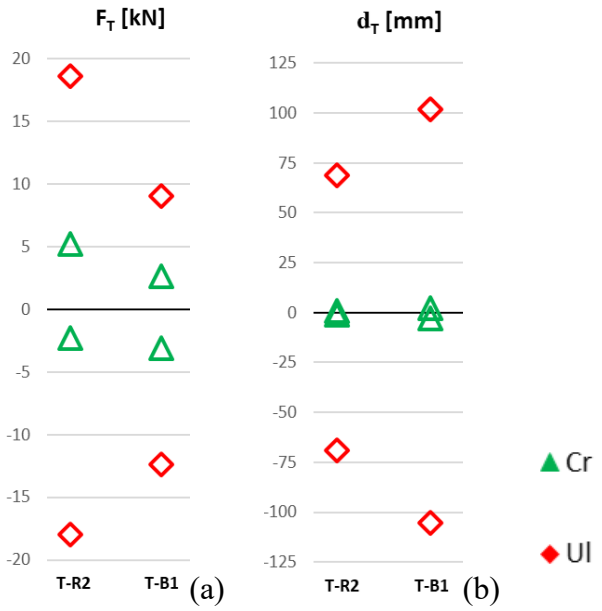


Figure 3.122 Main test results of "T" samples: first cracking and ultimate force (a) and deflection (b) values.

The cyclic tests allow also to draw the trends of the cycle stiffness, K_T (evaluated as the slope of the peak-to-peak line within each loop of the F_T–d_T curve) by varying the net deflection d_T (Figure 3.123a). The stiffness degradation with increasing deflection shows an approximately power-law trend; at the end of the tests, the cycle stiffness was less than 10% the initial value.

The cumulative input energy (E_{in}) and the dissipated hysteretic energy (E_{hys}) were quantified (Figure 3.123b), as well as the E_{hys}/E_{in} ratios (Figure 3.123c). E_{in} is the cumulative work to deform the sample from the beginning of the test to a specific target value of deflection. For each loading cycle, it corresponds to the area under the positive and negative branches of the hysteretic loop of the F_T-d_T graph. Similarly, the cumulative dissipated hysteretic energy E_{hys} is the sum of all the areas included in the hysteretic loops. Moreover, an approximate estimation of the equivalent hysteretic damping with varying target displacement was performed (Figure 3.123d).

In respect to the first cracking condition, the cumulative dissipated energy at collapse resulted more than 500 times greater in both cases. The damping ratio, ξ_{hys}, decreased as the deflection progressed and resulted about 11-12% at collapse.

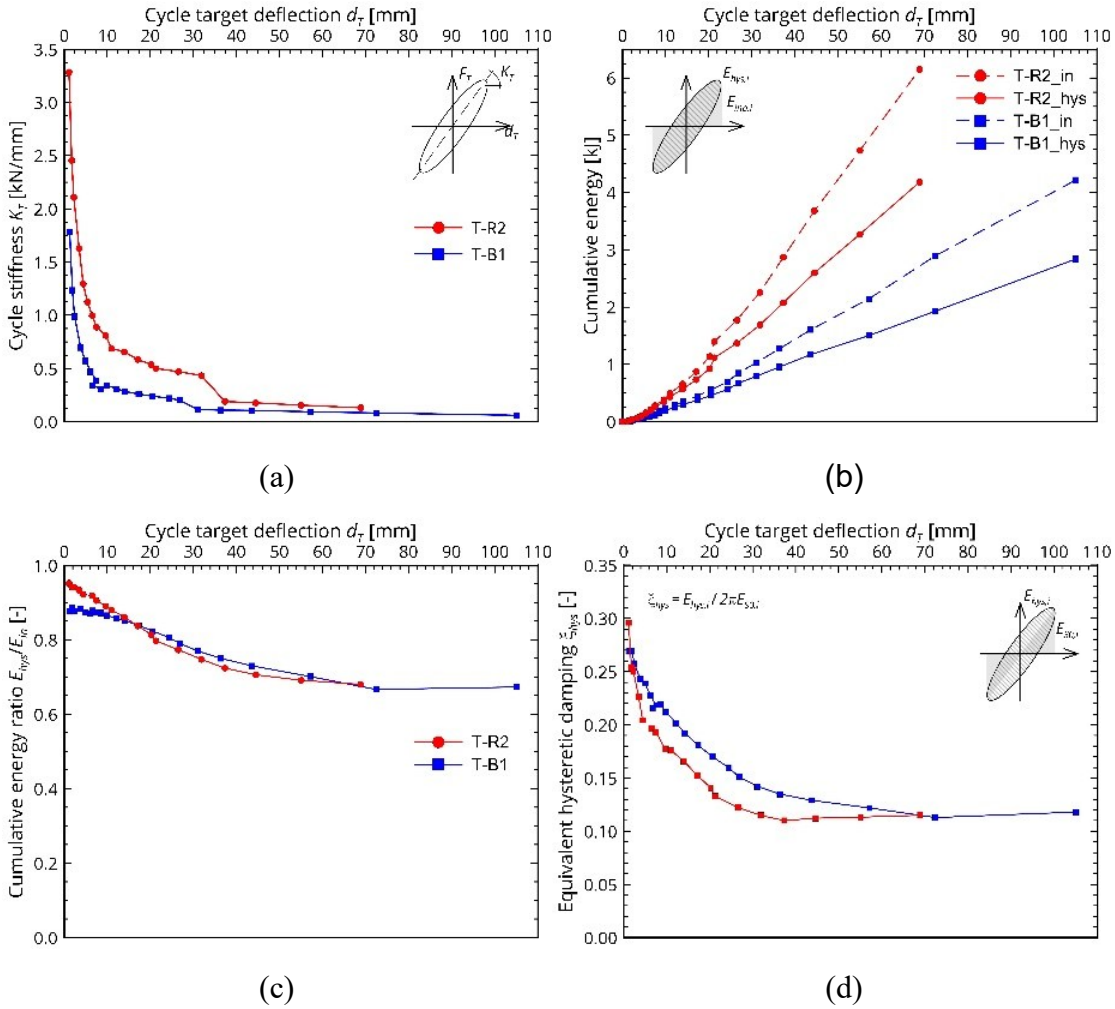


Figure 3.123 Roof ring beam stiffness and energy characteristics, varying the cycle target deflection d_m

3.8 Ring beams with externally-bonded FRP strips

In the following, experimental tests on the out of plane behaviour of masonry ring beams strengthened with externally bonded carbon fibre-reinforced polymer (CFRP) strips will be presented. The tests performed in this study were performed at the laboratory of the company Fibre Net in Pavia di Udine (Italy). The relevant literature review is discussed in section 3.7.

The tests reported and analysed in the following provide original new results. The campaign investigates on the seismic behaviour of full-scale masonry crowning beams with externally bonded CFRP strips.

3.8.1 Description of the samples

The samples for testing the masonry ring beams with externally bonded CFRP strips were C-shaped masonry samples ("C") and had nominal dimensions of 3650×1035 mm (l×b = central span × side, measured along the axes) and height h = 1000 mm. The first sample ("C-R2") was made of 350 mm-thick double-leaf rubble stone masonry and the other ("C-B1") of 250 mm-thick single-leaf solid clay brick masonry. A 200 mm–wide CFRP strip was bonded externally to each sample at mid-height around the outer perimeter, rounding the corners with a bend radius of 20 mm. Prior to installing the CFRP strip, a high-strength cementitious mortar layer was applied at mid-height of the wall to provide a uniform bonding surface. The mortar layer had a height of 250 mm and a thickness of 10 mm for specimen C-B1 and up to 30 mm for specimen C-R2. The CFRP strip was subsequently bonded to this mortar layer using epoxy resin. In the double-leaf rubble stone sample, transversal connectors (i.e "artificial diatons", as those described in section 3.2.1) were added to prevent leaves separation in the masonry.

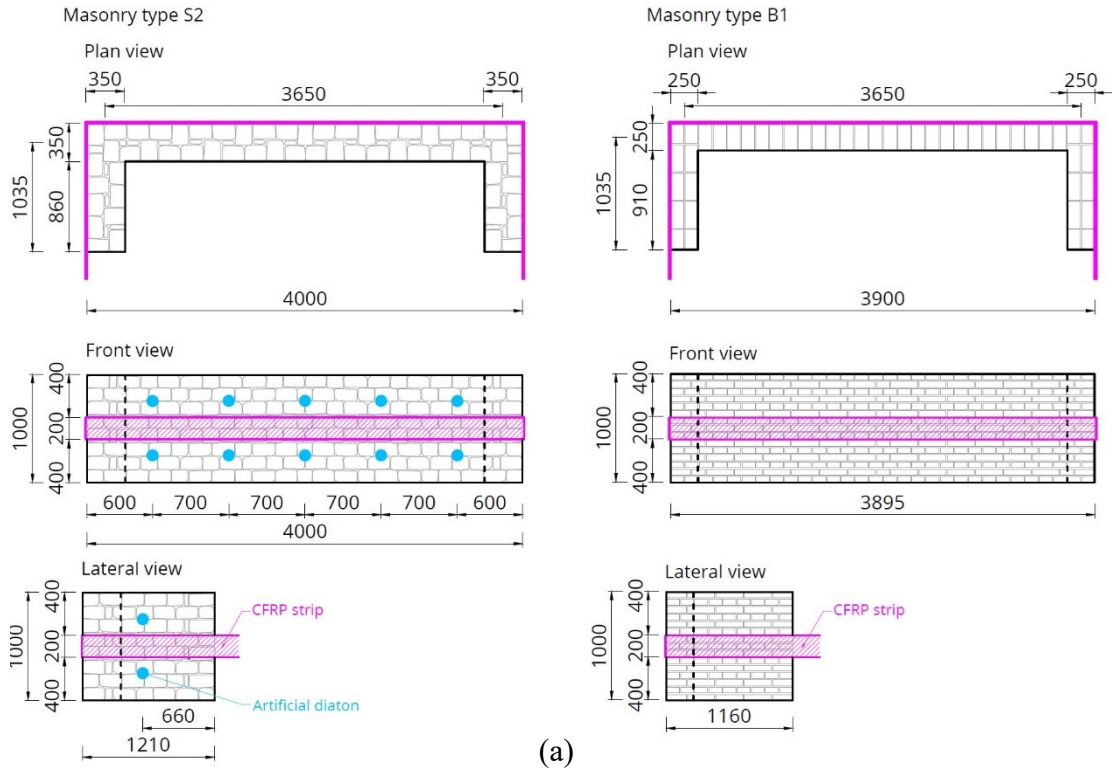


Figure 3.124 Main geometric characteristics of the C-shape masonry samples: (a) C-R2 and (b) C-B1

3.8.2 Test setup

The test setup for the "C" samples is schematized in Figure 3.125. Each sample laid on six trolleys, made with tubular steel profiles (dimension 250×360 mm) and steel ball bearings, which moved on a smooth horizontal surface with minimal friction (5 mm thick steel plates. The out-of-plane horizontal cyclic loading was applied at the midspan using a hydraulic jack. The ends of the sample wings were clamped to a reaction wall (horizontal stiff steel beam fixed to concrete blocks) via supports capable to prevent rotation about vertical axis but to allow lateral movement. Two vertical HEA 160 steel beams were used to transfer the load from the actuator to the specimen. There were loading plates between the HEA 160 and the specimen with allowed rotation about their vertical axis. The loading frame was placed on ball bearings to make slip friction negligible. Four "L" shaped steel rails were welded to the base steel plate. Two were used to keep the loading beams centred, and two were placed on the outer sides of the middle trolleys to allow for relative rotations.

The CFRP strips were anchored into the supports (by clamping), thus fixing the axial movement of the sample (in the direction of the loading) when the actuator was pushing. In the case when the actuator was pulling the sample, the wings pressed against a vertical steel beam.

The load was applied cyclically, alternatively pushing (positive loading) and pulling (negative loading), gradually increasing the amplitude of the deflection. When the CFRP strip at the midspan failed during pushing, the test was stopped, and the reinforcement continuity was restored just to prevent the separation of the two wall portions (no other influence on negative loading). Then, the test was restarted by pulling monotonically to induce the failure of the CFRP strip at the corners.

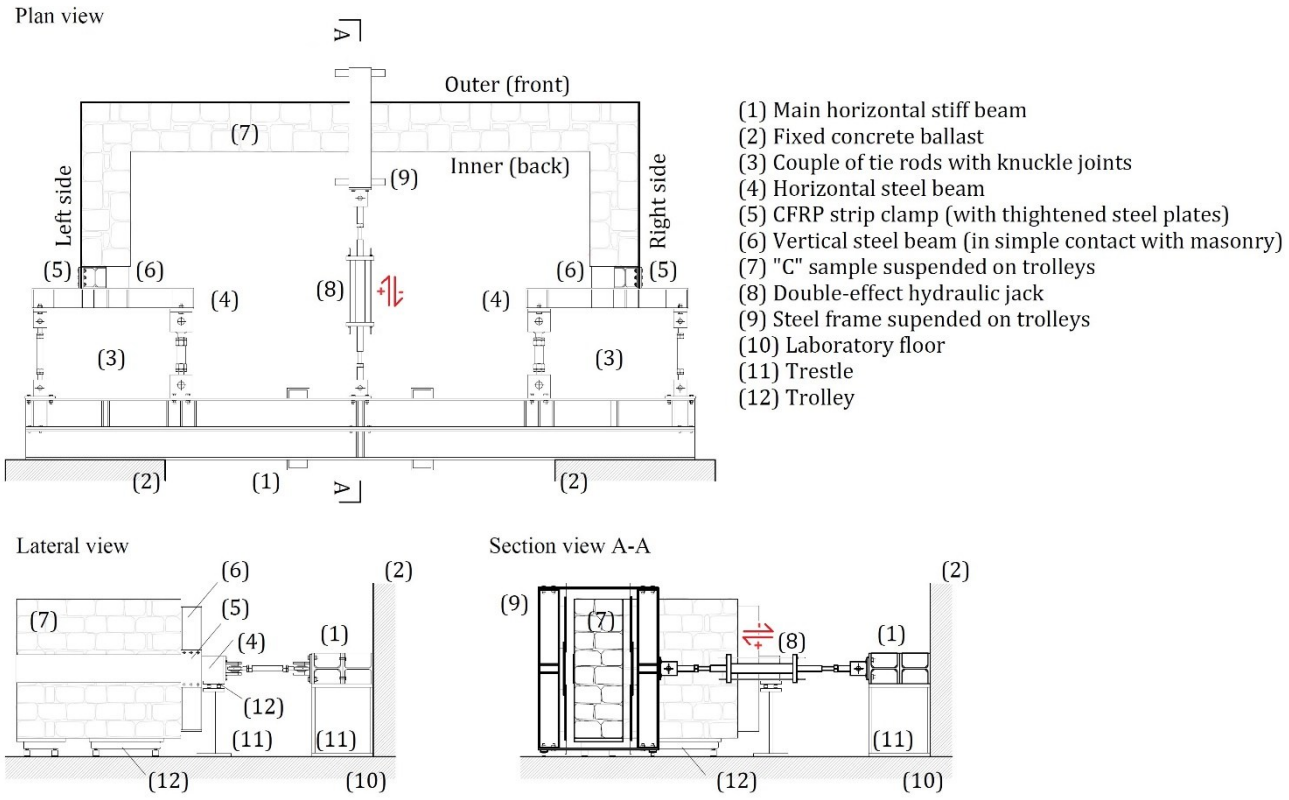


Figure 3.125 Experimental setup for "C" samples. The instrumentation is shown in the plan view

Each specimen was equipped with 28 displacement and two load transducers, as shown in Figure 3.126 and Figure 3.127. The forces in the actuator were measured by a pressure transducer mounted on the oil circuit of the actuator. The transducers are explained in Table 3.18.

Table 3.18 Instrumentation for the OOP tests on "C" samples

Transducer	Measurement
C_EXT_OD1, C_EXT_OD2, C_EXT_OD3, C_EXT OD4	Out-of-plane displacement of the middle section of the wall on the external side
C_INT_OD1, C_INT_OD2	Out-of-plane displacement of the middle section of the wall on the internal side
C_EXT_OD5, C_EXT_OD6	Out-of-plane displacement and rotation of the right corner of the wall
C_EXT_OD7, C_EXT_OD8	Out-of-plane displacement and rotation of the left corner of the wall
R_INT_OD1, R_INT_OD2	Out-of-plane displacement and rotation of the right end of the wall
L_INT_OD1, L_INT_OD2	Out-of-plane displacement and rotation of the left end of the wall
R_EXT_OD1, R_EXT_OD2	Out-of-plane lateral displacement and rotation of the right corner of the wall
L_EXT_OD1, L_EXT_OD2	Out-of-plane lateral displacement and rotation of the left corner of the wall
C_INT_IS C_EXT_IS1	(Horizontal) strain at the middle section of the wall (INT=internal side; EXT=external side)
C_EXT_IS2, C_EXT_IS3, R_EXT_IS, L_EXT_IS	(Horizontal) strain at the wall corners on the external side (C=central part of the wall; R=right part of the wall; L=left part of the wall)
R_INT_IS, L_INT_IS	(Horizontal) strain at the wall corners on the internal side
CRTL_R, CRTL_L	Out-of-plane displacement of the concrete blocks
P.INT, P.EXT	Pressure transducers to measure the load applied when the actuator is pushing (EXT) and when it's pulling (INT)

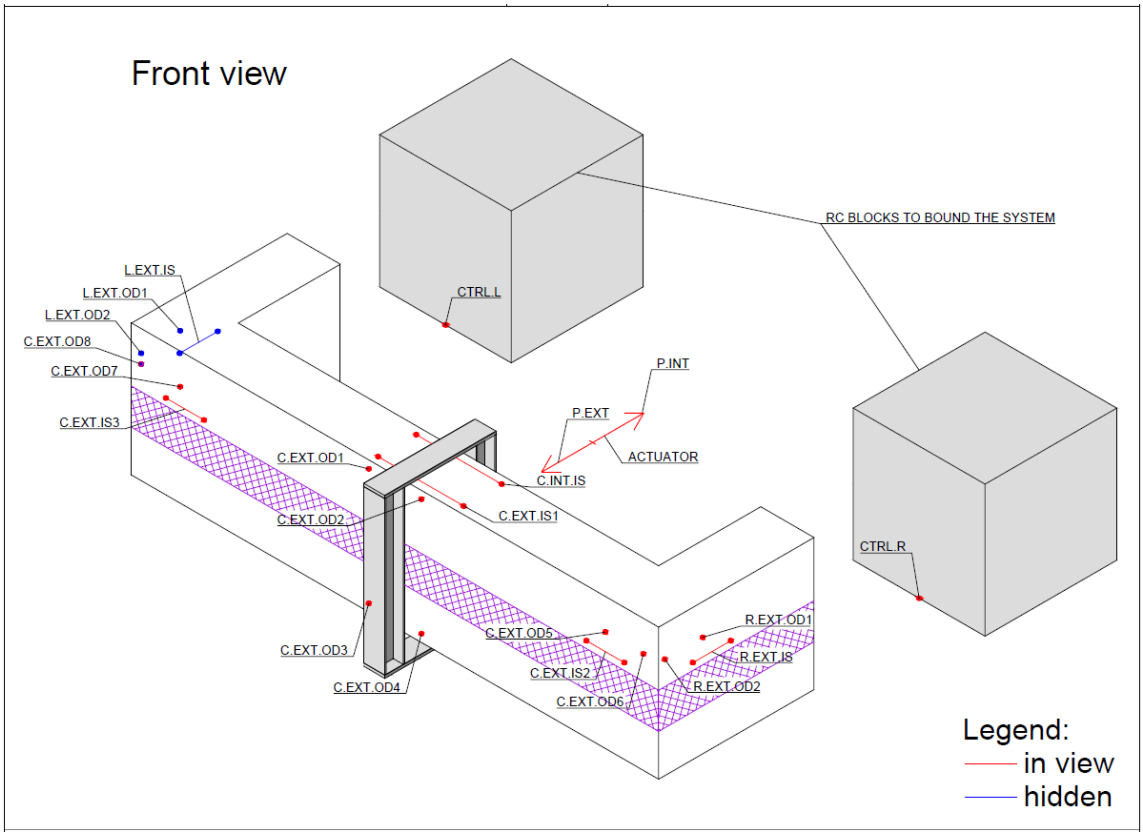


Figure 3.126 Out of plane bending of "C" samples tests setup, measurement instruments, external view

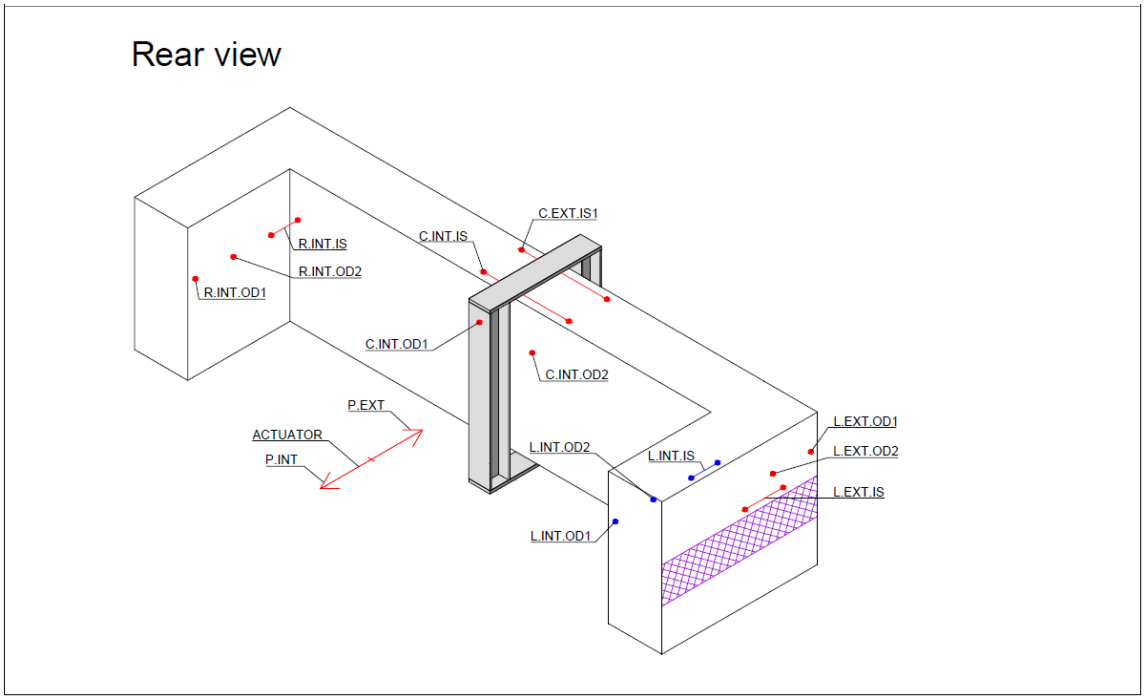


Figure 3.127 Out of plane bending of "C" samples tests setup, measurement instruments, internal view

The main results are summarized in the following. The global behaviour of the samples is described in terms of capacity curves, representing the out-of-plane horizontal load, F_C, varying the net horizontal deflection at the midspan, d_C.

Besides the deflection, the relative opening of the midspan crack (inner side, w_i, and external side, w_e) was monitored. Horizontal displacements at the wing extremities were also surveyed (left wing, h_L, and right one, h_R). In addition, pairs of displacement transducers were installed on the outer side of the wall, near the corners, enabling the survey of the corner rotations θ.

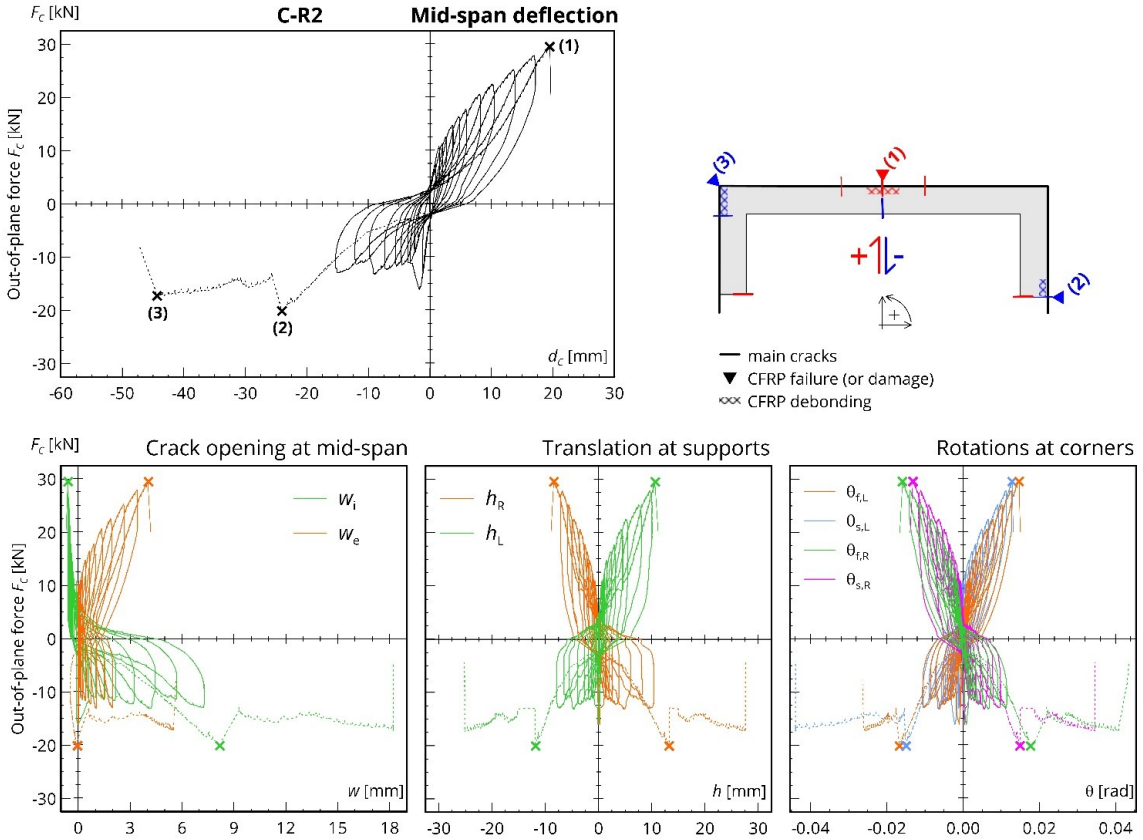
3.8.3 Results

3.8.3.1 Test C-R2

The first sub-vertical cracks occurred at midspan and located at the outer side, when pushing, while at the inner side, when pulling, once the flexural tensile strength of the masonry parallel to the bed joint was attained. In the former case, the load did not drop, owing to the CFRP strip; conversely, in the latter, it dropped down and later increased again. The stiffness reduction was significant in both cases but more pronounced when pulling. The progressive deflection in the pushing direction led to the onset of CFRP debonding at the midspan and to the opening of other nearly vertical cracks on the outer masonry surface (about 500 mm from the midspan). Finally, the tensile fracture failure of the CFRP strip in the vicinity of the midspan occurred. Looking the fractured reinforcement, it is observed that some local delamination occurred just around the crack: it involved both the GFRP-grout and the grout-masonry interfaces.

The test then proceeded monotonically in the pulling direction and induced the anticipated fracturing of impregnated fibres at the right clamp. This was likely caused by local stress concentration in the fibres due to rotation of the clamped supports, which might have aggravated the local weakening of the fibres. The fracturing caused a partial load decrease. Then, as the load was further increased, the cracking of the masonry close to the left corner and the tensile failure of the CFRP strip at the fold at the left corner, also accompanied by diffuse debonding, were attained. Actually, the extensive debonding phenomena at the corner was observed concurrently with the failure of the strip; it involved mainly the masonry-levelling grout interface, while the grout-CFRP bond remained effective.

Consistently with the crack pattern, the crack opening at midspan resulted higher for pulling than pushing. The inward horizontal translations at supports when pushing were slightly higher at the left side in positive load direction, and the opposite was observed when pulling. However, the corner rotations were almost symmetric.



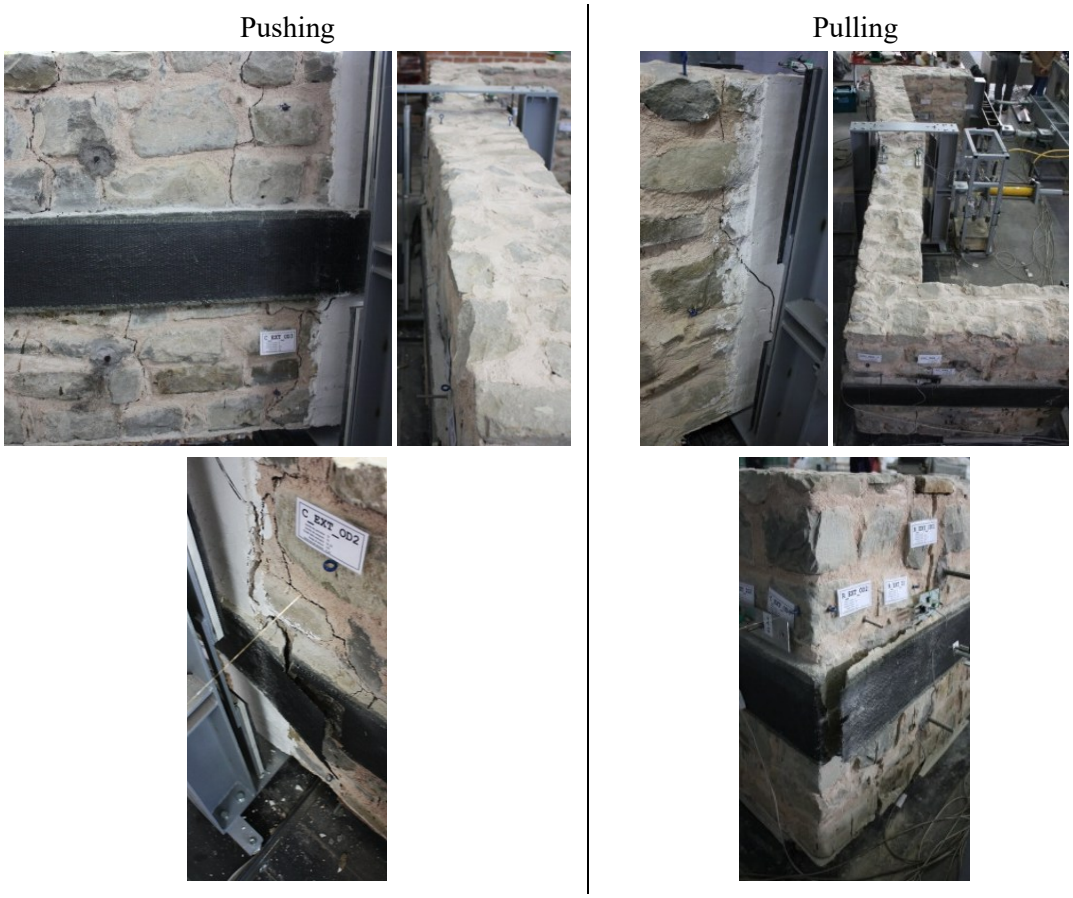
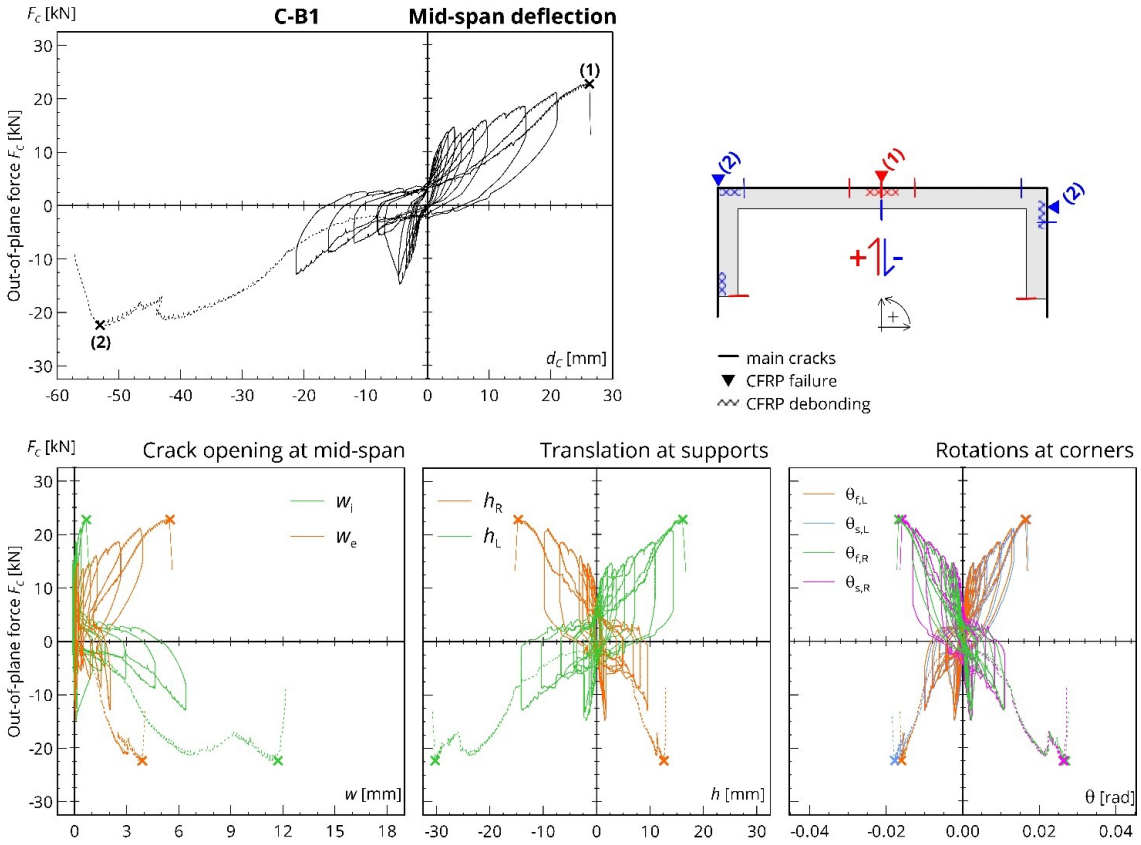


Figure 3.128 Main results of test C-R2

3.8.3.2 Test C-B1

The first crack, almost vertical, appeared in the masonry at the mid-span, on the outer side, for the attainment of the flexural tensile strength of the solid clay masonry parallel to the bed joint, when pushing. However, no significant load decrease occurred with the crack opening (just a slight stiffness degradation) because of the presence of the CFRP reinforcement. In contrast, the opening of a midspan vertical crack on the inner side, when pulling, induced a rapid load decrease. Afterwards, the load was gradually recovered in subsequent cycles but with a significant stiffness reduction. As the cyclic test progressed, the midspan crack alternatively opened on the outer side when pushing and on the inner side when pulling. As the deflection increased, a slight CFRP debonding was observed around the outer crack (masonry-grout interface), and new sub-vertical cracks opened at about 250–300 mm from the midspan section, as a consequence of the stress distribution effect of the CFRP strip). Because of these cracks, the stiffness reduced further. Some debonding also occurred near the right clamp, but the strip remained effective in carrying the tensile strength. The failure of the CFRP strip (tensile fracture of the fibres) occurred abruptly at the midspan with significant values of deflection. When loading monotonically in the opposite direction (pulling), the masonry began cracking in the vicinity of the corners and some diagonal and horizontal cracks appeared in the central part of the sample. The collapse occurred for the tensile failure of the CFRP strip at the left corner and, then, at the right side, near the corner bend. Some CFRP debonding was also observed in these sections, just before the failure.

The trend of the horizontal displacements at the wing extremities indicates quite comparable values of inward and outward lateral movement associated with a given deflection level. However, slightly higher translations occurred at the left side for both loading directions. The rotations at the corners almost coincided for both sides until achieving the positive peak value, after which a slightly asymmetrical behaviour occurred in the final loading cycle, with higher rotations at the right corner compared to the left. This was most likely due to the inhomogeneity of the masonry and imperfect symmetry of the damage. Consequently, the outward support translation was higher on the left than on the right side.



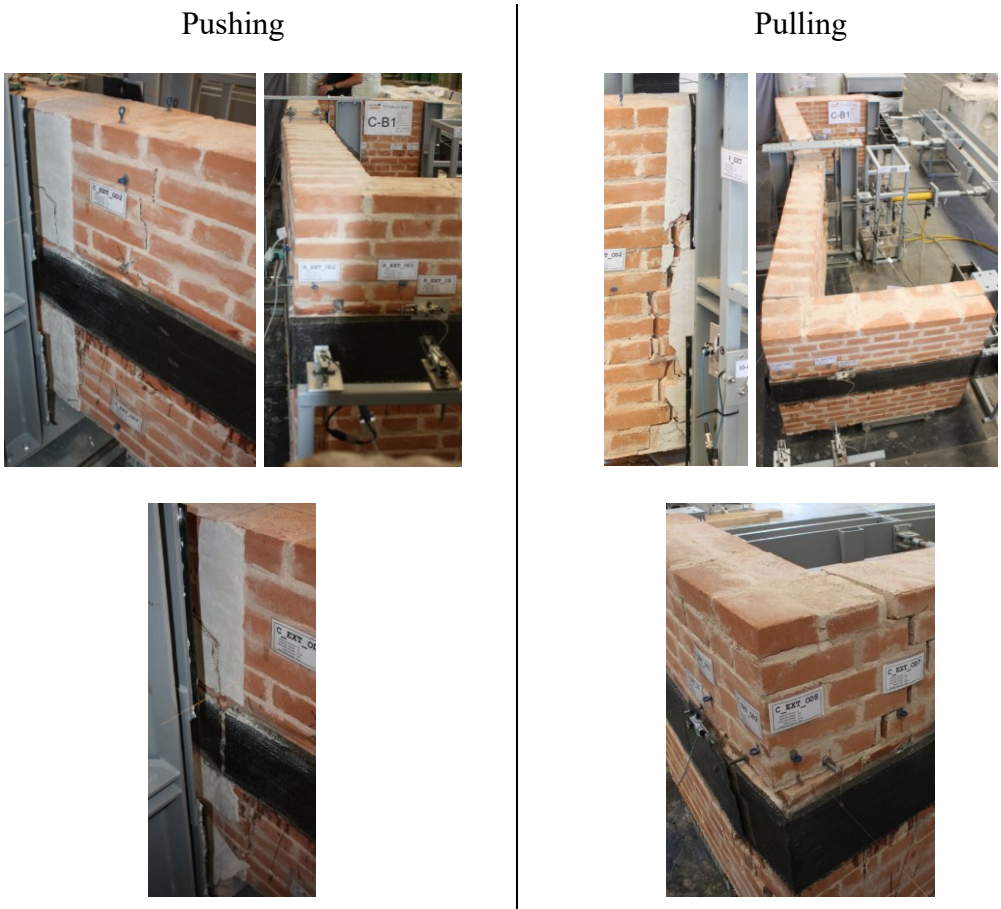


Figure 3.129 Main results of test C-B1

3.8.4 Analysis of results and comparison

The main results of the two tests in terms of load and deflection at first cracking (*Cr*) and at collapse (*Ul*) are summarised in Table 3.19 and Figure 3.130. Since the eccentric reinforcement intervened differently, depending on the loading direction, the envelope of the load-deflection capacity curves had asymmetric trend: when pushing, the trend is elastic-plastic with hardening (end of the elastic phase at first cracking); when pulling, a sudden load decrease interrupts the elastic stage at first cracking, then a plastic stage with hardening is detected. When pushing, the CFRP strip fractures at the mid span; when pulling, the CFRP strip fractured around the corners.

Sample C-R2 exhibited in pushing a peak resistance of +29.6 kN and a deflection 1/187 of the net span. The peak resistance and respective deflection in pulling were -20.3 kN, at 1/152 of the span and were lower than expected, since affected by the premature damage of fibres at the support and at the corner bend, as previously described.

Because of the smaller thickness, the resistances of C-B1 sample were lower (~22.6 kN for both loading directions). Because of different stiffness, the ultimate deflection for pulling (equal to 1/70 of the net span) resulted approximately twice that for pushing (1/140 of the net span).

Table 3.19 Main results of the tests on masonry ring beams with externally bonded FRP strips, in terms of load and deflection at first cracking (Cr) and at collapse (Ul)

		First cracking (*Cr*)		**Ultimate load (*Ul*)**	
Sample	**Load direction**	F_C **[kN]**	d_C **[mm]**	F_C **[kN]**	d_C **[mm]**
C-R2	Push (+)	+9.6	+1.2	+29.6	+19.5
	Pull (−)	−14.0	−1.2	−20.3*	−24.1*
C-B1	Push (+)	+10.4	+1.7	+22.9	+26.0
	Pull (−)	−14.8	−4.5	−22.2	−52.8

*premature damage of fibres

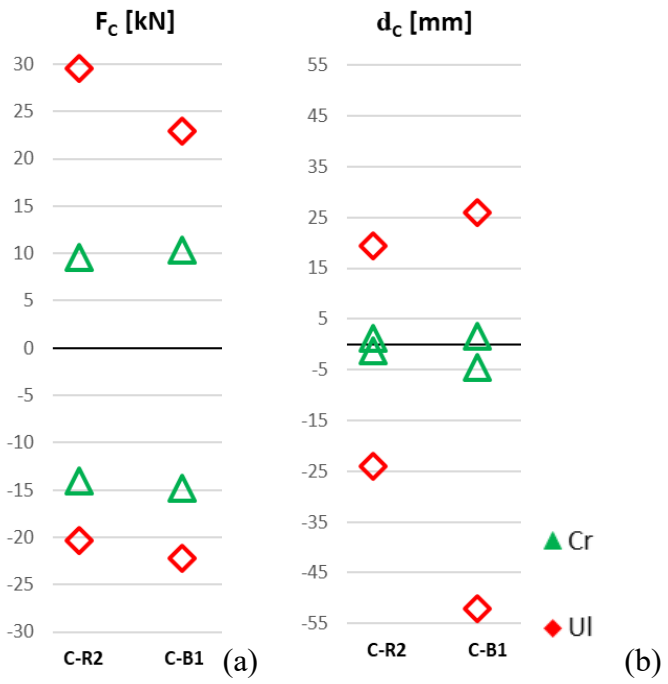


Figure 3.130 Main test results of "C" samples: first cracking and collapse force (a) and deflection (b) values

3.9 Pushover test on a full-scale masonry building

Testing entire structures is a fundamental step to check the effectiveness of the reinforcement at the global level, under the actual interactions among the resisting elements and actual boundary conditions; it also provides useful outputs for the validation of procedures and tools aimed at the global performance analysis. Nevertheless, as a consequence of the high costs and great complexity, full-scale tests on strengthened structures are currently rare.

3.9.1 Literature review

Gu et al. [190] tested a 1/3-scale, three-storey, solid brick masonry wall with openings under in-plane quasi-static cyclic loading. In this study the strength and size of the bricks and the mortar were not scaled accordingly due to challenges in determining compatible scale factors among structures and materials. They compared the behaviour before and after the repair by carbon FRP grids bonded with epoxy resin on one side and only at the areas of intensive cracking on the ground floor. Under an area-based reinforcement ratio of 18%, the walls' lateral resistance was restored to 82% of the undamaged wall, and ductility and energy dissipation capacity were effectively recovered or enhanced.

Triller et al. [194] performed quasi-static cyclic tests on a full-scale three-storey hollow-bricks masonry building, comparing the seismic response before and after the retrofitting with a double-side application of mortar coating reinforced with glass fibre grids. Glass fibre anchors were used to provide inter-storey connection and anchoring into the foundation. The building resistance increased by approximately 50%, and the deformation capacity and ductility tripled. It was also clearly pointed out the important role of adequate confining (wrapping) and anchoring the coating to the existing masonry.

The study made by Lucchini et al. [191] investigated, through full-scale quasi-static cyclic tests on a two-storey hollow-block masonry building, the effectiveness of the one-side application of a 30 mm thick mortar coating added with short steel fibres (i.e., Fibre Reinforced Mortar), combined with conventional steel reinforcing bars located at the base of the building to provide a connection with the foundation. In addition, steel connectors (about 6 connectors per square meter) were also installed to link the coating layer to the masonry walls. The strengthened configuration highlighted a significant increase of the lateral initial stiffness and resistance capacity (2.3 and 3.3 times higher, respectively), and ensured an effective ultimate drift of up to 0.4%.

Morici et al. [193] performed on-site pushover tests on two almost identical two-storey brick masonry buildings previously damaged by a seismic event. One was repaired by repointing the cracks, and the other was strengthened with a CRM coating reinforced by glass fibre-reinforced polymer meshes, applied on both sides of the load-bearing walls of the first level and only on the outer face at the second level. Horizontal steel tie-rods were also introduced on the intermediate floor and roof. Both structures were subjected to a monotonic, quasi-static lateral load. According to the test results, the second structure exhibited a resistance and top displacement capacity, which were respectively 2.8 and 1.8 times higher than those presented by the first one. It is worth remarking that the CRM benefits were not fully exploited because of some uplift at the base of the building, which clearly pointed out the importance of an effective connection of the coating at the foundations.

More complex than quasi-static loading tests is the shaking table test, in which the structure is subjected to a series of dynamic actions (simulating the earthquake ground motions) of increasing intensity.

Maddaloni et al. [271] studied the dynamic behaviour of a 1:2 scaled, single-storey simple building made of regular tuff masonry and covered by a flat timber floor with a cementitious deck. The as-built structure was damaged, repaired by means of cracks injection and stitching, and then externally retrofitted with a diffuse fibre-reinforced plastering of the facades combined with the top wrapping by glass fibre grids embedded in the mortar coating. The intervention prevented the activation of local failures, restored the original frequency and improved the building's resistance to a +40% input acceleration without any significant damage. The specimen behaved as a monolithic block with a rigid rotation at the base because it was not anchored into the foundation.

De Santis and de Felice [195] performed shaking table tests on a full-scale, tuff masonry room with openings covered by an inclined timber roof. The sample was tested both unstrengthened and after retrofitting with CRM applied on the outer surface of the two walls with openings. As compared to the unstrengthened specimen, the absolute base acceleration attained by the retrofitted structure under ultimate conditions was more than doubled, and the collapse moved from wall separation to in-plane mechanism. After adding a horizontal top steel tie bar on the unstrengthened wall, the acceleration resulted four times higher.

Juhásová et al. [196] carried out dynamic investigations on a single-level stone masonry room. At first, the configuration reinforced by means of polymer grids embedded in some bed joints was tested. Then, the structure was retrofitted by means of polymer grids bonded on the outer surface with a fibre-reinforced plaster. The maximum input acceleration of the repaired model was more than tripled; the damage pattern revealed an effective inhibition of the out-of-plane mechanism of the walls, in favour of a box-like behaviour, with most of the damage accumulated at the base (due to the lack of a plaster connection with the foundations).

Referring to strengthening methods other than fibre-based, it is worth mentioning the research work of Benedetti et al. [272], that tested on a shaking table a total of 24, half scaled, two-storey masonry buildings, made either of solid brick and stone masonry. The study compared the effectiveness of different traditional retrofitting techniques such as steel ties, steel beams and reinforced concrete bands, in preventing walls separation and improving the connection between slabs and walls. Similarly, Mazzon et al. [198] compared the dynamic tests results of two identical stone masonry houses, 2:3 scaled, and highlighted the capability of hydraulic lime grout injections to substantially increase the resistant capacity (+56% maximum input acceleration) without modifying the original frequency and modal deformations.

It is also significant to mention the shaking-table tests of Magenes et al. ([197], [44]) and Senaldi et al. [45], which was carried out to investigate on the effects of traditional seismic retrofitting techniques aimed at fostering the box-type global behaviour of the structure. The samples consisted of three full-scale, two-storey, double-leaf stone masonry buildings with flexible timber floors and roofs (single layer of planks). The 1st prototype [197] represented a vulnerable building without anti-seismic detailing and devices: the introduction, in the damaged configuration, of perimeter tie-rods at the floor and roof level and cable bracings under the roof, and the improvement of the connection of the ridge beam with the gable walls, let the structure to withstand an 18% greater maximum acceleration. In the 2nd prototype building [44], an additional layer of matchboard planks was applied to provide moderate in-plane stiffening of the wooden diaphragms, and the wall-to-diaphragm connections were improved by introducing steel ring beams on the intermediate floor, and reinforced masonry ring beams, at the top. Differently, the 3rd prototype building [45] had the roof diaphragm stiffened by multilayer plywood panels connected to perimeter reinforced concrete beams. The intermediate floor was stiffened

by a reinforced concrete slab provided with embedded bars for connection with the masonry. The buildings 2 and 3 were able to withstand, respectively, accelerations up to 1.84 and 2.37 times higher than the reference configuration.

In Vintzileou et al. [199], the shaking table tests of a 1/2 scaled, two-storey building showed that the stiffening of the wooden floors by means of an additional plank layer, combined with grout injections on the masonry infill walls, led to the doubling of the resisting accelerations. Similarly, Guerrini et al [43], tested a 1/2 scaled, three-storey, stone masonry aggregate composed of two units on a unidirectional shaking table, and obtained an 83% acceleration increase by installing floor tie rods and improving the wall-to-diaphragm assembly by means of steel devices connecting the floor joists with the outer wall face.

The experimental tests presented in this study concerned full-scale cyclic tests on a two-leaf rubble stone masonry building. The tests were carried out at the Laboratory of the University of Brescia.

The full-scale structure was designed to represent a historical rural stone masonry house typical of the Italian and Slovenian heritage [273]. In fact, in those countries, simple two/three-story rectangular buildings provided with wood-joist floors and a pitched timber roof covered by tiles are very common. The bearing walls are generally made of roughly sized stones and a modest amount of low strength lime mortar. The test was subdivided into two stages (test on the unstrengthened and on the retrofitted structure) to simulate a repairing intervention on a building that was pre-damaged by a significant seismic event. The intervention technique consisted of a CRM system applied on the building facades, with the addition of transverse injected steel connectors to increase the collaboration between the masonry wall leaves, steel tie rods at the first floor and on the roof rafters.

In the following, the main characteristic of the building, the strengthening intervention, and of the tests' arrangements are described in detail.

3.9.2 Scope and methods

The two-storey building consisted of four unreinforced stone masonry bearing walls (i.e., North, West, South, and East wall - Figure 3.131), a wooden intermediate floor (Figure 3.132a) and a gabled timber roof (Figure 3.132b). The 350 mm thick bearing walls were made with the same two-leaf stone masonry type used in the previous tests. The structure

had in-plane dimensions 5750x4350 mm, with a total height at rooftop of 6733 mm. The main geometric characteristics are schematically shown in Figure 3.133. Each pier was identified by a label indicating the wall orientation (*N*, *S*, *W*, *E*), followed by letter "*p*" for piers, the indication of the building level (1 or 2) and a sequential latter (*a*, *b*, *c*). The aspect ratio (height to width) of the longitudinal piers of the base floor ranged from 1.1 to 2.0.

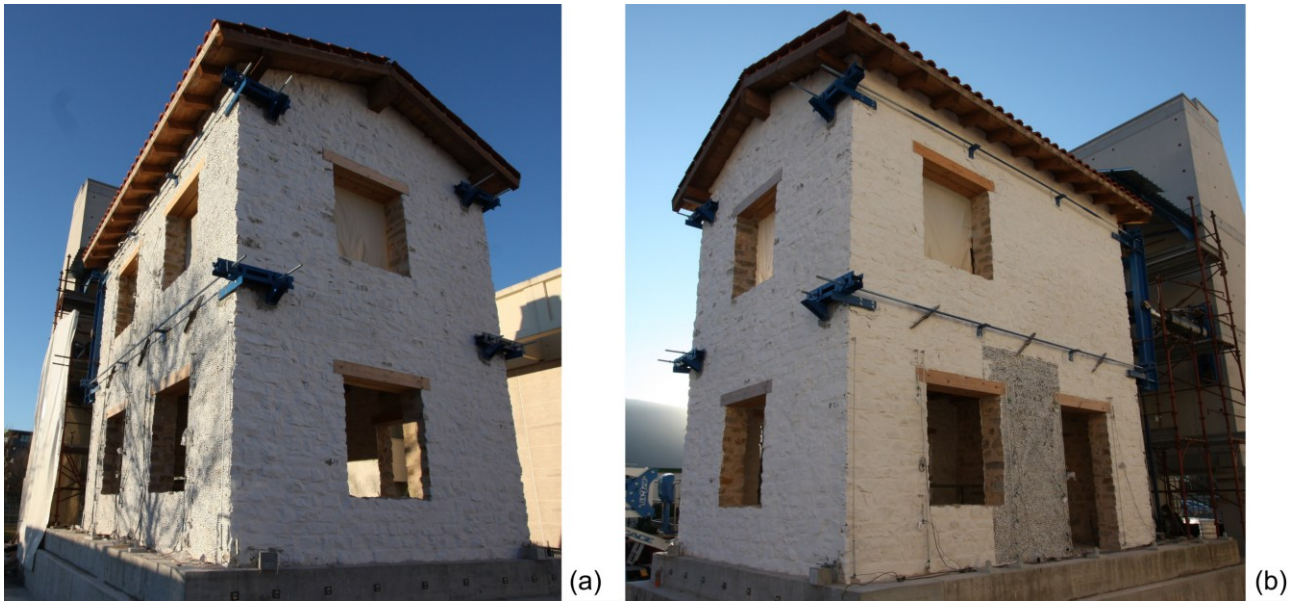


Figure 3.131 Views of the building from outside: (a) East and North walls; (b) North and West walls

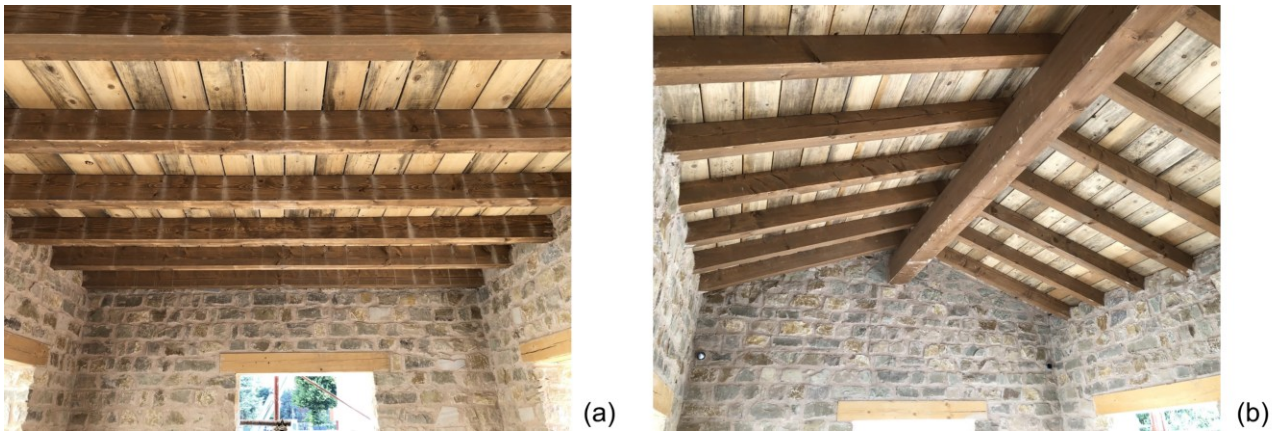


Figure 3.132 Views of the building from inside: intrados of the intermediate floor (a) and of the roof (b)

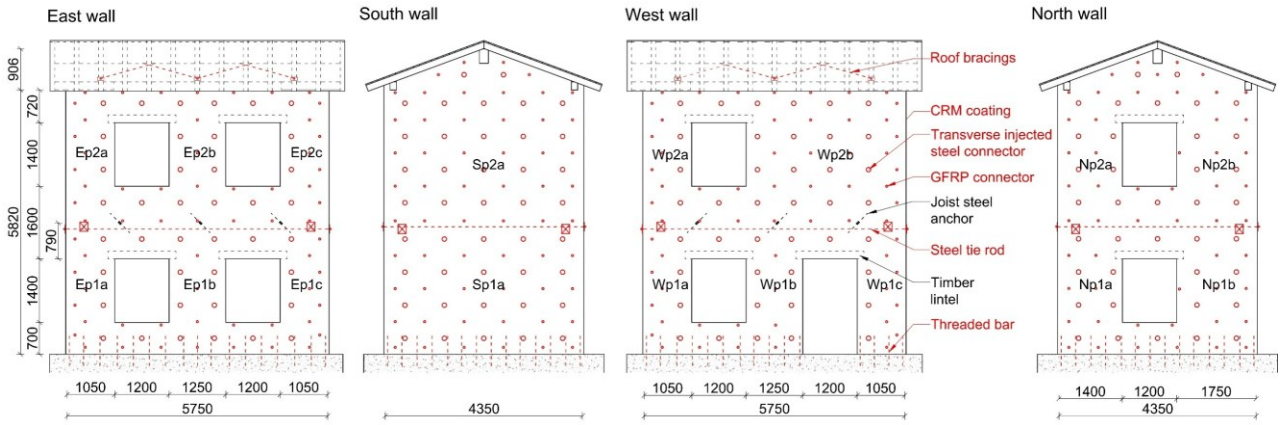


Figure 3.133 Side views of the building and coating connection details (dimensions in mm)

The walls of the building were connected to the foundation by 120x150x150 mm reinforced concrete blocks (teeth) embedded within the wall thickness to prevent potential sliding at the masonry-concrete interface (Figure 3.134a). The small blocks were anchored into the reinforced concrete (RC) foundation by 16 mm diameter steel bars. This was to simulate existing buildings, which typically have masonry foundations and cannot slide at contact with the foundations.

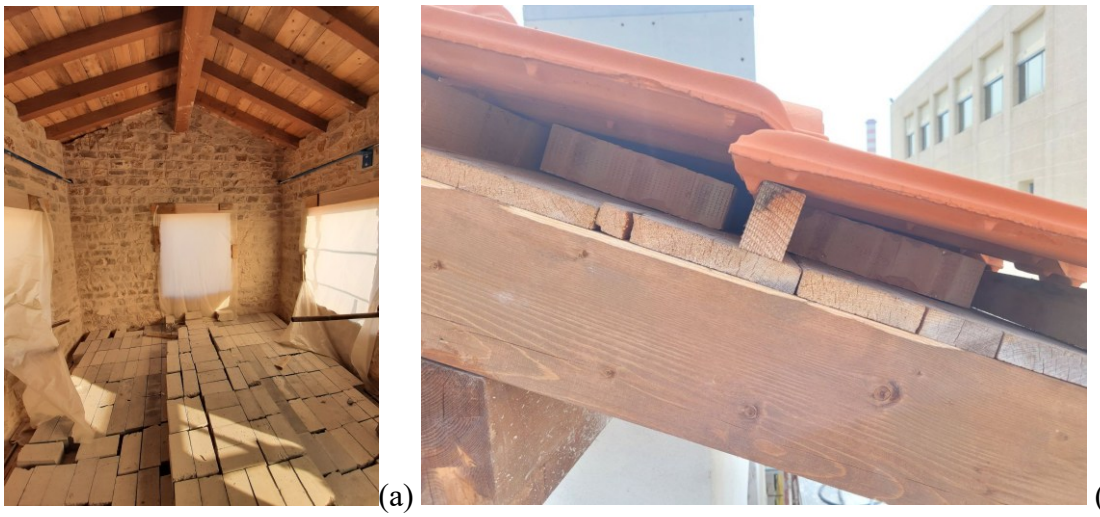
The intermediate wooden floor (Figure 3.132a) consisted of solid timber joists (cross-section of 120×160 mm, 3950 mm length) spaced at 600 mm, located into masonry pockets providing a support length of 150 mm. Timber boards (25 mm thick) were nailed to the floor joists. Three of the floor joists were connected to the East and West walls by means of steel anchors, 1800 mm spaced, passing through the masonry wall, and clamped by a steel wedge (Figure 3.131a,b; Figure 3.136a). The anchors were fastened to the floor joists through a plate using three wood screws per plate (Figure 3.134b). The wooden pitched roof consisted of 533 mm spaced solid timber joists (cross-section of 100×140 mm), connected at one end to a solid timber ridge beam (cross section of 200×320 mm). The opposite end was laid on the longitudinal walls. The roof was covered with 25 mm thick timber board planks, which were then overlaid with fired clay tiles. A couple of parallel wooden lintels (cross-section of 170×170 mm, 1500 mm length) was laid above each opening, provided with an end support of 150 mm on each side. All wooden elements were made of red spruce, with an average specific weight of 4.5 kN/m^3.



(a) (b)

Figure 3.134 (a) Reinforced concrete blocks embedded in the wall thickness to prevent potential sliding; (b) steel plate connected on the inside to the floor joist

The self-weights of the intermediate floor and the roof were equal to 0.2 kN/m^2 and 0.8 kN/m^2, respectively, considering a floor area equal to 4000x5400 mm^2 and a roof area of 5400×6500 mm. A total of 162 concrete blocks with dimensions 150x150x600 mm were placed on the intermediate floor Figure 3.135and 55x120x250 mm clay bricks on the roof to simulate the typical combination of vertical loads required by the Italian structural code for seismic conditions [15]. These additional blocks and bricks were uniformly spread over the floor/roof area. The total loads per unit area (i.e., self-weight and added load) applied on the intermediate floor and roof were 3.4 kN/m^2 and 1.4 kN/m^2, respectively. Note that the total area of the roof, which was considered in the calculation of the applied loads, was higher (i.e., 37.4 m^2) than that of the first floor (i.e., 21.6 m^2). The vertical stress at the base of the building was expected to range from a minimum of 0.16 MPa (South wall) to a maximum of 0.22 MPa (East wall) and on the intermediate floor, from 0.08 MPa to 0.11 MPa.



(a) (b)

Figure 3.135. Additional loads: (a) concrete blocks on the intermediate floor; (b) added bricks below roof tiles

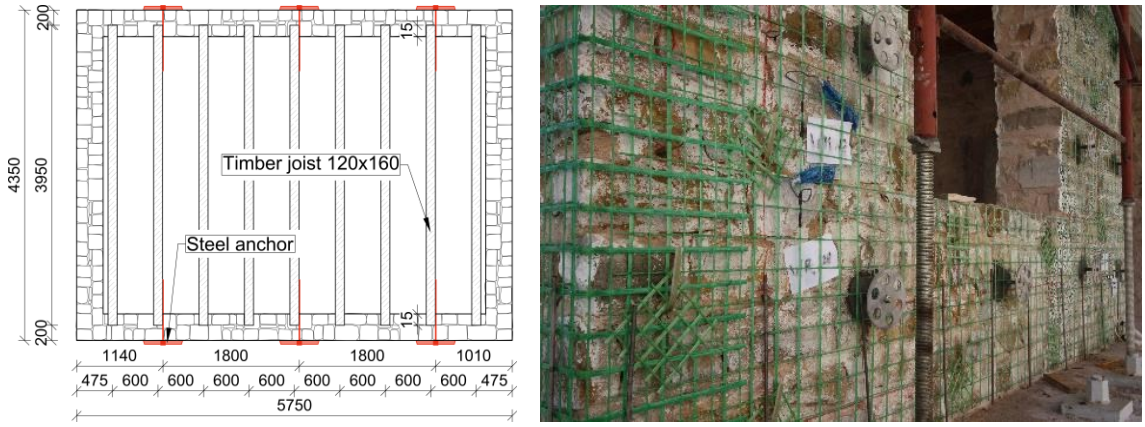
The seismic load on the structure was simulated by applying horizontal forces to the different floors, gradually increasing the amplitude of the deformation cycles (quasi-static cyclic tests). The first test, on the unreinforced masonry (URM) structure, was stopped close to the ultimate limit state when the damage was significant but repairable. Then, the repair and strengthening operations were carried out. The second test on the retrofitted masonry (RM) structure, was carried out up to near collapse.

3.9.3 Retrofitting technique

The adopted retrofitting approach consists of different interventions aiming at promoting the structure's "box behaviour" and improving the seismic resistance of the walls. To achieve the "box behaviour", the out-of-plane mechanisms must be first prevented. To this end, the test building was first provided with the longitudinal steel tie rods (Figure 3.133), located at the first-floor level, and the steel anchors (Figure 3.136a), frequently already present in existing masonry buildings, thus they were installed since the beginning of the first test. As discussed in the following, after testing the unstrengthened building, steel cable "X" bracings were also connected to the joist of the roof to improve its in-plane stiffness and further promote the global behaviour of the building. Finally, a series of techniques were used to improve the in-plane resistance and mutual interlocking of masonry walls. The walls were repaired by injecting the cracks with low-viscosity cementitious mortar to a depth of approximately 50 mm. Moreover, artificial diatons were installed and a layer of a CRM coating was applied on the outer surface of the perimeter walls to improve their seismic resistance (Figure 3.136b, Figure 3.137b). The blind hole

for the injected steel connector had a depth of 300 mm, to avoid interventions inside the building.

The GFRP mesh, produced in 2000 mm wide rolls, was applied to the four external facades of the building by ensuring an overlapping between adjacent strips of about 132 mm (i.e. two grid spacings). Moreover, along the four vertical corners of the building, GFRP angular mesh elements, with a 66×66 mm grid dimension and a width of 330 mm, were added to guarantee the continuity of the reinforcement at the walls' intersections. No angular elements were installed at windows' corners as the GFRP sheets were cut and placed so that the horizontal and vertical bars of the mesh resulted placed sufficiently close to each corner to effectively reduce the risk of diagonal crack formation. This decision was taken to simplify the procedure and limit its invasiveness.



(a) (b)

Figure 3.136 (a) Plan view of the steel anchors layout (dimensions in mm); (b) GFRP mesh and anchors just before the application of the mortar coating. Note the additional angular elements at the corner, the GFRP connectors, the head washers of the transverse injected steel connectors and the anchor bars with the foundation

The coating was anchored to the walls by GFRP L-shaped connectors (4/m^2) and artificial diatons (2/m^2), following the arrangement reported in Figure 3.133, and with the same characteristics reported in section 3.3. The L-shaped connectors were inserted into 16 mm diameter holes drilled in the masonry, for a depth of 300 mm. In front of each connector, a GFRP mesh device was positioned to distribute stresses within the coating; while, on each artificial diaton, a perforated stainless-steel washer with a nut welded at the centre was screwed on the head of the threaded bar, at a half thickness of the CRM coating, above the GFRP mesh.

Before applying the CRM coating, the mortar in masonry joints was removed for a depth of 10 mm and the masonry surface was washed with a high-pressure water cleaner. The washing removed the dirt, paint and moistened the masonry surface, which promoted a better adhesion of the CRM coating. The white paint was applied on the façade to make the detection of cracks easier during the test on the unreinforced building.

To increase the in-plane flexural resistance of the walls, the CRM coating was anchored to the foundation by 8 mm diameter stainless steel threaded bars (characteristic yield strength 200 MPa). The bars were anchored 250 mm deep into the RC foundation by epoxy resin, and 400 mm into the coating (Figure 3.137c). The bars were distributed along the entire perimeter of the building, three per meter, at about 10 mm from the masonry wall surface. The bars were installed beneath the GFRP mesh to avoid possible splitting failure mechanisms of the mortar coating. Previous pull-out tests [206], carried out on 6 mm diameter threaded steel bars showed that an approximate length of 50 times the diameter is enough to anchor the bars in the reinforced mortar coating.

Walls were connected by four additionally installed high strength steel rods (Class 8.8, 22 mm diameter threaded bars), placed along the internal surface of the perimeter walls, below the intermediate floor joists. They were anchored by 150x150x15 mm ribbed steel plates on the surface of the coating. At the roof level, eight tightened steel cable bracings (8 mm diameter) were installed on the timber rafters, in a “cross” configuration to increase the in-plane roof stiffness.

Note that no interventions were adopted to increase the in-plane stiffness of the timber floor, which remained flexible during both tests. However, the results of the cyclic tests together with the dynamic characterization discussed below, revealed that the adopted retrofitting intervention was able to promote the box response of the building, even without the adoption of devices to increase the floor stiffness.

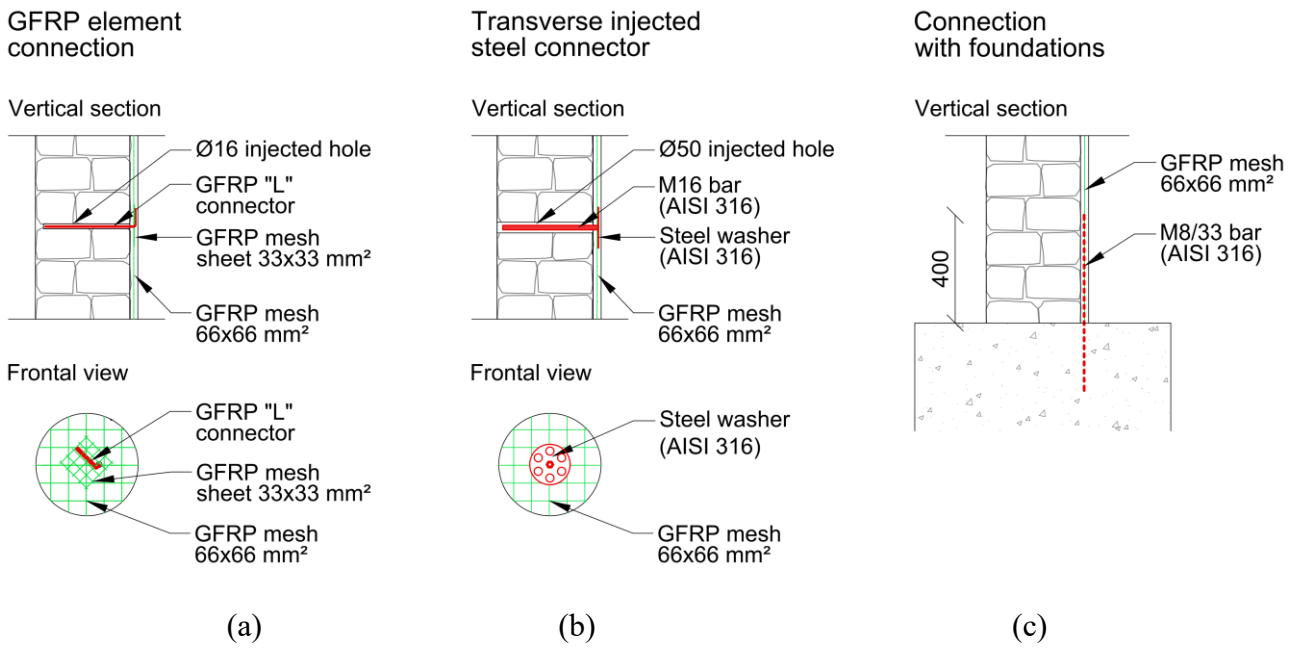
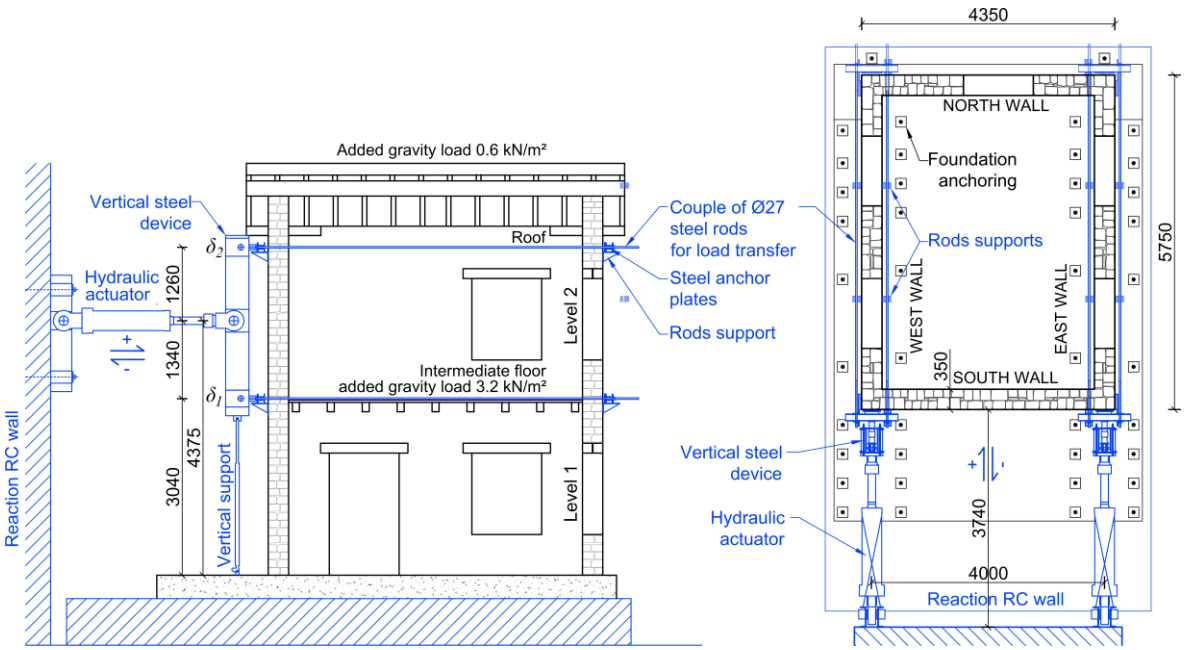


Figure 3.137 Details of the retrofitting intervention: connection to the wall with (a) GFRP elements, (b) transverse injected steel connectors and (c) connection to the foundation by steel bars

3.9.4 Test setup

The test setup is depicted in Figure 3.138. The lateral load (V_b) is applied by means of two hydraulic servo-controlled actuators (capacity 1500 kN each) installed on a reaction RC wall. One actuator is applied on the East wall and the other on the West wall. The load applied by each actuator was subdivided between the intermediate floor and the roof through a vertical steel beam hinged to the actuator, so that 51% of such force was applied at the top of the first level and 49% at the top of the second level of the building. This distribution was proportional to the product of the floor mass with the corresponding floor level.

The loading apparatus was located on the South side. When loading from the South to the North (positive loading direction), the actuator forces pushed against the South wall; when loading in the opposite direction (negative loading direction), the forces pulled on the North wall corners. The lateral force was transferred from the South to the North by four pairs of steel rods (27 mm diameter) placed at the sides of the two longitudinal walls, which were anchored at each end by a steel anchor plate. A gap was provided between the steel elements and the masonry to avoid undesired longitudinal constraints for the walls. The maximum displacement capacity of the testing apparatus was 150 mm in both loading directions.



(a)



(b)

Figure 3.138. Loading apparatus: (a) schematics section and plan view (dimensions in mm); (b) actual view.

The instrumentation used for the tests is shown in Figure 3.139. It consists of 52 displacement transducers, 2 load cells, 6 accelerometers and 2 camera setups for the DIC (digital image correlation) measurements. Two displacement transducers (HW, HE) with a stroke of 950 mm and two 1000 kN capacity load cells (CW, CE) were installed on the actuators to detect the pistons' stroke and the applied forces. Moreover, horizontal displacement transducers (H1SW, H1SE, H2SW, H2SE) with a stroke of 75 mm and four 1000 kN capacity load cells (C1SW, C2SW, C1SE, C2SE) were applied in each of the four loading areas of the South wall, to survey the lateral displacements of the building and the load distribution at the intermediate floor and the roof. The horizontal (BSW, BSE, BNW, BNE) and vertical displacements (V1W, V13W, V19E, V33E) at the base corners were also monitored. Many other linear potentiometers (100 mm stroke) were installed

on masonry piers and spandrels, to check vertical and diagonal displacements and the activation of cracks since the very early stages of the tests.

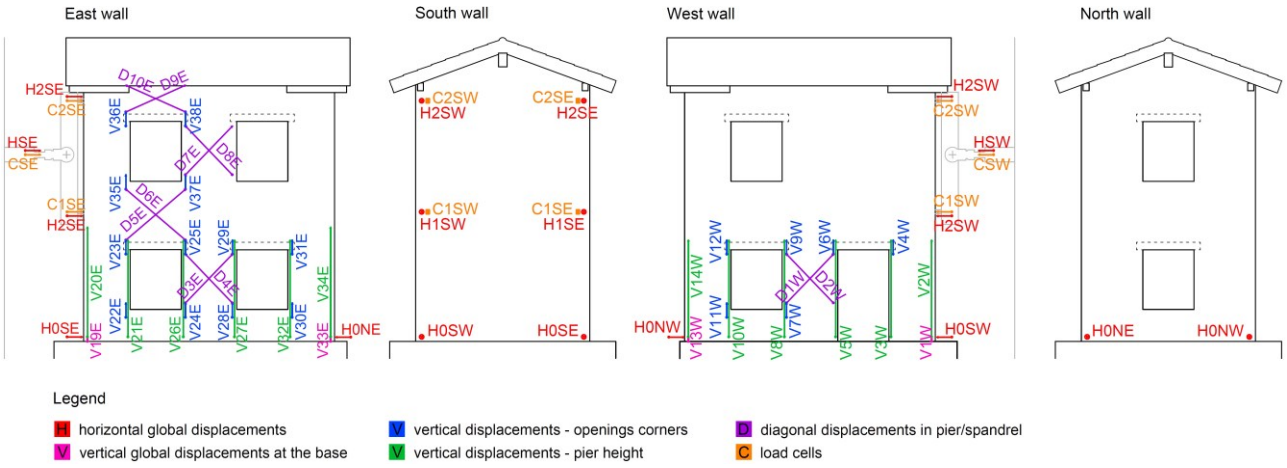


Figure 3.139. Load and displacement transducer set-up

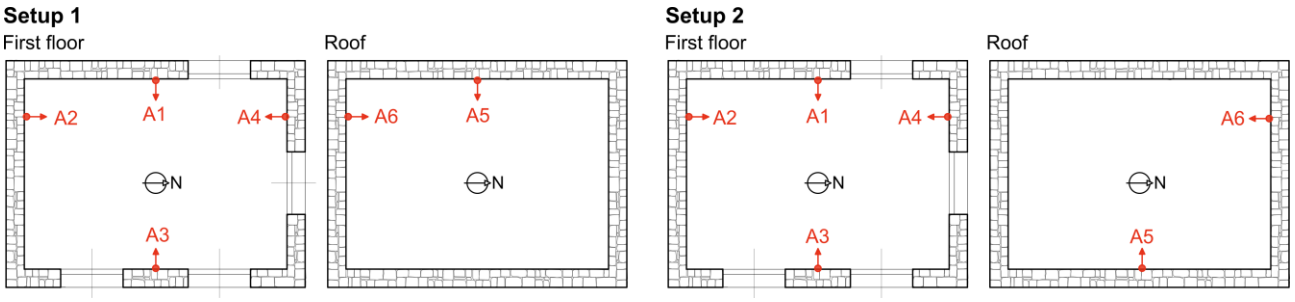


Figure 3.140. Accelerometer set-ups

The natural frequencies, mode shapes, and damping factors of the building were determined through a modal identification method for output-only systems. This method employed frequency domain decomposition as outlined in [274] and [275]. The investigation was carried out for four distinct configurations: the unreinforced masonry (URM) building prior to testing, the URM building post-testing, the retrofitted masonry (RM) building before testing, and the RM building after testing.

For the experimental process, six seismic accelerometers were positioned across two experimental setups that shared four reference sensors. The accelerometers (model 3741B122G, Figure 3.141) were chosen as they are the most suitable for measuring the vibrations of structures due to ambient excitations. Their measurement range is ± 0.5 g. The instruments effectively captured ambient-induced vibrations caused by external factors such as traffic and wind to allow for the estimation of the rigid body motions of the four walls at both the first floor and roof level, as shown in Figure 3.140. Data

acquisition was performed in the horizontal plane, in the transverse direction of the walls. The temporal data were sampled at a frequency of 300 Hz, with each measurement session having a minimum duration of 40 minutes.



Figure 3.141 Accelerometer

DIC systems were installed to measure displacements and crack formation on the entire surface of the East wall façade and a portion of the West wall.

Before the test, the surfaces were rendered visually regular with white paint, made with water and hydraulic lime powder. Then, a random black speckle pattern was applied to allow the software to detect the surface. The photos were automatically shot with constant time intervals, while the maximum displacement (in positive and negative load directions) photos were shot manually. The outputs were plotted as major strain views of the measured area (Figure 3.143a,b and Figure 3.147a,b).

The building was tested under quasi-static displacement load controls, to simulate earthquake load. Such a test guarantees a good correspondence of the damage to what can be expected in an actual seismic event since, usually, the fundamental vibration mode of the building involves most of its mass and its deformation increases along the structure height. Moreover, quasi-static testing gives insight into the hysteretic response, dissipated energy between cycles and damage evolution. Moreover, some previous experimental studies on buildings [276] and walls [277] have shown that quasi-static cyclic testing usually provides a more demanding environment than a dynamic excitation simulating a seismic event.

In the tests, the horizontal displacement at the roof of the building was gradually increased, and each displacement amplitude was repeated twice in both directions. The experiments were controlled through a computer software, so that both actuators simultaneously reached the same top displacement at West and East walls. The net structure displacement

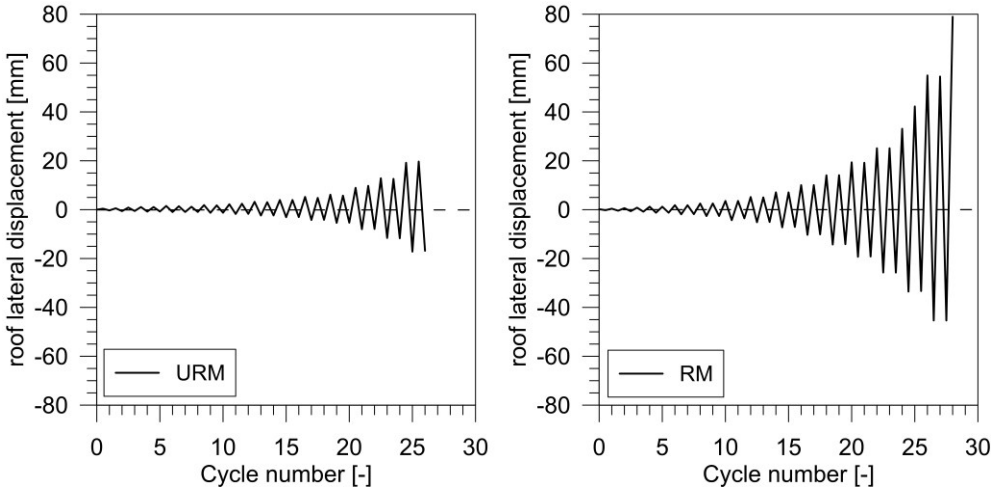
at the top was calculated using the following relation (with reference to the instruments as indicated in Figure 3.139).

$$\delta_2 = \frac{(H2SE + H2SW) - (BSE + BSW)}{2} \qquad (3.9)$$

Also the net lateral average displacement of the first floor, δ_1, was continuously surveyed during the test:

$$\delta_1 = \frac{(H1SE + H1SW) - (BSE + BSW)}{2} \qquad (3.10)$$

Unlike δ_2, the displacement δ_1 was not directly controlled, and its value depends on the structure's response. The loading cycles are presented in Figure 3.142.



(a) (b)

Figure 3.142 Loading cycles for the (a) unreinforced structure test and (b) for the retrofitted one.

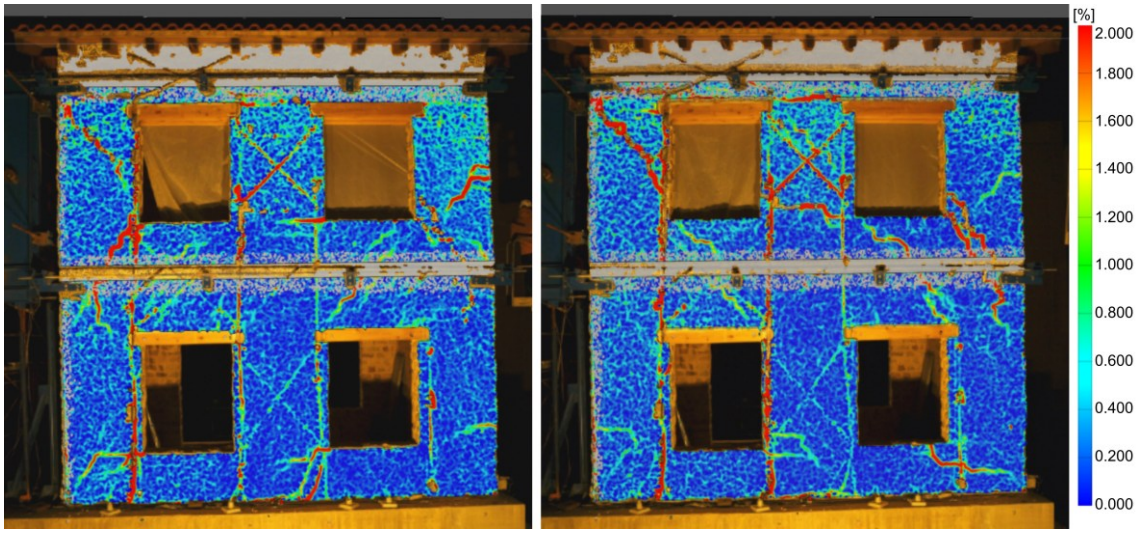
In the following, the results of the tests are reported, analysed, and discussed, including data and considerations on the effectiveness of the retrofitting technique, on dissipated energy and on damping factors.

3.9.5 Results of the pushover tests

3.9.5.1 Test on the URM building

The Unreinforced Masonry (URM) building was tested about six months after its construction. The crack pattern at the end of the test is illustrated in Figure 3.143. In more detail, in Figure 3.143a,b are shown the maximum strains of the East wall detected with

the DIC system, whereas Figure 3.143c reports a sketch of the cracks directly surveyed on the West wall. Note that the path of the cracks followed mainly the mortar joints.



(a) (b)

Figure 3.143 URM building cracks (maximum strains) on the East wall at the end of the test, detected by the DIC System.

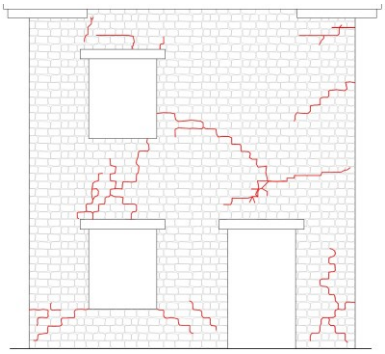


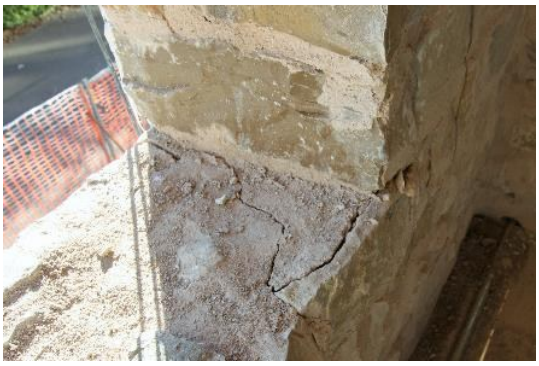
Figure 3.144 URM building cracks on the West wall at the end of the test

The significant events that occurred during the test of the URM building are summarized in Table 3.20and the experimental load-displacement curves, V_b-δ_2 and V_b-δ_1, are illustrated in Figure 3.146a, b. The curves are almost linear until the first flexural cracks occurred at the top and bottom of the pier Ep2b (see id. in Figure 3.133 for location), for a total lateral force V_b of about +66 kN. At the attainment of δ_2 = +1.2 mm, the stiffness of the building gradually started to reduce, as cracks developed close to the corners of openings on the first and second level and horizontal cracks occurred at the top of the pier Ep2a. A further reduction of the lateral stiffness was caused by visible diagonal shear cracks on the West and East wall spandrels above the windows of the first level (δ_2 = +2.1 mm). One of these cracks formed above the door and then extended to the window's

corner of the second level. With increasing lateral displacements, shear cracks formed on piers Ep2a and Ep2b, and the building attained the maximum capacity, equal to +267 kN. Then, the force slightly decreased to +251 kN as the existing cracks further expanded (Figure 3.145a). During the test, no building up-lift phenomena were observed at the base of the walls. The cracks at the first level were visibly thinner than those at the second level.

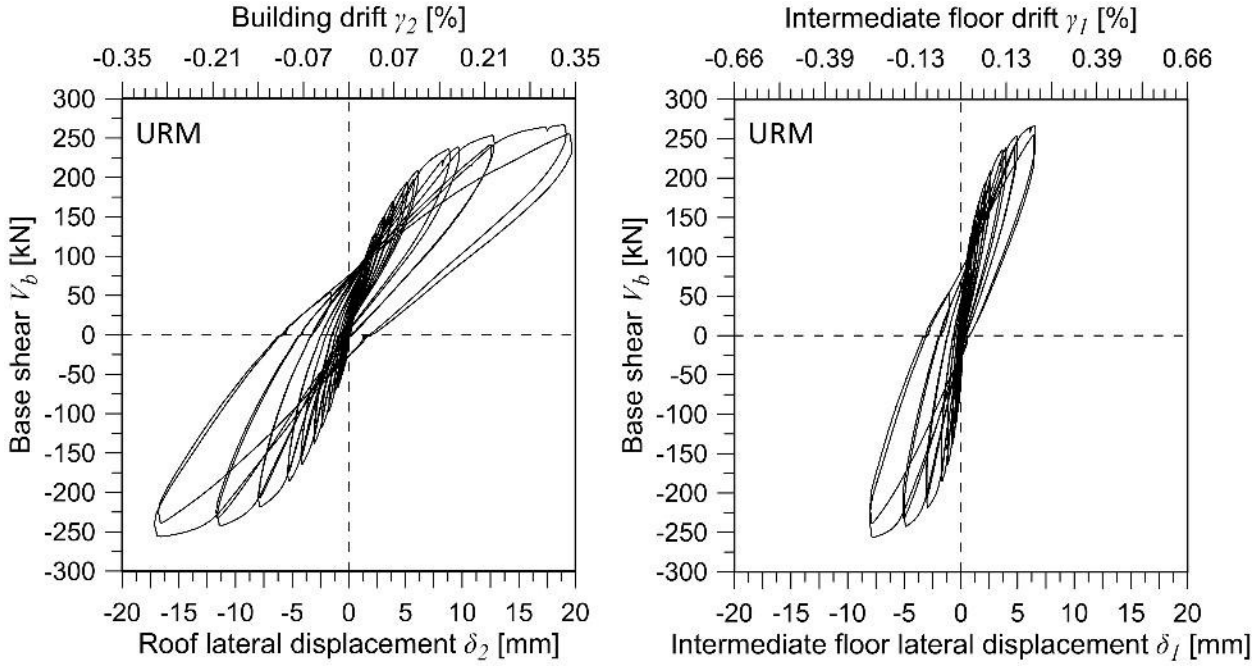
The transversal walls (South and North) exhibited some localized cracks around the loading points of the second level. Thin cracks also opened inside of the building, along the walls' intersections, evidencing a slight separation between orthogonal walls; moreover, a horizontal crack appeared at the base of the pier Np1b (Figure 3.145b), related to out-of-plane bending, involving also a portion of the pier Wp1a.

However, as mentioned above, the most significant cracks developed in the longitudinal walls and were due to in-plane mechanisms affecting mainly the piers of the second level, thus demonstrating a structural response governed by a story mechanism at the second level.


(a)

(b)

Figure 3.145 Diagonal crack in the bottom right corner of pier Ep2a (a) and horizontal crack at the base of pier Np1b (remarked in black) (b).



(a) (b)

Figure 3.146 URM: lateral load-displacement curves (a) V_b-δ_2 and (b) V_b-δ_1.

Table 3.20. Summary of main test events of the URM building: base shear Vb, intermediate floor lateral displacement δ1, roof lateral displacement δ2, intermediate floor drift γ1, building drift γ2.

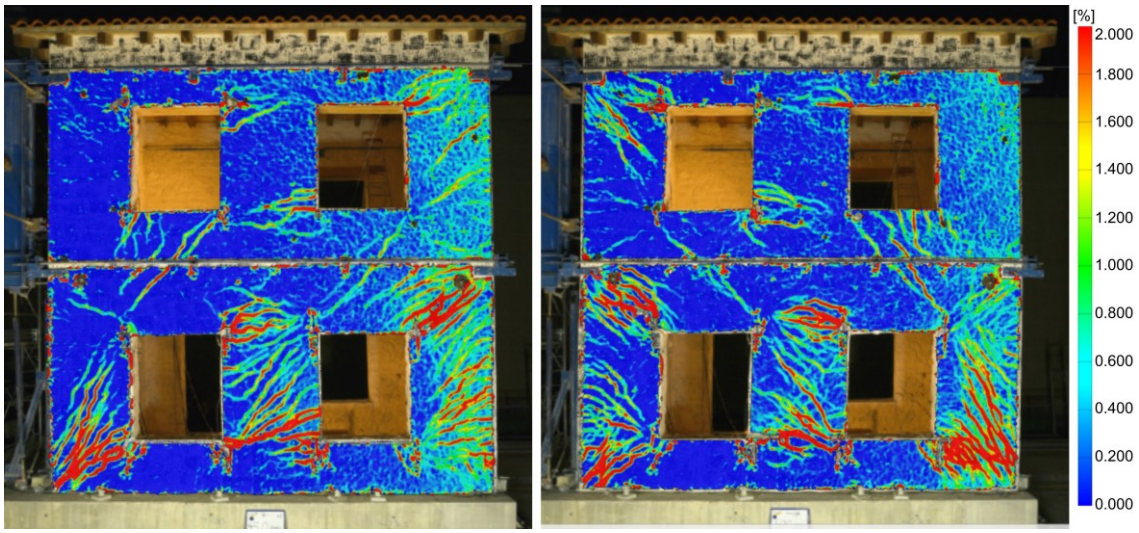
Event description	Vb [kN]	δ1 [mm]	δ2 [mm]	γ1 [%]	γ2 [%]
First flexural cracks at the top and bottom toes of the 2nd level pier Ep2b.	+66	+0.22	+0.85	+0.007	+0.015
	-45	-0.00	-0.53	-0.000	-0.020
New cracks at the openings' corners; horizontal cracks at the top of pier Ep2a; beginning of a gradual stiffness reduction.	+84	+0.43	+1.21	0.014	+0.021
	-67	-0.04	-0.97	-0.001	-0.017
Visible diagonal cracks in the East and West spandrels above the windows of the 1st level.	+125	+0.88	+2.14	+0.029	+0.038
	-97	-0.28	-1.75	-0.009	-0.031
Attainment of maximum capacity; diagonal cracks in piers Ep2a, Ep2c.	+267	+6.53	+18.95	+0.215	+0.336
	-256	-7.71	-16.60	-0.254	-0.294
Activation of story mechanism in the 2nd level.	+251	+6.46	19.58	0.213	0.347
	-239	-7.87	-16.63	-0.259	-0.295

3.9.5.2 Test on the RM building

Four months after the URM test, the building was strengthened and then tested 32 days later. Some negligible, minor microcracks were detected around the openings, in the coating, likely due to shrinkage.

The crack pattern at the end of the test is illustrated in Figure 3.147a,b (East wall) and Figure 3.147c (West wall); the experimental capacity curve V_b-δ_2 *is presented in Figure 3.150, in black color. A summary of the significant events during the test is reported in*

Table 3.21.



(a) (b)

Figure 3.147 RM building: cracks (maximum strains) on the East wall at the end of the test, detected by the DIC System for negative N-S (a) and positive S-N (b) loading directions

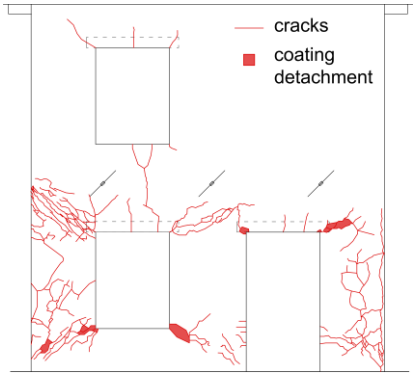


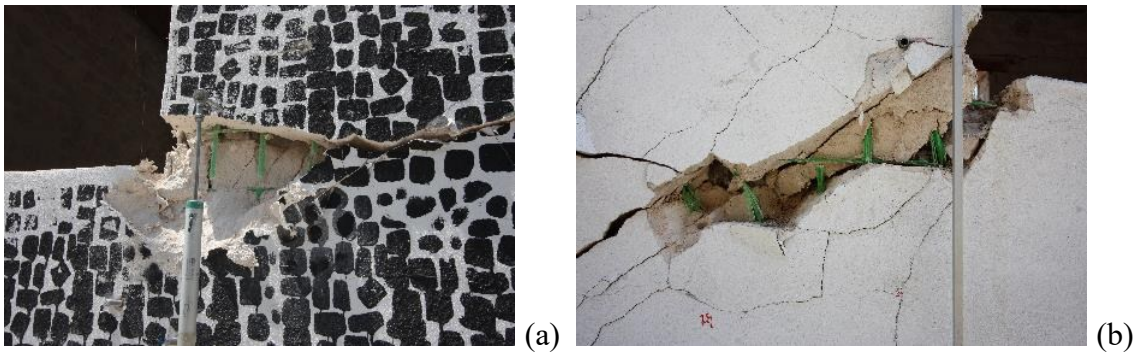
Figure 3.148 RM building: crack configuration on the West wall at the end of the test

The curve is almost linear until the first flexural cracks occurred at top and bottom of the piers of the first level, on the unreinforced wall side, at a displacement $\delta_2 = \pm 0.3$ mm. At almost $\delta_2 = +0.4$ mm, the stiffness of the building gradually started reducing, as cracks developed on the coating, close to the corners of the first level openings. With increasing lateral deflection, similar cracks occurred near the openings of the second level, while diagonal shear cracks appeared on the coating of the spandrels above the openings of the first level, causing a further reduction of the global stiffness. At about $\delta_2 = +3.2$ mm, the flexural cracks of the first level piers and the diagonal cracks of the spandrels began to spread locally and, contemporarily, diagonal shear cracks appeared in the piers. When

exceeding δ_2 = +9.2 mm, the cracks widely spread, causing a significant stiffness degradation. The maximum shear capacity was attained at +645 kN (δ_2 =+31.4 mm) and -590 kN (δ_2 = -30.5 mm). After the peak load, a graudal resistance decrease was observed. At δ_2 = -32.0 mm, the first level piers suffered a significant opening of their cracks, promoting a sharp reduction of the global lateral stiffness in the subsequent cycles. Once a decrease in post-peak resistance of about 15% was achieved, the test was conducted monotonically in the positive loading direction, up to near collapse. A sharp decrease of resistance from V_b = +573 kN to +509 kN occurred, as the GFRP mesh failed at the base of the piers Ep1b and Wp1a (Figure 3.149a,b). Only two transverse injected steel connectors, located at half height of the piers Ep1b and Wp1b, were crossed by the diagonal cracks, but no wall leaves separation was detected. The pier Wp2b did not show any damage.

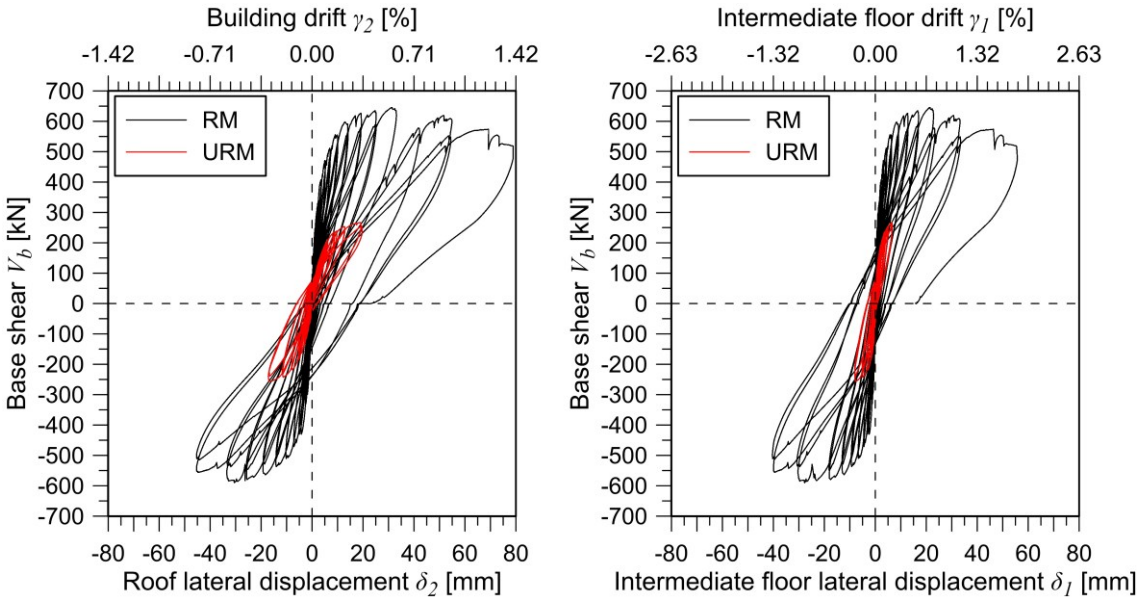
Close to the maximum displacement, a horizontal crack formed at the bottom of the piers Np1b and Wp1a, similarly to the URM test, causing a horizontal slippage of the North-West corner. In addition, some vertical splitting cracks occurred, from about δ_2 = +33.0 mm, along the threaded bars connecting the CRM coating of the South wall to the building foundation. The vertical uplift at the South wall base detected by the instrument V1W was about +16.6 mm at the maximum top lateral displacement in the positive loading direction. Differently, in the negative one, the same instrument detected -1.21 mm. At the North wall base, the uplifts detected by the instruments V13W and V33E were about +5.73 mm and +1.94 mm respectively, at the maximum top lateral displacement in the positive loading direction. In the negative one, V13W and V33E measured about -0.85 mm and -0.61 mm, respectively.

Based on the damage propagation discussed above, it may be observed that the response of the structure was governed by a story mechanism involving the first level.



(a) (b)

Figure 3.149 Mesh failure at the bottom left corner of the pier Ep1b (a) and at the bottom right corner of the pier Wp1a (b).



(a) (b)

Figure 3.150 Lateral load-displacement curves (a) V_b-δ_2 and (b) V_b-δ_1.

Table 3.21. Summary of main test events of the RM building: base shear Vb, intermediate floor lateral displacement δ1, roof lateral displacement δ2, intermediate floor drift γ1, building drift γ2

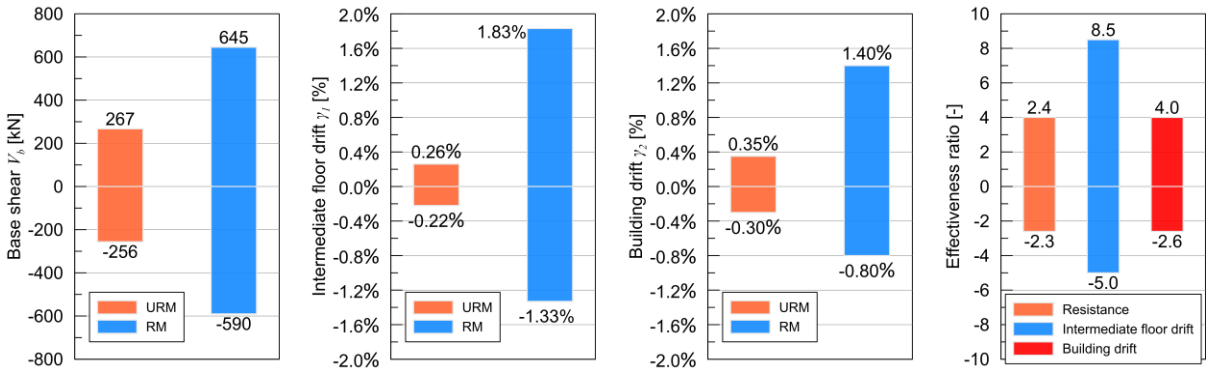
Event description	Vb [kN]	δ_1 [mm]	δ_2 [mm]	γ_1 [%]	γ_2 [%]
First horizontal cracks in the piers at 1st level on the unreinforced wall side (East and West walls).	+112	+0.21	+0.30	+0.007	+0.005
	-68	-0.06	-0.31	-0.002	-0.005
Cracks in piers, at the openings' corners at 1st level; start of a gradual stiffness decrease.	+129	+0.27	+0.40	+0.009	+0.007
	-95	-0.00	-0.41	-0.000	-0.007
Cracks in piers, at the 2nd level openings' corners; diagonal cracks in the 1st level spandrels above the windows.	+249	+0.75	+1.20	+0.025	+0.021
	-227	-0.54	-1.22	-0.018	-0.022
Spread of horizontal cracks in the coating of piers and diagonal cracks on spandrels. Shear cracks on 1st level piers.	+399	+2.12	+3.19	+0.070	+0.057
	-391	-1.79	-3.31	-0.059	-0.059
Beginning of the uplift of the coating from the foundation in the South and North walls.	+419	+2.60	+4.10	+0.086	+0.073
	-441	-4.49	-6.90	-0.148	-0.122
Wide spread of cracks in the coating of the 1st level piers and spandrels.	+556	+5.77	+9.14	+0.190	+0.162
	-507	-6.11	-9.37	-0.201	-0.166
Attainment of maximum shear capacity.	+645	+21.51	+31.41	+0.708	+0.557
	-590	-27.76	-30.50	-0.913	-0.588
Significant opening of the piers' cracks of the 1st level; abrupt decrease of the global lateral stiffness.	-537	-29.68	-31.95	-0.976	-0.566
GFRP mesh failure at the base of piers Ep1b and Wp1a.	+509	+46.88	+69.28	+1.542	+1.28

3.9.6 Analysis of results and comparison

In the URM building, the damage (shear and bending cracks) occurred mainly in the walls of the second level because of the low axial force and the flexural response of the piers. The coating changed the response mechanism of the structure since, in the RM building, the flexural failure mechanism is governed by the amount of vertical mesh wires for piers and horizontal wires for spandrels, making the resistances of the elements comparable between the first and second level. Thus, the failure occurred in the first level, where the lateral forces were higher. This change in behaviour can clearly be seen in Figure 3.152b, where the displacements measured at the intermediate floor and at the roof are reported

in different significant steps, for both URM and RM building: the larger displacements in the unreinforced structure occurred in the upper level, while in the reinforced structure the displacements of the lower level were more significant. In the URM building, the test was interrupted after reaching the maximum load. The first cracks were reached at the same displacement values for the URM and RM building. The presence of the transverse steel injected connectors (density 2/m^2) was an effective solution to avoid the separation of wall leaves and to ensure the collaboration between the CRM coating and the masonry until the mesh rupture. The test on the reinforced building also showed the important role of the connections between the coating and the foundation, aimed at transferring tensile forces into the foundation and preventing significant vertical uplift and slip phenomena at the base.

The maximum values of V_b, δ_1, γ_1, δ_2 and γ_2 obtained in the URM and RM building tests are summarized in Figure 3.151. The effect of strengthening can also be assessed by comparing the hysteretic response of the two tests in Figure 3.150, which show that lateral resistance increased by about 2.4 times, the displacement capacity became four times higher.

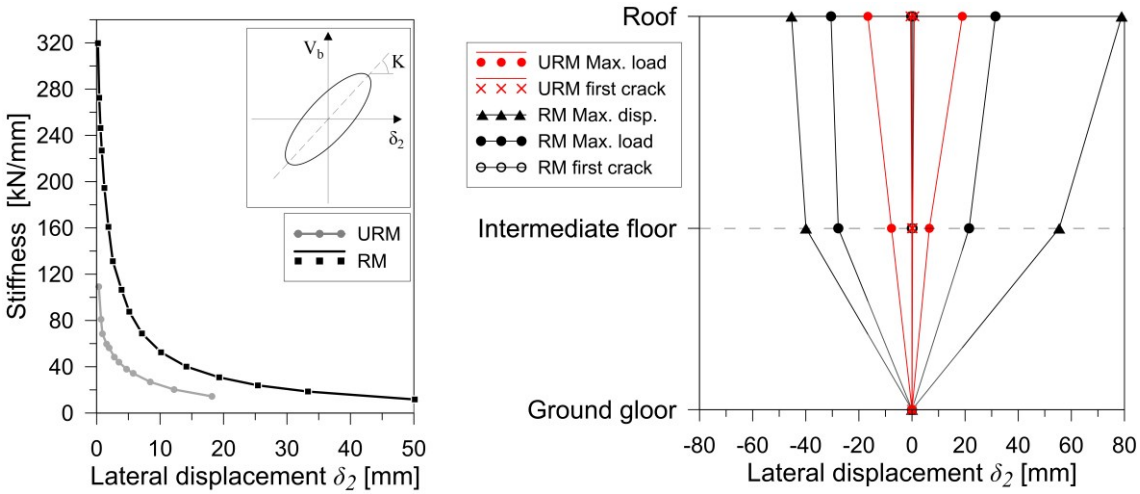


(a) (b) (c) (d)

Figure 3.151 Comparison between the URM and RM building: attained base shear Vb (a), intermediate floor lateral displacement δ1 (b), roof lateral displacement δ2 (c), and effectiveness ratio (d)

The cyclic tests allow also to draw the trends of the building's cycle stiffness, K (evaluated as the slope of the peak-to-peak line within each loop of the $V_b - \delta_2$ curve) by varying the distortion δ_2 (Figure 3.152a). The stiffness degradation with increasing distortion shows an approximately power-law trend, with a softer degradation in the strengthened (RM) building, in respect to the unstrengthened (URM) one. In the unstrengthened building, the

secant stiffness in the first cycle was 109 kN/mm and ultimately decreased to 14 kN/mm. The stiffness of the first cycle of the RM building was 320 kN/mm; the progressive damage caused the reduction of the lateral stiffness up to a minimum of 11.7 kN/mm. The RM building's stiffness, in the first cycle, exceeded that of the URM building by 2.9 times.



(a) (b)

Figure 3.152 URM and RM building: comparison in terms of (a) evolution of lateral stiffness and (b) deformed shape at different loading levels displacement

To investigate on the energy dissipation capacity, the cumulative input energy was compared against the dissipated hysteretic energy. The cumulative input energy, E_{in}, was calculated as the cumulative work needed to deform the building from the beginning of the test to a specific value of displacement.

In Figure 3.153, the total and dissipated cumulative energy determined at each loading cycle are plotted as a function of the lateral roof displacement, δ_2, for the URM and the RM building. Table 3.22 presents the values of E_{in} and E_{hys} at resistance peak ($\delta_{V,max}$) and at maximum displacement (δ_{max}). The dissipative capacity of the RM building was significantly larger than that of the URM one ($E_{hys,RM}$ was 8.4 times higher at maximum displacement). This is because the cracks in the strengthened building spread widely across the walls, whereas in plain masonry, the cracks appeared only in a limited number of mortar joints. The high redistribution of internal stresses in the coating thus resulted in increased strength and deformation capacities.

The cyclic curves of both tests clearly evidenced that most of the input energy was dissipated in hysteretic loops through progressive damage and crack propagation, as evidenced in Figure 3.154a, where the evolution of the E_{hys}/E_{in} energy ratios is reported.

The hysteretic energy varied between 41% and 53% of the total input energy, for the URM building, and between 41% and 64%, for the strengthened building and tended to increase after the peak load. In the RM building, only the positive half-cycle was considered for the determination of E_{hys} in the peak load cycle (± 33.0 mm, * in Figure 3.154a,b), due to an accidental disturbance on the measurement occurred in the negative half-cycle. This and the cycle after it were not repeated a second time.

Table 3.22. Values of cumulative input energy E_{in} and dissipated hysteresis E_{hys} at resistance peak ($\delta_{V,max}$) and at maximum displacement (δ_{max}), for URM and RM.

Test	Ein [kJ]		Ehys [kJ]		Ehys/Etot	
	$\delta_{Vb,max}$	δ_{max}	$\delta_{Vb,max}$	δ_{max}	$\delta_{Vb,max}$	δ_{max}
URM	26.7	32.8	12.6	15.9	0.47	0.48
RM	146.4	288.6	61.6	133.7	0.42	0.46

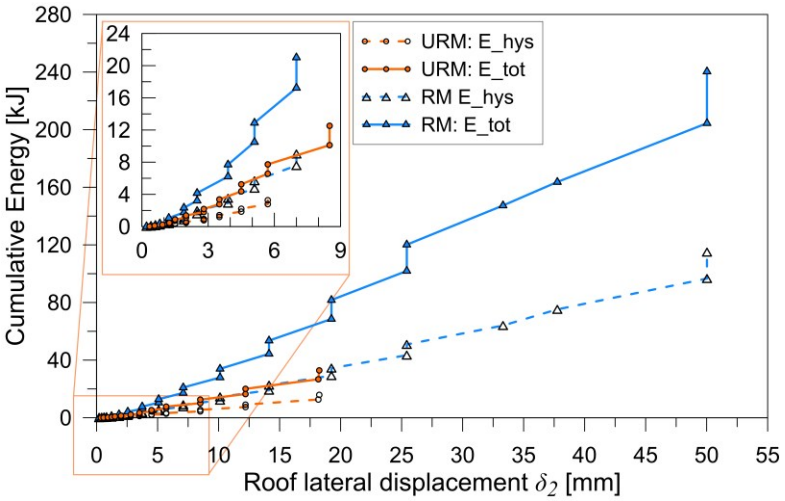
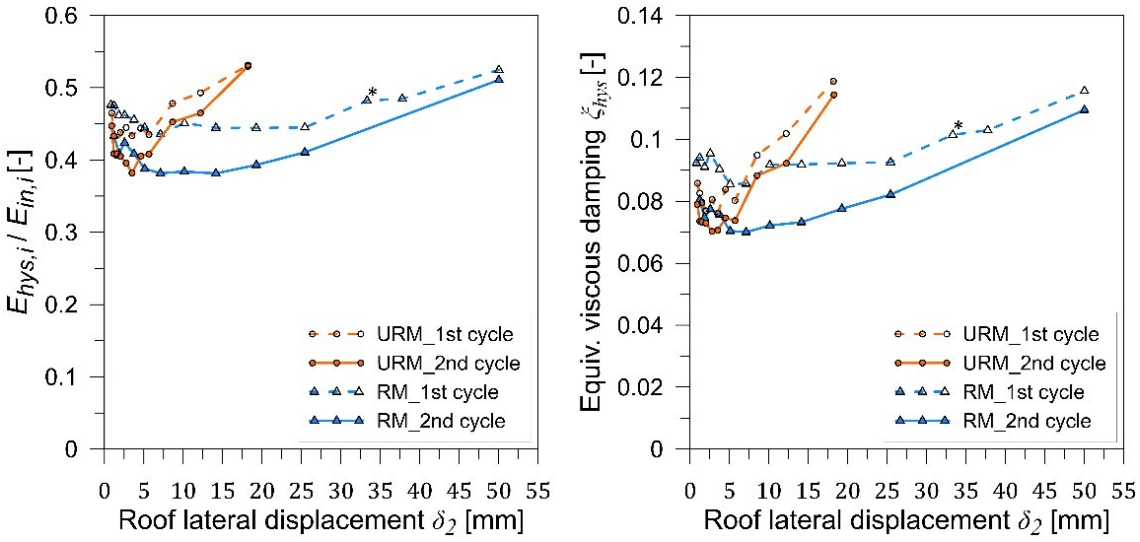


Figure 3.153 Comparison between the URM and RM building in terms of cumulative dissipated E_{hys} and total E_{in} energies

An approximate estimation of the equivalent hysteretic damping with varying target displacement was performed (accordingly to the procedure reported in FEMA 440 [247]) (Figure 3.154b).

The curves of the base shear versus the roof lateral displacement δ2 were considered for the determination of the equivalent hysteretic damping (Figure 3.146a and Figure 3.150a). The trends of the equivalent damping, calculated for the URM and RM building at the end of the first loading cycles, are reported Figure 3.154b. The difference in ξhys among the two cycles was quite evident in the early stages. The gap reduced as δ2 increased and after the peak load condition, ξhys almost coincided in the two cycles. Considering the

initial cycles, the URM and RM specimens exhibited an initial hysteretic damping of about 8% and 9%, respectively, and maintained almost constant values till the attainment of the peak load. Then, ξhys tended to increase and, at the end of the test, reached about 12% for both buildings. These values are comparable to those previously adopted by Gattesco and Boem [278], who considered ξhys of about 10% for the ultimate limit state, both in the case of URM and RM buildings. Similar values were also obtained by Magenes [80] and Javed [279] for URM masonry.



(a) (b)

Figure 3.154 Comparison between the URM and RM building in terms of (a) E_{hys}/E_{in} ratio, varying the lateral roof displacement δ_2 and (b) evolution of the equivalent hysteretic damping ratio ξ_{hys}.

3.9.7 Vibration analysis

The natural frequencies, mode shapes and damping factors of the building were evaluated for four different configurations: URM building, before and after testing, and RM building, before and after testing. The main results are reported in

Table 3.23 and the different mode shapes are schematized in Figure 3.155.

Table 3.23. Natural frequencies, f, deformed shape id., with reference to Figure 3.155, DS, and damping, ξ0, of the building, for the first five vibration modes

Mode	Undamaged URM			Damaged URM			Undamaged RM			Damaged RM		
	f [Hz]	*DS*	ξ_0 [%]	*f* [Hz]	*DS*	ξ_0 [%]	*f* [Hz]	*DS*	ξ_0 [%]	*f* [Hz]	*DS*	ξ_0 [%]
1	10.38	a	1.6	8.692	b	1.6	11.63	a	1.1	7.84	b	2.3
2	11.53	b	2.1	8.834	a	2.4	12.89	b	3.6	9.186	a	1.2
3	12.52	c	0.8	13.2	d	0.8	13.38	c	3.3	11.52	c	3.3
4	15.26	d	0.9	14.13	e	0.9	14.77	d	3	13.74	d	0.9
5	16.68	e	1.7	17.95	f	1.7	-	-	-	15.77	e	1

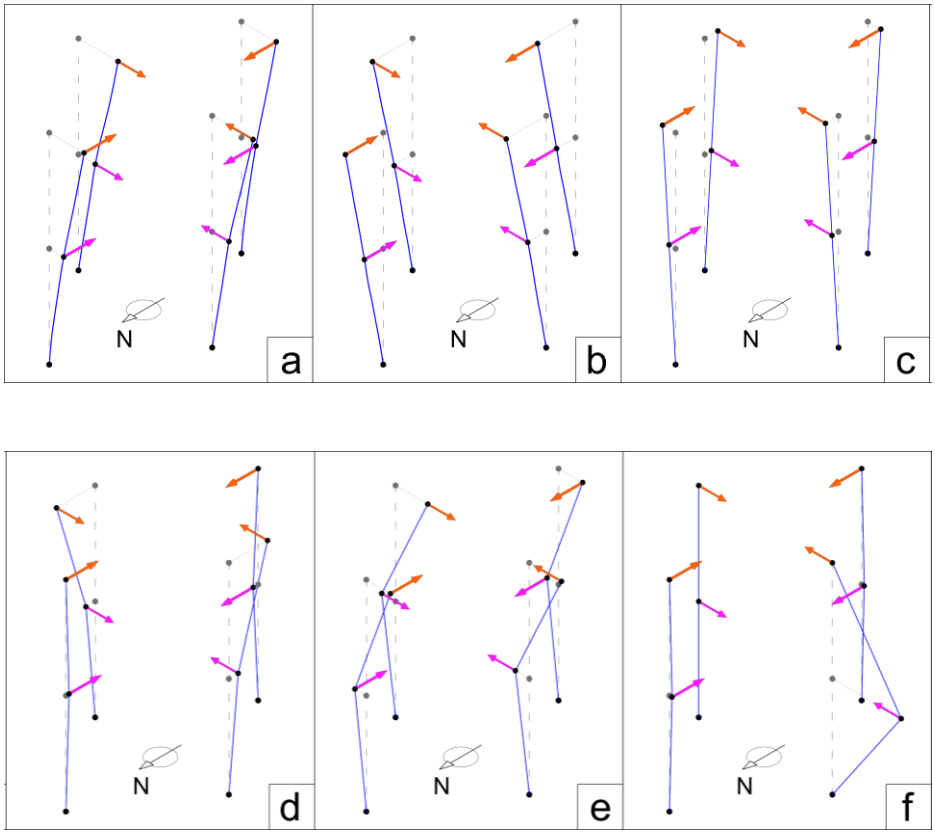


Figure 3.155 Vibration mode shapes.

In the undamaged URM building, mode 1 was translational in the transversal direction (type "a" mode shape in Figure 3.155) and mode 2 in the longitudinal one ("b"); mode 3 was rotational about the vertical axis ("c"); mode 4 described longitudinal walls oscillating out of plane in phase opposition ("d"); in mode 5 the longitudinal walls oscillate out of plane with floors in phase opposition ("e").

In the damaged URM building, the fundamental vibrating modes were inversed: modes 1 and 2 were translational in the longitudinal ("b") and transversal direction ("a"), respectively. Comparing with the undamaged configuration, the frequency of the mode shape "a" decreased by -14.9% and that of "b" by -24.6%. This is reasonably related to a stiffness degradation due to the damaging. The rotational mode about the vertical axis was not detected. Mode 3 described the out of plane oscillation of the longitudinal walls in phase opposition ("d"); in mode 4 the longitudinal walls oscillated out of plane, with floors in phase opposition ("e"). Mode 5 identified a local out of plane mechanism of the West longitudinal wall ("f").

Even though mode 5 could not be identified in the undamaged RM building, the mode shapes 1 to 4 were those of the undamaged URM building, with a frequency increase of at most 12%. Thus, the retrofitting intervention did not significantly alter the vibration response of the original structure.

In the damaged RM building, modes 1 and 2 were translational in the longitudinal ("b") and transversal ("a") direction, respectively; mode 3 was rotational about the vertical axis (“c”); modes 4 and 5 were of type “d” and "e", respectively. As for the RM, the damage induced an evident frequency decrease. The change was -21.0% with respect to the undamaged RM building, for the mode shape "a", and of -39.2% for "b".

The vibration analysis also provided preliminary information on the damping capacity of the structure. Since the recorded environmental excitation was very low, the values of ξ_0 reported in Table 3.23 referred to the structure’s initial, inherent viscous damping. In particular, the values related to the dominant vibration modes (1 and 2) were observed to fail within the range 1.1-3.6%. These values align with those previously obtained in the literature for traditional stone masonry structures ([198], [280]). However, it was not possible to recognize a clear influence of damage or retrofit operations on the damping values.

4 Analytical estimation of the seismic behaviour of CRM strengthened structural elements

The National Research Council (CNR) has issued guidelines for the design of FRP and FRCM strengthening systems, which are the guidelines CNR DT 200 R1/2013 [261] and CNR DT 215/2018 [11], respectively; however, to date, there are no specific design provisions for CRM systems, despite their widespread practical use. In professional practice, engineers often rely on correlations and design approaches originally developed for FRCM systems adapting them to CRM applications based on available technical documentation and experimental evidence demonstrating the system's effectiveness. Thus, the responsibility for the proper use and design of CRM strengthening remains largely to the designer.

The **in-plane shear** resistance of TRM-strengthened masonry elements is typically evaluated as the sum of the contributions of the plain masonry and the TRM layer(s). It is generally assumed, as evidenced by Ferrara et al. [124], that the shear capacity of the TRM is governed by the tensile failure of the textile, while the masonry reaches its maximum strength. The allowable maximum stress on the textile may also be reduced by the codes to account for potential premature debonding. This approach has shown good agreement with diagonal compression test results for thin FRCM systems (≤10 mm), but it tends to be less accurate for thicker systems (>15 mm). As a result, in the analytical interpretation of these tests on CRM-strengthened masonry, some authors [169,171] have proposed considering the tensile strength of the mortar as the governing parameter for predicting the peak load, while the textile mainly contributes to providing ductile post-cracking behaviour. Moreover, applying reduction factors to account for debonding often leads to overly conservative estimates of maximum strength in CRM systems, where debonding is typically observed only at advanced damage stages, as also observed during the tests. In a previous study, Gattesco and Boem [174] empirically evaluated a correction factor to account for the fact that the peak strengths of the TRM layer(s) and the masonry, may not be attained simultaneously. All previous evaluations were based on diagonal compression tests. In 2017, Gams et al. [138] performed shear-compression tests on FRCM-strengthened masonry piers, proving that when failure is governed by diagonal cracking, the lateral resistance can be evaluated considering only the tensile resistance of the textile crossing the diagonal crack, since at this stage the masonry is widely damaged.

However, for such systems, debonding may prevent the full exploitation of the fibre tensile capacity.

The in-plane bending resistance of TRM-strengthened masonry elements, is typically evaluated by performing a cross-sectional analysis under combined bending and axial loading, with the same approach adopted for reinforced concrete beams, as also suggested by CNR DT 215/2018 [11] and ACI 549.6R-20 [10]. This analysis is based on several key assumptions:

a) Strain compatibility is assumed to hold between the masonry and the TRM layer;
b) Plane sections remain plane even after the load is applied;
c) the contribution of the TRM layer in compression is neglected;
d) The axial load is considered to be acting at the mid-span.

Typically, a bilinear constitutive law for masonry in compression and a linear response of FRP until failure is assumed. The failure of FRP may be in different modes (e.g. fibre fracture, pull-out/sliding of fibres), which is considered in the equations by setting an appropriate value for ultimate strain of the fibres. The guideline CNR DT 215/2018 provides analytical expressions for calculating the capacity, considering three different failure modes: compressive failure of masonry, tensile failure of FRP and bilinear compression in masonry, and tensile failure of FRP and elastic compression in masonry. An effective anchoring of the TRM layer at the masonry panels extremities is required to include it in the evaluation of the in-plane flexural strength (at least 300 mm below and above [10]).

A critical issue within the current regulatory framework also concerns the behavior of CRM systems in single-sided applications and the mechanical connection between the reinforcement and the substrate. In such configurations, adhesion must be entirely ensured by connectors, which are required but neither quantified nor explicitly described in the existing guidelines. Additionally, for FRCM systems the guidelines recommend reducing the shear strength contribution of the TRM layer by 30% when the coating is applied on one side only. However, this reduction was not confirmed by the analytical validation of the experimental results presented in the following sections.

A similar approach to that of in-plane bending resistance was considered in the evaluation of the **out-of-plane bending resistance** of TRM-strengthened masonry. Analytical models available in the literature generally estimate the flexural strength based on the

strain compatibility method; however, as noted by Sagar et al. [188] and Tripathy et al. [281], the expressions used to define the moment capacity differ among authors. Various parameters have been considered in these formulations, though not always simultaneously, including TRM delamination [282], the tensile contribution of masonry [283], potential shear failure [26], and the introduction of strain reduction factors to account for both masonry shear failure and TRM debonding [184].

A different approach, based on limit analysis, was proposed by De Santis et al. [249], who assumed that masonry and TRM attain their ultimate strengths simultaneously. In this case, premature debonding was incorporated through a correction coefficient applied to the estimated resistance.

Based on the experimental evidences herein discussed, simple analytical models have been developed for the prediction of the strength and deformability characteristics of the masonry walls strengthened with the CRM technique that was developed in this study.

4.1 Analytic estimation of the in-plane resistance of piers

Table 4.1. List of symbols

t	masonry pier thickness
b	masonry pier width
l	masonry pier height (i.e. “effective length”)
t_c	Plaster thickness
E_m	masonry Young’s modulus
G_m	masonry shear modulus (~$1/3E_m$)
i	number of CRM-strengthened sides (1-2)
t_c	plaster nominal thickness
E_c	plaster Young’s modulus
G_c	plaster shear modulus (~$0.4E_c$)
η	coefficient related to the pier static scheme (e.g. 3 for cantilever, 12 for shear type)
I	second bending moment of the uncracked pier cross section ($tb^3/12$)
σ_0	mean vertical compressive stress on the pier
τ_0	equivalent masonry shear strength for $\sigma_0 = 0$ (for “Turnšek and Čačovič” formula)
β	pier slenderness factor ($1.0 \leq \beta = l/b \leq 1.5$)
χ	effectiveness reduction factor (=1 for CRM)
γ	model coefficient (=2)
A_G	net cross section of a GFRP wire
T_G	mean tensile resistance of a GFRP wire
s	GFRP mesh grid pitch
l_f	CRM effective length (=l, but ≤b)
$\varepsilon_{lim,G}$	limit tensile strain of GFRP
E_G	GFRP Young’s modulus
f_m	masonry compressive strength
α	coefficient of bending moment distribution (e.g. 1 for cantilever, 2 for shear type)
x	depth of the neutral axis of the cracked cross-section

To schematize analytically, in a simplified way, the in-plane lateral performances of masonry piers, an elastic-plastic behaviour is considered (Figure 4.1). To estimate the stiffness, resistance and ultimate displacement capacities, well-known correlations available in the literature were considered for the unstrengthened masonry. For CRM

strengthened masonry, the correlations need to be adjusted to account for the CRM contribution.

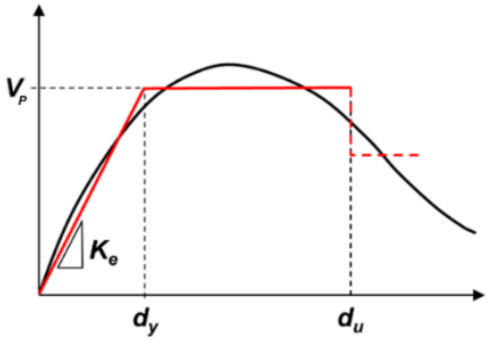


Figure 4.1 Generic, simplified elastic-plastic schematization of the in-plane lateral performances of masonry piers (red line), in comparison with actual performances (black line)

To evaluate the pier stiffness, K_e, both the flexural and shear deformability are considered, as indicated in Eq.(4.1). In case of CRM strengthened masonry, equivalent Young and shear moduli were considered, evaluating the average values between masonry and mortar coating, weighted on the respective thickness, as per Eq. (4.2) and Eq. (4.3).

$$K_e = \frac{1}{\frac{l^3}{\eta I E} + \frac{1.2 l}{G b t}} \tag{4.1}$$

$$E_{m(CRM)} = \frac{E_m\, t + E_c\, i\, t_c}{t} \tag{4.2}$$

$$G_{m(CRM)} = \frac{G_m\, t + G_c\, i\, t_c}{t} \tag{4.3}$$

For the evaluation of the pier's in-plane lateral resistance, V_P, the weakest mechanism between shear failure (due to diagonal cracking), $V_{P,d}$, and bending, $V_{P,f}$, is considered:

$$V_P = min\,(V_{P,d}; V_{P,f}) \tag{4.4}$$

The typical crack patterns that occur during seismic events are illustrated in Figure 4.2. For these mechanisms to activate, the diagonal masonry strut should not prematurely fail in compression:

$$V_P \leq 0.25 \cdot b \cdot t \cdot f_m \tag{4.5}$$

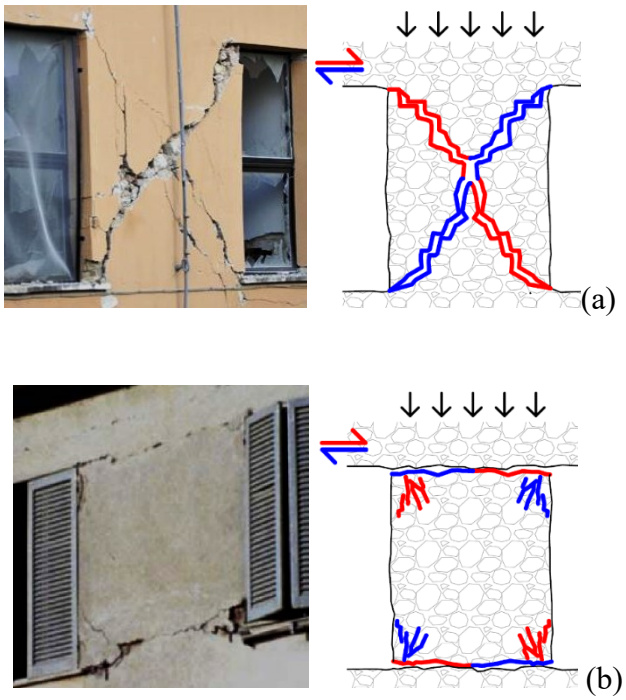


Figure 4.2 Typical in-plane failure mechanism of masonry piers: diagonal cracking (a) and bending (b)

For the unstrengthened masonry piers (suffix URM), different resistant models can be found in the literature to estimate the pier shear strength $V_{P,d(URM)}$. For example, the well-known "Turnšek and Čačovič" correlation [284], suitable for both regular and irregular masonry, can be applied, according to C8.7.1.16 in [65]:

$$V_{P,d(URM)} = \frac{1.5\tau_0}{\beta} b \cdot t \sqrt{1 + \frac{\sigma_o}{1.5\tau_0}} \tag{4.6}$$

The in-plane bending resistance of the unreinforced masonry piers is mainly due to the masonry compressive resistance and the stabilizing effect of the vertical loads ([7.8.2] in [65]):

$$V_{P,f(URM)} = \frac{\alpha M_{P(URM)}}{l} = \frac{\alpha}{l} \frac{\sigma_o b^2 t}{2} \left(1 - \frac{\sigma_o}{0.85 f_m}\right) \tag{4.7}$$

Both mechanisms benefit from the contribution of the CRM system, as the fibre-based composite material (the mesh wires), crossing both the diagonal and the horizontal cracks, limits their opening, fostering a wider stress diffusion. However, to be effective against the bending failure, the CRM system has to be sufficiently extended beyond the pier end sections.

Due to the lack of specific correlations for the evaluation of the resistance of CRM strengthened masonry pier (suffix CRM), reference is herein made to CNR-DT 215/2018 [11], which is referred to FRCM systems, since it has several similarities with the proposed CRM system.

According to it, the contribution given by the wires along the loading direction crossing the diagonal crack shall be added to that of the unstrengthened masonry:

$$V_{P,d(CRM)} = V_{P,d(URM)} + \chi \frac{1}{\gamma} \cdot i \cdot \frac{A_G}{s} \cdot l_f \cdot \varepsilon_{\lim,G} \cdot E_G \tag{4.8}$$

Note that, if the tensile failure of the fibres is attained, the factor $A_G \cdot \varepsilon_{lim,G} \cdot E_G$ corresponds to the tensile resistance of a single wire, T_G.

For the in-plane bending failure mechanism of the CRM strengthened masonry pier, the tensile-resistant contribution of the vertical wires crossing the horizontal cracks at the end sections are accounted. The moment capacity $M_{P(CRM)}$ can be evaluated by performing a reinforced cross-sectional analysis under combined bending and axial loading at the ultimate limit state, assuming conservation of plane sections, perfect bond among materials, masonry cracked in tension and plastic in compression, fibre mesh with linear-elastic behaviour in tension until the limit strain. The eccentricity of the mesh is not considered. Typically, the compressive behavior of the masonry material is considered elastic up to a strain of 0.2%. After this point, it behaves as perfectly plastic until it reaches the ultimate compressive strain (ε_{mu}) of 0.35%.

Alternatively, a simplified approach may be adopted by considering the first FRP bar positioned along the tensioned edge, thereby simplifying the formulation as expressed in Eq.(4.9) and illustrated in Figure 4.3.

$$V_{P,f(CRM)} = \frac{\alpha M_{P(CRM)}}{l} = \frac{\alpha}{l}\left[0.8x \cdot f_m \cdot t\left(\frac{b}{2} - 0.4x\right) + \chi \frac{i \cdot A_G \cdot \varepsilon_{\lim,G} \cdot E_G}{s} \cdot \frac{(b-x)}{2}\left(\frac{b}{6} + \frac{x}{3}\right)\right] \tag{4.9}$$

With:

$$x = b \cdot t\left(\sigma_0 + \chi \frac{i A_G \cdot \varepsilon_{\lim,G} \cdot E_G}{2s \cdot t}\right) \Big/ \left(0.8 \cdot f_m \cdot t + \chi \frac{i \cdot A_G \cdot \varepsilon_{\lim,G} \cdot E_G}{2s}\right)$$

In which:

$(b - x)/s$ is the number of tensed FRP bars;

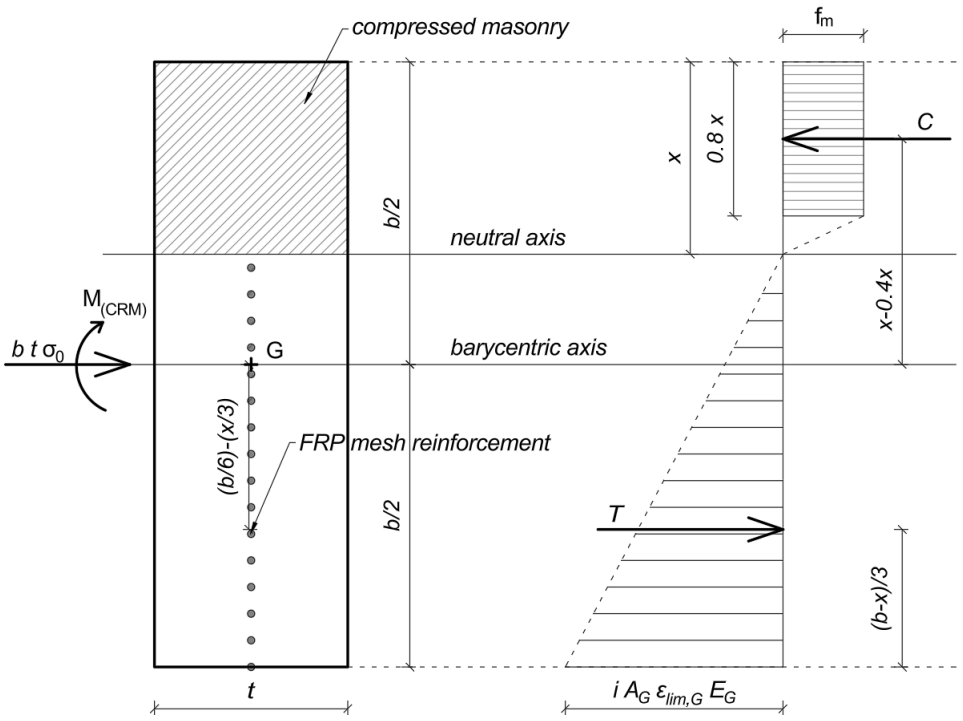


Figure 4.3 Cross-section of the wall: stress profiles, and load resultant in tension (T) and in compression (C)

It is observed that the plaster contribution on strength is neglected in both mechanisms. It is also worth noting that the introduction of effective transversal connectors in multiple-leaves masonry could be grossly considered by increasing the masonry shear strength, τ_0. Appropriate coefficients (range 1.2-1.5, depending on masonry type) are provided in C8.5.II of [65].

The ultimate displacement capacity of the masonry pier, d_{Pu}, is evaluated on the basis of the chord rotation limits at the pier extremities, θ_{Pu}. For unstrengthened masonry, the values provided in C8.7.1.3.1.1 of [65] can be applied - Eq. (4.10).

$$\theta_{Pu(URM)} = \begin{cases} 0.005 & if \ V_{P,d(URM)} < V_{P,f(URM)} \\ 0.010 & if \ V_{P,d(URM)} \geq V_{P,f(URM)} \end{cases} \tag{4.10}$$

For CRM masonry, in the lack of any guidance, doubled values could be considered, based on experimental evidences - Eq. (4.11).

$$\theta_{PU(CRM)} = \begin{cases} 0.010 & if\ V_{P,d(CRM)} < V_{P,f(CRM)} \\ 0.020 & if\ V_{P,d(CRM)} \geq V_{P,f(CRM)} \end{cases} \tag{4.11}$$

4.1.1 Application and validation

The analytical model described in section 4.1 is adopted to evaluate the lateral performances of the experimental tests on the pier samples resumed in section 1.1.

The values of the unstrengthened masonry shear strength (τ_0) considered in the formulations are calculated from the experimental tests obtained for the unstrengthened pier samples (P-R2U, P-B2U and P-B2U in sections 3.4.4, 3.4.4.4 and 3.4.4.7). In particular, since the diagonal cracking failure was attained in all the unstrengthened samples, Eq.(4.6) is solved for τ_0. For the resistance $V_{P,d(URM)}$, a bilinearization of the backbone capacity curves is performed according to the Italian Code (C7.3.4.2 of [65]) and the mean plastic value between positive and negative loading directions is considered.

For the Young's modulus, E_m, and the compressive strength, f_m, a preliminary estimation was done on the basis of values provided by the Italian code (Tab.C8.5.I in [65]), by performing a linear interpolation within the provided ranges for the different masonry types, starting from the values of shear strength τ_0. Actually, for the rubble stone sample, the values estimated by this procedure resulted slightly higher than the results of the monotonic compressive tests on masonry wallets (section 3.1). Therefore, those experimental outcomes were assumed as consistent and representative and were thus prudentially set as input parameters for masonry R2. Conversely, for the solid brick masonry (both B2 and B1), the results of the monotonic compressive tests on masonry wallets (section 3.1) provided values of both E_m and f_m significantly higher than Tab.C8.5.I. In this case, these latter calculated values were set as input parameters, since prudentially believed to be more representative for a masonry that is subjected to cyclic loading and whose orientation of principal compressive stresses deviate from the vertical. The parameters used in the analytic evaluations are presented in Table 4.2.

The main results are summarized in Figure 4.4, Figure 4.5 and Figure 4.6. and compared graphically with the experimental capacity curves. It is worth to note that the elastic deformability of the apparatus ($1/K_{add,P}$, experimentally measured as 1/56000 mm/N) is added to that of the samples, as it is not negligible.

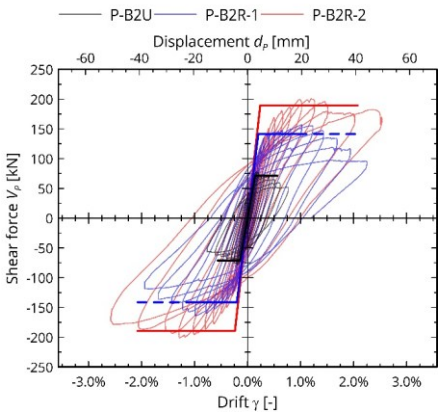
Table 4.2. Main parameters used in the estimation of stiffness and strength of masonry piers tested in-plane

b	[mm]	1500
l	[mm]	1960
t_c	[mm]	30
E_c	[GPa]	10
G_c	[GPa]	4

σ_0	[MPa]	0.5
A_G	[mm^2]	3.8
T_G	[kN]	5.11
s	[mm]	66
l_f	[mm]	1500

η	[-]	12
α	[-]	2

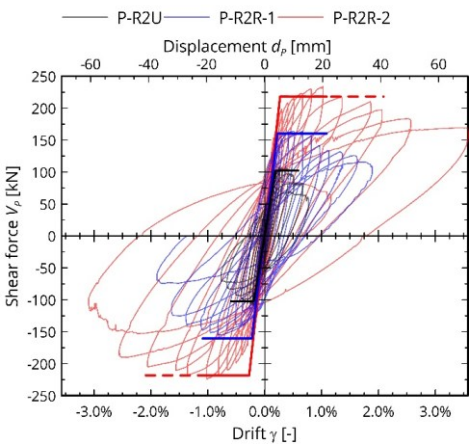
		P-R2U	P-R2R-1	P-R2R-2
t	[mm]	350	350	350
f_m	[MPa]	2.48	2.48	2.48
τ_0	[MPa]	0.071	0.071	0.071
i	[-]	-	1	2
χ	[-]	-	1.0	1.0
E	[MPa]	1074.2	1931.3	2788.5
G	[MPa]	358.1	700.9	1043.8
K_e	[N/mm]	54214	103178	152022
$K_{add,P}$	[N/mm]	56000	56000	56000
x	[mm]	-	437.3	490.6
M_P	[kNm]	150.2	190.9	221.0
$V_{P,f}$	[kN]	153.2	194.8	225.5
$V_{P,d}$	[kN]	102.2	160.2	218.3
V_P	**[kN]**	**102.2**	**160.2**	**218.3**
Mode	[-]	Shear	Shear	Shear*
$d_{P,e}$	**[mm]**	**3.71**	**4.41**	**5.33**
$d_{P,u}$	**[mm]**	**11.6**	**21.4**	**21.4 (41.0)**



(*) 1.3 is the amplification factor of the shear strength in multiple-leaves solid brick masonry, to account for the benefits of effective transversal connectors (since leaves separation actually occurred in P-B2U, but not in P-B2R-1 and P-B2R-2).

(**) since $V_{P,f}$ and $V_{P,d}$ are very close, a combined shear/bending failure is expected, thus $d_{P,u}$ could likely reach values related to flexure.

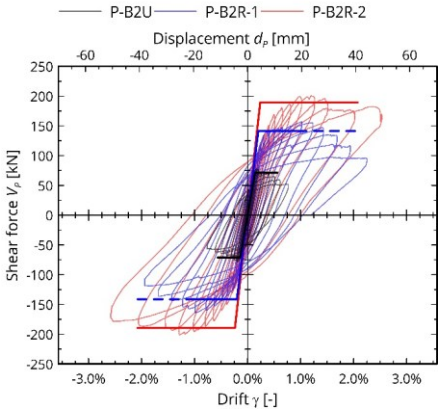
		P-R2U	P-R2R-1	P-R2R-2
t	[mm]	350	350	350
f_m	[MPa]	2.48	2.48	2.48
τ_0	[MPa]	0.071	0.071	0.071
i	[-]	-	1	2
χ	[-]	-	1.0	1.0
E	[MPa]	1074.2	1931.3	2788.5
G	[MPa]	358.1	700.9	1043.8
K_e	[N/mm]	54214	103178	152022
$K_{add,P}$	[N/mm]	56000	56000	56000
x	[mm]	-	437.3	490.6
M_P	[kNm]	150.2	190.9	221.0
$V_{P,f}$	[kN]	153.2	194.8	225.5
$V_{P,d}$	[kN]	102.2	160.2	218.3
V_P	**[kN]**	**102.2**	**160.2**	**218.3**
Mode	[-]	Shear	Shear	Shear*
$d_{P,e}$	**[mm]**	**3.71**	**4.41**	**5.33**
$d_{P,u}$	**[mm]**	**11.6**	**21.4**	**21.4 (41.0)**



(*) since $V_{P,f}$ and $V_{P,d}$ are very close, a combined shear/bending failure is expected, thus $d_{P,u}$ could likely reach values related to flexure.

Figure 4.4 Analytic results concerning the R2 masonry pier samples and comparison with the experimental behaviour

		P-B2U	**P-B2R-1**	**P-B2R-2**
t	[mm]	250	250	250
f_m	[MPa]	2.98	2.98	2.98
τ_0	[MPa] (*)	0.068	0.068x1.3	0.068x1.3
i	[-]	-	1	2
χ	[-]	-	1.0	1.0
E	[MPa]	1335.7	2535.7	3735.7
G	[MPa]	445.2	925.2	1405.2
K_e	[N/mm]	48150	97104	145939
$K_{add,P}$	[N/mm]	56000	56000	56000
x	[mm]	-	386.4	450.3
M_P	[kNm]	112.9	153.6	185.7
$V_{P,f}$	[kN]	115.2	156.8	189.5
$V_{P,d}$	[kN]	71.2	141.3	199.3
V_P	[kN]	71.2	141.3	199.3
Mode	[kN]	71.2	141.3	189.5
$d_{P,e}$	[-]	Shear	Shear**	Bending
$d_{P,u}$	[mm]	2.75	3.98	4.68
M_P	[mm]	11.1	21.1 (40.7)	40.7



(*) 1.3 is the amplification factor of the shear strength in multiple-leaves solid brick masonry, to account for the benefits of effective transversal connectors (since leaves separation actually occurred in P-B2U, but not in P-B2R-1 and P-B2R-2).

(**) since $V_{P,f}$ and $V_{P,d}$ are very close, a combined shear/bending failure is expected, thus $d_{P,u}$ could likely reach values related to flexure.

Figure 4.5 Analytic results concerning the B2 masonry pier samples and comparison with the experimental behaviour

		P-B1U	P-B1R-1
t	[mm]	250	250
f_m	[MPa]	3.84	3.84
τ_0	[MPa]	0.108	0.108
i	[-]	-	1
χ	[-]	-	1.0
E	[MPa]	1638.6	2838.6
G	[MPa]	546.2	1026.2
K_e	[N/mm]	59069	108041
$K_{add,P}$	[N/mm]	56000	56000
x	[mm]	-	304.2
$M_{P(CRM)}$	[kNm]	119.1	163.2
$V_{P,f(CRM)}$	[kN]	121.5	166.5
$V_{P,d(URM)}$	[kN]	94.2	94.2
$V_{P,d(CRM)}$	[kN]	-	152.3
$V_{P(CRM)}$	[kN]	94.2	152.3
Mode	[-]	Shear	Shear
$d_{P,e(CRM)}$	[mm]	3.28	4.13
$d_{P,u(CRM)}$	[mm]	11.5	21.3

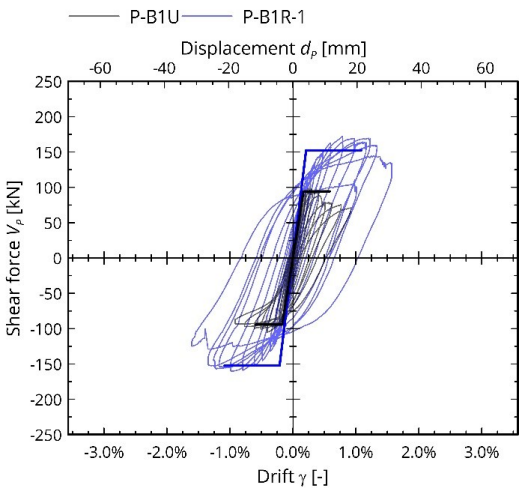


Figure 4.6 Analytic results concerning the B1 masonry pier samples and comparison with the experimental behaviour

The estimated in-plane elastic-plastic behaviour of piers shows a good correlation with the experimental results for all masonry types, and the failure mechanisms are correctly identified by the analytic models, with a slight underestimation of the peak load. The following comparisons are made considering the mean peak strength values between the positive and negative loading directions.

The prediction for P-R2R-1, which had coating on one side and failed in shear, overestimates the capacity by 0.4%. The prediction for P-R2R-2, which had coating on both sides and failed in combined shear/bending, underestimates the capacity by 4.8 % in shear and 1.7% in bending.

For sample P-B2R-1, which had coating on one side and failed in shear, the model underestimates the strength by 12.0%. For P-B2R-2, which had coating on both sides and failed in bending, the model underestimated the strength by 5.7%. Finally, for sample P-B1-R1, which had coating on one side and failed in predominantly in shear, the model underestimated strength by 8.4%.

4.2 Analytic estimation of the in-plane resistance of spandrels

Table 4.3. List of symbols

t	masonry spandrel thickness
b	masonry spandrel width
l	masonry spandrel height (i.e. “effective length”)
b_h	average height of a masonry row
b'	net masonry spandrel height (typically, lintel is not considered)
ρ	coefficient = $b'/4b_h$
d_{eff}	effective overlap length of blocks
E_m	masonry Young’s modulus
G_m	masonry shear modulus (~$1/3E_m$)
i	number of CRM-strengthened sides (1-2)
t_c	plaster nominal thickness
E_c	plaster Young’s modulus
G_c	plaster shear modulus (~$0.4E_c$)
η	coefficient related to the spandrel static scheme (e.g. 3 for cantilever, 12 for shear type)
I	second bending moment of the uncracked spandrel cross section ($tb^3/12$)
σ_0	mean compressive stress on the spandrel. Max. between horizontal compressive stress (if known) and vertical one (evaluated on the basis of the floor load and the diffusion of vertical stresses in adjacent piers). However, it is typically assumed = 0.
σ_{0P}	vertical compressive stress on the piers adjacent to the spandrel
f_m	masonry compressive strength (vertical direction)
$f_{m,h}$	masonry compressive strength (horizontal direction)
$\varepsilon_{lim,m}$	limit compressive strain of the masonry (typically assumed equal to 0.0035.)
τ_0	equivalent masonry shear strength for $\sigma_0 = 0$ (for “Turnšek and Čačovič” formula)
f_{v0}	masonry shear strength for $\sigma_0 = 0$ (shove test)
β	spandrel slenderness factor ($1.0 \leq \beta = l/b \leq 1.5$)
χ	effectiveness reduction factor (=1 for CRM)
γ	model coefficient (=2)
A_G	net cross section of a GFRP wire
T_G	mean tensile resistance of a GFRP wire
s	GFRP mesh grid pitch
l_f	CRM effective length (=l, but ≤b’)
$\varepsilon_{lim,G}$	limit tensile strain of GFRP
E_G	GFRP Young’s modulus
H_P	Tensile resisting element strength
A_s	Tensile resisting elements area
$\varepsilon_{s,y}$	Tensile resisting elements yielding deformation
E_s	Tensile resisting elements Young modulus
α	coefficient of bending moment distribution (e.g. 1 for cantilever, 2 for shear type)
x	depth of the neutral axis of the cracked cross-section

The empirical evidence has shown that the in-plane behavior of unreinforced masonry spandrels without horizontal ties can be schematized analytically, in a simplified way, as an elastic-brittle behaviour with some residual resistance (Figure 4.7a). Differently, when a horizontal tensile-resistant element is provided (e.g. a steel rod, a reinforced concrete ring beam, a metallic profile, the CRM reinforcement, a fibre-based composite strip, etc.) an elastic-plastic behaviour it is more appropriate (Figure 4.7b).

To estimate the stiffness, resistance and ultimate displacement capacities, well-known correlations available in the literature were be considered for the unstrengthened masonry. For CRM strengthened masonry, the correlations were adjusted to account for the CRM contribution.

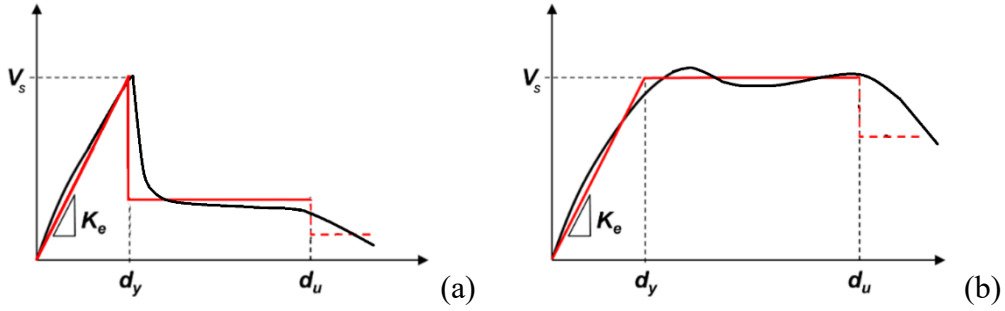


Figure 4.7 Generic, simplified elastic-brittle (a) or elastic-plastic (b) schematization of the in-plane lateral performances of masonry spandrels (red line), in comparison with actual performances (black line).

The spandrel stiffness was evaluated similarly to piers, according to Eq.(4.1), with l being the spandrel height, b the spandrel width and t the spandrel thickness. In the case of CRM-strengthened masonry, equivalent Young's and shear moduli were adopted, as defined in Eq. (4.2) and Eq. (4.3).

For the evaluation of the spandrel's in-plane lateral resistance, V_S, the weakest mechanism between shear failure, $V_{S,d}$, and bending, $V_{S,f}$, is considered:

$$V_S = \min(V_{S,d}; V_{S,f}) . \tag{4.12}$$

The typical crack patterns that occur during seismic events are illustrated in Figure 4.8. For these mechanisms to activate, the diagonal masonry strut should not prematurely fail in compression:

$$V_S \leq 0.25 \cdot b \cdot t \cdot f_m \tag{4.13}$$

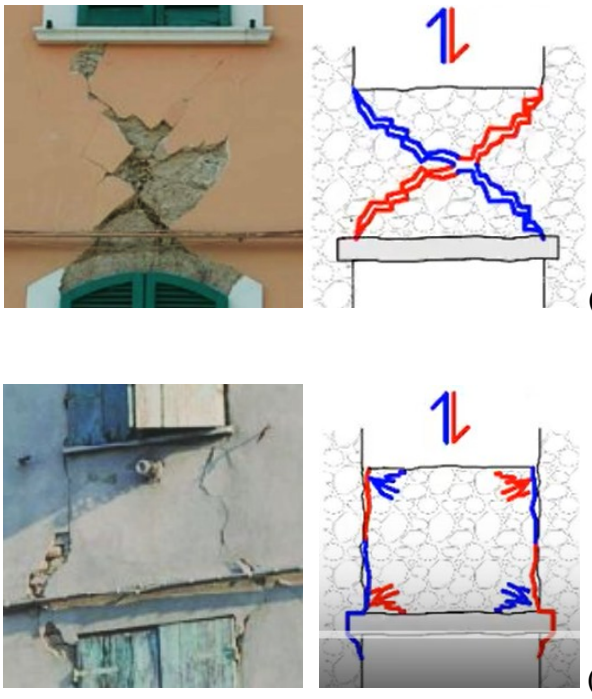


Figure 4.8 Typical in-plane failure mechanism of masonry spandrels: diagonal cracking (a) and bending (b).

For the unstrengthened masonry spandrels (suffix URM), different resistant models can be found in the literature to estimate $V_{S,d(URM)}$. As for piers, the "Turnšek and Čačovič" correlation was considered, according to Eq.(4.14), being σ_0 equal to zero in the calculations and considering conservatively the spandrels net height b' (without the lintel).

$$V_{P,d(URM)} = \frac{1.5\tau_0}{\beta} b' \cdot t \sqrt{1 + \frac{\sigma_o}{1.5\tau_0}} \qquad (4.14)$$

When failure is dominated by the shear mechanism, a residual resistance, $V'_{S,d(URM)}$, shall be considered. $V'_{S,d(URM)}$ can be estimated proportionally to $V_{S,d(URM)}$ according to the Italian code [65]:

- 0.6 for r.c. or steel lintel;
- 0.4 for timber lintel;
- 0.1 for masonry arch.

To estimate the in-plane bending resistance of unreinforced masonry spandrels without an effective horizontal tie (suffix *t0*), Eq.(4.15) can be used with the additional expression

for $f_{t,eq}$ (given in 7.3.4 in FEMA 306 [57]), which considers the contribution of block-to-block interaction (cohesion and friction) at the spandrel's ends:

$$V_{S,f(URM,t0)} = \frac{\alpha M_{S(URM,t0)}}{l} = \frac{\alpha}{l}\frac{2}{3} f_{t,eq} \cdot t \cdot b_h \cdot b \cdot \rho \tag{4.15}$$

With:

$$f_{t,eq} = \frac{d_{eff}}{b_h}\left(f_{V0} + 0.65 \cdot \sigma_{0P}\right)$$

When failure is dominated by the bending mechanism, a residual resistance, $V'_{S,f(URM)}$, shall be considered. $V'_{S,f(URM)}$ can be estimated by neglecting the cohesion contribution (i.e. assuming $f_{v0} = 0$ in Eq.(4.15).

Both mechanisms benefit from the contribution of the CRM system, as the fibre-based composite material (the mesh wires), crossing both the diagonal and the vertical cracks, limits their opening, fostering a wider stress diffusion. However, to be effective against the bending failure, the CRM system has to be sufficiently extended beyond the spandrel area.

In the lack of specific correlations for the evaluation of the resistance of CRM strengthened masonry spandrel (suffix CRM), reference is herein made to CNR-DT 215/2018 [11]. As for piers, the contribution given by the wires along the loading direction crossing the diagonal crack is considered in addition to that of the unstrengthened masonry:

$$V_{S,d(CRM)} = V_{S,d(URM)} + \chi \frac{1}{\gamma} \cdot i \cdot \frac{A_G}{s} \cdot l_f \cdot \varepsilon_{\lim,G} \cdot E_G. \tag{4.16}$$

Note that, if the tensile failure of the fibres is attained, the factor $A_G \cdot \varepsilon_{\lim,G} \cdot E_G$ corresponds to the tensile resistance of a single wire, T_G. It is also observed that, coherently with the behavior of the unreinforced masonry spandrel (Figure 4.7a), its residual resistance, $V'_{S,d(URM)}$, should prudentially be considered, instead of the peak one, $V_{S,d(URM)}$.

For the bending failure mechanism, the simplified formulation is similar to that of piers, and determined with Eq.(4.17). The tensile-resistant contribution of the horizontal wires crossing the vertical cracks at the end sections are accounted. Conservatively, the net masonry spandrel height, *b'*, is considered; however, in presence of a lintel that effectively indents at the extremities, the gross height, *b*, can be assumed instead of *b'*.

$$V_{S,f(CRM)} = \frac{\alpha M_{S(CRM)}}{l} = \frac{\alpha}{l}\left[0.8x \cdot f_{m,h} \cdot t\left(\frac{b'}{2} - 0.4x\right) + \chi \frac{i \cdot A_G \cdot \varepsilon_{\lim,G} \cdot E_G}{s} \cdot \frac{(b'-x)}{2}\left(\frac{b'}{6} + \frac{(b'-x)}{3}\right)\right] \quad (4.17)$$

$$\text{with} \quad x = b' \cdot t\left(\sigma_0 + \chi \frac{i A_G \cdot \varepsilon_{\lim,G} \cdot E_G}{2s \cdot t}\right) \Big/ \left(0.8 \cdot f_{m,h} \cdot t + \chi \frac{i \cdot A_G \cdot \varepsilon_{\lim,G} \cdot E_G}{2s}\right).$$

Note that, for this correlation to provide reliable results, it is necessary to ensure that the masonry does not reach the ultimate compressive strain while the fibre wires are still in the elastic range.

If a horizontal tensile-resistant element is provided (e.g. steel tie), with a ductile material behaviour, the simplified formulation can be developed considering two main failure modes:

1) Failure of the FRP mesh in tension;
2) Failure of masonry in compression.

The position of the neutral axis that separates the two failure modes $x_{2/3}$ is determined with Eq.(4.18)

$$x_{2/3} = \frac{\varepsilon_{lim,m}}{\varepsilon_{lim,m} + \varepsilon_{lim,G}} \quad (4.18)$$

The reinforced cross-sectional analysis is developed below for the case in which the tensile-resistant element is positioned along the barycentric axis of the section and is characterized by an elastic-perfectly plastic material behaviour.

In the case of mesh tensile failure, the moment capacity $M_{S(CRM)}$ is determined according to Eq.(4.19). In this case, the deformation of the tensile-resistant element is considered yielded ($\varepsilon_s \geq \varepsilon_{s,y}$).

$$M_{S(CRM)} = 0.8\, x\, t\, f_{m,h} \left(\frac{b'}{2} - 0.4\, x\right) + i\, \frac{T_G}{s}\left(\frac{b' - x}{2}\right)\left(\frac{b'}{6} + \frac{x}{3}\right) \quad (4.19)$$

With:

$$x = \frac{b'\left(\frac{H_P}{b'} + i\, \frac{T_G}{2\, s}\right)}{0.8\, f_{m,h}\, t + i\, \frac{T_G}{2\, s}}$$

In the case of masonry compressive failure, the moment capacity $M_{S(CRM)}$ is determined according to Eq.(4.20).

$$M_{S(CRM)}=0.8\,x\,t\,f_{m,h}\left(\frac{b'}{2}-0.4\,x\right)+E_G\,t_G\,\frac{\varepsilon_{lim,m}}{2\,x}\left(\frac{b'-x}{2}\right)^2\left(\frac{b'}{6}+\frac{x}{3}\right) \tag{4.20}$$

With t_G being the equivalent thickness of the FRP mesh as if it was a homogeneous material, determined based on its tensile strength, Eq.(4.21)

$$t_G=\frac{\left(\frac{b}{s}\right)A_G}{b}=\frac{T_G}{s\,E_G\,\varepsilon_{lim,G}} \tag{4.21}$$

And x being determined by solving the quadratic equation, according to Eq.(4.22)

$$x=\frac{-B\pm\sqrt{B^2-4\,A\,C}}{2\,A} \tag{4.22}$$

In case the tensile resisting elements deformation ε_s is lower than $\varepsilon_{s,y}$, the constants of the quadratic equations are determined through Eqs.(4.23). While, if the tensile yielding of the steel is attained, the tensile resistance of the steel tie(s) H_P is considered and the constants are determined through Eqs.(4.24).

$$\begin{aligned} A&=0.8\,t\,f_{m,h}-E_f\,t_f\,\frac{\varepsilon_{lim,m}}{2}\\ B&=E_G\,t_G\,\varepsilon_{lim,m}\,b'\\ C&=-E_f\,t_f\,\frac{\varepsilon_{lim,m}}{2}\,(b')^2-E_S\,A_S\,\frac{\varepsilon_{lim,m}}{2}\,b' \end{aligned} \tag{4.23}$$

$$\begin{aligned} A&=0.8\,t\,f_{m,h}-E_f\,t_f\,\frac{\varepsilon_{lim,m}}{2}\\ B&=E_G\,t_G\,\varepsilon_{lim,m}\,b'-H_P\\ C&=-E_f\,t_f\,\frac{\varepsilon_{lim,m}}{2}\,(b')^2 \end{aligned} \tag{4.24}$$

As for the piers, the plaster contribution is neglected in both mechanisms, and the introduction of effective transversal connectors in multiple-leaves masonry could be considered by increasing the masonry shear strength, τ_0.

The ultimate displacement capacity of the masonry spandrel, d_{Su}, is evaluated on the basis of the chord rotation limits at the spandrel extremities, θ_{Su}.

For unstrengthened masonry spandrels without effective horizontal tie, the residual resistance for both failure mechanisms, is maintained up to $\theta_{Su(URM,t0)}$ = 0.015 (C8.7.1.3.1.1 of [65]).

For CRM masonry, in the lack of any guidance, doubled values could be considered, based on experimental evidence ($\theta_{Su(CRM)}$ = 0.030).

4.2.1 Application and validation

The analytical model described in section 0 is adopted to evaluate the lateral performances of the experimental tests on the spandrel samples resumed in section 1.1.

The mechanical characteristics of the unstrengthened masonry (E_m, τ_0, f_m) considered in the formulations are those already applied for the masonry piers in section 4.1.1. The masonry horizontal compressive strength, $f_{m,h}$, is taken as $f_m/2$. The value of f_{v0} for R2 masonry is calculated from the experimental test S-R2U (section 3.5.4.1 and 3.5.4.3), by solving Eq. (4.15) for f_{v0} (for the resistance $V_{P,d(URM)}$, the peak load is taken and the mean value between positive and negative loading directions is considered). Coherently to the approach already adopted for the piers, for the solid brick samples, the values were taken from Tab.C8.5.I in [65] (linear interpolation within the provided range, starting from the values of shear strength τ_0). The parameters used in the analytic evaluations are presented in Table 4.4.

The main results are summarized in Figure 4.9 and compared graphically with the experimental capacity curves. It is worth to note that, regarding the displacements estimation, the elastic deformability of the lateral masonry piers ($1/K_{add,S}$, quantified analytically of the basis of a cantilever static scheme) is added to that of the spandrel, since the displacement transducers monitoring the spandrel distortion in the experimental tests were actually located at the inner corner of the metallic lever beams at the base.

Table 4.4. Main parameters used in the estimation of stiffness and strength of masonry spandrels tested in-plane

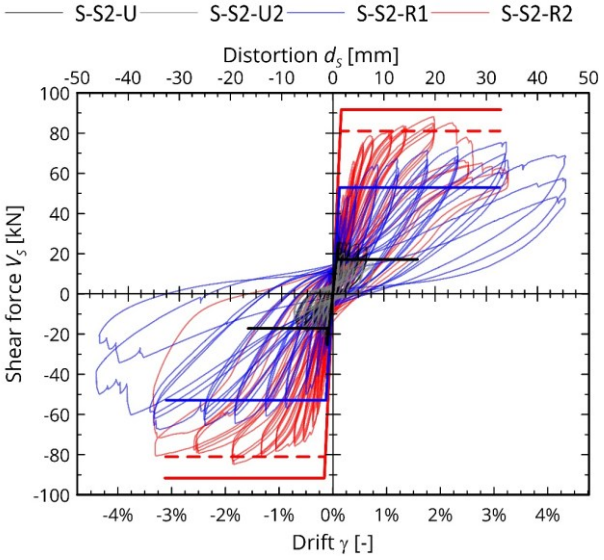
Main data									
l	[mm]	1050		A_G	[mm^2]	3.8		η	[-]	12
t_c	[mm]	30		T_G	[kN]	5.11		α	[-]	2

		S-R2U	**S-B2U**	**S-B1U**
b	[mm]	1170	1095	1095

E_c	[GPa]	10		s	[mm]	66		σ_{0P}	[MPa]	0.33
G_c	[GPa]	4		l_f	[mm]	1050				

d_{eff}	[mm]	80	125	65
b_h	[mm]	111	65	65
b'	[GPa]	1000	845	845
f_{v0}	[MPa]	0.103	0.208	0.248

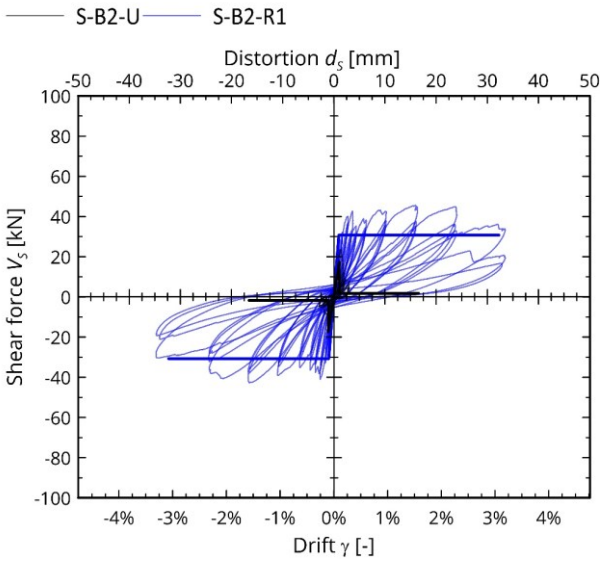
		S-R2U	S-R2R-1	S-R2R-2
t	[mm]	350	350	350
$f_{m,h}$	[MPa]	1.24	1.24	1.24
τ_0	[MPa]	0.071	0.071	0.071
i	[-]	-	1	2
χ	[-]	-	1.0	1.0
E	[MPa]	1074.2	1931.3	2788.5
G	[MPa]	358.1	700.9	1043.8
K_e	[N/mm]	95097	183181	271117
$K_{add,S}$	[N/mm]	32400	51000	69600
x	[mm]	-	117.4	213.3
M_S	[kNm]	13.3	31.5	56.7
$V_{S,f}$	[kN]	25.4	59.9	108.0 (81.0)*
$V_{S,d}$	[kN]	35.5	52.9	91.6
V_S	**[kN]**	**25.4**	**52.9**	**91.6 (81.0)**
Mode	[-]	Bending	Shear°	Sh. (Bend)
$d_{S,e}$	**[mm]**	**1.05**	**1.33**	**1.65 (1.46)**
$d_{S,u}$	**[mm]**	**16.5**	**32.5**	**32.8 (32.7)**



(*) calculated with α=1.5, as "in between" the shear-type and the cantilever scheme, to account grossly for the anomaly in the vertical loading system, as evidenced in section 3.5.4.4.

(°) since $V_{S,f}$ and $V_{S,d}$ are very close, a combined shear/bending failure is expected.

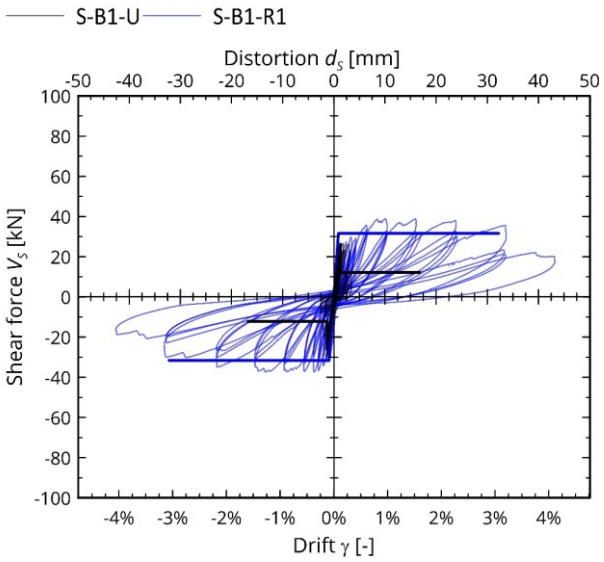
		S-B2U	S-B2R-1
t	[mm]	250	250
$f_{m,h}$	[MPa]	1.49	1.49
τ_0	[MPa]	0.068	0.068x1.3*
i	[-]	-	1
χ	[-]	-	1.0
E	[MPa]	1335.7	2535.7
G	[MPa]	445.2	925.2
K_e	[N/mm]	77051	157094
$K_{add,S}$	[N/mm]	20500	39100
x	[mm]	-	97.0
M_S	[kNm]	24.2	16.1
$V_{S,f}$	[kN]	46.0	30.7
$V_{S,d}$	[kN]	17.4	35.0
V_S	**[kN]**	**17.4**	**30.7**
Mode	[-]	Shear	Bending°
$d_{S,e}$	**[mm]**	**1.07**	**0.98**
$d_{S,u}$	**[mm]**	**16.6**	**32.3**



(*) 1.3 is the amplification factor of the shear strength in multiple-leaves roughly-cut stone solid brick masonry, to account for the benefits of effective transversal connectors.

(°) since $V_{S,f}$ and $V_{S,d}$ are very close, a combined shear/bending failure is expected.

		S-B1U	S-B1R-1
t	[mm]	250	250
$f_{m,h}$	[MPa]	1.92	1.92
τ_0	[MPa]	0.108	0.108
i	[-]	-	1
χ	[-]	-	1.0
E	[MPa]	1638.6	2838.6
G	[MPa]	546.2	1026.2
K_e	[N/mm]	94523	174588
$K_{add,S}$	[N/mm]	25400	43700
x	[mm]	-	77.3
M_S	[kNm]	13.8	16.6
$V_{S,f}$	[kN]	26.2	31.6
$V_{S,d}$	[kN]	27.7	35.5
V_S	**[kN]**	**26.2**	**31.6**
Mode	[-]	Bending°	Bending°



(°) since $V_{S,f}$ and $V_{S,d}$ are very close, a combined shear/bending failure is expected.

$d_{S,e}$	**[mm]**	**1.31**	**0.90**
$d_{S,u}$	**[mm]**	**16.8**	**32.2**

Figure 4.9 Analytic results concerning the masonry spandrel samples and comparison with the experimental behaviour

The estimated in-plane elastic-plastic behavior of the strengthened spandrels generally tended to underestimate the experimental results of the tested specimens, all of which exhibited a combined shear-bending failure mode. In particular, the analytical predictions of strength showed better alignment with the strength values observed during the repeated loading cycles, rather than with the initial peak loads. The following comparisons are made considering the mean peak strength values between the positive and negative loading directions.

For specimen S-R2R-1, strengthened on one side, the analytical model underestimates the capacity by 16.2% in bending.

For specimen S-R2R-2, strengthened on both sides, the model underestimates the capacity by 6.3% in bending and overestimates it by 6.0% in shear. In this case, the shear action due to bending was calculated assuming $\alpha = 1.5$, representing an intermediate condition between the shear-type and cantilever loading schemes, to account for the anomaly in the vertical loading system discussed in Section 3.5.4.4.

For specimen S-B2R-1, with one-sided coating, the model underestimates the capacity by 30.4% in bending and 20.6% in shear, whereas for specimen S-B1R-1, also strengthened on one side, the underestimation is 17.2% in bending and 6.9% in shear.

4.3 Analytic estimation of the out-of-plane resistance of piers

Table 4.5. List of symbols

t	masonry wall thickness
b	masonry wall width
l	masonry wall height
E_m	masonry Young's modulus
G_m	masonry shear modulus (~$1/3E_m$)
t_c	plaster nominal thickness
E_c	plaster Young's modulus
G_c	plaster shear modulus (~$0.4E_c$)
η	coefficient related to the wall static scheme (e.g. 48 for three-point bending)
I	second bending moment of the uncracked cross section ($bt^3/12$)
σ_0	mean vertical compressive stress on the wall
f_{v0}	masonry shear strength for $\sigma_0 = 0$ (shove test)
A_G	net cross section of a GFRP wire
T_G	mean tensile resistance of a GFRP wire
s	GFRP mesh grid pitch
$\varepsilon_{lim,G}$	limit tensile strain of GFRP
E_G	GFRP Young's modulus
n_G	number of GFRP wires subjected to tension = 1+int(b/s)
c	covering of GFRP mesh (typically, = $t_c/2$)
f_m	masonry compressive strength
$f_{c,f}$	plaster flexural strength
α	coefficient of bending moment distribution (e.g. = 4 for three-point bending)
α_e	plaster/masonry modular ratio = E_c/E_m
x	depth of the neutral axis of the cracked cross-section

To schematize analytically, in a simplified way, the out-of-plane lateral performances of masonry piers:

- an elastic-plastic behaviour with linear softening can be considered when the unstrengthened masonry is on the tensed side (Figure 4.10a);
- an elastic-plastic behaviour with linear hardening can be considered when the CRM layer is on the tensed side (Figure 4.10b).

To estimate the stiffness, resistance and ultimate displacement capacities, well-known correlations available in the literature can be considered for the unstrengthened masonry side. For CRM strengthened masonry side, the correlations need to be adjusted, so to

account for the CRM contribution. The procedure for calculating strengthened pier in bending presented below follows the CNR 215/2018 [11].

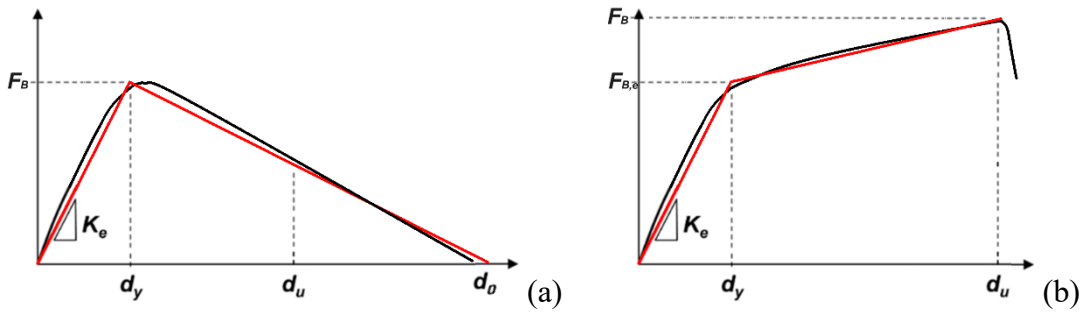


Figure 4.10 Generic, simplified elastic-brittle (a) or elastic-plastic (b) schematization of the out-of-plane performances of masonry walls (red line), in comparison with actual performances (black line).

To evaluate the pier stiffness, K_e, just the flexural deformability can be accounted, as indicated in Eq.(4.25), where a three-point bending static scheme is considered. In case of CRM strengthened masonry, equivalent Young modulus shall be considered, evaluating the average values between masonry and mortar coating, weighted on the respective thickness.

$$K_e = \frac{\eta I E}{\beta^3} . \tag{4.25}$$

Typically, during seismic events, masonry panels subjected to out-of-plane seismic actions exhibit maximum bending moment at the centre of the panel and negligible stresses at the edges (Figure 4.11). Such mechanism is likely to activate in masonry types not prone to disaggregation or leaves-separation phenomena.

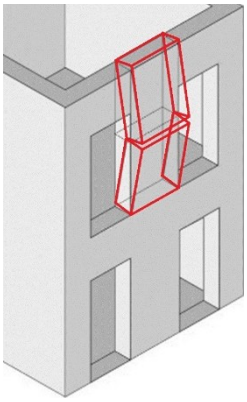


Figure 4.11 Typical out-of-plane failure mechanism of masonry walls.

The wall out-of-plane resistance related to bending, F_B, when the unstrengthened masonry is on the tensed side (suffix U) is mainly due to the masonry compressive resistance and the stabilizing effect of the vertical loads (7.8.2.2.3 in [65]:

$$F_{B,f(U)} = \frac{\alpha M_{B(U)}}{l} = \frac{\alpha}{l}\frac{\sigma_o b t^2}{2}\left(1-\frac{\sigma_o}{0.85 f_m}\right). \tag{4.26}$$

For this mechanism to activate, the masonry should not prematurely fail in shear in the cracked sections:

$$F_{B,f} \le f_v \cdot b \cdot x. \quad \text{with} \quad f_v = f_{v0} + 0.4 \cdot \sigma_0, \tag{4.27}$$

where f_{v0} shall be taken equal to zero, due to cyclic action.

When the CRM layer is on the tension side, the fibre-based composite material (the mesh wires) crossing the cracks, limits their opening, fostering a wider stress diffusion. In the lack of specific guidelines for the evaluation of the resistance of CRM strengthened masonry pier (suffix R), reference is herein made to CNR-DT 215/2018 [11]:

$$F_{B,u(R)} = \frac{\alpha M_{B,u(R)}}{l} = \frac{\alpha}{l}\left[0.8x \cdot f_m \cdot b \cdot (y_G - 0.4x) + n_G \cdot A_G \cdot \varepsilon_{\lim,G} \cdot E_G \cdot (t + t_c - c - y_G)\right] \tag{4.28}$$

with $x = (\sigma_0 \cdot b \cdot t + n_G \cdot A_G \cdot \varepsilon_{lim,G} \cdot E_G)/(0.8 \cdot f_m \cdot b)$,

and $y_G = \left[\frac{b}{2}(t + t_c)^2 + n_G \cdot A_G \cdot (t + t_c - c)\right]/[b \cdot (t + t_c) + n_G \cdot A_G]$.

The moment capacity $M_{B,u(R)}$ is evaluated by analysing a reinforced section subjected to combined compression and bending in cracked conditions, assuming conservation of plane sections, perfect bond among materials, masonry and plaster cracked in tension and plastic in compression, fibre mesh with linear-elastic behaviour in tension until reaching the limit strain. Note that, if the tensile failure of the fibres is attained, the factor $A_G \cdot \varepsilon_{lim,G} \cdot E_G$ corresponds to the tensile resistance of a single wire, T_G.

The conventional elastic limit force of the bi-linear curve (Figure 4.10b), $F_{B,e(R)}$, can be calculated from the bending moment related to first cracking, $M_{B,e(R)}$:

$$F_{B,e(R)} = \frac{\alpha M_{B,e(R)}}{l} = \frac{\alpha}{l}\left[\frac{b\cdot(t+t_c)^2}{6}\cdot\left(\sigma_0 + \frac{f_{c,f}}{\alpha_e}\right)\right] \quad (4.29)$$

According to C8.7.1.2.1.6 of [65], the ultimate out-of-plane deflection of the unstrengthened wall, $d_{Bu(U)}$, corresponds to 60% of the displacement for which $F_{B(U)} = 0$ ($d_{B0(U)}$), that is evaluated on the basis of equilibrium analysis of rigid blocks.

For CRM masonry, the ultimate deflection $d_{Bu(R)}$ corresponds to the attainment of the limit strain in tensed GFRP wires. Based on the experimental evidences, it is taken as $l/50$.

4.3.1 Application and validation

The analytical model described in section 4.3 is adopted to evaluate the lateral performances of the experimental out-of-plane bending tests resumed in section 3.6.

The mechanical characteristics of the unstrengthened masonry considered in the formulations are those already applied for the masonry piers and spandrels in §4.1.1 and §4.2.1.

To evaluate $d_{B0(U)}$, the contribution of the sample only was considered, thus $d_{B0(U)} = t/3$. The parameters used in the analytic evaluations are presented in Table 4.6.

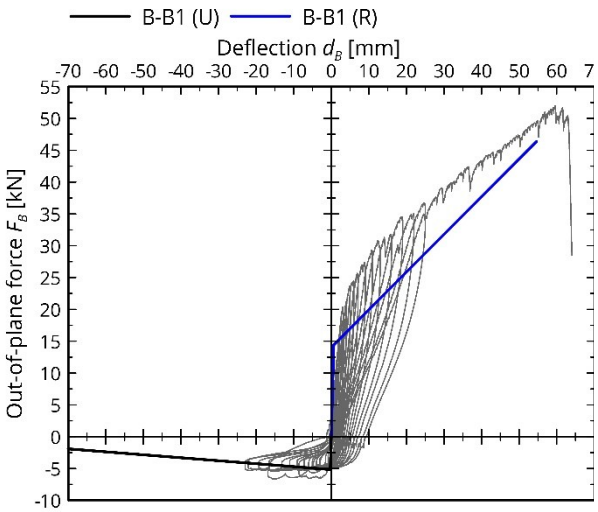
The main results are summarized in Figure 4.12 and compared graphically with the experimental capacity curves.

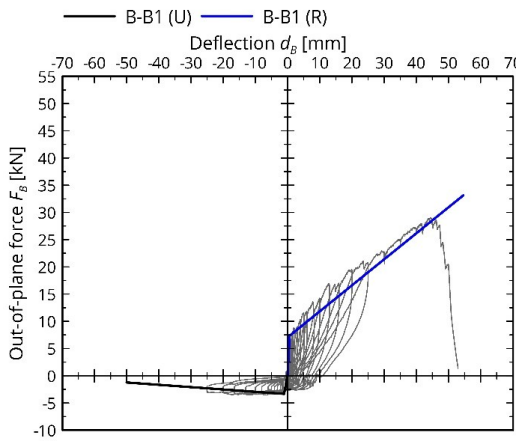
Table 4.6. Main parameters used in the estimation of stiffness and strength of masonry piers tested out-of-plane.

Main data									
b	[mm]	1030		n_G	[-]	16		η	[-]	48
l	[mm]	2730		A_G	[mm^2]	3.8		α	[-]	4
t_c	[mm]	30		T_G	[kN]	5.11		α_e	[-]	8
E_c	[GPa]	10		s	[mm]	66		$f_{c,f}$	[MPa]	3.0

		B-R2	B-B2	B-B1
t	[mm]	350	250	250
f_m	[MPa]	2.48	2.98	3.84
E_m	[MPa]	1074.2	1335.7	1638.6
E	[MPa]	1931.3	2535.7	2838.6
σ_0	[MPa]	0.034	0.032	0.032
K_e	[N/mm]	21459	11271	12618
y_G	[mm]	~190	~140	~140
$M_{B(U)}$	[kNm]	2.5	1.3	1.3
$M'_{B(U)}$	[kNm]*	3.5	2.3	2.3
$F_{B,f(U)}$	**[kN]**	**5.2**	**3.3**	**3.3**
$d_{B,e(U)}$	**[mm]**	**0.24**	**0.30**	**0.26**
$d_{B,u(U)}$	**[mm]**	**70.0**	**50.0**	**50.0**
$x_{(C)}$	[mm]	46.6	37.0	28.7
$M_{B(C)}$	[kN]	30.6	21.6	21.9
$M'_{B(C)}$	[kN]*	31.6	22.6	22.9
$F_{B,f(C)}$	**[kN]**	**46.3**	**33.1**	**33.6**
$M_{B,e(C)}$	[kN]	8.84	4.02	4.84
$M'_{B,e(C)}$	[kN]*	9.84	5.02	5.84
$F_{B,e(C)}$	**[kN]**	**14.4**	**7.4**	**8.6**
$d_{B,e(C)}$	**[mm]**	**0.67**	**0.65**	**0.68**
$d_{B,u(C)}$	**[mm]**	**54.6**	**54.6**	**54.6**

(*) evaluated by adding to M_B the additional contribution due to the friction of the testing apparatus (approximately 1 kNm)





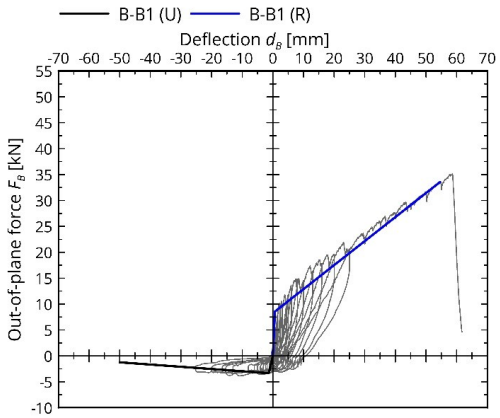


Figure 4.12 Analytic results concerning the out-of-plane tests and comparison with the experimental behaviour.

The estimated out-of-plane elastic-plastic behavior of the strengthened piers correctly reproduces the experimental strength, although with maximum errors of about 15 %. The value of $F_{B,e(R)}$ is generally underestimated by the model, as also the displacement at first cracking $d_{B,e(R)}$, particularly the latter, which is significantly lower than the experimental observations.

For the unstrengthened specimens, the analytical predictions showed good correlation with the experimental results in terms of strength.

For the B-R2 specimen, the model underestimates the strength capacity by 11.0%, while the strength at first cracking is underestimated by 29.4%.

For the B-B2 specimen, the analytical model overestimates the strength capacity by 14.1%, whereas the strength at first cracking is underestimated by 16.2%.

For the B-B1 specimen, the model underestimates the strength capacity by 4.3%, while the strength at first cracking is underestimated by 12.2%.

4.4 Analytic estimation of resistance of roof ring beams with FRP meshes embedded in mortar joints

Table 4.7. List of symbols

t	masonry beam thickness
b	masonry beam height
l	Masonry beam span
E_m	masonry Young's modulus
η	coefficient related to the beam static scheme (e.g. =48 for 3 point bending)
I	second bending moment of the uncracked beam cross section ($tb^3/12$)
A_G	net cross section of a GFRP wire
n_B	number of bed joints with GFRP embedded
T_G	mean tensile resistance of a GFRP wire
s	GFRP grid pitch
$\varepsilon_{lim,G}$	limit tensile strain of GFRP
E_G	GFRP Young's modulus
n_G	total number of GFRP wire levels in a single bedjoint
n'_G	number of GFRP wire levels in tension in a single bedjoint
c	covering (distance between the outer GFRP wires and the tensed edge of the cross section
$f_{m,f}$	masonry flexural strength (horizontal mending)
α	coefficient of bending moment distribution (e.g.=4 for 3 point bending)
α_G	GFRP/masonry modular ratio = E_G / E_m

To schematize analytically, in a simplified way, the out-of-plane lateral performances of masonry beams with FRP mesh embedded in the bed joints, a tri-linear behaviour with final plastic stage can be considered (Figure 4.13).

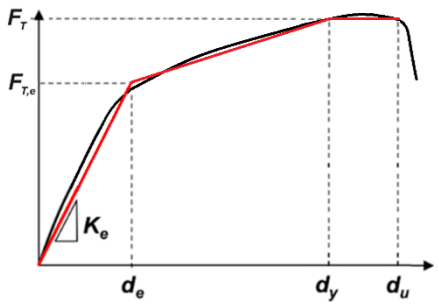


Figure 4.13 Generic, simplified tri-linear schematization of the out-of-plane performances of masonry beams with GFRP meshes embedded in the bed joints (red line), in comparison with actual performances (black line).

To evaluate the beam stiffness, K_e, just the flexural deformability of the masonry can be accounted, as indicated in Eq.).

$$K_e = \frac{\eta \, I E_m}{l^3} \tag{4.30}$$

Typically, during seismic events, masonry roof ring beams subjected to out-of-plane seismic actions exhibit maximum bending moment at the centre of the span. Such mechanism is likely to activate in masonry types not prone to disaggregation or leaves-separation phenomena.

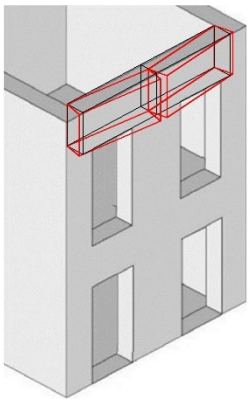


Figure 4.14 Typical out-of-plane failure mechanism of masonry ring beams.

In masonry beams with GFRP meshes embedded in the bed joints, the out-of-plane resistance, $F_{T,u(R)}$, was evaluated by analysing a reinforced section subjected to bending in cracked conditions, assuming conservation of plane sections, perfect bond among materials, masonry cracked in tension and plastic in compression, fibre mesh with linear-elastic behaviour in tension until reaching the limit strain.

$$F_{T,u(R)} = \frac{\alpha M_{Tu(R)}}{l} = \frac{\alpha}{l}\frac{\varepsilon_{\lim,G}\cdot E_G\cdot I_{id}}{\alpha_G(t-c-x_{id})} \tag{4.31}$$

with $x_{id} = \dfrac{\alpha_G\cdot n_B A_G\cdot n'_G}{b}\left(-1+\sqrt{1+\dfrac{2\,b\cdot(t-c)-bs\cdot(n'_G-1)}{\alpha_G\cdot n_B A_G\cdot n'_G}}\right)$ and

$$I_{id} = \frac{b\cdot x_{id}^3}{3} + \alpha_G\cdot n_B A_G\cdot n'_G(t-c-x_{id})^2 - \alpha_G\cdot n_B A_G\cdot s(t-c-x_{id})(n'_G-1)\,n'_G + \alpha_G\cdot n_B A_G\cdot s^2\,(2n'_G-1)(n'_G-1)\,n'_G/6$$

Since n'_G is unknown, a first attempt value corresponding to the total number of wire levels n_G can be set, and equilibrium calculated. If the calculated neutral axis, x_{id}, is compatible with the assumption, the result is correct; otherwise, the procedure continues iteratively by reducing n'_G until a good solution is found.

Note that, if the tensile failure of the fibres is attained, the factor $\varepsilon_{\lim,G}\cdot E_G$ corresponds to the tensile strength of the wires, T_G/A_G.

The conventional elastic limit force of the bi-linear curve (Figure 4.13), $F_{T,e(R)}$, can be calculated from the bending moment related to the masonry first cracking, $M_{T,e(R)}$:

$$F_{T,e(R)} = \frac{\alpha M_{T,e(R)}}{l} = \frac{\alpha}{l}\frac{b\cdot t^2}{6}\cdot f_{m,f}. \tag{4.32}$$

Note that the contribution of the reinforcement is neglected as this is unlikely to contribute to the first cracking resistance of the masonry beam.

For GFRP reinforced masonry, the deflection d_y, based on the experimental evidences, it is taken as $5*l/t$, and $d_u = 1.5*d_y$.

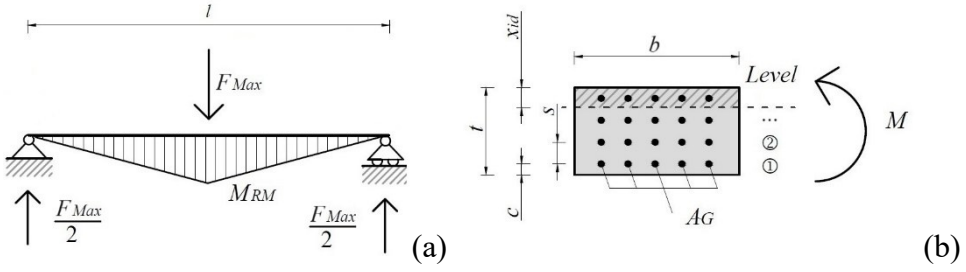


Figure 4.15 "T" samples: (a) static scheme assumed for the evaluation of the ultimate and first cracking load and (b) schematisation of the reinforced masonry cross-section.

4.4.1 Application and validation

The analytical model described in section 4.4 is adopted to evaluate the lateral performances of the CONSTRAIN experimental out-of-plane bending tests of masonry ring beams resumed in section 3.7.

The mechanical characteristics of masonry and GFRP wire considered in the formulations are those already applied in sections 4.1.1, 4.2.1 and 4.3.1. The values of $f_{m,f}$ are calculated from the average first cracking load measured in the experimental tests on the ring beams, solving Eq.(4.32) for $f_{m,f}$. The parameters used in the analytic evaluations are presented in Table 4.8.

The main results are summarized in Figure 4.16 and compared graphically with the experimental capacity curves.

Table 4.8. Main parameters used in the estimation of stiffness and strength of ring beams tested out-of-plane

Main data					
l	[mm]	3000	E_G	[MPa]	72816
η	[-]	48	T_G	[kN]	5.11
α	[-]	4	A_G	[mm^2]	3.8
			s	[mm]	66

		T-R2	T-B1
t	[mm]	350	250
b	[mm]	660	465
E_m	[MPa]	1074.2	1638.6
$f_{m,f}$	[MPa]	0.235	0.442
n_b	[-]	4	6 (5*)
n_G	[-]	5	4
n'_G	[-]	4	3
c	[mm]	43	26
K_e	[N/mm]	4503	1764
$M_{T,e}$	[kNm]	3.17	2.14
I_{id}		1.52.E+8	4.5(3.84*) E+7
x_{id}	[mm]	45.1	33.7 (31.3*)
$M_{T,u(R)}$	[kN]	11.5	10.2 (8.6*)
$F_{T,e}$	**[kN]**	**4.22**	**2.85**
$F_{T,u(R)}$	**[kN]**	**15.4**	**13.6 (11.5*)**
$d_{T,e(R)}$	**[mm]**	**0.94**	**1.62**
$d_{T,y(R)}$	**[mm]**	**42.9**	**60.0**
$d_{T,u(R)}$	**[mm]**	**64.3**	**90.0**

*Assuming the ineffectiveness of the GFRP mesh in the upper bed joint

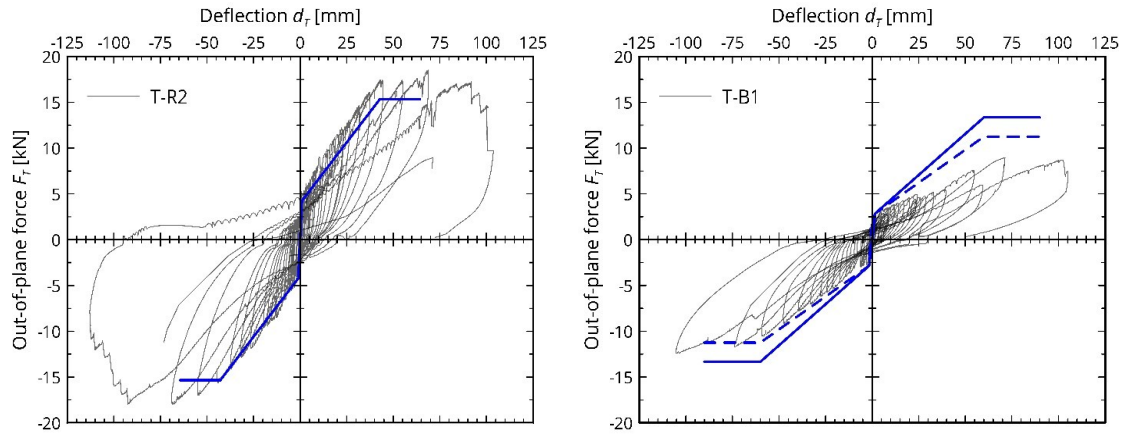


Figure 4.16 Analytic results concerning the out-of-plane tests and comparison with the experimental behaviour

The estimated out-of-plane elastic-plastic behavior of the strengthened beams generally reproduces the experimental response, although with some deviations. The value of $F_{T,u(R)}$ is underestimated by the model, as is the ultimate displacement $d_{B,u(R)}$. This discrepancy is particularly evident for specimen T-B1, where the predicted ultimate strength is

significantly lower than the experimental value. This difference is likely due to the continuous horizontal discontinuity that developed along the upper bed joint near failure, which reduced the effectiveness of the reinforcement mesh embedded in that joint. Conversely, the strength at first cracking is well captured by the model, showing only minimal deviations. The following comparisons refer to the mean peak strength values between the positive and negative loading directions.

For the T-R2 specimen, the model underestimates the strength capacity by 15.8% and the ultimate displacement by 6.7%, while the strength at first cracking is overestimated by 12.5% and the displacement at first cracking by 4.4%.

For specimen T-B1, the model overestimates the strength capacity by 27.1% and the ultimate displacement by 13.0%. However, when the last reinforcement layer is not considered, the overestimation of the strength capacity decreases to 7.5%. In this case, the predicted strength at first cracking matches the experimental result, while the displacement at first cracking is underestimated by 35.2%.

4.5 Analytic estimation of resistance of ring beams with externally-bonded FRP strips

Table 4.9. List of symbols

t	thickness of the masonry cross section
b	width of the masonry cross section
l	beam span
E_m	masonry Young's modulus
E_C	CFRP Young's modulus
α_C	ratio of the CFRP and masonry Young's moduli (modular ratio) = E_C /E_m
A_C	CFRP cross section
f_C	maximum stress of the CFRP
x_{id}	idealised depth of the neutral axis of the cracked, homogenised cross-section
I_{id}	second moment of area of the cracked, homogenised cross-section

The static system of the "C" samples to evaluate the resistance is different for pulling (Figure 4.17a) and pushing (Figure 4.17b). For the positive loading (pushing), the system has free rotation at the extremities (vertical crack is free to occur at the inner side of the wings). In the opposite direction (pulling), the rotations are constrained at the extremities (assuming an effective continuity of the CFRP reinforcement), and a moment hinge is at the midspan (representing the vertical crack in masonry at the inner side).

However, according to the static systems, the resistance F_{Max} is the same for both cases - Eq.(4.33):

$$F_{Max} = 4\frac{M_{RM}}{l} \tag{4.33}$$

being M_{RM} the resisting bending moment and F_{Max} the respective load.

The resisting bending moment M_{RM} of the CFRP reinforced cross section (Figure 4.17c) can be estimated according to Eq.(4.34) assuming, for simplicity, that plane cross-sections remain planar after deflection, perfect bond between the reinforcement and masonry, masonry has zero tensile strength and a linear-elastic response in compression, the CFRP reinforcement has a linear-elastic response in tension until reaching maximum stress f_F.

$$M_{RM} = \frac{f_C \cdot I_{id}}{\alpha_C (t - x_{id})}, \tag{4.34}$$

$$x_{id} = \frac{\alpha_C \cdot A_C}{b}\left(-1 + \sqrt{1 + \frac{2bt}{\alpha_C \cdot A_C}}\right) \tag{4.35}$$

$$I_{id} = \frac{b \cdot x_{id}^3}{3} + \alpha_C \cdot A_C (t - x_{id})^2 \tag{4.36}$$

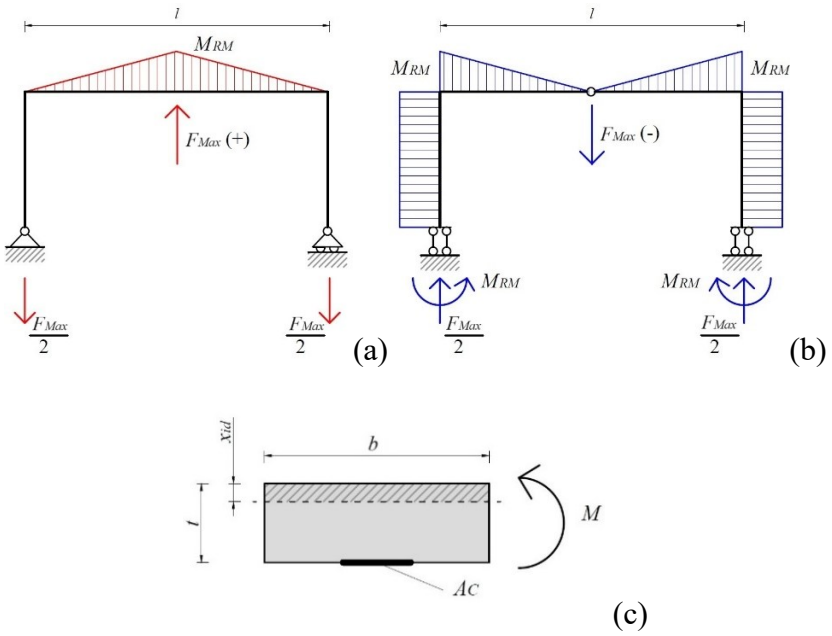


Figure 4.17 "C" samples: static scheme for the evaluation of the resistance in (a) positive and (b) negative directions and (c) reinforced masonry cross-section.

4.5.1 Application and validation

The analytical results in terms of strength capacity are reported in

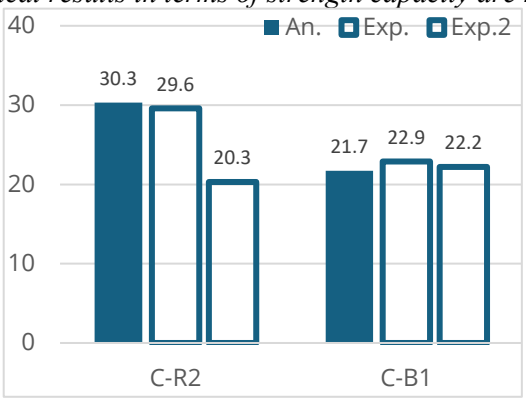


Figure 4.18, also in comparisons with the experimental outcomes.

Main data		
l	[mm]	3650
b	[mm]	1000
E_F	[MPa]	353000
A_F	[mm^2]	66.6
f_F	[MPa]	1314

		C-R2	C-B1
t	[mm]	350	250
E_m	[MPa]	1074.2	1638.6
α_F	[-]	329	215
x_{id}	[mm]	103.8	71.6
I_{id}	[mm^4]	1.7E+09	5.8E+08
M_{RM}	[kN·m]	27.6	19.8
F_{Max}	[kN]	30.3	21.7

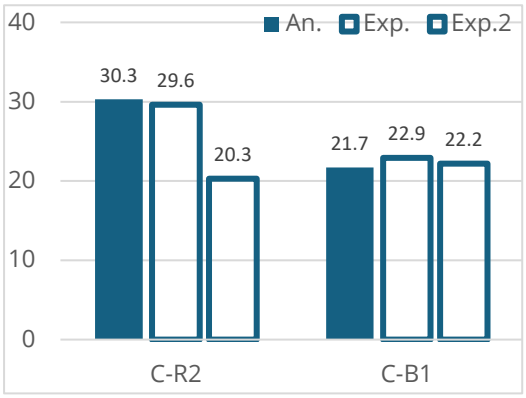


Figure 4.18 Analytic results concerning the out-of-plane tests and comparison with the experimental behaviour.

For specimen C-R2, the estimated strength capacity closely matches the resistance measured in the positive loading direction. When considering the mean strength value between the two loading directions, the model overestimates the resistance by 21.4%. However, the lower resistance observed in the pulling direction was likely due to fibre fracturing near the right clamp, as noted in section3.8.3.

For specimen C-B1, the analytical model shows good agreement with the experimental results, underestimating the strength capacity by only 3.8%.

5 Numerical modelling

In the literature, several numerical analyses have been conducted to simulate the behavior of TRM-strengthened masonry elements, with the aim of assessing the properties of the strengthening system on both in-plane and out-of-plane performance.

As discussed in section 1.4.1, modelling strategies for unreinforced masonry elements are generally based either on discrete element approaches or on continuum-based finite element methods [66–69]. As for unreinforced masonry, discrete modelling of TRM-strengthened masonry involves the explicit representation of the mortar matrix, fibre grid, and interface layers (i.e., grid-matrix and matrix-masonry interfaces), each described with its own nonlinear material law. This approach allows for a detailed investigation of local interactions among components. By contrast, continuum FE approaches typically assume perfect bonding between the components, with the equivalent mechanical properties of the TRM system calibrated through tensile and shear bond tests on TRM coupons. This latter strategy is generally more computationally efficient and thus more suitable for large-scale structural analyses.

Most numerical studies in the literature focus on calibrating material parameters based on laboratory tests, later extending these models to case-study applications. Nonlinear constitutive laws are usually adopted to differentiate between tensile and compressive behavior, commonly using Rankine-type models for tension and Von Mises, Hill for compression or the Smeared Crack (SC) or Concrete Damage Plasticity (CDP) formulations. The textile reinforcement is generally modelled as an elastic-brittle material in tension, while the matrix–masonry and textile-matrix interfaces are described either by a perfect bond or by nonlinear shear bond-slip relationships. When a perfect bond is assumed, debonding is typically represented by calibrating the tensile strength of the TRM coating elements. In case perfect bond is assumed, typically debonding is modelled by appropriately calibrating the tensile strength of the TRM coating elements. The application of DEM or FDEM modelling approaches to the simulation of TRM-strengthened masonry elements is still at an early stage of development [285,286].

The main software used in the literature to model TRM-strengthened masonry are Midas FEA, Diana, Abaqus, Ansys and self-made sub-routines for the FEA software. In-plane performance of TRM was used to simulate both diagonal compression and shear-

compression tests. A series of diagonal compression tests were simulated by Basili et al. [146,287], modelling separately the mortar matrix and the embedded mesh, using the SC model for the former and an elastic-brittle behaviour for the latter. A perfect bond was assumed between the FRCM coating and the masonry and the debonding effect was accounted indirectly with reduced tensile resistance of the textile. The same approach was adopted by Garofano et al. [288] for modelling shear-compression tests, although the numerical simulations did not correctly reproduce the experimental stiffness in the pre-peak branch, resulting in a softer initial response. Differently, Wang et al. [289] modelled the embedded mesh as a grid perfectly bonded to the mortar matrix, which was represented by a shell layer fully connected to the shell elements simulating the masonry. The bond behaviour between fibres and mortar was indirectly accounted for by calibrating an appropriate tensile softening law for the mortar. Corradi et al. [290] proposed a different modelling approach for CRM-strengthened masonry, in which both the masonry and the mortar matrix were represented by solid elements with homogeneous material properties, while the FRP grid bars were modelled using truss elements. Diagonal compression tests were simulated under the assumption of a perfect bond among all components. Castori et al. [291] refined this method by adopting a discrete approach for masonry and reducing the tensile strength of the grid to account for debonding. In contrast, Lignola et al. [292] modelled the TRM as an equivalent homogeneous material, accounting for both the contributions of the mortar matrix and the embedded fibres. Ungureanu et al. [293] adopted three distinct contact interface elements in Ansys (bricks-mortar, TRM-bricks, TRM-mortar) to detect any possible contact separation between the TRM system and the URM panels. The model by Murgo et al. [294] employed nonlinear shear interfaces between the truss elements representing the FRCM grid and the bi-dimensional elements representing the mortar matrix, while a perfect bond was assumed between the mortar and the bricks. The bricks were modelled as linear-elastic bi-dimensional elements, with nonlinear interfaces representing the mortar-brick interaction.

5.1 Detail finite element analysis modelling

In this study, the simulation of the in-plane behaviour of masonry piers and spandrels will be performed, based on a continuum macro-modelling approach.

Some of the specimens that were tested during the project have been modelled with the FEA software Abaqus v. 6.12 [295]. In particular in this Section, the results of the numerical modelling of shear-compression tests on piers and shear-bending tests on spandrels is presented. At the end of each sub-section involving one of the models, a direct comparison between the experimental and numerical behaviour is reported. The modelling considered only the monotonical behaviour of the samples and the numerical curves were compared to the experimental ones.

5.1.1 Material properties

Careful consideration was given to the mechanical characterization of the masonry and reinforcement materials. Concrete, which constitute the material of the top and bottom RC elements, was assumed as an indefinitely elastic and isotropic material.

The mechanical characteristics of materials are summarized in *Table 5.1*.

Table 5.1. Mechanical properties of the materials used in the models

Material	Elasticity modulus [MPa]	Density [kg/m^3]	Poisson modulus ν [-]
Reinforced concrete	40000	2500	0.2
Stone masonry	1074	2100	0.43
Single leaf brick masonry	2183	1800	0.43
Two leaf brick masonry	2183	1800	0.43
Reinforcement plaster	9000	1800	0.43

5.1.2 Post-failure behaviour

The masonry and the reinforcement were described in the form of an equivalent, homogeneous and isotropic material having a linear elastic behaviour up to failure, based on the test results and on what reported in scientific literature [26,152]. The post-cracked behaviour was based on an appropriate calibration of the Concrete Damaged Plasticity (CDP) mechanical model. This mechanical model, developed by Lubliner et al. 1989 [296] for RC components and further elaborated by Lee and Fenves (1998) [297], well applies to materials with a quasi-brittle behaviour such as masonry. Recent examples for

masonry structural systems can be found in Pandey et al. and Xiong et al. (2014) [298,299]. In the CDP model, the yield surface function considers different evolution of strength under tensile and compressive stresses (Figure 5.1). In this study, the main input parameters were defined in accordance with [152]. The dilation angle φ and the ratio fb0/fc0 between the equibiaxial compressive failure stress to the uniaxial compressive one, specifically, were assumed equal to 40° and 1.16 respectively. The ratio of the second stress invariant on the tensile meridian (K) was assumed equal to 1, while the eccentricity parameter, that defines the rate at which the function approaches the asymptote was assumed equal to 0.1. Tension stiffening effects and post-cracked compressive behaviour for the masonry were described in the form of stress-strain post-failure relationships in Table 5.2.

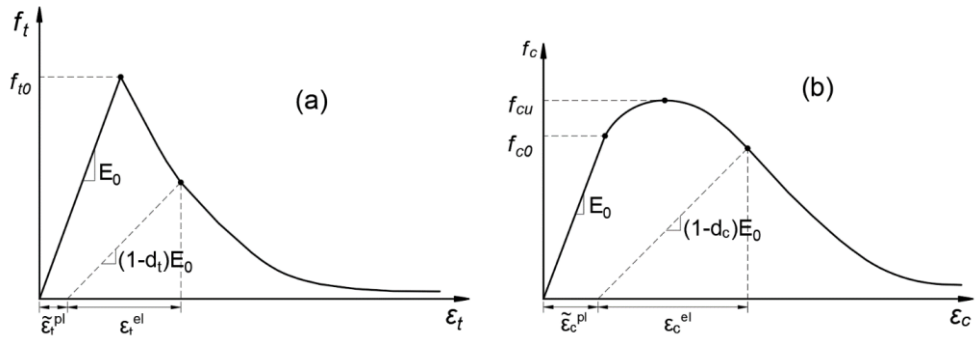


Figure 5.1 Mechanical behaviour of masonry under uniaxial (a) tension and (b) compression (Abaqus)

Table 5.2: Tension stiffening stress-strain multilinear relationships for the masonry

Post-failure behaviour (masonry)			
Stone masonry			
Tensile behaviour		Compressive behaviour	
ft (MPa)	εt,pl(-)	fc (MPa)	εc,pl(-)
0.13	0	2.5	0
0.13	0.0042	3.5	0.0035
0.0013	0.01	3.5	0.005
Single leaf brick masonry			
Tensile behaviour		Compressive behaviour	
ft (MPa)	εt,pl(-)	fc (MPa)	εc,pl(-)
0.15	0	2	0
0.15	0.005	4	0.002
0.08	0.015	5	0.0035
		6.25	0.0069
		6.86	0.0105
		6	0.011
		1	0.014
Two leaf brick masonry			
Tensile behaviour		Compressive behaviour	
ft (MPa)	εt,pl(-)	fc (MPa)	εc,pl(-)
0.12	0	2	0
0.12	0.001	4	0.002
0.01	0.01	5	0.0035
		6.25	0.0069
		6.86	0.0105
		6	0.011
		1	0.014

5.1.3 Modelling of the reinforcement coating

In order to represent the reinforcement, two modelling approaches were considered and compared to reduce the computational complexity of the model. Initially, the modelling involved the simulation of the CRM tensile tests presented in Gattesco *et al*. [202] (Figure 5.2). A first model was constituted by 4 nodes shell elements (S4R), representing the mortar, with the GFRP mesh acting as a rebar layer embedded in the middle of the shell

ply as a reinforcement. A second model was realized with an equivalent homogeneous material, constituted by 3D solid, 8-node brick elements (C3D8R). The post-cracked behaviour was based on an appropriate calibration of the CDP mechanical model.

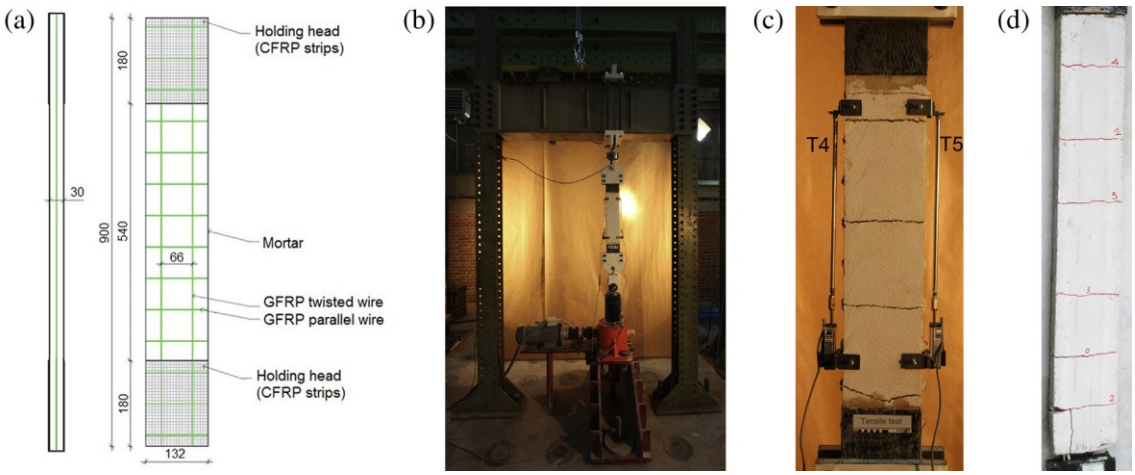


Figure 5.2 Tensile test: (a) GFRP reinforced mortar layer samples, (b) test setup and view of samples (c) and (d) crack pattern at the end of the tests

Considering the results given by the two different approaches and the computational costs, the equivalent homogeneous material proved to be a better solution. The comparison between the numerical result obtained with the latter model and the experimental curves is reported in Figure 5.3.

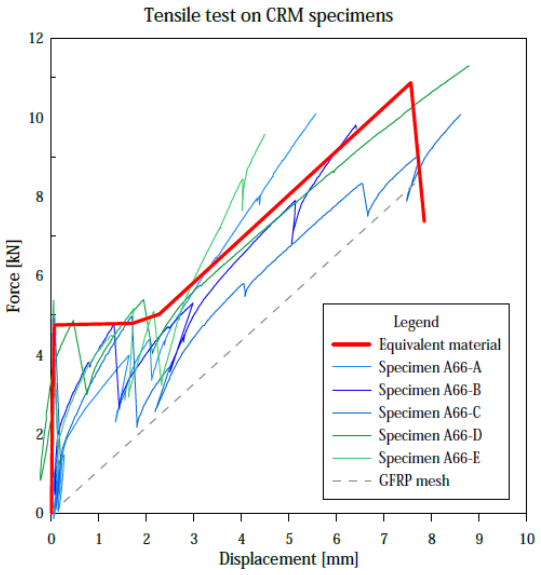


Figure 5.3 Comparison between the numerical and the experimental curves of the CRM tensile tests

The comparison shows a good correlation between the model and the experimental behaviour; thus, this type of modelling was adopted for all the reinforced specimens. The

brick elements representing the reinforcement were connected to the masonry elements with a tie constrain, which connects two separate surfaces together so that there is no relative motion between them. The mesh defined for the reinforced plaster was compatible with the masonry mesh, with prismatic elements having a square section and a side equal to 66 mm, by the thickness of the coating, equal to 35 mm for the rubblestone masonry specimens and 30 mm for the brick masonry ones.

Tension stiffening effects and post-cracked compressive behaviour of the reinforcement were described in the form of stress-strain post-failure relationships in Table 5.3.

Table 5.3. Tension stiffening stress-strain multilinear relationships for the reinforcement

Post-failure behaviour (reinforcement)			
Stone masonry			
Tensile behaviour		Compressive behaviour	
f_t (MPa)	$\varepsilon_{t,pl}$(-)	f_c (MPa)	$\varepsilon_{c,pl}$(-)
1.30	0	18	0
1.30	0.005	20	0.0005
2.30	0.02	20	0.002
0.1	0.021		
Single leaf brick masonry			
Tensile behaviour		Compressive behaviour	
f_t (MPa)	$\varepsilon_{t,pl}$(-)	f_c (MPa)	$\varepsilon_{c,pl}$(-)
2.26	0	22	0
2.26	0.005	30	0.0004
3.2	0.0187	30	0.004
0.1	0.02		
Two leaf brick masonry			
Tensile behaviour		Compressive behaviour	
f_t (MPa)	$\varepsilon_{t,pl}$(-)	f_c (MPa)	$\varepsilon_{c,pl}$(-)
2.26	0	22	0
2.26	0.005	30	0.0004
3.2	0.0187	30	0.004
0.1	0.02		

5.2 Shear-compression numerical models

In accordance with the test setup presented in 3.4.3, the numerical models of the shear-compression test piers consisted of two concrete beams, the masonry wall and the reinforcement were derived. Concrete, masonry, and reinforcement elements were described in the form of 3D solid, 8-node brick elements available in the ABAQUS/Standard element library (C3D8R). A regular mesh pattern with a constant mesh size of 66 mm was used. The interaction between the elements constituting the masonry and the concrete components, having coincident mesh nodes at the contact surfaces, was guaranteed by means of merged nodes on the boundary of the adjacent elements.

The upper stiff steel element was described in the form of a rigid body constraint about a reference node. The latter acted on the nodes of the elements of the top concrete beam, lying on a X-Z plane, restraining the out of plane translations in the Z-axis direction, and the rotations about the three axes (uz = urx = ury = urz = 0).

To account for the deformations of the steel base plate that were observed during the experimental tests, in the numerical model a series of spring elements, directed in the Y direction, rigidly connected to the ground, were modelled. Their stiffness was determined considering a simplified static scheme, with the steel plate performing as a fixed beam, in correspondence of the anchor bolts and loaded by two concentrated forces located at the points where the RC beam brackets are welded to the plate.

The nodes located at the base of the model were constrained to prevent translations in the X an Z directions ($u_x = u_z = 0$), as displayed in Figure 5.4.

A quasi-static dynamic implicit analysis, considering geometric nonlinearities, in displacement control was carried out to overcome convergence problems due to the formation of cracks. An appropriate loading time history was defined to avoid dynamic effects, thus maintaining a static behaviour. The analysis was performed in two steps. In the first step, uniformly distributed vertical loads were applied on the upper nodes of the elements of the top concrete beam, acting as an equivalent vertical pressure (σ_0=0.5 MPa). Gravity loads were also considered. In the second step, the static loads from the previous analysis were maintained and a horizontal lateral displacements u_x, with a monotonic linear rising time history, was imposed to the nodes of the top concrete element, as

presented in Figure 5.4. For the stone masonry, the thickness of each element was equal to 0.0875 m.

5.2.1 Stone masonry piers

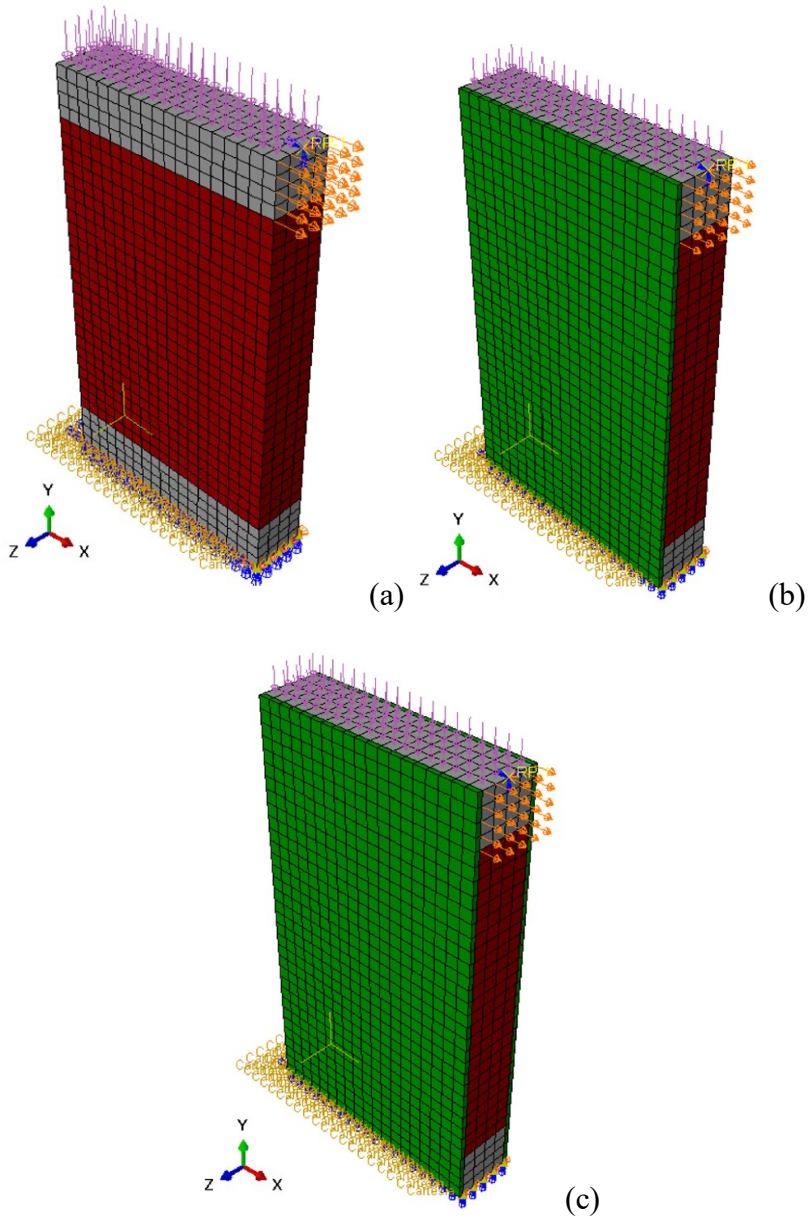


Figure 5.4 Numerical model FE-P-R2U (a); FE-P-R2R-1 (b) and FE-P-R2R-2 (c)

5.2.1.1 Unreinforced FEM

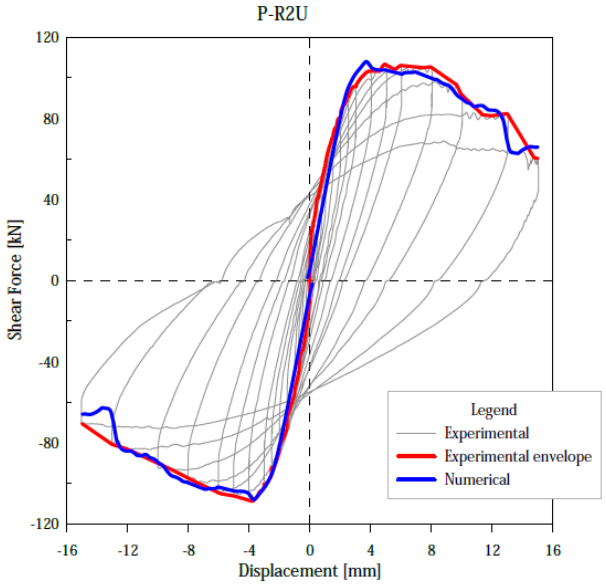


Figure 5.5 Model FE-P-R2U: comparison between numerical and experimental curves of shear force - top displacement

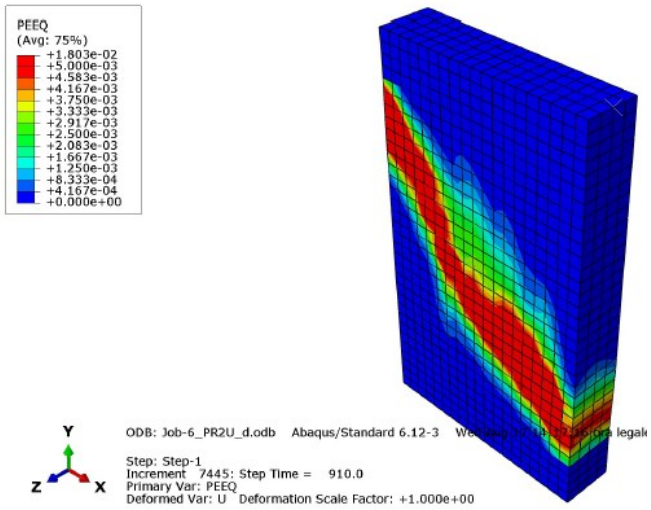


Figure 5.6 Model FE-P-R2U: equivalent plastic strain distribution at the end of the simulation.

Imposed Displacement	Observation
2.5 mm	First vertical crack at the middle of the wall
4 mm	Peak resistance
5 mm	The crack became diagonal, indicating a shear response
15 mm	Failure due to diagonal shear cracking. Damage is concentrated in a principal crack.

From the diagram reported in Figure 5.5, a good agreement between the numerical results and the experimental measures can be observed.

Considering the experimental trend, a good calibration of the masonry parameters was obtained. The numerical model well fits the shear force peak, and quite well the descending branch in positive and negative loading directions. It has to be considered that the equivalent homogenous material used for the masonry cannot take into account for the interaction between the stone elements and the mortar, thus the distribution of the crack is linear and perpendicular to the main tensile direction.

It can also be noted that there are some shear force drops at numerical level. These occurred at significant crack propagation during the analysis.

5.2.1.2 One side reinforced FEM

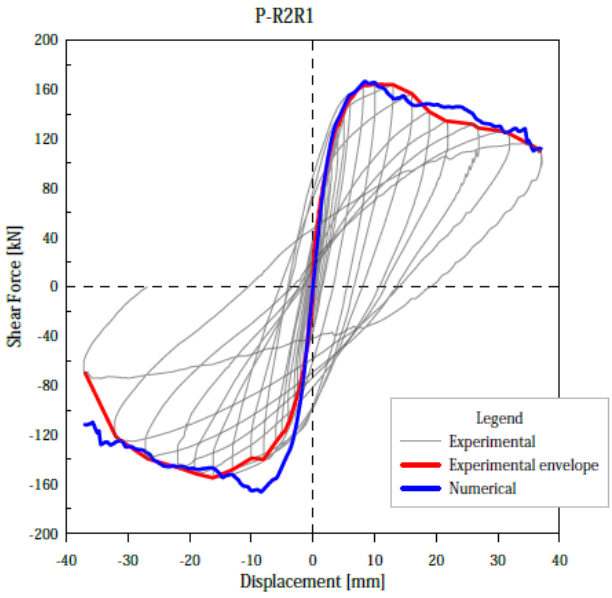


Figure 5.7 Model FE-P-R2R-1: comparison between numerical and experimental curves of shear force – top displacement

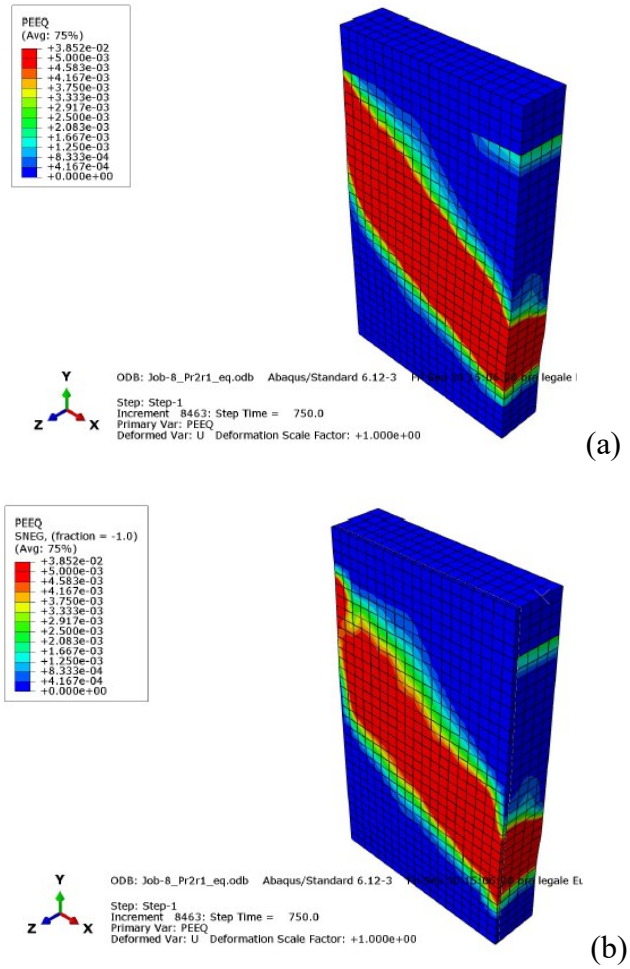


Figure 5.8 Model FE-P-R2R-1: equivalent plastic strain distribution at the end of the simulation on the masonry side (a) and on the reinforced side (b)

Imposed Displacement	Observation
2.6 mm	First vertical crack at the middle of the wall on the coating and the unstrengthened side.
2.6 mm – 6 mm	The vertical crack propagates.
6 mm – 14 mm	Peak resistance is reached. The main vertical crack in the masonry became diagonal. The damage is more distributed in the reinforcement, but still with a diagonal pattern.
14 mm – 33 mm	The diagonal shear crack propagates untill failure. Damage is more distributed than in the unreinforced specimen.

As can be noted in Figure 5.7, a good agreement between experimental and numerical trends was reached. A good calibration of the reinforced parameters was obtained, maintaining the masonry behaviour of the unreinforced specimen. The numerical model well fits the shear force peak and the descending branch in positive direction. The

descending branch in the negative direction fits well the experimental trend, in terms of peak shear force, and quite well the trend after the peak. It has to be considered that the analysis was monotonic and could not consider the accumulation of damage that occurred in the cyclic test.

5.2.1.3 Two side reinforced FEM

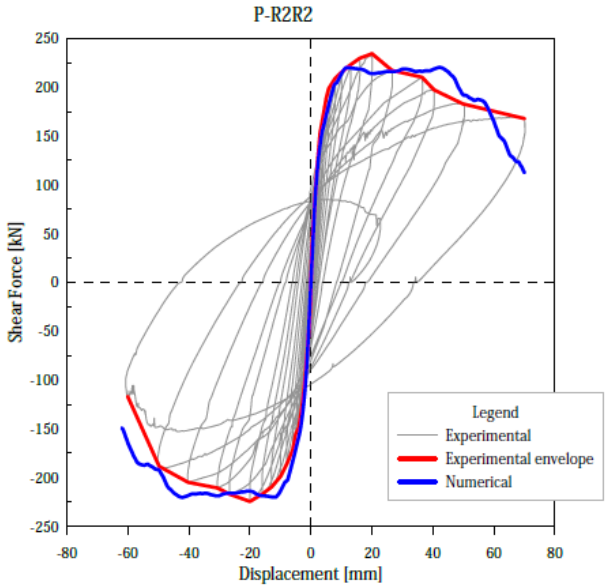


Figure 5.9 Model FE-P-R2R-2: comparison between numerical and experimental curves of shear force – top displacement

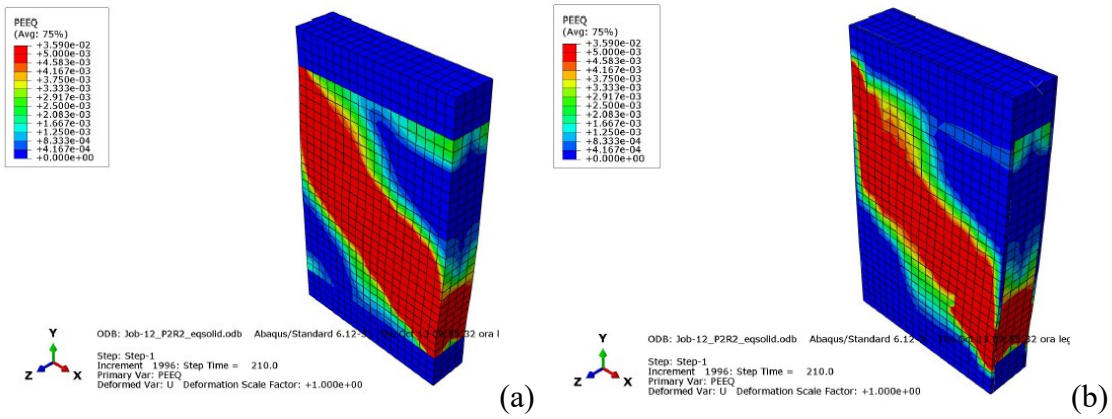


Fig. 1: Model FE-P-R2R-2: equivalent plastic strain distribution at the end of the simulation on the masonry side (a) and on the reinforced side (b)

Imposed Displacement	Observation
4 mm	First horizontal crack appeared at the top corner between masonry and RC top beam.
8 mm	From the horizontal crack, an inclined propagation caused the appearing of a diagonal crack which interest the whole high of the masonry elements.
10 mm – 18 mm	Peak resistance is reached. The vertical crack and the horizontal ones (at the top and at the base of the masonry) propagation indicates a combinate shear and flexural failure.
18 mm – 40 mm	The diagonal cracks propagates vertically, causing a spread of damage in the specimen. As seen in the experimental trend, a combination of shear and flexural mechanisms can be observed.
40 mm – 70 mm	Damage continued untile failure

As can be noted in Figure 5.9, a good agreement between experimental and numerical trends was reached. Material behaviours remained the same as previous simulations. The shear force peak is slightly underestimated compared to the experimental one (-5.9%), but the numerical descending branch fits quite well the trend obtained experimentally. It is important to note that, particularly in the negative direction, it is well estimated the moment and the drop in resistance that occurs after the breakage of the GFRP mesh.

5.2.2 Single leaf brick masonry specimens

To resemble the experimental test, the concrete beams used in the unreinforced model had a width of 350 mm, while the reinforced sample's concrete beams had a width of 250 mm (Figure 5.10). The width of the masonry has been modified to 0.25 m and the thickness of each element is equal to 62.5 mm.

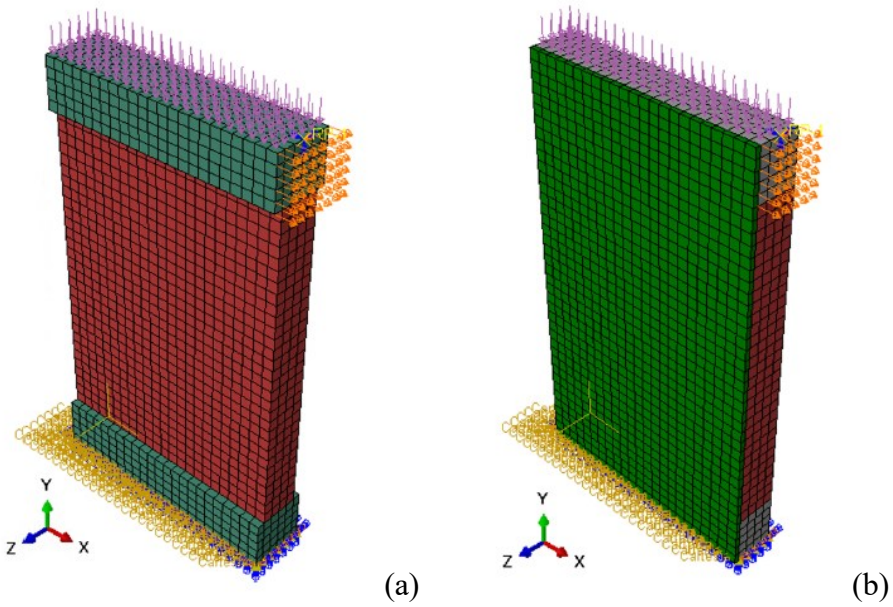


Figure 5.10 Numerical model FE-P-B1U (a); FE-P-B1R (b)

5.2.2.1 Unreinforced FEM

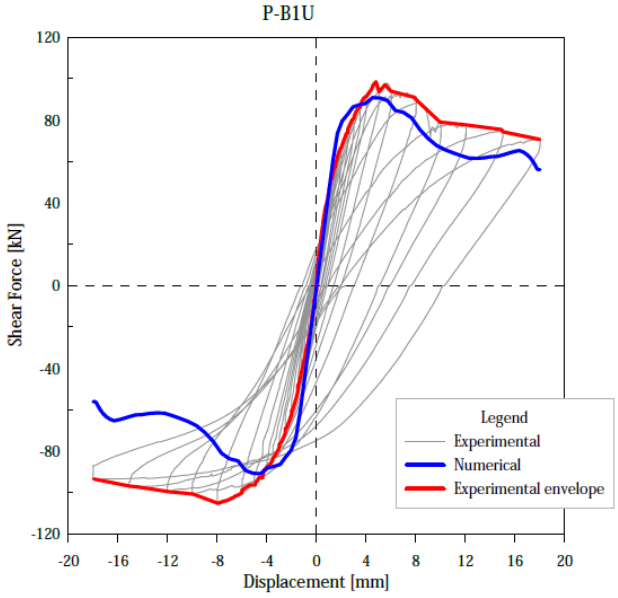


Figure 5.11 Model FE-P-B1U: comparison between numerical and experimental curves of shear force – top displacement

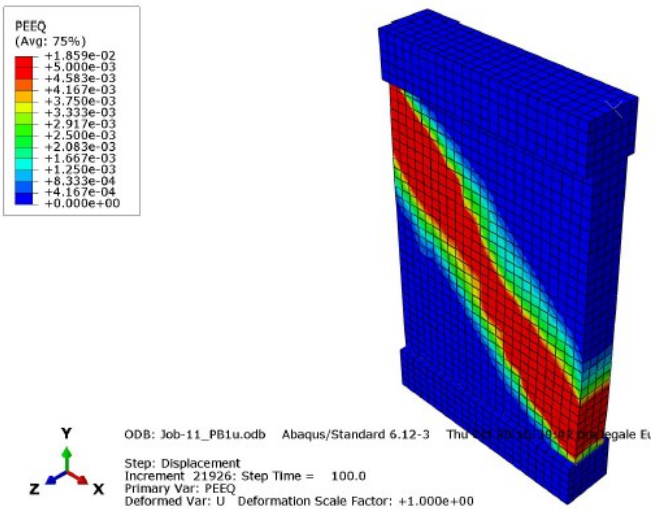


Figure 5.12 Model FE-P-B1U: equivalent plastic strain distribution at the end of the simulation

Imposed Displacement	Observation
1.5 mm	First horizontal crack appeared at the top left corner.
2 mm	A central vertical crack formed at the centre of the specimen, while the horizontal cracks grew.
3.5 mm	The vertical crack propagates diagonally, indicating a shear failure.
4 mm – 6 mm	Peak force is reached.
6 mm – 18 mm	The diagonal crack continued propagating until the end of the test.

As can be noted in Figure 5.11, a quite good agreement between experimental and numerical trends was reached. The shear force peak is fairly underestimated compared to the experimental one (-7.7% in the positive side and -13.6% in the negative one), but the numerical descending branch fits quite well the trend obtained experimentally, particularly for the positive direction. The homogenization of the material allows only a partial capture of the crack pattern, which experimentally occurs in the mortar joints, but it is adequate to identify the failure mechanism as early as the first crack appears.

5.2.2.2 One side reinforced FEM

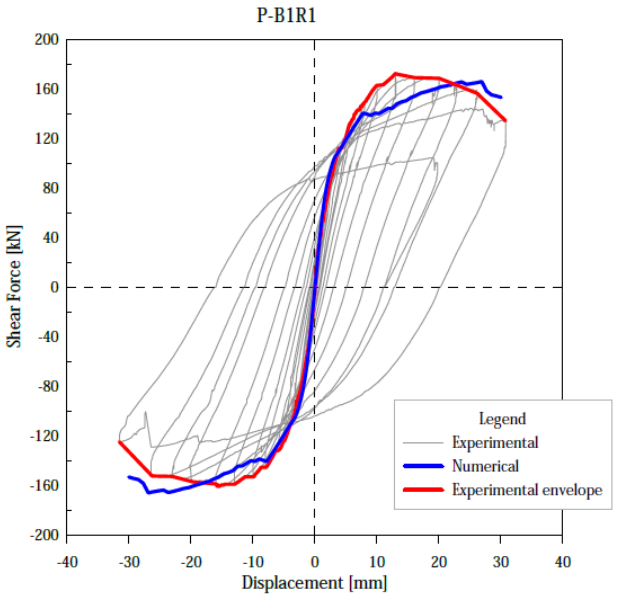


Figure 5.13 Model FE-P-B1R: comparison between numerical and experimental curves of shear force – top displacement

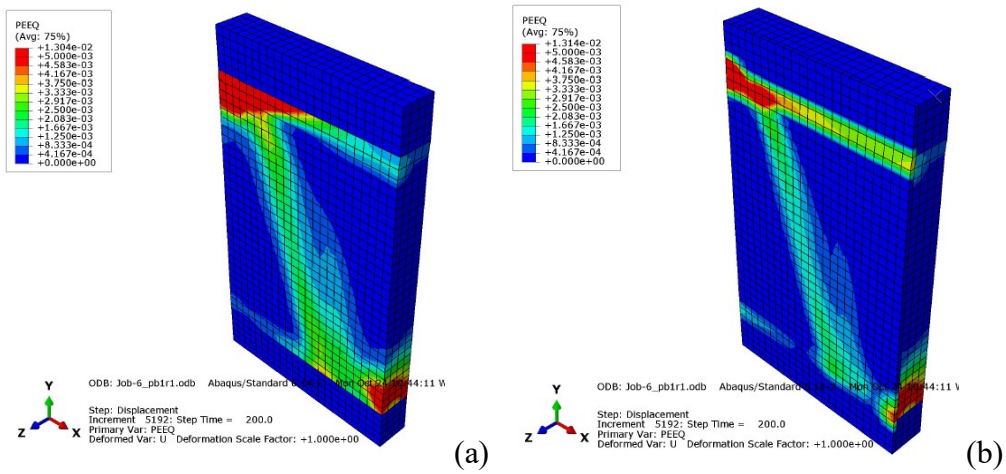


Figure 5.14 Model FE-P-B1R: equivalent plastic strain distribution at the end of the simulation on the masonry side (a) and on the reinforced side (b)

Imposed Displacement	Observation
3 mm	First horizontal crack appeared at the top left corner both in the reinforcement and in the masonry.
3 mm – 14 mm	The horizontal crack propagates horizontally, with a pure bending failure behaviour.
14 mm – 33 mm	The horizontal cracks propagate both in the top and in the bottom area of the specimen, in addition a diagonal damage is present.

As can be noted in Figure 5.13, a good agreement between experimental and numerical trends was reached. The shear force peak fits the experimental one, but not at the same displacements. The initial stiffness decrease fits well the experimental behaviour and the numerical descending branch happens at the same time as the experimental one, which occurs when the GFRP mesh tears. Through the analysis of the crack pattern, the first failure mechanism that occurs is of a flexural type.

5.2.3 Two leaf brick masonry specimens

The dimensions used in these models are the same as the FE-P-B1 models.

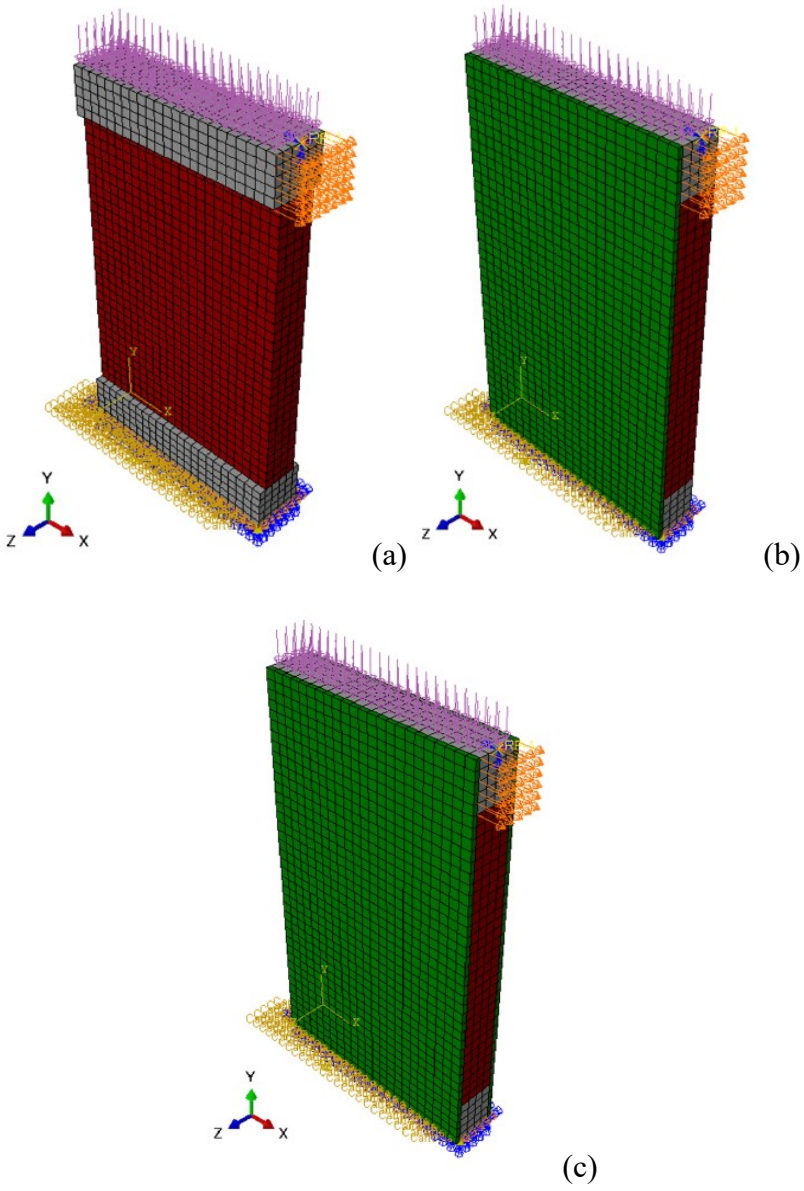


Figure 5.15 Numerical model FE-P-B2U (a); FE-P-B2R-1 (b) and FE-P-B2R-2 (c)

5.2.3.1 Unreinforced FEM

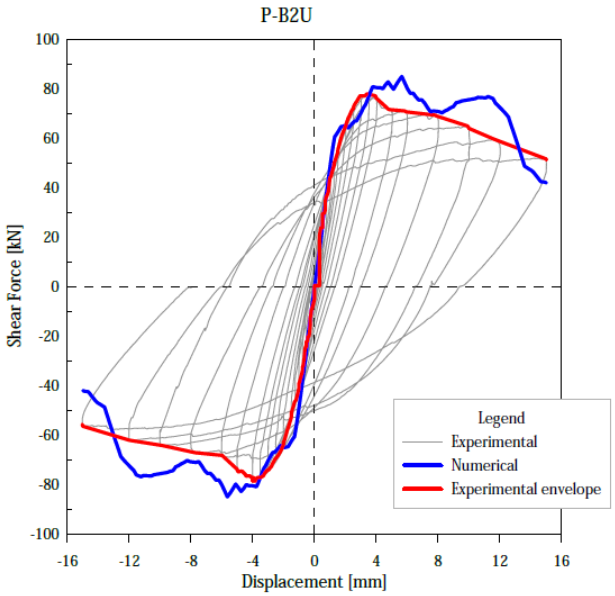


Figure 5.16 Model FE-P-B2U: comparison between numerical and experimental curves of shear force – top displacement

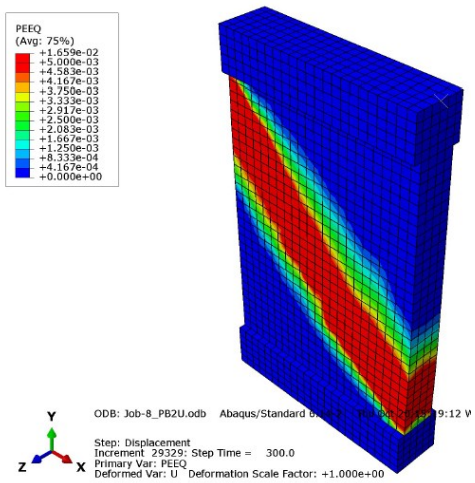


Figure 5.17 Model FE-P-B2U: equivalent plastic strain distribution at the end of the simulation

Imposed Displacement	Observation
2 mm	The first diagonal crack started creating at the centre of the specimen.
4 mm – 6 mm	Peak resistance is reached.
6 mm – 15 mm	The diagonal crack propagates until failure, indicating a shear failure mechanism.

As can be noted in Figure 5.16, a fairly good agreement between experimental and numerical trends was reached. The masonry behaviour is the same used for the single-leaf specimen, scaled on the experimental resistance obtained for the double-leaf masonry. The shear force peak fits the experimental one, with a slight overestimation (+8.2%). The numerical descending branch fits well the trend obtained experimentally, both for the positive and the negative direction.

5.2.3.2 One side reinforced FEM

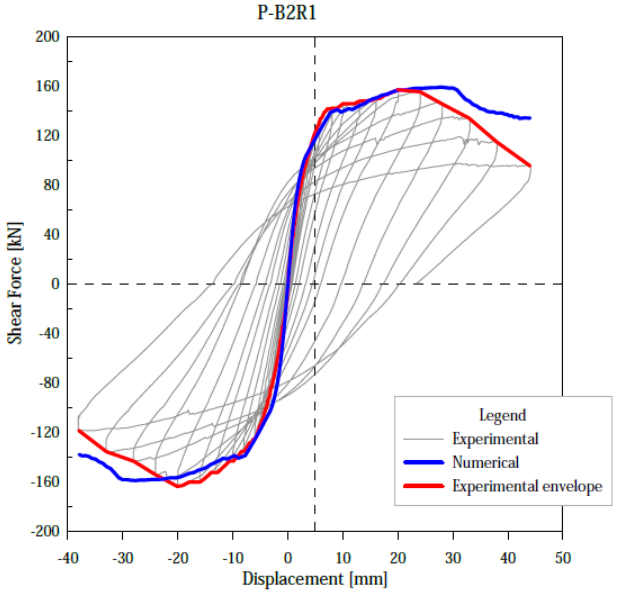


Figure 5.18 Model FE-P-B2R-1: comparison between numerical and experimental curves of shear force – top displacement.

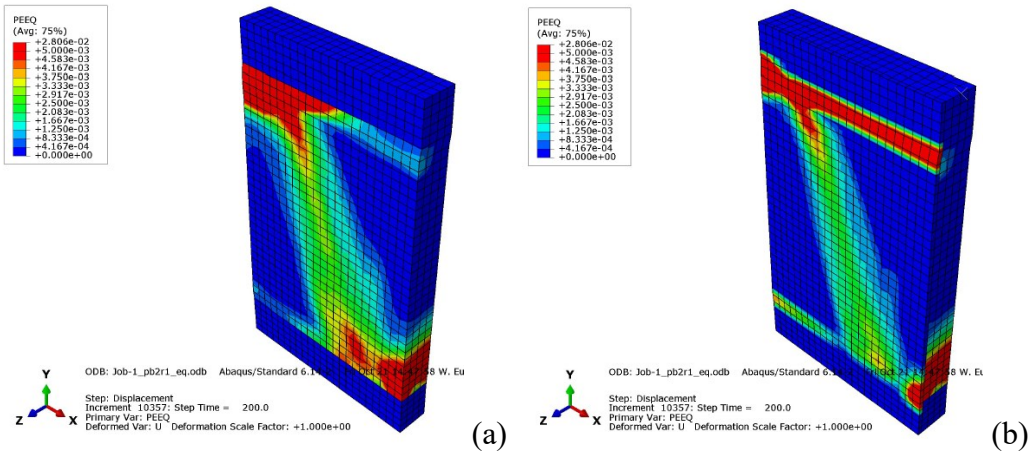


Figure 5.19 Model FE-P-B2R-1: equivalent plastic strain distribution at the end of the simulation on the masonry side (a) and on the reinforced side (b)

Imposed Displacement	Observation
2 mm	The first horizontal crack started creating at the top of the specimen.
2 mm – 8 mm	Propagation of horizontal cracks.
8 mm – 30 mm	The peak force is reached, the horizontal cracks propagated and a diagonal damage is observed, starting from the top corner. Flexural failure is dominant.
30 mm – 40 mm	The cracks propagated further, with reduce stiffness in shear-displacement trend.

As can be noted in Figure 5.18, a good agreement between experimental and numerical trends was reached. The masonry behaviour is the same used for the unreinforced specimen, the reinforcement behaviour remains the same as the previous analysis. The shear force peak fits the experimental one, although the descending branch is slightly underestimated and it happens at a higher displacement value. The flexural failure mode is correctly evaluated with the numerical model.

5.2.3.3 Two side reinforced FEM

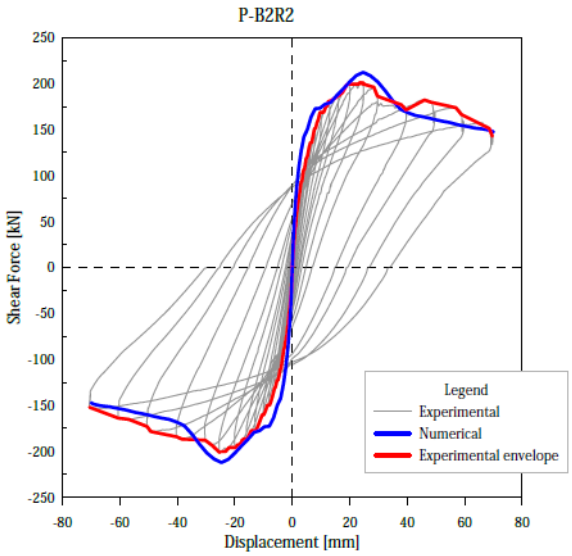


Figure 5.20 Model FE-P-B2R-2: comparison between numerical and experimental curves of shear force – top displacement

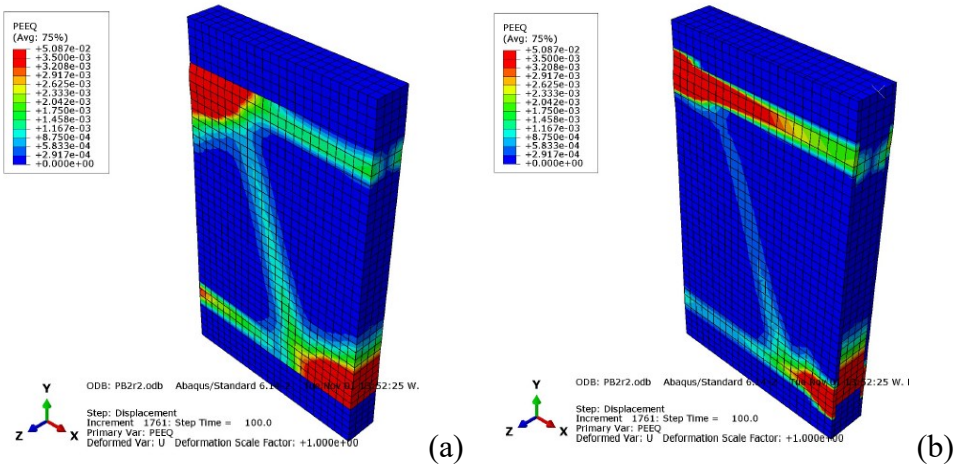


Figure 5.21 Model FE-P-B2R-2: equivalent plastic strain distribution at the end of the simulation on the masonry side (a) and on the reinforced side (b)

Imposed Displacement	Observation
2 mm	The first horizontal crack started creating in the reinforcement at the top of the specimen.
2 mm – 10 mm	The horizontal crack propagated, affecting the entire width of the sample.
25 mm	Peak resistance is reached. A horizontal crack at the base of the specimen started propagating. Flexural failure is dominant.
30 mm	A diagonal damage started propagating in the specimen.
30 mm – 70 mm	Cracks continue to propagate both in the corner of the specimen and in diagonal, until the final displacement is reached.

As can be noted in Figure 5.20, a good agreement between experimental and numerical trends was reached. The masonry behaviour is the same used for the unreinforced specimen and the reinforcement behaviour remains the same as previous analysis. The shear force peak fits the experimental one, as well as the descending branch. The flexural failure mode is correctly evaluated with the numerical model.

5.3 Shear-bending numerical models

In accordance with the test setup presented in section 3.5.3, the numerical models of the shear-bending test spandrels consisted of two masonry piers, modelled from mid-height of the lower opening to mid-height of the upper one, the masonry spandrel, four concrete beams, two steel beams and the reinforcement. Concrete, masonry, steel and the reinforcement were described in the form of 3D solid, 8-node brick elements available in the ABAQUS/Standard element library (C3D8R). A regular mesh pattern with a constant mesh size of 66 mm was used. The structural interaction between elements constituting the masonry and the concrete components, having coinciding mesh nodes at the contact surfaces, was guaranteed by means of merged nodes on the boundary of the elements.

The specimen was restrained by two rotational hinges, the first one allowed rotation and sliding and the latter one allowed only rotation. In the numerical model these conditions were represent by restraining the steel beam nodes located in the points where the hinges were positioned in the experimental specimen.

For the stone specimens, the wooden lintel was modelled with an orthotropic material, considering average mechanical properties of spruce timber. The connection with the masonry was assured by rigid connectors at the top of the lintel, which guaranteed solidary displacements between the elements. The other lintel surfaces were modelled in contact with the masonry, so that there was no interpenetration. For the brick specimens, the lintel was modelled with the same behaviour as the masonry.

A quasi-static dynamic implicit analysis, considering geometric nonlinearities, in displacement control was carried out to overcome convergence problems due to the formation of cracks. An appropriate loading time history was defined to avoid dynamic effects, thus maintaining a static behaviour. The analysis was performed in two steps. In the first step, uniformly distributed vertical loads were applied on both piers on the upper nodes of the top concrete beams, acting as an equivalent vertical pressure (σ_0=0.33 MPa). Gravity loads were also considered.

In the second step, the static loads from the previous analysis were maintained and a vertical lateral displacement u_y, with a monotonic linear rising time history, was imposed to the nodes at the ends of the steel beams located under the lintel. The results obtained in this way are equivalent to the ones obtained by applying the forces, experimentally measured and applied with the two actuators, at the steel beam ends (as it has been done

in the experimental test). The applied displacements are derived from the experimentally measured ones, corresponding on the effects given by applying the external forces from the two actuators.

The spandrel drift was evaluated by considering the vertical displacements of the nodes at base of the two steel beams under the lintel, and dividing the difference between these two displacements by the spandrel span. The shear force was evaluated at the mid-section of the spandrel, with the Free Body Cut feature provided by the software.

5.3.1 Stone masonry specimens

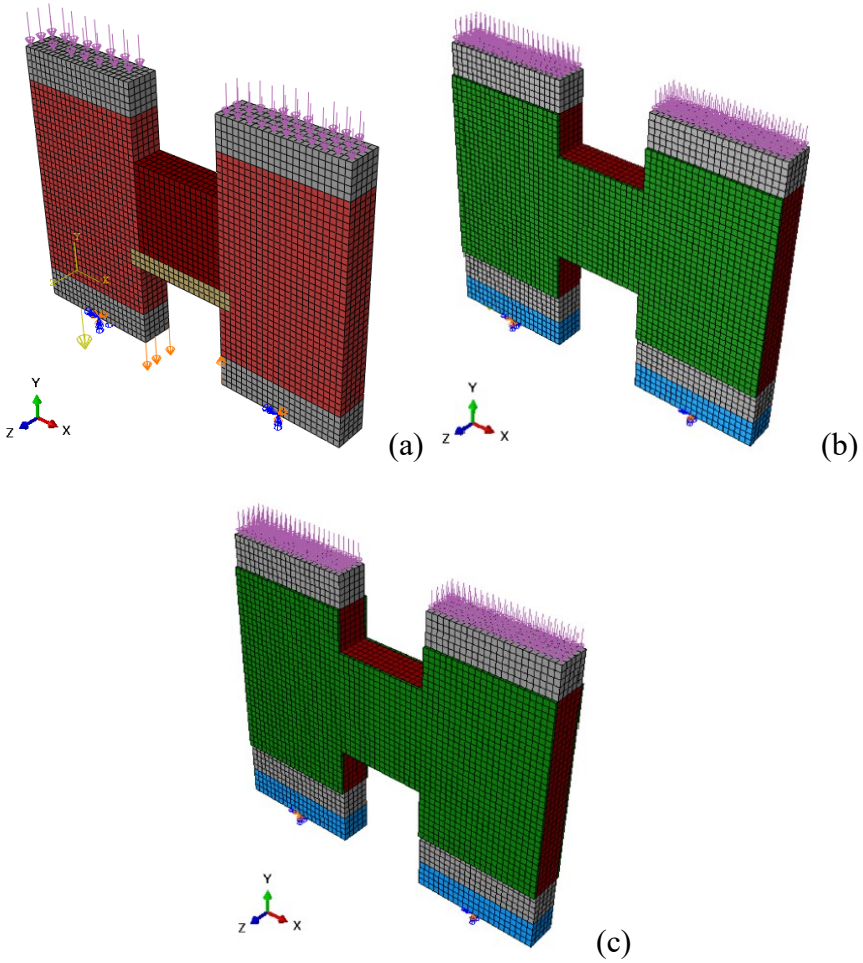


Figure 5.22 Numerical model FE-S-R2U (a); FE-S-R2R-1 (b) and FE-S-R2R-2 (c)

5.3.1.1 Unreinforced FEM

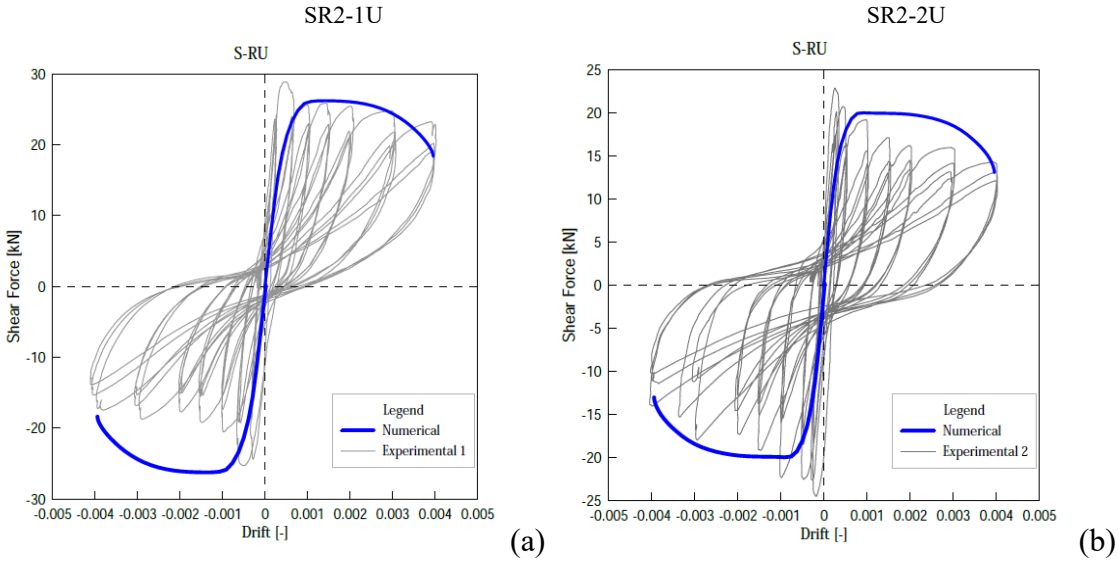


Figure 5.23 Model FE-S-R2U: comparison between numerical and experimental curves of shear force – spandrel drift for the first specimen SR2-1U (a) and the second one SR2-2U(b)

The SR2-1U specimen is the spandrel that, after the unreinforced test, has been reinforced on one side, while the SR2-2U specimen has been reinforced on both sides.

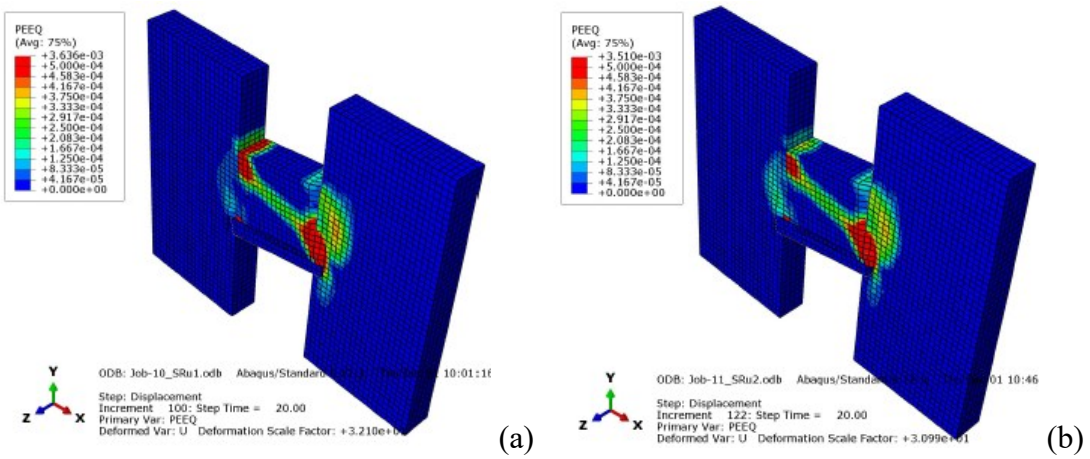


Figure 5.24 Model FE-S-R2U: equivalent plastic strain distribution at the end of the simulation for the specimen 1 (a) and the specimen 2 (b)

Drift	Observation
0.03%	A first vertical crack compared at the top angle of the spandrel
0.08%	The diagonal crack formed in the spandrel.
0.1%	The peak shear force is reached. In this moment both the vertical and the diagonal cracks are wider.
0.4%	The cracks grew until the end of the test, a damage is also observed on the interface between the masonry and the wood lintel

From the diagrams reported in Figure 5.23, a good agreement between the numerical results and the experimental measures can be observed. The two specimens differ in tensile strength by about 20%, in fact the second one has lower experimental force peak (80% lower than the sample 1 shear force peak).

Considering the experimental trends, a good calibration of the masonry parameters was obtained. The numerical model fits the descending branch in positive and negative loading directions, while a slight under-estimation is observed for the shear force peak (about -10%). It can be noted an underestimation of the stiffness in the initial elastic phase, despite a higher elastic modulus considered compared to the experimental results in the compression test on masonry. This can be explained considering the experimental trend of the compression tests, bearing in mind that the spandrel is subjected to low compressions, and noted that in the first phase (with low compression) the behaviour is stiffer. It has to be considered that the equivalent homogenous material used for the masonry cannot take into account for the interaction between the stone elements and the mortar, thus the distribution of the crack is linear and perpendicular to the main tensile direction.

The numerical descending branch of the negative curve of specimen SR2-1U and of that of the positive curve of specimen SR2-2U evidence an overestimation over the experimental results, probably due to damage accumulated at the formation of the first cracks.

5.3.1.2 One side reinforced FEM

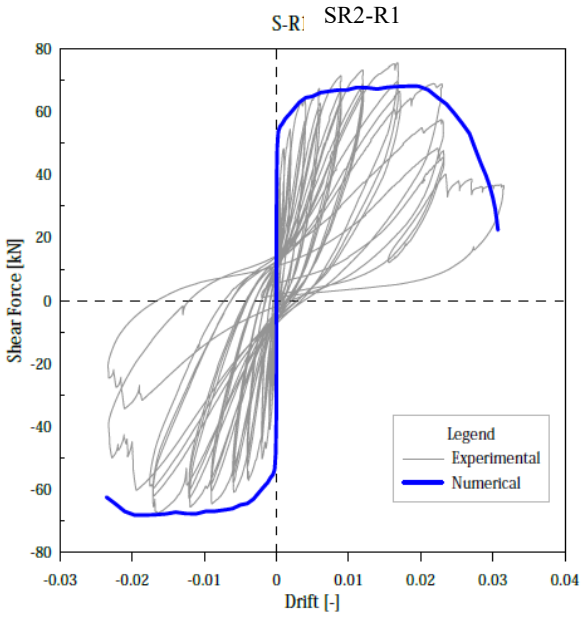


Figure 5.25 Model FE-S-R2R-1: comparison between numerical and experimental curves of shear force - spandrel drift.

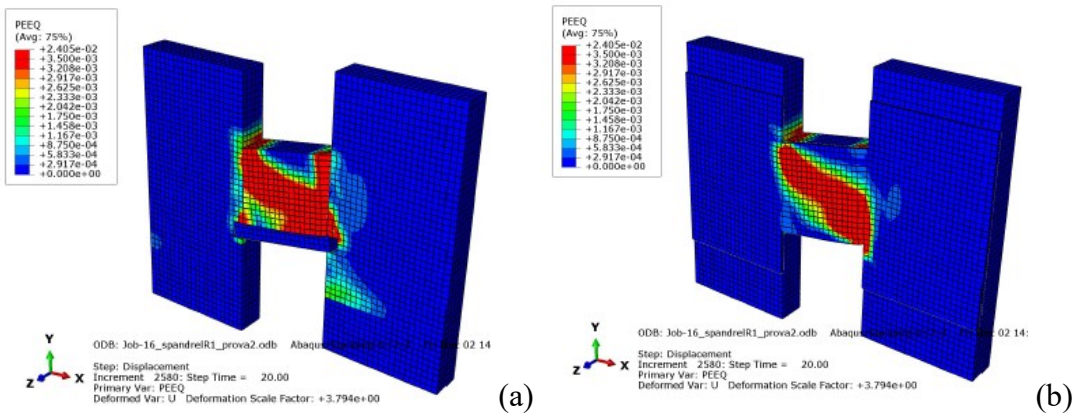


Figure 5.26 Model FE-S-R2R-1: equivalent plastic strain distribution at the end of the simulation on the masonry side (a) and on the reinforced side (b)

Drift	Observation
0.10%	Two cracks formed at the top corner and on the bottom corner of the spandrel, more significantly on the masonry elements.
0.15%	A diagonal crack started forming both on the masonry and on the reinforcement
0.15% - 0.70%	The cracks grew and spread over the entire area of the spandrel
0.70% - 3%	Progressive damage until failure of the GFRP mesh.

As can be noted in Figure 5.25, a good agreement between experimental and numerical trends was reached. The masonry behaviour is the same used for piers, the reinforcement behaviour remains the same as previous analysis. The shear force peak fits well the experimental one, in this case the evaluation of the stiffness is better. The positive peak is slightly underestimated (-9.8%), but the negative one is evaluated correctly. The numerical descending branches fit well the experimental ones, as well as the resistance drop occurred at the mesh rupture.

5.3.1.3 *Two side reinforced FEM*

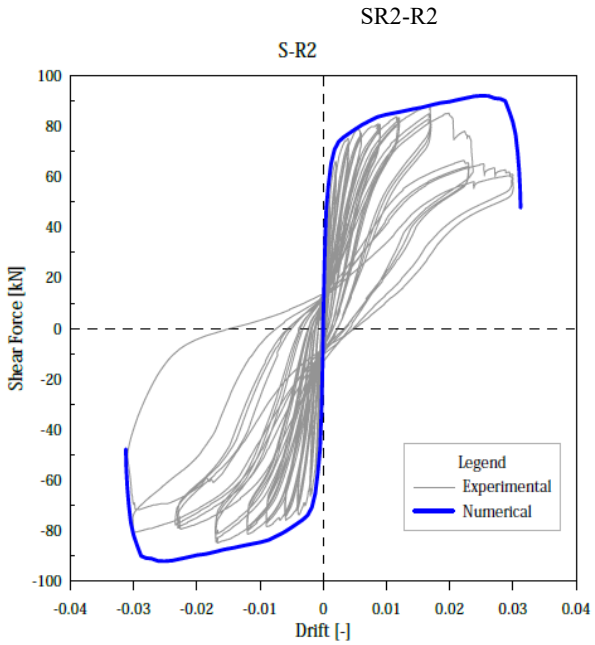


Figure 5.27 Model FE-S-R2R-2: comparison between numerical and experimental curves of shear force – spandrel drift

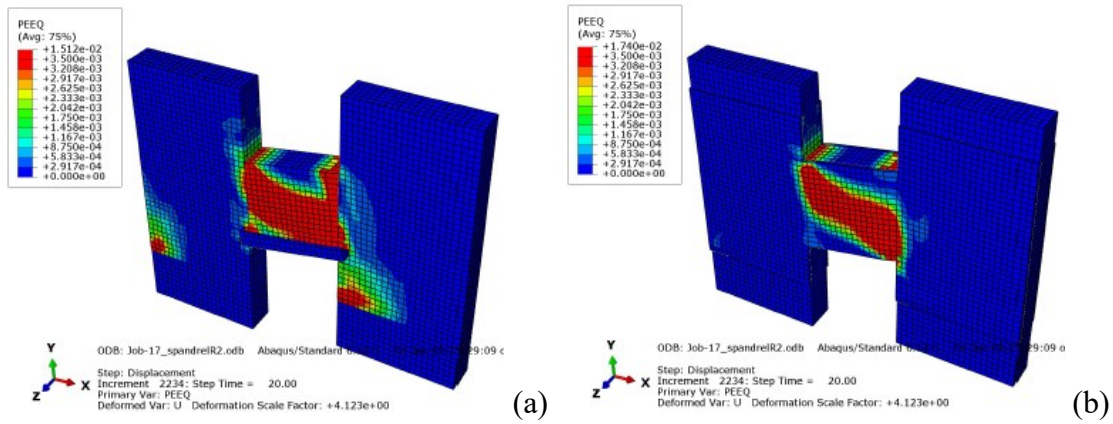


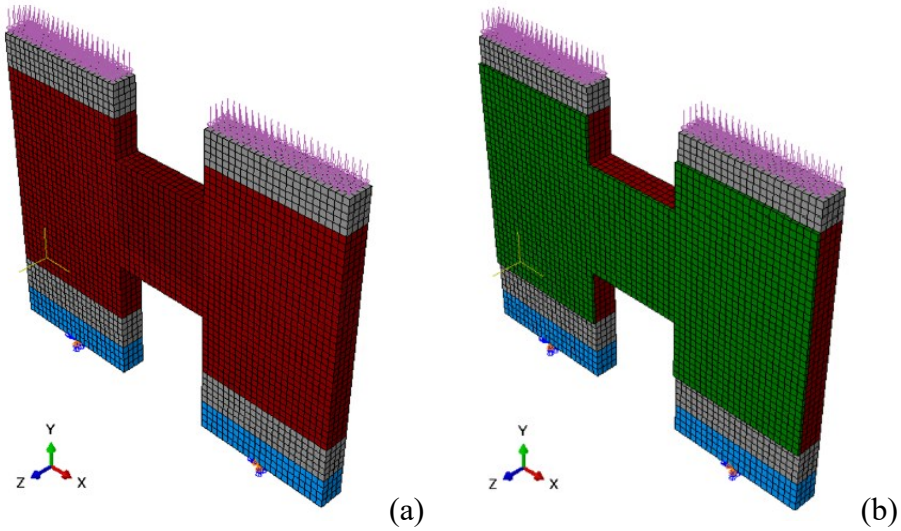
Figure 5.28 Model FE-S-R2R-2: equivalent plastic strain distribution at the end of the simulation on the masonry side (a) and on the reinforced side (b)

Drift	Observation
0.15%	The first vertical crack formed at the top corner of the spandrel.
0.25%	A diagonal crack started forming both on the masonry and on the reinforcement.
0.25% - 0.80%	The cracks grew and reach the entire height of the spandrel.
0.80% - 3%	The vertical crack grew significantly and a concentrated damage can be noted in the corners of the spandrel. The flexural failure can be clearly individuated.

As can be noted in Figure 5.27, a good agreement between experimental and numerical trends was reached. The masonry behaviour is the same used for the piers and the reinforcement behaviour remains the same as previous analysis. The shear force peak is in good agreement with the experimental one, considering an average between positive and negative directions. Also, in this case the stiffness is properly evaluated. The numerical descending branch fits the experimental one in the negative direction, identifying correctly also the stiffness drop. The positive trend is slightly more resistant than the experimental one (+4.2%), and the stiffness drop is slightly shifted in terms of drift.

5.3.2 Single leaf brick masonry specimens

To resemble the experimental test, the concrete beams used in the unreinforced model had a width of 0.35 m, while the reinforced sample's concrete beams had a width of 0.25 m. The width of the masonry has been modified to 0.25 m and the thickness of each element is equal to 0.0625 m.



(a) (b)

Figure 5.29 Numerical model FE-S-B1U (a); FE-S-B1R (b)

5.3.2.1 Unreinforced FEM

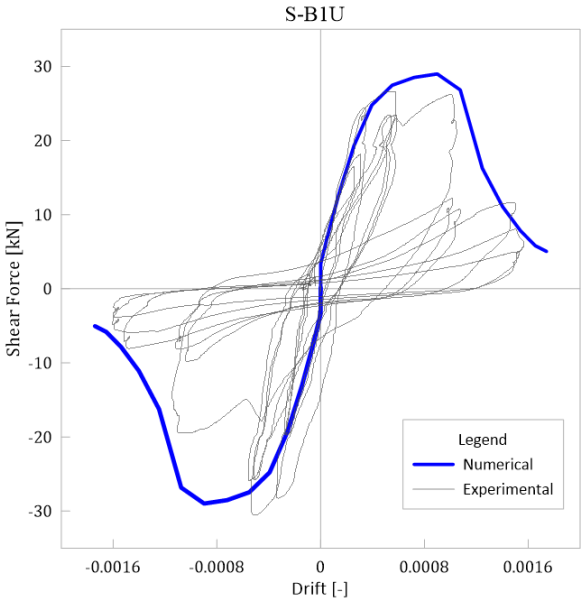


Figure 5.30 Model FE-S-B1U: comparison between numerical and experimental curves of shear force – spandrel drift

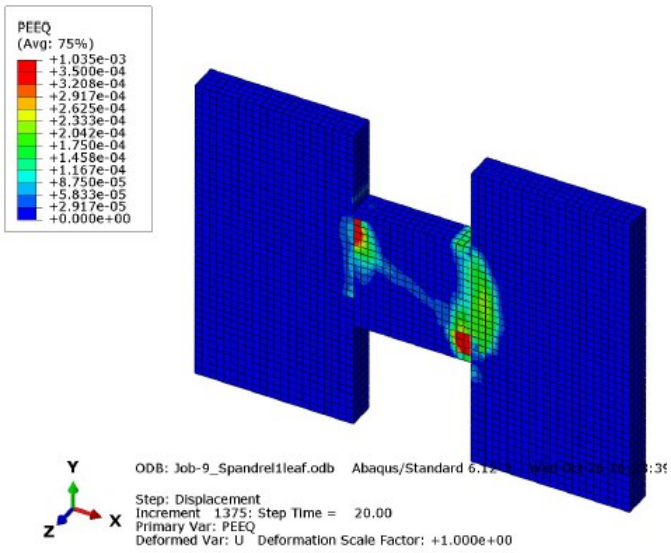


Figure 5.31 Model FE-S-B1U: equivalent plastic strain distribution at the end of the simulation.

Drift	Observation
0.014%	The first damage can be noted in the lintel. A first vertical crack compared at the top angle of the spandrel
0.02% - 0.08%	The peak resistance is reached. The vertical crack propagated and a diagonal crack formed in the spandrel.
0.15%	End of the test, damage is consistent at lintel level and on the diagonal crack formed in the spandrel.

As can be noted in Figure 5.30, a good agreement between experimental and numerical trends was reached. The masonry behaviour is the same used for the piers. Considering what observed in the experimental test, a particular attention was paid to the lintel behaviour. In fact, the lintel was defined as the masonry material, but with a reduced tensile strength due to its orientation. The calibration was considered reasonable, since numerically the first damage of the lintel was well fitted. The shear force peak was averagely slightly underestimated (-1.8%), but the numerical descending branch fits the experimental curve both in the positive and negative directions.

5.3.2.2 One side reinforced FEM

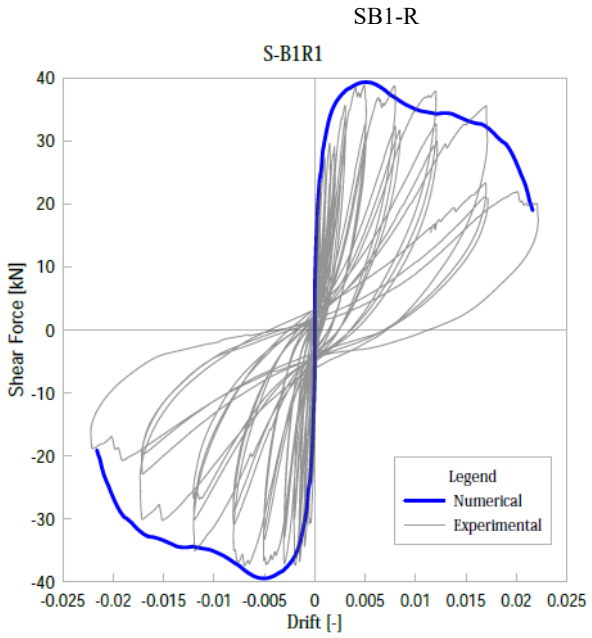


Figure 5.32 Model FE-S-B1R: comparison between numerical and experimental curves of shear force – spandrel drift

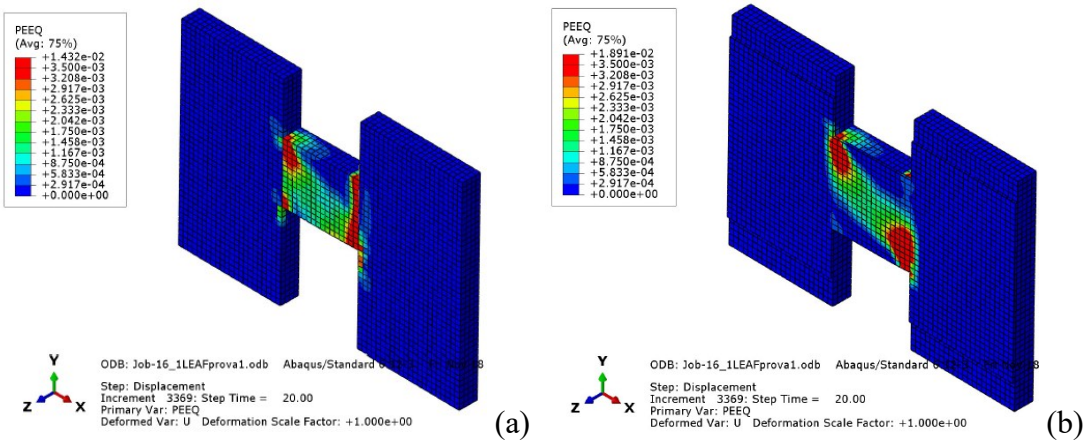


Figure 5.33 Model FE-S-B1R: equivalent plastic strain distribution at the end of the simulation on the masonry side (a) and on the reinforced side (b)

Drift	Observation
0.045%	The first vertical crack appeared in the spandrel, at the interface with the pier.
0.05% - 0.3%	The vertical crack propagated and a diagonal crack started to form in the masonry at spandrel level.
0.3% - 0.56%	After reaching the maximum resistance, the cracks propagated further and affected the entire dimension of the spandrel.
0.56% - 2.2%	Cracks continue to spread over the spandrel vertically and diagonally till the end of the test.

As can be noted in Figure 5.32, a good agreement between experimental and numerical trends was reached. The masonry behaviour is the same used for the unreinforced model and the reinforcement has the same behaviour of the previous analysis. Considering the high level of damage reached in the unreinforced test, the following considerations were taken into account in the numerical modelling:

- after the test the lintel was completely detached from the spandrel, for this reason it was neglected in the model;
- the vertical cracks at the interface between spandrel and piers were significant. For this reason, spandrel and piers were not considered to be perfectly adherent, but a friction value of 0.30 has been considered at the interface. This allows to consider the interlocking provided at the already formed crack level;
- a reduction of 30% of the masonry tensile strength has to be taken into account.

Neglecting these considerations in the analysis means a non-negligible overestimation of the maximum resistance of the specimen.

It can be noted that the shear force peak fits the experimental one, with a slight overestimation (averagely +3.3%), and the descending branches fit well the trends obtained in the test.

5.3.3 Two leaf brick masonry specimens

The dimensions used in these models are the same as the FE-S-B1 models.

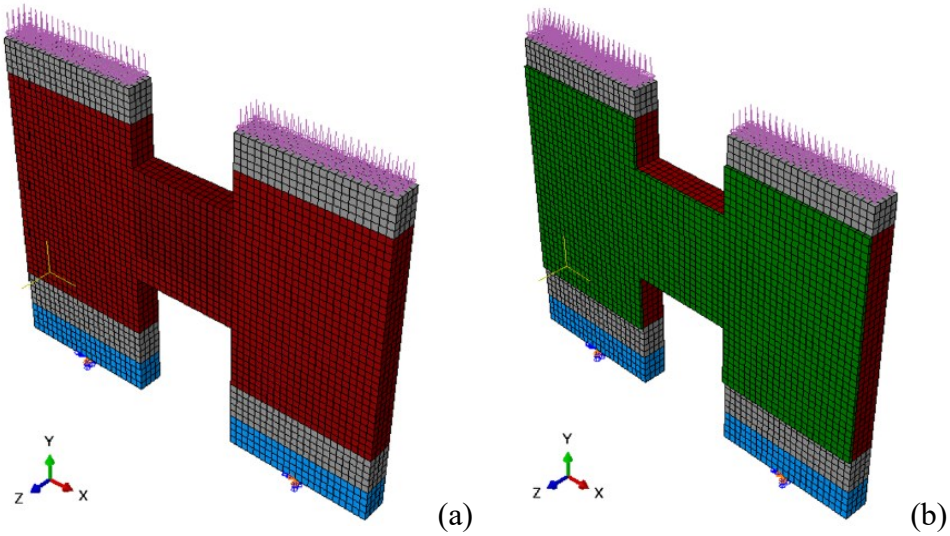


Figure 5.34 Numerical model FE-S-B2U (a) and FE-S-B2R-1 (b)

5.3.3.1 Unreinforced FEM

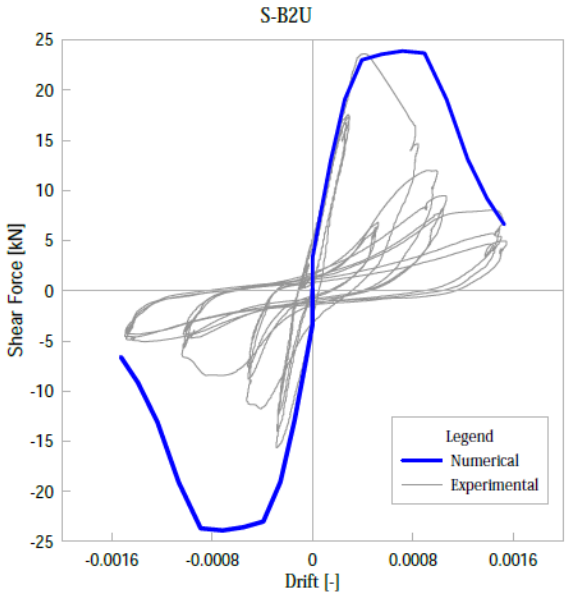


Figure 5.35 Model FE-S-B2U: comparison between numerical and experimental curves of shear force – spandrel drift.

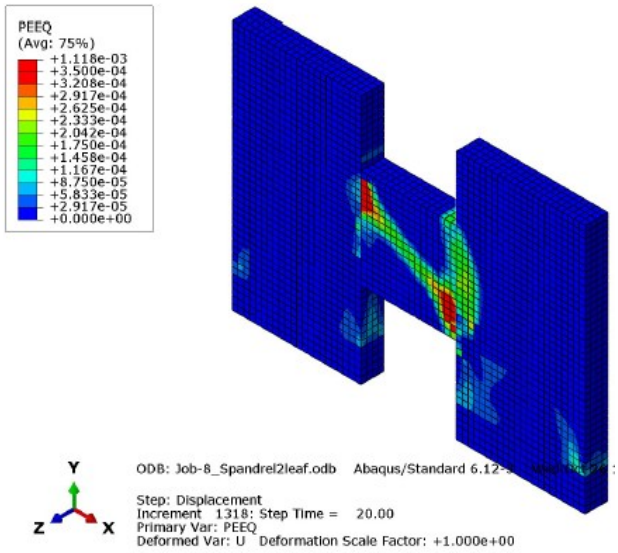


Figure 5.36 Model FE-S-B2U: equivalent plastic strain distribution at the end of the simulation

Drift	Observation
0.02%	The first damage can be noted in the lintel.
0.05%	A first vertical crack compared at the top angle of the spandrel. The peak force is reached.
0.08%	A diagonal crack started propagating in the centre of the spandrel.
0.08% - 0.16%	Both the vertical and the diagonal cracks propagated through the entire dimension of the spandrel. An important damage was also present on the lintel corner.

As can be noted in Figure 5.35, a good agreement between experimental and numerical trends was reached. The masonry behaviour is the same used for the piers. As done for the single-leaf specimen, the lintel was defined as the masonry material but considering a reduced tensile strength, because of the different tensile direction. The behaviour considered was the same as the previous one. The first stiffness degradation due to the damage accumulated in the lintel was well fitted. Also, the shear force peak fits well the experimental one in the positive direction, while the negative direction was not considered due to the problems occurred during the experimental test. The descending branch fits the experimental one both in the positive and in the negative direction, with a slight overestimation of the softening.

5.3.3.2 One side reinforced FEM

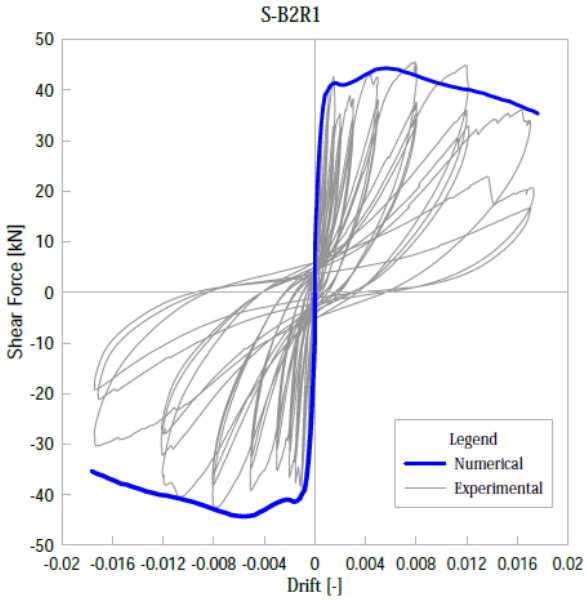


Figure 5.37 Model FE-S-B2R-1: comparison between numerical and experimental curves of shear force – spandrel drift

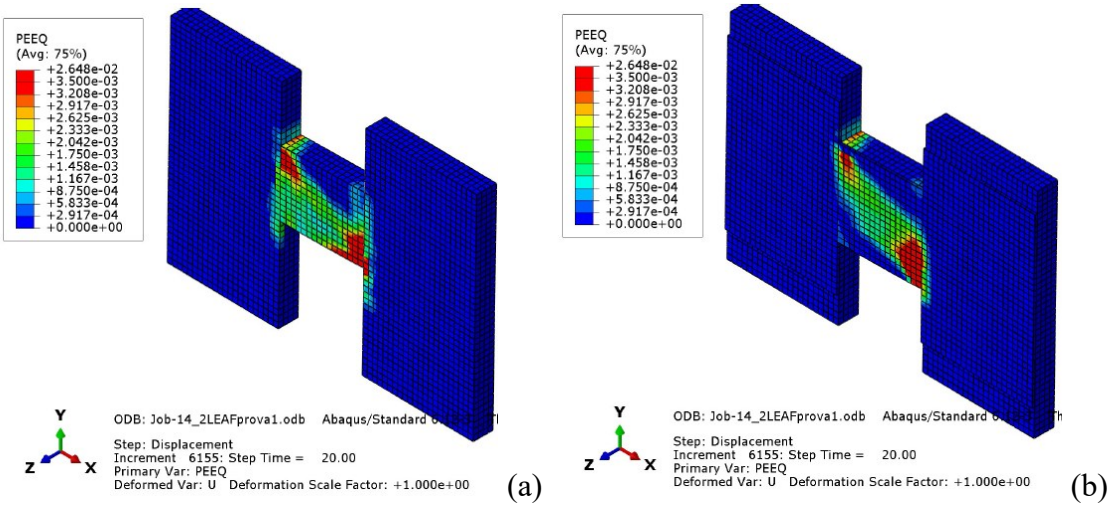


Figure 5.38 Model FE-S-B2R-1: equivalent plastic strain distribution at the end of the simulation on the masonry side (a) and on the reinforced side (b)

Drift	Observation
0.05%	The first vertical crack appeared in the spandrel, at the interface with the pier.
0.15%	The vertical crack propagated in the masonry and in addition a diagonal crack started forming in the spandrel. Damage started appearing also in the reinforcement.
0.50%	The maximum resistance is reached. Vertical cracks interested both the masonry and the reinforcement, while a diagonal crack created in the masonry propagated.
0.50% - 1.72%	Cracks continue to spread over the spandrel vertically and horizontally till the end of the test, interesting the entire dimension of the spandrel both in the masonry and in the reinforcement.

As can be noted in Figure 5.37, a good agreement between experimental and numerical trends was reached. The masonry behaviour and the reinforcement one is the same used for previous analysis. Also, in this case, considering the high level of damage reached in the unreinforced test, the following considerations were taken into account in the numerical modelling:

- after the test the lintel was completely detached from the spandrel, for this reason it has been neglected in the model;
- a reduction of 30% of the masonry tensile strength has to be taken into account.

Neglecting these considerations in the analysis means a non-negligible overestimation of the maximum resistance of the specimen.

The shear force peak fits the experimental one (with less than 1% overestimation), and the descending branches fit well the trends obtained in the test.

5.4 Equivalent frame modelling

In this section, numerical pushover analyses are conducted using the Midas Gen software [300], and the equivalent frame method to perform a parametric study on the behavior of CRM-strengthened structures. This approach enables the analysis of entire buildings without requiring excessive computational time. The validated method is subsequently applied to model the pilot building tests presented in Section 1.1.

5.4.1 Equivalent frame method

As discussed in section 1.4.1, the Equivalent Frame Method (EFM) [85] for the modelling of masonry walls and structures basically consists in schematizing the structure into an equivalent frame system composed of vertical and horizontal resisting structural macro-elements (i.e. the piers and the spandrels) connected by means of rigid nodes (Figure 5.39a). Each macro-element is represented as a beam element along its principal centroid axis, with nodes positioned at the intersections with the centroid axes of the orthogonal connected elements. Infinitely rigid segments at the ends of the masonry macro-elements allow to model the reduced deformability of the structural nodes.

The length of the deformable part of a pier, i.e the effective length l_{eff}, can be calculated by applying Eq.(5.1):

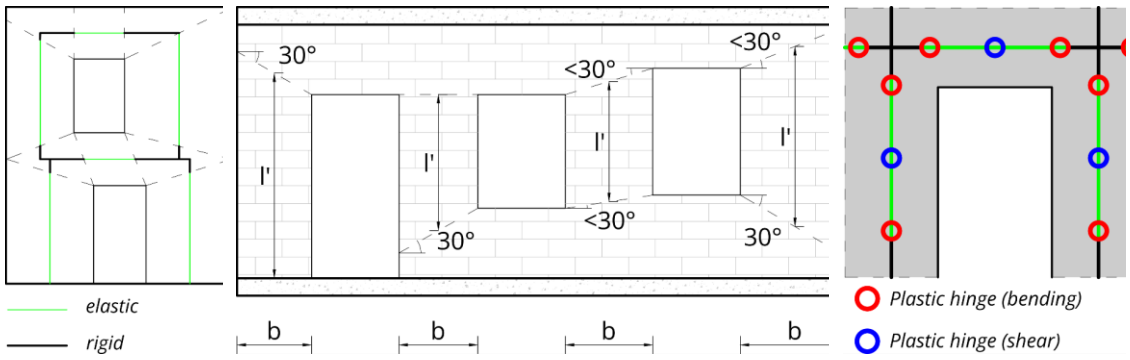
$$l_{eff} = l' + \frac{b(H - l')}{3l'} \leq H \tag{5.1}$$

being l' the conventional length (determined accordingly to Figure 5.39b), b the pier width, and H the net interstory height. The effective deformable portion is located proportionally to the length of the lower and upper rigid parts, as specified by Eq.(5.2).

$$l_{\inf,eff} = l_{\inf}\left(1 - \frac{l_{eff} - l'}{l_{\inf} + l_{\sup}}\right) \quad \text{and} \quad l_{\sup,eff} = l_{\sup}\left(1 - \frac{l_{eff} - l'}{l_{\inf} + l_{\sup}}\right) \tag{5.2}$$

being, l_{inf} and l_{sup} the conventional length of the lower and upper rigid parts of the vertical element ($l_{inf} + l' + l_{sup} = H$).

The elastic deformation of the structural elements depends on the elasticity of the beam elements, while the inelastic response is lumped in rotational and shear plastic hinges. The rotational plastic hinges at the ends of the beam elements simulate the inelastic in-plane bending response, while the shear plastic hinge at mid-length represents the inelastic in-plane shear response.



(a) (b) (c)

Figure 5.39 Modelling of a masonry wall accordingly to the Equivalent frame method (a), definition of the effective pier length (b), and location of the lumped plasticity hinges (c)

5.4.2 The software Midas Gen

The software Midas GEN allows to carry out nonlinear static pushover analysis for masonry buildings. The modelling of the structure is based on the Equivalent frame model with lumped plasticity. The user is asked to preliminary define:

- the geometry of the equivalent frame;
- the vertical loads;
- the masonry mechanical properties;
- the behaviour of the lumped plasticity hinges.

- **Geometry**

The user models the masonry structure according to the "Equivalent Frame" method (Figure 5.40), by using beam elements, and provides the effective lengths of the piers and spandrels and of the rigid nodes. The rigid beams forming the rigid nodes of the structure can be modelled separately from pier/spandrel elements or by defining beam-end-offset constraints applied on piers/spandrel elements. The user must be careful in assigning the self-weights of such rigid portions, to avoid double counting. An effective strategy that was used in this study, is to apply the beam-end offset constraints option to vertical elements (therefore, having the masonry self-weight) in combination with a separate modelling of the horizontal rigid elements (assigning them zero self-weight).

The user also defines the beams cross sections (bending deformation is always considered, the shear one is optional but is activated by default). For the proper assignment of the plastic capacities, the Y-local axis of the beam has to be arranged along the wall thickness (i.e. perpendicular to the wall plane).

The piers of the ground floor are typically fixed at the base. To properly apply floor diaphragm constraints, the user shall keep attention in constraining only the nodes at the top of the piers, keeping free all the other nodes at that level.

- **Vertical loads**

The vertical loads transmitted by the floors can be assigned manually as nodal or distributed loads. The "assign floor load" option allows also automatic assignment, once floor typology (i.e. one/two way) and the nodes of the loading area are selected.

The masonry self-weights (defined in the material properties) shall also be activated.

- **Material properties**

Masonry is assumed as an equivalent isotropic material. The user provides the basic masonry mechanical characteristics in terms of self-weight, Young's modulus and shear modulus (or Poisson's ratio).

- **Lumped plasticity features**

The user selects the type of masonry element (pier or spandrel) and defines the non-linear masonry characteristics:

- for the piers: the shear strength (τ_0), the vertical compressive strength (f_m) and the vertical stress distribution coefficient (0.85 by default);
- for the spandrels: the shear strength (τ_0), the horizontal compressive strength ($f_{m,h}$) and the horizontal tie resistance (H_p).

The hinges to be activated for the pushover analysis of masonry buildings are, typically, in-plane shear, at the beam centre (*Fz*), and in-plane bending (*My*), at both beam ends. Axial compression can also be activated (*Fx*).

The user is asked also to select the strength formulations: for the purposes of this study, "existing masonry" and "irregular masonry type" options are suggested. Thus:

- for pier elements, the shear resistance ($V_{P,d(URM)}$) and the bending resistance ($M_{P(URM)}$) are determined through Eqs. (5.3) and (5.4), respectively:

$$V_{P,d(URM)}=\frac{1.5\tau_0}{\beta} b_P \cdot t_P \sqrt{1+\frac{\sigma_o}{1.5\tau_0}} \tag{5.3}$$

$$M_{P(URM)}=\frac{\sigma_o b_P^2 t_P}{2}\left(1-\frac{\sigma_o}{0.85 f_m}\right) \tag{5.4}$$

- for spandrel elements, the shear resistance ($V_{S,d(URM)}$) and the bending resistance ($M_{S(URM)}$) are determined through Eqs. (5.5) and (5.6), respectively.

$$V_{S,d(URM)}=\frac{1.5\tau_0}{\beta} b_S \cdot t_S \sqrt{1+\frac{\sigma_o}{1.5\tau_0}} \quad (5.5)$$

$$M_{S(URM)}=\frac{H_S b_S}{2}\left(1-\frac{H_P}{0.85 f_{m,h} h_S t_S}\right) \quad (5.6)$$

Where:

t_P	masonry pier thickness
b_P	masonry pier width
l_P	masonry pier height (i.e. “effective length”)
t_S	masonry spandrel thickness
b_S	masonry spandrel height
l_S	masonry spandrel length (i.e. “effective length”)
σ_0	mean compressive stress on the pier/spandrel
f_m	masonry vertical compressive strength
$f_{m,h}$	masonry horizontal compressive strength
τ_0	equivalent masonry shear strength for $\sigma_0 = 0$
β	pier/spandrel slenderness factor ($1.0 \leq \beta = l/b \leq 1.5$)
H_p	tensile resistance of the horizontal tie (however, limited to $0.4 \cdot f_{m,h} \cdot b_S \cdot t_S$)

Basically, for the in-plane shear mechanism the software considers the Turnšek-Čačovič formulation [63]. For in-plane bending mechanism of piers, it accounts only for the masonry compressive resistance and the stabilizing effect of the vertical loads. For the strength in-plane bending mechanism of spandrels, it assumes the presence of an effective horizontal tie, otherwise the resistance is null.

As observed in section 0, spandrels without a horizontal tie have a bending resistance, even though small, due to the interaction between adjacent blocks at the spandrel ends, as evidenced also from the experimental tests on the unstrengthened spandrel samples. Thus, in this case, the user shall “force” the software for a proper evaluation of the bending resistance. For example, a fictitious horizontal tie resistance ($H_{P,fit}$) can be set, based on the actual resistance expected for the spandrel.

For each hinge type, the user defines the post-elastic behaviour (FEMA type, Figure 5.41). Point “B” is automatically determined (based on the elastic stiffness of the element and the resistance). The user defines “C”, “D” and “E” (in terms of both strength ratio, in respect to point “B”, and deformation capacities) and can opt/opt out for the total strength loss at the reaching of point “E” (kept constant by default).

Based on the provided hinges properties, the software automatically calculates the lateral strength and displacement capacities of masonry piers and spandrels; the axial stress level is automatically updated at each analysis step. The software considers the mean axial stress in the element to determine the resistance of hinges.

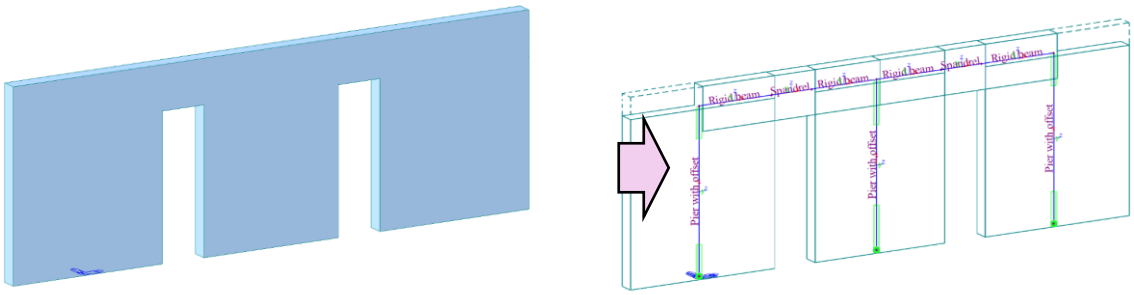


Figure 5.40 "Equivalent frame" model schematization.

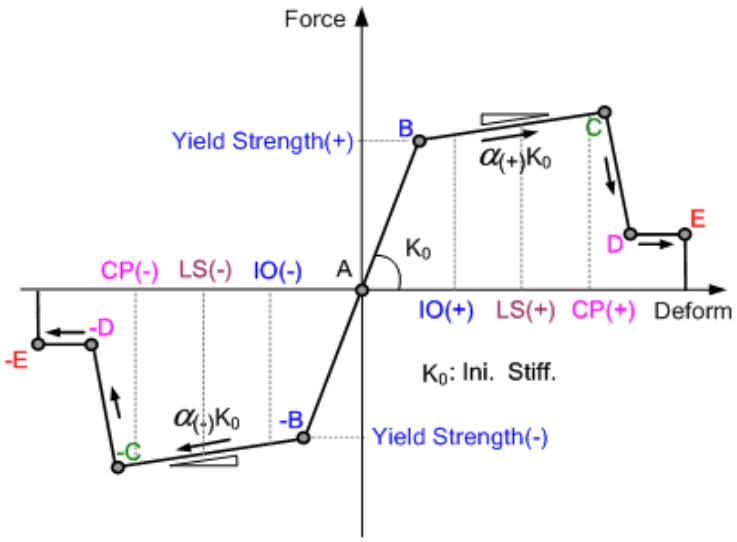


Figure 5.41 Plastic hinge behaviour (according to FEMA 356 [301])

- **Analysis features**

The user sets up the pushover analysis under displacement control (of a master node, i.e. the mass centre at the roof level), specifying the lateral load pattern, the target displacement and the number of steps. The vertical loads shall be preliminary applied.

Different lateral load patterns can be applied: proportional to a static load case defined by the user, uniform acceleration (proportional to the mass at each story level), proportional to a mode shape, normalized mode shape times mass (the load pattern for the pushover analysis is derived by multiplying the normalized mode shape by the mass). The last three

types require eigenvalue analysis to be previously performed; to that, it is essential to define the masses of the structure (e.g. the self-weights and added loads can be converted into masses). After the analysis, the user can check the calculated strength of each inelastic hinge at each step.

- **How to account for CRM**

The software performs the pushover analysis by automatically evaluating the in-plane resistance and displacement characteristics of the piers and spandrels, by automatically applying the analytical correlations previously presented, that are suitable for URM. Currently, the software does not include an automatic procedure to account for the CRM contribution. Thus, for CRM strengthened masonry, the user shall "force" the software by providing "fictitious" equivalent masonry properties, to account also for the CRM reinforcement contribution. In fact, the software does not allow to modify the correlations for the resistance estimation, but just the masonry material parameters and plastic hinges drift limits.

For CRM strengthened elements (both piers and spandrels), the "spandrel element type" shall be selected in the software and equivalent material parameters values $\tau_{0,eq}$ (masonry shear strength) and $H_{P,eq}$ have to be set, according to Eqs. (5.7) and (5.8):

$$\tau_{0,eq}=-\frac{\sigma_0}{3}+\sqrt{\frac{\sigma_o^2}{9}+\left(\frac{\beta V_{d(CRM)}}{1.5bt}\right)^2} \tag{5.7}$$

$$H_{P,eq}=\frac{2M_{(CRM)}}{b} \tag{5.8}$$

where:

$V_{d(CRM)}$ Resistance of the CRM strengthened masonry element in shear (related to the in-plane diagonal cracking mechanism)

M_{CRM} Resistance of the CRM strengthened masonry element in bending (related to the in-plane bending mechanism)

The values of $V_{d(CRM)}$ and M_{CRM} shall be calculated analytically by the user, applying the correlations presented in sections 4.1 and 0 for CRM. Note also that the masonry compressive strength shall be set fictitiously to a high value (e.g. 1000 MPa). For spandrel elements, it is assumed $\sigma_0 = 0$ in Eq.(5.7). Also increased ultimate drift values has to be assigned to CRM strengthened masonry elements, as also discussed in sections 4.1 and 0.

- **Validation**

For the validation of the procedure, two benchmark examples (a pier and a spandrel element), represented in Figure 5.42, are considered, and the comparison between numerical simulations and analytical calculations are made. The masonry and CRM characteristics adopted are reported in Table 5.4.

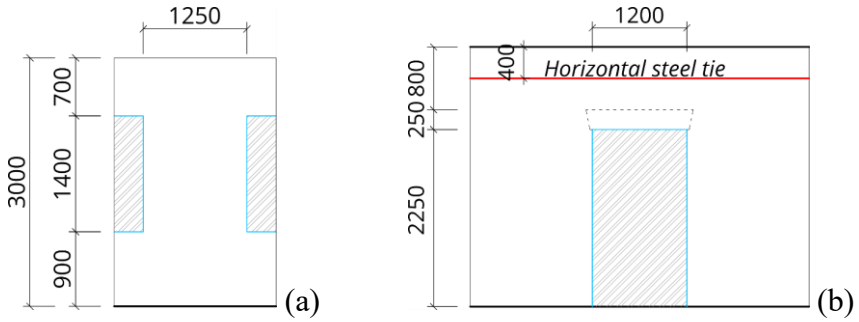


Figure 5.42 Benchmark examples: (a) pier and (b) spandrel elements (measures in mm)

Table 5.4. Main characteristics for the benchmark examples.

ID	Value	Unit	Description
t_m	250	mm	masonry thickness
b'	800	mm	net masonry spandrel height (typically, lintel is not considered)
E_m	1500	MPa	secant Young's modulus of masonry
G_m	500	MPa	shear modulus of masonry (E_m/3)
f_m	3.45	MPa	vertical compressive strength
$f_{m,h}$	1.725	MPa	horizontal compressive strength (f_m/2)
τ_0	0.09	MPa	equivalent masonry shear strength under zero vertical stress
H_p	100	kN	resistance of the horizontal tie of the spandrel
T_G	5.11	kN	tensile resistance of a GFRP wire.
s	66	mm	GFRP mesh grid pitch
t_c	30	mm	mortar coating thickness
E_c	10000	MPa	secant Young's modulus of the coating mortar
H_p	100	kN	tensile resistance of the horizontal steel tie

To schematize analytically, in a simplified way, the in-plane lateral performances of masonry piers and spandrels, an elastic-plastic behaviour is considered. To estimate the stiffness, resistance and ultimate displacement capacities, the analytical correlations presented in sections 4.1 and 0 are adopted. The pier is subjected to a vertical stress of

0.3 MPa and both the shear-type (*st*) and the cantilever (*ct*) beam static schemes are considered. The spandrel is assumed to have an effective horizontal steel tie.

Table 5.5. Analytical calculations concerning the benchmark pier (shear-type scheme).

Pier_st_0.3		**URM**	**R1**	**R2**
i	[-]	-	1	2
χ	[-]	-	1.0	1.0
f_m	[MPa]	3.45	3.45	3.45
E	[MPa]	1500	2700	3900
G	[MPa]	500	980	1460
K_e	[kN/mm]	42.7	80.9	119.0
x	[mm]	-	195.1	248.3
M_P	[kNm]	52.6	84.8	112.6
$V_{P,f}$	[kN]	56.1	90.4	120.1
$V_{P,d}$	[kN]	50.5	98.9	147.3
V_P	[kN]	50.5	90.4	120.1
Mode	[-]	Diag. cracking	Bending	Bending
$d_{P,e}$	[mm]	1.18	1.18	1.08
$d_{P,u}$	[mm]	9.4	37.5	37.5

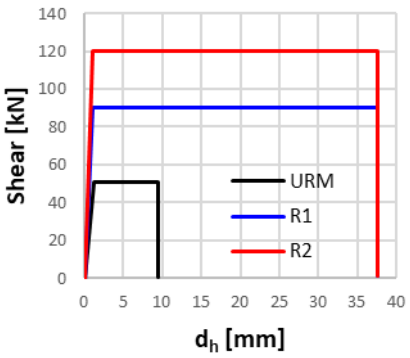


Table 5.6. Analytical calculations concerning the benchmark pier (cantilever beam scheme).

Pier_ct_0.3		**URM**	**R1**	**R2**
i	[-]	-	1	2
χ	[-]	-	1.0	1.0
f_m	[MPa]	3.45	3.45	3.45
E	[MPa]	1500	2700	3900
G	[MPa]	500	980	1460
K_e	[kN/mm]	19.8	36.5	53.2
x	[mm]	-	195.1	248.3
M_P	[kNm]	52.6	84.8	112.6
$V_{P,f}$	[kN]	22.2	35.8	47.6
$V_{P,d}$	[kN]	50.5	98.9	147.3
V_P	[kN]	22.2	35.8	47.6
Mode	[-]	Bending	Bending	Bending
$d_{P,e}$	[mm]	1.12	1.00	0.92
$d_{P,u}$	[mm]	18.8	37.5	37.5

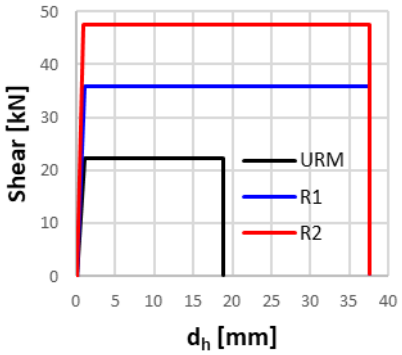
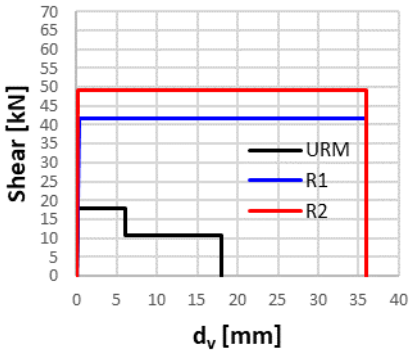


Table 5.7. Analytical calculations concerning the benchmark spandrel.

Spandrel		**URM**	**R1**	**R2**
i	[-]	-	1	2
χ	[-]	-	1.0	1.0
f_{hd}	[MPa]	1.73	1.73	1.73
E	[MPa]	1500	2700	3900
G	[MPa]	500	980	1460
K_e	[kN/mm]	66.9	128.1	189.1
x	[mm]	-	301.0	309.7
M_S	[kNm]	26.4	29.0*	29.5*
$V_{S,f}$	[kN]	43.9	48.4	49.2
$V_{S,d}$	[kN]	18.0	41.8	72.7
$V'_{S,d}$	[kN]	10.8	-	-
V_S	[kN]	18.0	41.8	49.2
Mode	[-]	Diag. cracking	Diag. cracking	Bending
$d_{S,e}$	[mm]	0.27	0.21	0.26
$d_{S,u}$	[mm]	6.0	36.0	36.0



* In both reinforced configurations, bending failure occurs due to masonry crushing, so the R2 configuration results in only a slight increase in the bending resistance in respect to the R1 configuration.

Legend:	
i	number of CRM-strengthened sides (1-2)
χ	effectiveness reduction factor (=1 for CRM at both-sides, ≤1 at one side)
K_e	elastic stiffness
x	depth of the neutral axis of the cracked cross-section
M	resisting bending moment
V_f	in-plane lateral resistance related to bending mechanism
V_d	in-plane lateral resistance related to diagonal cracking mechanism
V	in-plane lateral resistance
d_e	yield displacement
d_u	ultimate displacement

For piers, the vertical axial compression is simulated by applying a vertical force to the upper node and the pushover analysis is performed by gradually increasing the lateral displacement of the upper node. The plotted graphs represent the base shear, F_P, varying the net horizontal displacement d_h between the top and the bottom of the effective pier length l_{eff}.

For spandrels, the pushover analysis is performed by gradually increasing the nodal rotation at the two base supports while controlling the horizontal displacement of the node at the top-right node. The plotted graphs represent the shear acting on the spandrel, F_S, against the distortion (i.e. net displacement d_v between the spandrel ends, determined orthogonally in respect to the direction of the adjacent rigid parts).

The geometric nonlinearities are considered by the pushover analyses. In both cases, the self-weight is not considered.

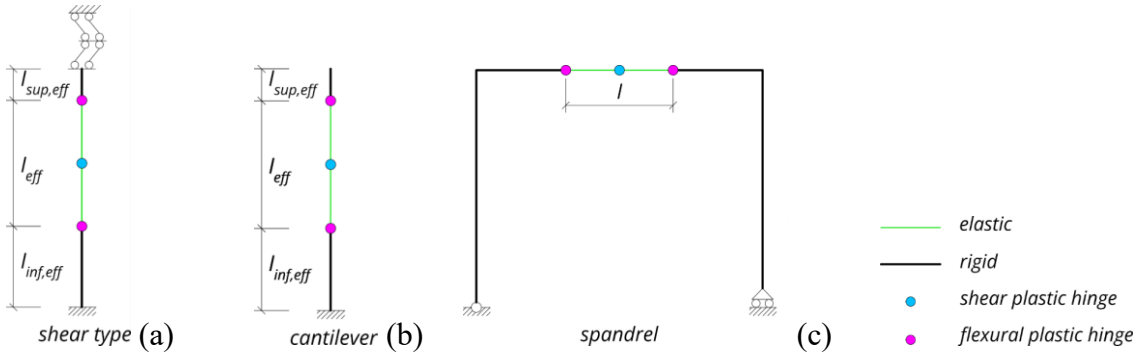
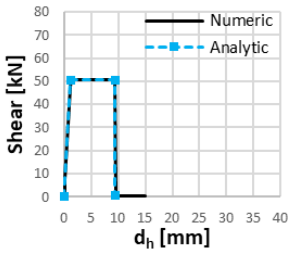
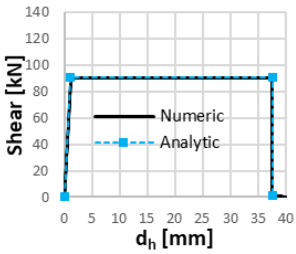
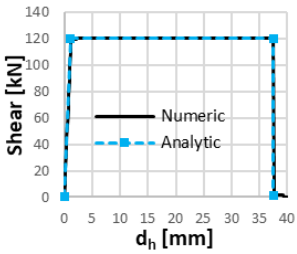
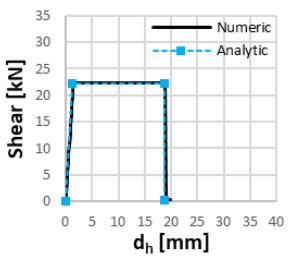
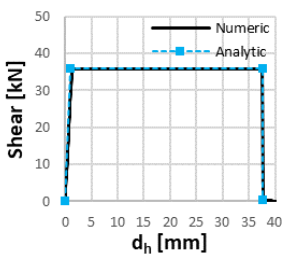
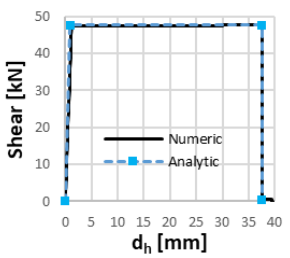
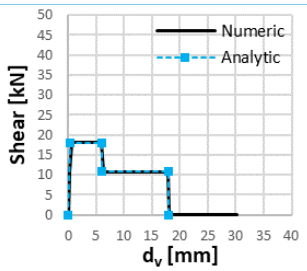
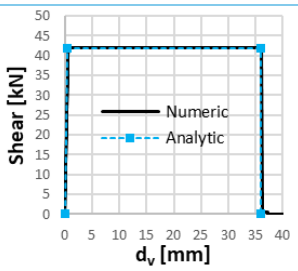
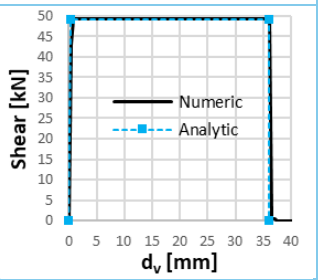


Figure 5.43 Schematization of the validation numerical models for the pier, according to (a) a shear-type or (b) a cantilever beam scheme, and for the spandrel

ID:	**URM_Pier_st_0.3**		**R1_Pier_st_0.3 ($H_{p,eq}$=135.6kN, $\tau_{0,eq}$=0.232MPa)**		**R2_Pier_st_0.3 ($H_{p,eq}$=180.2kN, $\tau_{0,eq}$=0.382MPa)**	
State:	Unstrengthened		Strengthened on one side		Strengthened on two sides	
Axial stress:	0.3 MPa		0.3 MPa		0.3 MPa	
Capacity curve:						
Yield point:	1.31 mm	50.5 kN	1.20 mm	90.3 kN	1.10 mm	120.0 kN
Collapse:	9.38 mm	50.5 kN	37.5 mm	90.4 kN	37.5 mm	120.1 kN
Failure mode:	Diagonal cracking		Bending		Bending	

ID:	**URM_Pier_ct_0.3**	**R1_Pier_ct_0.3 ($H_{p,eq}$=135.6kN, $\tau_{0,eq}$=0.232MPa)**	**R2_Pier_ct_0.3 ($H_{p,eq}$=180.2kN, $\tau_{0,eq}$=0.382MPa)**
State:	Unstrengthened	Strengthened on one side	Strengthened on two sides
Axial stress:	0.3 MPa	0.3 MPa	0.3 MPa
Capacity curve:			

Yield point:	1.53 mm	22.2 kN	1.35 mm	35.8 kN	1.20 mm	47.5 kN
Collapse:	18.7 mm	22.2 kN	37.5 mm	35.8 kN	37.5 mm	47.6 kN
Failure mode:	Bending		Bending		Bending	

ID:	**URM_Spandrel**		**R1_Spandrel ($H_{p,eq}$=72.6kN, $\tau_{0,eq}$=0.209MPa)**		**R2_Spandrel ($H_{p,eq}$=73.8kN, $\tau_{0,eq}$=0.364MPa)**	
State:	Unstrengthened		Strengthened on one side		Strengthened on two sides	
H_p	100 kN		100 kN		100 kN	
Capacity curve:						
Yield point:	0.55 mm	18.0 kN	0.72 mm	41.8 kN	0.76 mm	49.2 kN
Collapse:	17.8 mm	10.8 kN	36.0 mm	41.8 kN	36.1 mm	49.2 kN
Failure mode:	Diagonal cracking		Diagonal cracking		Bending	

It is observed that for both piers and spandrels, the analytical and numerical predictions coincide, in terms both of capacity curves and failure mode. It is thus concluded that the adopted procedure allows the software to correctly reproduce in a simplified way the behaviour of both unstrengthened and CRM strengthened masonry.

5.4.3 Benchmark examples

A series of benchmark models, including individual structural elements (piers and spandrels), portal frames, and single- and double-story walls, are analysed to simulate their seismic behavior using the equivalent frame method. Each configuration is examined in three conditions: unstrengthened (URM), strengthened on one side (R1), and strengthened on both sides (R2).

5.4.3.1 Material properties

For the numeric study herein presented, a solid brick masonry with characteristics reported in Table 5.8 is considered. The chord rotation limits for the piers and spandrels are given in accordance with the Italian Code [65].

Table 5.8. Masonry characteristics *adopted.*

symbol	value	unit	description
t	250	mm	Thickness
γ_m	18	kN/m^3	Self-weight
$E_{lim,m,c}$	0.35	%	Limit compressive strain of masonry
E_m	1500	MPa	Secant Young modulus
G_m	500	MPa	Shear modulus (E_m/3)
f_m	3.45	MPa	Vertical compressive strength
$f_{m,h}$	1.725	MPa	Horizontal compressive strength
f_{v0}	0.20	MPa	Masonry shear strength for $\sigma_0 = 0$ (shove test)
τ_0	0.09	MPa	Masonry shear strength for $\sigma_0 = 0$ (diagonal cracking mechanism)
b_h	65	mm	average height of a masonry row
d_{eff}	65	mm	effective overlap length of bricks
Chord rotation limits			
$\theta_{Pu(d)}$	0.005	-	for piers (shear failure)
$\theta_{Pu(f)}$	0.010	-	for piers (bending failure)
$\theta_{Su(t0)}$	0.015	-	for spandrels without effective horizontal tie (residual resistance)
$\theta_{Su(t1,f)}$	0.020	-	for spandrels with effective horizontal tie (bending resistance)
$\theta_{Su(t1,d)}$	0.005	-	for spandrels with effective horizontal tie (shear resistance)

5.4.3.2 Reinforcement properties

The strengthening used for the reinforced configurations consists of a natural hydraulic lime mortar coating, strengthened with a Glass Fibre-Reinforced Polymer (GFRP) mesh. The mechanical properties of the reinforcement are reported in Table 5.9. The chord rotation limits for the piers and spandrels are generally set in accordance with the experimental findings.

Note that in all the simulations, the resistance contribution of the CRM system is assumed as not subjected to any effectiveness reduction, even in case of one side application, according to the experimental findings.

Table 5.9: Masonry and CRM characteristics adopted.

symbol	value	unit	description
t_c	30	mm	Thickness of the coating
γ_c	18	kN/m^3	Plaster self-weight
E_c	10000	MPa	Plaster Young modulus
G_c	4000	MPa	Plaster shear modulus (~0.4E_c)
T_G	5.11	kN	Mean tensile resistance of a GFRP wire
A_G	3.8	mm^2	Dry fibre cross section of a GFRP wire
s	66	mm	GFRP grid pitch
$\varepsilon_{lim,G}$	1.85	%	Limit tensile strain of GFRP
E_G	72.7	GPa	GFRP Young modulus (referred to the dry fibre cross section)
Chord rotation limits			
$\theta_{Pu(d)}$	0.010	-	for piers (shear failure)
$\theta_{Pu(f)}$	0.020	-	for piers (bending failure)
θ_{Su}	0.030	-	for spandrels (both shear and bending failure)

5.4.3.3 Geometric features

The benchmark examples consist in a series of piers and spandrels, portal frames, single- and double-story walls and an entire building. The main features are presented in this section.

- **Pier elements**

Four pier configurations, with a height of 1400 mm and varying aspect ratios are considered (Figure 5.44). A vertical compression is applied at the top; the self-weight is neglected.

The capacity curves for single masonry piers varying aspect ratio and the vertical stress are analysed. Both the shear-type and the cantilever beam schemes are investigated.

The Identification (ID) of each case study is in the form "Pier_A_B_C_D_E"

- A represents the beam static scheme: *st* for shear-type, *ct* for cantilever;
- B is for the total height in meters: e.g. *h3*;
- C is for the aspect ratio: *a* for 1.0, *b* for 1.5, *c* for 2.0 and *d* for 0.8;
- D is for the axial stress: 01-03-05 for 0.1, 0.3 or 0.5 MPa, respectively;
- E is for the strengthened configuration: R1 and R2 for strengthening on one and two sides, respectively. If this part is omitted, it indicates an unstrengthened structure.

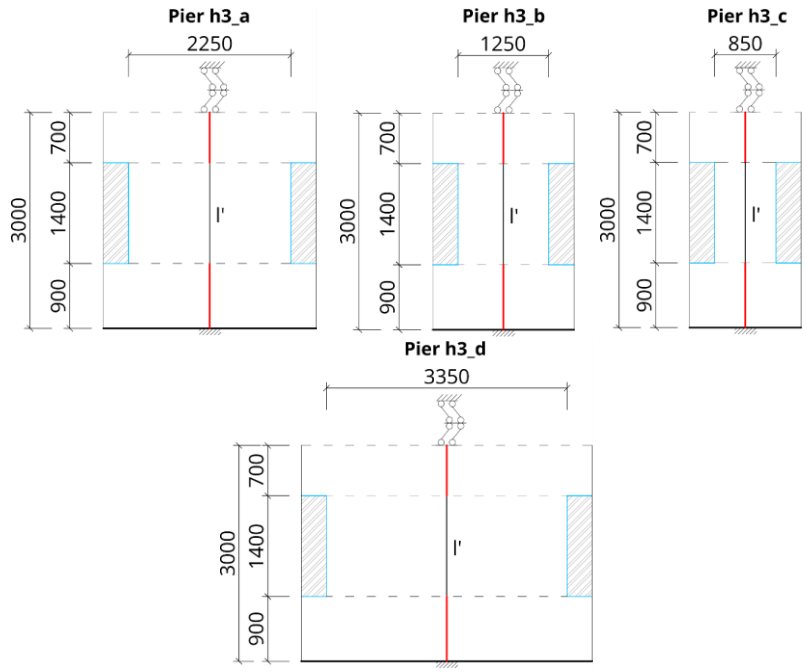


Figure 5.44 Pier elements (measures in mm)

- **Spandrel elements**

Three spandrel configurations with a length of 1200 mm, with varying aspect ratios are considered (Figure 5.45). The compressive stress on adjacent piers, σ_{0P}, is 0.3 MPa; self-weight is neglected.

Two different spandrel configurations are analysed:

- t_1, provided with effective horizontal tie (H_P = 100 kN is assumed for the tensile resistance of the horizontal tie);
- t_0, without any effective horizontal tie;

The spandrels are assumed to include a masonry arch, which, according to the Italian Code, limits the residual shear strength to 10%. In contrast, when a tensile-resisting element is present, the residual shear strength is increased to 60%.

Note that, in case of spandrels provided with both an effective horizontal tie and CRM, both tensile failure of the mesh and crushing of the masonry were considered as potential failure modes.

The ID of each case study is in the form “Spandrel_A_B_C_D”

- A is for the total length in meters: e.g. *L1.2*;
- B is for the aspect ratio: 1.0, 1.5 and 0.8;
- C is for the spandrel configuration: *t1* or *t0;*

- D is for the strengthened configuration: R1 and R2 for strengthening on one and two sides, respectively. If this part is omitted, it indicates an unstrengthened structure.

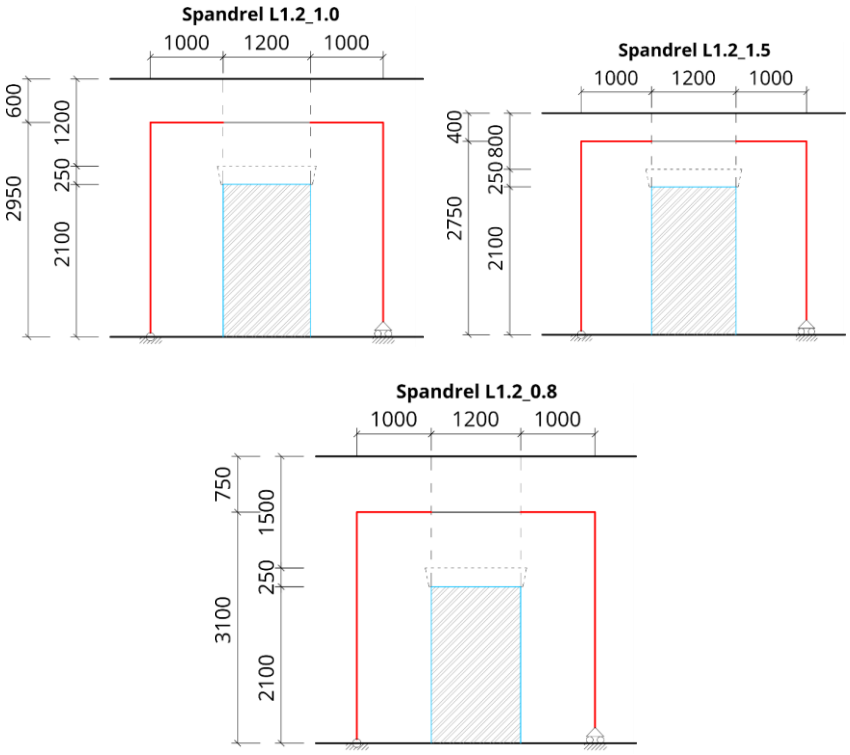


Figure 5.45 Spandrel elements (measures in mm)

- **Portal frames**

Portal frames representing a symmetric wall with a door opening in the middle are considered (Figure 5.46). Fixed supports are assigned at the bottom of the piers, simulating a stiff foundation. A vertical compression is applied at the top; the self-weight is neglected.

The ID of each case study is in the form "Portal frame A_B_C_D_E_F"

- A is for the total wall width in meters: e.g. *L5.2*;
- B is for the axial stress on the piers: 01-03-05 for 0.1, 0.3 or 0.5 MPa, respectively.
- C is for the spandrel length in meters: e.g. *1.2*;
- D is for the spandrel aspect ratio: 1.0, 1.5 and 0.8;
- E is for the spandrel configuration: t_1 or t_0 (see spandrel elements);
- F is for the strengthened configuration: R1 and R2 for strengthening on one and two sides, respectively. If this part is omitted, it indicates an unstrengthened structure.

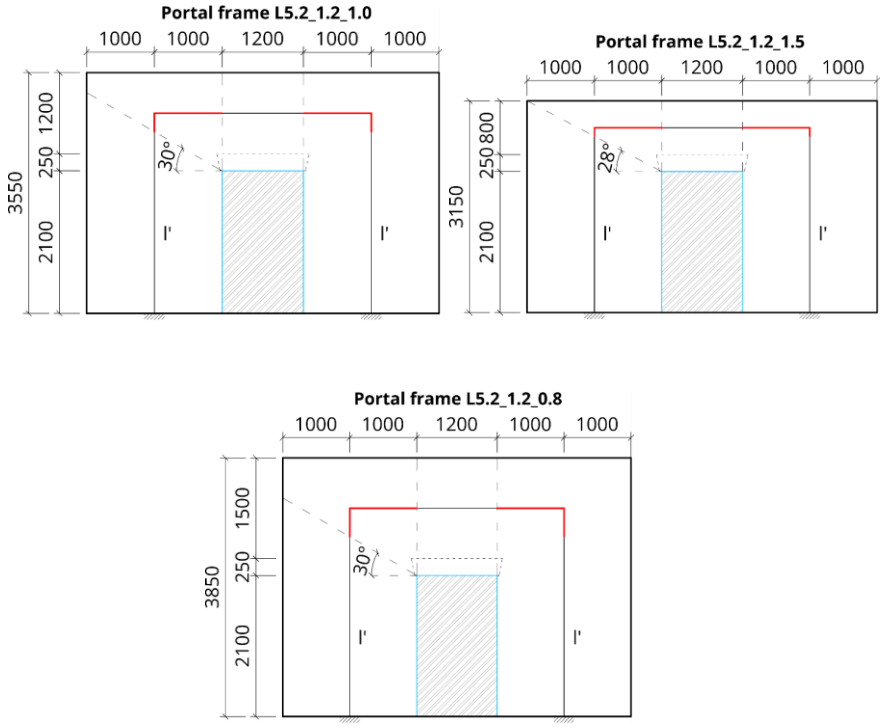


Figure 5.46 Portal frames (measures in mm)

- **Single-story walls**

Single-story walls representing a symmetric wall with two window openings are considered (Figure 5.47). Fixed supports are assigned at the bottom of the piers, simulating a stiff foundation. A vertical compression is applied at the top; the self-weight is also considered. The capacity curves varying the aspect ratio and the vertical stress are analysed. Spandrel configuration *t1* is considered (see spandrel elements).

The ID of each case study is in the form "Single-story wall A_B_C_D":

- A is for the total height in meters: e.g. *h3.35*;
- B is for the pier aspect ratio: *1a* for 1.0, *1b* for 1.5, *1c* for 2.0;
- C is for the axial stress on the piers of the first floor (in addition to the self-weight): 01-03-05 for 0.1, 0.3 or 0.5 MPa, respectively;
- D is for the strengthened configuration: R1 and R2 for strengthening on one and two sides, respectively. If this part is omitted, it indicates an unstrengthened structure.

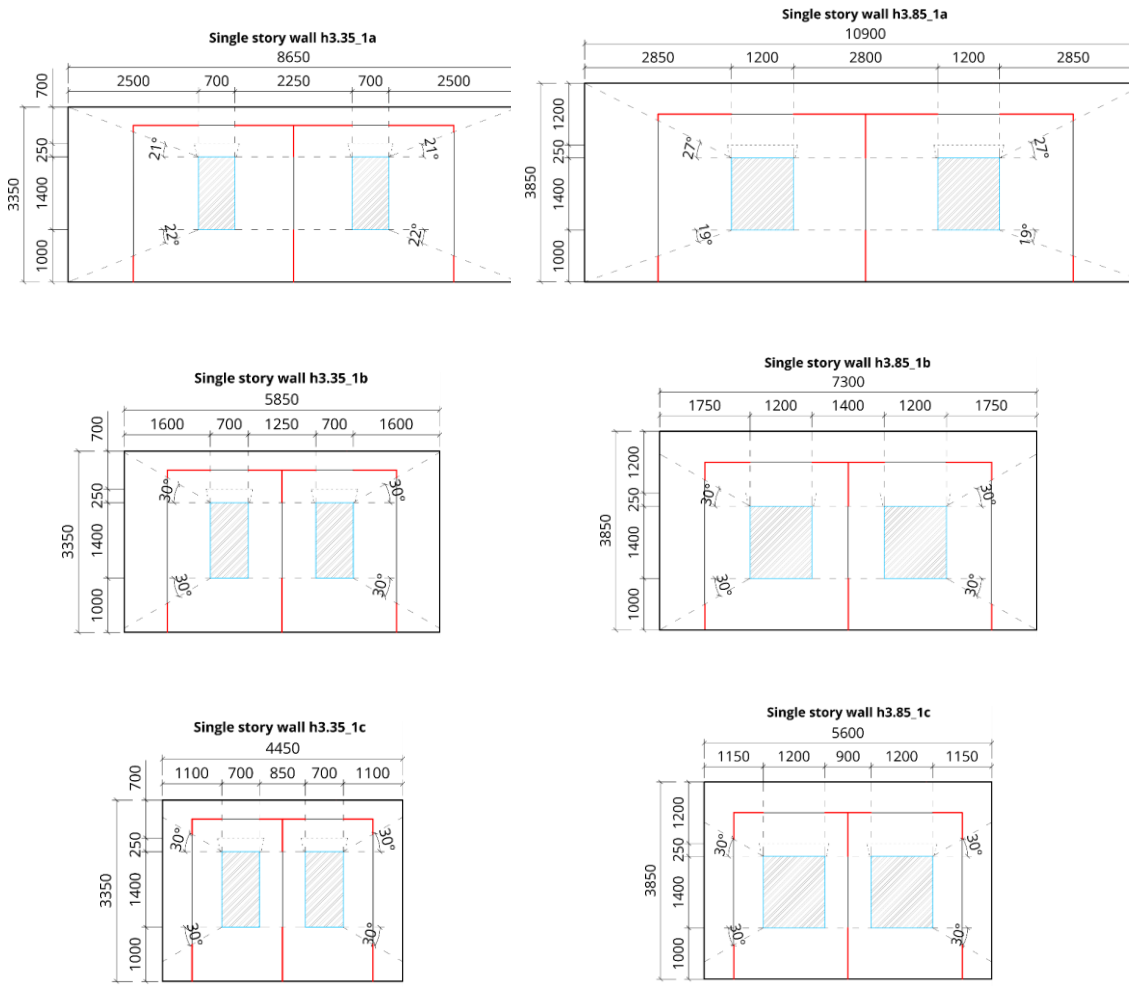


Figure 5.47 Single-story walls (measures in mm)

- **Two-story walls**

Two two-story walls configurations are considered (Figure 5.48). Fixed supports are assigned at the bottom of the piers, simulating a stiff foundation. A vertical compression is applied at the top; the self-weight is also considered. The capacity curves varying the vertical stress are analysed. Spandrel configuration t_1 is considered (see spandrel elements).

The ID of each case study is in the form "Two-story wall_A_B_C":

- A is for the total height in meters: e.g. *h6*;
- B is for the average axial stress on the piers of the first floor (in addition to the self-weight): 01-03-05 for 0.1, 0.3 or 0.5 MPa, respectively;
- C is for the strengthened configuration: R1 and R2 for strengthening on one and two sides, respectively. If this part is omitted, it indicates an unstrengthened structure.

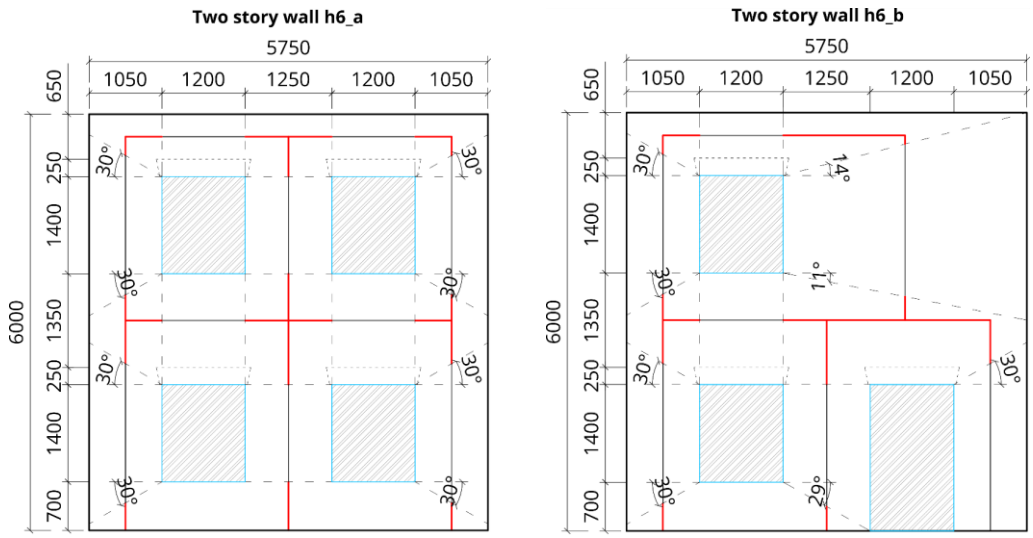


Figure 5.48 Two-story walls (measures in mm)

5.4.3.4 Analyses

The input tables for the mechanical parameters considered for the masonry, in the three different configurations (non-reinforced, strengthened on one side and on two sides), are provided in Figure 5.49. Moreover, the additional properties set for the behavior of the plastic hinges are summarized in Figure 5.50 and Figure 5.51, for piers, and Figure 5.52, Figure 5.53 and Figure 5.54, for spandrels.

Some general remarks before presenting the results:

- The resistance capacity of the CRM strengthened elements depends also on their axial stress level. However, $\tau_{0,eq}$ and $H_{P,eq}$, have been calculated with reference to the axial force due to vertical loads only. Therefore, any possible variation of axial force during the pushover analysis (and, consequently, of the resistance of the CRM strengthened elements) is not considered in this simplified approach.
- In spandrel elements, conservatively, the net masonry spandrel height, *b'*, is considered (the height of the jack arch is neglected).

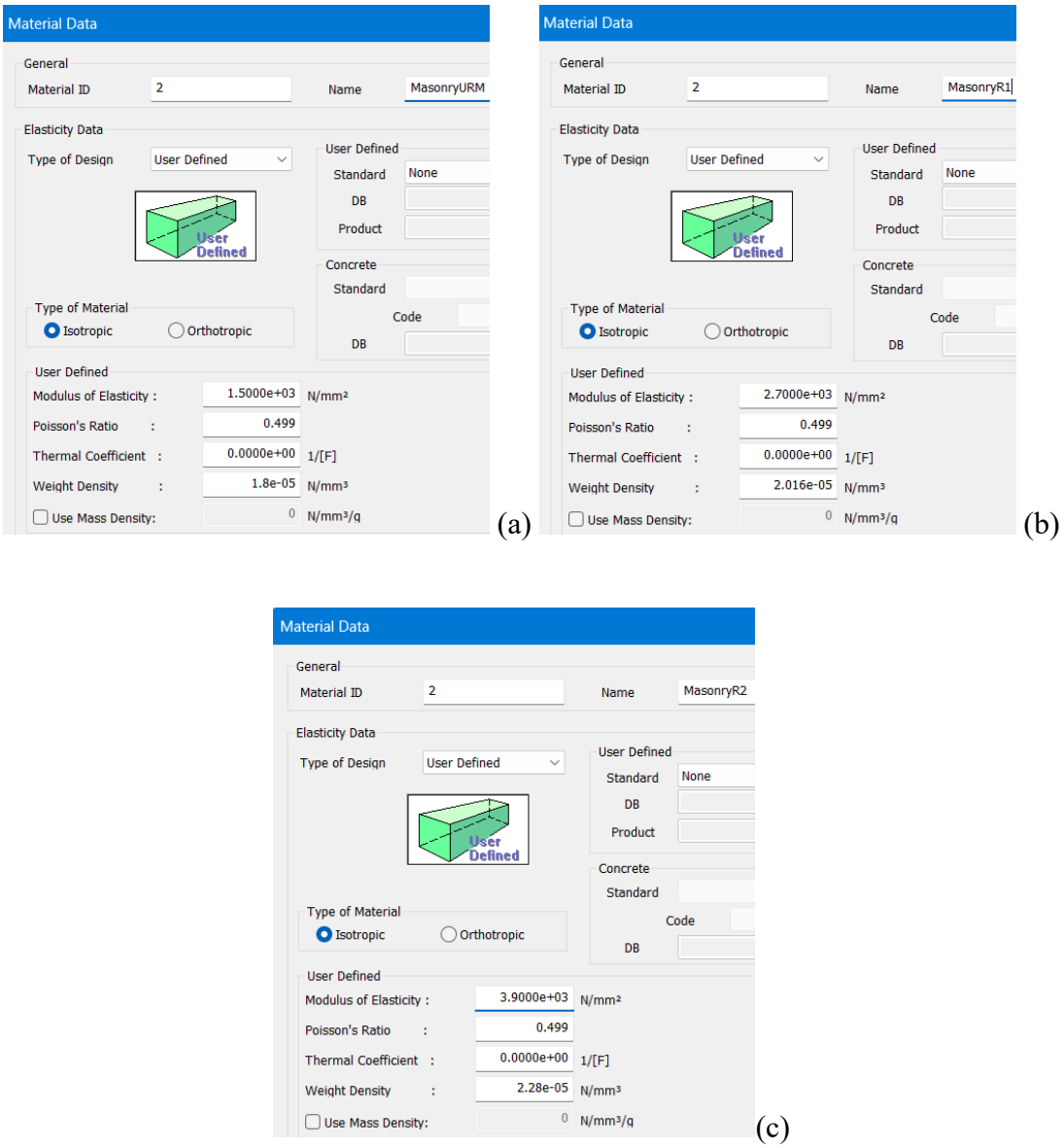


Figure 5.49 Material data for masonry: (a) unreinforced; (b) strengthened on one side; (c) strengthened on two sides

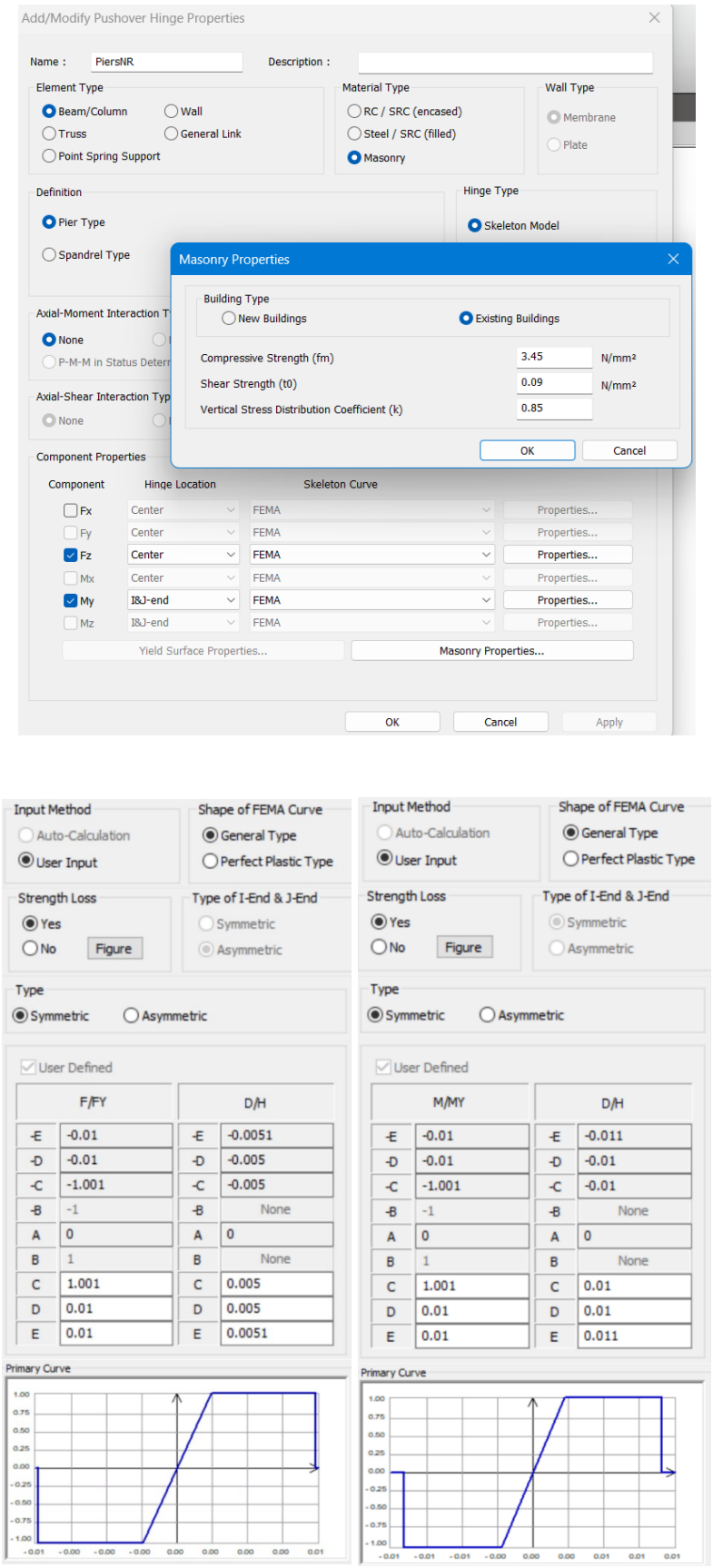


Figure 5.50 Characteristics of the plastic hinges for unreinforced masonry piers in Midas Gen

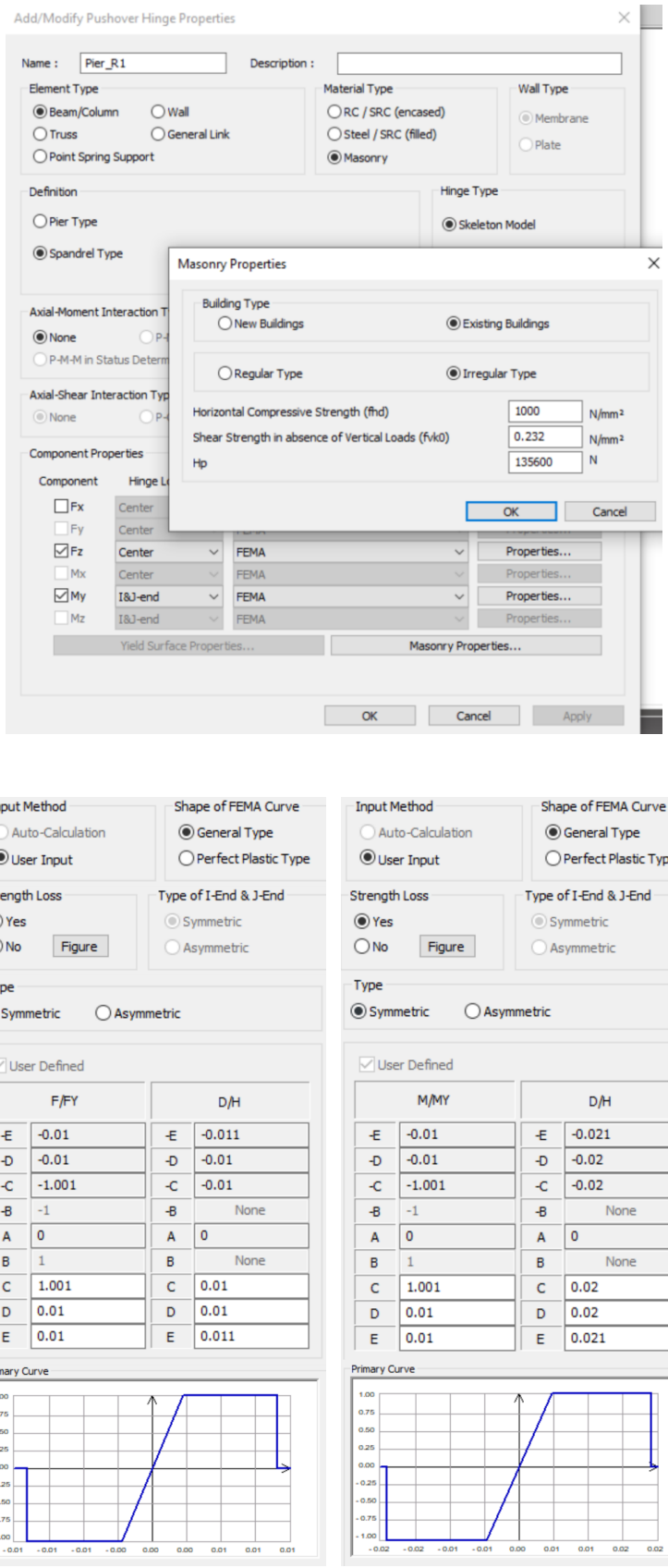


Figure 5.51 Characteristics of the plastic hinges for reinforced masonry piers in Midas Gen

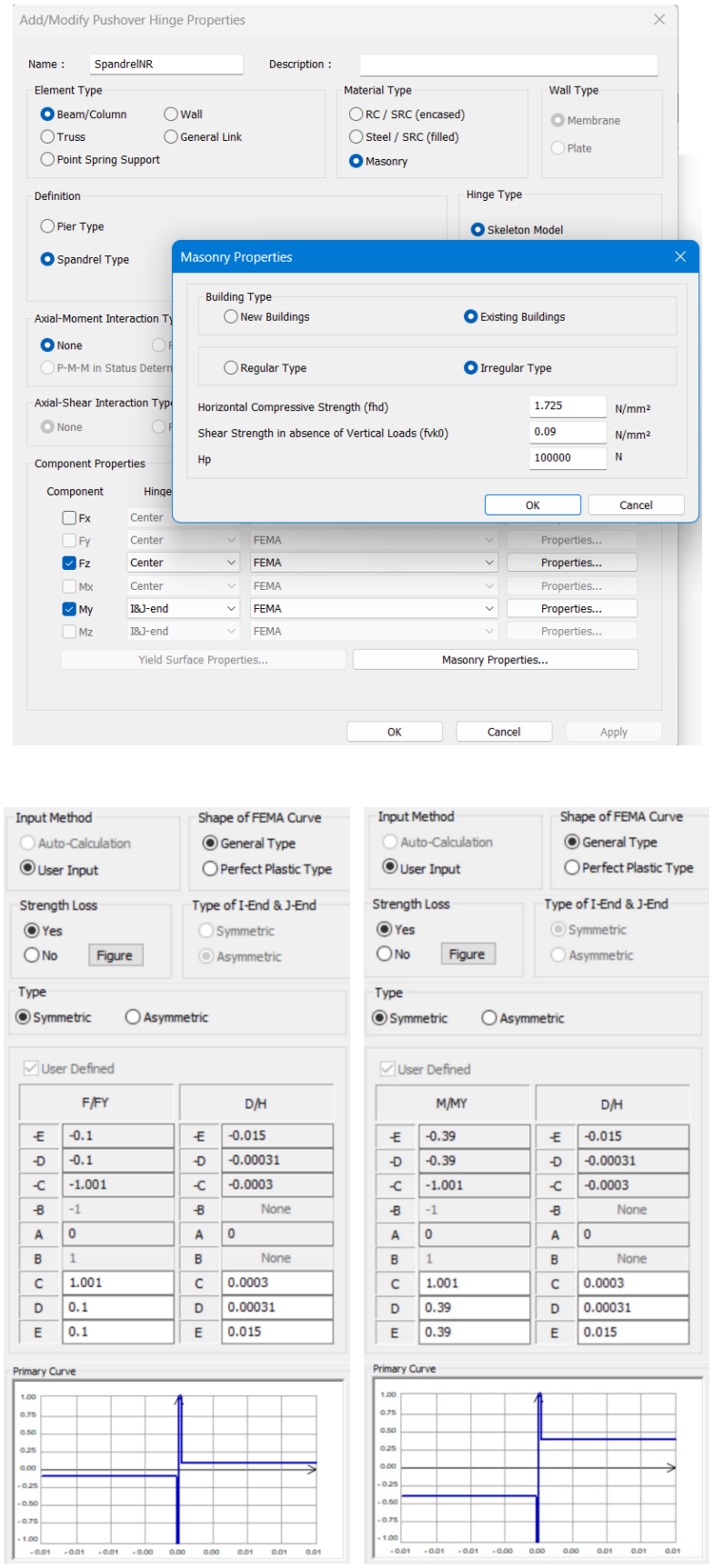


Figure 5.52 Characteristics of the plastic hinges in Midas Gen for: unreinforced masonry spandrels with horizontal tie (case t_1)

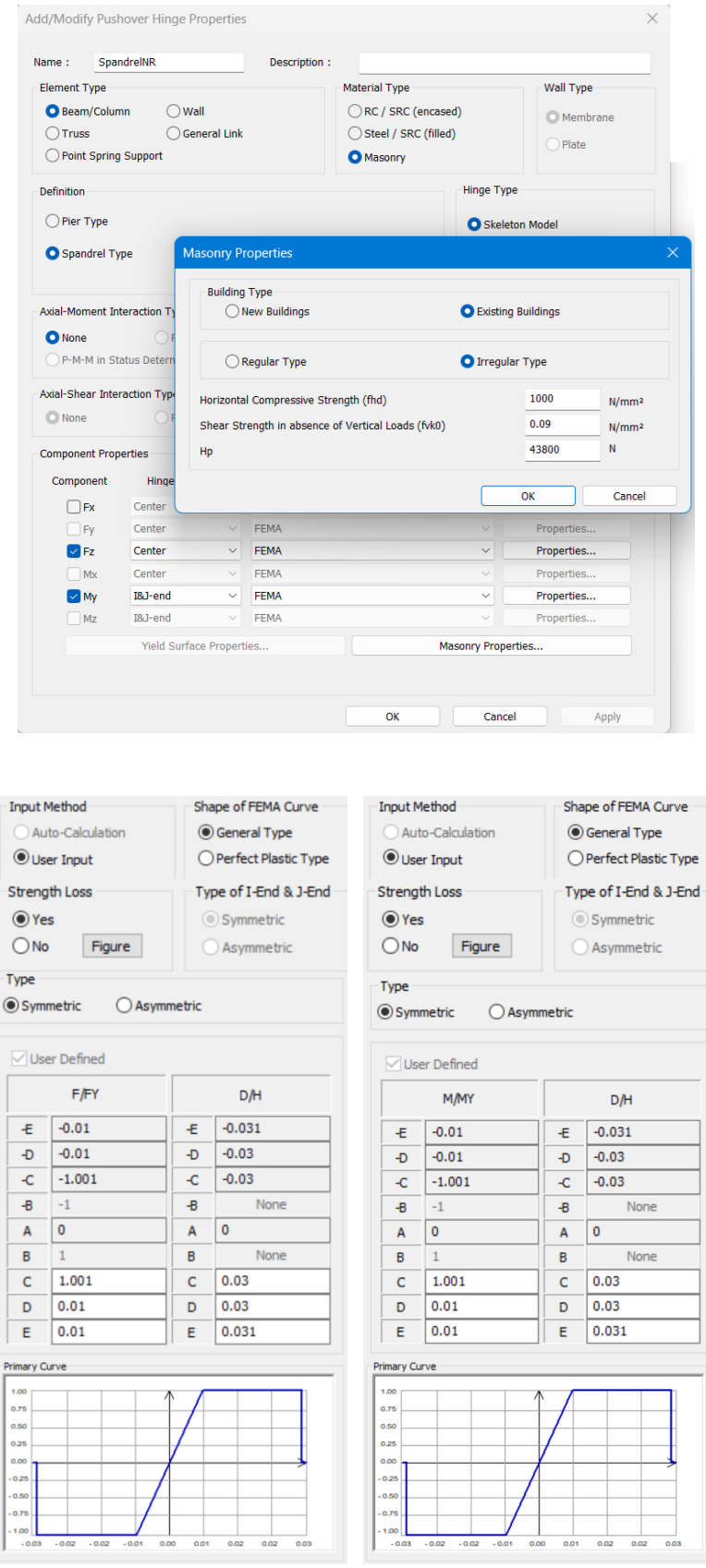


Figure 5.53 Characteristics of the plastic hinges in Midas Gen for: unreinforced masonry spandrels without horizontal tie (case t_0)

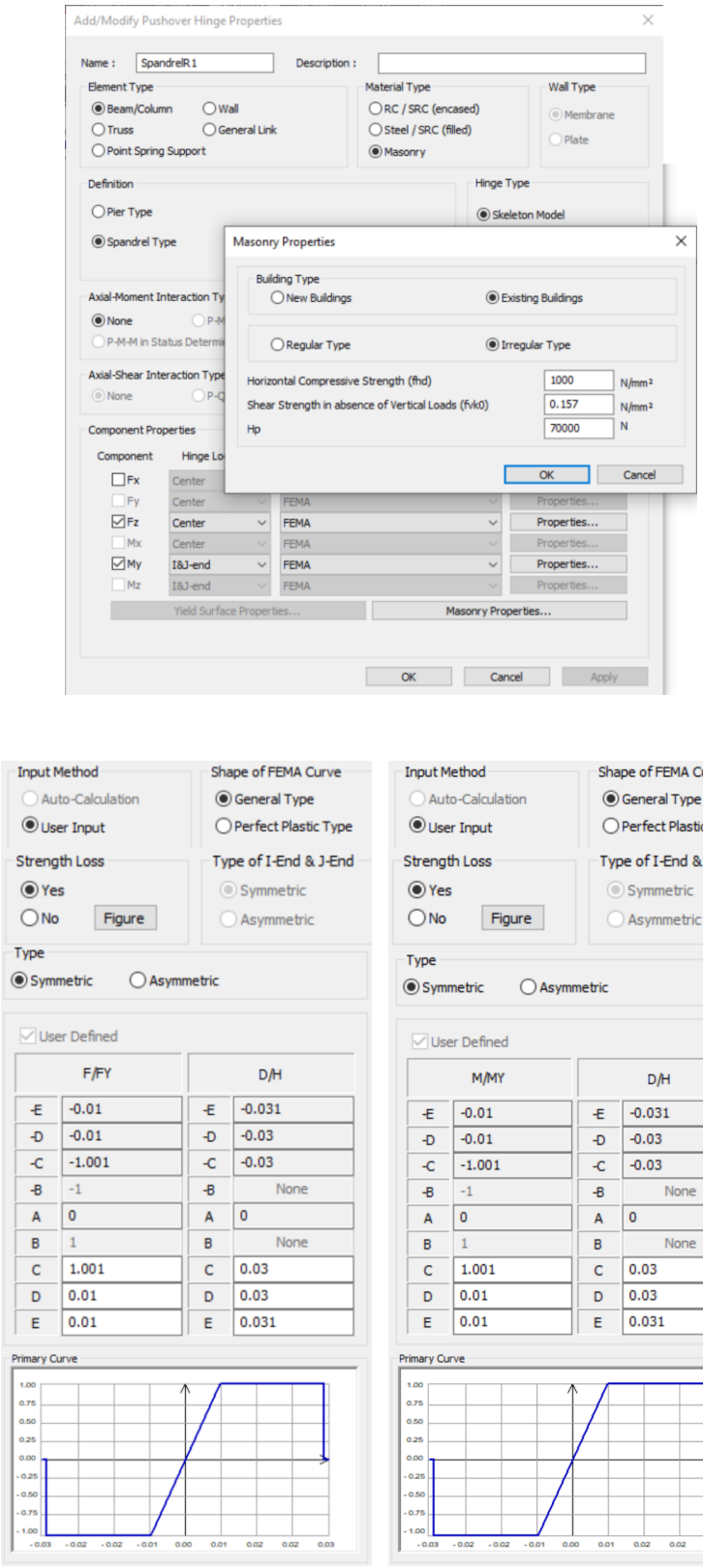


Figure 5.54 Characteristics of the plastic hinges in Midas Gen for reinforced masonry spandrels

- **Pier elements**

The complete set of capacity curves for masonry piers are reported in Appendix B. The modelling approach adopted is schematized in Figure 5.55. The vertical stress is simulated by applying a vertical force to the upper node, before performing the pushover analysis.

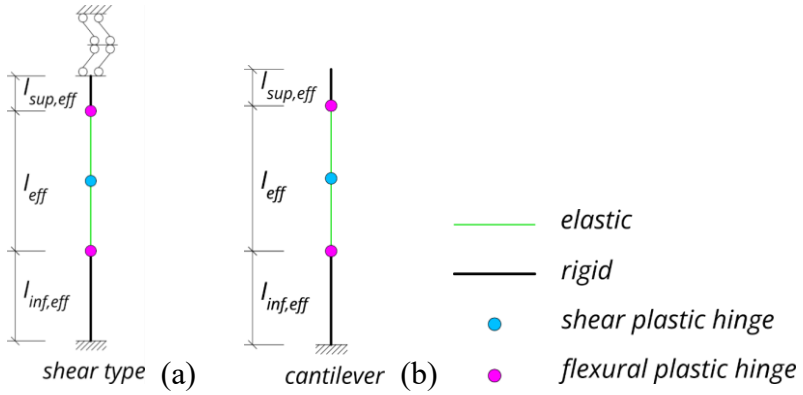


Figure 5.55 Modelling of a single pier, according to a shear-type (a) or a cantilever (b) scheme

The pushover analysis is performed by scaling the horizontal force at the upper node while controlling its horizontal displacement. In the graphs, the base shear, F, is plotted against the net horizontal displacement d between the top and the bottom of the effective pier length l_{eff}.

Generally, in the cantilever elements, the lower flexural hinge activates, as it is the most stressed under bending moment. In shear-type elements dominated by bending, both flexural hinges activate simultaneously, due to the symmetric distribution of the bending moment. In shear-type pier elements vulnerable to shear, the plastic hinge located in the centre of the element activates.

- **Spandrel elements**

The complete set of capacity curves of the masonry spandrels are reported in Appendix B. The modelling approach adopted is presented in Figure 5.56. It consists of a portal frame with piers and nodal areas modelled as rigid elements. Only the spandrels are considered as elastic and the respective plastic hinges are activated.

The pushover analysis is performed by gradually increasing the nodal rotation at the two base supports while controlling the horizontal displacement of the node at the top-right. No self-weights or additional vertical loads are considered. In the graphs, the shear acting on the spandrel, *F*, is plotted against the net vertical displacement *d* between the left and right end of the spandrel length *l*.

In unstrengthened spandrels (t_0), the model predicts either a bending or a shear brittle failure, followed by a post-cracking phase, as illustrated in Figure 5.57a,b. This residual capacity, associated with the bending failure mechanism is governed by the block-to-block interaction mechanism, while the cohesion contribution is neglected (i.e., $f_{v0}=0$ in Eq.(4.15)). In contrast, the residual capacity for the shear mechanism is limited to 10%. For unreinforced t_1 spandrel configurations, the chord rotation limits depend on the governing failure mechanism (0.005 for diagonal cracking and 0.02 for bending), while the residual strength for diagonal cracking is set at 0.6% and maintained up to a chord rotation of 0.015 (Figure 5.57c).

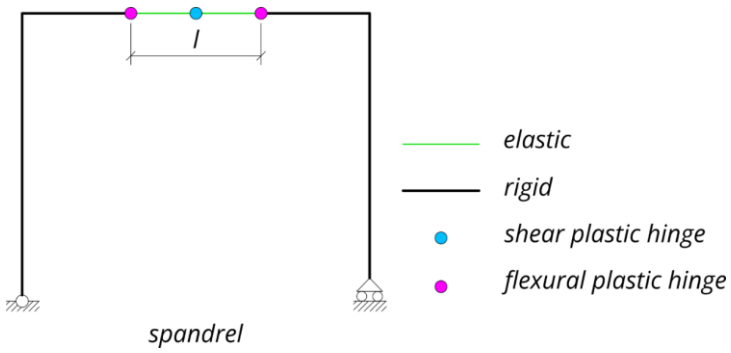


Figure 5.56 Modelling of a single spandrel

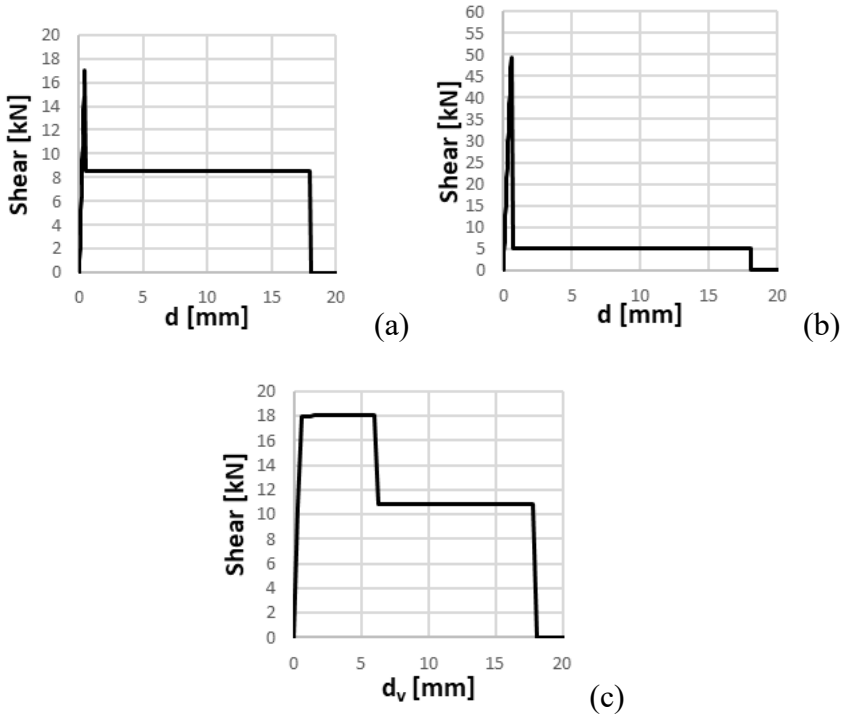


Figure 5.57 Capacity curve for unstrengthened masonry spandrels (a) L1.2_1.5_t0, (b) L1.2_0.8_t0 and (c) L1.2_1.5_t1

- **Portal frames**

The complete set of capacity curves of the portal frames are reported in Appendix B; the modelling approach adopted is presented in Figure 5.58. The masonry self-weight is not considered.

The pushover analysis is performed by gradually increasing the nodal displacement of the corner nodes (from left to right). The total base shear, *F*, is plotted against the lateral displacement, *d*.

It is observed that, as the lateral displacement progresses, the axial compression decreases in the left pier and increases in the right one. This aspect, in the unstrengthened configuration, likely results in a higher resistance of the right pier, compared to the left one. Differently, in the reinforced configurations, the variation of axial load on the piers' resistance in neglected.

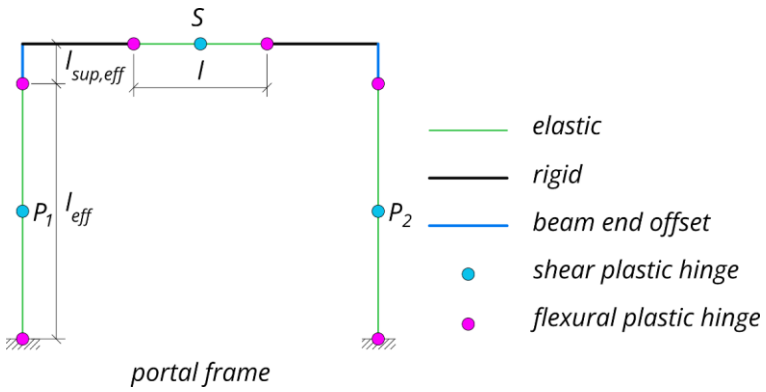


Figure 5.58 Modelling of a portal frame

The results show that the higher resistance of the URM spandrels in t_1 configurations allows for a better exploitation of the piers' lateral performance, than in t_0 cases. However, the impact of the tie is greatly mitigated in the R1-R2 configurations, as the CRM provides the spandrel with an effective coupling effect for the piers.

- **Single-story walls**

The capacity curves of the single-story walls are reported in Appendix B; the modelling approach adopted is presented in Figure 5.59. The masonry self-weight is considered.

The pushover analysis is performed by gradually increasing the nodal displacement of the corner nodes (from left to right). The total base shear, *F*, is plotted against the lateral displacement, *d*.

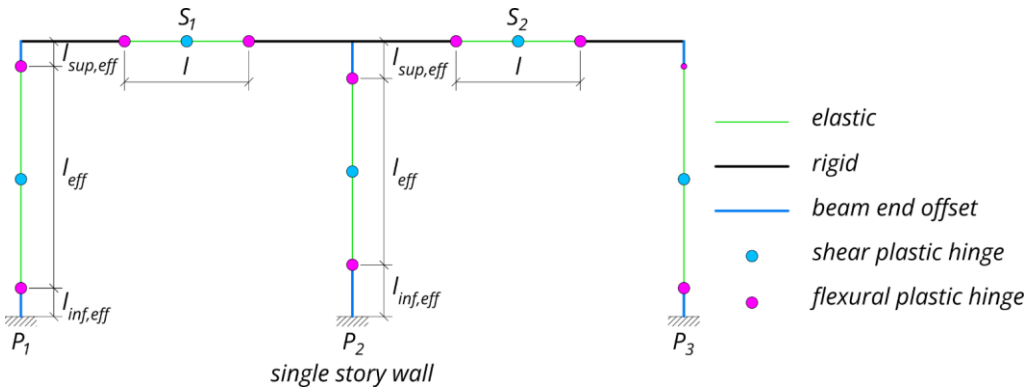


Figure 5.59 Modelling of a single-story wall

The resistances of the 3.85 m tall wall result generally higher than those of the 3.35 m one under the same configuration assumptions (URM, R1 or R2). Similar conclusions as for the Portal frame can be drawn.

- **Two-story walls**

The capacity curves obtained for the two-story walls are reported in Appendix B; the modelling approach adopted is presented in Figure 5.60.

The pushover analysis is performed by gradually increasing the lateral forces applied on the left corner nodes. Two force distributions are considered: one proportional to the fundamental mode shape (id. "mode") and one proportional to story masses (id. "mass"). The total base shear, F, is plotted against the lateral displacement at top of the second story, d. The masonry self-weight is considered. For the case study "two-story wall h6_b", the analyses were performed for both the left-to-right (+) and right-to-left (-) loading directions.

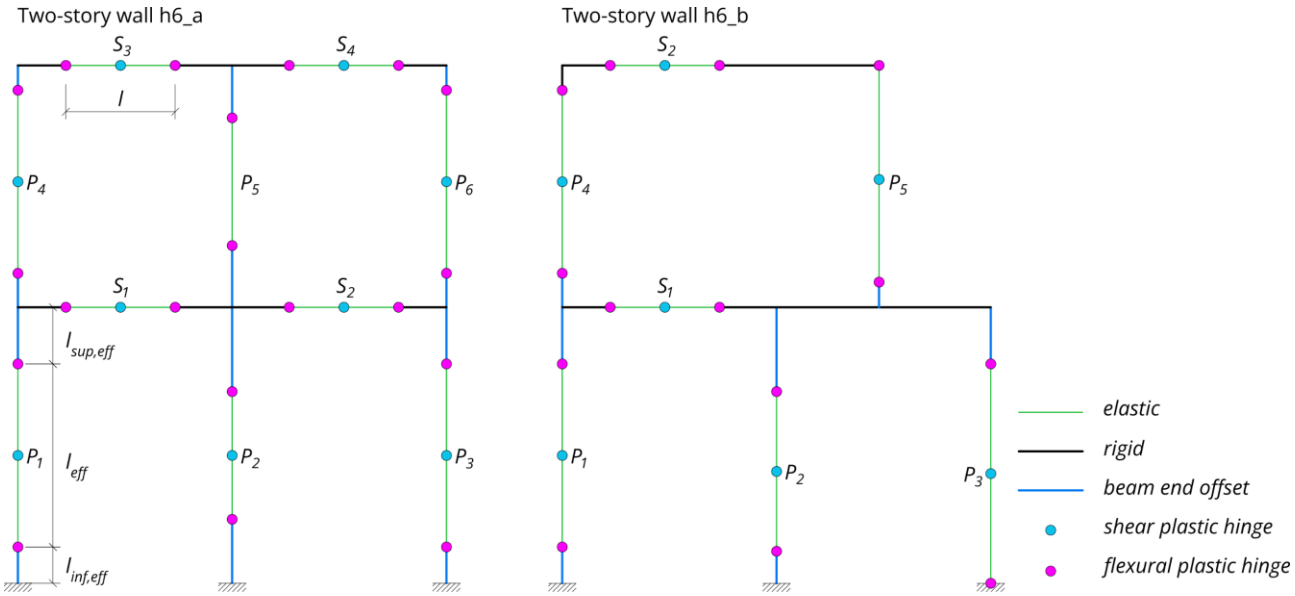


Figure 5.60 Modelling of two-story walls

5.5 Pilot building simulation using the Equivalent frame model

The building was analysed using an equivalent frame model implemented in the Midas Gen software. The geometric characteristics of the structure are described in Section 1.1. The loading apparatus was also modelled to account for the distribution of forces between the two longitudinal walls. It was represented through rigid elements, while the connections between the apparatus and the building were defined to avoid introducing any unintended stiffness. The lengths of the piers and of the rigid zones, shown in Figure 5.61, were determined according to Dolce's rule [85].

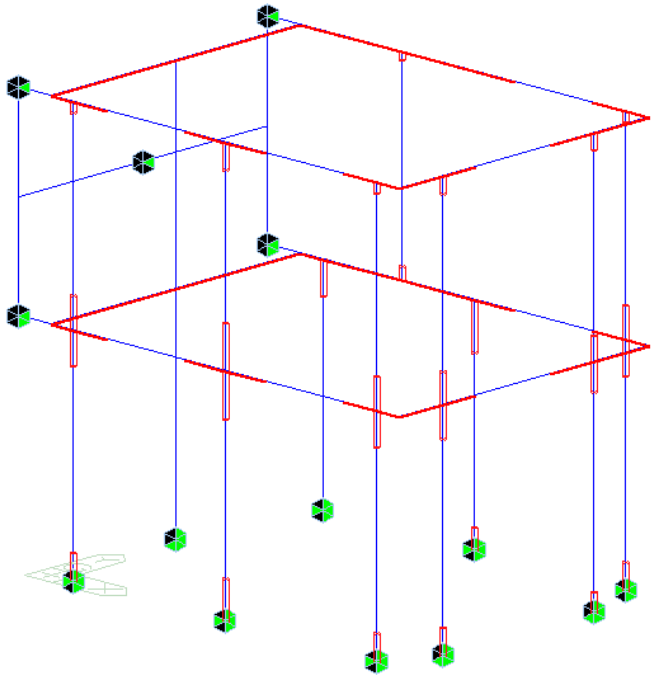


Figure 5.61 Equivalent frame model of the pilot building (red segments are rigid)

5.5.1 Material properties

The mechanical characteristics of the masonry used in the analysis are based on the previous experimental evidence. The material properties are summarized in Table 5.10.

Table 5.10. Masonry mechanical parameters used to calculate the plastic hinge resistances

E_m [Mpa]	1050	Masonry Young's modulus
G_m [Mpa]	350	Masonry shear modulus
f_m [Mpa]	2.4	Masonry compressive reisistance in the vertical direction
f_{hm} [Mpa]	1.2	Masonry reisistance in the horizontal direction
τ_0 [Mpa]	0.08	Masonry shear reisstance in absence of normal tension
ρ [kN/m^3]	21.0	Masonry self weight
ε_{c2} [‰]	0.002	Limit strain at constant compressive resistance (Figure 5.62)
ε_{cu} [‰]	0.01	Ultimate strain

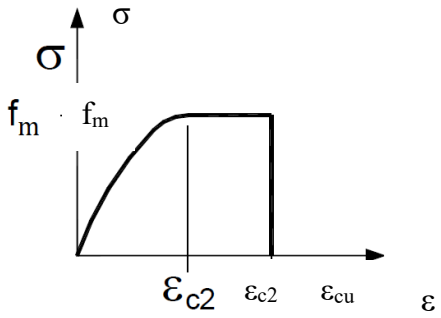


Figure 5.62 Simplified constitutive law for masonry

The mechanical characteristics of materials for strengthening (GFRP mesh and mortar for coating) were obtained from technical data sheets and previous tests on the materials. Their mechanical properties are reported in Table 5.11.

Table 5.11. Material properties of materials for strengthening

GFRP mesh			Coating mortar		
T_G	5.60	kN	f_c	15	MPa
E_s	25000	MPa	$f_{t,c}$	1.1	MPa
ε_{su}	14.5	‰	E_c	5000	MPa
Mesh pitch	66	mm			

The additional GFRP mesh installed at the corners was considered when calculating the bending resistance of side longitudinal piers. Ten vertical reinforcement mesh strands were considered in the most distant position from the compressed edge and double reinforcement bars up to 330 mm from the tensioned edge were also considered.

The elastic and shear moduli were increased to account for the coating. The thickness of the beam element sections remained 350 mm, but an equivalent weight density was used to consider the added weight of the mortar coating.

The drifts and the residual strengths used for the plastic hinges are reported in Table 5.12. The drift values were adjusted according to the previous experimental evidence.

5.5.2 Plastic hinges properties

Table 5.12. Drifts used to model plastic hinges in the numerical model of the URM pilot building

URM pier				
Point	Flexural hinge		Shear hinge	
	Resistance	Drift	Resistance	Drift
A.	0	0	0	0
B.	$M_{Rd,b(U)}$	$\delta_{B(M)}$	$V_{Rd,dc(U)}$	$\delta_{B(V)}$
C.	$M_{Rd,b(U)}$	1.0%	$V_{Rd,dc(U)}$	0.5%
D.	$0.3 \cdot M_{Rd,b(U)}$	1.5 %	$0.5 \cdot V_{Rd,dc(U)}$	0.8%
E.	$0.3 \cdot M_{Rd,b(U)}$	2.0 %	$0.5 \cdot V_{Rd,dc(U)}$	0.85%
URM spandrel				
Point	Flexural hinge		Shear hinge	
	Resistance	Drift	Resistance	Drift
A.	0	0	0	0
B.	M_{R1}	$\delta_{B(M)}$	V_{R2}	$\delta_{B(V)}$
C.	M_{R1}	1.5%	$0.7 \cdot V_{R2}$	0.2%
D.	$0.3 \cdot M_{R1}$	1.5%	$0.3 \cdot V_{R2}$	0.5%
E.	$0.3 \cdot M_{R1}$	2.0%	$0.3 \cdot V_{R2}$	0.6%

The drifts used for the strengthened plastic hinges were calibrated to reproduce the observed behaviour. The drifts used in the analysis are reported in Table 5.13.

Table 5.13. Drifts used to model plastic hinges in the numerical model of the strengthened pilot building

RM pier				
Point	Flexural hinge		Shear hinge	
	Resistance	Drift	Resistance	Drift
A.	0	0	0	0
B.	$M_{Rd,b(URM)}$	$\delta_{B(M)}$	$V_{Rd,dc(URM)}$	$\delta_{B(V)}$
C.	$M_{Rd,b(URM)}$	1.8%	$V_{Rd,dc(URM)}$	0.8%
D.	$0.5 \cdot M_{Rd,b(URM)}$	4.0 %	$0.6 \cdot V_{Rd,dc(URM)}$	1.6%
E.	$0.5 \cdot M_{Rd,b(URM)}$	4.2 %	$0.6 \cdot V_{Rd,dc(URM)}$	1.8%

RM Spandrel		
Point	Flexural hinge	
	Resistance	Drift
A.	0	0
B.	M_{R1}	$\delta_{B(M)}$
C.	M_{R1}	1.5%
D.	$0.3 \cdot M_{R1}$	1.5%
E.	$0.3 \cdot M_{R1}$	2.0%

The calculated values for the piers' strength show that all piers and spandrels fail in bending. The exception is the large pier in the West wall, which fails in shear.

5.5.3 Numerical analysis of the unreinforced pilot building

A pushover analysis was conducted by imposing lateral displacement on the middle node of the horizontal element connecting the two vertical elements of the loading apparatus. Supports to fix the translations and the rotation in the wall plane were applied at the base of the ground story pier elements.

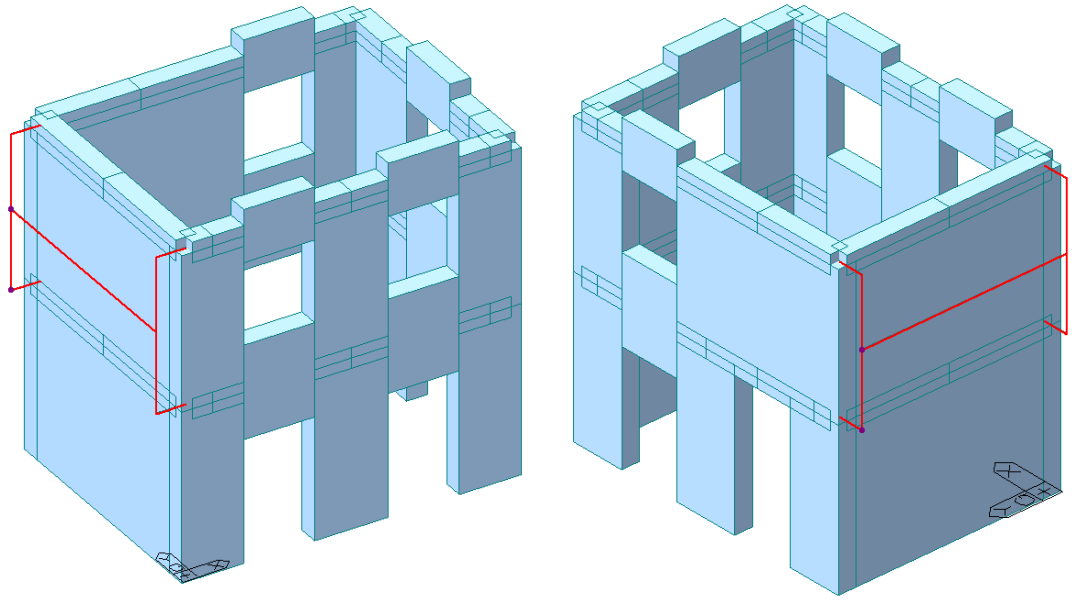


Figure 5.63 Equivalent frame model of the pilot building (extruded view)

5.5.3.1 Modal analysis

The results of the modal analysis are presented in Table 5.14. The predominant X direction mode is shown in Figure 5.64. The first mode of vibration is a translational mode in *Y* direction, while the second one is translational in *X* direction. Consequently, *X* direction will be referred to as the second mode of vibration, while *Y* direction will be referred as the first one. The participanting masses associated with the first and second vibration modes are 84.51% and 93.75%, respectively. The structure vibrates predominantly in the second mode. The periods of vibration in the *Y* and *X* directions are equal to 0.175 s and 0.161 s, respectively. It must be noted that the elastic modulus of the masonry was considered halved to account for the cracked state, as suggested by the Italian Building Code [15].

Table 5.14. Results of modal analysis

EIGENVALUE ANALYSIS													
	Mode No	Frequency			Period	Tolerance							
		(rad/sec)		(cycle/sec)	(sec)								
	1	35.8769		5.7100	0.1751	5.6095e-49							
	2	38.9631		6.2012	0.1613	5.3118e-48							
MODAL PARTICIPATION MASSES PRINTOUT													
	Mode No	TRAN-X		TRAN-Y		TRAN-Z		ROTN-X		ROTN-Y		ROTN-Z	
		MASS(%)	SUM(%)	MASS(%)	SUM(%)	MASS(%)	SUM(%)	MASS(%)	SUM(%)	MASS(%)	SUM(%)	MASS(%)	SUM(%)
	1	0.5493	0.5493	84.5131	84.5131	0.0000	0.0000	0.0000	0.0000	0.0000	0.0000	7.9345	7.9345
	2	93.7511	94.3003	0.3517	84.8648	0.0000	0.0000	0.0000	0.0000	0.0000	0.0000	0.2653	8.1998

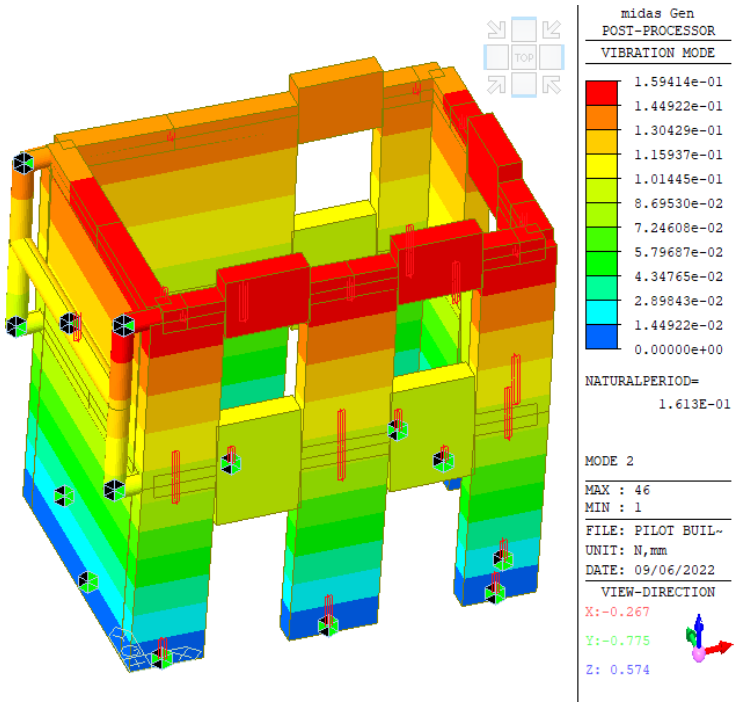


Figure 5.64 Second vibration mode (first translational mode in X direction)

5.5.3.2 Pushover analysis

In the pushover analysis, the actual vertical loads acted on the structure, and the distribution of horizontal forces depended on the stiffness of the longitudinal walls. The model included the loading apparatus to simulate horizontal force distribution properly. The geometric nonlinearities were considered in the analyses, although the out-of-plane behaviour of the elements was not considered. The pushover analysis was performed up to a 2nd story displacement of 50 mm. The resulting pushover curve is presented in Figure 5.65, and key observations of the model behaviour are presented in Table 5.15. The failure mechanism is shown in Figure 5.66.

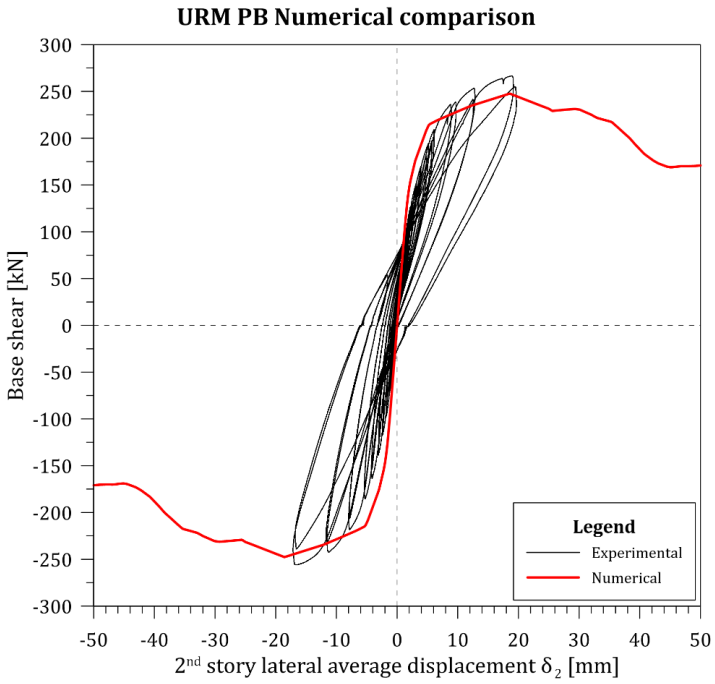


Figure 5.65 Pilot building numerical comparison with the equivalent frame model

Table 5.15. Equivalent frame model behaviour

Top floor displacement [mm]	Observation
2.4	Flexural cracking (point B reached) in all spandrels of East and West walls and piers of the top floor.
5.6	Shear cracking (point B) of the middle pier of the West wall on the 1st story
27.0	Failure (point E) of the middle pier of the West wall on the 1st story
29.0	Cracking (point B) in the middle pier of the East wall on the 2nd story
32.8	Near collapse (point D) in the southern spandrel of the East wall.
35.2	Maximum resistance (point C) at the base of most of the 1st story piers.
40.0	Failure (point E) of the southern spandrel of the East wall.

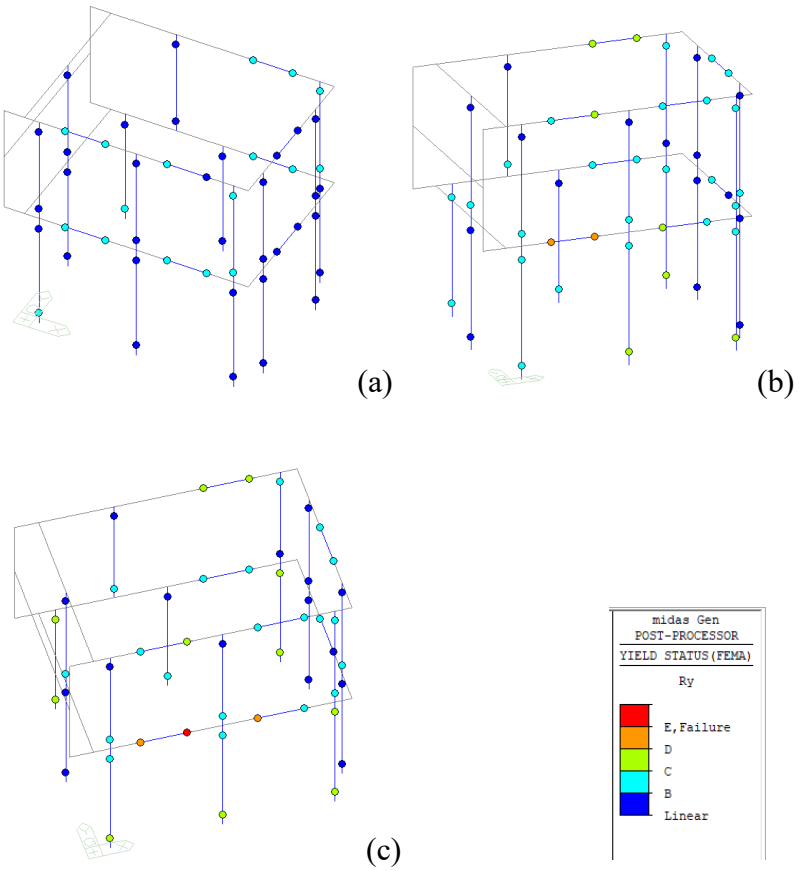


Figure 5.66 Numerical model hinge status of yielding by FEMA, positive loading direction: Top story displacement equal to 2.4 mm (a); 32.8 mm (b); 40.0 mm (c)

Even though the numerical pushover curve reproduces the stiffness and resistance of the building quite well, the numerical model indicates a 1st story collapse mechanism (in the test, there was a 2nd story collapse). The difference can be attributed to the effect of corner piers, which interact with the cross walls. This interaction causes the middle pier on 2nd story to be the weakest of the three and the first to damage. In the test, the middle pier was damaged first too.

5.5.4 Numerical analysis of the strengthened pilot building

The analysis was performed with displacement imposed on the middle node of the horizontal beam, connecting the two vertical beam elements of the loading apparatus. Plastic hinges were assigned to the pier and spandrel beam elements.

5.5.4.1 Modal analysis

The results of the modal analysis are presented Table 5.16. The first mode of vibration is a translational mode in Y direction, while the second one is translational in X direction. The predominant mode of vibration in X direction is shown in Figure 5.67. The participating masses associated with the first and second mode of vibration are 85.36% and 93.47%, respectively. The structure vibrates predominantly in the second mode. The periods of vibration in the Y and X directions are equal to 0.154 s and 0.142 s, respectively. That is a decrease of 12.3 % in Y and 11.7 % in X directions, which is caused by the global stiffness increase of the structure due to the coating. It must be noted that the elastic moduli of the materials were halved to account for the cracked cross-section, as suggested by the NTC 2018 standard in chapter 7.2.6.

Table 5.16. Results of modal analysis

Node	Mode	UX		UY		UZ		RX		RY		RZ	
EIGENVALUE ANALYSIS													
	Mode No	Frequency				Period		Tolerance					
		(rad/sec)		(cycle/sec)		(sec)							
	1	40.9249		6.5134		0.1535		1.5835e-47					
	2	44.2169		7.0373		0.1421		1.3619e-46					
MODAL PARTICIPATION MASSES PRINTOUT													
	Mode No	TRAN-X		TRAN-Y		TRAN-Z		ROTN-X		ROTN-Y		ROTN-Z	
		MASS(%)	SUM(%)	MASS(%)	SUM(%)	MASS(%)	SUM(%)	MASS(%)	SUM(%)	MASS(%)	SUM(%)	MASS(%)	SUM(%)
	1	0.5290	0.5290	85.3638	85.3638	0.0000	0.0000	0.0000	0.0000	0.0000	0.0000	7.0602	7.0602
	2	93.4709	93.9999	0.3614	85.7252	0.0000	0.0000	0.0000	0.0000	0.0000	0.0000	0.2060	7.2662

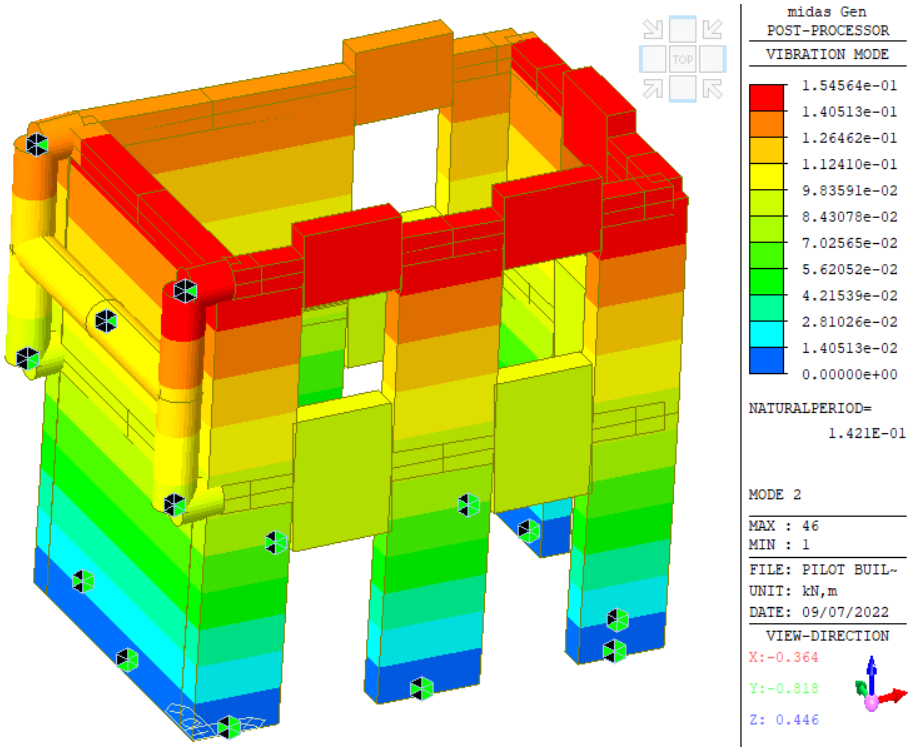
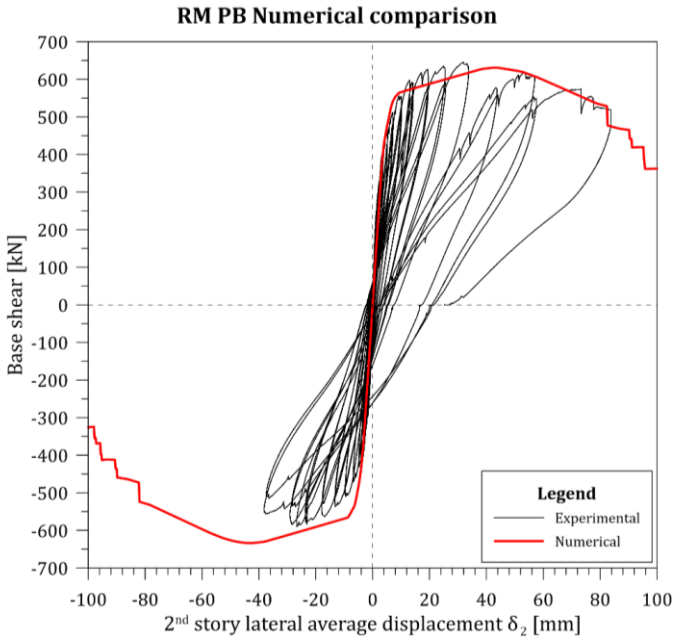


Figure 5.67 Second vibration mode (translational in the X direction)

5.5.4.2 Pushover analysis

The pushover analysis considers nonlinear static behaviour. After applying vertical loads, the horizontal displacements are imposed until a 2nd story displacement reaches 100 mm in the *X* direction. The loads were applied in positive and negative loading directions. Hence, there were two pushover analyses for the strengthened building. The resulting

pushover curves are presented in Figure 5.68. Key observations of the model behaviour



are presented in

Figure 5.68 Pilot building numerical comparison with the equivalent frame model

Table 5.17. The collapse mechanism evolution is shown in Figure 5.69.

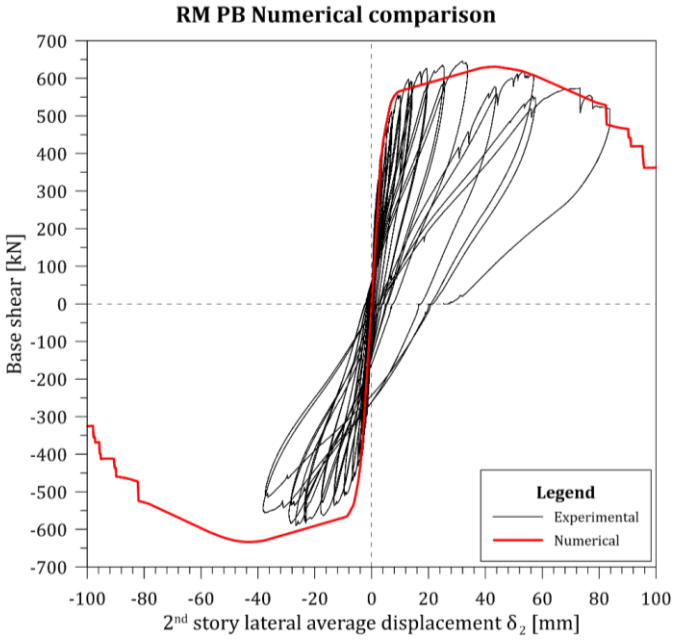


Figure 5.68 Pilot building numerical comparison with the equivalent frame model

Table 5.17. Equivalent frame model behaviour

Top floor displacement [mm]	Observation
4.0	Flexural cracking (point B) in the 1st story piers of the longitudinal walls
5.2	Flexural cracking (point B) of the southernmost 1st story spandrel pier of the East wall
6.4	Flexural cracking (point B) of the 2nd story spandrel West wall
8.0	Flexural cracking (point B) of the 2nd story middle pier of the East wall
8.6	Flexural cracking (point B) of all the 1st story spandrels of the longitudinal walls and in the 2nd story northernmost spandrel of the East wall
13.2	Flexural cracking (point B) in the 2nd story northernmost piers of the longitudinal walls
36.0	Flexural cracking (point B) in the 2nd story southernmost spandrel of the East wall.
41.6	Maximum bending resistance (point C) in the middle piers of the 1st storey of the longitudinal walls
44.0	Maximum bending resistance (point C) in all of the 1st storey piers of the longitudinal walls, except for the corner pier adjacent to the door.
53.2	Maximum bending resistance (point C) in all of the 1st storey piers of the longitudinal walls.
79.0	Near collapse (point D) in the middle 1st story pier of the East wall
82.4	Failure (point E) of the middle pier on the 1st storey of the East wall
86.0	Near collapse (point D) of the middle pier on the 1st story of the West wall
90.2	Failure (point E) of the middle pier on 1st storey of the West wall
95.6	Failure (point E) of all the 1st story piers of the longitudinal walls

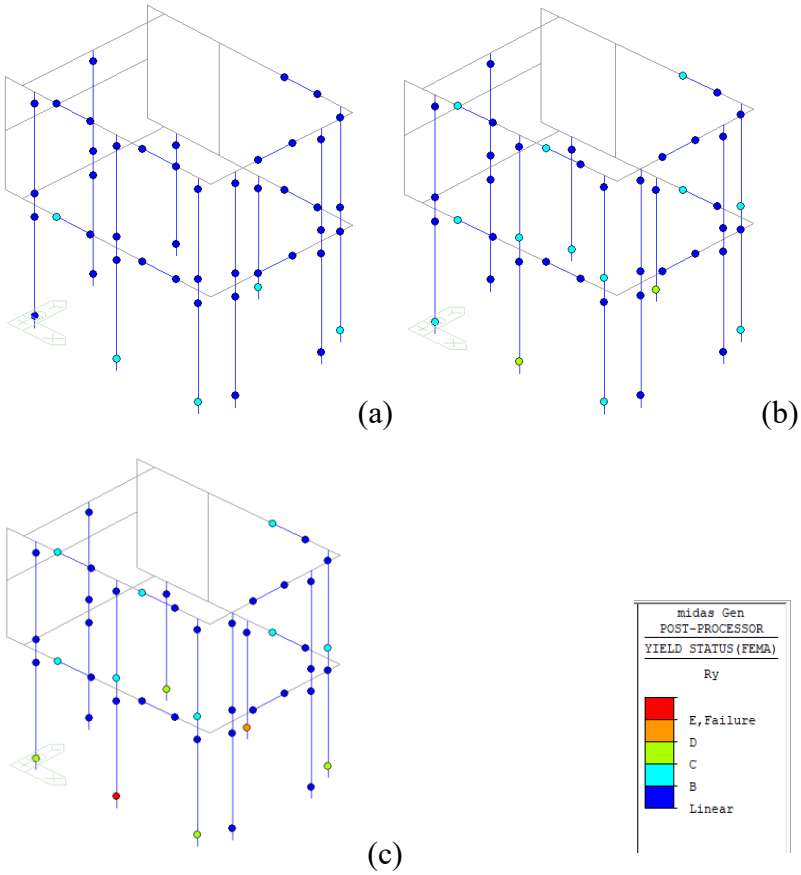


Figure 5.69 Numerical model hinge status of yielding by FEMA, positive loading direction: Top story displacement equal to 5.2 mm (a); 41.6 mm (b); 86.0 mm (c)

The numerical pushover curve reproduces the stiffness and resistance of the building quite well. The match is better in the positive direction of loading. The resistance in the simulations was highly influenced by the additional reinforcement added in the corner piers of the longitudinal walls. The behaviour observed in the numerical model evidence a 1st story collapse mechanism characterized by the formation of flexural hinges at the base and the top of the piers; the same mechanism was observed in the experimental test.

6 Conclusions and future work

6.1 Summary

The present work was motivated by the lack of experimental and numerical data on historic masonry structures strengthened using the Composite Reinforced Mortar (CRM) technique, particularly for single-sided interventions and the comparison with double-sided strengthening. The primary objective of this thesis was to investigate the effectiveness of CRM interventions in enhancing the seismic performance of unreinforced masonry (URM) elements and buildings, and to assess the reliability of numerical modelling approaches for their analysis.

The study integrated laboratory testing, advanced numerical simulations, and parametric analyses. Laboratory campaigns included material characterization of CRM composites, accelerated ageing tests to assess durability, and structural tests on masonry elements and a pilot building. These tests allowed the identification of mechanical response mechanisms, assessment of load-bearing and deformation capacities, and evaluation of the influence of key parameters such as mesh density, mortar properties, and boundary conditions. The experimental results also provided the basis for analytical correlations for estimating the strength of CRM-reinforced elements and guidance on deformation capacity. Particular attention was given to two-leaf walls, addressing the separation problem experimentally through the use of artificial diatons.

Advanced numerical models were developed using Abaqus, with detailed nonlinear material behavior at the masonry, mortar, and reinforcement interface levels. These models helped interpret the interactions among the components and evaluate the impact of key parameters on local and global responses. For larger-scale applications, the equivalent frame method was employed, calibrated on the pilot building tests, demonstrating its potential for efficient assessment of whole-building seismic performance.

6.2 Conclusions

6.2.1 Effectiveness of CRM reinforcement

The experimental campaign conducted in this study has confirmed the effectiveness of the Composite Reinforced Mortar (CRM) system for the seismic strengthening of historic masonry, both in single-sided and double-sided applications. Full-scale in-plane (IP) and out-of-plane (OOP) cyclic tests on single- and double-leaf masonry walls and in-plane tests on spandrels demonstrated that the CRM coating, consisting of hydraulic lime mortar reinforced with GFRP mesh and properly anchored through connectors, significantly improves structural performance.

Key findings from the experiments include:

- **In-plane (IP) performance**

For the considered historic **two-wythe stone masonry**, the one side strengthening on masonry piers increased the resistance and the displacement at maximum resistance by 47 % and 175 %, respectively. The capacity for energy dissipation improved about 2.5 times, and the ultimate displacement increased by 135 %. OOP bending tests on piers strengthened on one side were performed to obtain information for design against local failures. If the coating is applied on both sides of the wall, the resistance to in-plane loads increased to 111 %, more than double that on only one side, and the displacement and energy dissipation capacity improved by 301 % and tenfold, respectively. For the spandrels, the strengthening increased the peak resistance by 2.8 and 3.4 times that of the unstrengthened sample, for the case of coating on one or two sides, respectively. Furthermore, the strengthening provided considerable additional ductility, displacement capacity and energy dissipation, with ultimate drifts more than five times greater and dissipated energy more than thirty times larger.

For the considered **single leaf brick masonry**, the one side strengthening on masonry piers increased the resistance and the displacement at maximum resistance by 63% and 119%, respectively. The capacity for energy dissipation improved about 4.4 times, and the ultimate displacement increased by 80 %. For the spandrel, the coating on one side increased the peak resistance by 33%. The drifts in the strengthened sample reached 1.5% at peak load and 3.2% at collapse, which is one order of magnitude greater than for the

unstrengthened sample. Furthermore, the strengthening provided considerable additional energy dissipation capacity, which increased by 25 times.

For the considered **double-leaf brick masonry**, the one side strengthening on masonry piers increased the resistance and the displacement at maximum resistance by 105% and 447%. The capacity for energy dissipation improved about 4.4 times, and the ultimate displacement increased by 179 %. If the coating is applied on both sides of the wall, the resistance to in-plane loads increased to 157 %, and the displacement and energy dissipation capacity improved by 301 % and elevenfold, respectively. %. For the spandrel, the coating on one side increased the peak resistance by 125%. The drifts in the strengthened sample reached 1.5% at peak load and 3.2% at collapse, which is one order of magnitude greater than for the unstrengthened sample. Furthermore, the strengthening provided considerable additional energy dissipation capacity, which increased by 66 times.

The pushover test on the **two-leaf rubble stone masonry building**, showed that the coating on one side increased the lateral by approximately 2.4 times. Moreover, the displacement capacity and the total dissipated energy increased by approximately 4.0 times and 7.2 times, respectively. The results of this study also highlight that one-side application of a CRM system can effectively mitigate and delay the propagation of cracks in masonry under lateral loads of similar magnitude. In the URM building, the damage (shear and bending cracks) occurred mainly in the second level walls due to the low value of the axial load in the piers. On the contrary, in the RM building, the flexural resistance of the reinforced piers is mainly due to the CRM system, and thus, the collapse occurred at the first level, where the horizontal forces are higher. Moreover, the CRM coating promoted the activation of a "box behaviour" of the whole building that led to a kinematic mechanism involving the global overturning of the structure. The evaluation of the equivalent viscous damping coefficient of the URM building ranged from 8 % to 12 % and was quite similar for the RM building. This information can be useful to evaluate the resisting acceleration with the use of the Capacity spectrum method [302].

- **Out-of-plane (OOP) performance**

The out-of-plane tests on masonry piers, conducted under a three-point bending configuration, showed that single-sided CRM strengthening increased the bending resistance by a factor of 8.5 to 10.6. In addition, the displacement capacity exhibited a substantial improvement.

The reinforcement enabled a diffuse cracking pattern from the central section, rather than a single localized failure observed on the unstrengthened side. Full exploitation of the GFRP mesh was observed at collapse, indicating that the desired failure mechanisms were achieved.

Masonry ring beams strengthened with externally bonded CFRM strips and those with GFRP meshes embedded in the bed joints were tested under horizontal cyclic loading. Although these techniques are present in current guidelines, the literature referring to experimental results on full-scale configurations and load reversal is limited.

The tests on the C shaped samples showed the effectiveness of the one-sided carbon fibre reinforced polymer strip in increasing the resistance and displacement capacity in both loading directions.. The continuity of the carbon strips around the corners and at the orthogonal walls was thus crucial to achieve effectiveness. The tests also highlighted the possibility of accidental local damage in the fibres (e.g. for an inadequate bend radius or anchorage of the strip) that might reduce the effectiveness of the intervention. No particular influences were related to the type of masonry, only to the thickness.

The tests on simply supported masonry beams with GFRP meshes embedded in the bed joints proved beneficial in increasing both strength and displacement capacities, when compared with the first cracking occurrence. The diffuse reinforcement enabled the formation of several nearly vertical cracks in the masonry, spread over a wide area of the sample until the failure at the centre. With increased masonry thickness, the resistance increased, but the ultimate deflection was reduced. But tests also showed that, especially in masonry with straight bed joints, such as the solid bricks, discontinuity within the bed joint could arise and reduce the mesh contribution. Thus, close attention should be paid to fully embed the mesh within the mortar and remove any voids. However, in actual applications, gravitational loads acting on the beam provide additional stabilizing action.

- **Composite action and connection details**

The test on the two-leaf rubble stone masonry building demonstrated that employing two transverse injected connectors per square meter was found to be an effective measure in preventing the separation of masonry leaves, as evidenced by the absence of wall bulging phenomena in the reinforced masonry test. Also, the test on the repaired building evidenced the importance of the connection between the coating and the foundation.

Proper connection details, such as vertical rebars, must be adopted to prevent vertical uplift phenomena and improve the global flexural capacity of the building.

Effective anchoring, including artificial diatons in double-leaf walls, was essential to prevent premature separation of masonry leaves also in tests on single structural elements and to ensure that the coating acted compositely with the masonry. Debonding between coating and masonry was observed during the tests on piers and spandrels, which eventually spread over larger areas. However, because of the good connection, the coating and the elements acted as a composite element until collapse.

- **Other observations:**

Differently from previous findings in diagonal compression tests on FRCM strengthened masonry [177], no eccentric phenomena related to the asymmetrical stiffness occurred. This is because the boundary conditions in these tests (continuity with the lateral piers) were much more realistic than those of the isolated panels investigated in the literature. Finally, the low-medium axial stress level in the panels (more consistent with actual configurations) mitigated this occurrence.

6.2.2 Durability of CRM composites

Durability and long-term performance of composite strengthening systems remain a critical concern for the rehabilitation of masonry structures. The results of the present study demonstrate that environmental exposure at elevated temperature in alkaline conditions, significantly affects the mechanical behavior of TRM and FRP materials, with notable reductions in tensile strength and elongation at break, observed in both dry fibreglass yarns and GFRP grids. Moreover, the tests highlighted practical issues in current testing regulations, such as slippage and difficulties in clamping dry fibre yarns, which can influence the reliability and reproducibility of experimental measurements.

After 3000 hours of conditioning, tensile tests revealed that the strength of dry fibreglass yarns decreased by 65% and 84% at 23°C and 40°C, respectively. The current observations can be the criticalities of the clamping system proposed in the guidelines for testing: the radiused clamps caused partial premature fibre breaks. Additionally, wrapping the yarn on the steel cylinder increased slippage. Using wedge jaws with glued tabs provided the most reliable measurements.

For the FRP grids, strength reductions depended on both the exposure conditions and the fibre orientation. WARP fibres consistently retained higher strength than WEFT fibres, with differences of 5-10% in most cases. After 3000 h at 40 °C, the strength of WARP fibres decreased to 76% under Environment A and 64% under Environment C, while WEFT fibres dropped to 69% and 60%, respectively. On average, Environment C was more aggressive than Environment A. Failure modes also varied with orientation: WARP samples fractured mainly near the first node, whereas WEFT samples showed longitudinal fibre breaks along the sample.

Although the mortar was classified as M15, it exhibited significantly higher strengths after 28 days, showing a compressive strength of approximately 23 MPa in compression and 4 MPa in flexural tension.

The FRCM system did not achieve the anticipated tensile performance because the dry fibreglass mesh slipped within the mortar, emphasizing the necessity of including adhesion-promoting components in the design of composite systems. In some tests, cracks appeared outside the gauge length, highlighting the challenge of accurately monitoring displacements during tensile testing.

Although accelerated ageing tests are effective for identifying degradation trends but still require correlation with real-time exposure to predict service life. Future research should aim to establish these correlations.

6.2.3 Analytical estimation of the seismic behaviour of CRM-strengthened masonry

The analytical correlations deriving from the FRCM guidelines, appropriately calibrated to adapt to the CRM system, correctly estimate the in-plane elastic-plastic behaviour of piers. Results shows a good correlation with the experimental data for all masonry types, and the failure mechanisms are correctly identified by the analytic models, with a slight underestimation of the peak load. For spandrels, the correlations generally tended to underestimate the experimental results of the tested specimens. In particular, the analytical predictions of strength showed better alignment with the strength values observed during the repeated loading cycles, rather than with the initial peak loads.

The proposed analytical approach for estimating the out-of-plane behaviour of masonry piers, correctly reproduces the experimental strength, although with maximum errors of about 15 %. The strength at first cracking is generally underestimated by the model, as also the displacement at first cracking. Also, for the unstrengthened specimens, the

analytical predictions showed good correlation with the experimental results in terms of strength.

For the roof ring beams strengthened with GFRP meshes embedded in mortar joints or with the externally-bonded CFRP strips, the proposed analytical approach for the first cracking and maximum strength prediction, based on the simple bending resistance of unreinforced or reinforced cross-sections, respectively, was shown to be reliable. In the former case, the full, uncracked masonry cross section was considered; in the latter, cracked masonry with zero tensile strength and only tensile strength of fibres. This simple approach was effective, although the maximum strength prediction did not account for premature failures, for example, due to local damage of fibres (CFRP strips) or to row separations (GFRP meshes in bed joints). However, this can be roughly addressed by reducing the maximum allowable stress of the reinforcement, as well as the effective fibre amount.

6.2.4 Numerical modelling insights

The numerical investigations carried out in this study highlighted the complementary roles of detailed and simplified modelling approaches for the analysis of CRM-strengthened masonry structures.

The detailed finite element models developed in Abaqus, accounting for material nonlinearities in both the masonry and the reinforced mortar matrix, were able to accurately reproduce the experimentally observed failure mechanisms, crack patterns, and load-displacement responses at the structural element scale. As such, they provide a reliable reference for the validation of analytical correlations and for the interpretation of experimental results.

At the building scale, simplified models based on the equivalent frame method, implemented in Midas Gen, demonstrated their capability to capture the global seismic response of CRM-strengthened buildings with a limited computational effort. Although these models rely on idealized constitutive laws and concentrated plasticity, their calibration against experimental data allowed a realistic representation of strength hierarchy, stiffness degradation, and displacement capacity. The application to benchmark wall configurations and to the pilot building test confirmed that, when properly calibrated, equivalent frame models can provide reliable estimates of global seismic performance,

making them suitable for practical engineering assessments and preliminary design studies.

Overall, the combined use of detailed and simplified numerical approaches proved to be an effective strategy: refined models support the understanding and calibration of simplified methods, while equivalent frame models enable the extension of experimental findings to real-scale structures with a limited computational cost.

6.3 Future Work

Although the present research provides a comprehensive experimental and numerical assessment of CRM strengthening systems, several aspects require further investigation.

First, large-scale experimental validation beyond the pilot building remains an important step to confirm the applicability of the proposed analytical and numerical approaches to more complex and irregular structures. Additional full-scale tests on multi-story buildings would be particularly valuable to further investigate load redistribution, out-of-plane interactions, and global failure mechanisms.

Second, the experimental results presented in this thesis offer a solid basis for the development and validation of advanced numerical models aimed at extensive parametric studies. Future work should focus on systematically investigating the influence of geometric parameters, masonry typologies, reinforcement layouts, and connector arrangements on the seismic performance of CRM-strengthened elements and structures.

Further long-term experimental studies are also needed to better assess the durability of CRM systems under combined environmental cycling and sustained loading. A key challenge remains the correlation between accelerated ageing test results and the actual long-term behaviour of strengthened masonry in real exposure conditions, which is essential for reliable service-life predictions.

Finally, future research should address aspects not covered in this study, such as the economic efficiency and practical feasibility of single-sided versus double-sided CRM applications, as well as the integration of out-of-plane response within simplified global analysis frameworks. These developments would further support the adoption of CRM systems in design practice and contribute to the formulation of dedicated guidelines and code provisions.

References

[1] Atalić J, Uroš M, Šavor Novak M, Demšić M, Nastev M. The Mw5.4 Zagreb (Croatia) earthquake of March 22, 2020: impacts and response. Bull Earthq Eng 2021;19:3461–89. https://doi.org/10.1007/s10518-021-01117-w.

[2] Augenti N, Parisi F. Learning from Construction Failures due to the 2009 L'Aquila, Italy, Earthquake. J Perform Constr Facil 2010;24:536–55. https://doi.org/10.1061/(ASCE)CF.1943-5509.0000122.

[3] Fragomeli A. Comportamento degli edifici in muratura nella sequenza sismica dell'Italia centrale del 2016 - Parte 1: Quadro generale. Progett Sismica 2017:49–77. https://doi.org/10.7414/PS.8.2.49-77.

[4] Fragomeli A, Galasco A, Graziotti F. Comportamento degli edifici in muratura nella sequenza sismica dell'Italia centrale del 2016 - Parte 2: Esempi di centri colpiti. Progett Sismica 2017:75–98. https://doi.org/10.7414/PS.8.3.75-98.

[5] Freddi F, Novelli V, Gentile R, Veliu E, Andreev S, Andonov A, et al. Observations from the 26th November 2019 Albania earthquake: the earthquake engineering field investigation team (EEFIT) mission. Bull Earthq Eng 2021;19:2013–44. https://doi.org/10.1007/s10518-021-01062-8.

[6] Manfredi G. Danni. Aquila Il Progetto CASE Complessi Antisismici Sostenibili Ed Ecocompatibili Ed IUSS Press 2010:35–41.

[7] Parisi F, Luca FD, Petruzzelli F, Risi RD, Chioccarelli E, Iervolino I. Field inspection after the May 20th and 29th 2012 Emilia- Romagna earthquakes 2012.

[8] Ghiassi B, Lourenco PB. Long-term Performance and Durability of Masonry Structures: Degradation Mechanisms, Health Monitoring and Service Life Design. Woodhead Publishing; 2018.

[9] Collepardi M. Degradation and restoration of masonry walls of historical buildings. Mater Struct 1990;23:81–102. https://doi.org/10.1007/BF02472568.

[10] ACI 549-L, RILEM TC 250. ACI 549.6R-20 Guide to Design and Construction of Externally Bonded Fabric-Reinforced Cementitious Matrix (FRCM) and Steel-Reinforced Grout (SRG) Systems for Repair and Strengthening Masonry Structures 2020.

[11] CNR. CNR DT 215/2018 Instructions for planning, execution and control of Static Consolidation Interventions through the use of Fibre-reinforced composites with inorganic matrix 2020.

[12] Chopra AK. Dynamics of structures: theory and applications to earthquake engineering. 4th ed. Upper Saddle River, New Jersey: Prentice Hall; 2012.

[13] Paulay T, Priestley MJN. Seismic design of reinforced concrete and masonry buildings. New York: Wiley; 1992. https://doi.org/10.1002/9780470172841.

[14] CEN. EN 1998-1:2004/A1:2013 - Eurocode 8: Design of structures for earthquake resistance - Part 1: General rules, seismic actions and rules for buildings 2013.

[15] Ministero delle Infrastrutture e dei Trasporti. Decreto 17 gennaio 2018: Aggiornamento delle «Norme tecniche per le costruzioni». 2018.

[16] Drysdale RG, Hamid AA, Baker DJ. Masonry structures: Behavior and design. Prentice-Hall, Englewood Cliffs, New Jersey, USA; 1993.

[17] Magenes G, Calvi GM. In-plane seismic response of brick masonry walls. Earthq Eng Struct Dyn 1997;26:1091–112. https://doi.org/10.1002/(SICI)1096-9845(199711)26:11%253C1091::AID-EQE693%253E3.0.CO;2-6.

[18] Tomaževič M. Earthquake-Resistant Design of Masonry Buildings. vol. 1. Imperial College Press; 1999.

[19] Marques R. Masonry Box Behavior. In: Beer M, Kougioumtzoglou IA, Patelli E, Au IS-K, editors. Encycl. Earthq. Eng., Berlin, Heidelberg: Springer Berlin Heidelberg; 2014, p. 1–18. https://doi.org/10.1007/978-3-642-36197-5_155-1.
[20] Hendry AW, Sinha BP, Davies SR. Design of masonry structures. 3rd ed. London: E & FN Spon; 2004.
[21] Samarasinghe W. The in-plane failure of Brickwork. Tesi di Dottorato. University of Edinburg, 1980.
[22] Beyer K, Dazio A. Quasi-Static Cyclic Tests on Masonry Spandrels. Earthq Spectra 2012;28:907–29. https://doi.org/10.1193/1.4000063.
[23] Gams M, Tomaževič M. Experimental simulation of seismic response of masonry walls, 2012.
[24] Gattesco N, Macorini L, Dudine A. Experimental Response of Brick-Masonry Spandrels under In-Plane Cyclic Loading. J Struct Eng 2015;142:04015146. https://doi.org/10.1061/(ASCE)ST.1943-541X.0001418.
[25] Gattesco, N, Clemente I, Noè S. Experimental investigation on the behavior of spandrels in ancient masonry buildings, Beijing, China: 2008.
[26] Gattesco N, Boem I. Out-of-plane behavior of reinforced masonry walls: Experimental and numerical study. Compos Part B Eng 2017;128:39–52. https://doi.org/10.1016/j.compositesb.2017.07.006.
[27] Godio M, Vanin F, Zhang S, Beyer K. Quasi-static shear-compression tests on stone masonry walls with plaster: Influence of load history and axial load ratio. Eng Struct 2019;192:264–78. https://doi.org/10.1016/j.engstruct.2019.04.041.
[28] Magenes G, Penna A, Rota M, Galasco A, Senaldi I. Shaking table test of a full scale stone masonry building with stiffened floor and roof diaphragms 2012.
[29] Parker CK, Tanner JE, Varela JL. Evaluation of ASTM Methods to Determine Splitting Tensile Strength in Concrete, Masonry, and Autoclaved Aerated Concrete. Masonry, ASTM International100 Barr Harbor Drive, PO Box C700, West Conshohocken, PA 19428-2959; 2008, p. 62–73. https://doi.org/10.1520/STP45706S.
[30] Petry S, Beyer K. Influence of boundary conditions and size effect on the drift capacity of URM walls. Eng Struct 2014;65:76–88. https://doi.org/10.1016/j.engstruct.2014.01.048.
[31] Spyrakos C, Francioso A. Shaking Table Test and Pushover Analysis on a Scaled Masonry Building, 2012.
[32] Vasconcelos G, Lourenço PB. In-Plane Experimental Behavior of Stone Masonry Walls under Cyclic Loading. J Struct Eng 2009;135:1269–77. https://doi.org/10.1061/(ASCE)ST.1943-541X.0000053.
[33] CEN. EN 772-1:2011+A1:2015 Methods of test for masonry units- Part 1: Determination of compressive strength 2015.
[34] European Union. EN 1996-1-1: Eurocode 6: Design of masonry structures - Part 1-1: General rules for reinforced and unreinforced masonry structures. 2005.
[35] CEN. EN 1015-11: Methods of test for mortar for masonry - Part 11: Determination of flexural and compressive strength of hardened mortar 2019.
[36] CEN. EN 1052-3:2002/A1:2007 Methods of test for masonry - Part 3: Determination of initial shear strength 2007.
[37] CEN. EN 1052-1:1998 Methods of test for masonry - Part 1: Determination of compressive strength 1998.
[38] C15 Committee. ASTM C1314 Test Method for Compressive Strength of Masonry Prisms 2021. https://doi.org/10.1520/C1314-21.

[39] C15 Committee. ATSM E519 Test Method for Diagonal Tension (Shear) in Masonry Assemblages 2007. https://doi.org/10.1520/E0519-07.
[40] Graziotti F, Magenes G, Penna A. Experimental cyclic behaviour of stone masonry spandrels, 2012.
[41] Augenti N, Parisi F, Prota A, Manfredi G. In-Plane Lateral Response of a Full-Scale Masonry Subassemblage with and without an Inorganic Matrix-Grid Strengthening System. J Compos Constr 2011;15:578–90. https://doi.org/10.1061/(ASCE)CC.1943-5614.0000193.
[42] Ismail N, Ingham JM. In-plane and out-of-plane testing of unreinforced masonry walls strengthened using polymer textile reinforced mortar. Eng Struct 2016;118:167–77. https://doi.org/10.1016/j.engstruct.2016.03.041.
[43] Guerrini G, Senaldi I, Graziotti F, Magenes G, Beyer K, Penna A. Shake-Table Test of a Strengthened Stone Masonry Building Aggregate with Flexible Diaphragms. Int J Archit Herit 2019;13:1078–97. https://doi.org/10.1080/15583058.2019.1635661.
[44] Magenes G, Penna A, Senaldi IE, Rota M, Galasco A. Shaking Table Test of a Strengthened Full-Scale Stone Masonry Building with Flexible Diaphragms. Int J Archit Herit 2014;8:349–75. https://doi.org/10.1080/15583058.2013.826299.
[45] Senaldi I, Magenes G, Penna A, Galasco A, Rota M. The Effect of Stiffened Floor and Roof Diaphragms on the Experimental Seismic Response of a Full-Scale Unreinforced Stone Masonry Building. J Earthq Eng 2014;18:407–43. https://doi.org/10.1080/13632469.2013.876946.
[46] Rinaldin G, Amadio C, Gattesco N. Review of experimental cyclic tests on unreinforced and strengthened masonry spandrels and numerical modelling of their cyclic behaviour. Eng Struct 2016;132:609–23. https://doi.org/10.1016/j.engstruct.2016.11.063.
[47] Tomaževič M, Lutman M, Petković L. Seismic Behavior of Masonry Walls: Experimental Simulation. J Struct Eng 1996;122:1040–7. https://doi.org/10.1061/(ASCE)0733-9445(1996)122:9(1040).
[48] Binda L, Saisi A, Tiraboschi C. Investigation procedures for the diagnosis of historic masonries. Constr Build Mater 2000;14:199–233. https://doi.org/10.1016/S0950-0618(00)00018-0.
[49] C15 Committee. ASTM C1197 Test Method for In Situ Measurement of Masonry Deformability Properties Using the Flatjack Method 2014. https://doi.org/10.1520/C1197-14A.
[50] RILEM TC 177-MDT. RILEM recommendation MDT. D.5—in-situ stress-strain behaviour tests based on the flat jack. Mater Struct 2004;37:497–501. https://doi.org/10.1007/BF02481589.
[51] RILEM TC 177-MDT. RILEM recommendation MDT. D. 4: In-situ stress tests based on the flat jack. Mater Struct 2004;37:491–6. https://doi.org/10.1007/BF02481588.
[52] C15 Committee. ASTM C1531 Test Methods for In Situ Measurement Of Masonry Mortar Joint Shear Strength Index 2003. https://doi.org/10.1520/C1531-03.
[53] RILEM TC 127-MS. MS-B.4 Determination of shear strength index for masonry unit/mortar junction. Mater Struct 1996;29:459–63. https://doi.org/10.1007/BF02486276.
[54] Borri A, Castori G, Corradi M. Determination of Shear Strength of Masonry Panels Through Different Tests. Int J Archit Herit 2015;9:913–27. https://doi.org/10.1080/15583058.2013.804607.

[55] Boschi S, Galano L, Vignoli A. Mechanical characterisation of Tuscany masonry typologies by in situ tests. Bull Earthq Eng 2019;17:413–38. https://doi.org/10.1007/s10518-018-0451-4.
[56] Corradi M, Borri A, Vignoli A. Experimental study on the determination of strength of masonry walls. Constr Build Mater 2003;17:325–37. https://doi.org/10.1016/S0950-0618(03)00007-2.
[57] Federal Emergency Management Agency. ATC FEMA 306: Evaluation of earthquake damaged concrete and masonry wall buildings – Basic Procedures Manual. 1999.
[58] ACI 530-05 Building Code Requirements for Masonry Structures and Commentary. 2005.
[59] DIN 1053-100 Masonry: Design on the Basis of Semi-Probabilistic Safety Concept. 2004.
[60] Cattari S, Magenes G, editors. Uso dei software di calcolo nella verifica sismica degli edifici in muratura v3.0. IT: Doppiavoce; 2024.
[61] Magenes G, Calvi GM. In-plane seismic response of brick masonry walls. Earthq Eng Struct Dyn 1997;26:1091–112. https://doi.org/10.1002/(SICI)1096-9845(199711)26:11%253C1091::AID-EQE693%253E3.0.CO;2-6.
[62] Calderini C, Cattari S, Lagomarsino S. In-plane strength of unreinforced masonry piers. Earthq Eng Struct Dyn 2009;38:243–67. https://doi.org/10.1002/eqe.860.
[63] Turnšek V, Čačovič F. Some experimental results on the strength of brick masonry walls. Proc 2nd Int Brick Mason Conf Stoke--Trent 1971:149–56.
[64] Turnšek V, Sheppard P. The shear and flexural resistance of masonry walls, NIGRO, Naša kniga; 1980, p. 517–73.
[65] Ministero delle Infrastrutture e dei Trasporti. Circolare 21 gennaio 2019, n. 7 C.S.LL.PP.: Istruzioni per l'applicazione dell'«Aggiornamento delle "Norme tecniche per le costruzioni"» di cui al decreto ministeriale 17 gennaio 2018. 2019.
[66] Angelillo M, Lourenço PB, Milani G. Masonry behaviour and modelling. In: Angelillo M, editor. Mech. Mason. Struct., vol. 551, Vienna: Springer Vienna; 2014, p. 1–26. https://doi.org/10.1007/978-3-7091-1774-3_1.
[67] Lourenço PB. COMPUTATIONAL STRATEGIES FOR MASONRY STRUCTURES: MULTI-SCALE MODELLING, DYNAMICS, ENGINEERING APPLICATIONS AND OTHER CHALLENGES, Bilbao, Spain: 2013.
[68] Marques R, Lourenço PB. Possibilities and comparison of structural component models for the seismic assessment of modern unreinforced masonry buildings. Comput Struct 2011;89:2079–91. https://doi.org/10.1016/j.compstruc.2011.05.021.
[69] Zizi M, Chisari C, Rouhi J, De Matteis G. Comparative analysis on macroscale material models for the prediction of masonry in-plane behavior. Bull Earthq Eng 2022;20:963–96. https://doi.org/10.1007/s10518-021-01275-x.
[70] Gambarotta L, Lagomarsino S. DAMAGE MODELS FOR THE SEISMIC RESPONSE OF BRICK MASONRY SHEAR WALLS. PART I: THE MORTAR JOINT MODEL AND ITS APPLICATIONS. Earthq Eng Struct Dyn 1997;26:423–39. https://doi.org/10.1002/(SICI)1096-9845(199704)26:4%253C423::AID-EQE650%253E3.0.CO;2-%2523.
[71] Bui TT, Limam A, Sarhosis V, Hjiaj M. Discrete element modelling of the in-plane and out-of-plane behaviour of dry-joint masonry wall constructions. Eng Struct 2017;136:277–94. https://doi.org/10.1016/j.engstruct.2017.01.020.
[72] Lemos JV. Modelling the Dynamics of Masonry Structures with Discrete Elements. Open Constr Build Technol J 2016;10:210–9. https://doi.org/10.2174/1874836801610010210.

[73] Lemos JV. Discrete Element Modeling of Masonry Structures. Int J Archit Herit 2007;1:190–213. https://doi.org/10.1080/15583050601176868.
[74] Baraldi D, Reccia E, Cecchi A. In plane loaded masonry walls: DEM and FEM/DEM models. A critical review. Meccanica 2018;53:1613–28. https://doi.org/10.1007/s11012-017-0704-3.
[75] Chen X, Wang H, Chan AHC, Agrawal AK. Dynamic failure of dry-joint masonry arch structures modelled with the combined finite–discrete element method. Comput Part Mech 2020;7:1017–28. https://doi.org/10.1007/s40571-019-00297-2.
[76] Calderini C, Lagomarsino S. Continuum Model for In-Plane Anisotropic Inelastic Behavior of Masonry. J Struct Eng 2008;134:209–20. https://doi.org/10.1061/(ASCE)0733-9445(2008)134:2(209).
[77] Lourenço PB, Rots JG, Blaauwendraad J. Continuum Model for Masonry: Parameter Estimation and Validation. J Struct Eng 1998;124:642–52. https://doi.org/10.1061/(ASCE)0733-9445(1998)124:6(642).
[78] Tomaževič M. The computer program POR. Rep ZRMK 1978;846.
[79] Lagomarsino S, Penna A, Galasco A, Cattari S. TREMURI program: An equivalent frame model for the nonlinear seismic analysis of masonry buildings. Eng Struct 2013;56:1787–99. https://doi.org/10.1016/j.engstruct.2013.08.002.
[80] Magenes G. A method for pushover analysis in seismic assessment of masonry buildings. Proc. 12th World Conf. Earthq. Eng. Auckl. N. Z. 30 January - 4 Febr. 2000, New Zealand: Upper Hutt, New Zealand: New Zealand Society for Earthquake Engineering; 2000.
[81] Pasticier L, Amadio C, Fragiacomo M. Non-linear seismic analysis and vulnerability evaluation of a masonry building by means of the SAP2000 V.10 code. Earthq Eng Struct Dyn 2008;37:467–85. https://doi.org/10.1002/eqe.770.
[82] Petrovčič S, Kilar V. Seismic failure mode interaction for the equivalent frame modeling of unreinforced masonry structures. Eng Struct 2013;54:9–22. https://doi.org/10.1016/j.engstruct.2013.03.050.
[83] Roca P, Molins C, Marí AR. Strength Capacity of Masonry Wall Structures by the Equivalent Frame Method. J Struct Eng 2005;131:1601–10. https://doi.org/10.1061/(ASCE)0733-9445(2005)131:10(1601).
[84] Caliò I, Marletta M, Pantò B. A new discrete element model for the evaluation of the seismic behaviour of unreinforced masonry buildings. Eng Struct 2012;40:327–38. https://doi.org/10.1016/j.engstruct.2012.02.039.
[85] Dolce M. "Schematizzazione e modellazione per azioni nel piano delle pareti", Ordine degli Ingegneri, Potenza 1989.
[86] Moon FL, Yi T, Leon RT, Kahn LF. Recommendations for Seismic Evaluation and Retrofit of Low-Rise URM Structures. J Struct Eng 2006;132:663–72. https://doi.org/10.1061/(ASCE)0733-9445(2006)132:5(663).
[87] Berti M, Salvatori L, Orlando M, Spinelli P. Unreinforced masonry walls with irregular opening layouts: reliability of equivalent-frame modelling for seismic vulnerability assessment. Bull Earthq Eng 2017;15:1213–39. https://doi.org/10.1007/s10518-016-9985-5.
[88] Cattari S, D'Altri AM, Camilletti D, Lagomarsino S. Equivalent frame idealization of walls with irregular openings in masonry buildings. Eng Struct 2022;256:114055. https://doi.org/10.1016/j.engstruct.2022.114055.
[89] Senaldi I, Guerrini G, Solenghi M, Graziotti F, Penna A, Beyer K. Numerical modelling of the seismic response of a half-scale stone masonry aggregate prototype, Ascoli-Piceno: 2019.

[90] Tomić I, Beyer K. Shake-table test on a historical masonry aggregate: prediction and postdiction using an equivalent-frame model. Bull Earthq Eng 2024;22:6225–58. https://doi.org/10.1007/s10518-023-01765-0.
[91] Vanin F, Penna A, Beyer K. Equivalent-Frame Modeling of Two Shaking Table Tests of Masonry Buildings Accounting for Their Out-Of-Plane Response. Front Built Environ 2020;6:42. https://doi.org/10.3389/fbuil.2020.00042.
[92] Boscotrecase L, Piccarreta F. Edifici in muratura in zona sismica. Palermo: Flaccovio; 2006.
[93] Galano L, Betti M. Elementi di statica delle costruzioni storiche in muratura. Bologna: Esculapio; 2019.
[94] Ministero per i Beni e le Attività Culturali. Linee Guida per la valutazione e riduzione del rischio sismico del patrimonio culturale - allineamento alle nuove Norme tecniche per le costruzioni",. 2010.
[95] Milano L, Mannella A, Morisi C, Martinelli A. Schede illustrative dei principali meccanismi di collasso locali negli edifici esistenti in muratura e dei relativi modelli cinematici di analisi 2009;Allegato alle Linee Guida per la Riparazione e il Rafforzamento di elementi strutturali, Tamponature e Partizioni. Dipartimento della Protezione Civile.
[96] Bui TT, Limam A, Sarhosis V, Hjiaj M. Discrete element modelling of the in-plane and out-of-plane behaviour of dry-joint masonry wall constructions. Eng Struct 2017;136:277–94. https://doi.org/10.1016/j.engstruct.2017.01.020.
[97] Lemos J. Discrete Element Modeling of the Seismic Behavior of Masonry Construction. Buildings 2019;9:43. https://doi.org/10.3390/buildings9020043.
[98] Mendes N, Zanotti S, Lemos JV. Seismic Performance of Historical Buildings Based on Discrete Element Method: An Adobe Church. J Earthq Eng 2020;24:1270–89. https://doi.org/10.1080/13632469.2018.1463879.
[99] Psycharis IN, Lemos JV, Papastamatiou DY, Zambas C, Papantonopoulos C. Numerical study of the seismic behaviour of a part of the Parthenon Pronaos. Earthq Eng Struct Dyn 2003;32:2063–84. https://doi.org/10.1002/eqe.315.
[100] Çaktı E, Saygılı Ö, Lemos JV, Oliveira CS. Discrete element modeling of a scaled masonry structure and its validation. Eng Struct 2016;126:224–36. https://doi.org/10.1016/j.engstruct.2016.07.044.
[101] Galvez F, Sorrentino L, Ingham J, Dmytro D. One way bending capacity prediction of unreinforced masonry walls with varying cross section configurations, The International Masonry Society: Whyteleafe, UK: 2018.
[102] Godio M, Beyer K. Evaluation of force-based and displacement-based out-of-plane seismic assessment methods for unreinforced masonry walls through refined model simulations. Earthq Eng Struct Dyn 2019;48:454–75. https://doi.org/10.1002/eqe.3144.
[103] Calderini C, Lagomarsino S. Seismic Response of Masonry Arches Reinforced by Tie-Rods: Static Tests on a Scale Model. J Struct Eng 2015;141:04014137. https://doi.org/10.1061/(ASCE)ST.1943-541X.0001079.
[104] Giuriani E, Marini A. Wooden Roof Box Structure for the Anti-Seismic Strengthening of Historic Buildings. Int J Archit Herit 2008;2:226–46. https://doi.org/10.1080/15583050802063733.
[105] Giuriani E. Consolidamento degli edifici storici. Torino: UTET scienze tecniche; 2011.
[106] Gelfi P, Giuriani E, Marini A. Stud Shear Connection Design for Composite Concrete Slab and Wood Beams. J Struct Eng 2002;128:1544–50. https://doi.org/10.1061/(ASCE)0733-9445(2002)128:12(1544).

[107] Gattesco N, Macorini L. Strengthening and Stiffening Ancient Wooden Floors with Flat Steel Profiles. Proc. 5th Int. Conf. Struct. Anal. Hist. Constr. Possibilities Numer. Exp. Tech. 6-8 Novemb. 2006, vol. 1, New Delhi, India: Macmillan India Ltd.; 2006, p. 405–12.
[108] Gattesco N, Macorini L. In-plane stiffening techniques with nail plates or CFRP strips for timber floors in historical masonry buildings. Constr Build Mater 2014;58:64–76. https://doi.org/10.1016/j.conbuildmat.2014.02.010.
[109] Gattesco N, Macorini L. High reversibility technique for in-plane stiffening of wooden floors. In: Fodde E, editor. Struct. Anal. Hist. Constr. Preserv. Saf. Significance, CRC Press; 2008, p. 1035–42. https://doi.org/10.1201/9781439828229.ch118.
[110] Dolce M, Manfredi G. ReLUIS: Linee guida per riparazione e rafforzamento di elementi strutturali, tamponature e partizioni. Napoli: Doppiavoce; 2011.
[111] Corradi M, Tedeschi C, Binda L, Borri A. Experimental evaluation of shear and compression strength of masonry wall before and after reinforcement: Deep repointing. Constr Build Mater 2008;22:463–72. https://doi.org/10.1016/j.conbuildmat.2006.11.021.
[112] Gkournelos PD, Triantafillou TC, Bournas DA. Seismic upgrading of existing masonry structures: A state-of-the-art review. Soil Dyn Earthq Eng 2022;161:107428. https://doi.org/10.1016/j.soildyn.2022.107428.
[113] Licciardello L, Rots J, Esposito R. Performance of Unreinforced Masonry Strengthened with Bed Joint Reinforced Repointing. 12th Int. Conf. Struct. Anal. Hist. Constr., CIMNE; 2021. https://doi.org/10.23967/sahc.2021.188.
[114] Penazzi D, Valluzzi MR, Saisi A, Binda L, Modena C. REPAIR AND STRENGTHENING OF HISTORIC MASONRY BUILDINGS IN SEISMIC AREAS, Bethlehem, Palestine: 2001.
[115] Valluzzi MR, Binda L, Modena C. Mechanical behaviour of historic masonry structures strengthened by bed joints structural repointing. Constr Build Mater 2005;19:63–73. https://doi.org/10.1016/j.conbuildmat.2004.04.036.
[116] Binda L, Saisi A, Tedeschi C. Masonry: COMPATIBILITY OF MATERIALS USED FOR REPAIR OF MASONRY BUILDINGS: RESEARCH AND APPLICATIONS. In: Kourkoulis SK, editor. Fract. Fail. Nat. Build. Stones, Dordrecht: Springer Netherlands; 2006, p. 167–82. https://doi.org/10.1007/978-1-4020-5077-0_11.
[117] Miranda L, Milosevic J, Bento R. Cyclic behaviour of stone masonry walls strengthened by grout injection. Mater Struct 2017;50:47. https://doi.org/10.1617/s11527-016-0911-8.
[118] Uranjek M, Bosiljkov V, Žarnić R, Bokan-Bosiljkov V. In situ tests and seismic assessment of a stone-masonry building. Mater Struct 2012;45:861–79. https://doi.org/10.1617/s11527-011-9804-z.
[119] Valluzzi MR, Da Porto, F., Modena, C. Behaviour of multi-leaf stone masonry walls strengthened by different intervention techniques 2001:11.
[120] Zigler R. EVALUATION OF MASONRY GROUTING EFFECTIVENESS USING THERMOGRAPHY AND ULTRASONIC METHODS. Staveb Obz - Civ Eng J 2019;28. https://doi.org/10.14311/CEJ.2019.04.0041.
[121] Lanas J, Alvarez-Galindo JI. Masonry repair lime-based mortars: factors affecting the mechanical behavior. Cem Concr Res 2003;33:1867–76. https://doi.org/10.1016/S0008-8846(03)00210-2.
[122] Ehsani M, Saasatmanesh H. Seismic retrofit of URM Walls with Fiber Composites. TMS J 1996.

[123] Triantafillou TC, Fardis MN. Strengthening of historic masonry structures with composite materials. Mater Struct 1997;30:486–96.
[124] Ferrara G, Caggegi C, Martinelli E, Gabor A. Shear capacity of masonry walls externally strengthened using Flax-TRM composite systems: experimental tests and comparative assessment. Constr Build Mater 2020;261:120490. https://doi.org/10.1016/j.conbuildmat.2020.120490.
[125] Menna C, Asprone D, Durante M, Zinno A, Balsamo A, Prota A. Structural behaviour of masonry panels strengthened with an innovative hemp fibre composite grid. Constr Build Mater 2015;100:111–21. https://doi.org/10.1016/j.conbuildmat.2015.09.051.
[126] Boem I. Masonry Elements Strengthened with TRM: A Review of Experimental, Design and Numerical Methods. Buildings 2022;12:1307. https://doi.org/10.3390/buildings12091307.
[127] Aiello MA, Ghiassi B, Lourenço PB. FRP-strengthened masonry. Long-Term Perform. Durab. Mason. Struct., Elsevier; 2019, p. 209–38. https://doi.org/10.1016/B978-0-08-102110-1.00007-8.
[128] Chowdhury EU, Eedson R, Bisby LA, Green MF, Benichou N. Mechanical Characterization of Fibre Reinforced Polymers Materials at High Temperature. Fire Technol 2011;47:1063–80. https://doi.org/10.1007/s10694-009-0116-6.
[129] Donnini J, De Caso Y Basalo F, Corinaldesi V, Lancioni G, Nanni A. Fabric-reinforced cementitious matrix behavior at high-temperature: Experimental and numerical results. Compos Part B Eng 2017;108:108–21. https://doi.org/10.1016/j.compositesb.2016.10.004.
[130] Papanicolaou CG, Triantafillou TC, Karlos K, Papathanasiou M. Textile-reinforced mortar (TRM) versus FRP as strengthening material of URM walls: in-plane cyclic loading. Mater Struct 2006;40:1081–97. https://doi.org/10.1617/s11527-006-9207-8.
[131] Al-Salloum YA, Siddiqui NA, Elsanadedy HM, Abadel AA, Aqel MA. Textile-Reinforced Mortar versus FRP as Strengthening Material for Seismically Deficient RC Beam-Column Joints. J Compos Constr 2011;15:920–33. https://doi.org/10.1061/(ASCE)CC.1943-5614.0000222.
[132] ACI Committee 440. State-of-the-art report on fiber reinforced plastic (FRP) reinforcement for concrete structures. Detroit, Mich.: American Concrete Institute; 2002.
[133] EOTA. EAD 340275-00-0104: Externally-bonded composite systems with inorganic matrix for strengthening of concrete and masonry structures 2018.
[134] ISO/TC 38/SC 23. ISO 1144:2016 - Textiles Universal system for designating linear density (Tex System) 2016.
[135] Consiglio Superiore LL PP. Linea Guida per la identificazione, la qualificazione ed il controllo di accettazione di compositi fibrorinforzati a matrice inorganica (FRCM) da utilizzarsi per il consolidamento strutturale di costruzioni esistenti. 2022.
[136] Consiglio Superiore LL PP. Linea Guida per la identificazione, la qualificazione ed il controllo di accettazione dei sistemi a rete preformata in materiali compositi fibrorinforzati a matrice polimerica da utilizzarsi per il consolidamento strutturale di costruzioni esistenti con la tecnica dell'intonaco armato CRM (Composite Reinforced Mortar). 2019.
[137] Angiolilli M, Gregori A, Pathirage M, Cusatis G. Fiber Reinforced Cementitious Matrix (FRCM) for strengthening historical stone masonry structures: Experiments

and computations. Eng Struct 2020;224:111102. https://doi.org/10.1016/j.engstruct.2020.111102.
[138] Gams M, Tomaževič M, Berset T. Seismic strengthening of brick masonry by composite coatings: an experimental study. Bull Earthq Eng 2017;15:4269–98. https://doi.org/10.1007/s10518-017-0136-4.
[139] Corradi M, Borri A, Poverello E, Castori G. The Use of Transverse Connectors as Reinforcement of Multi-leaf Walls. Mater Struct 2017;50. https://doi.org/10.1617/s11527-016-0977-3.
[140] Del Zoppo M, Di Ludovico M, Prota A. Analysis of FRCM and CRM parameters for the in-plane shear strengthening of different URM types. Compos Part B Eng 2019;171:20–33. https://doi.org/10.1016/j.compositesb.2019.04.020.
[141] Gams M, Boem I, Gattesco N, Rizzi E, Dudine A. Experimental study on the seismic enhancement of brick masonry spandrels using a single-sided composite reinforced mortar coating. Bull Earthq Eng 2024;22:2531–52. https://doi.org/10.1007/s10518-024-01868-2.
[142] Gattesco N, Rizzi E, Dudine A, Gams M. A new method of seismic strengthening stone masonry with CRM coatings on one side. Constr Build Mater 2023;407:133565. https://doi.org/10.1016/j.conbuildmat.2023.133565.
[143] Gattesco N, Rizzi E, Bez A, Dudine A. Study on the effectiveness of a CRM system: in-plane and out-of-plane cyclic tests on masonry piers. Procedia Struct Integr 2023;44:2230–7. https://doi.org/10.1016/j.prostr.2023.01.285.
[144] Gattesco N, Boem I, Rizzi E, Dudine A, Gams M. Cyclic tests on two-leaf rubble stone masonry spandrels strengthened with CRM coating on one or both sides. Eng Struct 2023;296:116965. https://doi.org/10.1016/j.engstruct.2023.116965.
[145] Proença J, Gago AS, Cardoso J, Cóias V, Paula R. Development of an innovative seismic strengthening technique for traditional load-bearing masonry walls. Bull Earthq Eng 2012;10:113–33. https://doi.org/10.1007/s10518-010-9210-x.
[146] Basili M, Vestroni F, Marcari G. Brick masonry panels strengthened with textile reinforced mortar: experimentation and numerical analysis. Constr Build Mater 2019;227:117061. https://doi.org/10.1016/j.conbuildmat.2019.117061.
[147] Gattesco N, Rizzi E, Boem I, Dudine A, Gams M. Seismic strengthening of existing brick masonry with CRM coatings on one side. Bull Earthq Eng 2025. https://doi.org/10.1007/s10518-025-02181-2.
[148] Gattesco N, Rizzi E, Boem I, Facconi L, Minelli F, Dudine A, et al. Full-scale cyclic tests on a stone masonry building to investigate the effectiveness of a one-side application of the composite reinforced mortar system. Eng Struct 2023;296:116967. https://doi.org/10.1016/j.engstruct.2023.116967.
[149] Marcari G, Basili M, Vestroni F. Experimental investigation of tuff masonry panels reinforced with surface bonded basalt textile-reinforced mortar. Compos Part B Eng 2017;108:131–42. https://doi.org/10.1016/j.compositesb.2016.09.094.
[150] D'Ambrisi A, Mezzi M, Caporale A. Experimental investigation on polymeric net-RCM reinforced masonry panels. Compos Struct 2013;105:207–15. https://doi.org/10.1016/j.compstruct.2013.05.017.
[151] Garcia-Ramonda L, Pelà L, Roca P, Camata G. Cyclic shear-compression testing of brick masonry walls repaired and retrofitted with basalt textile reinforced mortar. Compos Struct 2022;283:115068. https://doi.org/10.1016/j.compstruct.2021.115068.
[152] Gattesco N, Amadio C, Bedon C. Experimental and numerical study on the shear behavior of stone masonry walls strengthened with GFRP reinforced mortar

coating and steel-cord reinforced repointing. Eng Struct 2015;90:143–57. https://doi.org/10.1016/j.engstruct.2015.02.024.
[153] Guerreiro J, Proença J, Ferreira JG, Gago A. Experimental characterization of in-plane behaviour of old masonry walls strengthened through the addition of CFRP reinforced render. Compos Part B Eng 2018;148:14–26. https://doi.org/10.1016/j.compositesb.2018.04.045.
[154] Hračov S, Pospíšil S, Garofano A, Urushadze S. In-plane cyclic behaviour of unfired clay and earth brick walls in both unstrengthened and strengthened conditions. Mater Struct 2016;49:3293–308. https://doi.org/10.1617/s11527-015-0720-5.
[155] Mercedes L, Bernat-Maso E, Gil L. In-plane cyclic loading of masonry walls strengthened by vegetal-fabric-reinforced cementitious matrix (FRCM) composites. Eng Struct 2020;221:111097. https://doi.org/10.1016/j.engstruct.2020.111097.
[156] Messali F, Metelli G, Plizzari G. Experimental results on the retrofitting of hollow brick masonry walls with reinforced high performance mortar coatings. Constr Build Mater 2017;141:619–30. https://doi.org/10.1016/j.conbuildmat.2017.03.112.
[157] Papanicolaou C, Triantafillou T, Lekka M. Externally bonded grids as strengthening and seismic retrofitting materials of masonry panels. Constr Build Mater 2011;25:504–14. https://doi.org/10.1016/j.conbuildmat.2010.07.018.
[158] Tomaževič M, Gams M, Berset T. Strengthening of stone masonry walls with composite reinforced coatings. Bull Earthq Eng 2015;13:2003–27. https://doi.org/10.1007/s10518-014-9697-7.
[159] Torres B, Ivorra S, Javier Baeza F, Estevan L, Varona B. Textile reinforced mortars (TRM) for repairing and retrofitting masonry walls subjected to in-plane cyclic loads. An experimental approach. Eng Struct 2021;231:111742. https://doi.org/10.1016/j.engstruct.2020.111742.
[160] Türkmen ÖS, De Vries BT, Wijte SNM, Vermeltfoort AT. Quasi-static cyclic in-plane testing of masonry walls strengthened with a single-sided fabric-reinforced cementitious matrix overlay and flexible anchorage. J Build Pathol Rehabil 2019;4:8. https://doi.org/10.1007/s41024-019-0043-y.
[161] Almeida JAPP, Pereira EB, Barros JAO. Assessment of overlay masonry strengthening system under in-plane monotonic and cyclic loading using the diagonal tensile test. Constr Build Mater 2015;94:851–65. https://doi.org/10.1016/j.conbuildmat.2015.07.040.
[162] Angiolilli M, Gregori A, Cattari S. Performance of Fiber Reinforced Mortar coating for irregular stone masonry: Experimental and analytical investigations. Constr Build Mater 2021;294:123508. https://doi.org/10.1016/j.conbuildmat.2021.123508.
[163] Babaeidarabad S, De Caso F, Nanni A. URM Walls Strengthened with Fabric-Reinforced Cementitious Matrix Composite Subjected to Diagonal Compression. J Compos Constr 2014;18:04013045. https://doi.org/10.1061/(ASCE)CC.1943-5614.0000441.
[164] Benedetti A. In Plane Behaviour of Masonry Walls Reinforced with Mortar Coatings and Fibre Meshes. Int J Archit Herit 2019;13:1029–41. https://doi.org/10.1080/15583058.2019.1618972.
[165] Borri A, Corradi M, Sisti R, Buratti C, Belloni E, Moretti E. Masonry wall panels retrofitted with thermal-insulating GFRP-reinforced jacketing. Mater Struct 2016;49:3957–68. https://doi.org/10.1617/s11527-015-0766-4.

[166] Borri A, Castori G, Corradi M, Speranzini E. Shear behavior of unreinforced and reinforced masonry panels subjected to in situ diagonal compression tests. Constr Build Mater 2011;25:4403–14. https://doi.org/10.1016/j.conbuildmat.2011.01.009.
[167] Carozzi FG, D'Antino T, Poggi C. In-situ experimental tests on masonry panels strengthened with Textile Reinforced Mortar composites. Procedia Struct Integr 2018;11:355–62. https://doi.org/10.1016/j.prostr.2018.11.046.
[168] Casacci S, Gentilini C, Di Tommaso A, Oliveira DV. Shear strengthening of masonry wallettes resorting to structural repointing and FRCM composites. Constr Build Mater 2019;206:19–34. https://doi.org/10.1016/j.conbuildmat.2019.02.044.
[169] D'Antino T, Carozzi FG, Poggi C. Diagonal shear behavior of historic walls strengthened with composite reinforced mortar (CRM). Mater Struct 2019;52:114. https://doi.org/10.1617/s11527-019-1414-1.
[170] Del Zoppo M, Di Ludovico M, Balsamo A, Prota A. In-plane shear capacity of tuff masonry walls with traditional and innovative Composite Reinforced Mortars (CRM). Constr Build Mater 2019;210:289–300. https://doi.org/10.1016/j.conbuildmat.2019.03.133.
[171] Donnini J, Maracchini G, Lenci S, Corinaldesi V, Quagliarini E. TRM reinforced tuff and fired clay brick masonry: Experimental and analytical investigation on their in-plane and out-of-plane behavior. Constr Build Mater 2021;272:121643. https://doi.org/10.1016/j.conbuildmat.2020.121643.
[172] Garcia-Ramonda L, Pelá L, Roca P, Camata G. In-plane shear behaviour by diagonal compression testing of brick masonry walls strengthened with basalt and steel textile reinforced mortars. Constr Build Mater 2020;240:117905. https://doi.org/10.1016/j.conbuildmat.2019.117905.
[173] Gattesco N, Boem I, Dudine A. Diagonal compression tests on masonry walls strengthened with a GFRP mesh reinforced mortar coating. Bull Earthq Eng 2015;13:1703–26. https://doi.org/10.1007/s10518-014-9684-z.
[174] Gattesco N, Boem I. Experimental and analytical study to evaluate the effectiveness of an in-plane reinforcement for masonry walls using GFRP meshes. Constr Build Mater 2015;88:94–104. https://doi.org/10.1016/j.conbuildmat.2015.04.014.
[175] Marcari G, Basili M, Vestroni F. Experimental investigation of tuff masonry panels reinforced with surface bonded basalt textile-reinforced mortar. Compos Part B Eng 2017;108:131–42. https://doi.org/10.1016/j.compositesb.2016.09.094.
[176] Oskouei AV, Jafari A, Bazli M, Ghahri R. Effect of different retrofitting techniques on in-plane behavior of masonry wallettes. Constr Build Mater 2018;169:578–90. https://doi.org/10.1016/j.conbuildmat.2018.02.197.
[177] Parisi F, Iovinella I, Balsamo A, Augenti N, Prota A. In-plane behaviour of tuff masonry strengthened with inorganic matrix–grid composites. Compos Part B Eng 2013;45:1657–66. https://doi.org/10.1016/j.compositesb.2012.09.068.
[178] Prota A, Marcari G, Fabbrocino G, Manfredi G, Aldea C. Experimental In-Plane Behavior of Tuff Masonry Strengthened with Cementitious Matrix–Grid Composites. J Compos Constr 2006;10:223–33. https://doi.org/10.1061/(ASCE)1090-0268(2006)10:3(223).
[179] Wang X, Lam CC, Iu VP. Comparison of different types of TRM composites for strengthening masonry panels. Constr Build Mater 2019;219:184–94. https://doi.org/10.1016/j.conbuildmat.2019.05.179.
[180] Yardim Y, Lalaj O. Shear strengthening of unreinforced masonry wall with different fiber reinforced mortar jacketing. Constr Build Mater 2016;102:149–54. https://doi.org/10.1016/j.conbuildmat.2015.10.095.

[181] Babaeidarabad S, Caso FD, Nanni A. Out-of-Plane Behavior of URM Walls Strengthened with Fabric-Reinforced Cementitious Matrix Composite. J Compos Constr 2014;18:04013057. https://doi.org/10.1061/(ASCE)CC.1943-5614.0000457.
[182] Cevallos OA, Olivito RS, Codispoti R, Ombres L. Flax and polyparaphenylene benzobisoxazole cementitious composites for the strengthening of masonry elements subjected to eccentric loading. Compos Part B Eng 2015;71:82–95. https://doi.org/10.1016/j.compositesb.2014.10.055.
[183] D'Ambra C, Lignola GP, Prota A, Sacco E, Fabbrocino F. Experimental performance of FRCM retrofit on out-of-plane behaviour of clay brick walls. Compos Part B Eng 2018;148:198–206. https://doi.org/10.1016/j.compositesb.2018.04.062.
[184] Harajli M, ElKhatib H, San-Jose JT. Static and Cyclic Out-of-Plane Response of Masonry Walls Strengthened Using Textile-Mortar System. J Mater Civ Eng 2010;22:1171–80. https://doi.org/10.1061/(ASCE)MT.1943-5533.0000128.
[185] Kariou FA, Triantafyllou SP, Bournas DA, Koutas LN. Out-of-plane response of masonry walls strengthened using textile-mortar system. Constr Build Mater 2018;165:769–81. https://doi.org/10.1016/j.conbuildmat.2018.01.026.
[186] Martins A, Vasconcelos G, Fangueiro R, Cunha F. Experimental assessment of an innovative strengthening material for brick masonry infills. Compos Part B Eng 2015;80:328–42. https://doi.org/10.1016/j.compositesb.2015.06.012.
[187] Papanicolaou CG, Triantafillou TC, Papathanasiou M, Karlos K. Textile reinforced mortar (TRM) versus FRP as strengthening material of URM walls: out-of-plane cyclic loading. Mater Struct 2007;41:143–57. https://doi.org/10.1617/s11527-007-9226-0.
[188] Sagar SL, Singhal V, Rai DC, Gudur P. Diagonal Shear and Out-of-Plane Flexural Strength of Fabric-Reinforced Cementitious Matrix–Strengthened Masonry Walletes. J Compos Constr 2017;21:04017016. https://doi.org/10.1061/(ASCE)CC.1943-5614.0000796.
[189] Valluzzi MR, Da Porto F, Garbin E, Panizza M. Out-of-plane behaviour of infill masonry panels strengthened with composite materials. Mater Struct 2014;47:2131–45. https://doi.org/10.1617/s11527-014-0384-6.
[190] Gu J-B, Tao Y, Xin R, Yang Z, Shi Q-X. Seismic Performance of Multistorey Masonry Structure with Openings Repaired with CFRP Grid. Adv Civ Eng 2018;2018:1–11. https://doi.org/10.1155/2018/4374876.
[191] Lucchini S, Facconi L, Minelli F, Plizzari G. Cyclic Test on a Full-Scale Unreinforced Masonry Building Repaired with Steel Fiber-Reinforced Mortar Coating. J Struct Eng 2021;147:04021059. https://doi.org/10.1061/(ASCE)ST.1943-541X.0003020.
[192] Magenes G, Kingsley G, Calvi GM. Seismic Testing of a Full-Scale, Two-Story Masonry Building: Test Procedure and Measured Experimental Response 1995. https://doi.org/10.13140/RG.2.1.4590.2962.
[193] Morici M, Gioiella L, Micozzi F, Zona A, Dudine A, Grassia S, et al. Push 'o ver: in situ pushover tests on as built and strengthened existing brickwork constructions. Procedia Struct Integr 2023;44:830–7. https://doi.org/10.1016/j.prostr.2023.01.108.
[194] Triller P, Tomaževič M, Gams M. Seismic strengthening of clay block masonry buildings with composites: an experimental study of a full scale three-storey building model. Bull Earthq Eng 2019;17:4049–80. https://doi.org/10.1007/s10518-019-00609-0.

[195] De Santis S, de Felice G. Shake table tests on a tuff masonry structure strengthened with composite reinforced mortar. Compos Struct 2021;275:114508. https://doi.org/10.1016/j.compstruct.2021.114508.
[196] Juhásová E, Sofronie R, Bairrão R. Stone masonry in historical buildings — Ways to increase their resistance and durability. Eng Struct 2008;30:2194–205. https://doi.org/10.1016/j.engstruct.2007.07.008.
[197] Magenes G, Penna A, Galasco A. A full-scale shaking table test on a two-storey stone masonry building 2010.
[198] Mazzon N, Valluzzi MR, Aoki T, Garbin E. Shaking Table Tests on Two Multi-Leaf Stone Masonry Buildings 2009;In: Proc. of the 11th Canadian Masonry Symposium, Toronto (Canada), May 31st-June 3rd, Mc Master University.
[199] Vintzileou E, Mouzakis C, Adami C-E, Karapitta L. Seismic behavior of three-leaf stone masonry buildings before and after interventions: Shaking table tests on a two-storey masonry model. Bull Earthq Eng 2015;13:3107–33. https://doi.org/10.1007/s10518-015-9746-x.
[200] De Santis S, Carozzi FG, De Felice G, Poggi C. Test methods for Textile Reinforced Mortar systems. Compos Part B Eng 2017;127:121–32. https://doi.org/10.1016/j.compositesb.2017.03.016.
[201] Kouris LAS, Triantafillou TC. State-of-the-art on strengthening of masonry structures with textile reinforced mortar (TRM). Constr Build Mater 2018;188:1221–33. https://doi.org/10.1016/j.conbuildmat.2018.08.039.
[202] Gattesco N, Boem I. Characterization tests of GFRM coating as a strengthening technique for masonry buildings. Compos Struct 2017;165:209–22. https://doi.org/10.1016/j.compstruct.2017.01.043.
[203] Bellini A, Incerti A, Bovo M, Mazzotti C. Effectiveness of FRCM Reinforcement Applied to Masonry Walls Subject to Axial Force and Out-Of-Plane Loads Evaluated by Experimental and Numerical Studies. Int J Archit Herit 2018;12:376–94. https://doi.org/10.1080/15583058.2017.1323246.
[204] Alecci V, Misseri G, Rovero L, Stipo G, De Stefano M, Feo L, et al. Experimental investigation on masonry arches strengthened with PBO-FRCM composite. Compos Part B Eng 2016;100:228–39. https://doi.org/10.1016/j.compositesb.2016.05.063.
[205] Garmendia L, Larrinaga P, García D, Marcos I. Textile-Reinforced Mortar as Strengthening Material for Masonry Arches. Int J Archit Herit 2014;8:627–48. https://doi.org/10.1080/15583058.2012.704480.
[206] Boem I, Gattesco N. Cyclic behavior of masonry barrel vaults strengthened through Composite Reinforced Mortar, considering the role of the connection with the abutments. Eng Struct 2021;228:111518. https://doi.org/10.1016/j.engstruct.2020.111518.
[207] Gattesco N, Boem I, Andretta V. Experimental behaviour of non-structural masonry vaults reinforced through fibre-reinforced mortar coating and subjected to cyclic horizontal loads. Eng Struct 2018;172:419–31. https://doi.org/10.1016/j.engstruct.2018.06.044.
[208] CNR. CNR-DT 203/2006 Guide for the Design and Construction of Concrete Structures Reinforced with Fiber-Reinforced Polymer Bars 2007.
[209] Boem I. Characterization of Textile-Reinforced Mortar: State of the Art and Detail-Level Modeling with a Free Open-Source Finite-Element Code. J Compos Constr 2022;26:04022060. https://doi.org/10.1061/(ASCE)CC.1943-5614.0001240.
[210] Caggegi C, Carozzi FG, De Santis S, Fabbrocino F, Focacci F, Hojdys Ł, et al. Experimental analysis on tensile and bond properties of PBO and aramid fabric

reinforced cementitious matrix for strengthening masonry structures. Compos Part B Eng 2017;127:175–95. https://doi.org/10.1016/j.compositesb.2017.05.048.
[211] Carozzi FG, Bellini A, D'Antino T, De Felice G, Focacci F, Hojdys Ł, et al. Experimental investigation of tensile and bond properties of Carbon-FRCM composites for strengthening masonry elements. Compos Part B Eng 2017;128:100–19. https://doi.org/10.1016/j.compositesb.2017.06.018.
[212] De Santis S, Ceroni F, De Felice G, Fagone M, Ghiassi B, Kwiecień A, et al. Round Robin Test on tensile and bond behaviour of Steel Reinforced Grout systems. Compos Part B Eng 2017;127:100–20. https://doi.org/10.1016/j.compositesb.2017.03.052.
[213] Leone M, Aiello MA, Balsamo A, Carozzi FG, Ceroni F, Corradi M, et al. Glass fabric reinforced cementitious matrix: Tensile properties and bond performance on masonry substrate. Compos Part B Eng 2017;127:196–214. https://doi.org/10.1016/j.compositesb.2017.06.028.
[214] Lignola GP, Caggegi C, Ceroni F, De Santis S, Krajewski P, Lourenço PB, et al. Performance assessment of basalt FRCM for retrofit applications on masonry. Compos Part B Eng 2017;128:1–18. https://doi.org/10.1016/j.compositesb.2017.05.003.
[215] De Carvalho Bello CB, Boem I, Cecchi A, Gattesco N, Oliveira DV. Experimental tests for the characterization of sisal fiber reinforced cementitious matrix for strengthening masonry structures. Constr Build Mater 2019;219:44–55. https://doi.org/10.1016/j.conbuildmat.2019.05.168.
[216] Olivito RS, Codispoti R, Cevallos OA. Bond behavior of Flax-FRCM and PBO-FRCM composites applied on clay bricks: Experimental and theoretical study. Compos Struct 2016;146:221–31. https://doi.org/10.1016/j.compstruct.2016.03.004.
[217] Trochoutsou N, Di Benedetti M, Pilakoutas K, Guadagnini M. Mechanical Characterisation of Flax and Jute Textile-Reinforced Mortars. Constr Build Mater 2021;271:121564. https://doi.org/10.1016/j.conbuildmat.2020.121564.
[218] Karbhari VM, Chin JW, Hunston D, Benmokrane B, Juska T, Morgan R, et al. Durability Gap Analysis for Fiber-Reinforced Polymer Composites in Civil Infrastructure. J Compos Constr 2003;7:238–47. https://doi.org/10.1061/(ASCE)1090-0268(2003)7:3(238).
[219] Righetti L, Corradi M, Borri A, Castori G, Sisti R, Osofero AI. Durability of GFRP grids for masonry structures. Int J Forensic Eng 2016;3:164. https://doi.org/10.1504/IJFE.2016.075990.
[220] Borri A, Castori G, Corradi M, Sisti R. Ageing Problems of GFRP Grids Used for Masonry Reinforcement. Key Eng Mater 2014;624:413–20. https://doi.org/10.4028/www.scientific.net/KEM.624.413.
[221] Micelli F, Aiello MA. Residual tensile strength of dry and impregnated reinforcement fibres after exposure to alkaline environments. Compos Part B Eng 2019;159:490–501. https://doi.org/10.1016/j.compositesb.2017.03.005.
[222] C27 Committee. ASTM C1666/C1666M-08 Specification for Alkali Resistant (AR) Glass Fiber for GFRC and Fiber-Reinforced Concrete and Cement 2015. https://doi.org/10.1520/C1666_C1666M-08.
[223] CEN. EN 15422:2008 Precast concrete products - Specification of glassfibres for reinforcement of mortars and concretes 2008.
[224] EOTA. EAD 260002-00-0301 2017.

[225] D30 Committee. ASTM D7750-12 Test Method for Cure Behavior of Thermosetting Resins by Dynamic Mechanical Procedures using an Encapsulated Specimen Rheometer 2017. https://doi.org/10.1520/D7750-12R17.
[226] EOTA. EAD 340392-00-0104: CRM (composite reinforced mortar) systems for strengthening concrete and masonry structures 2018.
[227] ISO. ISO 3341: Textile glass - Yarns - Determination of breaking force and breaking elongation 2008.
[228] Boem I. Enhancement of the Seismic Peformances of Hystoric Masonry Buildings through Glass Fiber-Reinforced Mortar. Tesi di Dottorato. Università degli Studi di Trieste, 2016.
[229] ISO. ISO 10406-1:2008 - Fibre-reinforced Polymer (FRP), reinforcement of concrete - Test methods, Part 1: FRP bars and grids 2008.
[230] ISO. ISO 3374: Reinforcement products - Mats and fabrics - Determination of mass per unit area 2000.
[231] CEN. EN 998-2:2016 Specification for mortar for masonry - Part 2: Masonry mortar 2016.
[232] CEN. EN 1015-6:1998 Methods of test for mortar for masonry - Part 6: Determination of bulk density of fresh mortar 1998.
[233] CEN. EN 13412:2006 Products and systems for the protection and repair of concrete structures - Test methods - Determination of modulus of elasticity in compression 1998.
[234] ISO. ISO 527-1:2019 - Plastics - Determination of tensile properties - Part 1: General principles 2019.
[235] ASTM. ASTM D695 Standard Test Method for Compressive Properties of Rigid Plastics 2023. https://doi.org/10.1520/D0695-23.
[236] American Concrete Institute. ACI 440.3R-04 - Guide Test Methods for Fiber-Reinforced Polymers (FRPs) for Reinforcing or Strengthening Concrete Structures 2004.
[237] ISO/TC 164. EN ISO 6892-1 - Metallic materials - Tensile testing - Part 1: Method of test at room temperature 2009.
[238] Micelli F, Corradi M, Aiello M, Borri A. Properties of Aged GFRP Reinforcement Grids Related to Fatigue Life and Alkaline Environment. Appl Sci 2017;7:897. https://doi.org/10.3390/app7090897.
[239] Lu C, Ni M, Chu T, He L. Comparative Investigation on Tensile Performance of FRP Bars after Exposure to Water, Seawater, and Alkaline Solutions. J Mater Civ Eng 2020;32:04020170. https://doi.org/10.1061/(ASCE)MT.1943-5533.0003243.
[240] Boem I, Gattesco N, Rizzi E, Dudine A, Gams M. Fibre-based composite materials for the seismic strengthening of masonry ring beams: cyclic tests on full-scale samples. Mater Struct 2025;58:97. https://doi.org/10.1617/s11527-025-02617-w.
[241] Roselli G, Mirabile Gattia D, AlShawa O, Cinaglia P, Di Girolami G, Francola C, et al. Mortar analysis of historic buildings damaged by recent earthquakes in Italy. Eur Phys J Plus 2019;134:540. https://doi.org/10.1140/epjp/i2019-13024-2.
[242] CEN. EN 12390-13: Testing hardened concrete - Part 13: Determination of secant modulus of elasticity in compression 2021.
[243] ISO. ISO 10406-1: Fibre-reinforced polymer (FRP) reinforcement of concrete — Test methods — Part 1: FRP bars and grids 2015.
[244] Castori G, Borri A, Marco Corradi, Righetti. Structural analysis of transversal steel connectors applied on multi-leaf walls, Halifax, Canada: 2017.

[245] Oats RC, Dai Q, Head M. Digital Image Correlation Advances in Structural Evaluation Applications: A Review. Pract Period Struct Des Constr 2022;27:03122007. https://doi.org/10.1061/(ASCE)SC.1943-5576.0000725.
[246] Howlader MK, Masia MJ, Griffith MC. Digital image correlation for the analysis of in-plane tested unreinforced masonry walls. Structures 2021;29:427–45. https://doi.org/10.1016/j.istruc.2020.11.051.
[247] ATC. FEMA 440: Improvement of Nonlinear Static Seismic Analysis Procedures. 2005.
[248] Padalu PKVR, Singh Y, Das S. Efficacy of basalt fibre reinforced cement mortar composite for out-of-plane strengthening of unreinforced masonry. Constr Build Mater 2018;191:1172–90. https://doi.org/10.1016/j.conbuildmat.2018.10.077.
[249] De Santis S, De Canio G, de Felice G, Meriggi P, Roselli I. Out-of-plane seismic retrofitting of masonry walls with Textile Reinforced Mortar composites. Bull Earthq Eng 2019;17:6265–300. https://doi.org/10.1007/s10518-019-00701-5.
[250] Ismail N, Ingham JM. In-plane and out-of-plane testing of unreinforced masonry walls strengthened using polymer textile reinforced mortar. Eng Struct 2016;118:167–77. https://doi.org/10.1016/j.engstruct.2016.03.041.
[251] Fiorentino G, Forte A, Pagano E, Sabetta F, Baggio C, Lavorato D, et al. Damage patterns in the town of Amatrice after August 24th 2016 Central Italy earthquakes. Bull Earthq Eng 2018;16:1399–423. https://doi.org/10.1007/s10518-017-0254-z.
[252] Mercimek Ö. Seismic failure modes of masonry structures exposed to Kahramanmaraş earthquakes (Mw 7.7 and 7.6) on February 6, 2023. Eng Fail Anal 2023;151:107422. https://doi.org/10.1016/j.engfailanal.2023.107422.
[253] Sorrentino L, Cattari S, Da Porto F, Magenes G, Penna A. Seismic behaviour of ordinary masonry buildings during the 2016 central Italy earthquakes. Bull Earthq Eng 2019;17:5583–607. https://doi.org/10.1007/s10518-018-0370-4.
[254] D'Ayala D, Speranza E. Definition of Collapse Mechanisms and Seismic Vulnerability of Historic Masonry Buildings. Earthq Spectra 2003;19:479–509. https://doi.org/10.1193/1.1599896.
[255] Podestà S, Scandolo L. Earthquakes and Tie-Rods: Assessment, Design, and Ductility Issues. Int J Archit Herit 2019;13:329–39. https://doi.org/10.1080/15583058.2018.1563239.
[256] Tomaževič M, Lutman M, Weiss P. Seismic Upgrading of Old Brick-Masonry Urban Houses: Tying of Walls with Steel Ties. Earthq Spectra 1996;12:599–622. https://doi.org/10.1193/1.1585898.
[257] Guadagnuolo M, Faella G. Simplified Design of Masonry Ring-Beams Reinforced by Flax Fibers for Existing Buildings Retrofitting. Buildings 2020;10:12. https://doi.org/10.3390/buildings10010012.
[258] Borri A, Castori G, Grazini A. Retrofitting of masonry building with reinforced masonry ring-beam. Constr Build Mater 2009;23:1892–901. https://doi.org/10.1016/j.conbuildmat.2008.09.012.
[259] Sisti R, Corradi M, Borri A. An experimental study on the influence of composite materials used to reinforce masonry ring beams. Constr Build Mater 2016;122:231–41. https://doi.org/10.1016/j.conbuildmat.2016.06.120.
[260] Jasieńko J, Raszczuk K, Frąckiewicz P, Kleszcz K, Bednarz Ł. Strengthening of masonry rings with composite materials. Herit Sci 2021;9:11. https://doi.org/10.1186/s40494-021-00485-5.
[261] CNR. CNR DT 200 R1 Instructions for the Design, Execution and Control of Static Consolidation Interventions through the use of Fiber-reinforced Composites 2014.

[262] Aiello MA, Bencardino F, Cascardi A, D'Antino T, Fagone M, Frana I, et al. Masonry columns confined with fabric reinforced cementitious matrix (FRCM) systems: A round robin test. Constr Build Mater 2021;298:123816. https://doi.org/10.1016/j.conbuildmat.2021.123816.
[263] Babatunde SA. Review of strengthening techniques for masonry using fiber reinforced polymers. Compos Struct 2017;161:246–55. https://doi.org/10.1016/j.compstruct.2016.10.132.
[264] Bertolli V, Sneed LH, Focacci F, D'Antino T. Shear Strengthening of RC Beams with U-Wrapped FRCM Composites: State of the Art and Assessment of Available Analytical Models. J Compos Constr 2025;29:04024091. https://doi.org/10.1061/JCCOF2.CCENG-4736.
[265] Drobiec Ł. Study of impact of bed joint reinforcement on load-carrying capacity and crack resistance of masonry walls made of calcium silicate units. J Build Eng 2021;33:101841. https://doi.org/10.1016/j.jobe.2020.101841.
[266] Liang X, Peng J, Ren R. A state-of-the-art review: Shear performance of the concrete beams reinforced with FRP bars. Constr Build Mater 2023;364:129996. https://doi.org/10.1016/j.conbuildmat.2022.129996.
[267] Vaculik J, Visintin P, Burton NG, Griffith MC, Seracino R. State-of-the-art review and future research directions for FRP-to-masonry bond research: Test methods and techniques for extraction of bond-slip behaviour. Constr Build Mater 2018;183:325–45. https://doi.org/10.1016/j.conbuildmat.2018.06.103.
[268] Valluzzi MR, Oliveira DV, Caratelli A, Castori G, Corradi M, De Felice G, et al. Round Robin Test for composite-to-brick shear bond characterization. Mater Struct 2012;45:1761–91. https://doi.org/10.1617/s11527-012-9883-5.
[269] Triantafillou TC. Strengthening of Masonry Structures Using Epoxy-Bonded FRP Laminates. J Compos Constr 1998;2:96–104. https://doi.org/10.1061/(ASCE)1090-0268(1998)2:2(96).
[270] Anil Ö, Tatayoğlu M, Demirhan M. Out-of-plane behavior of unreinforced masonry brick walls strengthened with CFRP strips. Constr Build Mater 2012;35:614–24. https://doi.org/10.1016/j.conbuildmat.2012.04.058.
[271] Maddaloni G, Di Ludovico M, Balsamo A, Maddaloni G, Prota A. Dynamic assessment of innovative retrofit techniques for masonry buildings. Compos Part B Eng 2018;147:147–61. https://doi.org/10.1016/j.compositesb.2018.04.038.
[272] Benedetti D, Carydis P, Pezzoli P. Shaking table tests on 24 simple masonry buildings. Earthq Eng Struct Dyn 1998;27:67–90. https://doi.org/10.1002/(SICI)1096-9845(199801)27:1%253C67::AID-EQE719%253E3.0.CO;2-K.
[273] Langé S. L' eredità romanica: la casa europea in pietra. Jaca Book; 2020.
[274] Brincker R, Zhang L, Andersen P. Modal identification of output-only systems using frequency domain decomposition. Smart Mater Struct 2001;10:441–5. https://doi.org/10.1088/0964-1726/10/3/303.
[275] Brincker R, Ventura C, Andersen P. Damping estimation by Frequency Domain Decomposition. 2001.
[276] Paulson TJ, Abrams DP. Correlation between Static and Dynamic Response of Model Masonry Structures. Earthq Spectra 1990;6:573–91. https://doi.org/10.1193/1.1585587.
[277] Tomaževič M, Lutman M, Petković L. Seismic Behavior of Masonry Walls: Experimental Simulation. J Struct Eng 1996;122:1040–7. https://doi.org/10.1061/(ASCE)0733-9445(1996)122:9(1040).

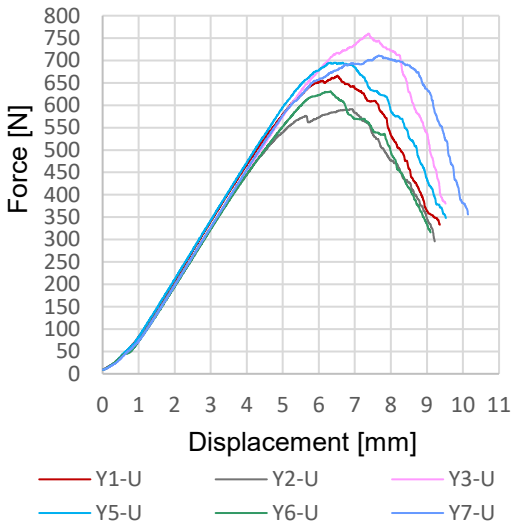
[278] Gattesco N, Boem I. Assessment of the seismic capacity increase of masonry buildings strengthened through the application of GFRM coatings on the walls. Int J Mason Res Innov 2017;2:300. https://doi.org/10.1504/IJMRI.2017.087433.
[279] Javed M. Seismic Risk Assessment of Unreinforced Brick Masonry Buildings System of Northern Pakistan, PhD Thesis, Department of Civil Engineering, University of Engineering and Technology, Peshawar, Pakistan. 2009.
[280] Elmenshawi A, Sorour M, Mufti A, Jaeger LG, Shrive N. Damping mechanisms and damping ratios in vibrating unreinforced stone masonry. Eng Struct 2010;32:3269–78. https://doi.org/10.1016/j.engstruct.2010.06.016.
[281] Tripathy D, Meghwal P, Singhal V. Strengthening of Lime Mortar Masonry Wallettes Using Fiber-Reinforced Cementitious Matrix. J Compos Constr 2020;24:04020075. https://doi.org/10.1061/(ASCE)CC.1943-5614.0001086.
[282] D'Antino T, Carozzi FG, Colombi P, Poggi C. Out-of-plane maximum resisting bending moment of masonry walls strengthened with FRCM composites. Compos Struct 2018;202:881–96. https://doi.org/10.1016/j.compstruct.2018.04.054.
[283] Padalu PKVR, Singh Y, Das S. Out-of-plane flexural behaviour of masonry wallettes strengthened using FRP composites and externally bonded grids: Comparative study. Compos Part B Eng 2019;176:107302. https://doi.org/10.1016/j.compositesb.2019.107302.
[284] Turnšek V., Čačovič F. Some experimental results on the strength of brick masonry walls. HWH West KH Speed Br Ceram Reasearch Assoc - Lond Ed Proc 2nd Int Brick-Mason Conf Stoke--Trent UK Br Ceram Res Assoc 1971:149–56.
[285] Angiolilli M, Gregori A, Cusatis G. Simulating the Nonlinear Mechanical Behavior of FRCM-strengthened Irregular Stone Masonry Walls. Int J Archit Herit 2023;17:938–54. https://doi.org/10.1080/15583058.2021.2001114.
[286] Gobbin F, De Felice G, Lemos JV. A Discrete Element Model for Masonry Vaults Strengthened with Externally Bonded Reinforcement. Int J Archit Herit 2021;15:1959–72. https://doi.org/10.1080/15583058.2020.1743792.
[287] Basili M, Marcari G, Vestroni F. Nonlinear analysis of masonry panels strengthened with textile reinforced mortar. Eng Struct 2016;113:245–58. https://doi.org/10.1016/j.engstruct.2015.12.021.
[288] Garofano A, Ceroni F, Pecce M. Modelling of the in-plane behaviour of masonry walls strengthened with polymeric grids embedded in cementitious mortar layers. Compos Part B Eng 2016;85:243–58. https://doi.org/10.1016/j.compositesb.2015.09.005.
[289] Wang X, Ghiassi B, Oliveira DV, Lam CC. Modelling the nonlinear behaviour of masonry walls strengthened with textile reinforced mortars. Eng Struct 2017;134:11–24. https://doi.org/10.1016/j.engstruct.2016.12.029.
[290] Corradi M, Borri A, Castori G, Sisti R. Shear strengthening of wall panels through jacketing with cement mortar reinforced by GFRP grids. Compos Part B Eng 2014;64:33–42. https://doi.org/10.1016/j.compositesb.2014.03.022.
[291] Castori G, Corradi M, Sperazini E. Full size testing and detailed micro-modeling of the in-plane behavior of FRCM–reinforced masonry. Constr Build Mater 2021;299:124276. https://doi.org/10.1016/j.conbuildmat.2021.124276.
[292] Lignola GP, Bilotta A, Ceroni F. Assessment of the effect of FRCM materials on the behaviour of masonry walls by means of FE models. Eng Struct 2019;184:145–57. https://doi.org/10.1016/j.engstruct.2019.01.035.
[293] Ungureanu D, Țăranu N, Ghiga DA, Isopescu DN, Mihai P, Cozmanciuc R. Diagonal Tensile Test on Masonry Panels Strengthened with Textile-Reinforced Mortar. Materials 2021;14:7021. https://doi.org/10.3390/ma14227021.

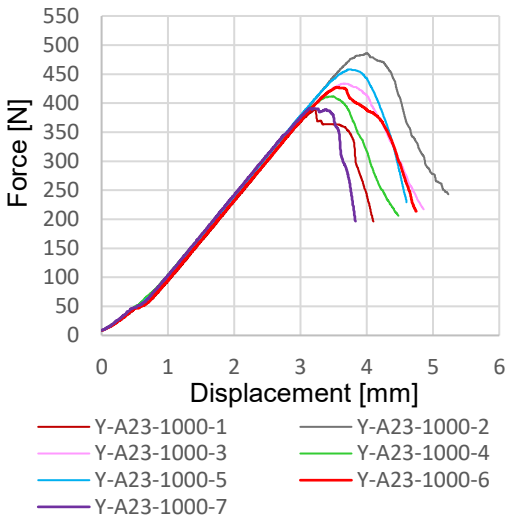
[294] Murgo FS, Ferretti F, Mazzotti C. A discrete-cracking numerical model for the in-plane behavior of FRCM strengthened masonry panels. Bull Earthq Eng 2021;19:4471–502. https://doi.org/10.1007/s10518-021-01129-6.
[295] Dassault Systèmes Simulia Corp. Abaqus v6.12-3 2012.
[296] Lubliner J, Oliver J, Oller S, Oñate E. A plastic-damage model for concrete. Int J Solids Struct 1989;25:299–326. https://doi.org/10.1016/0020-7683(89)90050-4.
[297] Lee J, Fenves GL. Plastic-Damage Model for Cyclic Loading of Concrete Structures. J Eng Mech 1998;124:892–900. https://doi.org/10.1061/(ASCE)0733-9399(1998)124:8(892).
[298] Pandey AK, Bisht RS. Numerical Modelling of Infilled Clay Brick Masonry under Blast Loading. Adv Struct Eng 2014;17:591–606. https://doi.org/10.1260/1369-4332.17.4.591.
[299] Xiong XY, Xue RJ, Zhang S, Wang LJ. The Finite Element Analysis on Seismic Performance of Ring Beam and Constructional Column with Different Storey in Masonry Building. Adv Mater Res 2014;919–921:1016–9. https://doi.org/10.4028/www.scientific.net/AMR.919-921.1016.
[300] CSPFea S.c. MIDAS Gen 2021.
[301] Federal Emergency Management Agency. ATC FEMA 356: Prestandard and commentary for the seismic rehabilitation of buildings. 2000.
[302] ATC - Applied Technology Council. ATC-40: Seismic Evaluation and Retrofit of Concrete Buildings ATC-40. 1996.

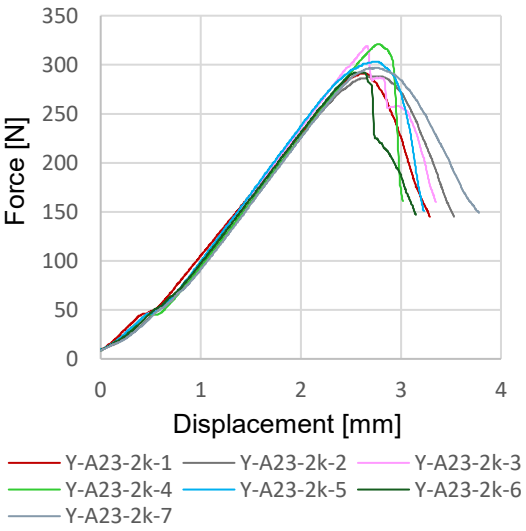
Appendix A

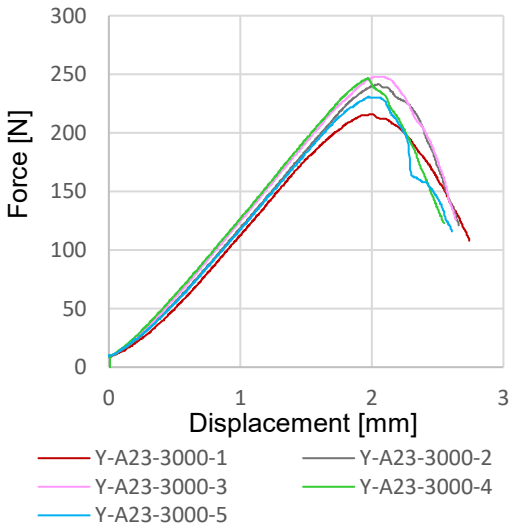
This appendix presents the complete results of the tensile tests on yarns and on GFRP meshes. analyses carried out on the benchmark models described in Sections 2.5 and 2.6.

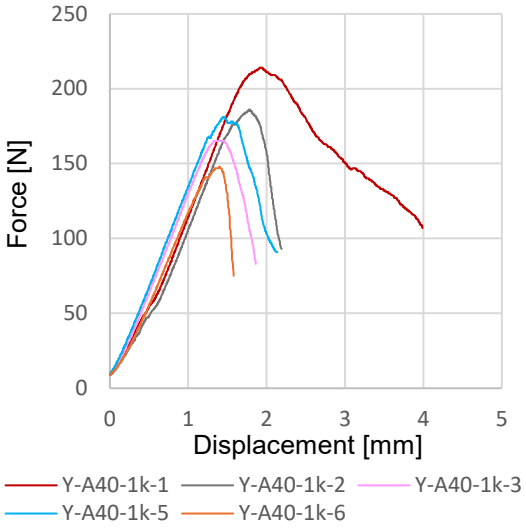
- **Force-displacement plots of the yarn tensile tests that exhibited valid failure modes**

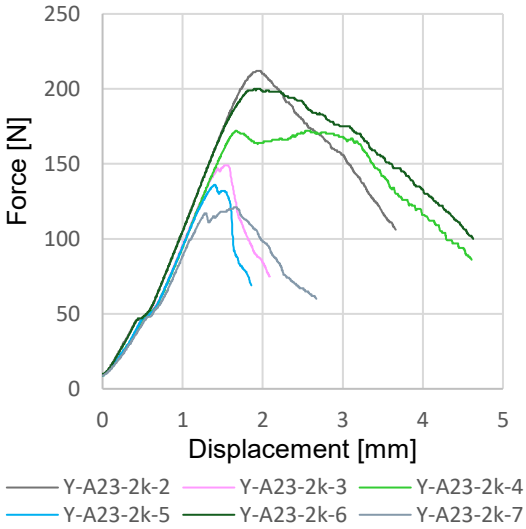


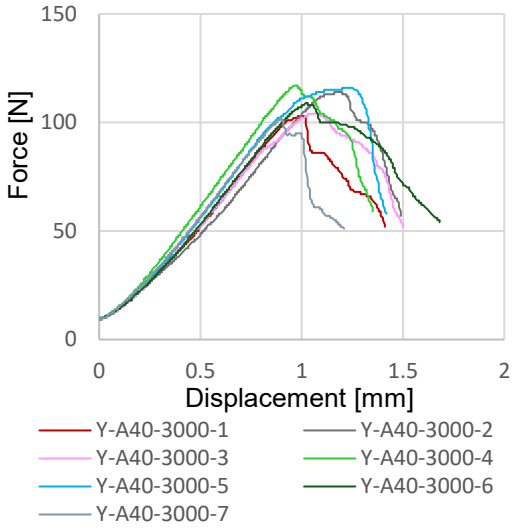




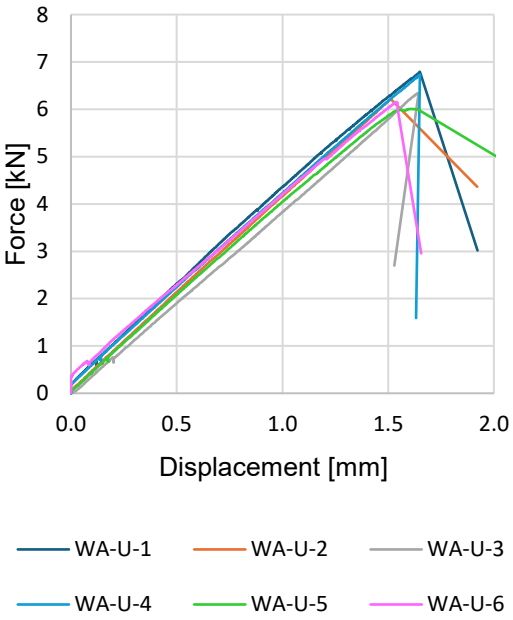


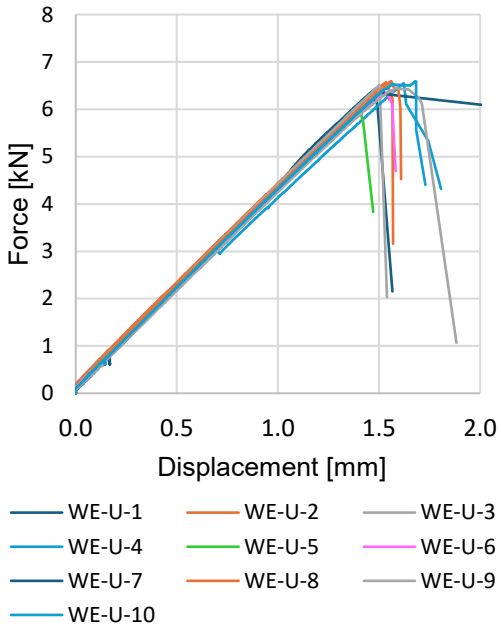

250
200
150
100
50
0
Force [N]
0
1
2
3
4
5
Displacement [mm]
Y-A40-1k-1
Y-A40-1k-2
Y-A40-1k-3
Y-A40-1k-5
Y-A40-1k-6

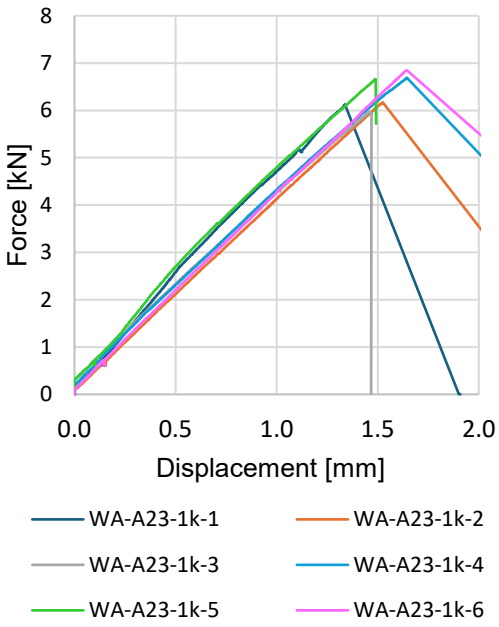

250
200
150
100
50
0
Force [N]
0
1
2
3
4
5
Displacement [mm]
Y-A23-2k-2
Y-A23-2k-3
Y-A23-2k-4
Y-A23-2k-5
Y-A23-2k-6
Y-A23-2k-7

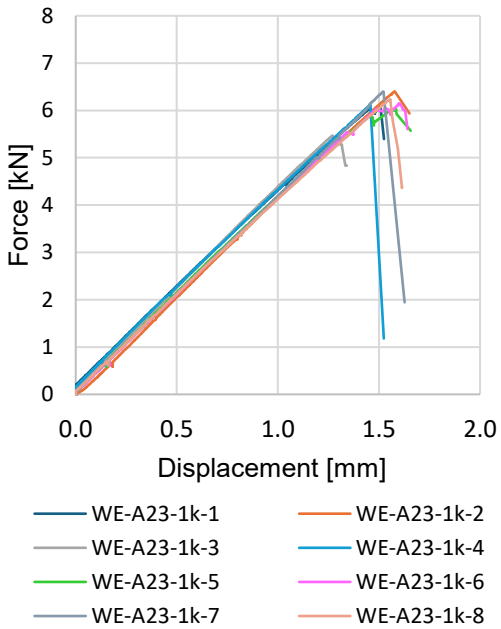

150
100
50
0
Force [N]
0
0.5
1
1.5
2
Displacement [mm]
Y-A40-3000-1
Y-A40-3000-2
Y-A40-3000-3
Y-A40-3000-4
Y-A40-3000-5
Y-A40-3000-6
Y-A40-3000-7

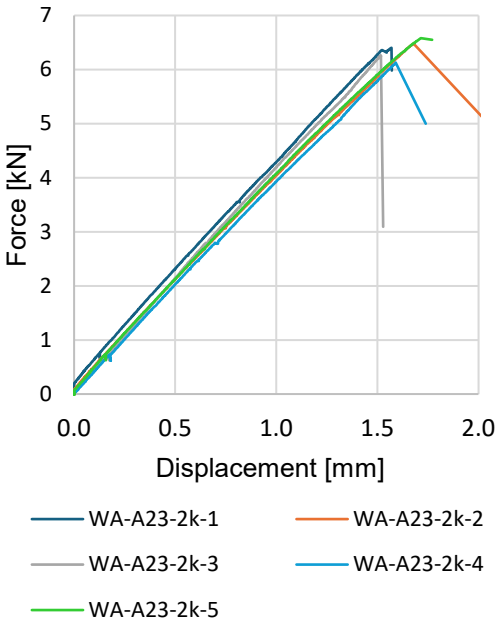
- **Force-displacement plots of the tensile GFRP meshes tests**

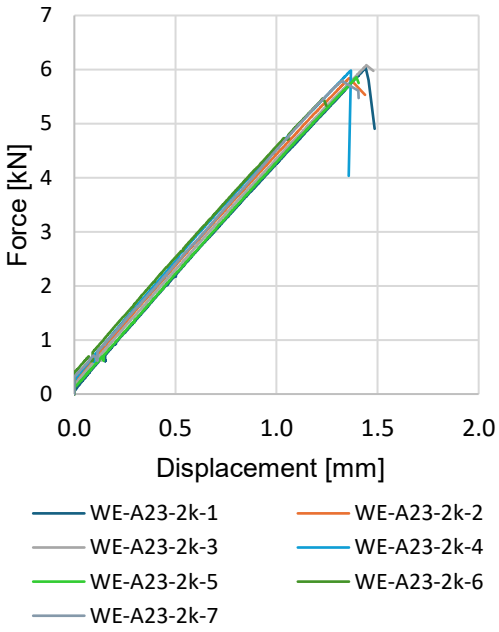


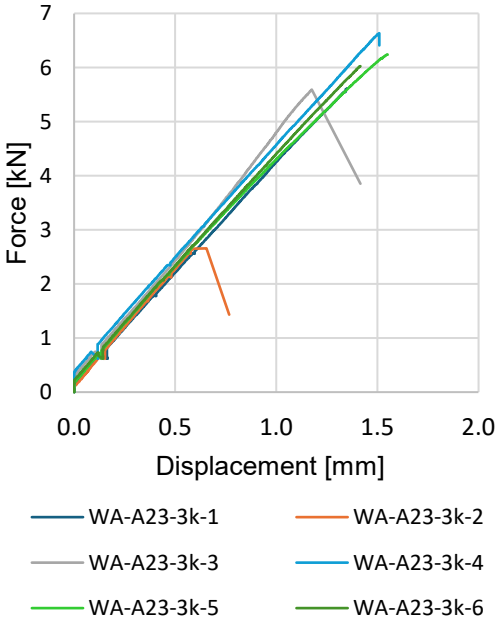


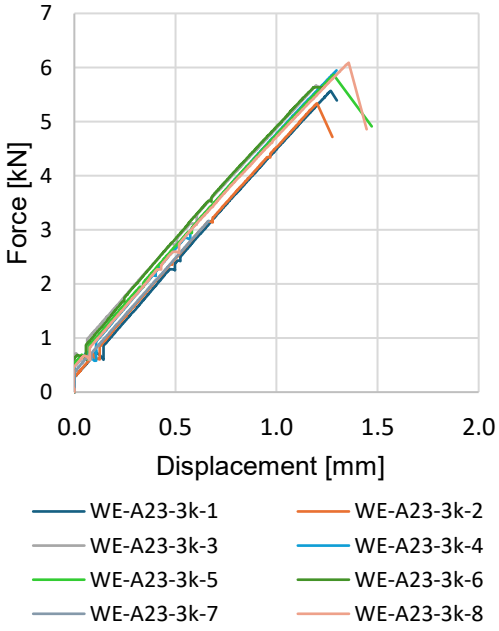


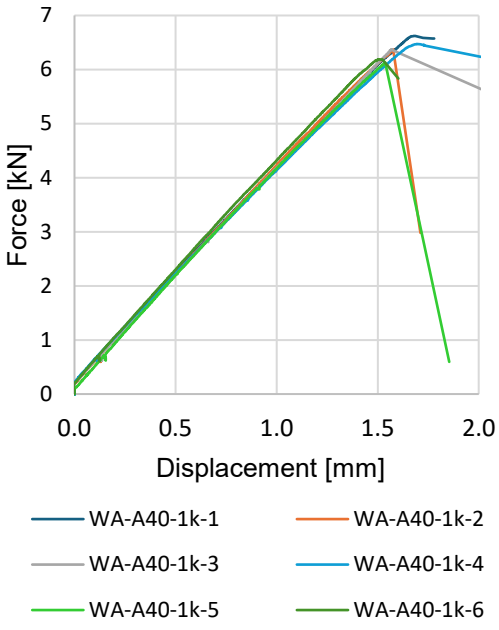


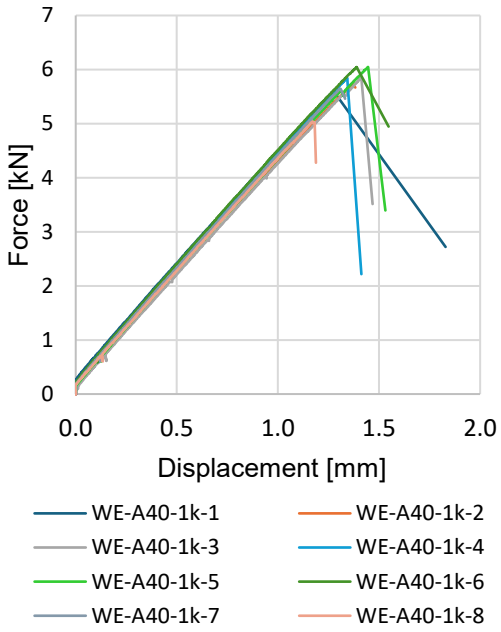

Force [kN]
Displacement [mm]
WA-A23-2k-1
WA-A23-2k-2
WA-A23-2k-3
WA-A23-2k-4
WA-A23-2k-5

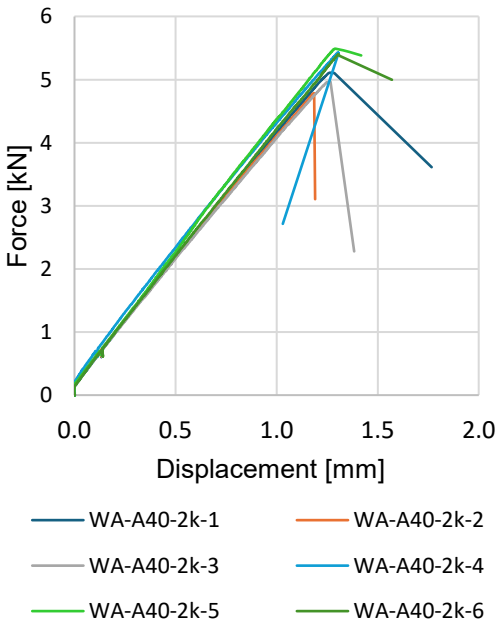

Force [kN]
Displacement [mm]
WE-A23-2k-1
WE-A23-2k-2
WE-A23-2k-3
WE-A23-2k-4
WE-A23-2k-5
WE-A23-2k-6
WE-A23-2k-7

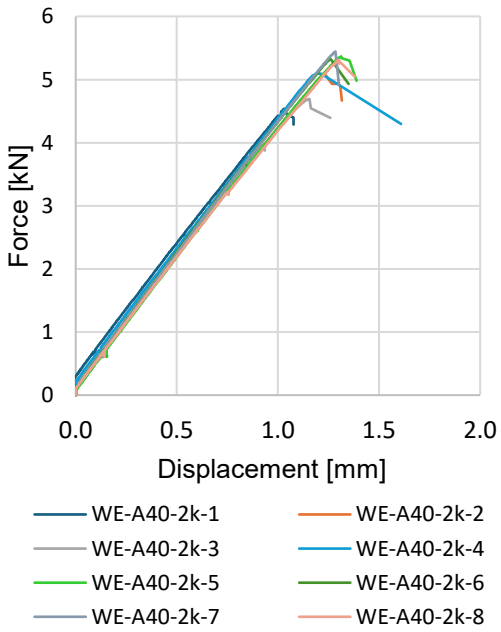

Force [kN]
Displacement [mm]
WA-A23-3k-1
WA-A23-3k-2
WA-A23-3k-3
WA-A23-3k-4
WA-A23-3k-5
WA-A23-3k-6

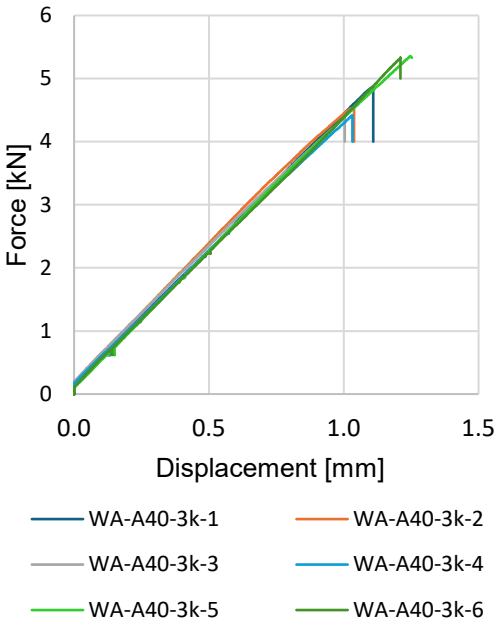

Force [kN]
Displacement [mm]
WE-A23-3k-1
WE-A23-3k-2
WE-A23-3k-3
WE-A23-3k-4
WE-A23-3k-5
WE-A23-3k-6
WE-A23-3k-7
WE-A23-3k-8

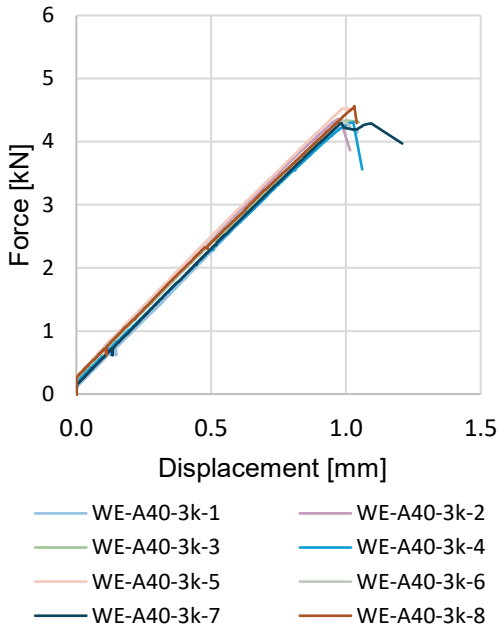

Force [kN]
Displacement [mm]
WA-A40-1k-1
WA-A40-1k-2
WA-A40-1k-3
WA-A40-1k-4
WA-A40-1k-5
WA-A40-1k-6

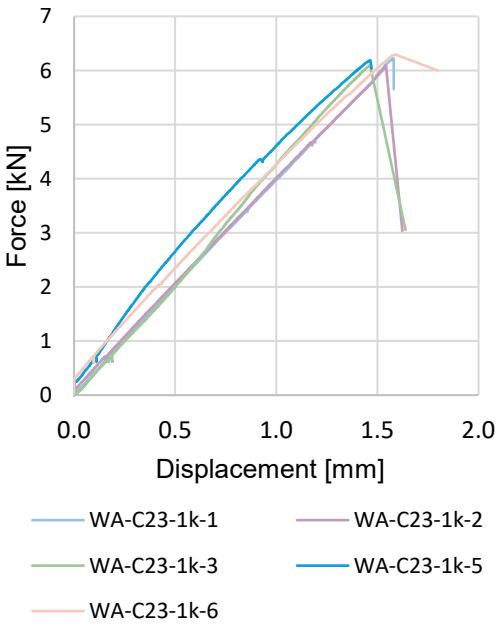

Force [kN]
Displacement [mm]
WE-A40-1k-1
WE-A40-1k-2
WE-A40-1k-3
WE-A40-1k-4
WE-A40-1k-5
WE-A40-1k-6
WE-A40-1k-7
WE-A40-1k-8

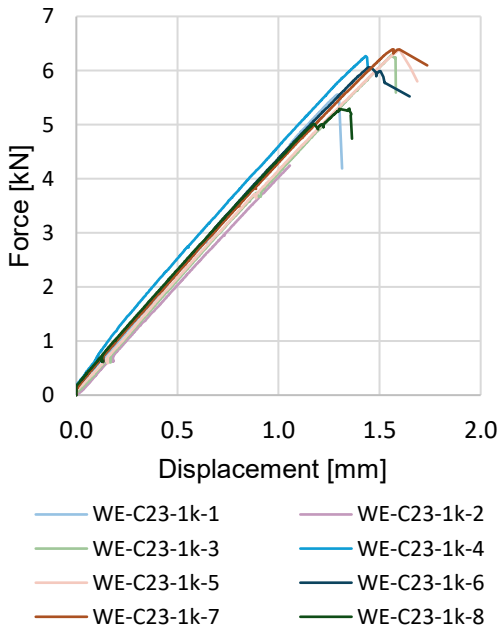

Force [kN]
Displacement [mm]
WA-A40-2k-1
WA-A40-2k-2
WA-A40-2k-3
WA-A40-2k-4
WA-A40-2k-5
WA-A40-2k-6

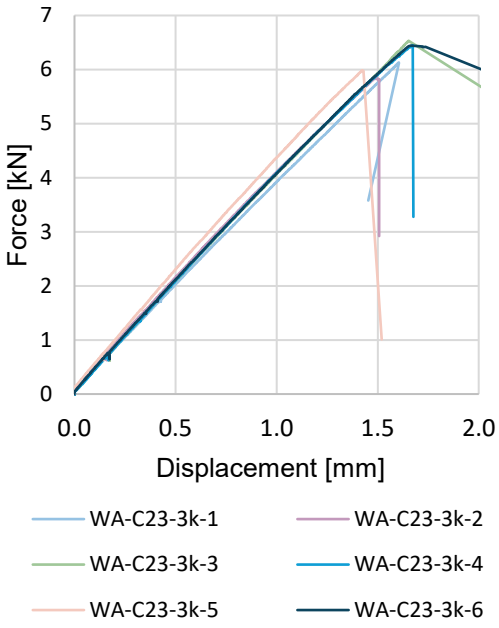

Force [kN]
Displacement [mm]
WE-A40-2k-1
WE-A40-2k-2
WE-A40-2k-3
WE-A40-2k-4
WE-A40-2k-5
WE-A40-2k-6
WE-A40-2k-7
WE-A40-2k-8

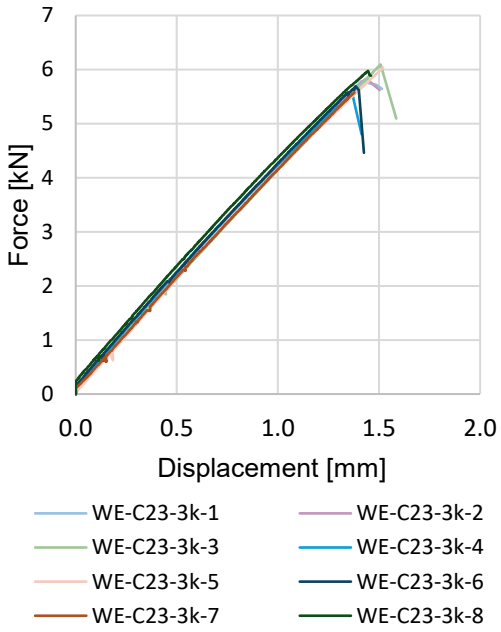

Force [kN]
Displacement [mm]
WA-A40-3k-1
WA-A40-3k-2
WA-A40-3k-3
WA-A40-3k-4
WA-A40-3k-5
WA-A40-3k-6

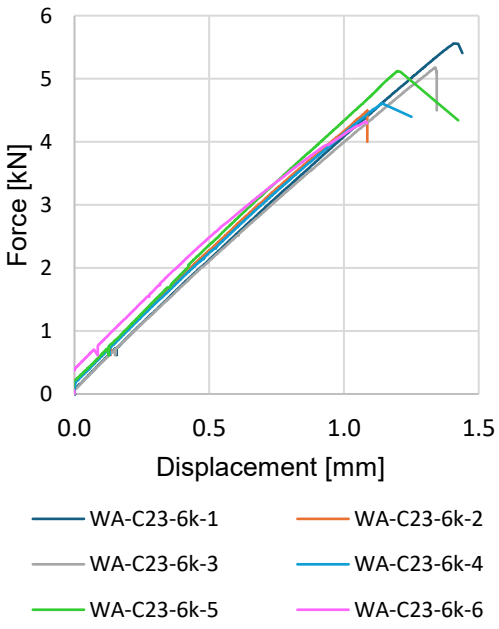

Force [kN]
Displacement [mm]
WE-A40-3k-1
WE-A40-3k-2
WE-A40-3k-3
WE-A40-3k-4
WE-A40-3k-5
WE-A40-3k-6
WE-A40-3k-7
WE-A40-3k-8

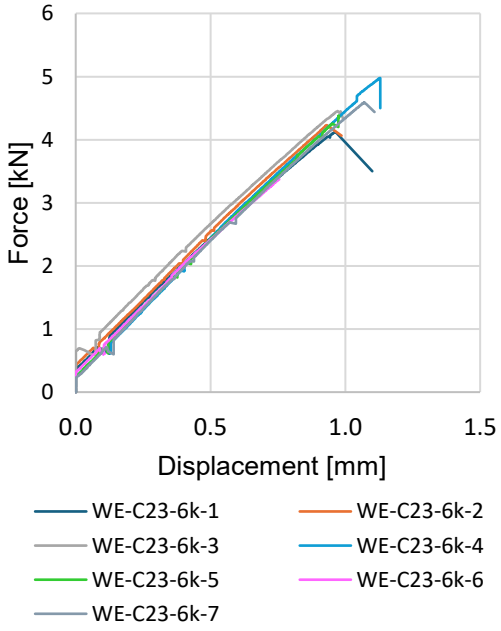

Force [kN]
Displacement [mm]
WA-C23-1k-1
WA-C23-1k-2
WA-C23-1k-3
WA-C23-1k-5
WA-C23-1k-6

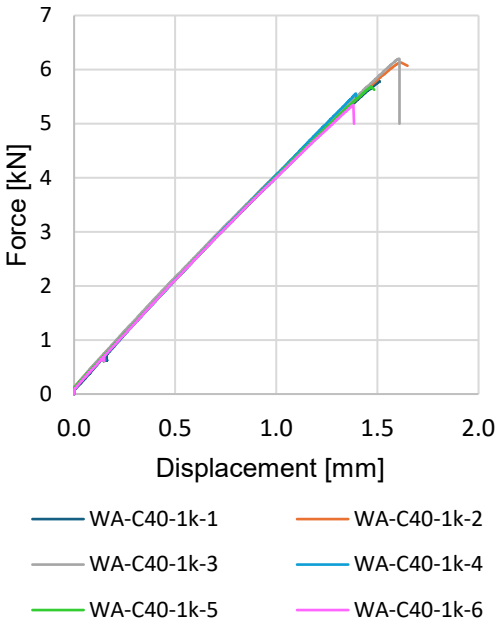

Force [kN]
Displacement [mm]
WE-C23-1k-1
WE-C23-1k-2
WE-C23-1k-3
WE-C23-1k-4
WE-C23-1k-5
WE-C23-1k-6
WE-C23-1k-7
WE-C23-1k-8

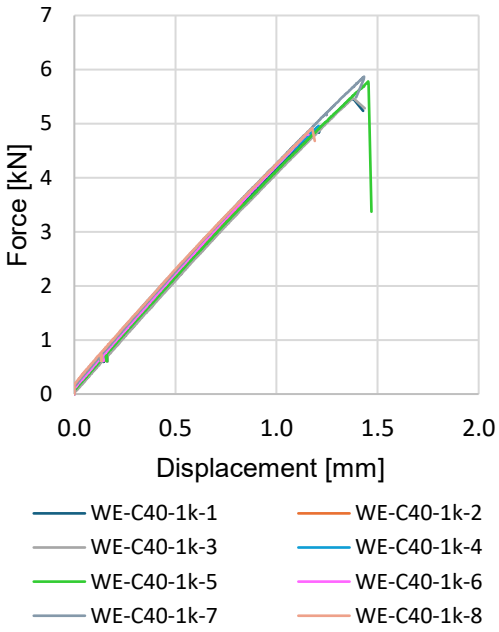

Force [kN]
Displacement [mm]
WA-C23-3k-1
WA-C23-3k-2
WA-C23-3k-3
WA-C23-3k-4
WA-C23-3k-5
WA-C23-3k-6

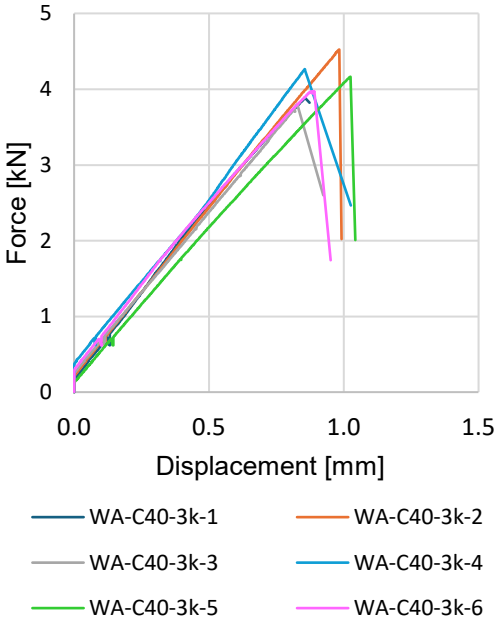

Force [kN]
Displacement [mm]
WE-C23-3k-1
WE-C23-3k-2
WE-C23-3k-3
WE-C23-3k-4
WE-C23-3k-5
WE-C23-3k-6
WE-C23-3k-7
WE-C23-3k-8

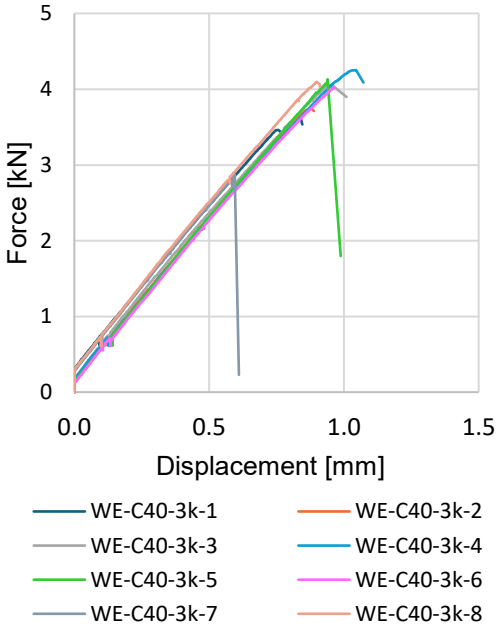

Force [kN]
Displacement [mm]
WA-C23-6k-1
WA-C23-6k-2
WA-C23-6k-3
WA-C23-6k-4
WA-C23-6k-5
WA-C23-6k-6

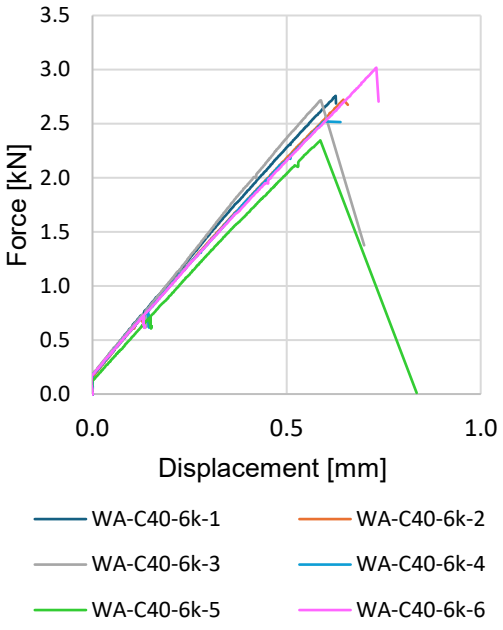

Force [kN]
Displacement [mm]
WE-C23-6k-1
WE-C23-6k-2
WE-C23-6k-3
WE-C23-6k-4
WE-C23-6k-5
WE-C23-6k-6
WE-C23-6k-7

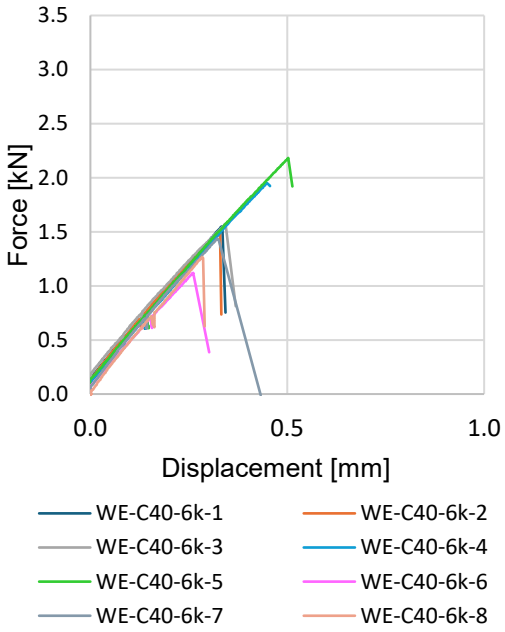

Force [kN]
Displacement [mm]
WA-C40-1k-1
WA-C40-1k-2
WA-C40-1k-3
WA-C40-1k-4
WA-C40-1k-5
WA-C40-1k-6

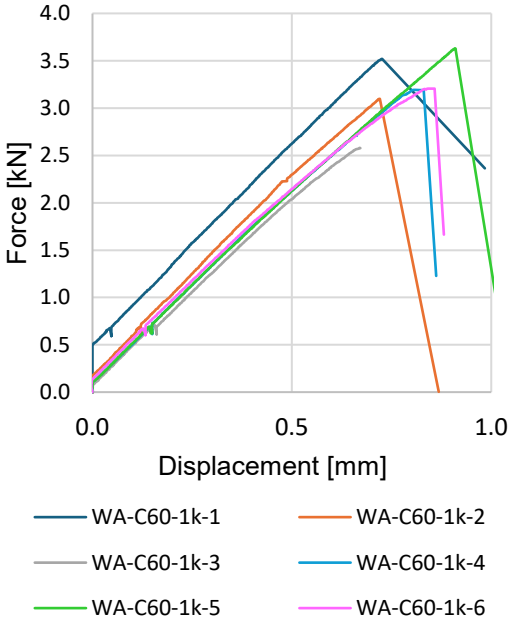

Force [kN]
Displacement [mm]
WE-C40-1k-1
WE-C40-1k-2
WE-C40-1k-3
WE-C40-1k-4
WE-C40-1k-5
WE-C40-1k-6
WE-C40-1k-7
WE-C40-1k-8

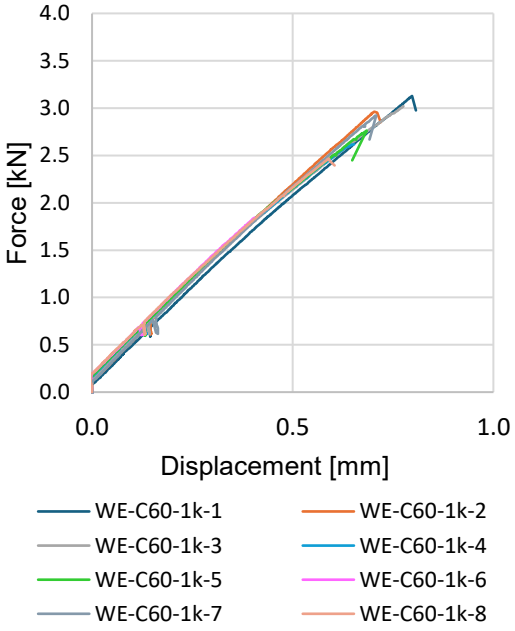

Force [kN]
Displacement [mm]
WA-C40-3k-1
WA-C40-3k-2
WA-C40-3k-3
WA-C40-3k-4
WA-C40-3k-5
WA-C40-3k-6

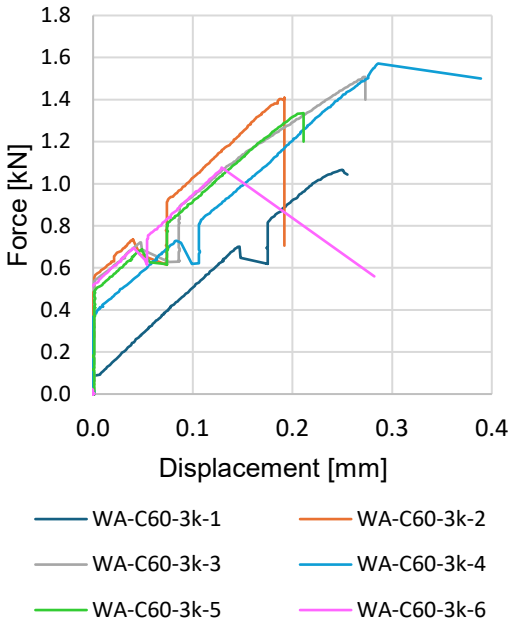

Force [kN]
Displacement [mm]
WE-C40-3k-1
WE-C40-3k-2
WE-C40-3k-3
WE-C40-3k-4
WE-C40-3k-5
WE-C40-3k-6
WE-C40-3k-7
WE-C40-3k-8

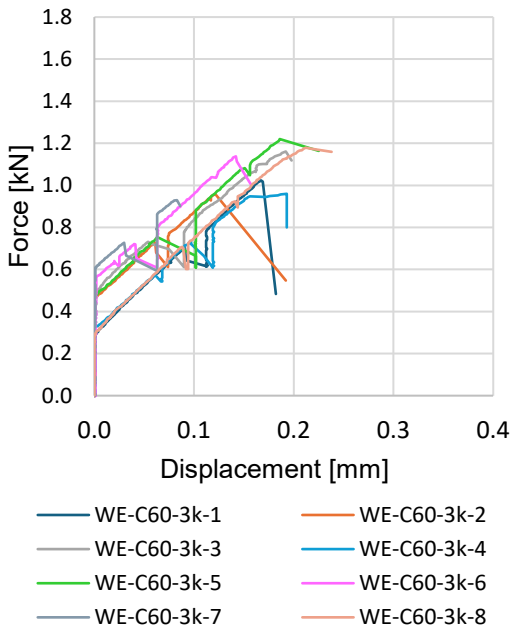

Force [kN]
Displacement [mm]
WA-C40-6k-1
WA-C40-6k-2
WA-C40-6k-3
WA-C40-6k-4
WA-C40-6k-5
WA-C40-6k-6

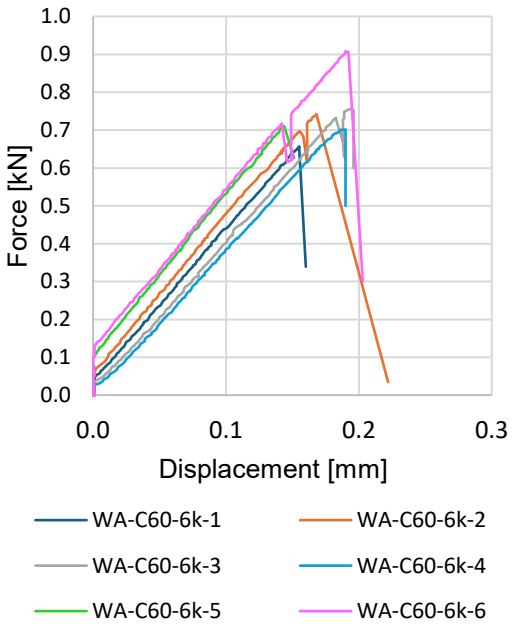

Force [kN]
Displacement [mm]
WE-C40-6k-1
WE-C40-6k-2
WE-C40-6k-3
WE-C40-6k-4
WE-C40-6k-5
WE-C40-6k-6
WE-C40-6k-7
WE-C40-6k-8

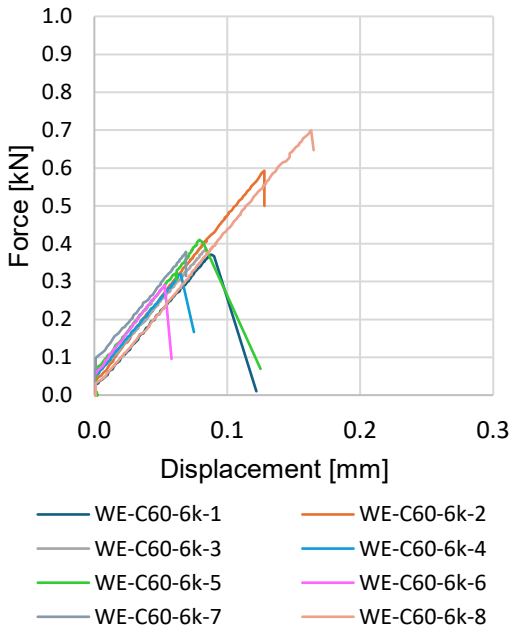

Force [kN]
Displacement [mm]
WA-C60-1k-1
WA-C60-1k-2
WA-C60-1k-3
WA-C60-1k-4
WA-C60-1k-5
WA-C60-1k-6


Force [kN]
Displacement [mm]
WE-C60-1k-1
WE-C60-1k-2
WE-C60-1k-3
WE-C60-1k-4
WE-C60-1k-5
WE-C60-1k-6
WE-C60-1k-7
WE-C60-1k-8


Force [kN]
Displacement [mm]
WA-C60-3k-1
WA-C60-3k-2
WA-C60-3k-3
WA-C60-3k-4
WA-C60-3k-5
WA-C60-3k-6


Force [kN]
Displacement [mm]
WE-C60-3k-1
WE-C60-3k-2
WE-C60-3k-3
WE-C60-3k-4
WE-C60-3k-5
WE-C60-3k-6
WE-C60-3k-7
WE-C60-3k-8


Force [kN]
Displacement [mm]
WA-C60-6k-1
WA-C60-6k-2
WA-C60-6k-3
WA-C60-6k-4
WA-C60-6k-5
WA-C60-6k-6


Force [kN]
Displacement [mm]
WE-C60-6k-1
WE-C60-6k-2
WE-C60-6k-3
WE-C60-6k-4
WE-C60-6k-5
WE-C60-6k-6
WE-C60-6k-7
WE-C60-6k-8

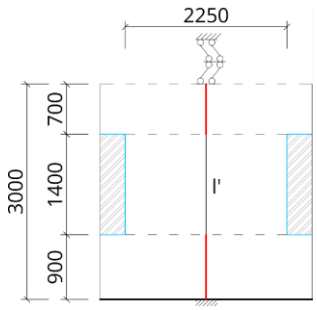
Appendix B

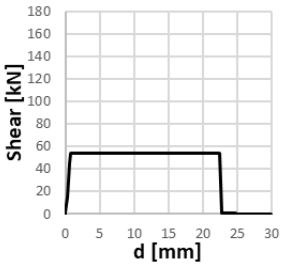
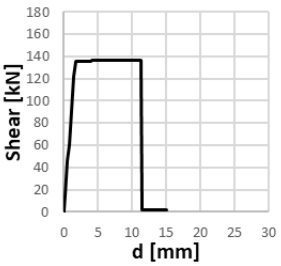
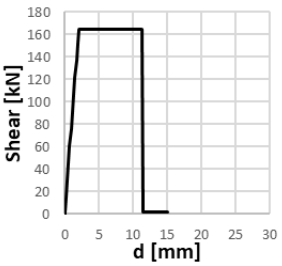
This appendix presents the complete results of the numerical analyses carried out on the benchmark models described in Section 5.4.3. The study includes individual structural elements (piers and spandrels), portal frames, and single- and double-story wall configurations. Each model was analysed in three conditions: unstrengthened (URM), strengthened on one side (R1), and strengthened on both sides (R2), using the equivalent frame method implemented in Midas Gen.

The results reported herein include the full set of pushover curves, capacity parameters, and failure modes for each configuration, complementing the main discussion provided in Section 5.4.3.

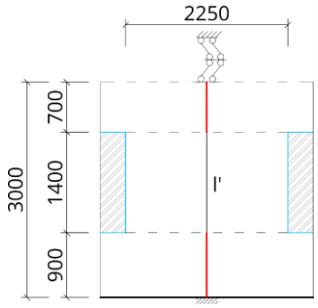
Simplified numerical analyses on pier elements

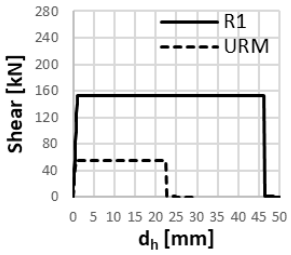
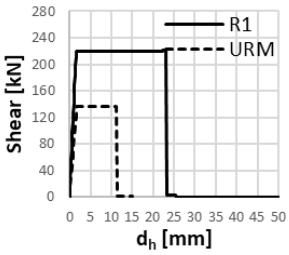
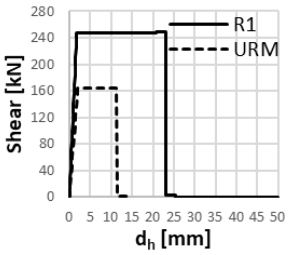
- **Pier st_h3_a**



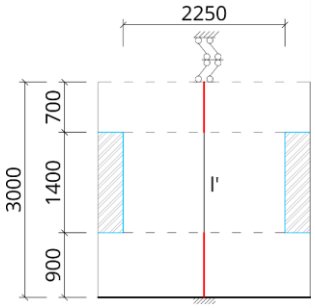
ID:	Pier_st_h3_a_01		Pier_st_h3_a_03		Pier_st_h3_a_05	
Axial stress:	0.1 MPa		0.3 MPa		0.5 MPa	
Capacity curve:						
	d [mm]	*F* [kN]	*d* [mm]	*F* [kN]	*d* [mm]	*F* [kN]
	0.00	0.0	0.00	0.0	0.00	0.0
	0.02	1.5	0.02	1.5	0.02	1.5
	0.19	15.2	0.56	45.7	0.56	45.7
	0.38	30.4	0.94	76.1	1.13	91.3
	0.56	45.7	1.31	106.5	1.88	152.2
	0.75	54.2	1.69	135.9	2.06	164.2
	22.50	54.2	11.25	136.0	11.25	164.3
	22.69	0.5	11.44	1.4	11.44	1.6
	24.94	0.0	15.00	0	15.00	0.0
Yield point:	0.75 mm	54.2 kN	1.69 mm	135.9 kN	2.06 mm	164.2 kN
Collapse:	24.8 mm	54.2 kN	11.3 mm	136.0 kN	11.25 mm	164.3 kN
Failure mode:	Bending		Diagonal cracking		Diagonal cracking	

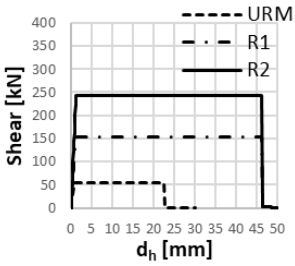
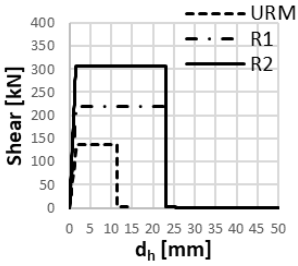
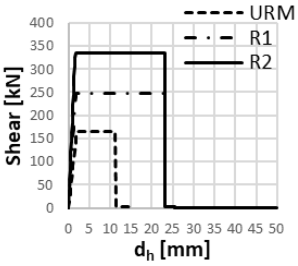
- **Pier st_h3_a_R1**



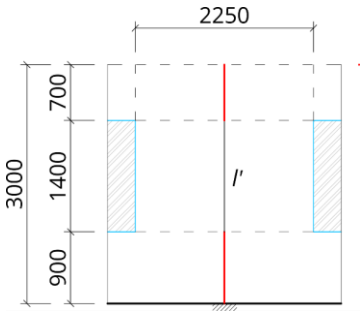
ID:	Pier_st_h3_a_01_R1		Pier_st_h3_a_03_R1		Pier_st_h3_a_05_R1	
Masonry properties:	$\tau_{0,eq}$=0.194MPa;$H_{p,eq}$=157.4kN		$\tau_{0,eq}$=0.186MPa;$H_{p,eq}$=244.2kN		$\tau_{0,eq}$=0.178MPa;$H_{p,eq}$=318.7kN	
Axial stress:	0.1 MPa		0.3 MPa		0.5 MPa	
Capacity curve:						
	d [mm]	*F* [kN]	*d* [mm]	*F* [kN]	*d* [mm]	*F* [kN]
	0.00	0.0	0.00	0.0	0.00	0.0
	0.20	28.3	0.20	28.3	0.20	28.3
	1.00	141.3	1.50	211.9	1.70	240.1
	1.10	153.3	1.60	220.2	1.80	247.9
	46.2	153.4	23.1	220.4	23.1	248.2
	46.3	0.0	23.2	0.0	23.2	0.0
Yield point:	1.10 mm	153.3 kN	1.60 mm	220.2 kN	1.80 mm	247.9 kN
Collapse:	46.2 mm	153.4 kN	23.1 mm	220.4 kN	23.1 mm	248.2 kN
Failure mode:	Bending		Diagonal cracking		Diagonal cracking	

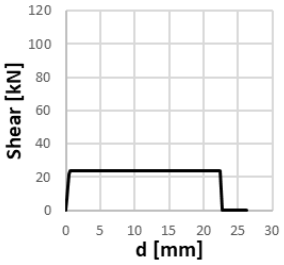
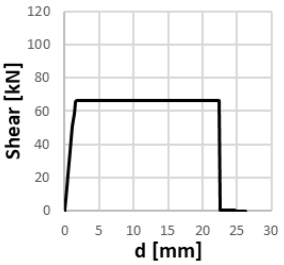
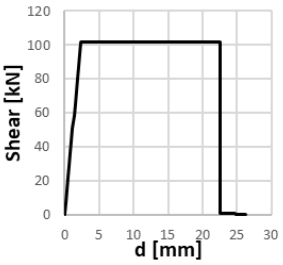
- **Pier st_h3_a_R2**



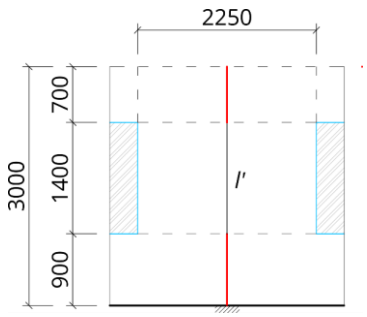
ID:	Pier_st_h3_a_01_R2		Pier_st_h3_a_03_R2		Pier_st_h3_a_05_R2	
Masonry properties:	$\tau_{0,eq}$=0.299MPa;$H_{p,eq}$=248.8kN		$\tau_{0,eq}$=0.287MPa;$H_{p,eq}$=324.4kN		$\tau_{0,eq}$=0.273MPa;$H_{p,eq}$=388.4kN	
Axial stress:	0.1 MPa		0.3 MPa		0.5 MPa	
Capacity curve:						
	d [mm]	*F* [kN]	*d* [mm]	*F* [kN]	*d* [mm]	*F* [kN]
	0.00	0.0	0.00	0.0	0.00	0.0
	0.20	40.8	0.20	40.8	0.20	40.8
	1.10	224.4	1.50	306.0	1.60	326.4
	1.20	242.2	1.60	307.2	1.70	334.4
	46.2	242.5	23.1	307.6	23.1	334.7
	46.3	0.0	23.2	0.0	23.2	0.0
Yield point:	1.10 mm	242.2 kN	1.60 mm	307.2 kN	1.70 mm	334.4 kN
Collapse:	46.2 mm	242.5 kN	23.1 mm	307.6 kN	23.1 mm	334.7 kN
Failure mode:	Bending		Diagonal cracking		Diagonal cracking	

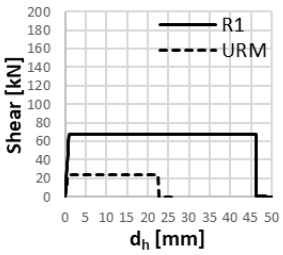
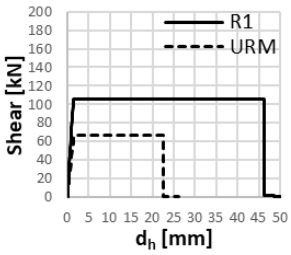
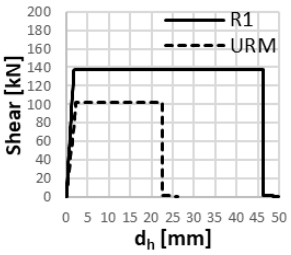
- **Pier ct_h3_a**



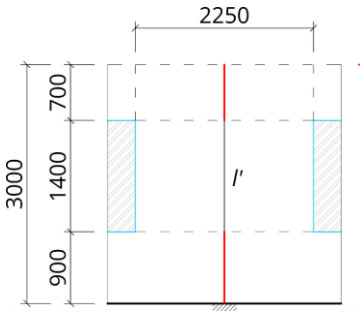
ID:	Pier_ct_h3_a_01	Pier_ct_h3_a_03	Pier_ct_h3_a_05
Axial stress:	0.1 MPa	0.3 MPa	0.5 MPa
Capacity curve:			
	d [mm] *F* [kN] 0.00 0.0 0.02 0.7 0.17 7.3 0.33 14.6 0.50 21.9 0.66 23.7 22.46 23.7 22.62 0.2 30.00 0.0	*d* [mm] *F* [kN] 0.00 0.0 0.02 0.7 0.50 21.9 1.16 51.0 1.49 65.6 1.65 66.0 22.47 66.1 22.62 0.7 30.00 0.0	*d* [mm] *F* [kN] 0.00 0.0 0.02 0.7 0.66 29.2 1.33 58.3 1.99 87.5 2.48 101.7 22.48 101.8 22.62 1.0 30.00 0.0
Yield point:	0.66 mm 23.7 kN	1.65 mm 66.0 kN	2.48 mm 101.7 kN
Collapse:	25.5 mm 23.7 kN	22.5 mm 66.1 kN	22.5 mm 101.8 kN
Failure mode:	Bending	Bending	Bending

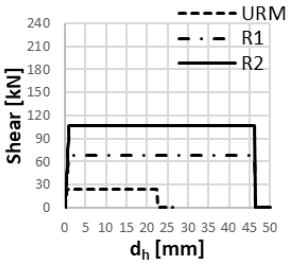
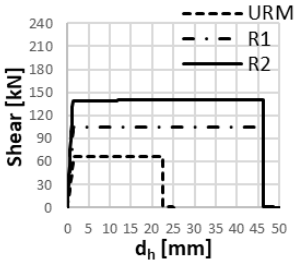
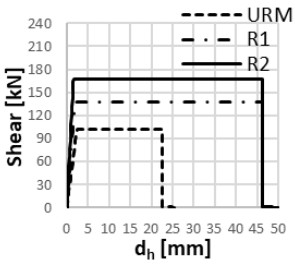
- **Pier ct_h3_a_R1**



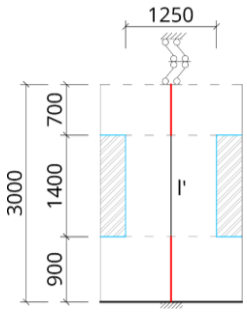
ID:	Pier_ct_h3_a_01_R1	Pier_ct_h3_a_03_R1	Pier_ct_h3_a_05_R1
Masonry properties:	$\tau_{0,eq}$=0.194MPa;$H_{p,eq}$=157.4kN	$\tau_{0,eq}$=0.186MPa;$H_{p,eq}$=244.2kN	$\tau_{0,eq}$=0.178MPa;$H_{p,eq}$=318.7kN
Axial stress:	0.1 MPa	0.3 MPa	0.5 MPa
Capacity curve:			
	d [mm] / *F* [kN] 0.00 / 0.0 0.20 / 15.2 0.80 / 60.8 0.90 / 67.8 46.2 / 67.8 46.3 / 0.0	*d* [mm] / *F* [kN] 0.00 / 0.0 0.20 / 15.2 1.30 / 98.9 1.40 / 105.1 46.2 / 105.2 46.3 / 0.0	*d* [mm] / *F* [kN] 0.00 / 0.0 0.20 / 15.2 1.80 / 136.9 1.90 / 137.2 46.2 / 137.3 46.3 / 0.0
Yield point:	0.90 mm 67.8 kN	1.40 mm 105.1 kN	1.90 mm 137.2 kN
Collapse:	46.2 mm 67.8kN	46.2 mm 105.2 kN	46.2 mm 137.3 kN
Failure mode:	Bending	Bending	Bending

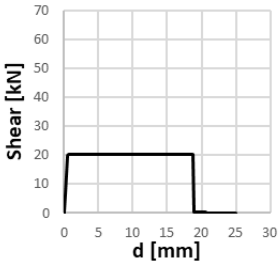
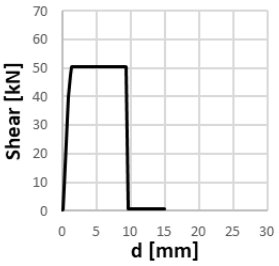
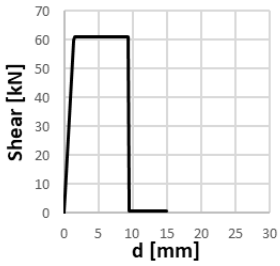
- **Pier ct_h3_a_R2**



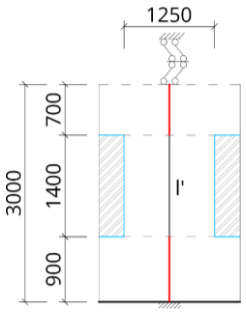
ID:	Pier_ct_h3_a_01_R2	Pier_ct_h3_a_03_R2	Pier_ct_h3_a_05_R2
Masonry properties:	$\tau_{0,eq}$=0.299MPa;$H_{p,eq}$=248.8kN	$\tau_{0,eq}$=0.287MPa;$H_{p,eq}$=324.4kN	$\tau_{0,eq}$=0.273MPa;$H_{p,eq}$=388.4kN
Axial stress:	0.1 MPa	0.3 MPa	0.5 MPa
Capacity curve:			
	d [mm] *F* [kN] 0.00 0.0 0.20 22.0 0.90 98.8 1.00 107.1 46.2 107.2 46.3 0.0	*d* [mm] *F* [kN] 0.00 0.0 0.20 22.0 1.20 131.8 1.30 139.6 46.2 139.8 46.3 0.0	*d* [mm] *F* [kN] 0.00 0.0 0.20 22.0 1.50 164.7 1.60 167.2 46.2 167.3 46.3 0.0
Yield point:	1.00 mm 107.1 kN	1.30 mm 139.6 kN	1.60 mm 167.2 kN
Collapse:	46.2 mm 107.2 kN	46.2 mm 139.8 kN	46.2 mm 167.3 kN
Failure mode:	Bending	Bending	Bending

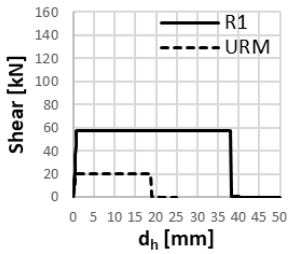
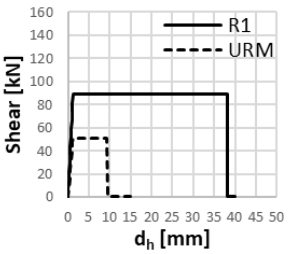
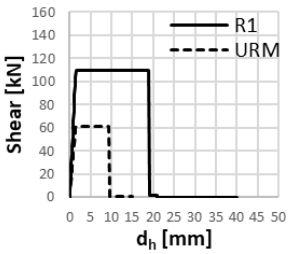
- **Pier st_h3_b**



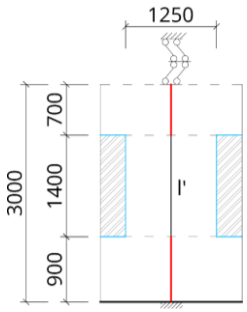
ID:	Pier_st_h3_b_01	Pier_st_h3_b_03	Pier_st_h3_b_05
Axial stress:	0.1 MPa	0.3 MPa	0.5 MPa
Capacity curve:			
	d [mm] *F* [kN] 0.00 0.0 0.02 0.7 0.16 6.7 0.31 13.3 0.47 20.0 0.63 20.1 18.75 20.1 18.91 0.2 25.00 0.0	*d* [mm] *F* [kN] 0.00 0.0 0.02 0.8 0.38 16.0 0.75 32.0 1.13 48.0 1.31 50.5 9.38 50.5 9.56 0.5 15.00 0.0	*d* [mm] *F* [kN] 0.00 0.0 0.02 0.7 0.31 13.3 0.78 33.3 1.25 53.3 1.56 61.0 9.38 61.1 9.53 0.6 15.00 0.0
Yield point:	0.63 mm 21.1 kN	1.31 mm 50.5 kN	1.56 mm 61.0 kN
Collapse:	18.8 mm 21.1 kN	9.38 mm 50.5 kN	9.38 mm 61.1 kN
Failure mode:	Bending	Diagonal cracking	Diagonal cracking

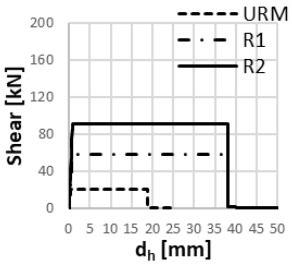
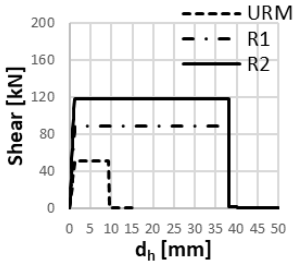
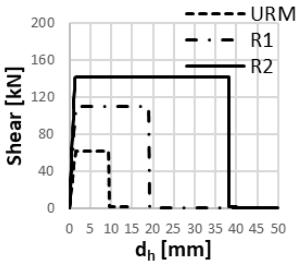
- **Pier st_h3_b_R1**



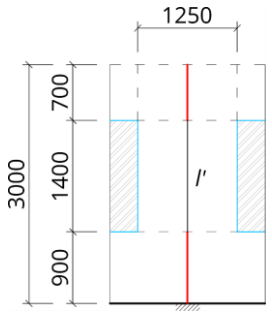
ID:	Pier_st_h3_b_01_R1	Pier_st_h3_b_03_R1	Pier_st_h3_b_05_R1
Masonry properties:	$\tau_{0,eq}$=0.242MPa;$H_{p,eq}$=87.4kN	$\tau_{0,eq}$=0.232MPa;$H_{p,eq}$=135.6kN	$\tau_{0,eq}$=0.221MPa;$H_{p,eq}$=177.1kN
Axial stress:	0.1 MPa	0.3 MPa	0.5 MPa
Capacity curve:			
	d [mm] / *F* [kN] 0.00 / 0.0 0.20 / 14.9 0.70 / 52.2 0.80 / 57.3 38.1 / 57.4 38.2 / 0.0	*d* [mm] / *F* [kN] 0.00 / 0.0 0.20 / 14.9 1.10 / 82.0 1.20 / 88.9 38.1 / 89.0 38.2 / 0.0	*d* [mm] / *F* [kN] 0.00 / 0.0 0.20 / 14.9 1.40 / 104.4 1.50 / 109.4 19.0 / 109.5 19.1 / 0.0
Yield point:	0.80 mm 57.3 kN	1.20 mm 88.9 kN	1.50 mm 109.4 kN
Collapse:	38.1 mm 57.4 kN	38.1 mm 89.0 kN	19.0 mm 109.5 kN
Failure mode:	Bending	Bending	Diagonal cracking

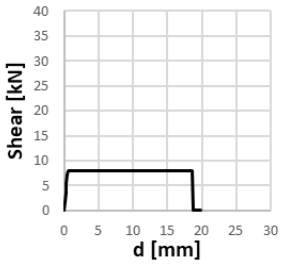
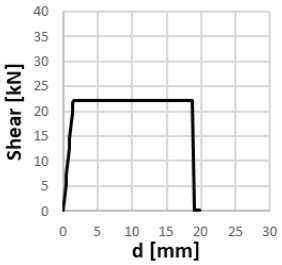
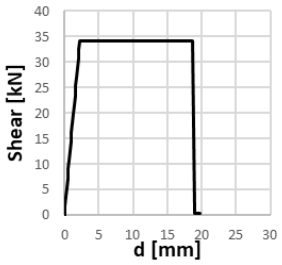
- **Pier st_h3_b_R2**



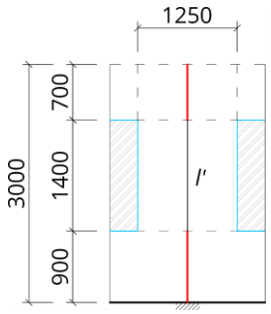
ID:	Pier_st_h3_b_01_R2	Pier_st_h3_b_03_R2	Pier_st_h3_b_05_R2
Masonry properties:	$\tau_{0,eq}$=0.396MPa;$H_{p,eq}$=138.2kN	$\tau_{0,eq}$=0.382MPa;$H_{p,eq}$=180.2kN	$\tau_{0,eq}$=0.365MPa;$H_{p,eq}$=215.8kN
Axial stress:	0.1 MPa	0.3 MPa	0.5 MPa
Capacity curve:			
	d [mm] / *F* [kN] 0.00 / 0.0 0.20 / 21.5 0.80 / 86.1 0.90 / 90.6 38.1 / 90.7 38.2 / 0.0	*d* [mm] / *F* [kN] 0.00 / 0.0 0.20 / 21.5 1.00 / 107.6 1.10 / 118.1 38.1 / 118.2 38.2 / 0.0	*d* [mm] / *F* [kN] 0.00 / 0.0 0.20 / 21.5 1.30 / 139.9 1.40 / 141.4 38.1 / 141.6 38.2 / 0.0
Yield point:	0.90 mm / 90.6 kN	1.10 mm / 118.1 kN	1.40 mm / 141.4 kN
Collapse:	38.1 mm / 90.7 kN	38.1 mm / 118.2 kN	38.1 mm / 141.6 kN
Failure mode:	Bending	Bending	Bending

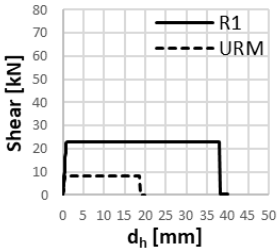
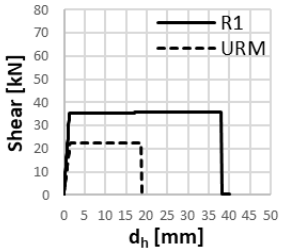
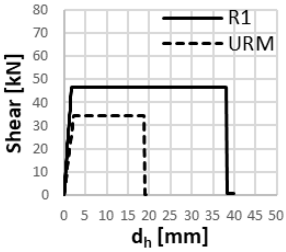
- **Pier ct_h3_b**



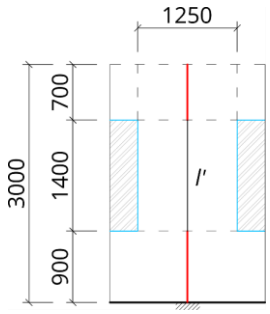
ID:	Pier_ct_h3_b_01	Pier_ct_h3_b_03	Pier_ct_h3_b_05
Axial stress:	0.1 MPa	0.3 MPa	0.5 MPa
Capacity curve:			
	d [mm] *F* [kN] 0.00 0.0 0.02 0.2 0.12 1.8 0.23 3.6 0.47 7.2 0.59 8.0 18.66 8.0 18.82 0.1 20.00 0.0	*d* [mm] *F* [kN] 0.00 0.0 0.02 0.2 0.12 1.8 0.47 7.2 0.94 14.5 1.53 22.2 18.73 22.2 18.94 0.2 20.00 0.0	*d* [mm] *F* [kN] 0.00 0.0 0.02 0.2 0.59 9.0 1.17 18.1 1.64 25.3 2.22 34.2 18.69 34.2 18.94 0.3 20.00 0.0
Yield point:	0.59 mm 8.0 kN	1.53 mm 22.2 kN	2.22 mm 34.2 kN
Collapse:	18.7 mm 8.0 kN	18.7 mm 22.2 kN	18.7 mm 34.2 kN
Failure mode:	Bending	Bending	Bending

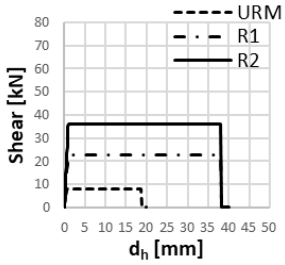
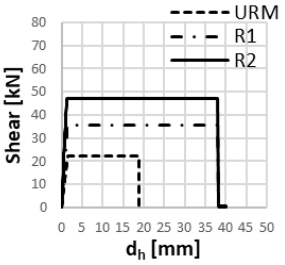
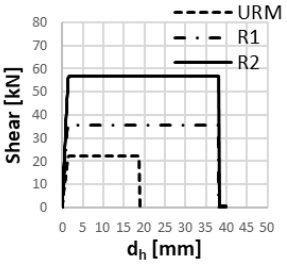
- **Pier ct_h3_b_R1**



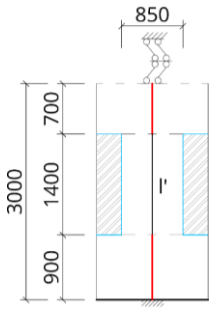
ID:	Pier_ct_h3_b_01_R1	Pier_ct_h3_b_03_R1	Pier_ct_h3_b_05_R1
Masonry properties:	$\tau_{0,eq}$=0.242MPa;$H_{p,eq}$=87.4kN	$\tau_{0,eq}$=0.232MPa;$H_{p,eq}$=135.6kN	$\tau_{0,eq}$=0.221MPa;$H_{p,eq}$=177.1kN
Axial stress:	0.1 MPa	0.3 MPa	0.5 MPa
Capacity curve:			
	d [mm] / *F* [kN] 0.00 / 0.0 0.15 / 4.1 0.76 / 20.4 0.83 / 22.4 38.1 / 22.9 38.2 / 0.0	*d* [mm] / *F* [kN] 0.00 / 0.0 0.15 / 4.1 1.29 / 34.7 1.36 / 35.5 38.1 / 35.6 38.2 / 0.0	*d* [mm] / *F* [kN] 0.00 / 0.0 0.15 / 4.1 1.66 / 44.9 1.74 / 46.4 38.1 / 46.4 38.3 / 0.0
Yield point:	0.83 mm / 22.4 kN	1.36 mm / 35.6 kN	1.74 mm / 46.4 kN
Collapse:	38.1 mm / 22.9 kN	38.1 mm / 35.6 kN	38.1 mm / 46.4 kN
Failure mode:	Bending	Bending	Bending

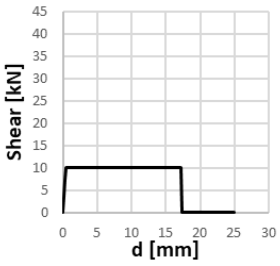
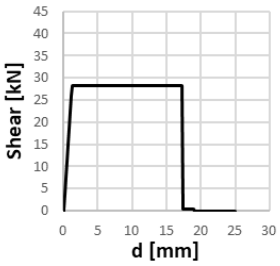
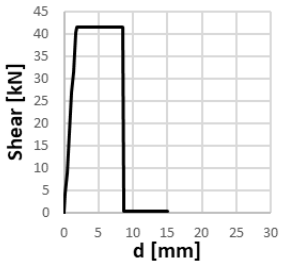
- **Pier ct_h3_b_R2**



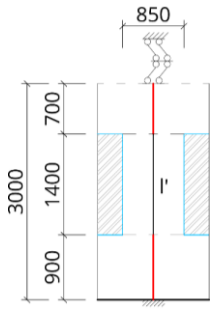
ID:	Pier_ct_h3_b_01_R2	Pier_ct_h3_b_03_R2	Pier_ct_h3_b_05_R2
Masonry properties:	$\tau_{0,eq}$=0.396MPa;$H_{p,eq}$=138.2kN	$\tau_{0,eq}$=0.382MPa;$H_{p,eq}$=180.2kN	$\tau_{0,eq}$=0.365MPa;$H_{p,eq}$=215.8kN
Axial stress:	0.1 MPa	0.3 MPa	0.5 MPa
Capacity curve:			
	d [mm] *F* [kN] 0.00 0.0 0.15 5.9 0.91 35.3 0.99 36.2 38.1 36.2 38.2 0.0	*d* [mm] *F* [kN] 0.00 0.0 0.15 5.9 1.21 47.1 1.29 47.2 38.1 47.2 38.2 0.0	*d* [mm] *F* [kN] 0.00 0.0 0.15 5.9 1.44 55.9 1.52 56.5 38.1 56.6 38.1 0.0
Yield point:	0.99 mm 36.2 kN	1.29 mm 47.2 kN	1.52 mm 56.5 kN
Collapse:	38.1 mm 36.2 kN	38.1 mm 47.2 kN	38.1 mm 56.6 kN
Failure mode:	Bending	Bending	Bending

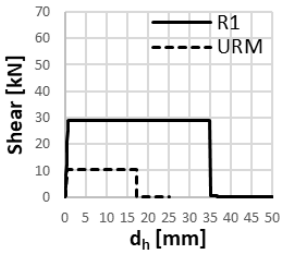
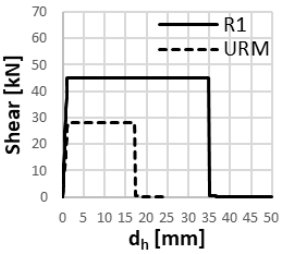
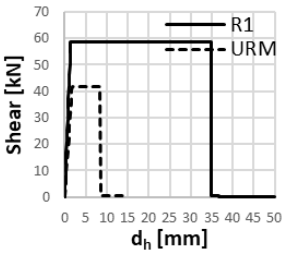
- **Pier st_h3_c**



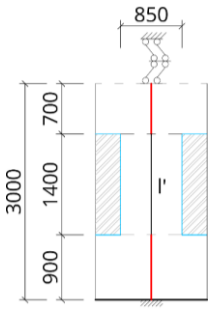
ID:	Pier_st_h3_c_01	Pier_st_h3_c_03	Pier_st_h3_c_05
Axial stress:	0.1 MPa	0.3 MPa	0.5 MPa
Capacity curve:			
	d [mm] *F* [kN] 0.00 0.0 0.02 0.4 0.16 3.7 0.31 7.5 0.47 10.1 17.19 10.1 17.34 0.1 25.00 0.0	*d* [mm] *F* [kN] 0.00 0.0 0.02 0.4 0.47 11.2 0.78 18.7 1.09 26.2 1.25 28.2 17.19 28.2 17.34 0.3 25.00 0.0	*d* [mm] *F* [kN] 0.00 0.0 0.02 0.4 0.75 17.9 1.31 31.4 1.50 35.9 1.88 41.5 8.44 41.5 8.63 0.4 15.00 0.0
Yield point:	0.47 mm 10.1 kN	1.25 mm 28.2 kN	1.88 mm 41.5 kN
Collapse:	17.2 mm 10.1 kN	17.2 mm 28.2 kN	8.44 mm 41.5 kN
Failure mode:	Bending	Bending	Diagonal cracking

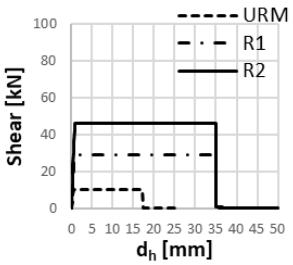
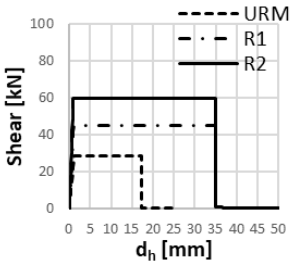
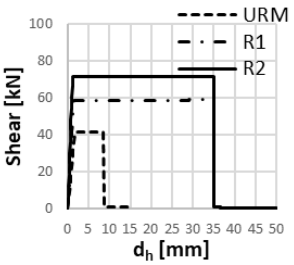
- **Pier st_h3_c_R1**



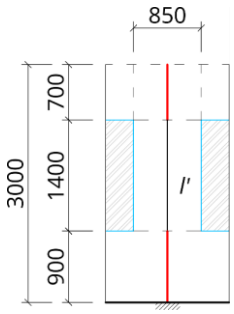
ID:	Pier_st_h3_c_01_R1	Pier_st_h3_c_03_R1	Pier_st_h3_c_05_R1
Masonry properties:	$\tau_{0,eq}$=0.242MPa;$H_{p,eq}$=59.5kN	$\tau_{0,eq}$=0.232MPa;$H_{p,eq}$=92.2kN	$\tau_{0,eq}$=0.221MPa;$H_{p,eq}$=120.4kN
Axial stress:	0.1 MPa	0.3 MPa	0.5 MPa
Capacity curve:			
	d [mm] / *F* [kN] 0.00 / 0.0 0.20 / 8.4 0.60 / 25.1 0.70 / 29.0 34.9 / 29.0 35.0 / 0.0	*d* [mm] / *F* [kN] 0.00 / 0.0 0.20 / 8.4 1.00 / 41.9 1.10 / 44.9 34.9 / 44.9 35.0 / 0.0	*d* [mm] / *F* [kN] 0.00 / 0.0 0.20 / 8.4 1.30 / 54.5 1.40 / 58.6 34.9 / 58.7 35.0 / 0.0
Yield point:	0.70 mm 29.0 kN	1.10 mm 44.9 kN	1.40 mm 58.6 kN
Collapse:	34.9 mm 29.0 kN	34.9 mm 44.9 kN	34.9 mm 58.7 kN
Failure mode:	Bending	Bending	Bending

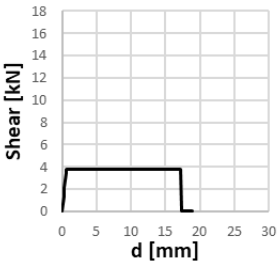
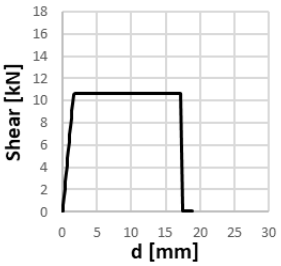
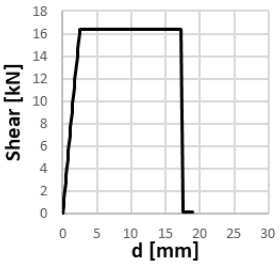
- **Pier st_h3_c_R2**



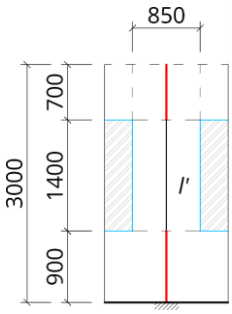
ID:	Pier_st_h3_c_01_R2	Pier_st_h3_c_03_R2	Pier_st_h3_c_05_R2
Masonry properties:	$\tau_{0,eq}$=0.396MPa;$H_{p,eq}$=94.0kN	$\tau_{0,eq}$=0.382MPa;$H_{p,eq}$=122.5kN	$\tau_{0,eq}$=0.365MPa;$H_{p,eq}$=146.7kN
Axial stress:	0.1 MPa	0.3 MPa	0.5 MPa
Capacity curve:			
	d [mm] / *F* [kN] 0.00 / 0.0 0.20 / 12.1 0.70 / 42.3 0.80 / 45.8 34.9 / 45.8 35.0 / 0.0	*d* [mm] / *F* [kN] 0.00 / 0.0 0.20 / 12.1 0.90 / 54.4 1.00 / 59.6 34.9 / 59.7 35.0 / 0.0	*d* [mm] / *F* [kN] 0.00 / 0.0 0.20 / 12.1 1.10 / 66.5 1.20 / 71.4 34.9 / 71.5 35.0 / 0.0
Yield point:	0.80 mm / 45.8 kN	1.00 mm / 59.6 kN	1.20 mm / 71.4 kN
Collapse:	34.9 mm / 45.8 kN	34.9 mm / 59.7 kN	34.9 mm / 71.5 kN
Failure mode:	Bending	Bending	Bending

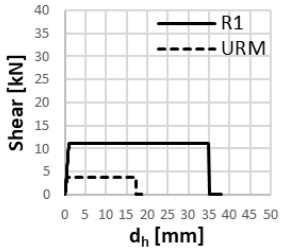
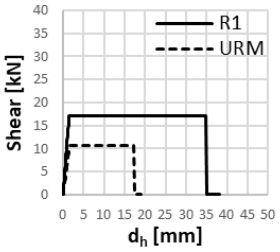
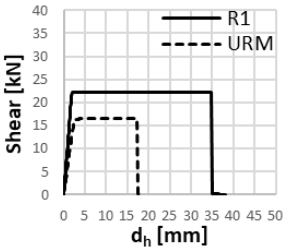
- **Pier ct_h3_c**



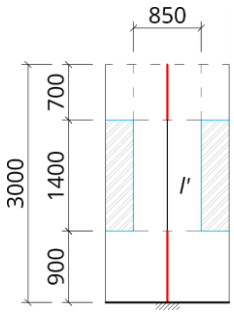
ID:	Pier_ct_h3_c_01	Pier_ct_h3_c_03	Pier_ct_h3_c_05
Axial stress:	0.1 MPa	0.3 MPa	0.5 MPa
Capacity curve:			
	d [mm] *F* [kN] 0.00 0.0 0.01 0.1 0.21 1.4 0.32 2.1 0.43 2.8 0.53 3.5 0.64 3.8 17.17 3.8 17.35 0.0 19.00 0.0	*d* [mm] *F* [kN] 0.00 0.0 0.01 0.1 0.11 0.7 0.32 2.1 0.64 4.2 1.17 7.7 1.71 10.7 17.17 10.7 17.47 0.1 19.00 0.0	*d* [mm] *F* [kN] 0.00 0.0 0.01 0.1 0.43 2.8 1.06 7.0 1.38 9.1 1.81 11.9 2.56 16.4 17.20 16.4 17.59 0.2 19.00 0.0
Yield point:	0.64 mm 3.8 kN	1.71 mm 10.7 kN	2.56 mm 16.4 kN
Collapse:	17.2 mm 3.8 kN	17.2 mm 10.7 kN	17.2 mm 16.4 kN
Failure mode:	Bending	Bending	Bending

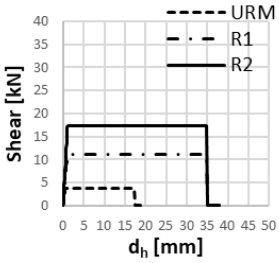
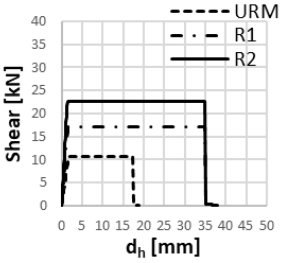
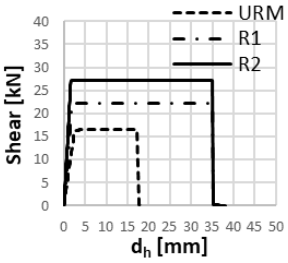
- **Pier ct_h3_c_R1**



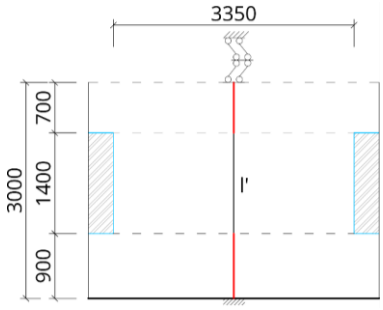
ID:	Pier_ct_h3_c_01_R1	Pier_ct_h3_c_03_R1	Pier_ct_h3_c_05_R1
Masonry properties:	$\tau_{0,eq}$=0.242MPa;$H_{p,eq}$=59.5kN	$\tau_{0,eq}$=0.232MPa;$H_{p,eq}$=92.2kN	$\tau_{0,eq}$=0.221MPa;$H_{p,eq}$=120.4kN
Axial stress:	0.1 MPa	0.3 MPa	0.5 MPa
Capacity curve:			
	d [mm] *F* [kN] 0.00 0.0 0.21 2.4 0.89 10.3 0.96 11.0 34.9 11.0 35.1 0.0	*d* [mm] *F* [kN] 0.00 0.0 0.21 2.4 1.44 16.7 1.51 17.1 34.8 17.1 35.1 0.0	*d* [mm] *F* [kN] 0.00 0.0 0.21 2.4 1.92 22.2 2.00 22.3 34.9 22.3 35.1 0.0
Yield point:	0.96 mm 11.0 kN	1.51 mm 17.1 kN	2.00 mm 22.3 kN
Collapse:	34.9 mm 11.0 kN	34.8 mm 17.1 kN	34.9 mm 22.3 kN
Failure mode:	Bending	Bending	Bending

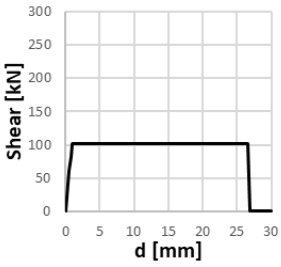
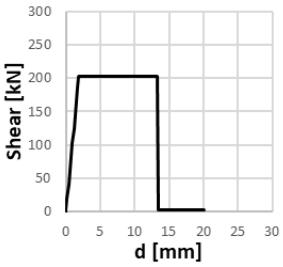
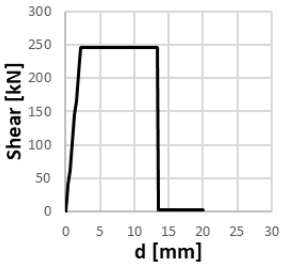
- **Pier ct_h3_c_R2**



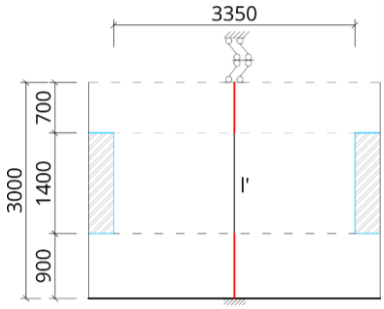
ID:	Pier_ct_h3_c_01_R2	Pier_ct_h3_c_03_R2	Pier_ct_h3_c_05_R2
Masonry properties:	$\tau_{0,eq}$=0.396MPa;$H_{p,eq}$=94.0kN	$\tau_{0,eq}$=0.382MPa;$H_{p,eq}$=122.5kN	$\tau_{0,eq}$=0.365MPa;$H_{p,eq}$=146.7kN
Axial stress:	0.1 MPa	0.3 MPa	0.5 MPa
Capacity curve:			
	d [mm] / *F* [kN] 0.00 / 0.0 0.21 / 3.4 1.03 / 17.2 1.10 / 17.4 34.9 / 17.4 35.1 / 0.0	*d* [mm] / *F* [kN] 0.00 / 0.0 0.21 / 3.4 1.30 / 21.7 1.37 / 22.7 34.9 / 22.7 35.1 / 0.0	*d* [mm] / *F* [kN] 0.00 / 0.0 0.21 / 3.4 1.58 / 26.3 1.65 / 27.2 34.9 / 27.2 35.1 / 0.0
Yield point:	1.10 mm 17.4 kN	1.37 mm 22.7 kN	1.65 mm 27.2 kN
Collapse:	34.9 mm 17.4 kN	34.9 mm 22.7 kN	34.9 mm 27.2 kN
Failure mode:	Bending	Bending	Bending

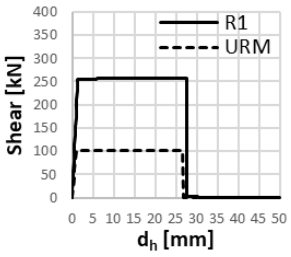
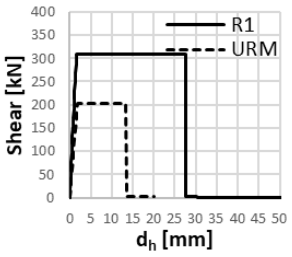
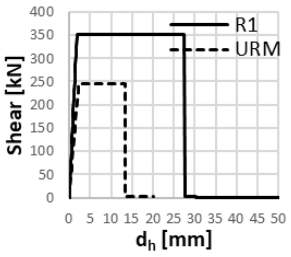
- **Pier st_h3_d**



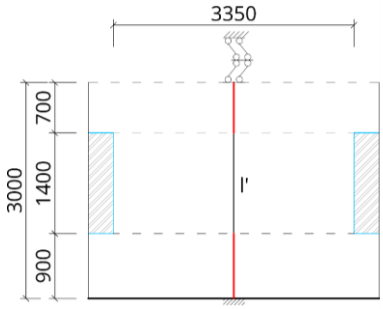
ID:	Pier_st_h3_d_01	Pier_st_h3_d_03	Pier_st_h3_d_05
Axial stress:	0.1 MPa	0.3 MPa	0.5 MPa
Capacity curve:			
	d [mm] *F* [kN] 0.00 0.0 0.02 2.1 0.19 20.8 0.38 41.6 0.75 83.1 0.94 101.3 26.63 101.4 26.81 1.0 30.00 0.0	*d* [mm] *F* [kN] 0.00 0.0 0.02 2.1 0.56 62.3 1.13 124.7 1.69 187.0 1.88 203.0 13.31 203.2 13.50 2.0 20.00 0.0	*d* [mm] *F* [kN] 0.00 0.0 0.02 2.1 0.75 83.1 1.50 166.2 1.88 207.8 2.25 245.2 13.31 245.5 13.50 2.5 20.00 0.0
Yield point:	0.94 mm 101.3 kN	1.88 mm 203.0 kN	2.25 mm 245.2 kN
Collapse:	26.6 mm 101.3 kN	13.3 mm 203.2 kN	13.3 mm 245.2 kN
Failure mode:	Bending	Diagonal cracking	Diagonal cracking

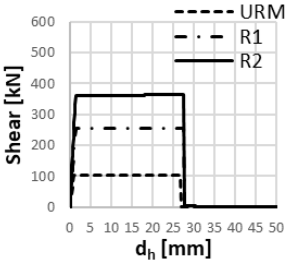
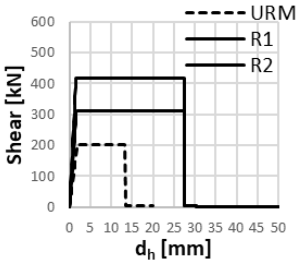
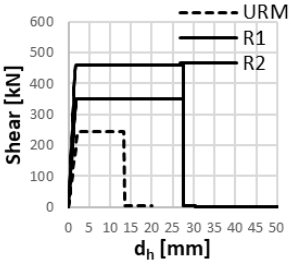
- **Pier st_h3_d_R1**



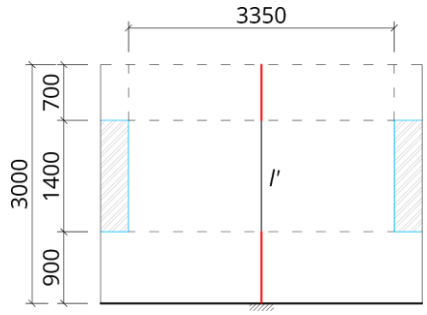
ID:	Pier_st_h3_d_01_R1	Pier_st_h3_d_03_R1	Pier_st_h3_d_05_R1
Masonry properties:	$\tau_{0,eq}$=0.173MPa;$H_{p,eq}$=234.3kN	$\tau_{0,eq}$=0.166MPa;$H_{p,eq}$=363.5kN	$\tau_{0,eq}$=0.159MPa;$H_{p,eq}$=474.5kN
Axial stress:	0.1 MPa	0.3 MPa	0.5 MPa
Capacity curve:			
	d [mm] / *F* [kN] 0.00 / 0.0 0.20 / 38.4 1.30 / 249.5 1.40 / 255.8 27.5 / 256.1 27.6 / 0.0	*d* [mm] / *F* [kN] 0.00 / 0.0 0.20 / 38.4 1.60 / 307.1 1.70 / 309.7 27.5 / 310.0 27.6 / 0.0	*d* [mm] / *F* [kN] 0.00 / 0.0 0.20 / 38.4 1.80 / 345.5 1.90 / 351.5 27.5 / 351.8 27.6 / 0.0
Yield point:	1.40 mm 255.8 kN	1.70 mm 309.7 kN	1.90 mm 351.5 kN
Collapse:	27.5 mm 256.1 kN	27.5 mm 310.0 kN	27.5 mm 351.8 kN
Failure mode:	Diagonal cracking	Diagonal cracking	Diagonal cracking

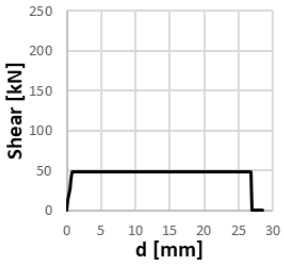
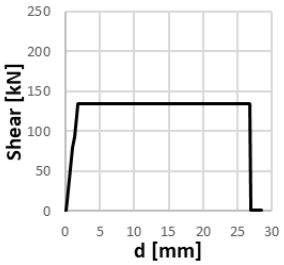
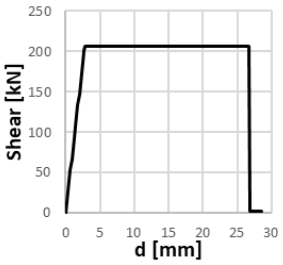
- **Pier st_h3_d_R2**



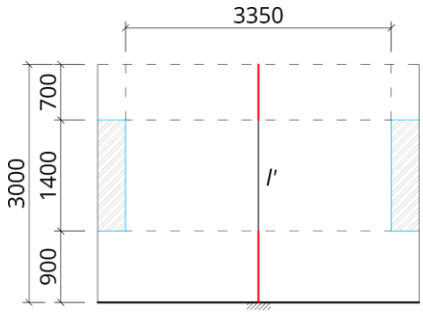
ID:	Pier_st_h3_d_01_R2		Pier_st_h3_d_03_R2		Pier_st_h3_d_05_R2	
Masonry properties:	$\tau_{0,eq}$=0.257MPa;$H_{p,eq}$=370.5kN		$\tau_{0,eq}$=0.246MPa;$H_{p,eq}$=483.0kN		$\tau_{0,eq}$=0.235MPa;$H_{p,eq}$=578.3kN	
Axial stress:	0.1 MPa		0.3 MPa		0.5 MPa	
Capacity curve:						
	d [mm]	*F* [kN]	*d* [mm]	*F* [kN]	*d* [mm]	*F* [kN]
	0.00	0.0	0.00	0.0	0.00	0.0
	0.20	55.4	0.20	55.4	0.20	55.4
	1.30	360.4	1.50	415.8	1.60	443.5
	1.40	362.3	1.60	416.1	1.70	459.1
	27.5	362.7	27.5	416.5	27.5	459.6
	27.6	0.0	27.6	0.0	27.6	0.0
Yield point:	1.40 mm	362.3 kN	1.60 mm	416.1 kN	1.70 mm	459.1 kN
Collapse:	27.5 mm	362.7 kN	27.5 mm	416.5 kN	27.5 mm	459.6 kN
Failure mode:	Diagonal cracking		Diagonal cracking		Diagonal cracking	

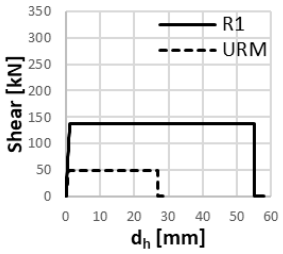
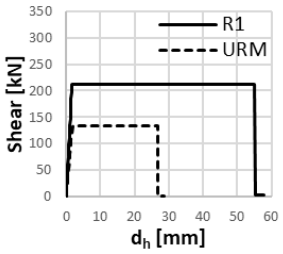
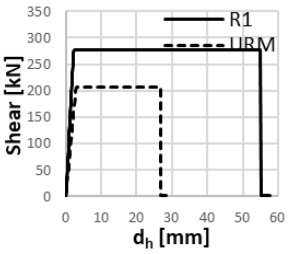
- **Pier ct_h3_d**



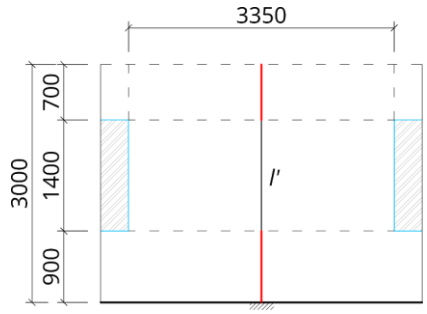
ID:	Pier_ct_h3_d_01	Pier_ct_h3_d_03	Pier_ct_h3_d_05
Axial stress:	0.1 MPa	0.3 MPa	0.5 MPa
Capacity curve:			
	d [mm] / *F* [kN] 0.00 / 0.0 0.02 / 1.3 0.18 / 13.4 0.36 / 26.8 0.54 / 40.1 0.72 / 48.1 26.72 / 48.1 26.89 / 0.5 28.50 / 0.0	*d* [mm] / *F* [kN] 0.00 / 0.0 0.02 / 1.3 0.54 / 40.1 1.09 / 80.3 1.63 / 120.4 1.99 / 134.1 26.74 / 134.2 26.89 / 1.3 28.50 / 0.0	*d* [mm] / *F* [kN] 0.00 / 0.0 0.02 / 1.3 0.72 / 53.5 1.99 / 147.2 2.35 / 173.9 2.90 / 206.5 26.75 / 206.7 26.89 / 2.1 28.50 / 0.0
Yield point:	0.72 mm 48.1 kN	1.99 mm 134.1 kN	2.9 mm 206.5 kN
Collapse:	26.7 mm 48.1 kN	26.7 mm 134.2 kN	26.7 mm 206.7 kN
Failure mode:	Bending	Bending	Bending

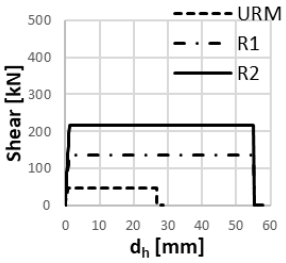
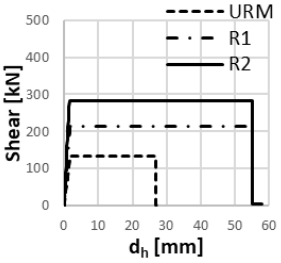
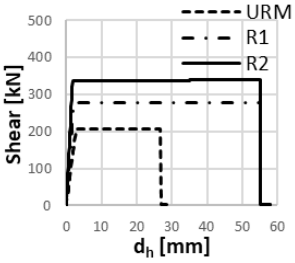
- **Pier ct_h3_d_R1**



ID:	Pier_ct_h3_d_01_R1	Pier_ct_h3_d_03_R1	Pier_ct_h3_d_05_R1
Masonry properties:	$\tau_{0,eq}$=0.173MPa;$H_{p,eq}$=234.3kN	$\tau_{0,eq}$=0.166MPa;$H_{p,eq}$=363.5kN	$\tau_{0,eq}$=0.159MPa;$H_{p,eq}$=474.5kN
Axial stress:	0.1 MPa	0.3 MPa	0.5 MPa
Capacity curve:			
	d [mm] / *F* [kN] 0.00 / 0.0 0.19 / 24.7 1.07 / 136.1 1.17 / 137.0 55.1 / 137.2 55.2 / 0.0	*d* [mm] / *F* [kN] 0.00 / 0.0 0.19 / 24.7 1.66 / 210.3 1.75 / 212.6 55.1 / 212.8 55.2 / 0.0	*d* [mm] / *F* [kN] 0.00 / 0.0 0.19 / 24.7 2.14 / 272.1 2.24 / 277.4 55.1 / 277.7 55.2 / 0.0
Yield point:	1.17 mm / 137.0 kN	1.75 mm / 212.6 kN	2.24 mm / 277.4 kN
Collapse:	55.1 mm / 137.2 kN	55.1 mm / 212.8 kN	55.1 mm / 277.7 kN
Failure mode:	Bending	Bending	Bending

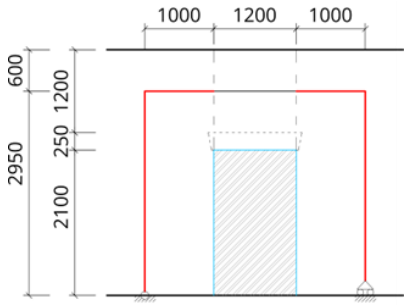
- **Pier ct_h3_d_R2**

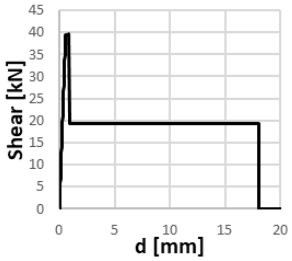
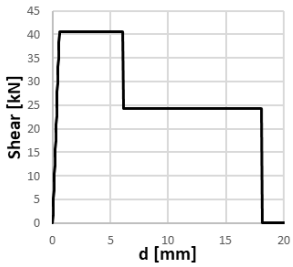


ID:	Pier_ct_h3_d_01_R2		Pier_ct_h3_d_03_R2		Pier_t_h3_d_05_R2	
Masonry properties:	$\tau_{0,eq}$=0.257MPa;$H_{p,eq}$=370.5kN		$\tau_{0,eq}$=0.246MPa;$H_{p,eq}$=483.0kN		$\tau_{0,eq}$=0.235MPa;$H_{p,eq}$=578.3kN	
Axial stress:	0.1 MPa		0.3 MPa		0.5 MPa	
Capacity curve:						
	d [mm]	*F* [kN]	*d* [mm]	*F* [kN]	*d* [mm]	*F* [kN]
	0.00	0.0	0.00	0.0	0.00	0.0
	0.19	35.7	0.19	35.7	0.19	35.7
	1.27	216.6	1.46	268.0	1.75	321.6
	1.36	216.7	1.56	282.4	1.85	338.1
	55.1	216.9	55.1	282.7	55.1	338.4
	55.2	0.0	55.2	0.0	55.2	0.0
Yield point:	1.36 mm	216.7 kN	1.56 mm	282.4 kN	1.85 mm	338.1 kN
Collapse:	55.1 mm	216.9 kN	55.1 mm	282.7 kN	55.1 mm	338.4 kN
Failure mode:	Bending		Bending		Bending	

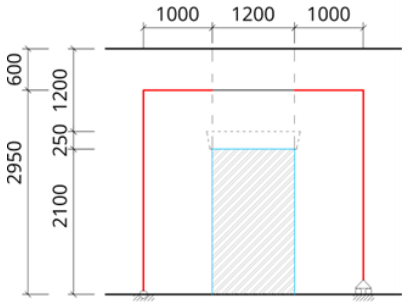
Simplified numerical analyses on spandrel elements

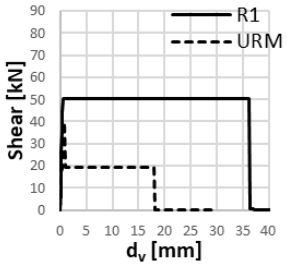
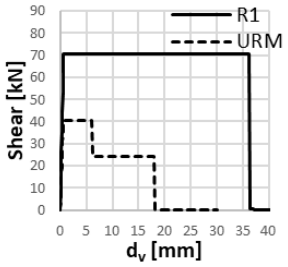
- **Spandrel L1.2_1.0**



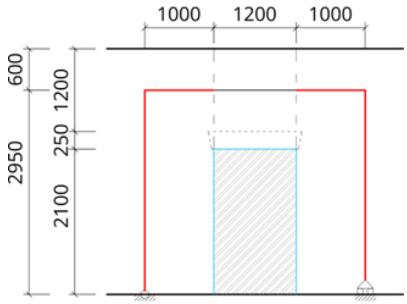
ID:	Spandrel_L1.2_1.0_t0	Spandrel_L1.2_1.0_t1
Masonry properties:	$H_{p,fit}$ = 39.5 kN	
Capacity curve:	 *d* [mm] *F* [kN] 0.00 0.0 0.83 39.5 0.91 19.4 18.0 19.4 18.1 0.0	 *d* [mm] *F* [kN] 0.00 0.0 0.60 40.5 6.07 40.5 6.15 24.3 18.0 24.3 18.1 0.0
Yield point:	0.83 mm 39.5 kN	0.60 mm 40.5 kN
Collapse:	18.0 mm 19.4 kN	18.0 mm 24.3 kN
Failure mode:	Bending	Diagonal cracking

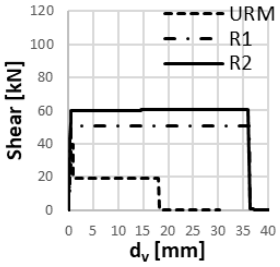
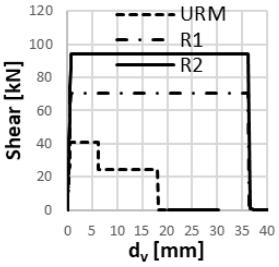
- **Spandrel L1.2_1.0_R1**



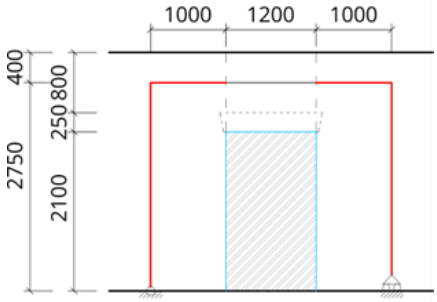
ID:	Spandrel_L1.2_1.0_t0_R1	Spandrel_L1.2_1.0_t1_R1
Masonry properties:	$\tau_{0,eq}$=0.112MPa;$H_{p,eq}$=55.1kN	$\tau_{0,eq}$=0.157MPa;$H_{p,eq}$=97.7kN
Capacity curve:		
	d [mm] *F* [kN] 0.00 0.0 0.08 8.9 0.49 50.4 36.1 50.5 36.3 0.0	*d* [mm] *F* [kN] 0.00 0.0 0.08 8.9 0.64 70.7 36.1 70.7 36.4 0.0
Yield point:	0.49 mm 50.4 kN	0.64 mm 70.7 kN
Collapse:	36.1 mm 50.5 kN	36.1 mm 70.7 kN
Failure mode:	Diagonal cracking	Diagonal cracking

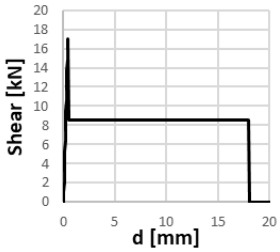
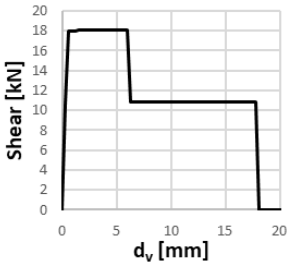
- **Spandrel L1.2_1.0_R2**



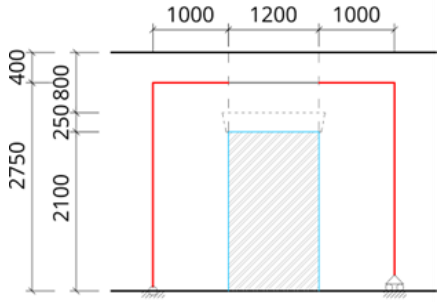
ID:	Spandrel_L1.2_1.0_t0_R2	Spandrel_L1.2_1.0_t1_R2
Masonry properties:	$\tau_{0,eq}$=0.215MPa;$H_{p,eq}$=60.2kN	$\tau_{0,eq}$=0.260MPa;$H_{p,eq}$=94.1kN
Capacity curve:	 *d* [mm] *F* [kN] 0.00 0.0 0.22 32.1 0.46 60.2 36.0 60.3 36.3 0.0	 *d* [mm] *F* [kN] 0.00 0.0 0.22 32.1 0.67 94.1 36.1 94.2 36.6 0.0
Yield point:	0.46 mm 60.2 kN	0.67 mm 94.1 kN
Collapse:	36.0 mm 60.3 kN	36.1 mm 94.2 kN
Failure mode:	Bending	Bending

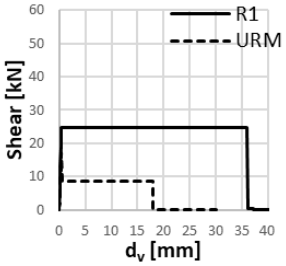
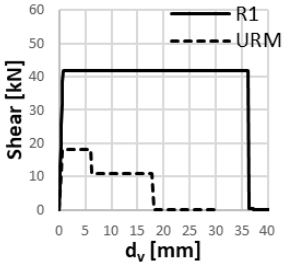
- **Spandrel L1.2_1.5**



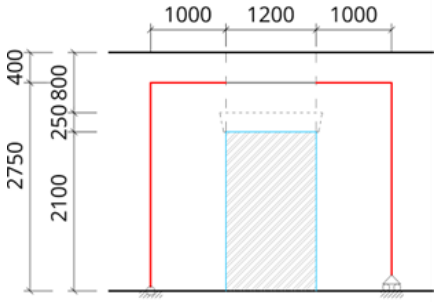
ID:	Spandrel_L1.2_1.5_t0	Spandrel_L1.2_1.5_t1
Masonry properties:	$H_{p,fit}$ = 26.3 kN	
Capacity curve:	 *d* [mm] *F* [kN] 0.00 0.0 0.43 17.0 0.49 17.0 18.0 8.6 18.0 0.0	 *d* [mm] *F* [kN] 0.00 0.0 0.55 18.0 5.98 18.0 6.31 10.8 17.8 10.8 18.1 0.0
Yield point:	0.43 mm 17.0 kN	0.55 mm 18.0 kN
Collapse:	18.0 mm 8.6 kN	17.8 mm 10.8 kN
Failure mode:	Bending	Diagonal cracking

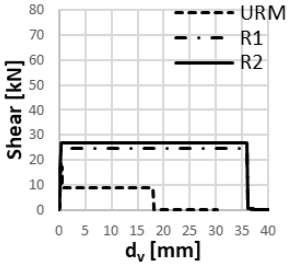
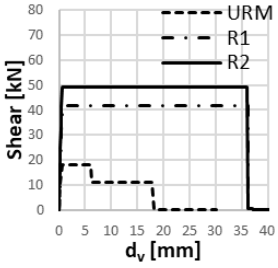
- **Spandrel L1.2_1.5_R1**



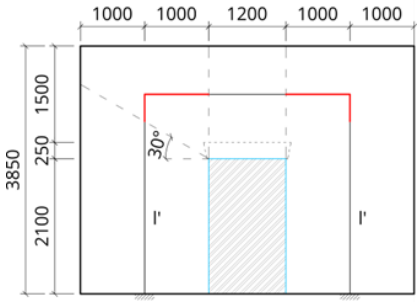
ID:	Spandrel_L1.2_1.5_t0_R1	Spandrel_L1.2_1.5_t1_R1
Masonry properties :	$\tau_{0,eq}$=0.164MPa;$H_{p,eq}$=36.8kN	$\tau_{0,eq}$=0.209MPa;$H_{p,eq}$=76.1kN
Capacity curve:	 *d* [mm] *F* [kN] 0.00 0.0 0.10 6.4 0.39 24.5 36.0 24.6 36.2 0.0	 *d* [mm] *F* [kN] 0.00 0.0 0.10 6.4 0.74 41.8 36.2 41.8 36.3 0.0
Yield point:	0.39 mm 24.5 kN	0.74 mm 41.8 kN
Collapse:	36.0 mm 24.6 kN	36.2 mm 41.8 kN
Failure mode:	Bending	Diagonal cracking

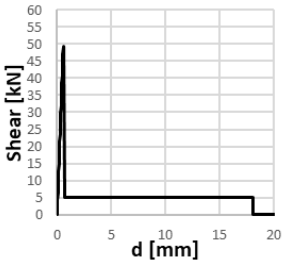
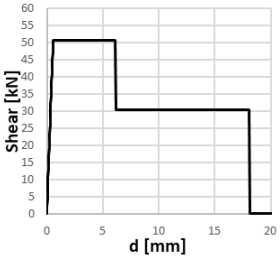
- **Spandrel L1.2_1.5_R2**



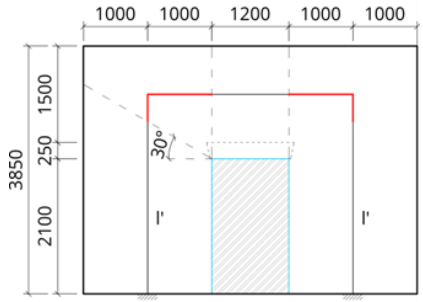
ID:	Spandrel_L1.2_1.5_t0_R2	Spandrel_L1.2_1.5_t1_R2
Masonry properties:	$\tau_{0,eq}$=0.319MPa;$H_{p,eq}$=40.2kN	$\tau_{0,eq}$=0.364MPa;$H_{p,eq}$=73.8kN
Capacity curve:	 *d* [mm] *F* [kN] 0.00 0.0 0.18 16.4 0.38 26.8 36.0 26.8 36.2 0.0	 *d* [mm] *F* [kN] 0.00 0.0 0.18 16.4 0.55 49.2 36.0 49.2 36.3 0.0
Yield point:	0.38 mm 26.8 kN	0.55 mm 49.2 kN
Collapse:	36.0 mm 26.8 kN	36.0 mm 49.2 kN
Failure mode:	Bending	Bending

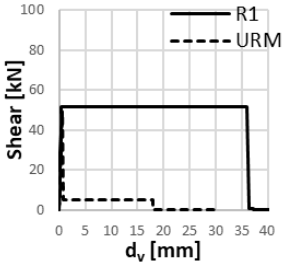
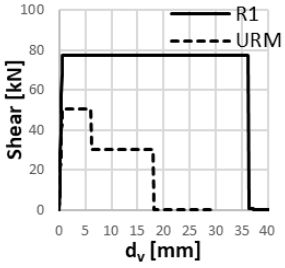
- **Spandrel L1.2_0.8**



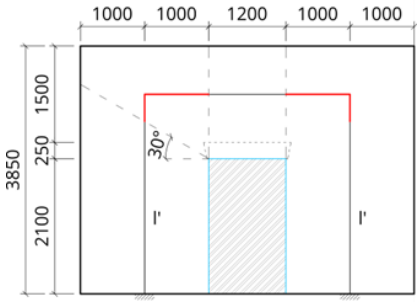
ID:	Spandrel_L1.2_0.8_t0	Spandrel_L1.2_1.5_t1
Masonry properties :	$H_{p,fit}$ = 49.4 kN	
Capacity curve:		
	d [mm] *F* [kN] 0.00 0.0 0.55 49.4 0.71 5.0 18.0 5.0 18.0 0.0	*d* [mm] *F* [kN] 0.00 0.0 0.57 50.6 6.10 50.7 6.19 30.4 18.1 30.4 18.2 0.0
Yield point:	0.55 mm 49.4 kN	0.57 mm 50.6 kN
Collapse:	18.0 mm 5.0 kN	18.0 mm 30.4 kN
Failure mode:	Diagonal cracking	Diagonal cracking

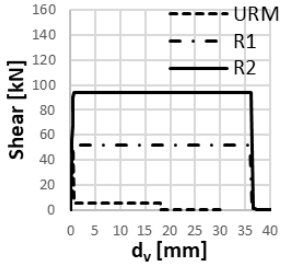
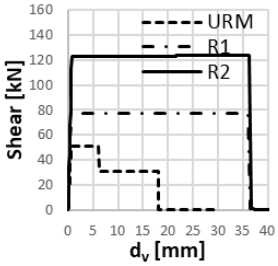
- **Spandrel L1.2_0.8_R1**



ID:	Spandrel_L1.2_0.8_t0_R1	Spandrel_L1.2_0.8_t1_R1
Masonry properties :	$\tau_{0,eq}$=0.092MPa;$H_{p,eq}$=68.9kN	$\tau_{0,eq}$=0.137MPa;$H_{p,eq}$=113.3kN
Capacity curve:		
	d [mm] *F* [kN] 0.00 0.0 0.07 9.7 0.45 51.8 36.1 51.8 36.3 0.0	*d* [mm] *F* [kN] 0.00 0.0 0.07 9.7 0.57 77.1 36.1 77.1 36.4 0.0
Yield point:	0.45 mm 51.8 kN	0.57 mm 77.1 kN
Collapse:	36.1 mm 51.8 kN	36.1 mm 77.1 kN
Failure mode:	Diagonal cracking	Diagonal cracking

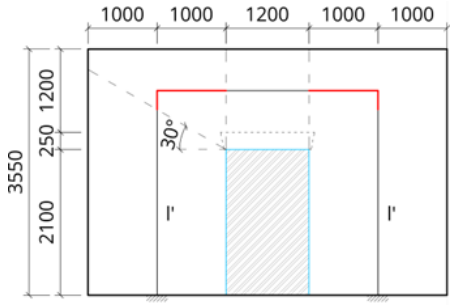
- **Spandrel L1.2_0.8_R2**

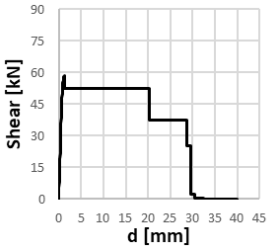
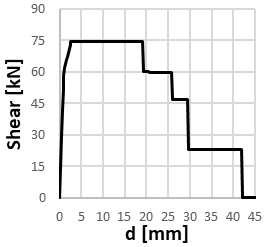


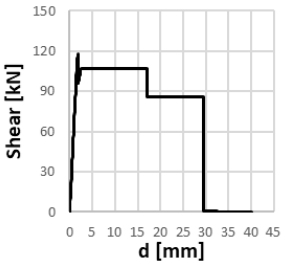
ID:	Spandrel_L1.2_0.8_t0_R2	Spandrel_L1.2_0.8_t1_R2
Masonry properties :	$\tau_{0,eq}$=0.174MPa;$H_{p,eq}$=75.3kN	$\tau_{0,eq}$=0.219MPa;$H_{p,eq}$=108.7kN
Capacity curve:		
	d [mm] *F* [kN] 0.00 0.0 0.20 34.0 0.61 94.1 36.1 94.1 36.5 0.0	*d* [mm] *F* [kN] 0.00 0.0 0.20 34.0 0.72 123.2 36.2 123.3 36.7 0.0
Yield point:	0.61 mm 94.1 kN	0.72 mm 123.2 kN
Collapse:	36.1 mm 94.1 kN	36.2 mm 123.3 kN
Failure mode:	Bending	Diagonal cracking

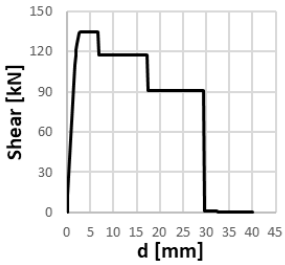
Simplified numerical analyses on portal frames

- **Portal frame L5.2_1.2_1.0**

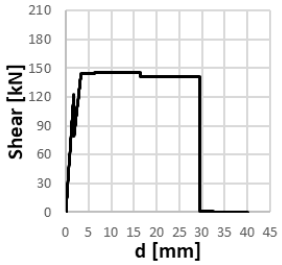
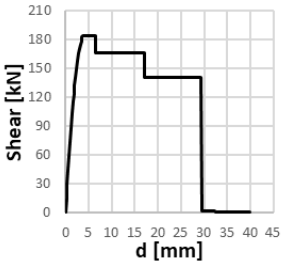


ID:	Portalframe_L5.2_01_1.2_1.0_t0 ($H_{p,fit}$ = 26.5kN)	Portalframe_L5.2_01_1.2_1.0_t1
Axial stress in piers:	0.1 MPa	
Capacity curve:		
	d [mm] *F* [kN] 0.00 0.0 0.20 13.8 0.56 38.7 1.08 58.1 1.36 58.3 1.40 52.3 20.4 52.3 20.4 37.6 28.7 37.4 28.7 25.1 29.5 25.1 29.5 0.0	*d* [mm] *F* [kN] 0.00 0.0 0.20 13.8 0.60 40.2 1.00 55.7 1.20 59.2 2.80 72.8 20.6 72.8 20.8 58.5 28.6 58.3 28.8 46.3 29.4 46.3
Yield point:	0.56 mm 38.7 kN	0.60 mm 40.2 kN
Maximum resistance:	1.36 mm 58.3 kN	20.6 mm 72.8 kN
Collapse:	28.7 mm 37.4 kN	28.6 mm 58.3 kN
Failure mode:	Bending in P1 (base then top), later contemporary bending in S (right) and P2 (base). Failure of P2 (top), then failure of S and finally failure of P1 (base) followed by P2 (base).	Bending in P1 (base then top), then bending in P2 (base), then bending in S (right). Failure of P1 (top then base), later in P2 (base) and finally in S (right).

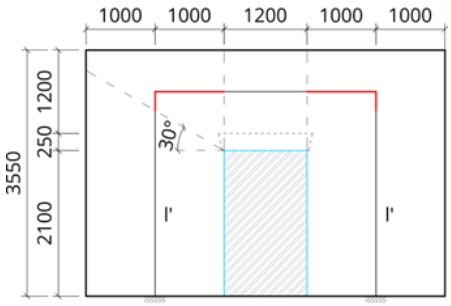
<table>
<tr><td>ID:</td><td>Portalframe_L5.2_03_1.2_1.0_t0
($H_{p,fit}$ = 39.5kN)</td><td>Portalframe_L5.2_03_1.2_1.0_t1</td></tr>
<tr><td>Axial stress in piers:</td><td colspan="2">0.3 MPa</td></tr>
<tr><td>Capacity curve:</td><td> 

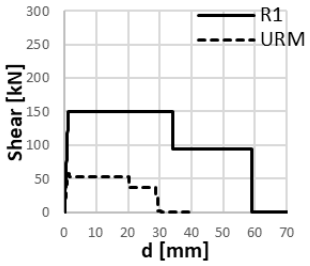
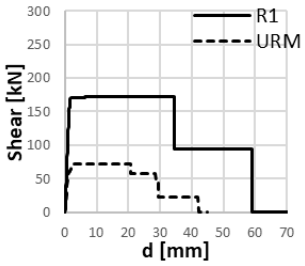
<table>
<tr><th>d [mm]</th><th>F [kN]</th></tr>
<tr><td>0.00</td><td>0.0</td></tr>
<tr><td>0.20</td><td>13.8</td></tr>
<tr><td>1.64</td><td>112.6</td></tr>
<tr><td>1.68</td><td>114.0</td></tr>
<tr><td>1.88</td><td>118.1</td></tr>
<tr><td>2.44</td><td>106.5</td></tr>
<tr><td>17.1</td><td>106.6</td></tr>
<tr><td>17.1</td><td>85.6</td></tr>
<tr><td>29.5</td><td>85.6</td></tr>
<tr><td>29.5</td><td>0.0</td></tr>
</table></td><td> 

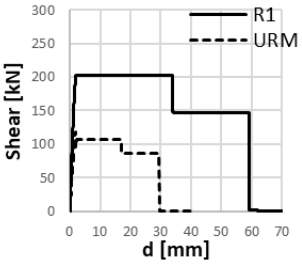
<table>
<tr><th>d [mm]</th><th>F [kN]</th></tr>
<tr><td>0.00</td><td>0.0</td></tr>
<tr><td>0.20</td><td>13.8</td></tr>
<tr><td>1.80</td><td>117.4</td></tr>
<tr><td>2.80</td><td>134.8</td></tr>
<tr><td>6.60</td><td>134.8</td></tr>
<tr><td>6.80</td><td>117.2</td></tr>
<tr><td>17.2</td><td>117.2</td></tr>
<tr><td>17.4</td><td>90.9</td></tr>
<tr><td>29.4</td><td>90.9</td></tr>
<tr><td>29.6</td><td>0.0</td></tr>
</table></td></tr>
<tr><td>Yield point:</td><td>1.64 mm 112.6 kN</td><td>1.80 mm 117.4 kN</td></tr>
<tr><td>Maximum resistance:</td><td>1.88 mm 118.1 kN</td><td>6.60 mm 134.8 kN</td></tr>
<tr><td>Collapse:</td><td>29.5 mm 85.6 kN</td><td>29.4 mm 90.9 kN</td></tr>
<tr><td>Failure mode:</td><td>Bending in P1 (base), then bending in S (left and right) and later in P2 (base). Failure of S and then contemporary failure of P1 and P2 (base).</td><td>Contemporary bending in P1 (base) and diagonal cracking in S and later bending in P2 (base). Failure of S and then contemporary failure of P1 and P2 (base).</td></tr>
</table>

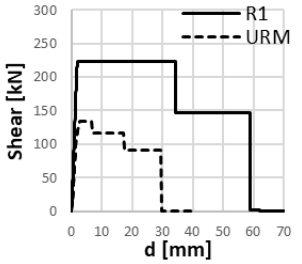
ID:	Portalframe_L5.2_05_1.2_1.0_t0 ($H_{p,fit}$ =52.5kN)	Portalframe_L5.2_05_1.2_1.0_t1
Axial stress in piers:	0.5 MPa	
Capacity curve:	 *d* [mm] *F* [kN] 0.00 0.0 0.20 13.8 1.80 79.5 3.36 143.7 3.44 144.9 16.5 145.0 16.5 140.7 29.5 140.7 29.5 0.0	 *d* [mm] *F* [kN] 0.00 0.0 0.20 13.8 1.80 121.7 3.00 168.6 3.80 183.8 6.60 183.8 6.80 166.2 17.0 166.3 17.2 139.9 29.4 140.0 29.6 0.0
Yield point:	1.80 mm 79.5kN	1.80 mm 121.7 kN
Maximum resistance:	16.5 mm 145.0 kN	6.60 mm 183.8 kN
Collapse:	29.5 mm 140.7 kN	29.4 mm 140.0 kN
Failure mode:	Diagonal cracking in S, then bending in P1 (base) and later P2 (base). Failure of S and then contemporary failure of P1 and P2 (base).	Diagonal cracking in S, then bending in P1 (base) and later P2 (base). Failure of S and then contemporary failure of P1 and P2 (base).

- **Portal frame L5.2_1.2_1.0_R1**

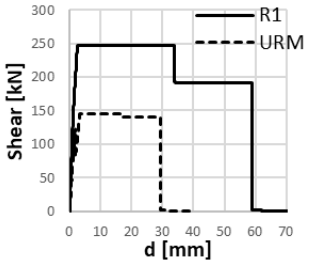


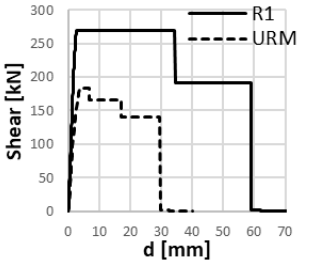
ID:	Portalframe_L5.2_01_1.2_1.0_t0_R1	Portalframe_L5.2_01_1.2_1.0_t1_R1
Masonry properties:	$\tau_{0,eq,P}$=0.237 MPa; $H_{p,eq,P}$=139.9 kN; $\tau_{0,eq,S}$=0.112 MPa; $H_{p,eq,S}$=55.1 kN	$\tau_{0,eq,P}$=0.237 MPa; $H_{p,eq,P}$=139.9 kN; $\tau_{0,eq,S}$=0.157 MPa; $H_{p,eq,S}$=97.7 kN
Axial stress in piers:	0.1 MPa	
Capacity curve:		
	d [mm] *F* [kN] 0.00 0.0 0.20 24.7 1.20 148.0 1.24 149.5 34.0 149.6 34.1 95.4 59.0 94.9 59.1 0.0	*d* [mm] *F* [kN] 0.00 0.0 0.20 24.7 1.24 151.1 1.68 169.8 1.72 171.5 34.4 171.6 34.5 94.8 59.0 94.9 59.1 0.0
Yield point:	1.20 mm 149.5 kN	1.24 mm 151.1 kN
Maximum resistance:	34.0 mm 149.6 kN	34.4 mm 171.6 kN
Collapse:	59.0 mm 94.9 kN	59.0 mm 94.9 kN
Failure mode:	Contemporary bending in P1 and P2 (base) and diagonal cracking in S. Failure of S, then failure of P1 and P2 (base).	Contemporary bending in P1 and P2 (base) and later diagonal cracking in S. Failure of S, then failure of P1 and P2 (base).

<table>
<tr><td>ID:</td><td>Portalframe_L5.2_03_1.2_1.0_t0_R1</td><td>Portalframe_L5.2_03_1.2_1.0_t1_R1</td></tr>
<tr><td>Masonry properties:</td><td>$\tau_{0,eq,P}$=0.227 MPa; $H_{p,eq,P}$=217.0 kN; $\tau_{0,eq,S}$=0.112 MPa; $H_{p,eq,S}$=55.1 kN</td><td>$\tau_{0,eq,P}$=0.227 MPa; $H_{p,eq,P}$=217.0 kN; $\tau_{0,eq,S}$=0.157 MPa; $H_{p,eq,S}$=97.7 kN</td></tr>
<tr><td>Axial stress in piers:</td><td colspan="2">0.3 MPa</td></tr>
<tr><td>Capacity curve:</td><td> 

<table>
<tr><th>d [mm]</th><th>F [kN]</th></tr>
<tr><td>0.00</td><td>0.0</td></tr>
<tr><td>0.20</td><td>24.7</td></tr>
<tr><td>1.24</td><td>151.1</td></tr>
<tr><td>1.92</td><td>201.7</td></tr>
<tr><td>34.00</td><td>201.9</td></tr>
<tr><td>34.1</td><td>147.2</td></tr>
<tr><td>59.00</td><td>147.2</td></tr>
<tr><td>59.1</td><td>0.0</td></tr>
</table></td><td> 

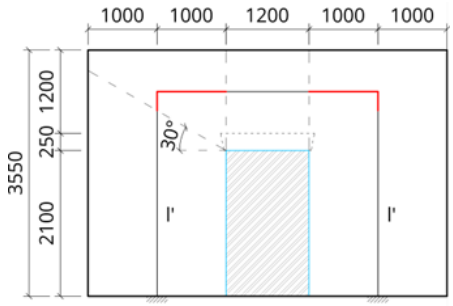
<table>
<tr><th>d [mm]</th><th>F [kN]</th></tr>
<tr><td>0.00</td><td>0.0</td></tr>
<tr><td>0.20</td><td>24.7</td></tr>
<tr><td>1.72</td><td>210.4</td></tr>
<tr><td>1.92</td><td>223.7</td></tr>
<tr><td>34.4</td><td>223.8</td></tr>
<tr><td>34.5</td><td>147.0</td></tr>
<tr><td>59.0</td><td>147.2</td></tr>
<tr><td>59.1</td><td>0.0</td></tr>
</table></td></tr>
<tr><td>Yield point:</td><td>1.24 mm 151.1 kN</td><td>1.72 mm 210.4 kN</td></tr>
<tr><td>Maximum resistance:</td><td>34.0 mm 201.9 kN</td><td>34.4 mm 223.8 kN</td></tr>
<tr><td>Collapse:</td><td>59.0 mm 147.2 kN</td><td>59.0 mm 147.2 kN</td></tr>
<tr><td>Failure mode:</td><td>Diagonal cracking in S, then contemporary bending in P1 and P2 (base). Failure of S, then failure of P1 and P2 (base).</td><td>Diagonal cracking in S, then contemporary bending in P1 and P2 (base). Failure of S, then failure of P1 and P2 (base).</td></tr>
</table>

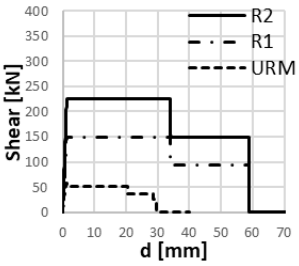
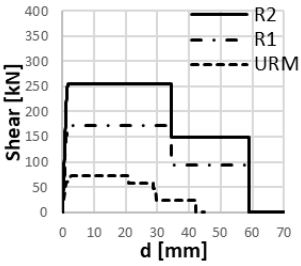
<table>
<tr><td>ID:</td><td>Portalframe_L5.2_05_1.2_1.0_t0_R1</td><td>Portalframe_L5.2_05_1.2_1.0_t1_R1</td></tr>
<tr><td>Masonry properties:</td><td>$\tau_{0,eq,P}$=0.216 MPa; $H_{p,eq,P}$=283.3 kN; $\tau_{0,eq,S}$=0.112 MPa; $H_{p,eq,S}$=55.1 kN</td><td>$\tau_{0,eq,P}$=0.216 MPa; $H_{p,eq,P}$=283.3 kN; $\tau_{0,eq,S}$=0.157 MPa; $H_{p,eq,S}$=97.7 kN</td></tr>
<tr><td>Axial stress in piers:</td><td colspan="2">0.5 MPa</td></tr>
<tr><td>Capacity curve:</td><td> 

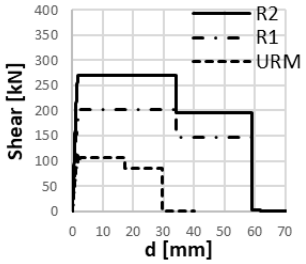
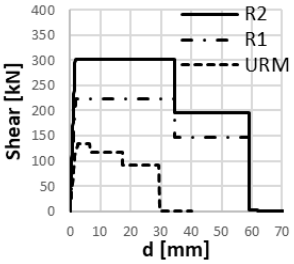
<table>
<tr><th>d [mm]</th><th>F [kN]</th></tr>
<tr><td>0.00</td><td>0.0</td></tr>
<tr><td>0.20</td><td>24.7</td></tr>
<tr><td>1.24</td><td>151.1</td></tr>
<tr><td>2.52</td><td>246.6</td></tr>
<tr><td>33.9</td><td>246.8</td></tr>
<tr><td>34.0</td><td>192.1</td></tr>
<tr><td>59.0</td><td>192.1</td></tr>
<tr><td>59.1</td><td>0.0</td></tr>
</table></td><td> 

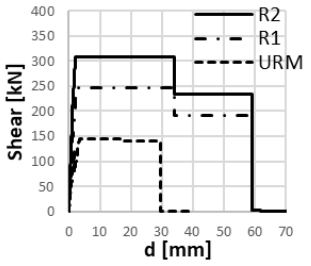
<table>
<tr><th>d [mm]</th><th>F [kN]</th></tr>
<tr><td>0.00</td><td>0.0</td></tr>
<tr><td>0.20</td><td>24.7</td></tr>
<tr><td>1.72</td><td>210.4</td></tr>
<tr><td>2.52</td><td>268.6</td></tr>
<tr><td>34.4</td><td>268.8</td></tr>
<tr><td>34.5</td><td>192.1</td></tr>
<tr><td>59.0</td><td>192.1</td></tr>
<tr><td>59.1</td><td>0.0</td></tr>
</table></td></tr>
<tr><td>Yield point:</td><td>1.24 mm 151.1 kN</td><td>1.72 mm 210.4 kN</td></tr>
<tr><td>Maximum resistance:</td><td>33.9 mm 246.8 kN</td><td>33.9 mm 268.8 kN</td></tr>
<tr><td>Collapse:</td><td>59.0 mm 192.1 kN</td><td>59.0 mm 192.1 kN</td></tr>
<tr><td>Failure mode:</td><td>Diagonal cracking in S, then contemporary bending in P1 and P2 (base). Failure of S, then failure of P1 and P2 (base).</td><td>Diagonal cracking in S, then contemporary bending in P1 and P2 (base). Failure of S, then failure of P1 and P2 (base).</td></tr>
</table>

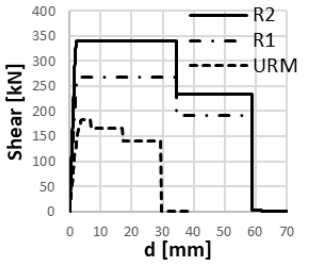
- **Portal frame L5.2_1.2_1.0_R2**



ID:	Portalframe_L5.2_01_1.2_1.0_t0_R2	Portalframe_L5.2_01_1.2_1.0_t1_R2
Masonry properties:	$\tau_{0,eq,P}$=0.386 MPa; $H_{p,eq,P}$=221.2 kN; $\tau_{0,eq,S}$=0.215 MPa; $H_{p,eq,S}$=69.1 kN	$\tau_{0,eq,P}$=0.386 MPa; $H_{p,eq,P}$=221.2 kN; $\tau_{0,eq,S}$=0.260 MPa; $H_{p,eq,S}$=97.7 kN
Axial stress in piers:	0.1 MPa	
Capacity curve:	 *d* [mm] *F* [kN] 0.00 0.0 0.20 35.3 1.20 209.6 1.36 224.8 34.0 225.0 34.1 150.0 59.0 150.0 59.1 0.0	 *d* [mm] *F* [kN] 0.00 0.0 0.20 35.3 1.36 237.1 1.64 253.9 1.68 255.8 34.4 256.0 34.5 150.0 59.0 150.0 59.1 0.0
Yield point:	1.20 mm 209.6 kN	1.36 mm 237.1 kN
Maximum resistance:	34.0 mm 225.0 kN	34.4 mm 256.0 kN
Collapse:	59.0 mm 150.0 kN	59.0 mm 150.0 kN
Failure mode:	Bending in S, then contemporary bending in P1 and P2 (base). Failure of S, then failure of P1 and P2 (base).	Contemporary bending in P1 and P2 (base) and later bending in S. Failure of S, then failure of P1 and P2 (base).

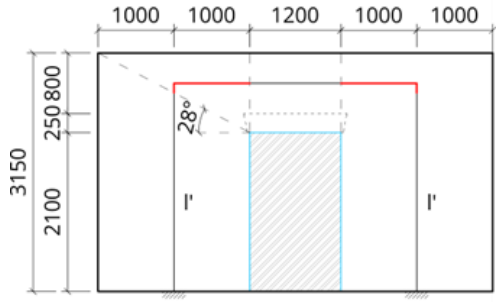
ID:	Portalframe_L5.2_03_1.2_1.0_t0 _R2	Portalframe_L5.2_03_1.2_1.0_t1_ R2
Masonry properties:	$\tau_{0,eq,P}$=0.371 MPa; $H_{p,eq,P}$=288.3 kN; $\tau_{0,eq,S}$=0.215 MPa; $H_{p,eq,S}$=69.1 kN	$\tau_{0,eq,P}$=0.371 MPa; $H_{p,eq,P}$=288.3 kN; $\tau_{0,eq,S}$=0.260 MPa; $H_{p,eq,S}$=97.7 kN
Axial stress in piers:	0.3 MPa	
Capacity curve:	 *d* [mm] *F* [kN] 0.00 0.0 0.20 35.3 1.2 209.6 1.76 270.1 34.0 270.4 34.1 195.5 59.0 195.5 59.1 0.0	 *d* [mm] *F* [kN] 0.00 0.0 0.20 35.3 1.68 294.6 1.76 301.3 34.4 301.5 34.2 195.5 59.0 195.5 59.1 0.0
Yield point:	1.20 mm 270.1 kN	1.68 mm 301.3 kN
Maximum resistance:	34.0 mm 270.4 kN	34.4 mm 301.5 kN
Collapse:	59.0 mm 195.5 kN	59.0 mm 195.5 kN
Failure mode:	Bending in S, then contemporary bending in P1 and P2 (base). Failure of S, then failure of P1 and P2 (base).	Bending in S, then contemporary bending in P1 and P2 (base). Failure of S, then failure of P1 and P2 (base).).

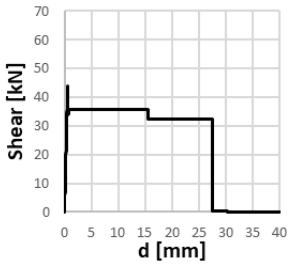
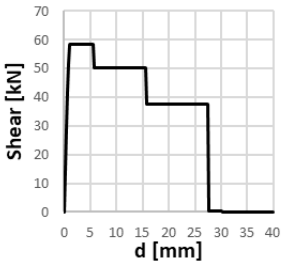
<table>
<tr><td>ID:</td><td>Portalframe_L5.2_05_1.2_1.0_t0_R2</td><td>Portalframe_L5.2_05_1.2_1.0_t1_R2</td></tr>
<tr><td>Masonry properties:</td><td>$\tau_{0,eq,P}$=0.355 MPa; $H_{p,eq,P}$=345.2 kN; $\tau_{0,eq,S}$=0.215 MPa; $H_{p,eq,S}$=69.1 kN</td><td>$\tau_{0,eq,P}$=0.355 MPa; $H_{p,eq,P}$=345.2 kN; $\tau_{0,eq,S}$=0.260 MPa; $H_{p,eq,S}$=97.7 kN</td></tr>
<tr><td>Axial stress in piers:</td><td colspan="2">0.5 MPa</td></tr>
<tr><td>Capacity curve:</td><td> 

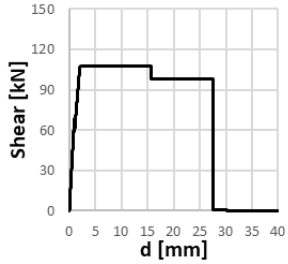
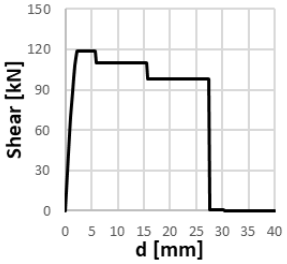
<table>
<tr><th>d [mm]</th><th>F [kN]</th></tr>
<tr><td>0.00</td><td>0.0</td></tr>
<tr><td>0.20</td><td>35.3</td></tr>
<tr><td>1.2</td><td>209.6</td></tr>
<tr><td>2.12</td><td>308.8</td></tr>
<tr><td>33.9</td><td>309.0</td></tr>
<tr><td>34.0</td><td>234.7</td></tr>
<tr><td>59.0</td><td>234.1</td></tr>
<tr><td>59.1</td><td>0.0</td></tr>
</table></td><td> 

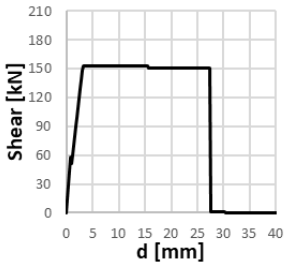
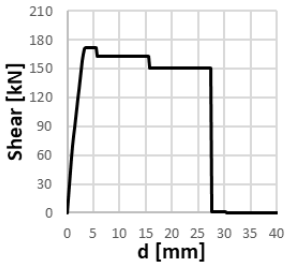
<table>
<tr><th>d [mm]</th><th>F [kN]</th></tr>
<tr><td>0.00</td><td>0.0</td></tr>
<tr><td>0.20</td><td>35.3</td></tr>
<tr><td>1.68</td><td>294.6</td></tr>
<tr><td>2.12</td><td>339.8</td></tr>
<tr><td>34.4</td><td>340.0</td></tr>
<tr><td>34.5</td><td>233.8</td></tr>
<tr><td>59.0</td><td>234.1</td></tr>
<tr><td>59.1</td><td>0.0</td></tr>
</table></td></tr>
<tr><td>Yield point:</td><td>1.20 mm 209.3 kN</td><td>1.68 mm 339.8 kN</td></tr>
<tr><td>Maximum resistance:</td><td>33.9 mm 309.0 kN</td><td>34.4 mm 340.0 kN</td></tr>
<tr><td>Collapse:</td><td>59.0 mm 234.1 kN</td><td>59.0 mm 234.1 kN</td></tr>
<tr><td>Failure mode:</td><td>Bending in S, then contemporary bending in P1 and P2 (base). Failure of S, then failure of P1 and P2 (base).</td><td>Bending in S, then contemporary bending in P1 and P2 (base). Failure of S, then failure of P1 and P2 (base).</td></tr>
</table>

- **Portal frame L5.2_1.2_1.5**

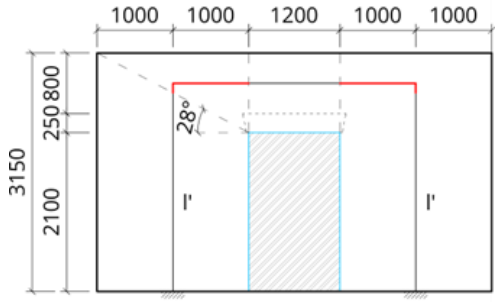


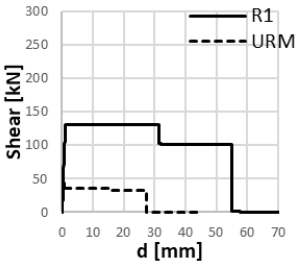
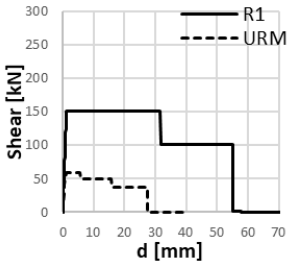
ID:	Portalframe_L5.2_01_1.2_1.5_t0 ($H_{p,fit}$ = 17.7kN)	Portalframe_L5.2_01_1.2_1.5_t1
Axial stress in piers:	0.1 MPa	
Capacity curve:		
	d [mm] *F* [kN] 0.00 0.0 0.20 14.5 0.66 43.8 0.76 35.8 15.5 35.8 15.6 32.4 27.5 32.4 27.5 0.0	*d* [mm] *F* [kN] 0.00 0.0 0.20 14.5 0.60 42.1 1.00 58.6 5.60 58.6 5.80 50.2 15.6 50.2 15.8 37.7 27.4 37.7 27.6 0.0
Yield point:	0.56 mm 40.5 kN	0.60 mm 42.1 kN
Maximum resistance:	0.66 mm 43.8 kN	5.60 mm 58.6 kN
Collapse:	27.5 mm 32.4 kN	27.4 mm 37.7 kN
Failure mode:	Contemporary bending in S and bending in P1 (base) and later in P2 (base). Failure of S and then contemporary failure of P1 and P2 (base).	Bending in P1 (base), then contemporary diagonal cracking in S and P2 (base). Failure of S and then contemporary failure of P1 and P2 (base).

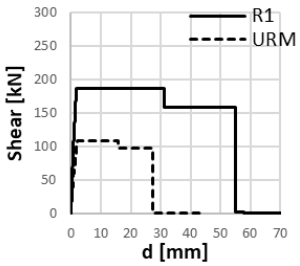
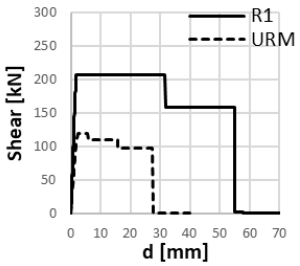
ID:	Portalframe_L5.2_03_1.2_1.5_t0 ($H_{p,fit}$ = 26.3kN)	Portalframe_L5.2_03_1.2_1.5_t1
Axial stress in piers:	0.3 MPa	
Capacity curve:	 *d* [mm] *F* [kN] 0.00 0.0 0.20 14.5 0.90 64.7 1.90 103.0 2.12 107.9 15.7 107.9 15.7 97.9 27.5 98.0 27.5 0.0	 *d* [mm] *F* [kN] 0.00 0.0 0.20 14.5 1.00 70.2 1.80 108.8 2.40 118.7 5.60 118.8 5.80 110.4 15.6 110.4 15.8 97.8 27.4 97.9 27.6 0.0
Yield point:	0.90 mm 64.7 kN	1.00 mm 70.2 kN
Maximum resistance:	15.7 mm 107.9 kN	5.60 mm 118.7 kN
Collapse:	27.5 mm 98.0 kN	27.4 mm 97.9 kN
Failure mode:	Bending in S, then bending in P1 and later in P2 (base). Failure of S and then contemporary failure of P1 and P2 (base).	Diagonal cracking in S, then bending in P1 (base) and later in P2 (base). Failure of S and then contemporary failure of P1 and P2 (base).

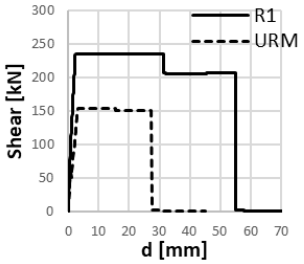
ID:	Portalframe_L5.2_05_1.2_1.5_t0 ($H_{p,fit}$ = 35.0kN)	Portalframe_L5.2_05_1.2_1.5_t1
Axial stress in piers:	0.5 MPa	
Capacity curve:	 *d* [mm] *F* [kN] 0.00 0.0 0.20 14.5 1.00 51.0 3.20 152.9 15.4 153.0 15.6 150.9 27.4 151.0 27.6 0.0	 *d* [mm] *F* [kN] 0.00 0.0 0.20 14.5 1.00 70.2 3.00 165.5 3.40 171.6 5.60 171.6 5.80 163.2 15.6 163.3 15.8 150.7 27.4 150.8 27.6 0.0
Yield point:	1.00 mm 51.0 kN	1.00 mm 70.2 kN
Maximum resistance:	15.4 mm 153.0 kN	5.60 mm 171.6 kN
Collapse:	27.4 mm 151.0 kN	27.4 mm 150.8 kN
Failure mode:	Diagonal cracking S, then bending in P1 (base) and in P2 (base). Failure of S and then contemporary failure of P1 and P2 (base).	Diagonal cracking in S, then bending in P1 (base) and later in P2 (base). Failure of S and then of P1 and P2.

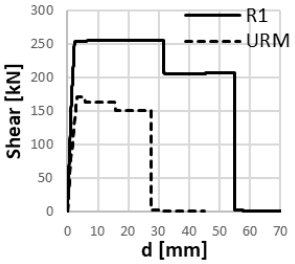
- **Portal frame L5.2_1.2_1.5_R1**



ID:	Portalframe_L5.2_01_1.2_1.5_t0_R1	Portalframe_L5.2_01_1.2_1.5_t1_R1
Masonry properties:	$\tau_{0,eq,P}$=0.230 MPa; $H_{p,eq,P}$=139.9 kN; $\tau_{0,eq,S}$=0.164 MPa; $H_{p,eq,S}$=36.8 kN	$\tau_{0,eq,P}$=0.230 MPa; $H_{p,eq,P}$=139.9 kN; $\tau_{0,eq,S}$=0.209 MPa; $H_{p,eq,S}$=76.1 kN
Axial stress in piers:	0.1 MPa	
Capacity curve:		
	d [mm] *F* [kN] 0.00 0.0 0.20 25.9 0.72 92.4 1.16 130.3 31.3 130.3 31.4 101.8 54.9 101.8 55.0 0.0	*d* [mm] *F* [kN] 0.00 0.0 0.20 25.9 1.16 148.9 1.20 150.4 31.6 150.5 31.7 101.8 54.9 101.8 55.0 0.0
Yield point:	0.72 mm 92.4 kN	1.16 mm 148.9 kN
Maximum resistance:	31.3 mm 130.3 kN	31.6 mm 150.5 kN
Collapse:	54.9 mm 101.8 kN	54.9 mm 101.8 kN
Failure mode:	Bending in S and later contemporary bending in P1 and P2 (base). Failure of S, then failure of P1 and P2 (base).	Contemporary bending in P1 and P2 (base) and diagonal cracking in S. Failure of S, then failure of P1 and P2 (base).

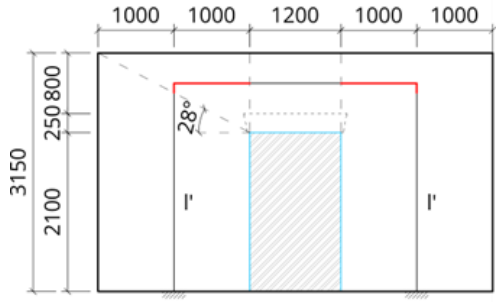
ID:	Portalframe_L5.2_03_1.2_1.5_t0 _R1	Portalframe_L5.2_03_1.2_1.5_t1_ R1
Masonry properties:	$\tau_{0,eq,P}$=0.220 MPa; $H_{p,eq,P}$=217.0 kN; $\tau_{0,eq,S}$=0.164 MPa; $H_{p,eq,S}$=36.8 kN	$\tau_{0,eq,P}$=0.220 MPa; $H_{p,eq,P}$=217.0 kN; $\tau_{0,eq,S}$=0.209 MPa; $H_{p,eq,S}$=76.1 kN
Axial stress in piers:	0.3 MPa	
Capacity curve:		
	d [mm] *F* [kN] 0.00 0.0 0.20 25.9 0.72 92.4 1.80 186.3 31.3 186.4 31.4 157.9 54.9 157.9 55.0 0.0	*d* [mm] *F* [kN] 0.00 0.0 0.20 25.9 1.20 155.0 1.80 206.4 31.6 206.5 31.7 157.9 54.9 157.9 55.0 0.0
Yield point:	0.72 mm 92.4 kN	1.20 mm 155.0 kN
Maximum resistance:	31.3 mm 186.4 kN	31.6 mm 206.5 kN
Collapse:	54.9 mm 157.9 kN	54.9 mm 157.9 kN
Failure mode:	Bending in S and later contemporary bending in P1 and P2 (base). Failure of S, then failure of P1 and P2 (base).	Diagonal cracking in S, then contemporary bending in P1 and P2 (base). Failure of S, then failure of P1 and P2 (base).

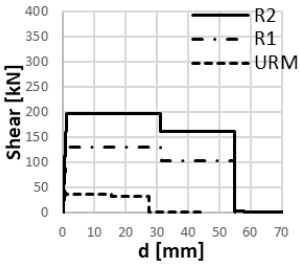
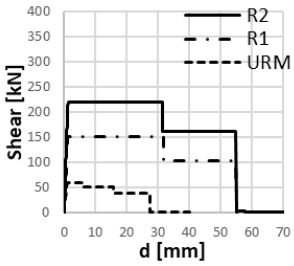
<table>
<tr><td>ID:</td><td>Portalframe_L5.2_05_1.2_1.5_t0_R1</td><td>Portalframe_L5.2_05_1.2_1.5_t1_R1</td></tr>
<tr><td>Masonry properties:</td><td>$\tau_{0,eq,P}$=0.210 MPa; $H_{p,eq,P}$=283.0 kN; $\tau_{0,eq,S}$=0.164 MPa; $H_{p,eq,S}$=36.8 kN</td><td>$\tau_{0,eq,P}$=0.210 MPa; $H_{p,eq,P}$=283.0 kN; $\tau_{0,eq,S}$=0.209 MPa; $H_{p,eq,S}$=76.1 kN</td></tr>
<tr><td>Axial stress in piers:</td><td colspan="2">0.5 MPa</td></tr>
<tr><td>Capacity curve:</td><td> 

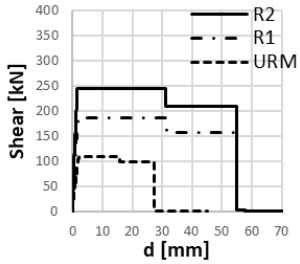
<table>
<tr><th>d [mm]</th><th>F [kN]</th></tr>
<tr><td>0.00</td><td>0.0</td></tr>
<tr><td>0.20</td><td>25.9</td></tr>
<tr><td>0.72</td><td>92.4</td></tr>
<tr><td>2.36</td><td>234.4</td></tr>
<tr><td>31.3</td><td>234.6</td></tr>
<tr><td>31.4</td><td>206.1</td></tr>
<tr><td>54.9</td><td>206.1</td></tr>
<tr><td>55.0</td><td>0.0</td></tr>
</table></td><td> 

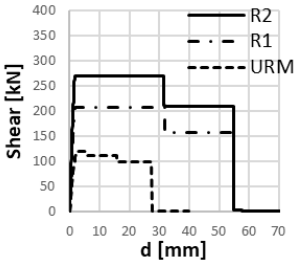
<table>
<tr><th>d [mm]</th><th>F [kN]</th></tr>
<tr><td>0.00</td><td>0.0</td></tr>
<tr><td>0.20</td><td>25.9</td></tr>
<tr><td>1.20</td><td>155.0</td></tr>
<tr><td>2.36</td><td>254.5</td></tr>
<tr><td>31.6</td><td>254.7</td></tr>
<tr><td>31.7</td><td>206.1</td></tr>
<tr><td>59.0</td><td>206.1</td></tr>
<tr><td>59.1</td><td>0.0</td></tr>
</table></td></tr>
<tr><td>Yield point:</td><td>0.72 mm 92.4 kN</td><td>1.20 mm 155.0 kN</td></tr>
<tr><td>Maximum resistance:</td><td>31.3 mm 234.6 kN</td><td>31.6 mm 254.7 kN</td></tr>
<tr><td>Collapse:</td><td>54.9 mm 206.1 kN</td><td>54.9 mm 206.1 kN</td></tr>
<tr><td>Failure mode:</td><td>Bending in S and later contemporary bending in P1 and P2 (base). Failure of S, then failure of P1 and P2 (base).</td><td>Diagonal cracking in S, then contemporary bending in P1 and P2 (base). Failure of S, then failure of P1 and P2 (base).</td></tr>
</table>

- **Portal frame L5.2_1.2_1.5_R2**

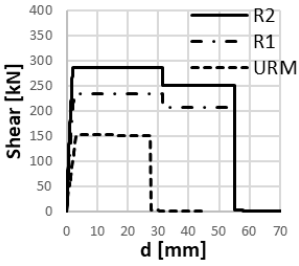
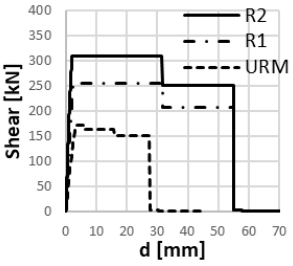


ID:	Portalframe_L5.2_01_1.2_1.5_t0_R2	Portalframe_L5.2_01_1.2_1.5_t1_R2
Masonry properties:	$\tau_{0,eq,P}$=0.372 MPa; $H_{p,eq,P}$=221.2 kN; $\tau_{0,eq,S}$=0.319 MPa; $H_{p,eq,S}$=46.1 kN	$\tau_{0,eq,P}$=0.372 MPa; $H_{p,eq,P}$=221.2 kN; $\tau_{0,eq,S}$=0.364 MPa; $H_{p,eq,S}$=76.1 kN
Axial stress in piers:	0.1 MPa	
Capacity curve:		
	d [mm] *F* [kN] 0.00 0.0 0.20 37.1 0.64 117.7 1.28 196.5 31.2 196.7 31.3 160.9 54.9 160.9 55.0 0.0	*d* [mm] *F* [kN] 0.00 0.0 0.20 37.1 1.04 192.1 1.28 219.8 31.5 219.9 31.6 160.9 54.9 160.9 55.0 0.0
Yield point:	0.64 mm 117.7 kN	1.04 mm 192.1 kN
Maximum resistance:	31.2 mm 196.7 kN	31.5 mm 219.9 kN
Collapse:	54.9 mm 160.9 kN	54.9 mm 160.9 kN
Failure mode:	Bending in S and later contemporary bending in P1 and P2 (base). Failure of S, then failure of P1 and P2 (base).	Contemporary bending in P1 and P2 (base) and diagonal cracking in S. Failure of S, then failure of P1 and P2 (base).

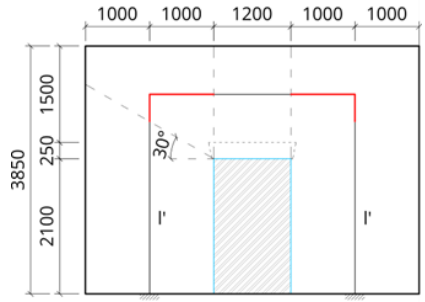
<table>
<tr><td>ID:</td><td>Portalframe_L5.2_03_1.2_1.5_t0 _R2</td><td>Portalframe_L5.2_03_1.2_1.5_t1_ R2</td></tr>
<tr><td>Masonry properties:</td><td>$\tau_{0,eq,P}$=0.357 MPa; $H_{p,eq,P}$=288.3 kN; $\tau_{0,eq,S}$=0.319 MPa; $H_{p,eq,S}$=46.1 kN</td><td>$\tau_{0,eq,P}$=0.357 MPa; $H_{p,eq,P}$=288.3 kN; $\tau_{0,eq,S}$=0.364 MPa; $H_{p,eq,S}$=76.1 kN</td></tr>
<tr><td>Axial stress in piers:</td><td colspan="2">0.3 MPa</td></tr>
<tr><td>Capacity curve:</td><td> 

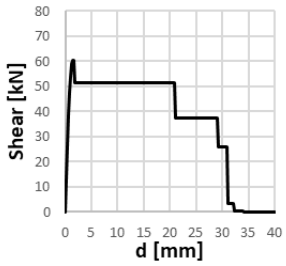
<table>
<tr><th>d [mm]</th><th>F [kN]</th></tr>
<tr><td>0.00</td><td>0.0</td></tr>
<tr><td>0.20</td><td>37.1</td></tr>
<tr><td>0.64</td><td>117.7</td></tr>
<tr><td>1.68</td><td>245.3</td></tr>
<tr><td>31.2</td><td>245.4</td></tr>
<tr><td>31.3</td><td>209.7</td></tr>
<tr><td>54.9</td><td>209.7</td></tr>
<tr><td>55.0</td><td>0.0</td></tr>
</table></td><td> 

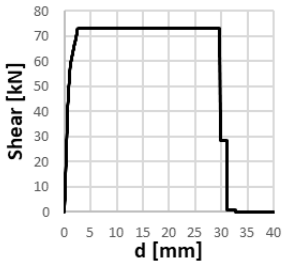
<table>
<tr><th>d [mm]</th><th>F [kN]</th></tr>
<tr><td>0.00</td><td>0.0</td></tr>
<tr><td>0.20</td><td>37.1</td></tr>
<tr><td>1.04</td><td>192.1</td></tr>
<tr><td>1.68</td><td>268.5</td></tr>
<tr><td>31.5</td><td>268.7</td></tr>
<tr><td>31.6</td><td>209.7</td></tr>
<tr><td>54.9</td><td>209.7</td></tr>
<tr><td>55.0</td><td>0.0</td></tr>
</table></td></tr>
<tr><td>Yield point:</td><td>0.64 mm 117.7 kN</td><td>1.04 mm 192.1 kN</td></tr>
<tr><td>Maximum resistance:</td><td>31.2 mm 245.4 kN</td><td>31.5 mm 268.7 kN</td></tr>
<tr><td>Collapse:</td><td>54.9 mm 209.7 kN</td><td>54.9 mm 209.7 kN</td></tr>
<tr><td>Failure mode:</td><td>Bending in S and later contemporary bending in P1 and P2 (base). Failure of S, then failure of P1 and P2 (base).</td><td>Diagonal cracking in S, then contemporary bending in P1 and P2 (base). Failure of S, then failure of P1 and P2 (base).</td></tr>
</table>

ID:	Portalframe_L5.2_05_1.2_1.5_t0_R2	Portalframe_L5.2_05_1.2_1.5_t1_R2
Masonry properties:	$\tau_{0,eq,P}$=0.341 MPa; $H_{p,eq,P}$=345.2 kN; $\tau_{0,eq,S}$=0.319 MPa; $H_{p,eq,S}$=46.1 kN	$\tau_{0,eq,P}$=0.341 MPa; $H_{p,eq,P}$=345.2 kN; $\tau_{0,eq,S}$=0.364 MPa; $H_{p,eq,S}$=76.1 kN
Axial stress in piers:	0.5 MPa	
Capacity curve:		
	d [mm] *F* [kN] 0.00 0.0 0.20 37.1 0.64 117.7 2.00 286.6 31.2 286.8 31.3 251.1 54.9 251.1 55.0 0.0	*d* [mm] *F* [kN] 0.00 0.0 0.20 37.1 1.04 192.1 2.00 309.9 31.5 310.1 31.6 251.1 54.9 251.1 55.0 0.0
Yield point:	0.64 mm 117.7 kN	1.04 mm 192.1 kN
Maximum resistance:	31.2 mm 286.8 kN	31.5 mm 310.1 kN
Collapse:	54.9 mm 251.1 kN	54.9 mm 251.1 kN
Failure mode:	Bending in S and later contemporary bending in P1 and P2 (base). Failure of S, then failure of P1 and P2 (base).	Diagonal cracking in S, then contemporary bending in P1 and P2 (base). Failure of S, then failure of P1 and P2 (base).

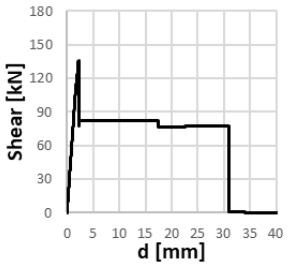
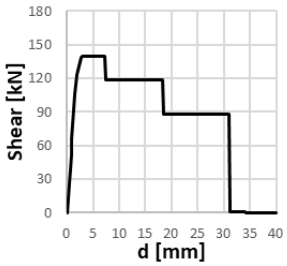
- **Portal frame L5.2_1.2_0.8**



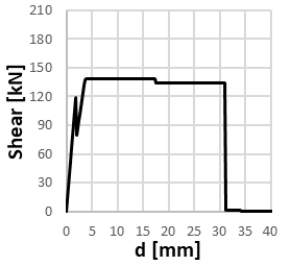
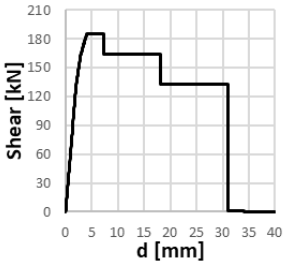
<table>
<tr><td>ID:</td><td>Portalframe_L5.2_01_1.2_0.8_t0
($H_{p,fit}$ = 33.1kN)</td><td>Portalframe_L5.2_01_1.2_0.8_t1</td></tr>
<tr><td>Axial stress in piers:</td><td colspan="2">0.1 MPa</td></tr>
<tr><td>Capacity curve:</td><td> 

<table>
<tr><th>d [mm]</th><th>F [kN]</th></tr>
<tr><td>0.00</td><td>0.0</td></tr>
<tr><td>0.20</td><td>13.2</td></tr>
<tr><td>0.60</td><td>38.6</td></tr>
<tr><td>1.20</td><td>59.0</td></tr>
<tr><td>1.40</td><td>60.3</td></tr>
<tr><td>1.60</td><td>60.3</td></tr>
<tr><td>1.80</td><td>51.6</td></tr>
<tr><td>20.8</td><td>51.6</td></tr>
<tr><td>21.0</td><td>37.5</td></tr>
<tr><td>29.0</td><td>37.4</td></tr>
<tr><td>29.2</td><td>25.9</td></tr>
</table></td><td> 

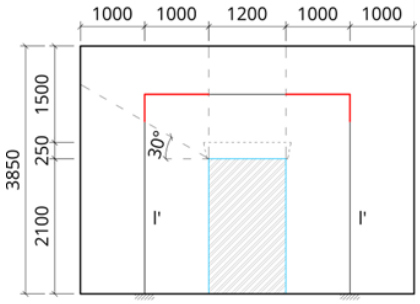
<table>
<tr><th>d [mm]</th><th>F [kN]</th></tr>
<tr><td>0.00</td><td>0.0</td></tr>
<tr><td>0.20</td><td>13.2</td></tr>
<tr><td>0.60</td><td>38.8</td></tr>
<tr><td>0.84</td><td>49.0</td></tr>
<tr><td>1.16</td><td>58.7</td></tr>
<tr><td>2.56</td><td>73.0</td></tr>
<tr><td>29.7</td><td>73.1</td></tr>
<tr><td>29.7</td><td>61.6</td></tr>
<tr><td>29.8</td><td>28.4</td></tr>
<tr><td>31.0</td><td>28.4</td></tr>
<tr><td>31.0</td><td>0.0</td></tr>
</table></td></tr>
<tr><td>Yield point:</td><td>0.60 mm 38.6 kN</td><td>0.60 mm 38.8 kN</td></tr>
<tr><td>Maximum resistance:</td><td>1.60 mm 60.3 kN</td><td>29.7 mm 73.1 kN</td></tr>
<tr><td>Collapse:</td><td>29.0 mm 37.4 kN</td><td>31.0 mm 28.4 kN</td></tr>
<tr><td>Failure mode:</td><td>Bending in P1 base then top. Then contemporary bending in S (right) and P2 (base). Failure in P1 (top), then in P1 (base) and later is S1 (right) and finally in P2 (base).</td><td>Bending in P1 base then top and later in P2 base and then in P2 top. Contemporary failure of P1 (base and top) and P2 (base and top).</td></tr>
</table>

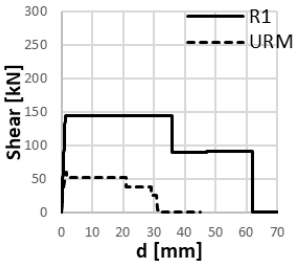
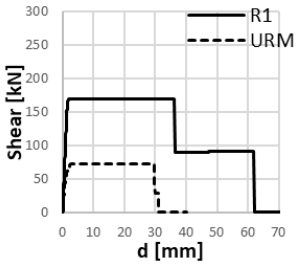
ID:	Portalframe_L5.2_03_1.2_0.8_t0 ($H_{p,fit}$ = 49.4kN)	Portalframe_L5.2_03_1.2_0.8_t1
Axial stress in piers:	0.3 MPa	
Capacity curve:		
	d [mm] *F* [kN] 0.00 0.0 0.20 13.2 1.64 108.1 2.22 135.9 2.24 77.4 2.40 82.0 17.4 82.0 17.4 77.0 31.0 77.1 31.0 0.0	*d* [mm] *F* [kN] 0.00 0.0 0.20 13.2 1.80 114.7 2.20 127.5 3.00 139.9 7.20 140.0 7.40 119.0 18.2 119.1 18.4 87.7 31.0 87.8 31.2 0.0
Yield point:	1.64 mm 108.1 kN	1.80 mm 114.7 kN
Maximum resistance:	2.22 mm 135.9 kN	7.20 mm 140.0 kN
Collapse:	31.0 mm 77.1 kN	31.0 mm 87.8 kN
Failure mode:	Bending in P1 (base), then diagonal cracking in S and later bending in P2 (base). Failure in S, then failure contemporary failure of P1 and P2.	Bending in P1 (base), then diagonal cracking in S and later bending in P2 (base). Failure in S, then failure contemporary failure of P1 and P2.

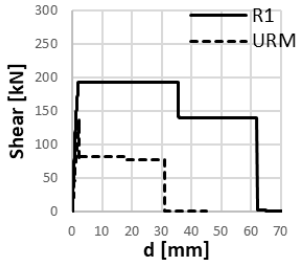
ID:	Portalframe_L5.2_05_1.2_0.8_t0 ($H_{p,fit}$ = 65.6kN)	Portalframe_L5.2_05_1.2_0.8_t1
Axial stress in piers:	0.5 MPa	

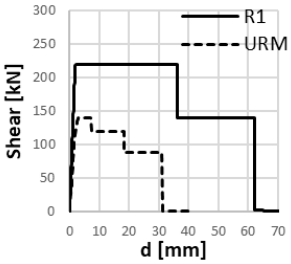
Capacity curve:	 *d* [mm] *F* [kN] 0.00 0.0 0.20 13.2 2.00 79.6 3.60 137.8 3.80 138.8 17.2 138.9 17.4 133.9 31.0 133.9 31.2 0.0	 *d* [mm] *F* [kN] 0.00 0.0 0.20 13.2 2.00 131.7 2.88 163.9 4.04 184.9 7.20 185.0 7.28 164.0 18.1 164.1 18.2 132.7 31.0 132.8 31.0 0.0
Yield point:	2.00 mm 79.6 kN	2.00 mm 131.7 kN
Maximum resistance:	17.2 mm 138.9 kN	7.20 mm 185.0 kN
Collapse:	31.0 mm 133.9 kN	31.0 mm 132.8 kN
Failure mode:	Diagonal cracking in S, then bending in P1 and P2 (base). Failure in S, then contemporary failure in P1 and P2 (base).	Diagonal cracking in S, then bending in P1 (base) and later in P2 (base). Failure in S, then contemporary failure in P1 and P2 (base).

- **Portal frame L5.2_1.2_0.8_R1**

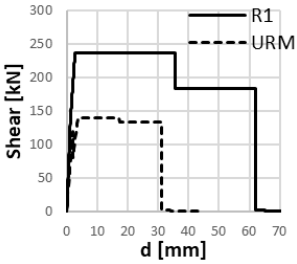
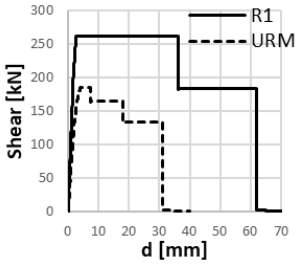


ID:	Portalframe_L5.2_01_1.2_0.8_t0_R1	Portalframe_L5.2_01_1.2_0.8_t1_R1
Masonry properties:	$\tau_{0,eq,P}$=0.241 MPa; $H_{p,eq,P}$=139.9 kN; $\tau_{0,eq,S}$=0.092 MPa; $H_{p,eq,S}$=68.9 kN	$\tau_{0,eq,P}$=0.241 MPa; $H_{p,eq,P}$=139.9 kN; $\tau_{0,eq,S}$=0.137 MPa; $H_{p,eq,S}$=113.3 kN
Axial stress in piers:	0.1 MPa	
Capacity curve:		
	d [mm] *F* [kN] 0.00 0.0 0.20 23.5 1.16 136.3 1.80 143.7 35.7 143.8 35.8 90.3 62.0 90.3 62.1 0.0	*d* [mm] *F* [kN] 0.00 0.0 0.20 23.5 1.28 149.4 1.80 169.8 36.1 169.9 36.2 90.3 62.0 90.3 62.1 0.0
Yield point:	1.16 mm 136.3 kN	1.28 mm 149.4 kN
Maximum resistance:	35.7 mm 143.8 kN	36.1 mm 169.9 kN
Collapse:	62.0 mm 90.3 kN	62.0 mm 90.3 kN
Failure mode:	Diagonal cracking in S and later contemporary bending in P1 and P2 (base). Failure of S, then failure of P1 and P2 (base).	Contemporary bending in P1 and P2 (base) and later diagonal cracking in S. Failure of S, then failure of P1 and P2 (base).

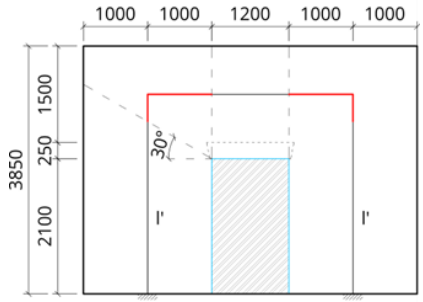
<table>
<tr><td>ID:</td><td>Portalframe_L5.2_03_1.2_0.8_t0_R1</td><td>Portalframe_L5.2_03_1.2_0.8_t1_R1</td></tr>
<tr><td>Masonry properties:</td><td>$\tau_{0,eq,P}$=0.230 MPa; $H_{p,eq,P}$=217.0 kN; $\tau_{0,eq,S}$=0.092 MPa; $H_{p,eq,S}$=68.9 kN</td><td>$\tau_{0,eq,P}$=0.230 MPa; $H_{p,eq,P}$=217.0 kN; $\tau_{0,eq,S}$=0.137 MPa; $H_{p,eq,S}$=113.3 kN</td></tr>
<tr><td>Axial stress in piers:</td><td colspan="2">0.3 MPa</td></tr>
<tr><td>Capacity curve:</td><td> 

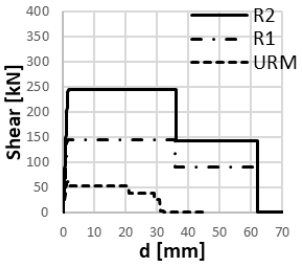
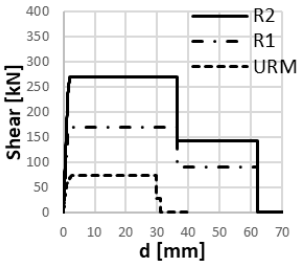
<table>
<tr><th>d [mm]</th><th>F [kN]</th></tr>
<tr><td>0.00</td><td>0.0</td></tr>
<tr><td>0.20</td><td>23.5</td></tr>
<tr><td>1.16</td><td>136.3</td></tr>
<tr><td>2.04</td><td>193.3</td></tr>
<tr><td>35.6</td><td>193.5</td></tr>
<tr><td>35.7</td><td>140.1</td></tr>
<tr><td>62.0</td><td>140.1</td></tr>
<tr><td>62.1</td><td>0.0</td></tr>
</table></td><td> 

<table>
<tr><th>d [mm]</th><th>F [kN]</th></tr>
<tr><td>0.00</td><td>0.0</td></tr>
<tr><td>0.20</td><td>23.5</td></tr>
<tr><td>1.80</td><td>207.8</td></tr>
<tr><td>2.00</td><td>219.5</td></tr>
<tr><td>36.1</td><td>219.6</td></tr>
<tr><td>36.2</td><td>140.1</td></tr>
<tr><td>62.0</td><td>140.1</td></tr>
<tr><td>62.1</td><td>0.0</td></tr>
</table></td></tr>
<tr><td>Yield point:</td><td>1.16 mm 136.3 kN</td><td>1.80 mm 207.8 kN</td></tr>
<tr><td>Maximum resistance:</td><td>35.7 mm 193.5 kN</td><td>36.1 mm 219.6 kN</td></tr>
<tr><td>Collapse:</td><td>62.0 mm 140.1 kN</td><td>62.0 mm 140.1 kN</td></tr>
<tr><td>Failure mode:</td><td>Diagonal cracking in S and later contemporary bending in P1 and P2 (base). Failure of S, then failure of P1 and P2 (base).</td><td>Diagonal cracking in S, then contemporary bending in P1 and P2 (base). Failure of S, then failure of P1 and P2 (base).</td></tr>
</table>

ID:	Portalframe_L5.2_05_1.2_0.8_t0_R1	Portalframe_L5.2_05_1.2_0.8_t1_R1
Masonry properties:	$\tau_{0,eq,P}$=0.220 MPa; $H_{p,eq,P}$=283.0 kN; $\tau_{0,eq,S}$=0.092 MPa; $H_{p,eq,S}$=68.9 kN	$\tau_{0,eq,P}$=0.220 MPa; $H_{p,eq,P}$=283.0 kN; $\tau_{0,eq,S}$=0.137 MPa; $H_{p,eq,S}$=113.3 kN
Axial stress in piers:	0.5 MPa	
Capacity curve:		
	d [mm] *F* [kN] 0.00 0.0 0.20 23.5 1.16 136.3 2.68 236.1 35.6 236.2 35.7 183.1 62.0 183.1 62.0 0.0	*d* [mm] *F* [kN] 0.00 0.0 0.20 23.5 1.80 207.8 2.64 262.2 36.1 262.4 36.2 182.8 62.0 182.8 62.1 0.0
Yield point:	1.16 mm 136.3 kN	1.80 mm 207.8 kN
Maximum resistance:	35.7 mm 236.2 kN	36.1 mm 262.4 kN
Collapse:	62.0 mm 183.1 kN	62.0 mm 182.8 kN
Failure mode:	Diagonal cracking in S and later contemporary bending in P1 and P2 (base). Failure of S, then failure of P1 and P2 (base).	Diagonal cracking in S, then contemporary bending in P1 and P2 (base). Failure of S, then failure of P1 and P2 (base).

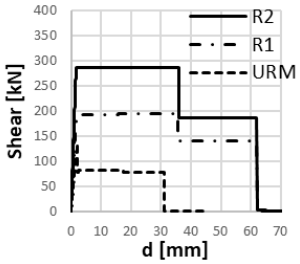
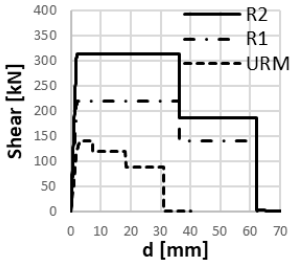
- **Portal frame L5.2_1.2_0.8_R2**



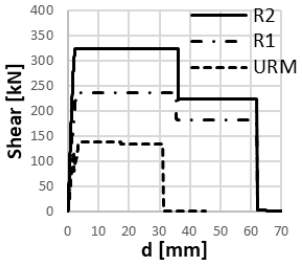
ID:	Portalframe_L5.2_01_1.2_0.8_t0_R2	Portalframe_L5.2_01_1.2_0.8_t1_R2
Masonry properties:	$\tau_{0,eq,P}$=0.393 MPa; $H_{p,eq,P}$=221.2 kN; $\tau_{0,eq,S}$=0.174 MPa; $H_{p,eq,S}$=86.4 kN	$\tau_{0,eq,P}$=0.393 MPa; $H_{p,eq,P}$=221.2 kN; $\tau_{0,eq,S}$=0.219 MPa; $H_{p,eq,S}$=113.3 kN
Axial stress in piers:	0.1 MPa	
Capacity curve:		
Yield point:	1.40 mm 233.9 kN	1.40 mm 233.9 kN
Maximum resistance:	36.0 mm 243.7 kN	36.4 mm 270.0 kN
Collapse:	62.0 mm 142.8 kN	62.0 mm 142.8 kN
Failure mode:	Contemporary bending in P1 and P2 (base) and later diagonal cracking in S. Failure of S, then failure of P1 and P2 (base).	Contemporary bending in P1 and P2 (base) and later diagonal cracking in S. Failure of S, then failure of P1 and P2 (base).

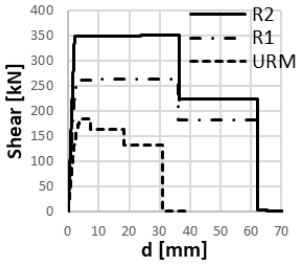
d [mm]	*F* [kN]
0.00	0.0
0.20	33.7
1.40	233.9
1.60	243.7
36.0	243.9
36.1	142.8
62.0	142.8
62.1	0.0

d [mm]	*F* [kN]
0.00	0.0
0.20	33.7
1.40	233.9
2.04	269.8
36.4	270.0
36.5	142.8
62.0	142.8
62.1	0.0

ID:	Portalframe_L5.2_03_1.2_0.8_t0_R2	Portalframe_L5.2_03_1.2_0.8_t1_R2
Masonry properties:	$\tau_{0,eq,P}$=0.379 MPa; $H_{p,eq,P}$=288.3 kN; $\tau_{0,eq,S}$=0.174 MPa; $H_{p,eq,S}$=86.4 kN	$\tau_{0,eq,P}$=0.379 MPa; $H_{p,eq,P}$=288.3 kN; $\tau_{0,eq,S}$=0.219 MPa; $H_{p,eq,S}$=113.3 kN
Axial stress in piers:	0.3 MPa	
Capacity curve:		
	d [mm] *F* [kN] 0.00 0.0 0.20 33.7 1.60 265.5 1.84 286.9 36.0 287.1 36.1 186.1 62.0 186.1 62.1 1.9	*d* [mm] *F* [kN] 0.00 0.0 0.20 33.7 1.84 305.7 2.00 313.0 36.4 313.3 36.5 186.1 62.0 186.1 62.1 0.0
Yield point:	1.60 mm 265.5 kN	1.84 mm 305.7 kN
Maximum resistance:	36.0 mm 287.1 kN	36.4 mm 313.0 kN
Collapse:	62.0 mm 186.1 kN	62.0 mm 186.1 kN
Failure mode:	Diagonal cracking in S and later contemporary bending in P1 and P2 (base). Failure of S, then failure of P1 and P2 (base).	Contemporary bending in P1 and P2 (base) and later diagonal cracking in S. Failure of S, then failure of P1 and P2 (base).

ID:	Portalframe_L5.2_05_1.2_0.8_t0_R2	Portalframe_L5.2_05_1.2_0.8_t1_R2
Masonry properties:	$\tau_{0,eq,P}$=0.362 MPa; $H_{p,eq,P}$=345.2 kN; $\tau_{0,eq,S}$=0.174 MPa; $H_{p,eq,S}$=86.4 kN	$\tau_{0,eq,P}$=0.362 MPa; $H_{p,eq,P}$=345.2 kN; $\tau_{0,eq,S}$=0.219 MPa; $H_{p,eq,S}$=113.3 kN
Axial stress in piers:	0.5 MPa	

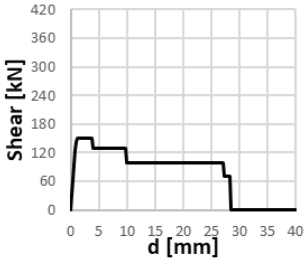
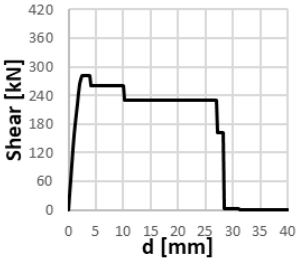
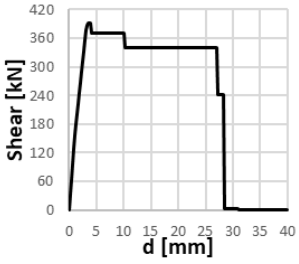
<table>
<tr>
<td>Capacity curve:</td>
<td>


<table>
<tr><th>d [mm]</th><th>F [kN]</th></tr>
<tr><td>0.00</td><td>0.0</td></tr>
<tr><td>0.20</td><td>33.7</td></tr>
<tr><td>1.6</td><td>265.5</td></tr>
<tr><td>2.24</td><td>323.6</td></tr>
<tr><td>36.0</td><td>323.8</td></tr>
<tr><td>36.1</td><td>222.2</td></tr>
<tr><td>62.0</td><td>222.2</td></tr>
<tr><td>62.1</td><td>2.2</td></tr>
</table>
</td>
<td>


<table>
<tr><th>d [mm]</th><th>F [kN]</th></tr>
<tr><td>0.00</td><td>0.0</td></tr>
<tr><td>0.20</td><td>33.7</td></tr>
<tr><td>2.04</td><td>336.7</td></tr>
<tr><td>2.20</td><td>349.7</td></tr>
<tr><td>36.4</td><td>349.9</td></tr>
<tr><td>36.5</td><td>222.1</td></tr>
<tr><td>62.0</td><td>222.1</td></tr>
<tr><td>62.1</td><td>0.0</td></tr>
</table>
</td>
</tr>
<tr><td>Yield point:</td><td>1.60 mm 265.5 kN</td><td>2.04 mm 336.7 kN</td></tr>
<tr><td>Maximum resistance:</td><td>36.0 mm 323.8 kN</td><td>36.4 mm 349.9 kN</td></tr>
<tr><td>Collapse:</td><td>62.0 mm 222.2 kN</td><td>62.0 mm 225.1 kN</td></tr>
<tr><td>Failure mode:</td><td>Diagonal cracking in S and later contemporary bending in P1 and P2 (base). Failure of S, then failure of P1 and P2 (base).</td><td>Diagonal cracking in S, then contemporary bending in P1 and P2 (base). Failure of S, then failure of P1 and P2 (base).</td></tr>
</table>

Simplified numerical analyses on single story walls

- **Single-story wall h.3.35_1a**

ID:	Singlestorywall_h3.35_1a_01	Singlestorywall_h3.35_1a_03	Singlestorywall_h3.35_1a_05
Axial stress:	0.1 MPa	0.3 MPa	0.5 MPa
Capacity curve:			
	d [mm] *F* [kN] 0.00 0.0 0.20 32.1 0.80 125.6 1.00 143.9 1.20 150.7 3.80 150.8 4.00 129.8 9.80 129.9 10.0 98.5 27.0 98.7 27.2 69.6 28.2 69.6 28.0 0.0	*d* [mm] *F* [kN] 0.00 0.0 0.20 32.1 1.00 157.9 2.00 265.4 2.20 275.4 2.40 281.5 3.80 281.6 4.00 260.6 10.0 260.7 10.2 229.4 27.0 229.6 27.2 161.9 28.2 161.9 28.4 0.0	*d* [mm] *F* [kN] 0.00 0.0 0.20 32.1 1.00 157.9 3.00 377.8 3.20 387.0 3.40 392.6 4.00 392.6 4.20 371.6 10.0 371.8 10.2 340.4 27.0 340.7 27.2 240.5 28.2 240.5 28.4 0.0
Yield point:	0.80 mm 125.6 kN	1.00 mm 157.9 kN	1.00 mm 157.9 kN
Maximum resistance:	3.80 mm 150.8 kN	3.80 mm 281.6 kN	4.00 mm 392.6 kN
Collapse:	27.0 mm 98.7 kN	27.0 mm 229.6 kN	27.0 mm 340.7 kN
Failure mode:	Bending in P1 (base), then contemporary diagonal cracking in S1 and S2 and bending in P2, later bending in P3 (base). Failure of S1 and S2, then bending failure of P2 (base), later failure of P1 and P3 (base).	Diagonal cracking in S1 and S2, then in order bending in P1, P2 and in P3 (base). Failure of S1 and S2, then bending failure of P2 (base), later failure of P1 (base) and P3 (base).	Diagonal cracking in S1 and S2, then contemporary bending in P1 and P2 (base) and finally in P3 (base). Failure of S1 and S2, then bending failure of P1 (base), later failure of P2 and P3 (base).

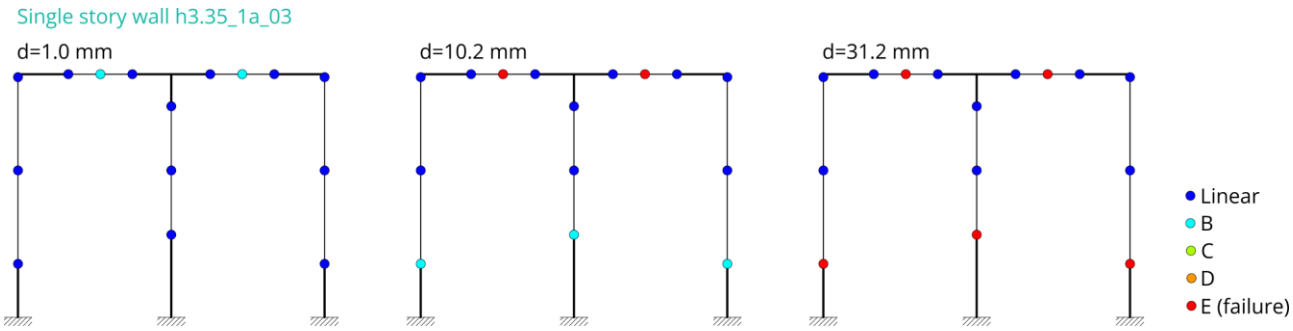
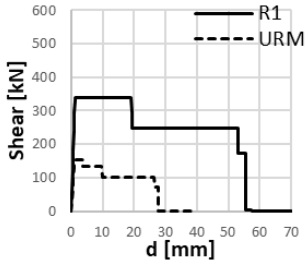
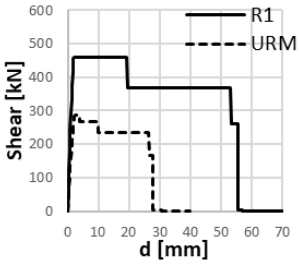
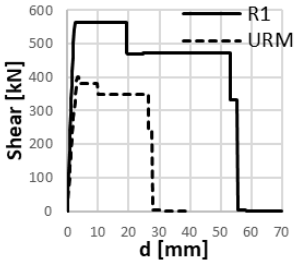
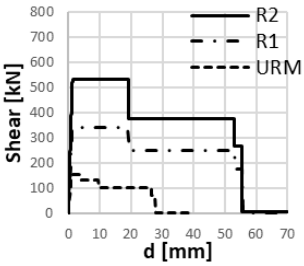
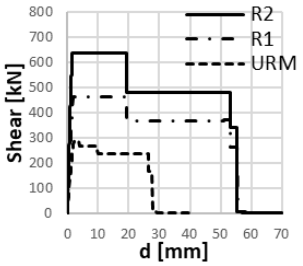
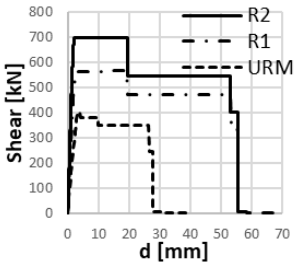


Figure 0.1 Failure mechanism of single-story wall h3.35_1a_03

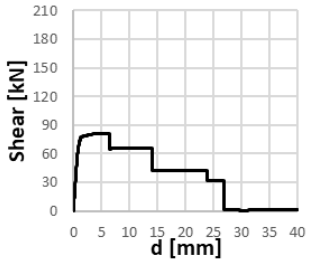
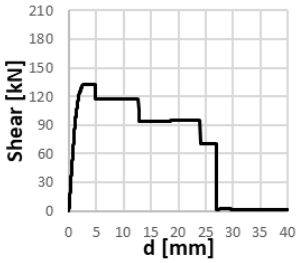
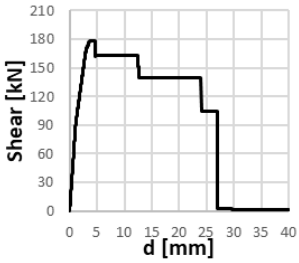
- **Single-story wall h3.35_1a_R1**

ID:	Singlestorywall_h3.35_1a_01_R1	Singlestorywall_h3.35_1a_03_R1	Singlestorywall_h3.35_1a_05_R1
Masonry properties:	$\tau_{0,eq,P1,P3}$=0.198MPa; $H_{p,eq,P1,P3}$=191.3kN; $\tau_{0,eq,P2}$=0.198MPa; $H_{p,eq,P2}$=173.1kN; $\tau_{0,eq,S}$=0.157MPa; $H_{p,eq,S}$=70.0kN	$\tau_{0,eq,P1,P3}$=0.189MPa; $H_{p,eq,P1,P3}$=285.6kN; $\tau_{0,eq,P2}$=0.189MPa; $H_{p,eq,P2}$=257.8kN; $\tau_{0,eq,S}$=0.157MPa; $H_{p,eq,S}$=70.0kN	$\tau_{0,eq,P1,P3}$=0.181MPa; $H_{p,eq,P1,P3}$=366.2kN; $\tau_{0,eq,P2}$=0.181MPa; $H_{p,eq,P2}$=330.2kN; $\tau_{0,eq,S}$=0.157MPa; $H_{p,eq,S}$=70.0kN
Axial stress:	0.1 MPa	0.3 MPa	0.5 MPa
Capacity curve:			
	d [mm] *F* [kN] 0.00 0.0 0.20 60.2 1.00 292.6 1.40 339.7 19.0 340.1 19.2 293.8 19.4 247.1 53.0 247.3 53.2 174.3	*d* [mm] *F* [kN] 0.00 0.0 0.20 60.2 1.00 292.6 2.00 460.3 19.2 460.8 19.4 368.3 19.6 367.4 53.0 368.0 53.2 259.6	*d* [mm] *F* [kN] 0.00 0.0 0.20 60.2 1.00 292.6 2.40 563.6 19.2 564.0 19.4 471.6 19.6 470.7 53.0 471.4 53.2 332.5
Yield point:	1.00 mm 292.6 kN	1.00 mm 292.6 kN	1.00 mm 292.6 kN
Maximum resistance:	19.2 mm 340.1 kN	19.2 mm 460.8 kN	19.2 mm 564.0 kN
Collapse:	53.0 mm 247.3 kN	53.0 mm 368.0 kN	53.0 mm 471.4 kN
Failure mode:	Diagonal cracking in S1 and S2, then contemporary bending in P1, P2 and P3 (base). Failure of S1 and S2, then bending failure of P2 (base), later failure of P1 and P3 (base).	Diagonal cracking in S1 and S2, then contemporary bending in Pi, P2 and P3 base). Failure of S1 and S2, then bending failure of P2 (base), later failure of P1 and P3 (base).	Diagonal cracking in S1 and S2, then contemporary bending in Pi, P2 and P3 base). Failure of S1 and S2, then bending failure of P2 (base), later failure of P1 and P3 (base).

- **Single-story wall h3.35_1a_R2**

ID:	Singlestorywall_h3.35_1a_01_R2	Singlestorywall_h3.35_1a_03_R2	Singlestorywall_h3.35_1a_05_R2
Masonry properties:	$\tau_{0,eq,P1,P3}$=0.308MPa; $H_{p,eq,P1,P3}$=292.3kN; $\tau_{0,eq,P2}$=0.308MPa; $H_{p,eq,P2}$=264.0kN; $\tau_{0,eq,S}$=0.260MPa; $H_{p,eq,S}$=70.0kN	$\tau_{0,eq,P1,P3}$=0.295MPa; $H_{p,eq,P1,P3}$=374.0kN; $\tau_{0,eq,P2}$=0.295MPa; $H_{p,eq,P2}$=337.4kN; $\tau_{0,eq,S}$=0.260MPa; $H_{p,eq,S}$=70.0kN	$\tau_{0,eq,P1,P3}$=0.282MPa; $H_{p,eq,P1,P3}$=442.8kN; $\tau_{0,eq,P2}$=0.281MPa; $H_{p,eq,P2}$=399.2kN; $\tau_{0,eq,S}$=0.260MPa; $H_{p,eq,S}$=70.0kN
Axial stress:	0.1 MPa	0.3 MPa	0.5 MPa
Capacity curve:			
	d [mm] *F* [kN] 0.00 0.0 0.20 86.3 0.98 423.5 1.3 527.1 1.32 530.3 19.2 530.6 19.3 376.4 53.0 376.4 53.1 265.3	*d* [mm] *F* [kN] 0.00 0.0 0.20 86.3 0.98 423.5 1.66 633.1 1.68 634.8 19.2 635.1 19.3 481.0 53.0 481.0 53.1 339.1	*d* [mm] *F* [kN] 0.00 0.0 0.20 86.3 0.98 423.5 1.96 696.3 1.98 697.5 19.2 697.8 19.3 543.7 53.0 543.7 53.1 401.1
Yield point:	0.98 mm 423.5 kN	0.98 mm 423.5 kN	0.98 mm 423.5 kN
R_{max}:	19.2 mm 530.6 kN	19.2 mm 635.1 kN	19.2 mm 697.8 kN
Collapse:	53.0 mm 376.4 kN	53.0 mm 481.0 kN	53.0 mm 543.7 kN
Failure mode:	Bending in S1 (left) and S2 (right), then diagonal cracking in S1 and S2 and later bending in S1 (right) and S2 (left). Finally, bending in P2 (base), followed by bending in P1 and P2 (base). Contemporary bending failure of S1 and diagonal cracking failure of S2. Finally, bending failure of P2 (base) and later failure of P1 and P3 (base).	Bending in S1 (left) and S2 (right), then diagonal cracking in S1 and S2 and later bending in S1 (right) and S2 (left). Finally, bending in P2 (base), followed by bending in P1 and P2 (base). Contemporary bending failure of S1 and diagonal cracking failure of S2. Finally, bending failure of P2 (base) and later failure of P1 and P3 (base).	Bending in S1 (left) and S2 (right), then diagonal cracking in S1 and S2 and later bending in S1 (right) and S2 (left). Finally, bending in P2 (base), followed by bending in P1 and P2 (base). Contemporary bending failure of S1 and diagonal cracking failure of S2. Finally, bending failure of P2 (base) and later failure of P1 and P3 (base).

- **Single-story wall h3.35_1b**

ID:	Singlestorywall_h3.35_1b_01	Singlestorywall_h3.35_1b_03	Singlestorywall_h3.35_1b_05
Axial stress:	0.1 MPa	0.3 MPa	0.5 MPa
Capacity curve:			
	d [mm] *F* [kN] 0.00 0.0 0.20 16.4 0.68 55.5 0.74 59.0 0.92 67.3 1.26 76.3 1.54 77.8 3.48 80.6 6.42 80.6 6.60 65.0 14.0 65.3 14.2 42.0 23.8 42.4 23.8 31.9 26.9 31.9 29.9 0.0	*d* [mm] *F* [kN] 0.00 0.0 0.20 16.4 1.14 93.3 1.84 122.1 2.56 132.9 4.82 133.0 4.94 117.3 12.7 117.7 12.7 105.9 12.9 105.9 13.0 94.2 24.0 97.4 24.0 70.6 26.9 70.5 26.9 0.0	*d* [mm] *F* [kN] 0.00 0.0 0.20 16.4 1.14 93.3 2.86 164.4 3.02 169.3 3.62 178.2 4.62 178.2 4.7 162.5 12.5 162.9 12.6 151.1 12.7 139.1 24 139.9 24.0 104.4 26.9 104.2 26.9 0.0
Yield point:	0.68 mm 55.5 kN	1.14 mm 93.3 kN	1.14 mm 93.3 kN
R_{max}:	6.42 mm 80.6 kN	4.82 mm 133.0 kN	4.62 mm 178.2 kN
Collapse:	23.8 mm 42.4 kN	24.0 mm 97.4 kN	24.0 mm 139.9 kN
Failure mode:	Bending in P1 (base), then bending in P2 (base + top), later contemporary bending in P1 (top) and P3 (base), followed by diagonal cracking in S2 and later in S2. Failure of S1 and S2, then bending failure of P2 (base), later contemporary failure of P1 and P3 (base).	Diagonal cracking in S1 and S2, then contemporary bending in P1 and P2 (base) and later in P3 (base). Failure of S1 and S2, then bending failure of P2 (base), later contemporary failure of P1 and P3 (base).	Diagonal cracking in S1 and S2, then bending in P2 (base), later bending in P1 (base) and lastly in P3 (base). Failure of S1 and S2, then bending failure of P2 (base), later contemporary failure of P1 and P3 (base).

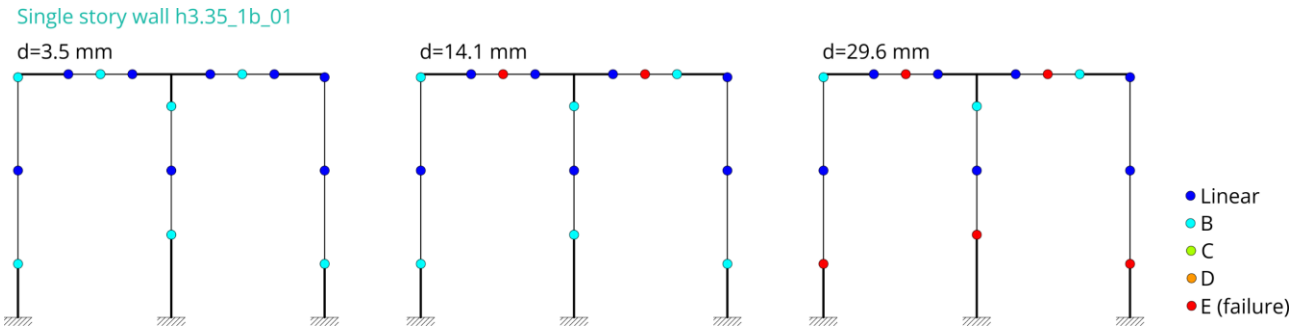
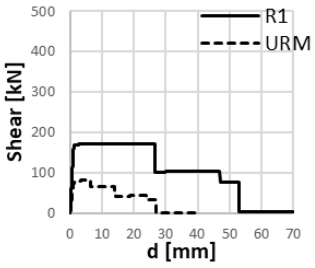
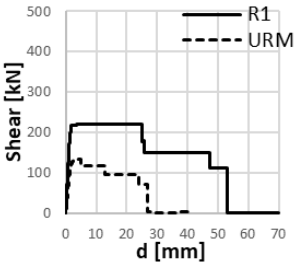
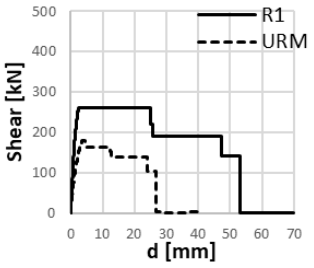
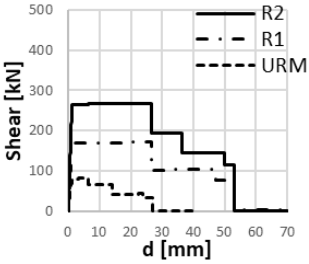
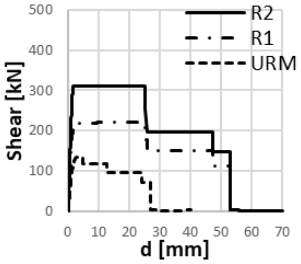
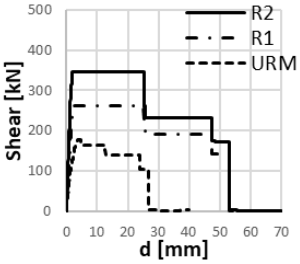


Figure 0.2 Failure mechanism of single-story wall h3.35_1b_01

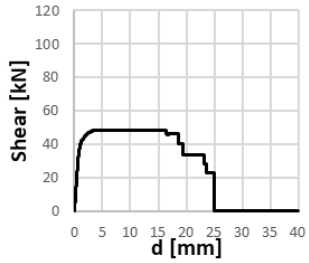
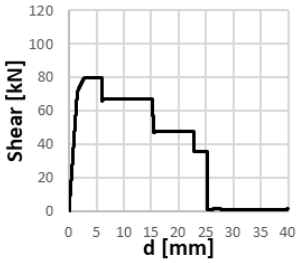
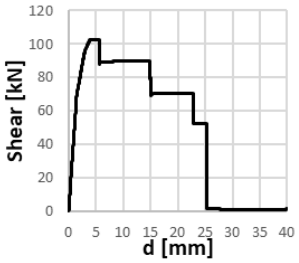
- **Single-story wall h3.35_1b_R1**

ID:	Singlestorywall_h3.35_1b_01_R1	Singlestorywall_h3.35_1b_03_R1	Singlestorywall_h3.35_1b_05_R1
Masonry properties:	$\tau_{0,eq,P1,P3}$=0.240MPa; $H_{p,eq,P1,P3}$=122.8kN; $\tau_{0,eq,P2}$=0.240MPa; $H_{p,eq,P2}$=96.7kN; $\tau_{0,eq,S}$=0.157MPa; $H_{p,eq,S}$=70.0kN	$\tau_{0,eq,P1,P3}$=0.229MPa; $H_{p,eq,P1,P3}$=183.1kN; $\tau_{0,eq,P2}$=0.229MPa; $H_{p,eq,P2}$=143.7kN; $\tau_{0,eq,S}$=0.157MPa; $H_{p,eq,S}$=70.0kN	$\tau_{0,eq,P1,P3}$=0.219MPa; $H_{p,eq,P1,P3}$=234.6kN; $\tau_{0,eq,P2}$=0.219MPa; $H_{p,eq,P2}$=183.9kN; $\tau_{0,eq,S}$=0.157MPa; $H_{p,eq,S}$=70.0kN
Axial stress:	0.1 MPa	0.3 MPa	0.5 MPa
Capacity curve:			
	d [mm] *F* [kN] 0.00 0.0 0.21 32.0 1.16 165.7 1.26 169.7 26.6 170.2 26.7 137.4 26.8 102.4 46.9 102.4 47.0 76.9 53.0 76.9 53.1 0.0	*d* [mm] *F* [kN] 0.00 0.0 0.21 32.0 1.12 167.9 1.89 218.5 25.0 219.7 25.1 183.5 25.2 177.9 25.8 177.9 25.9 149.0 47.3 149.0 47.4 110.8	*d* [mm] *F* [kN] 0.00 0.0 0.21 32.0 1.12 167.9 2.45 260.2 25.0 261.4 25.1 225.2 25.2 219.5 25.7 219.5 25.8 190.7 47.3 190.7 47.4 141.9
Yield point:	1.16 mm 165.7 kN	1.12 mm 167.9 kN	1.12 mm 167.9 kN
R_{max}:	26.6 mm 170.2 kN	25.0 mm 219.7 kN	25.0 mm 261.4 kN
Collapse:	46.9 mm 102.4 kN	47.3 mm 149.0 kN	47.3 mm 190.7 kN
Failure mode:	Diagonal cracking in S1 and S2, then bending in P1, P2 and P3 (base) and later in P2 (top). Failure of S1 and S2, then bending failure of P2 (base), later failure of P1 and P3 (base).	Diagonal cracking in S1 and S2, then bending in P2 (base and later in P1 and P3 (base). Finally bending in S1 (right) and S2 (left). Contemporary diagonal cracking failure of S2 and bending failure of S1, then bending failure of P2 (base), later failure of P1 and P3 (base).	Diagonal cracking in S1 and S2, then bending in P2 (base and later in P1 and P3 (base). Finally bending in S1 (right) and S2 (left). Contemporary diagonal cracking failure of S2 and bending failure of S1, then bending failure of P2 (base), later failure of P1 and P3 (base).

- **Single-story wall h3.35_1b_R2**

ID:	Singlestorywall_h3.35_1b_01_R2	Singlestorywall_h3.35_1b_03_R2	Singlestorywall_h3.35_1b_05_R2
Masonry properties:	$\tau_{0,eq,P1,P3}$=0.393MPa; $H_{p,eq,P1,P3}$=187.4kN; $\tau_{0,eq,P2}$=0.392MPa; $H_{p,eq,P2}$=147.2kN; $\tau_{0,eq,S}$=0.260MPa; $H_{p,eq,S}$=70.0kN	$\tau_{0,eq,P1,P3}$=0.378MPa; $H_{p,eq,P1,P3}$=239.6kN; $\tau_{0,eq,P2}$=0.377MPa; $H_{p,eq,P2}$=187.9kN; $\tau_{0,eq,S}$=0.260MPa; $H_{p,eq,S}$=70.0kN	$\tau_{0,eq,P1,P3}$=0.361MPa; $H_{p,eq,P1,P3}$=283.6kN; $\tau_{0,eq,P2}$=0.361MPa; $H_{p,eq,P2}$=222.2kN; $\tau_{0,eq,S}$=0.260MPa; $H_{p,eq,S}$=70.0kN
Axial stress:	0.1 MPa	0.3 MPa	0.5 MPa
Capacity curve:			
	d [mm] *F* [kN] 0.00 0.0 0.21 46.1 1.02 222.6 1.33 265.3 26.4 265.5 26.5 193.8 36.4 193.8 36.5 143.1 49.8 143.1 49.9 113.4 52.9 113.4 53.0 0.0	*d* [mm] *F* [kN] 0.00 0.0 0.21 46.1 1.12 245.8 1.68 310.1 25.2 310.4 25.3 195.9 47.2 195.9 47.3 146.1 52.9 146.1 53.0 0.0	*d* [mm] *F* [kN] 0.00 0.0 0.21 46.1 1.33 283.7 2.03 345.7 25.2 346.0 25.3 231.3 47.3 231.5 47.4 173.2 52.9 172.6 53.0 0.0
Yield point:	1.02 mm 222.6 kN	1.12 mm 245.8 kN	1.33 mm 283.7 kN
R_{max}:	26.4 mm 265.5 kN	25.2 mm 310.4 kN	25.2 mm 346.0 kN
Collapse:	36.4 mm 193.8 kN	47.2 mm 195.9 kN	47.3 mm 231.5 kN
Failure mode:	Bending in P2 (base) and in S1 (left) and S2 (right), then bending in P1 and P3 (base) and P2 (top). Bending failure of P2 (top then base), later bending failure of S1(left) and S2 (right). Finally, bending failure of P1 and P2 (base).	Bending in S1 (left) and S2 (right), then diagonal cracking in S1and S2 and bending in P2 (base). Later bending in P1 and P3 (base). Contemporary diagonal cracking failure of S1 and bending failure of S2. Then failure of P2 (base) and later of P1 and P3 (base).	Bending in S1 (left) and S2 (right), then diagonal cracking in S1and S2 and bending in P2 (base). Later bending in P1 and P3 (base). Contemporary diagonal cracking failure of S1 and bending failure of S2. Then failure of P2 (base) and later of P1 and P3 (base).

- **Single-story wall h3.35_1c**

ID:	Singlestorywall_h3.35_1c_01	Singlestorywall_h3.35_1c_03	Singlestorywall_h3.35_1c_05
Axial stress:	0.1 MPa	0.3 MPa	0.5 MPa
Capacity curve:			
	d [mm] *F* [kN] 0.00 0.0 0.20 9.4 0.66 31.0 1.04 39.4 1.26 42.2 2.52 46.9 3.72 48.5 16.5 48.6 16.6 45.7 18.6 46.5 18.6 40.2 19.3 40.2 19.3 33.9 23.1 33.8 23.1 27.9 23.6 27.9	*d* [mm] *F* [kN] 0.00 0.0 0.20 9.4 1.46 69.1 1.48 69.5 1.64 72.2 2.76 79.8 5.94 79.9 6.08 66.3 15.2 67.1 15.3 56.9 15.4 57.1 15.4 47.0 22.7 47.6 22.7 35.6 25.2 35.6 25.2 0.0	*d* [mm] *F* [kN] 0.00 0.0 0.20 9.4 1.48 69.5 2.84 94.2 2.98 96.1 3.92 102.5 5.56 102.5 5.72 88.8 14.84 89.7 15.02 69.5 22.8 70.3 22.82 52.6 25.2 52.5 25.2 0.0
Yield point:	0.66 mm 31.0 kN	1.46 mm 69.1 kN	1.48 mm 69.5 kN
R_{max}:	16.5 mm 48.6 kN	5.94 mm 79.9 kN	5.56 mm 102.5 kN
Collapse:	23.6 mm 27.9 kN	22.7 mm 47.6 kN	22.8 mm 70.3 kN
Failure mode:	Bending in P1 and P2 (base), then bending in P2 (top). Later bending in P1 (top), then bending in P3 (base) and later diagonal cracking in S2, followed by bending in S2 (right). Failure of P2 (base and top). Then failure of P1 (base and top) and later of P3 (base).	Contemporary diagonal racking in S1 and S2. Then bending in P1 and P2 and later in P3 (base). Failure of S1 and S2, then failure of P2 (base) and finally, contemporary failure of P1 and P3 (base).	Contemporary diagonal racking in S1 and S2. Then bending in P1 and P2 and later in P3 (base). Failure of S1 and S2, then failure of P2 (base) and finally, contemporary failure of P1 and P3 (base).

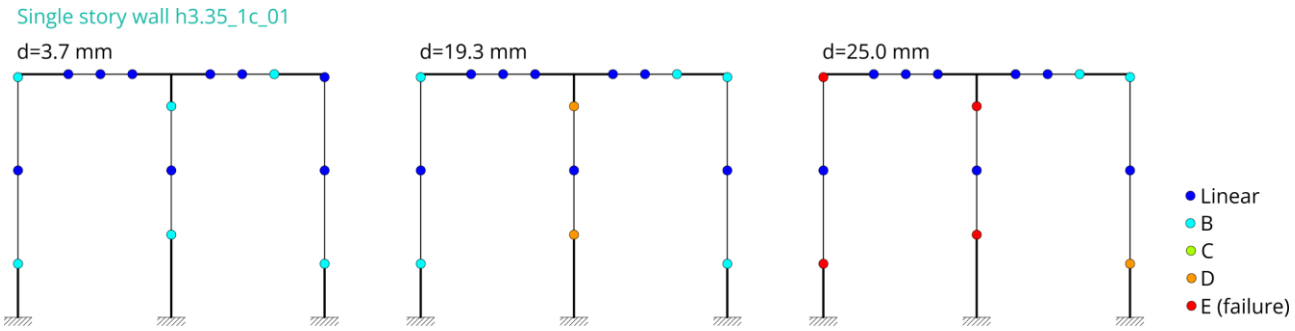


Figure 0.3 Failure mechanism of single-story wall h3.35_1c_01

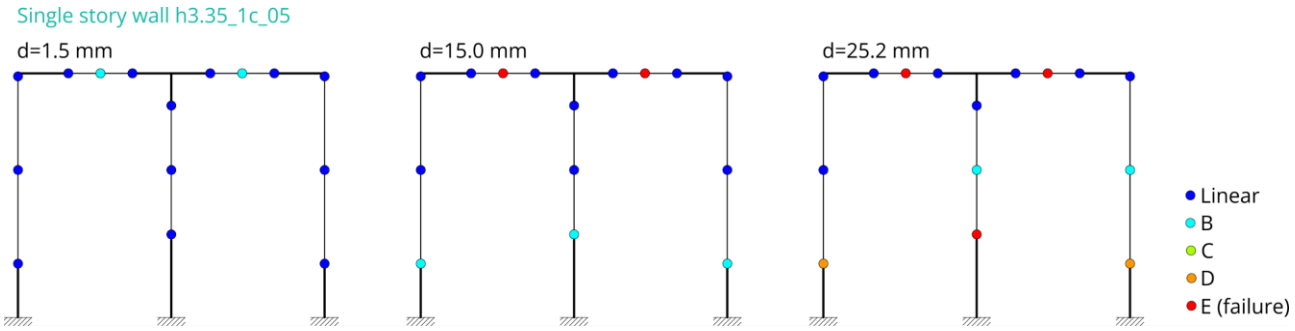
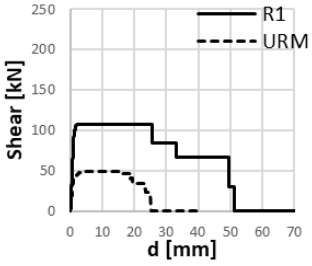
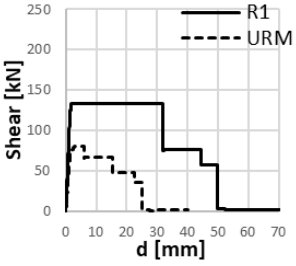
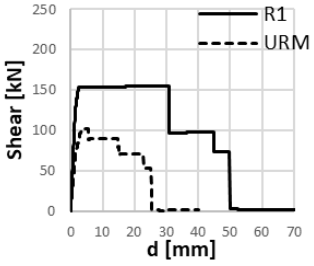
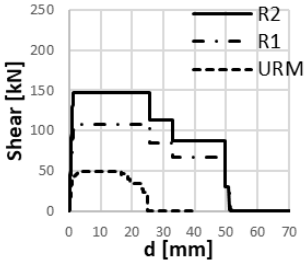
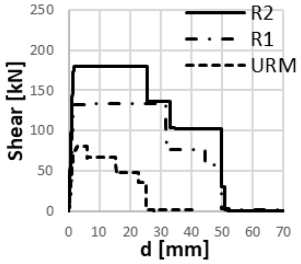
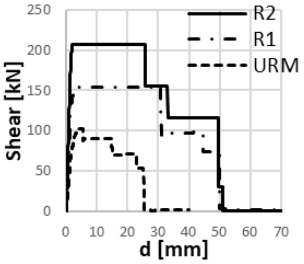


Figure 0.4 Failure mechanism of single-story wall h3.35_1c_05

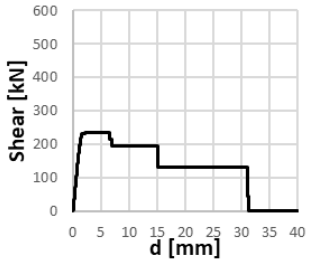
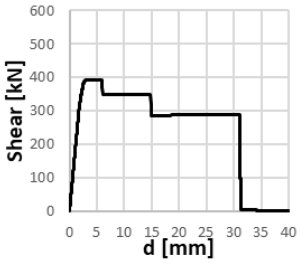
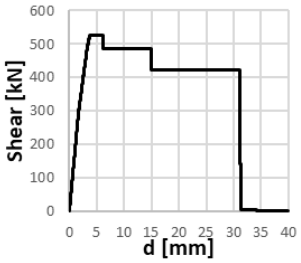
- **Single-story wall h3.35_1c_R1**

ID:	Singlestorywall_h3.35_1c_01_R1	Singlestorywall_h3.35_1b_03_R1	Singlestorywall_h3.35_1b_05_R1
Masonry properties:	$\tau_{0,eq,P1,P3}$=0.241MPa; $H_{p,eq,P1,P3}$=84.7kN; $\tau_{0,eq,P2}$=0.241MPa; $H_{p,eq,P2}$=66.2kN; $\tau_{0,eq,S}$=0.157MPa; $H_{p,eq,S}$=70.0kN	$\tau_{0,eq,P1,P3}$=0.230MPa; $H_{p,eq,P1,P3}$=126.1kN; $\tau_{0,eq,P2}$=0.230MPa; $H_{p,eq,P2}$=98.1kN; $\tau_{0,eq,S}$=0.157MPa; $H_{p,eq,S}$=70.0kN	$\tau_{0,eq,P1,P3}$=0.219MPa; $H_{p,eq,P1,P3}$=161.5kN; $\tau_{0,eq,P2}$=0.219MPa; $H_{p,eq,P2}$=125.4kN; $\tau_{0,eq,S}$=0.157MPa; $H_{p,eq,S}$=70.0kN
Axial stress:	0.1 MPa	0.3 MPa	0.5 MPa
Capacity curve:			
	d [mm] *F* [kN] 0.00 0.0 0.20 17.5 0.92 80.4 1.88 107.0 25.5 107.1 25.6 84.3 33.0 84.3 33.1 67.1 49.6 67.1 49.7 29.8 51.1 29.8 51.2 0.0	*d* [mm] *F* [kN] 0.00 0.0 0.20 17.5 1.40 121.2 1.88 132.9 31.7 132.9 31.8 76.3 44.5 76.3 44.6 57.4 49.7 57.4 49.8 0.0	*d* [mm] *F* [kN] 0.00 0.0 0.20 17.5 1.40 122.1 2.48 154.4 30.8 154.4 30.9 97.4 44.7 97.4 44.8 73.4 49.8 73.4 49.8 0.0
Yield point:	0.92 mm 80.4 kN	1.40 mm 121.2 kN	1.40 mm 122.1 kN
R_{max}:	25.5 mm 107.1 kN	31.7 mm 132.9 kN	30.8 mm 154.4 kN
Collapse:	33.0 mm 84.3 kN	44.5 mm 76.3 kN	44.7 mm 97.4 kN
Failure mode:	Bending in P2 (base then top), later bending in P1 and P3 (base) and finally bending in S1 (left) and S2 (right). Failure of P2 (base and top), then bending failure of S1 (left) and S2 (right) and later of P1 and P3 (base).	Diagonal cracking in S1 and S2, then bending in P2 (base) and lastly bending in P1 and P3 (base). Diagonal cracking failure of S1 and S2, then failure of P2 (base) and lastly failure of P1 and P3 (base).	Diagonal cracking in S1 and S2, then bending in P2 (base) and lastly bending in P1 and P3 (base). Diagonal cracking failure of S1 and S2, then failure of P2 (base) and lastly failure of P1 and P3 (base).

- **Single-story wall h3.35_1c_R2**

ID:	Singlestorywall_h3.35_1c_01_R2	Singlestorywall_h3.35_1c_03_R2	Singlestorywall_h3.35_1c_05_R2
Masonry properties:	$\tau_{0,eq,P1,P3}$=0.392MPa; $H_{p,eq,P1,P3}$=129.1kN; $\tau_{0,eq,P2}$=0.392MPa; $H_{p,eq,P2}$=100.6kN; $\tau_{0,eq,S}$=0.260MPa; $H_{p,eq,S}$=70.0kN	$\tau_{0,eq,P1,P3}$=0.377MPa; $H_{p,eq,P1,P3}$=165.0kN; $\tau_{0,eq,P2}$=0.377MPa; $H_{p,eq,P2}$=128.2kN; $\tau_{0,eq,S}$=0.260MPa; $H_{p,eq,S}$=70.0kN	$\tau_{0,eq,P1,P3}$=0.361MPa; $H_{p,eq,P1,P3}$=195.2kN; $\tau_{0,eq,P2}$=0.360MPa; $H_{p,eq,P2}$=151.4kN; $\tau_{0,eq,S}$=0.260MPa; $H_{p,eq,S}$=70.0kN
Axial stress:	0.1 MPa	0.3 MPa	0.5 MPa
Capacity curve:			
	d [mm] *F* [kN] 0.00 0.0 0.20 25.3 0.96 121.0 1.28 147.1 25.4 147.2 25.5 112.7 33.0 112.7 33.1 86.7 49.7 86.7 49.8 0.0	*d* [mm] *F* [kN] 0.00 0.0 0.20 25.3 1.24 155.8 1.68 179.4 25.5 179.6 25.6 136.1 33.0 136.1 33.2 102.5 49.6 102.5 49.7 0.0	*d* [mm] *F* [kN] 0.00 0.0 0.20 25.3 1.32 166.5 2.04 206.7 25.6 206.8 25.7 155.0 33.0 155.0 33.1 115.9 49.6 115.9 49.7 0.0
Yield point:	0.96 mm 121.0 kN	1.24 mm 155.8 kN	1.32 mm 166.5 kN
Maximum resistance:	25.4 mm 147.2 kN	25.5 mm 179.6 kN	25.6 mm 206.8 kN
Collapse:	33.0 mm 112.7 kN	33.0 mm 195.9 kN	33.0 mm 155.0 kN
Failure mode:	Bending in P2 (base then top), later contemporary bending in P1 and P3 (base) and bending in S1 (left) and S2 (right). Failure of P2 (top and base), then failure of P1 and P3 (base) and lastly bending failure of S1 (left) and S2 (right).	Bending in P2 (base then top), later bending in S1 (left) and S2 (right) and later bending in P1 and P3 (base). Failure of P2 (top and base), then failure of P1 and P3 (base) and lastly bending failure of S1 (left) and S2 (right).	Bending in S1 (left) and S2 (right), later bending in P2 (base then top) and lastly bending in P1 and P3 (base). Failure of P2 (top and base), then failure of P1 and P3 (base) and lastly bending failure of S1 (left) and S2 (right).

- **Single-story wall h3.85_1a**

ID:	Singlestorywall_h3.85_1a_01	Singlestorywall_h3.85_1a_03	Singlestorywall_h3.85_1a_05
Axial stress:	0.1 MPa	0.3 MPa	0.5 MPa
Capacity curve:			
	d [mm] *F* [kN] 0.00 0.0 0.20 34.9 0.86 150.7 1.18 194.9 1.44 222.8 1.82 232.3 2.78 235.3 6.56 235.4 6.58 214.4 6.84 214.5 6.86 193.5 15.1 193.5 15.2 130.8 31.0 130.8 31.1 42.9 31.3 42.9 31.3 0.0	*d* [mm] *F* [kN] 0.00 0.0 0.20 34.9 1.68 295.8 1.7 298.7 2.08 344.9 2.52 380.4 2.78 391.0 5.92 391.1 5.94 370.1 6.00 370.1 6.02 349.2 14.8 349.3 14.9 286.5 31.0 286.7 31.1 95.7 31.3 95.7 31.3 0.0	*d* [mm] *F* [kN] 0.00 0.0 0.20 34.9 1.68 295.8 1.7 298.7 3.26 489.0 3.64 519.3 3.84 527.0 6.08 527.1 6.16 485.1 15.0 485.3 15.0 422.5 31.0 422.8 31.1 140.5 31.3 140.5 31.3 0.0
Yield point:	0.86 mm 150.7 kN	1.68 mm 295.8 kN	1.68 mm 295.8 kN
R_{max}:	6.56 mm 235.4 kN	5.92 mm 391.1 kN	6.08 mm 527.1 kN
Collapse:	31.0 mm 130.8 kN	31.0 mm 286.7 kN	31.0 mm 422.8 kN
Failure mode:	Bending in P1 (base), then bending in P2 (base) followed by contemporary bending of P1 and P2 (top) and P3 (base). Then diagonal cracking in S2, followed by diagonal cracking in S1. Failure of S1 and S2. Later, failure in P1 (base), then P3 (base) and lastly P2 (base).	Diagonal cracking in S1 and S2, then bending in P1 (base) followed by P2 and P3 (base). Failure of S1 and S2, then bending failure of P1 and P3 and finally in P2 (base).	Diagonal cracking in S1 and S2, then bending in P1 (base) followed by P2 and P3 (base). Failure of S1 and S2, then bending failure of P1 and P3 and finally in P2 (base).

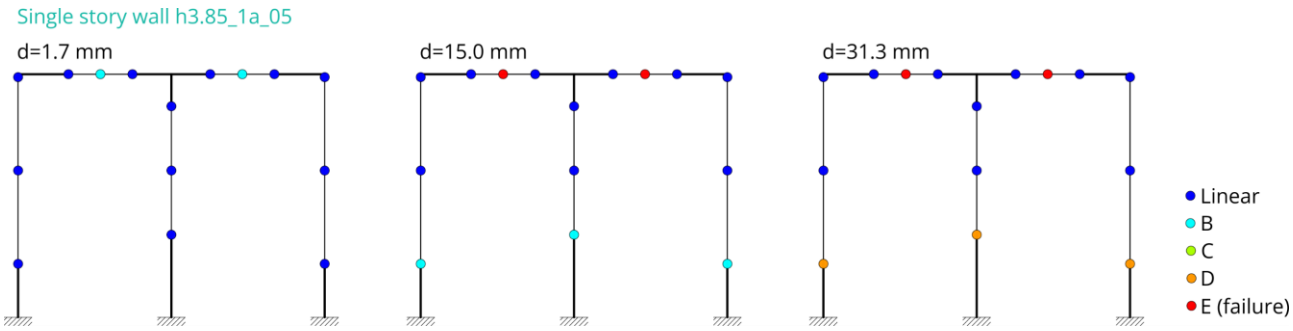
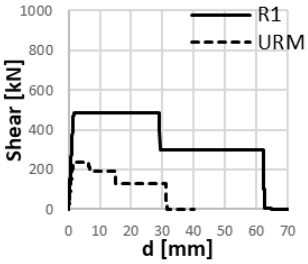
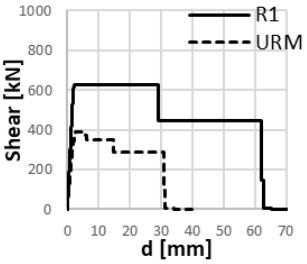
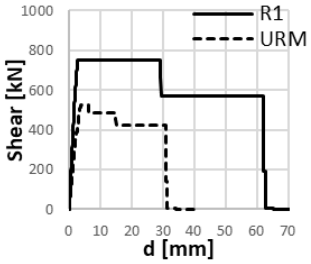
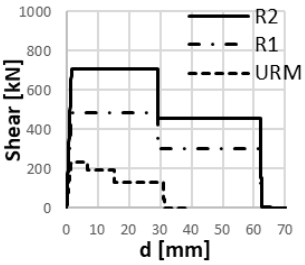
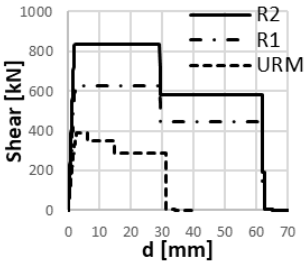
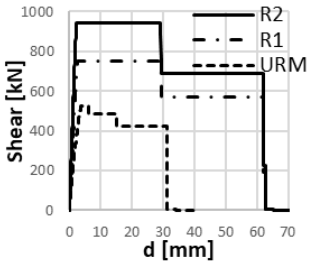


Figure 0.5 Failure mechanism of single-story wall h3.85_1a_05

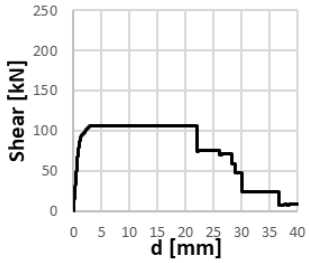
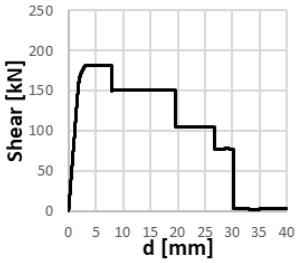
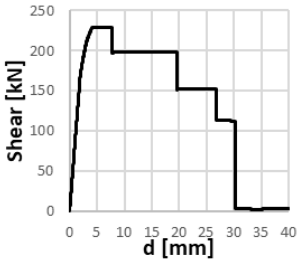
- **Single-story wall h3.85_1a_R1**

ID:	Singlestorywall_h3.85_1a_01_R1	Singlestorywall_h3.85_1a_01_R1	Singlestorywall_h3.85_1a_01_R1
Masonry properties:	$\tau_{0,eq,P1,P3}$=0.198MPa; $H_{p,eq,P1,P3}$=221.3kN; $\tau_{0,eq,P2}$=0.198MPa; $H_{p,eq,P2}$=220.3kN; $\tau_{0,eq,S}$=0.157MPa; $H_{p,eq,S}$=97.7kN	$\tau_{0,eq,P1,P3}$=0.189MPa; $H_{p,eq,P1,P3}$=328.3kN; $\tau_{0,eq,P2}$=0.189MPa; $H_{p,eq,P2}$=325.1kN; $\tau_{0,eq,S}$=0.157MPa; $H_{p,eq,S}$=97.7kN	$\tau_{0,eq,P1,P3}$=0.181MPa; $H_{p,eq,P1,P3}$=419.8kN; $\tau_{0,eq,P2}$=0.181MPa; $H_{p,eq,P2}$=414.6kN; $\tau_{0,eq,S}$=0.157MPa; $H_{p,eq,S}$=97.7kN
Axial stress:	0.1 MPa	0.3 MPa	0.5 MPa
Capacity curve:			
	d [mm] *F* [kN] 0.00 0.0 0.20 62.1 1.44 450.5 1.72 483.9 29.1 484.2 29.2 301.8 62.1 301.8 62.2 100.6 62.6 100.6 62.7 0.0	*d* [mm] *F* [kN] 0.00 0.0 0.20 62.1 1.72 537.2 2.20 628.8 29.2 629.2 29.3 446.9 62.1 446.9 62.2 148.4 62.6 148.4 62.7 0.0	*d* [mm] *F* [kN] 0.00 0.0 0.20 62.1 1.72 537.2 2.76 752.6 29.2 753.1 29.3 570.8 62.1 570.8 62.2 189.3 62.6 189.3 62.7 0.0
Yield point:	1.44 mm 450.5 kN	1.72 mm 537.2 kN	1.72 mm 537.2 kN
R_{max}:	29.1 mm 484.2 kN	29.2 mm 629.2 kN	29.2 mm 753.1 kN
Collapse:	62.1 mm 301.8 kN	62.1 mm 446.9 kN	62.1 mm 540.8 kN
Failure mode:	Bending in S1 (left) and S2 (right), then bending in P1 and P3 (base) and soon after in P2 (base). Lastly bending in S1 (right) and S2 (left). Bending failure of S1 and S2, then failure of P1 and P3 (base) and lastly of P2 (base).	Bending in S1 (left) and S2 (right), then bending in S1 (right) and S2 (left). Later bending in P1 and P3 (base) and soon after in P2 (base). Bending failure of S1 and S2, then failure of P1 and P3 (base) and lastly of P2 (base).	Bending in S1 (left) and S2 (right), then bending in S1 (right) and S2 (left). Later bending in P1 and P3 (base) and soon after in P2 (base). Bending failure of S1 and S2, then failure of P1 and P3 (base) and lastly of P2 (base).

- **Single-story wall h3.85_1a_R2**

ID:	Singlestorywall_h3.85_1a_01_R2	Singlestorywall_h3.85_1a_01_R2	Singlestorywall_h3.85_1a_01_R2
Masonry properties:	$\tau_{0,eq,P1,P3}$=0.305MPa; $H_{p,eq,P1,P3}$=336.2kN; $\tau_{0,eq,P2}$=0.306MPa; $H_{p,eq,P2}$=333.3kN; $\tau_{0,eq,S}$=0.260MPa; $H_{p,eq,S}$=97.7kN	$\tau_{0,eq,P1,P3}$=0.292MPa; $H_{p,eq,P1,P3}$=428.8kN; $\tau_{0,eq,P2}$=0.293MPa; $H_{p,eq,P2}$=423.9kN; $\tau_{0,eq,S}$=0.260MPa; $H_{p,eq,S}$=97.7kN	$\tau_{0,eq,P1,P3}$=0.279MPa; $H_{p,eq,P1,P3}$=506.9kN; $\tau_{0,eq,P2}$=0.280MPa; $H_{p,eq,P2}$=500.2kN; $\tau_{0,eq,S}$=0.260MPa; $H_{p,eq,S}$=97.7kN
Axial stress:	0.1 MPa	0.3 MPa	0.5 MPa
Capacity curve:			
	d [mm] *F* [kN] 0.00 0.0 0.20 88.7 1.44 641.0 1.80 709.4 29.1 709.8 29.2 457.7 62.1 457.7 62.2 152.1 62.6 152.1 62.7 0.0	*d* [mm] *F* [kN] 0.00 0.0 0.20 88.7 1.44 641.0 2.00 834.7 29.2 835.2 29.3 582.2 62.1 583.2 62.2 193.4 62.6 193.4 62.7 0.0	*d* [mm] *F* [kN] 0.00 0.0 0.20 88.7 1.44 641.0 2.32 940.3 29.2 940.9 29.4 688.9 62.1 688.9 62.2 228.2 62.6 228.2 62.7 0.0
Yield point:	1.44 mm 641.0 kN	1.44 mm 641.0 kN	1.44 mm 641.0 kN
R_{max}:	29.1 mm 709.8 kN	29.2 mm 835.2 kN	29.2 mm 940.9 kN
Collapse:	62.1 mm 457.7 kN	62.1 mm 583.2 kN	62.1 mm 688.9 kN
Failure mode:	Bending in S1 (left) and S2 (right), then bending in P1 and P3 (base) and soon after in P2 (base). Lastly bending in S1 (right) and S2 (left). Bending failure of S1 and S2, then failure of P1 and P3 (base) and lastly of P2 (base).	Bending in S1 (left) and S2 (right), then bending in S1 (right) and S2 (left). Later bending in P1 and P3 (base) and soon after in P2 (base). Bending failure of S1 and S2, then failure of P1 and P3 (base) and lastly of P2 (base).	Bending in S1 (left) and S2 (right), then bending in S1 (right) and S2 (left). Later bending in P1 and P3 (base) and soon after in P2 (base). Bending failure of S1 and S2, then failure of P1 and P3 (base) and lastly of P2 (base).

- **Single-story wall h3.85_1b**

ID:	Singlestorywall_h3.85_1b_01	Singlestorywall_h3.85_1b_03	Singlestorywall_h3.85_1b_05
Axial stress:	0.1 MPa	0.3 MPa	0.5 MPa
Capacity curve:			
	d [mm] *F* [kN] 0.00 0.0 0.20 17.3 0.78 67.9 1.06 83.5 1.44 94.4 3.04 106.4 3.30 106.6 22.1 106.7 22.1 74.6 26.0 75.8 26.1 70.4 28.1 71.1 28.2 58.1 28.9 58.1 28.9 46.9	*d* [mm] *F* [kN] 0.00 0.0 0.20 17.3 1.82 159.1 2.06 167.1 2.1 168.0 2.42 173.6 2.98 181.6 7.94 181.7 8.00 150.0 19.6 151.3 19.7 104.3 26.7 105.1 26.7 77.4 30.2 77.4 30.2 0.0	*d* [mm] *F* [kN] 0.00 0.0 0.20 17.3 1.94 169.9 1.96 170.8 2.54 193.8 3.1 211.9 4.02 228.1 4.1 229.2 7.8 229.3 7.9 198.0 19.54 198.9 19.7 152.3 26.7 152.8 26.72 112.6 30.18 112.4
Yield point:	0.78 mm 69.7 kN	1.82 mm 159.1 kN	1.94 mm 169.9 kN
R_{max}:	22.1 mm 106.7 kN	7.84 mm 181.7 kN	7.80 mm 229.3 kN
Collapse:	28.1 mm 71.1 kN	26.7 mm 105.1 kN	26.7 mm 152.8 kN
Failure mode:	Bending in P1 and P2 (base), then bending in P2 (top) followed by bending in P1 (top) and later inP3 (base); lastly bending of S2 (right) and diagonal cracking of S2. Bending failure of P2 (top), followed by P2 (base), later failure of the following bending hinges in order: P1 (base and top), P3 (base), S2 (right).	Contemporary bending of P1 (base) and diagonal cracking (DC) in P2, then contemporary DC in S1 and S2, followed by bending of P2 and P3 (base). Failure of S1 and S2, then bending failure of P2 (base) and lastly contemporary failure of P1 and P3 (base).	Diagonal cracking (DC) in S1 and S2 and then in P2, followed by bending of P1 (base), and later bending in P2 and P3 (base). Failure of S1 and S2, then bending failure of P2 (base) and lastly contemporary failure of P1 and P3 (base).

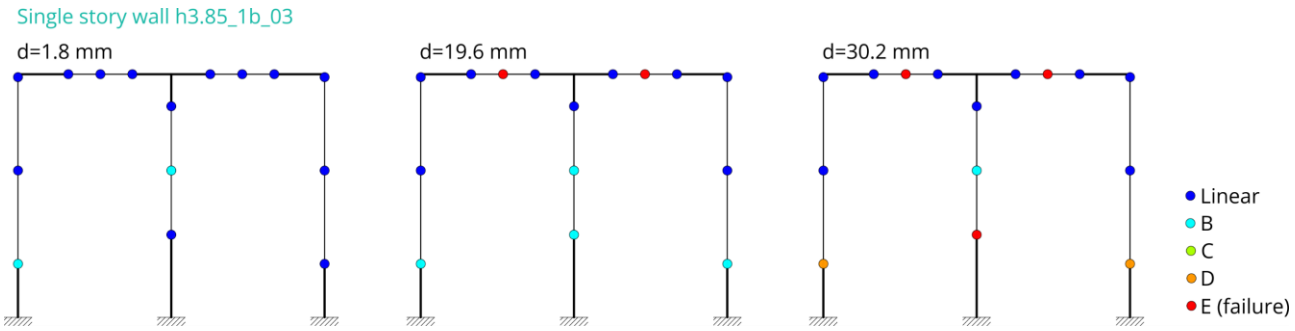


Figure 0.6 Failure mechanism of single-story wall h3.85_1b_03

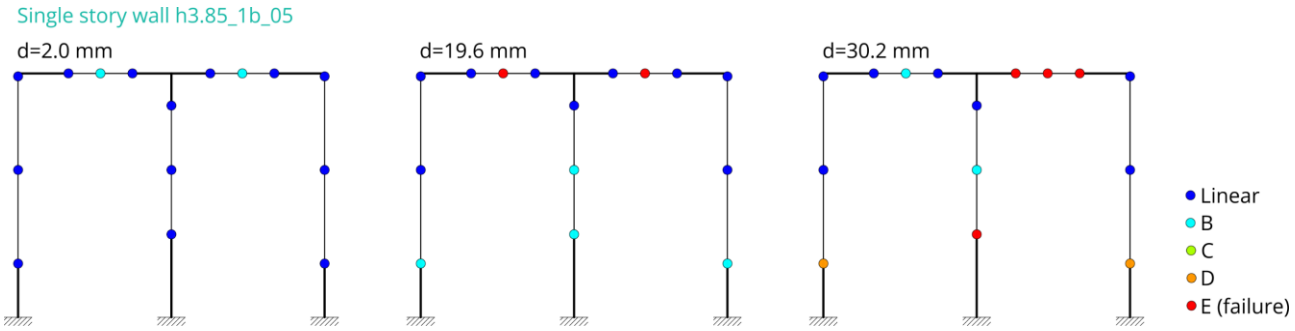
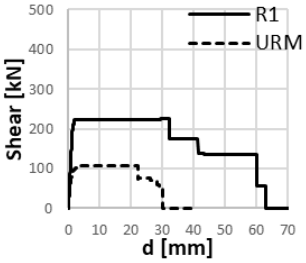
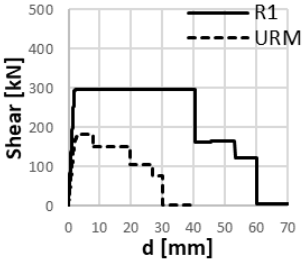
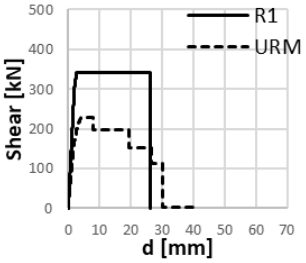
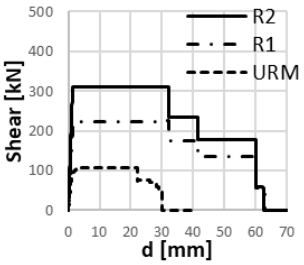
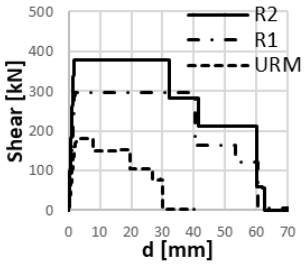
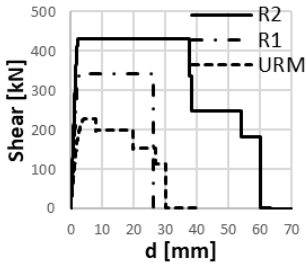


Figure 0.7 Failure mechanism of single-story wall h3.85_1b_05

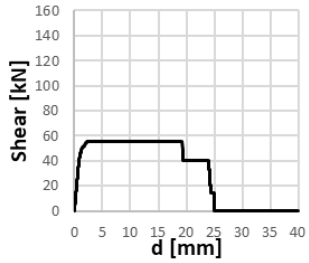
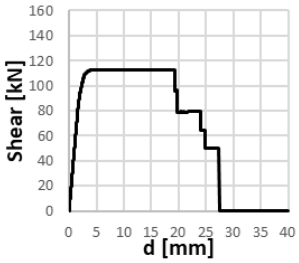
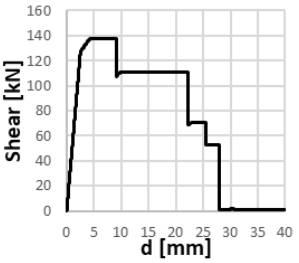
- **Single-story wall h3.85_1b_R1**

ID:	Singlestorywall_h3.85_1b_01_R1	Singlestorywall_h3.85_1b_01_R1	Singlestorywall_h3.85_1b_01_R1
Masonry properties:	$\tau_{0,eq,P1,P3}$=0.241MPa; $H_{p,eq,P1,P3}$=137.0kN; $\tau_{0,eq,P2}$=0.240MPa; $H_{p,eq,P2}$=112.0kN; $\tau_{0,eq,S}$=0.157MPa; $H_{p,eq,S}$=97.7kN	$\tau_{0,eq,P1,P3}$=0.230MPa; $H_{p,eq,P1,P3}$=202.6kN; $\tau_{0,eq,P2}$=0.229MPa; $H_{p,eq,P2}$=164.1kN; $\tau_{0,eq,S}$=0.157MPa; $H_{p,eq,S}$=97.7kN	$\tau_{0,eq,P1,P3}$=0.219MPa; $H_{p,eq,P1,P3}$=258.6kN; $\tau_{0,eq,P2}$=0.219MPa; $H_{p,eq,P2}$=208.6kN; $\tau_{0,eq,S}$=0.157MPa; $H_{p,eq,S}$=97.7kN
Axial stress:	0.1 MPa	0.3 MPa	0.5 MPa
Capacity curve:			
	d [mm] *F* [kN] 0.00 0.0 0.20 31.1 1.12 174.2 2.12 224.3 32.1 224.4 32.2 174.5 41.3 174.5 41.4 136.6 60.1 136.6 60.2 56.9 62.9 56.9 63.0 0.0	*d* [mm] *F* [kN] 0.00 0.0 0.20 31.1 1.60 250.3 2.20 297.0 40.3 297.3 40.4 162.5 53.1 164.5 53.2 121.6 60.2 121.6 60.3 0.0	*d* [mm] *F* [kN] 0.00 0.0 0.20 31.1 1.92 299.5 2.68 341.1 26.2 342.7 26.3 0.0
Yield point:	1.12 mm 174.2 kN	1.60 mm 250.3 kN	1.92 mm 299.5 kN
R_{max}:	32.1 mm 224.4 kN	40.3 mm 297.3 kN	26.2 mm 342.7 kN
Collapse:	41.3 mm 174.5 kN	53.1 mm 164.5 kN	26.2 mm 342.7 kN
Failure mode:	Bending in P2 (base), then bending in P2 (top) and P1, P3 (base) and later bending in S1 (left) and S2 (right), Failure of P2 (top then base). Later failure of P1 and P3 (base) and lastly of S1 (left) and S2 (right).	Diagonal cracking in S1 and S2. Then bending in P2 (base) and later in P1, P3 (base). Lastly, bending in P2 (top). Diagonal cracking failure of S1 and S2, then bending failure of P2 (base) and lastly of P1 and P3 (base).	Diagonal cracking in S1 and S2. Then bending in P2 (base) and later in P1, P3 (base). Lastly, diagonal cracking in P2. Diagonal cracking failure of P2 and total collapse.

- **Single-story wall h3.85_1b_R2**

ID:	Singlestorywall_h3.85_1b_01_R2	Singlestorywall_h3.85_1b_01_R2	Singlestorywall_h3.85_1b_01_R2
Masonry properties:	$\tau_{0,eq,P1,P3}$=0.392MPa; $H_{p,eq,P1,P3}$=207.4kN; $\tau_{0,eq,P2}$=0.391MPa; $H_{p,eq,P2}$=168.4kN; $\tau_{0,eq,S}$=0.260MPa; $H_{p,eq,S}$=97.7kN	$\tau_{0,eq,P1,P3}$=0.377MPa; $H_{p,eq,P1,P3}$=264.2kN; $\tau_{0,eq,P2}$=0.375MPa; $H_{p,eq,P2}$=213.4kN; $\tau_{0,eq,S}$=0.260MPa; $H_{p,eq,S}$=97.7kN	$\tau_{0,eq,P1,P3}$=0.360MPa; $H_{p,eq,P1,P3}$=312.0kN; $\tau_{0,eq,P2}$=0.359MPa; $H_{p,eq,P2}$=251.3kN; $\tau_{0,eq,S}$=0.260MPa; $H_{p,eq,S}$=97.7kN
Axial stress:	0.1 MPa	0.3 MPa	0.5 MPa
Capacity curve:			
	d [mm] *F* [kN] 0.00 0.0 0.20 44.7 1.16 259.2 1.52 309.4 32.0 309.6 32.1 234.5 41.3 234.5 41.4 177.5 60.1 177.5 60.2 56.9 62.6 56.9 62.7 0.0	*d* [mm] *F* [kN] 0.00 0.0 0.20 44.7 1.44 323.2 1.88 377.6 32.1 377.9 32.2 282.8 41.3 282.8 41.4 210.5 60.1 210.5 60.2 56.9 62.6 56.9 62.7 0.0	*d* [mm] *F* [kN] 0.00 0.0 0.20 44.7 1.44 323.2 2.28 430.1 37.6 430.4 37.7 336.7 38.3 336.7 38.4 247.5 53.9 247.5 54.0 181.9 60.2 181.9 60.3 0.0
Yield point:	1.16 mm 259.2 kN	1.44 mm 323.2 kN	1.44 mm 323.2 kN
R_{max}:	25.4 mm 309.6 kN	32.1 mm 377.9 kN	37.6 mm 430.4 kN
Collapse:	41.3 mm 234.5 kN	41.3 mm 282.8 kN	38.3 mm 336.7 kN
Failure mode:	Bending in P2 (base), then bending P2 (top). Later bending in S1 (left) and S2 (right) and bending in P1, P3 (base). Failure of P2 (top and later base). Later failure of P1 and P3 (base) and lastly of S1 (left) and S2 (right).	Bending in P2 (base), then bending in S1 (left) and S2 (right). Later bending in P1, P3 (base) and lastly in P2 (top). Failure of P2 (top and later base). Later failure of P1 and P3 (base) and lastly of S1 (left) and S2 (right).	Bending in S1 (left) and S2 (right), then bending in P2 (base) and later in S1 (right) and S2 (left). Lastly, bending in P1 and P3 (base). Bending failure of S1 and S2, then failure of P2 (base) and lastly of P1 and P3 (base).

- **Single-story wall h3.85_1c**

ID:	Singlestorywall_h3.85_1c_01	Singlestorywall_h3.85_1c_03	Singlestorywall_h3.85_1c_05
Axial stress:	0.1 MPa	0.3 MPa	0.5 MPa
Capacity curve:			
	d [mm] *F* [kN] 0.00 0.0 0.20 10.0 0.74 37.0 0.82 40.0 0.96 43.9 1.06 45.9 1.36 50.4 2.38 55.5 19.3 55.5 19.3 47.9 19.5 47.9 19.5 40.3 24.0 40.1 24.1 20.4 24.4 20.5 24.4 14.6	*d* [mm] *F* [kN] 0.00 0.0 0.20 10.0 1.68 84.4 1.72 85.9 2.04 94.8 2.38 102.0 2.86 109.2 3.90 112.7 19.4 112.8 19.4 96.0 19.6 96.3 19.7 78.9 24.1 79.7 24.1 64.1 24.8 64.3 24.8 49.7	*d* [mm] *F* [kN] 0.00 0.0 0.20 10.0 2.48 124.8 2.52 126.3 2.56 127.3 2.6 127.8 4.16 137.3 9.08 137.5 9.10 107.2 9.74 110.5 22.1 111.0 22.2 68.4 23.1 70.7 25.4 70.8 25.4 52.5 27.9 52.4 27.9 0.0
Yield point:	0.74 mm 37.0 kN	1.68 mm 84.4 kN	2.48 mm 124.8 kN
R_{max}:	19.3 mm 55.5 kN	19.4 mm 112.8 kN	9.08 mm 137.5 kN
Collapse:	24.0 mm 40.1kN	24.1 mm 79.7 kN	22.1 mm 111.0 kN
Failure mode:	Bending in P1 and P2 (base), later bending in P1 and P2 (top), then in P3 (base) and lastly in P3 (top). Failure of P2 (base + top), then bending failure of P3 (top), closely followed by contemporary failure of P1 (base + top) and P3 (base).	Contemporary bending in P1 and P2 (base), followed in order by: P2 (top), P1 (top), P3 (base), then diagonal cracking in S2 and bending is S2 (right). Bending failure of P2 (top), followed by P2 (base), later failure of the following bending hinges in order: P1 (base and top), P3 (base), S2 (diag. cracking).	Bending in P2 and P1 (base) and diagonal cracking in S2 and S1, then bending in P3 (base) and later DC in P2. Contemporary failure of S1 and S2, then failure of P2 (base) and finally contemporary bending failure of P1 and P3 (base).

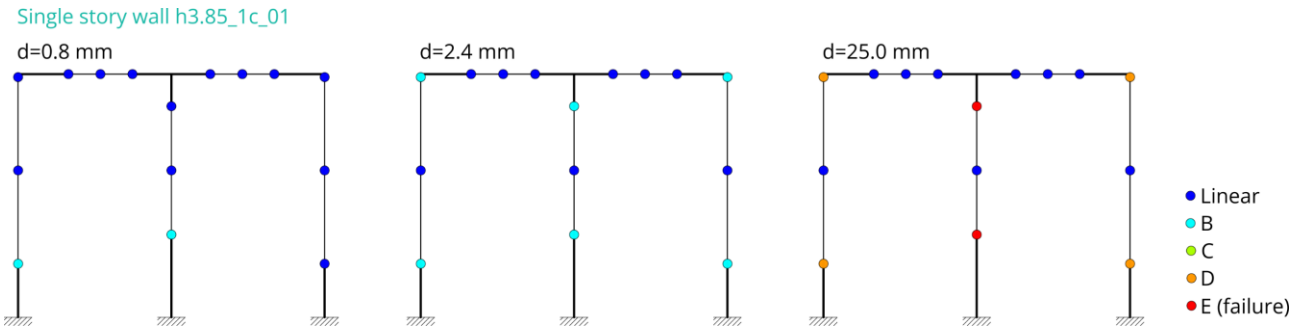


Figure 0.8 Failure mechanism of single-story wall h3.85_1c_01

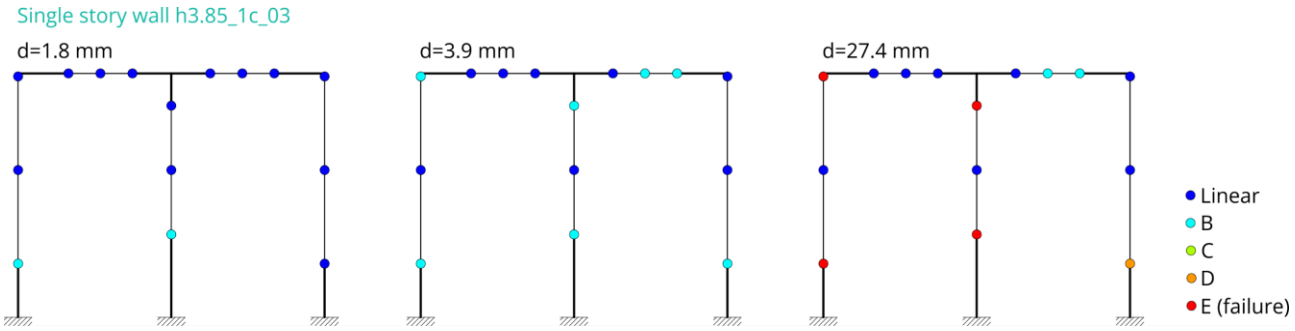


Figure 0.9 Failure mechanism of single-story wall h3.85_1c_03

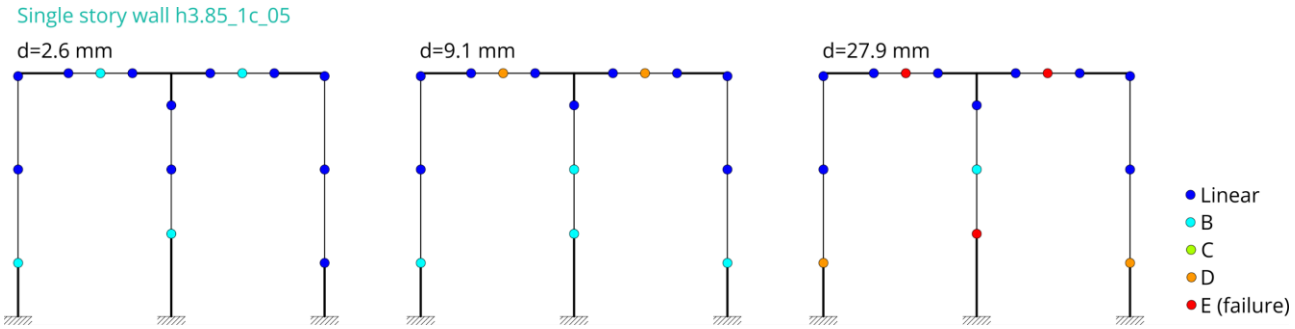
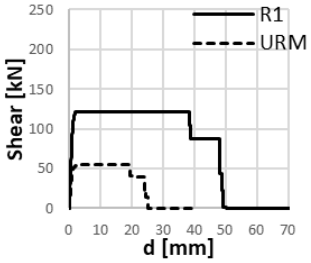
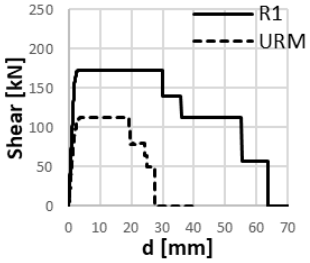
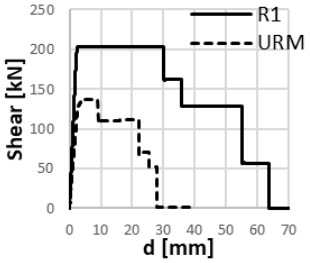
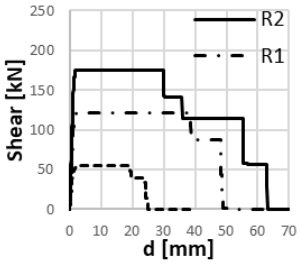
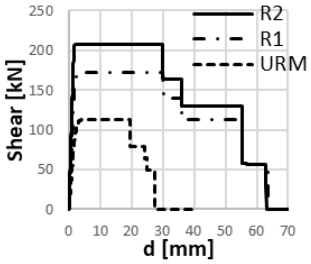
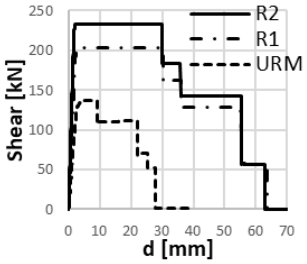


Figure 0.10 Failure mechanism of single-story wall h3.85_1c_05

- **Single-story wall h3.85_1c_R1**

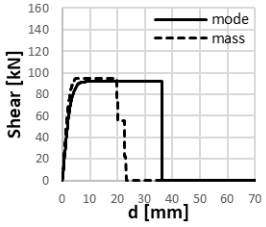
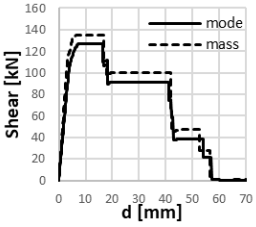
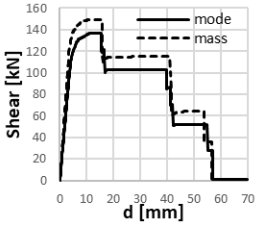
ID:	Singlestorywall_h3.85_1c_01_R1	Singlestorywall_h3.85_1c_01_R1	Singlestorywall_h3.85_1c_01_R1
Masonry properties:	$\tau_{0,eq,P1,P3}$=0.240MPa; $H_{p,eq,P1,P3}$=91.0kN; $\tau_{0,eq,P2}$=0.240MPa; $H_{p,eq,P2}$=73.5kN; $\tau_{0,eq,S}$=0.157MPa; $H_{p,eq,S}$=97.7kN	$\tau_{0,eq,P1,P3}$=0.230MPa; $H_{p,eq,P1,P3}$=134.0kN; $\tau_{0,eq,P2}$=0.229MPa; $H_{p,eq,P2}$=106.8kN; $\tau_{0,eq,S}$=0.157MPa; $H_{p,eq,S}$=97.7kN	$\tau_{0,eq,P1,P3}$=0.219MPa; $H_{p,eq,P1,P3}$=170.7kN; $\tau_{0,eq,P2}$=0.218MPa; $H_{p,eq,P2}$=135.2kN; $\tau_{0,eq,S}$=0.157MPa; $H_{p,eq,S}$=97.7kN
Axial stress:	0.1 MPa	0.3 MPa	0.5 MPa
Capacity curve:			
	d [mm] *F* [kN] 0.00 0.0 0.20 18.0 1.00 90.2 2.08 121.7 38.5 121.8 38.7 87.4 48.0 87.4 48.1 44.1 48.6 44.1 48.7 22.5 49.0 22.5 49.1 0.0	*d* [mm] *F* [kN] 0.00 0.0 0.20 18.0 1.48 133.0 2.64 172.2 30.0 172.6 30.2 139.7 35.8 139.7 35.9 112.8 55.2 112.8 55.3 57.1 63.6 57.1 63.7 0.0	*d* [mm] *F* [kN] 0.00 0.0 0.20 18.0 1.84 166.0 2.60 203.6 30.2 203.7 30.3 162.0 35.8 162.0 35.9 128.0 55.2 128.0 55.3 57.1 63.6 57.1 63.7 0.0
Yield point:	1.00 mm 90.2 kN	1.48 mm 133.0 kN	1.84 mm 166.0 kN
R_{max}:	38.5 mm 121.8 kN	30.0 mm 172.6 kN	30.2 mm 203.7 kN
Collapse:	48.0 mm 87.4 kN	35.8 mm 139.7 kN	35.8 mm 162.0 kN
Failure mode:	Bending in P2 (base then top), then bending in P1 and P3 (base). Lastly, bending in P1 and P3 (top). Bending failure of P2 (base and top), later bending failure of P1 and P3 (base) and lastly of P1 and P3 (top).	Bending in P2 (base then top), then bending in P1 and P3 (base). Lastly, bending in S1 (left) and S2 (right). Failure of P2 (top) and later P2 (base). Failure of P1 and P3 (base) and lastly bending failure of S1 (left) and S2 (right).	Bending in P2 (base then top), then bending in P1 and P3 (base). Lastly, bending in S1 (left) and S2 (right). Failure of P2 (top) and later P2 (base). Failure of P1 and P3 (base) and lastly bending failure of S1 (left) and S2 (right).

- **Single-story wall h3.85_1c_R2**

ID:	Singlestorywall_h3.85_1c_01_R2	Singlestorywall_h3.85_1c_01_R2	Singlestorywall_h3.85_1c_01_R2
Masonry properties:	$\tau_{0,eq,P1,P3}$=0.391MPa; $H_{p,eq,P1,P3}$=137.2kN; $\tau_{0,eq,P2}$=0.390MPa; $H_{p,eq,P2}$=109.7kN; $\tau_{0,eq,S}$=0.260MPa; $H_{p,eq,S}$=97.7kN	$\tau_{0,eq,P1,P3}$=0.376MPa; $H_{p,eq,P1,P3}$=174.3kN; $\tau_{0,eq,P2}$=0.374MPa; $H_{p,eq,P2}$=138.5kN; $\tau_{0,eq,S}$=0.260MPa; $H_{p,eq,S}$=97.7kN	$\tau_{0,eq,P1,P3}$=0.360MPa; $H_{p,eq,P1,P3}$=205.6kN; $\tau_{0,eq,P2}$=0.358MPa; $H_{p,eq,P2}$=162.6kN; $\tau_{0,eq,S}$=0.260MPa; $H_{p,eq,S}$=97.7kN
Axial stress:	0.1 MPa	0.3 MPa	0.5 MPa
Capacity curve:			
	d [mm] *F* [kN] 0.00 0.0 0.20 25.9 1.04 134.9 1.88 175.4 29.8 175.5 29.9 141.7 35.8 141.7 35.9 114.1 55.2 114.1 55.3 57.1 63.0 57.1 63.1 0.0	*d* [mm] *F* [kN] 0.00 0.0 0.20 25.9 1.32 171.0 1.8 206.9 29.9 207.1 30.0 164.4 35.8 164.4 35.9 129.5 55.3 129.5 55.4 57.1 63.0 57.1 63.1 0.0	*d* [mm] *F* [kN] 0.00 0.0 0.20 25.9 1.56 201.8 2.12 233.4 29.9 233.5 30.0 183.4 35.8 183.4 35.9 142.5 55.3 142.5 55.4 57.1 63.0 57.1 63.1 0.0
Yield point:	1.04 mm 134.9 kN	1.32 mm 171.0 kN	1.56 mm 201.8 kN
R_{max}:	29.8 mm 175.5 kN	29.9 mm 207.1 kN	29.9 mm 233.5 kN
Collapse:	35.8 mm 141.7 kN	35.8 mm 164.4 kN	35.8 mm 183.4 kN
Failure mode:	Bending in P2 (base), then bending P2 (top). Later bending in P1, P3 (base) and lastly in S1 (left) and S2 (right). Failure of P2 (top and later base). Later failure of P1 and P3 (base) and lastly of S1 (left) and S2 (right).	Bending in P2 (base), then bending P2 (top). Later bending in P1, P3 (base) and in S1 (left) and S2 (right). Failure of P2 (top and later base). Later failure of P1 and P3 (base) and lastly of S1 (left) and S2 (right).	Bending in P2 (base), then bending P2 (top) and in S1 (left) and S2 (right). Later bending in P1, P3 (base). Failure of P2 (top and later base). Later failure of P1 and P3 (base) and lastly of S1 (left) and S2 (right).

Simplified numerical analyses on two-story walls

- **Two-story wall h6_a**

ID:	Two-storywall_h6_a_01	Two-storywall_h6_a_03	Two-storywall_h6_a_05
Axial stress:	0.1 MPa	0.3 MPa	0.5 MPa
Capacity curve:			
Yield point:	1.50 mm 41.2 kN	2.80 mm 77.1 kN	3.90 mm 107.1 kN
R_{max}:	36.2 mm 92.1 kN	16.4 mm 126.7 kN	15.4 mm 137.1 kN
Collapse:	36.2 mm 92.1 kN	41.0 mm 91.4 kN	39.8 mm 103.0 kN
Failure mode (mode):	Bending in P1 (base), then in order: P1 (top), P2 (base), P4 (base and top), P2 (top), P5 (base and top), P3 (base). Diagonal cracking (DC) in S2 and later in S4. Finally bending in S2 (right) and later in S4 (right). Complete frame failure (not converging).	Bending (B) in P1 (base), then in order: P1 (top), diagonal cracking (DC) in S2, B in P2 (base), DC in P2, S4, S, B in P3 (base) and finally DC in S1. Contemporary DC failure of S2, S3 and S4, then DC failure of S1. Later failure of P2 (base) and lastly of P3, P1 (base).	Diagonal cracking (DC) in S2 then in order: bending (B) in P1 (base), DC in S1, S4, P2, S3, B in P2 and P3 (base). Contemporary DC failure of S3 and S4, then failure of S2 and S1 and later B failure of P2 (base), followed by contemporary B failure of P1 and P3 (base).

mode		mass		mode		mass		mode		mass	
d [mm]	*F* [kN]	*d* [mm]	*F* [kN]	*d* [mm]	*F* [kN]	*d* [mm]	*F* [kN]	*d* [mm]	*F* [kN]	*d* [mm]	*F* [kN]
0.00	0.0	0.00	0.0	0.00	0.0	0.00	0.0	0.00	0.0	0.00	0.0
1.50	41.2	1.4	48.9	2.80	77.1	2.6	91.4	3.90	107.1	4.80	137.2
1.90	51.2	1.8	61.2	6.00	122.2	6.2	134.4	4.50	116.6	5.00	138.4
2.20	58.3	1.9	63.6	16.4	126.7	16.7	135.2	6.90	130.7	6.70	144.4
2.30	60.1	2.6	77.7	16.5	109.9	16.8	106.3	11.4	137.1	9.20	148.8
2.90	69.7	3.3	87.1	18.1	111.3	17.8	107.8	15.4	137.1	15.7	148.9
3.30	75.3	4.7	94.8	18.2	103.9	17.9	97.4	15.5	119.6	15.8	114.7
3.40	76.3	19.8	94.9	18.3	104.2	41.9	100.3	16.6	114.0	15.9	115.0
4.00	81.2	20.0	75.0	18.4	89.6	42.0	66.3	16.7	100.4	16.0	109.6
5.40	88.9	21.1	55.6	41.0	91.4	42.3	66.7	39.8	103.0	41.0	115.0
6.90	90.9	22.4	55.4	41.1	74.5	42.4	44.7	39.9	85.2	41.1	100.5
8.50	91.7	22.6	48.6	42.0	75.3	52.6	47.7	41.2	86.9	41.3	100.8
5.90	90.4	22.7	22.6	42.1	58.2	52.7	27.4	41.3	69.9	41.4	80.4
10.4	92.1	23.0	22.6	42.7	58.8	56.6	27.4	42.0	70.7	41.5	80.6
36.2	92.1	23.1	0.3	42.8	37.3	56.7	0.7	42.1	50.9	41.6	60.5

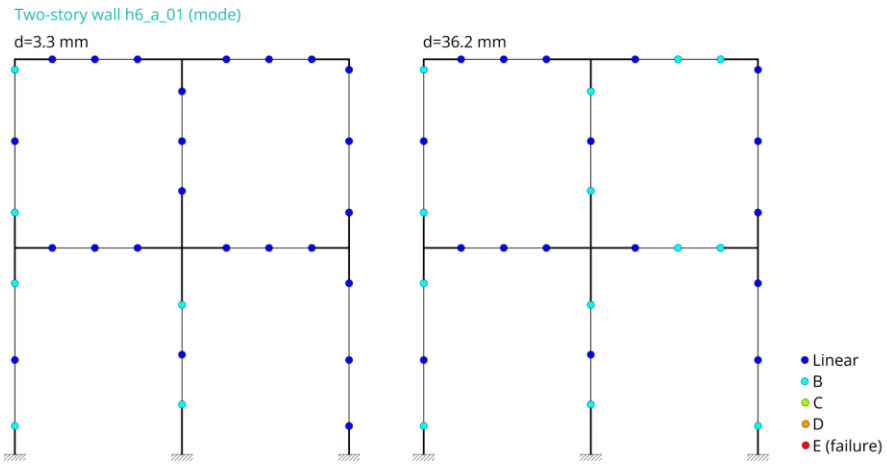


Figure 0.11 Failure mechanism of two-story wall h6_a_01

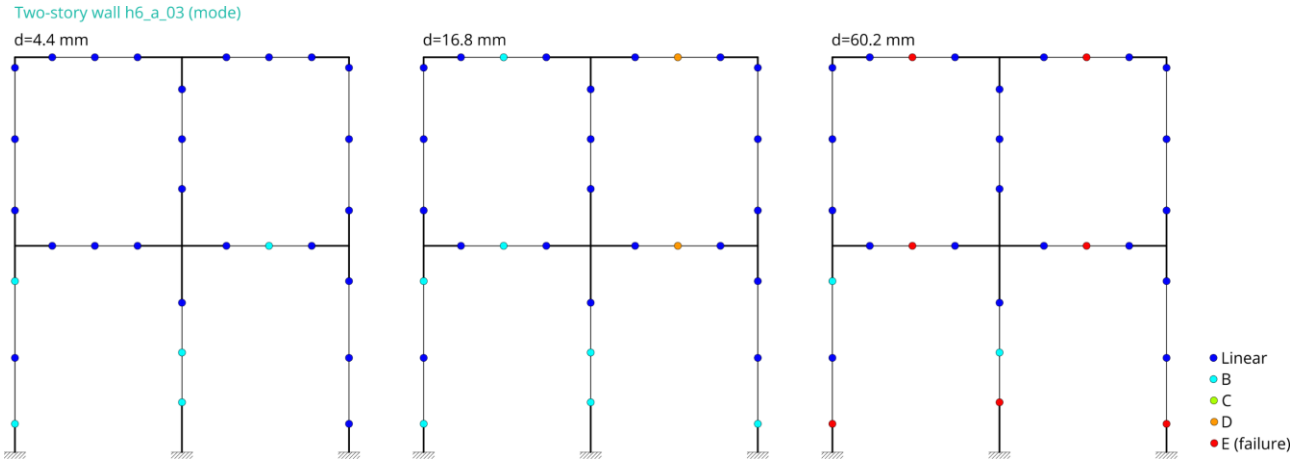


Figure 0.12 Failure mechanism of two-story wall h6_a_03

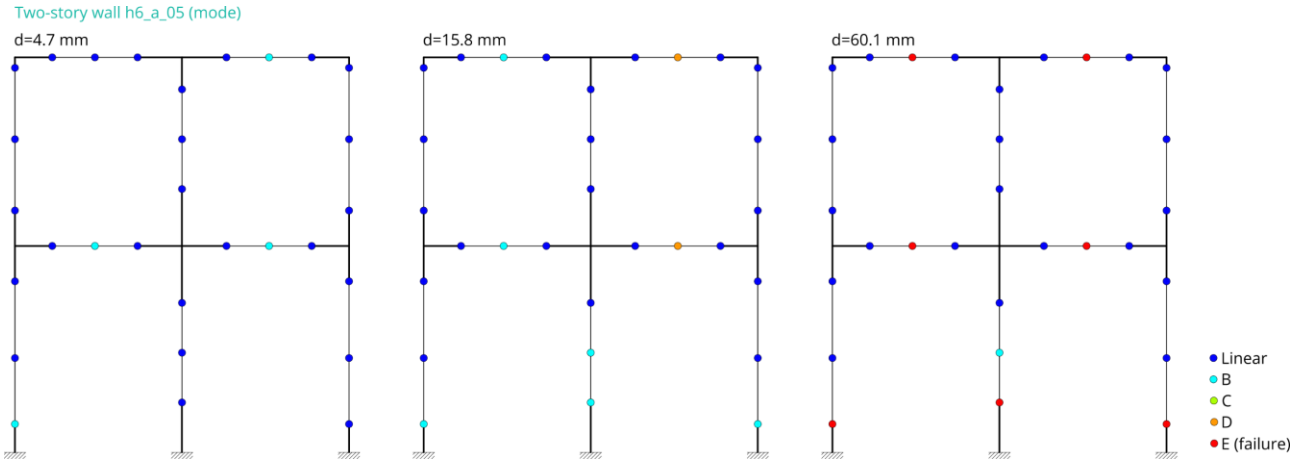
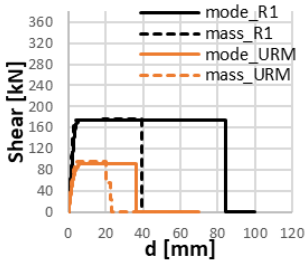
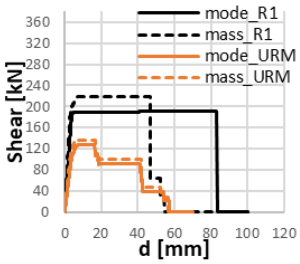
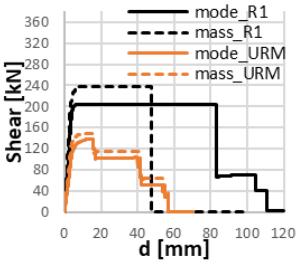


Figure 0.13 Failure mechanism of two-story wall h6_a_05

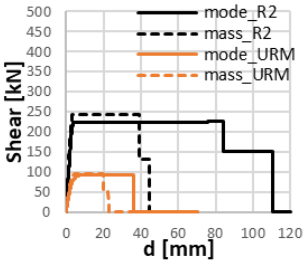
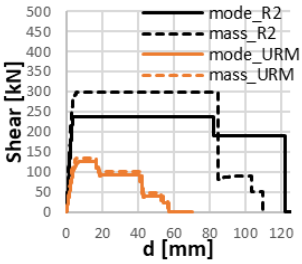
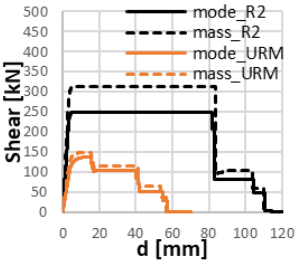
- **Two-story wall h6_a_R1**

ID:	Two-storywall_h6_a_01_R1	Two-storywall_h6_a_03_R1	Two-storywall_h6_a_05_R1

Axial stress:	0.1 MPa	0.3 MPa	0.5 MPa
Capacity curve:			
	mode: d [mm] / F [kN] 0.00 / 0.0 2.60 / 127.1 3.00 / 142.3 3.70 / 160.5 4.10 / 167.2 4.20 / 167.8 5.20 / 172.3 5.50 / 173.4 5.70 / 173.6 7.10 / 173.8 11.6 / 174.3 12.1 / 174.4 84.1 / 174.6 84.2 / 0.0 mass: d [mm] / F [kN] 0.00 / 0.0 2.20 / 136.2 2.50 / 149.9 3.10 / 168.4 3.50 / 174.5 3.70 / 175.1 39.2 / 175.2 39.3 / 0.0	mode: d [mm] / F [kN] 0.00 / 0.0 3.50 / 170.8 3.60 / 174.1 4.00 / 184.6 4.20 / 186.2 4.40 / 187.2 4.70 / 188.6 4.80 / 188.9 5.00 / 189.4 53.4 / 190.2 83.3 / 190.3 83.4 / 0.0 mass: d [mm] / F [kN] 0.00 / 0.0 2.90 / 180.0 3.20 / 194.3 3.40 / 197.1 6.80 / 218.3 7.00 / 219.2 7.10 / 219.5 46.9 / 219.7 47.0 / 64.1 52.2 / 64.1 52.3 / 32.1 54.5 / 32.1 54.6 / 0.0	mode: d [mm] / F [kN] 0.0 / 0.0 3.6 / 173.3 4.1 / 190.1 4.2 / 192.0 4.4 / 196.1 4.7 / 198.2 5.6 / 202.1 5.9 / 202.9 66.3 / 203.9 82.9 / 203.9 82.9 / 66.2 104.6 / 69.2 mass: d [mm] / F [kN] 0.0 / 0.0 3.2 / 199.1 3.3 / 200.5 3.7 / 210.0 4.5 / 223.8 4.6 / 224.3 6.6 / 236.7 6.6 / 236.9 6.8 / 237.2 47.6 / 237.5 47.7 / 0.0 0.0 / 0.0
Yield point:	2.60 mm 127.1 kN	3.50 mm 170.8 kN	3.60 mm 173.3 kN
Maximum resistance:	84.1 mm 174.6 kN	83.3 mm 190.3 kN	82.9 mm 203.9 kN
Collapse:	84.1 mm 174.6 kN	83.3 mm 190.3 kN	82.9 mm 66.2 kN
Failure mode (mode):	Bending (B) in P2 (base), then bending in P1 and P3 (base). Later in order: diagonal cracking (DC) in S2, B in P2 (top), DC in S1, B in S3 (left), B in P5 (top) and S4 right then left), B in P1 (top) and S3 (right). Complete failure at 84.1 mm.	Bending (B) in P2 (base), then diagonal cracking (DC) in S1 and S2. Then, in order: B in P1 and P3 (base), DC in P2, P4 and P3, B in S3 (left). Contemporary B failure of P1, DC failure of P2 and S4, and activation of bending in P3 (top). Lastly, B failure of P3 (base and top).	Diagonal cracking (DC) in S2 and later in S1. Bending (B) in S3 (left) and later in S4 (left). Later B in P2 (base) and in S3 and S4 (right). B in P1 and P3 (base). Later B in S1 (right) and lastly DC in P2. DC failure of S1 and S2 and B failure of S3 and S4. Later B failure of P2 (base), P1 (base) and lastly of P3 (base).

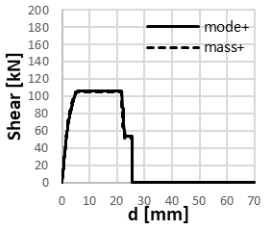
- **Two-story wall h6_a_R2**

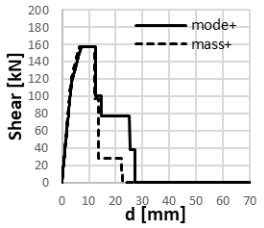
ID:	Two-storywall_h6_a_01_R2	Two-storywall_h6_a_03_R2	Two-storywall_h6_a_05_R2

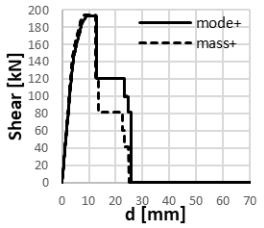
Axial stress:	0.1 MPa	0.3 MPa	0.5 MPa
Capacity curve:			
	mode: d [mm] / F [kN]; mass: d [mm] / F [kN] 0.00 / 0.0 / 0.0 / 0.0 2.50 / 175.2 / 2.1 / 186.7 2.90 / 197.2 / 2.4 / 207.1 3.20 / 206.4 / 3.3 / 241.0 3.40 / 214.5 / 3.4 / 242.5 3.60 / 218.3 / 3.5 / 243.5 3.90 / 224.6 / 39.1 / 243.5 7.50 / 224.9 / 39.2 / 188.5 83.8 / 224.9 / 39.3 / 188.5 83.9 / 149.8 / 39.4 / 132.4 110.2 / 149.8 / 44.6 / 132.4 110.2 / 0.0 / 44.6 / 0.0	mode: d [mm] / F [kN]; mass: d [mm] / F [kN] 0.00 / 0.0 / 0.0 / 0.0 2.80 / 196.6 / 2.6 / 227.1 3.10 / 213.1 / 3.3 / 267.9 3.10 / 215.7 / 3.7 / 282.5 3.20 / 217.7 / 4.1 / 287.4 3.50 / 228.3 / 5.4 / 296.4 3.80 / 237.3 / 5.7 / 297.8 3.80 / 237.7 / 84.5 / 298.0 70.6 / 238.7 / 84.6 / 89.5 82.1 / 238.7 / 103.5 / 89.5 82.2 / 191.2 / 103.6 / 50.9 122.1 / 191.2 / 109.7 / 50.9 122.1 / 0.0 / 109.8 / 0.0	mode: d [mm] / F [kN]; mass: d [mm] / F [kN] 0.00 / 0.0 / 0.0 / 0.0 2.80 / 196.6 / 2.9 / 258.9 3.10 / 216.4 / 3.2 / 279.9 3.50 / 233.5 / 3.3 / 283.0 3.60 / 239.1 / 3.5 / 293.4 3.70 / 240.6 / 3.7 / 300.7 4.90 / 248.4 / 3.7 / 301.8 5.00 / 248.6 / 4.9 / 311.8 81.5 / 249.7 / 24.4 / 312.4 83.3 / 82.1 / 83.9 / 312.4 104.6 / 82.1 / 83.9 / 103.2 104.6 / 46.9 / 103.9 / 103.2 110.8 / 46.9 / 103.9 / 58.8 110.8 / 0.0 / 110.1 / 58.8 110.2 / 0.0
Yield point:	2.50 mm 175.2 kN	2.80 mm 196.6 kN	2.80 mm 196.6 kN
R_{max}:	83.8 mm 224.9 kN	82.1 mm 238.7 kN	81.5 mm 249.7 kN
Collapse:	110.2 mm 149.8 kN	122.1 mm 191.2 kN	81.5 mm 249.7 kN
Failure mode (mode):	Bending (B) in P2 (base), then B in P1 and P3 (base) and in S3 (left). Then in order: B in S1 (left), S3 (right) and S4 (left and right), B in S2 (right), B in S1 (right) and S2 (left), B in P2 (top). Bending failure of all spandrels and P5 and P6 (base). Lastly, B failure of P4, P5 and P6.	Bending (B) in S3 (left), then B in P2 (base). Then in order: B in S3 (right) and S1 (left), B in S4 (left and right), B in S2 (right), B in S1 (right), B in S2 (left) and in P1 and P3 (base), B in P2 (top). Contemporary bending failure of S3, S4 and activation of bending in P4, P5 and P6 (base). Lastly, B failure of P4, P5 and P6 (base).	Bending (B) in S3 (left). Then, in order: contemporary B in S3 (right), S4 (left) and S1 (left), B in S2 (right), B in P2 (base)m B in S1 (right), B in P1 and P3 (base). Contemporary bending failure of S3 and S4 and activation of B in P4 and P6 (base). Later B failure of S1 and S2. Finally, B failure of P2, P1 and P3 (base).

- **Two-story wall h6_b**

ID:	Two-storywall_h6_b_01 (+)	Two-storywall_h6_b_03 (+)	Two-storywall_h6_b_05 (+)
σ:	0.1 MPa	0.3 MPa	0.5 MPa

<table>
<tr><td>Capacity curve:</td><td colspan="4"> 

<table>
<tr><th colspan="2">mode</th><th colspan="2">mass</th></tr>
<tr><th>d [mm]</th><th>F [kN]</th><th>d [mm]</th><th>F [kN]</th></tr>
<tr><td>0.00</td><td>0.0</td><td>0.00</td><td>0.0</td></tr>
<tr><td>1.30</td><td>43.8</td><td>1.30</td><td>47.4</td></tr>
<tr><td>4.60</td><td>100.9</td><td>4.30</td><td>100.9</td></tr>
<tr><td>5.50</td><td>105.4</td><td>5.10</td><td>104.7</td></tr>
<tr><td>5.60</td><td>105.8</td><td>21.5</td><td>104.8</td></tr>
<tr><td>21.8</td><td>105.9</td><td>21.6</td><td>84.6</td></tr>
<tr><td>21.9</td><td>85.9</td><td>21.9</td><td>84.6</td></tr>
<tr><td>22.2</td><td>85.9</td><td>22.0</td><td>65.4</td></tr>
<tr><td>22.3</td><td>67.1</td><td>22.3</td><td>65.4</td></tr>
<tr><td>22.5</td><td>67.1</td><td>22.4</td><td>57.7</td></tr>
<tr><td>22.6</td><td>59.6</td><td>22.7</td><td>57.7</td></tr>
<tr><td>22.8</td><td>59.6</td><td>22.8</td><td>51.5</td></tr>
<tr><td>22.9</td><td>53.9</td><td>25.4</td><td>50.9</td></tr>
<tr><td>24.7</td><td>53.3</td><td>25.5</td><td>0.0</td></tr>
<tr><td>25.6</td><td>0.0</td><td>70.0</td><td>0.0</td></tr>
<tr><td>70.0</td><td>0.0</td><td></td><td></td></tr>
</table></td><td colspan="4"> 

<table>
<tr><th colspan="2">mode</th><th colspan="2">mass</th></tr>
<tr><th>d [mm]</th><th>F [kN]</th><th>d [mm]</th><th>F [kN]</th></tr>
<tr><td>0.00</td><td>0.0</td><td>0.00</td><td>0.0</td></tr>
<tr><td>2.50</td><td>84.1</td><td>2.5</td><td>91.2</td></tr>
<tr><td>5.80</td><td>142.5</td><td>3.3</td><td>116.4</td></tr>
<tr><td>7.20</td><td>156.6</td><td>3.4</td><td>119.2</td></tr>
<tr><td>7.40</td><td>157.3</td><td>4.4</td><td>132.4</td></tr>
<tr><td>12.5</td><td>157.4</td><td>6.4</td><td>156.5</td></tr>
<tr><td>12.6</td><td>100.7</td><td>6.6</td><td>157.2</td></tr>
<tr><td>14.6</td><td>100.7</td><td>12.0</td><td>157.3</td></tr>
<tr><td>14.7</td><td>77.1</td><td>12.1</td><td>97.0</td></tr>
<tr><td>15.3</td><td>77.1</td><td>13.4</td><td>97.0</td></tr>
<tr><td>15.4</td><td>76.7</td><td>13.5</td><td>27.5</td></tr>
<tr><td>25.2</td><td>76.8</td><td>22.0</td><td>27.6</td></tr>
<tr><td>25.3</td><td>38.3</td><td>22.1</td><td>12.5</td></tr>
<tr><td>27.1</td><td>38.3</td><td>22.6</td><td>12.5</td></tr>
<tr><td>27.2</td><td>0.0</td><td>22.7</td><td>0.0</td></tr>
<tr><td>70.0</td><td>0.0</td><td>70.0</td><td>0.0</td></tr>
</table></td><td colspan="4"> 

<table>
<tr><th colspan="2">mode</th><th colspan="2">mass</th></tr>
<tr><th>d [mm]</th><th>F [kN]</th><th>d [mm]</th><th>F [kN]</th></tr>
<tr><td>0.00</td><td>0.0</td><td>0.00</td><td>0.0</td></tr>
<tr><td>3.50</td><td>121.5</td><td>3.40</td><td>127.7</td></tr>
<tr><td>4.10</td><td>139.6</td><td>4.30</td><td>153.8</td></tr>
<tr><td>4.50</td><td>148.2</td><td>4.80</td><td>160.9</td></tr>
<tr><td>7.50</td><td>185.4</td><td>7.10</td><td>189.0</td></tr>
<tr><td>9.10</td><td>192.7</td><td>8.30</td><td>194.8</td></tr>
<tr><td>12.9</td><td>192.8</td><td>12.5</td><td>122.0</td></tr>
<tr><td>13.0</td><td>120.8</td><td>13.6</td><td>122.0</td></tr>
<tr><td>13.1</td><td>120.8</td><td>13.7</td><td>81.7</td></tr>
<tr><td>23.3</td><td>120.9</td><td>22.4</td><td>81.8</td></tr>
<tr><td>23.4</td><td>100.0</td><td>22.5</td><td>60.1</td></tr>
<tr><td>23.8</td><td>100.0</td><td>22.9</td><td>60.1</td></tr>
<tr><td>23.9</td><td>99.8</td><td>23.0</td><td>59.9</td></tr>
<tr><td>24.5</td><td>99.8</td><td>23.3</td><td>59.9</td></tr>
<tr><td>24.6</td><td>81.8</td><td>23.4</td><td>41.0</td></tr>
<tr><td>25.7</td><td>81.7</td><td>24.8</td><td>40.8</td></tr>
<tr><td>25.8</td><td>0.0</td><td>24.9</td><td>0.0</td></tr>
<tr><td>70.0</td><td>0.0</td><td>70.0</td><td>0.0</td></tr>
</table></td></tr>
<tr><td>Yield point:</td><td colspan="2">1.30 mm</td><td colspan="2">43.8 kN</td><td colspan="2">2.50 mm</td><td colspan="2">84.1 kN</td><td colspan="2">3.50 mm</td><td colspan="2">121.5 kN</td></tr>
<tr><td>R_{max}:</td><td colspan="2">21.8 mm</td><td colspan="2">105.9 kN</td><td colspan="2">12.5 mm</td><td colspan="2">157.4 kN</td><td colspan="2">12.9 mm</td><td colspan="2">192.8 kN</td></tr>
<tr><td>Collapse:</td><td colspan="2">21.8 mm</td><td colspan="2">105.9 kN</td><td colspan="2">12.5 mm</td><td colspan="2">157.4 kN</td><td colspan="2">23.3 mm</td><td colspan="2">120.9 kN</td></tr>
<tr><td>Failure mode (mode+):</td><td colspan="4">Bending in P1 (base), then in order: P1 (top), P2 (base and top), P3 and P4 (base and top and later diagonal cracking in P3. Failure of P2 (base), then in order: failure of P2 (top), P1 (base), P1 (top) and finally, failure of P3 (base + top + diag. cracking).</td><td colspan="4">Bending (B) in P1 (base), then in order: P1 (top), diagonal cracking (DC) in P2 and S1, B in P2 and P3 (base) and DC in S2 and P3. Failure of most of the hinges at the left of P2 with bending failure of P2 (base). Then bending failure of P2 (top) and later P3 (base and top).</td><td colspan="4">Bending (B) in P1 (base), then in order: diagonal cracking (DC) in S1 and P2, B in P1 (top), B in P3 (base and top). DC failure of P2, then activation of DC hinge in P3 and later B failure of P1 (base), followed by P1 (top). Lastly, contemporary B and DC failure of P3 (all).</td></tr>
</table>

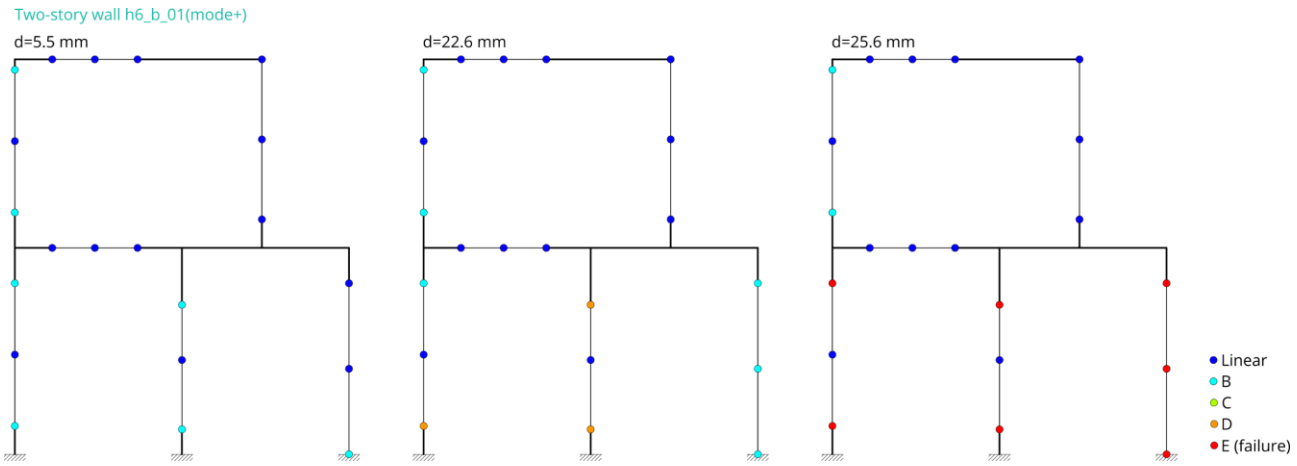


Figure 0.14 Failure mechanism of two-story wall h6_b_01 (mode+)

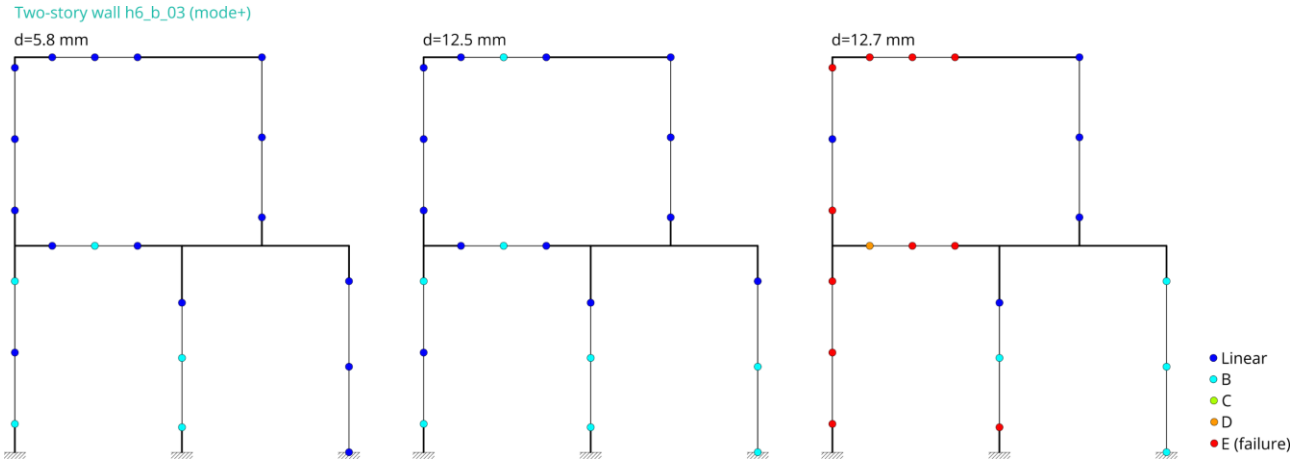


Figure 0.15 Failure mechanism of two-story wall h6_b_03 (mode+)

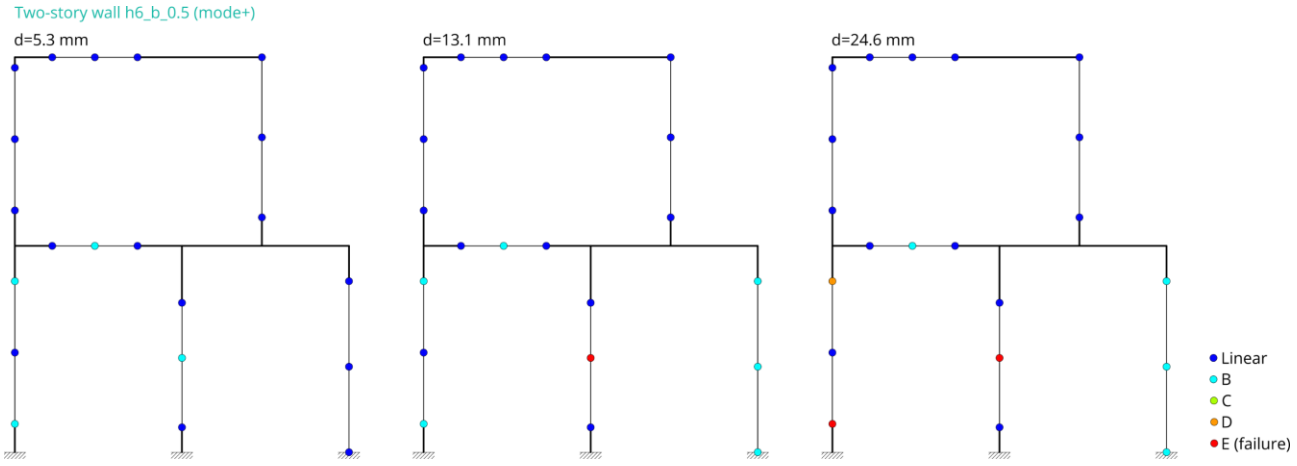
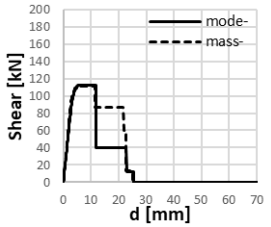
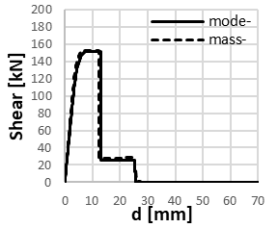
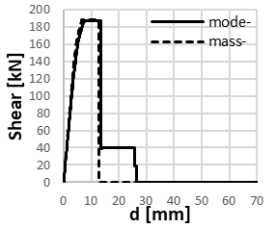


Figure 0.16 Failure mechanism of two-story wall h6_b_05 (mode+)

ID:	Two-storywall_h6_b_01 (-)	Two-storywall_h6_b_03 (-)	Two-storywall_h6_b_05 (-)

<table>
<tr><td>Axial stress:</td><td colspan="4">0.1 MPa</td><td colspan="4">0.3 MPa</td><td colspan="4">0.5 MPa</td></tr>
<tr><td>Capacity curve:</td><td colspan="4"> 
</td><td colspan="4"> 
</td><td colspan="4"> 
</td></tr>
<tr><td></td><td colspan="2">mode</td><td colspan="2">mass</td><td colspan="2">mode</td><td colspan="2">mass</td><td colspan="2">mode</td><td colspan="2">mass</td></tr>
<tr><td></td><td>d [mm]</td><td>F [kN]</td><td>d [mm]</td><td>F [kN]</td><td>d [mm]</td><td>F [kN]</td><td>d [mm]</td><td>F [kN]</td><td>d [mm]</td><td>F [kN]</td><td>d [mm]</td><td>F [kN]</td></tr>
<tr><td></td><td>0.00</td><td>0.0</td><td>0.00</td><td>0.0</td><td>0.00</td><td>0.0</td><td>0.00</td><td>0.0</td><td>0.00</td><td>0.0</td><td>0.00</td><td>0.0</td></tr>
<tr><td></td><td>1.80</td><td>58.8</td><td>1.70</td><td>61.9</td><td>3.30</td><td>107.8</td><td>3.30</td><td>120.0</td><td>3.70</td><td>125.5</td><td>3.7</td><td>138.3</td></tr>
<tr><td></td><td>3.90</td><td>105.4</td><td>3.40</td><td>103.9</td><td>3.70</td><td>117.5</td><td>3.60</td><td>127.8</td><td>5.00</td><td>158.7</td><td>4.4</td><td>157.4</td></tr>
<tr><td></td><td>5.00</td><td>111.6</td><td>4.60</td><td>110.8</td><td>4.40</td><td>132.3</td><td>3.80</td><td>132.2</td><td>5.40</td><td>166.0</td><td>4.9</td><td>167.0</td></tr>
<tr><td></td><td>5.30</td><td>112.6</td><td>11.4</td><td>110.8</td><td>4.50</td><td>133.4</td><td>4.00</td><td>134.9</td><td>5.50</td><td>167.1</td><td>5.3</td><td>173.2</td></tr>
<tr><td></td><td>11.8</td><td>112.6</td><td>11.5</td><td>86.6</td><td>4.70</td><td>135.5</td><td>4.30</td><td>138.4</td><td>6.70</td><td>181.0</td><td>6.4</td><td>186.8</td></tr>
<tr><td></td><td>11.9</td><td>39.8</td><td>21.7</td><td>86.6</td><td>6.00</td><td>147.5</td><td>5.40</td><td>149.3</td><td>6.80</td><td>181.8</td><td>6.5</td><td>187.6</td></tr>
<tr><td></td><td>22.6</td><td>39.9</td><td>21.8</td><td>59.8</td><td>6.30</td><td>148.6</td><td>6.00</td><td>151.7</td><td>7.40</td><td>186.5</td><td>6.6</td><td>188.5</td></tr>
<tr><td></td><td>22.9</td><td>12.7</td><td>22.6</td><td>59.8</td><td>7.50</td><td>151.9</td><td>6.30</td><td>152.4</td><td>13.4</td><td>187.3</td><td>12.8</td><td>188.6</td></tr>
<tr><td></td><td>25.3</td><td>12.4</td><td>22.7</td><td>13.6</td><td>12.9</td><td>152.0</td><td>12.4</td><td>152.5</td><td>13.5</td><td>38.6</td><td>12.9</td><td>0.0</td></tr>
<tr><td></td><td>25.4</td><td>5.7</td><td>24.9</td><td>13.6</td><td>13.0</td><td>25.7</td><td>12.5</td><td>27.6</td><td>25.7</td><td>40.4</td><td>70.0</td><td>0.0</td></tr>
<tr><td></td><td>25.5</td><td>0.1</td><td>25.0</td><td>6.2</td><td>25.3</td><td>25.7</td><td>25.3</td><td>28.2</td><td>25.8</td><td>18.6</td><td></td><td></td></tr>
<tr><td></td><td>27.5</td><td>0.0</td><td>25.1</td><td>6.2</td><td>25.4</td><td>11.5</td><td>25.4</td><td>13.1</td><td>26.3</td><td>18.8</td><td></td><td></td></tr>
<tr><td></td><td>70.0</td><td>0.0</td><td>25.2</td><td>0.1</td><td>25.6</td><td>11.6</td><td>25.7</td><td>13.2</td><td>26.4</td><td>0.0</td><td></td><td></td></tr>
<tr><td></td><td></td><td></td><td>70.0</td><td>0.0</td><td>25.7</td><td>0.0</td><td>25.8</td><td>0.0</td><td>70.0</td><td>0.0</td><td></td><td></td></tr>
<tr><td></td><td></td><td></td><td></td><td></td><td>70</td><td>0.0</td><td>70.0</td><td>0.0</td><td></td><td></td><td></td><td></td></tr>
<tr><td>Yield point:</td><td colspan="4">1.80 mm 58.8 kN</td><td colspan="4">3.30 mm 107.8 kN</td><td colspan="4">3.70 mm 125.5 kN</td></tr>
<tr><td>R_{max}:</td><td colspan="4">11.8 mm 112.6 kN</td><td colspan="4">12.9 mm 152.0 kN</td><td colspan="4">13.4 mm 187.3 kN</td></tr>
<tr><td>Collapse:</td><td colspan="4">11.8 mm 112.6 kN</td><td colspan="4">12.9 mm 152.0 kN</td><td colspan="4">13.4 mm 187.3 kN</td></tr>
<tr><td>Failure mode (mode-):</td><td colspan="4">Bending in P3 (base), then in order: bending in P3 (top), P2 (base), diagonal cracking in P2, bending in P1 (base and top), diagonal cracking in S1 and diagonal cracking in P1. Failure of most of the hinges at the left of P2 with bending failure of P2 (base). Then bending failure of P3 (base and top).</td><td colspan="4">Diagonal cracking (DC) in S1, then in order: bending (B) in P3 (base), DC in P2, B in P3 (top), DC in S2, B in P1 (base) and DC in P1. Contemporary DC failure of P1 and P2 and finally bending failure of P3 (base and top).</td><td colspan="4">Diagonal cracking (DC) in S1, then in order: DC in P2 and S2, bending in P3 (base and top), and lastly DC in P1. Contemporary DC failure of P1 and P2 and finally bending failure of P3 (base and top).</td></tr>
</table>

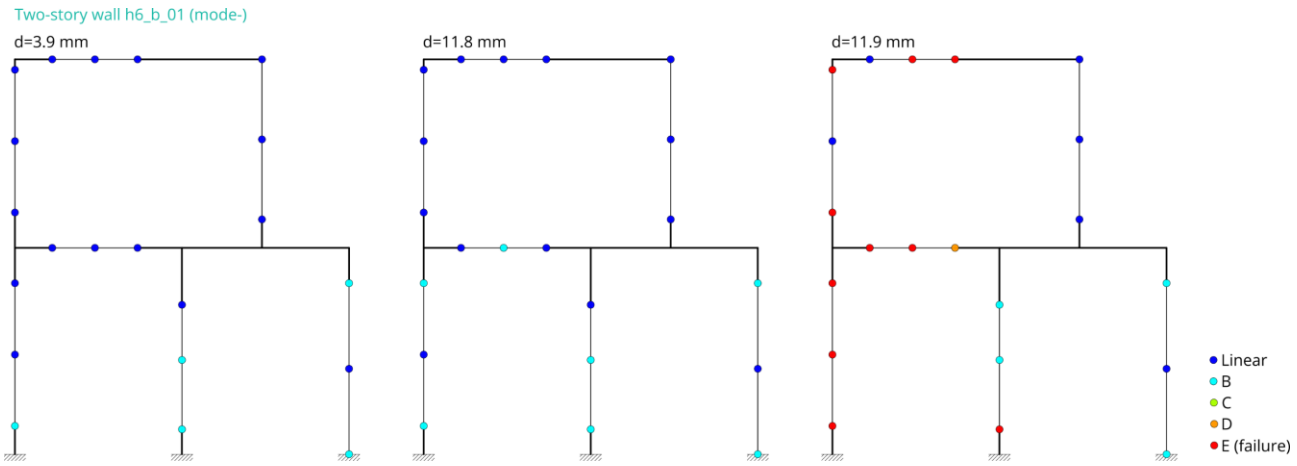


Figure 0.17 Failure mechanism of two-story wall h6_b_01 (mode-)

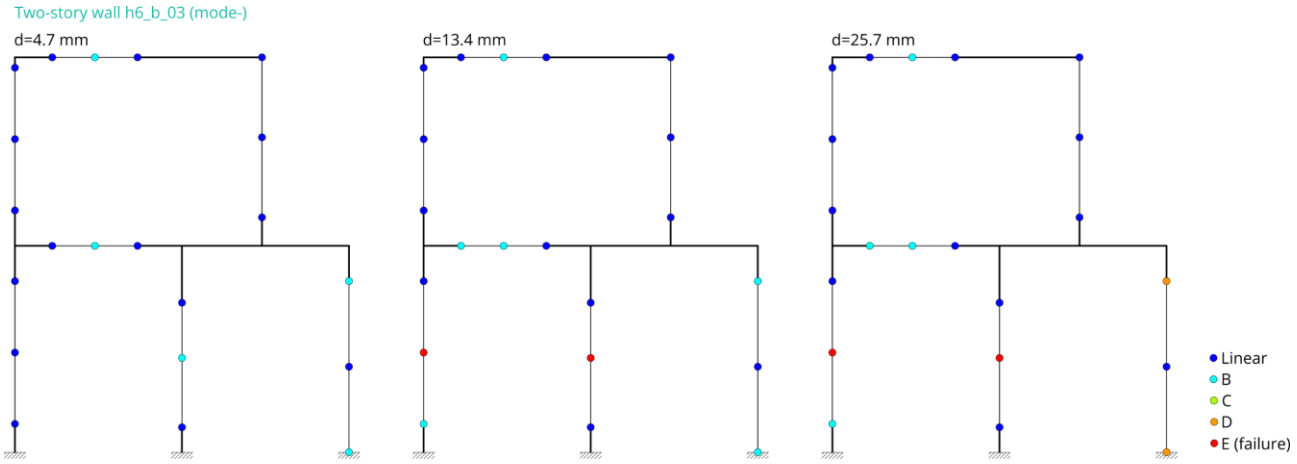


Figure 0.18 Failure mechanism of two-story wall h6_b_03 (mode-)

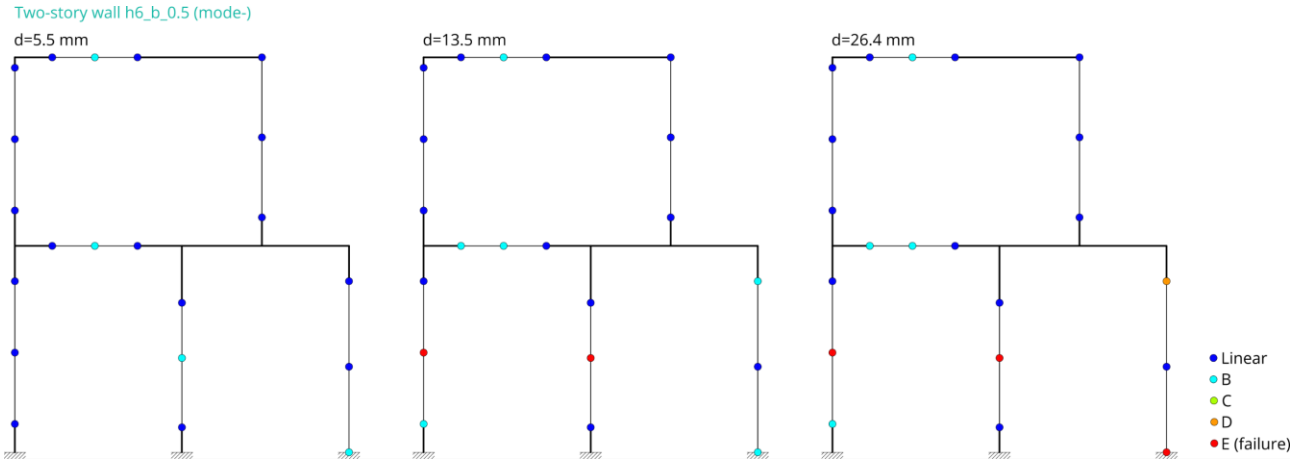
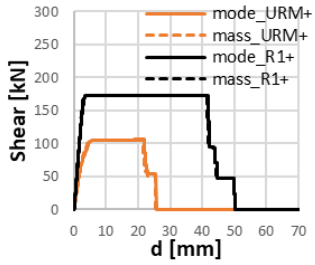
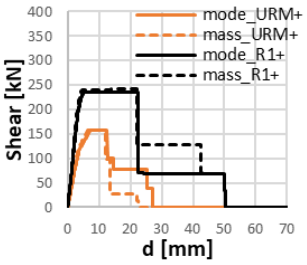
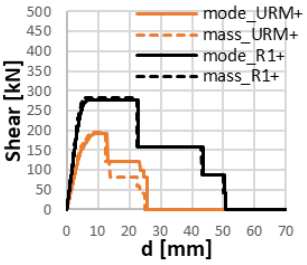


Figure 0.19 Failure mechanism of two-story wall h6_b_05 (mode-)

- **Two-story wall h6_b_R1**

ID:	Two-storywall_h6_b_01_R1 (+)	Two-storywall_h6_b_03_R1 (+)	Two-storywall_h6_b_05_R1 (+)
σ:	0.1 MPa	0.3 MPa	0.5 MPa
Capacity curve:			
Yield point:	2.30 mm 138.1 kN	3.20 mm 191.8 kN	3.20 mm 216.5 kN
R_{max}:	41.9 mm 172.9 kN	22.4 mm 235.9 kN	22.9 mm 278.1 kN
Collapse:	44.1 mm 93.7 kN	22.4 mm 235.9 kN	43.5 mm 157.7 kN
Failure mode (mode+):	Bending (B) in P1 and P2 (base). Then, in order: B in P3 (base), B in P2 (top), B in P1 (top), diagonal cracking (DC) in S1 and lastly B in P3 (top). Bending failure of P2 (base then top), later failure of P1 (base and top) and finally failure of P3 (base and top).	Bending (B) in P1 and diagonal cracking (DC) in S1. Then, in order: B in P2 (base), B in P3 (base) and lastly DC in P1 and P2. Diagonal cracking failure of P1 and P2, then bending failure of P3 (base and top).	Diagonal cracking (DC) in S1. Then, in order: bending (B) in P1 (base), B in P2 (base), B in S2 (right), B in P3 (base), DC in P2, B in S1 and S2 (left), DC in P1 and lastly B in P3 (top). Contemporary DC failure of P1 and B failure of P2 (base) and activation of B in P2 (top). Then failure of P2 (top) and lastly of P3 (base and top).

mode

d [mm]	F [kN]
0.00	0.0
2.30	138.1
2.80	157.3
3.20	169.0
3.35	171.6
3.45	172.4
3.50	172.8
41.9	172.9
41.9	93.7
44.1	93.7
44.1	46.6
49.9	46.6
50.0	0.0

mass

d [mm]	F [kN]
0.00	0.0
2.15	140.7
2.15	140.7
2.60	159.2
2.90	168.7
3.10	171.9
3.20	172.8
41.6	172.9
41.7	93.7
43.9	93.7
44.0	46.6
49.8	46.6
49.9	0.0

mode

d [mm]	F [kN]
0.00	0.0
3.20	191.8
3.35	197.5
4.15	220.2
4.65	230.4
5.30	235.7
22.4	235.9
22.4	69.5
50.0	69.5
50.1	0.0

mass

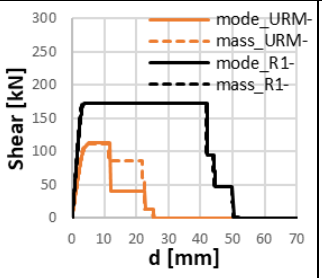
d [mm]	F [kN]
0.00	0.0
2.95	193.9
3.10	202.1
3.25	208.2
3.85	226.3
4.30	236.3
4.35	236.7
4.85	240.8
22.0	241.0
22.1	127.2
42.4	127.2
42.4	69.5
50.0	69.5
50.0	0.0

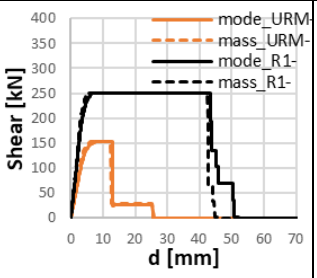
mode

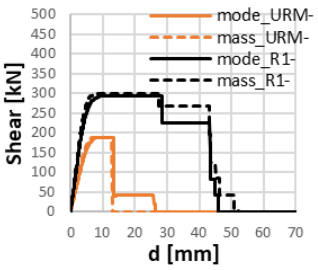
d [mm]	F [kN]
0.00	0.0
3.20	192.4
4.10	232.4
4.25	238.0
5.00	259.4
5.20	264.3
5.25	265.1
5.70	270.3
5.90	272.3
6.65	277.9
22.9	278.1
23.0	157.6
43.5	157.7
43.5	86.9

mass

d [mm]	F [kN]
0.00	0.0
3.30	216.5
3.75	238.1
3.90	244.5
4.80	271.7
4.85	272.8
5.10	276.1
5.95	283.0
22.4	283.2
22.5	157.7
43.0	157.7
43.1	86.9
50.1	86.2
50.1	0.0

<table>
<tr><td>ID:</td><td>Two-storywall_h6_b_01_R1 (-)</td><td>Two-storywall_h6_b_03_R1 (-)</td><td>Two-storywall_h6_b_05_R1 (-)</td></tr>
<tr><td>Axial stress:</td><td>0.1 MPa</td><td>0.3 MPa</td><td>0.5 MPa</td></tr>
<tr><td>Capacity curve:</td><td> 



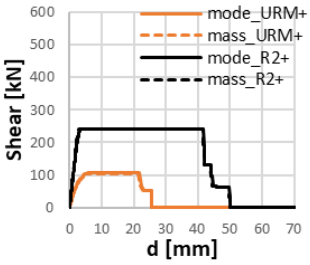
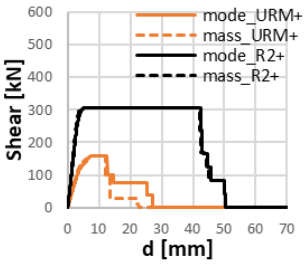
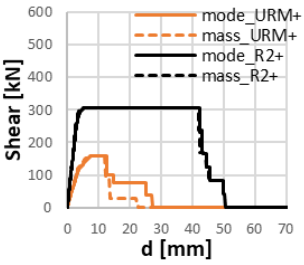

</td><td></td><td></td></tr>
<tr><td>Yield point:</td><td>2.40 mm 139.8 kN</td><td>3.10 mm 181.3 kN</td><td>3.10 mm 180.9 kN</td></tr>
<tr><td>R_{max}:</td><td>42.0 mm 172.9 kN</td><td>43.2 mm 250.6 kN</td><td>28.3 mm 293.4 kN</td></tr>
<tr><td>Collapse:</td><td>44.1 mm 96.7 kN</td><td>43.2 mm 250.6 kN</td><td>43.3 mm 224.5 kN</td></tr>
<tr><td>Failure mode (mode+):</td><td>Bending (B) in P1 and P2 (base). Then, in order: B in P3 (base), B in P2 (top), B in P1 (top), diagonal cracking (DC) in S1 and lastly B in P3 (top). Bending failure of P2 (base then top), later failure of P1 (base and top) and finally failure of P3 (base and top).</td><td>Diagonal cracking (DC) in S1, then in order: bending (B) in P1 (base), B in P2 (base), B in S2 (right), B in P3 (base), B in P2 (top), B in S2 (left), B in S1 (left) and lastly B in P1 and P3 (top). Failure of P2 (base then top), then failure of P1 (base and top) and lastly failure of P3 (base and top).</td><td>Diagonal cracking (DC) in S1, then in order: bending (B) in S2 (right), B in S2 (left) and P2 (base), B in P1 (base), B in S1 (left), DC in P3, B in P2 (top), and lastly B in P1 (top). DC failure of P3, then B failure of P2 (base) and lastly failure of P1 (base and top).</td></tr>
</table>

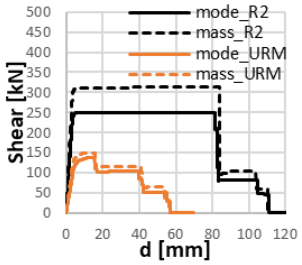
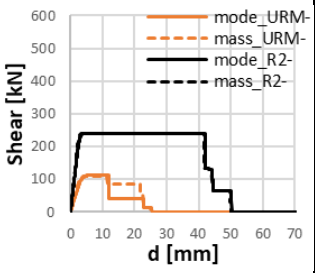
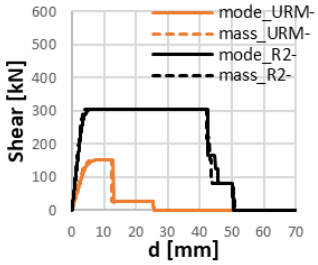
mode		*mass*	
d [mm]	*F* [kN]	*d* [mm]	*F* [kN]
0.00	0.0	0.00	0.0
2.40	139.8	2.15	140.4
3.05	164.3	2.20	142.6
3.10	165.6	2.75	165.3
3.30	168.8	2.80	166.3
3.40	169.7	2.95	168.8
3.80	172.8	3.40	172.8
42.0	172.9	41.7	172.9
42.0	93.7	41.7	93.7
44.1	93.7	44.0	93.7
44.2	46.6	44.0	46.6
50.0	46.6	49.9	46.6
50.0	0.0	49.9	0.0

mode		*mass*	
d [mm]	*F* [kN]	*d* [mm]	*F* [kN]
0.00	0.0	0.00	0.0
3.10	181.3	3.05	199.2
3.50	198.2	3.10	202.0
4.30	220.7	3.15	204.0
4.70	231.0	4.25	237.1
5.20	238.4	4.25	237.1
6.50	250.4	4.85	245.1
43.2	250.6	4.95	246.2
43.3	69.5	5.30	249.2
50.3	69.5	5.50	250.4
50.4	0.0	42.5	250.6
		42.5	65.7
		44.1	65.7
		44.1	0.0

mode		*mass*	
d [mm]	*F* [kN]	*d* [mm]	*F* [kN]
0.00	0.0	0.00	0.0
3.10	180.9	3.10	202.1
4.00	220.0	4.05	247.2
4.50	239.5	4.35	256.3
4.55	240.6	4.70	266.1
4.90	248.7	5.35	284.0
6.00	273.2	5.50	287.6
6.55	281.0	5.70	289.8
9.05	293.2	7.55	298.9
28.3	293.4	27.5	299.0
28.3	224.5	27.5	267.4
43.3	224.5	43.1	267.5
43.4	40.7	43.5	43.1
46.0	40.7	50.8	43.1
46.0	0.0	50.9	0.0

- **Two-story wall h6_b_R2**

ID:	Two-storywall_h6_b_01_R2 (+)				Two-storywall_h6_b_03_R2 (+)				Two-storywall_h6_b_05_R2 (+)			
σ:	0.1 MPa				0.3 MPa				0.5 MPa			
Capacity curve:												
	mode		*mass*		*mode*		*mass*		*mode*		*mass*	
	d [mm]	*F* [kN]	*d* [mm]	*F* [kN]	*d* [mm]	*F* [kN]	*d* [mm]	*F* [kN]	*d* [mm]	*F* [kN]	*d* [mm]	*F* [kN]
	0.00	0.0	0.00	0.0	0.00	0.0	0.00	0.0	0.00	0.0	0.00	0.0
	2.20	189.7	2.05	193.6	2.80	241.4	2.60	245.6	3.05	262.8	3.00	283.3
	2.30	196.2	2.15	200.4	3.00	252.7	2.65	249.0	3.25	278.5	3.05	286.9
	2.65	215.6	2.45	218.2	3.55	278.4	3.05	272.7	3.30	281.5	3.60	314.7
	3.00	230.7	2.80	233.9	4.15	295.4	3.15	277.7	3.40	286.4	4.60	345.1
	3.10	233.7	3.00	239.1	4.20	296.2	3.60	296.1	3.90	306.2	4.70	346.5
	3.35	238.5	3.05	239.7	4.45	299.7	3.70	298.7	4.10	311.9	4.95	348.4
	3.50	239.7	3.05	239.7	5.30	305.8	3.95	302.7	4.30	317.1	5.85	354.8
	41.8	239.9	41.6	239.9	5.30	305.8	4.40	305.8	5.20	338.7	9.55	354.9
	41.9	130.7	41.7	130.7	42.4	306.0	42.0	306.0	5.40	341.3	31.7	355.1
	44.1	130.7	43.9	130.7	42.5	165.9	42.1	165.9	6.95	352.1	31.7	218.9
	44.1	63.5	44.0	63.5	44.6	165.9	44.3	165.9	22.8	352.4	44.8	220.4
	49.9	63.5	49.8	63.5	44.6	82.8	44.3	82.8	22.8	96.3	44.9	96.3
	49.9	0.0	49.9	0.0	50.0	82.8	49.9	82.8	50.1	96.3	50.3	96.3
Yield point:	2.20 mm		189.7 kN		2.80 mm		241.4 kN		3.05 mm		262.8 kN	
R_{max}:	41.8 mm		239.9 kN		42.4 mm		306.0 kN		22.8 mm		352.4 kN	
Collapse:	44.1 mm		130.7 kN		44.6 mm		165.9 kN		22.8 mm		352.4 kN	
Failure mode (mode+):	Bending (B) in P2 (base), then in order: B in P1 (base), B in P3 (base), B in S1 (left), B in P2 (top), B in P3 (top) and lastly B in P1 (top). B failure of P2 (base then top), later failure of P1 (base and top) and lastly failure of P3 (base and top).				Bending (B) in P1 (base), then in order: B in P2 (base), B in S1 (left), B in P3 (base), B in S1 (right), B in P2 (top), B in S2 (right), B in P3 (top), B in P1 (top) and lastly B in S2 (left). B failure of P2 (base then top), later failure of P1 (base and top) and lastly failure of P3 (base and top).					Bending (B) in S1 (left), then in order: B in P1 (base), B in P2 (base), B in S1 (right), B in P3 (base), B in S2 (right), B in S2 (left), diagonal cracking (DC) in P2, B in P3 (top), and lastly DC in P1. B failure of P2 (base), DC failure of P1 and activation of B in P2 (top) later failure of P2 (top) and lastly failure of P3 (base and top).			

ID:	Two-storywall_h6_b_01_R2 (-)	Two-storywall_h6_b_03_R2 (-)	Two-storywall_h6_b_05_R2 (-)
Axial stress:	0.1 MPa	0.3 MPa	0.5 MPa
Capacity curve:			
	mode: d [mm] / F [kN] 0.00 / 0.0 2.30 / 192.2 2.35 / 195.5 2.90 / 225.2 3.00 / 228.7 3.50 / 238.0 3.65 / 239.7 41.9 / 239.9 42.0 / 130.7 44.2 / 130.7 44.2 / 63.5 50.0 / 63.5 50.0 / 0.0	*mass*: d [mm] / F [kN] 0.00 / 0.0 2.05 / 192.5 2.15 / 199.6 2.65 / 228.6 2.95 / 235.8 3.05 / 237.1 3.30 / 239.7 41.6 / 239.9 41.7 / 130.7 44.0 / 130.7 44.0 / 63.5 49.9 / 63.5 49.9 / 0.0	*mode*: d [mm] / F [kN] 0.00 / 0.0 2.80 / 234.5 2.90 / 242.0 3.00 / 247.7 3.45 / 270.3 3.70 / 282.4 3.75 / 283.9 3.80 / 285.2 3.85 / 285.9 5.15 / 304.1 5.40 / 305.8 42.6 / 306.0 42.7 / 165.9 44.8 / 165.9 44.8 / 82.8 50.2 / 82.8 50.2 / 0.0	*mass*: d [mm] / F [kN] 0.00 / 0.0 2.65 / 248.5 2.70 / 251.6 2.70 / 251.6 3.30 / 284.1 3.45 / 289.5 4.00 / 300.3 4.25 / 304.3 4.40 / 305.8 42.0 / 306.0 42.1 / 82.8 50.5 / 82.8 50.6 / 0.0	*mode*: d [mm] / F [kN] 0.00 / 0.0 2.70 / 226.2 3.15 / 260.5 3.40 / 278.5 3.45 / 281.3 3.60 / 289.4 3.65 / 291.0 4.65 / 323.1 4.70 / 324.3 6.45 / 349.1 7.30 / 354.9 43.4 / 355.2 43.4 / 96.3 50.4 / 96.3 50.5 / 0.0	*mass*: d [mm] / F [kN] 0.00 / 0.0 2.60 / 244.2 3.10 / 286.0 3.20 / 292.4 3.65 / 316.4 3.80 / 322.1 4.10 / 331.2 4.75 / 341.4 5.50 / 352.3 5.85 / 354.9 42.6 / 355.2 42.6 / 192.5 44.8 / 192.5 44.9 / 96.3 50.2 / 96.3 50.3 / 0.0
Yield point:	2.30 mm 192.2 kN	2.80 mm 234.5 kN	2.70 mm 226.2 kN
R_{max}::	41.9 mm 239.9 kN	42.6 mm 306.0 kN	43.4 mm 355.2 kN
Collapse:	44.2 mm 130.7 kN	44.8 mm 165.9 kN	43.4 mm 355.2 kN
Failure mode (mode+):	Bending (B) in P2 (base), then in order: B in P1 (base), B in P3 (base), B in S1 (left), B in P2 (top), B in P1 (top) and lastly B in P3 (top). B failure of P2 (base then top), later failure of P1 (base and top) and lastly failure of P3 (base and top).	Bending (B) in S1 (left), then in order: B in P2 (base), B in P1 (base), B in S2 (right), B in S1 (right), B in P2 (top), B in P3 (base), B in S2 (left), B in P3 (top) and lastly B in P1 (top). B failure of P2 (base and top), later failure of P1 (base and top) and lastly failure of P3 (base and top).	Bending (B) in S1 (left), then in order: B in S2 (right), B in P2, B in S2 (left), B in P1 (base), B in S1 (right), B in P2 (top), B in P3 (base), B in P3 (top), and lastly B in P1 (top). B failure of P2 (base and top), later failure of P1 (base and top) and lastly failure of P3 (base and top).